ADVANCES IN CHEMICAL PHYSICS VOL. 130 PART A
STUART A. RICE, Series Editor

Edited by
MIKITO TODA, TAMIKI KOMATSUZAKI,
TETSURO KONISHI, R. STEPHEN BERRY

GEOMETRIC STRUCTURES OF PHASE SPACE IN MULTI-DIMENSIONAL CHAOS

APPLICATIONS TO CHEMICAL REACTION DYNAMICS IN COMPLEX SYSTEMS

Part A

GEOMETRIC STRUCTURES OF PHASE SPACE IN MULTIDIMENSIONAL CHAOS

A SPECIAL VOLUME OF ADVANCES IN CHEMICAL PHYSICS
VOLUME 130

PART A

GEOMETRIC STRUCTURES OF PHASE SPACE IN MULTIDIMENSIONAL CHAOS

APPLICATIONS TO CHEMICAL REACTION DYNAMICS IN COMPLEX SYSTEMS

ADVANCES IN CHEMICAL PHYSICS
VOLUME 130

PART A

Edited by

**M. TODA, T. KOMATSUZAKI, T. KONISHI,
R. S. BERRY, and S. A. RICE**

Series Editor

STUART A. RICE

Department of Chemistry
and
The James Franck Institute
The University of Chicago
Chicago, Illinois

AN INTERSCIENCE PUBLICATION
JOHN WILEY & SONS, INC.

Published by John Wiley & Sons, Inc., Hoboken, New Jersey.
Published simultaneously in Canada.

Library of Congress Catalog Number: 58:9935

ISBN 0-471-70527-6 (Part A)
ISBN 0-471-71157-8 (Part B)
ISBN 0-471-71158-6 (Set)

Printed in the United States of America

10 9 8 7 6 5 4 3 2 1

CONTRIBUTORS TO VOLUME 130

YOJI AIZAWA, Department of Applied Physics, Faculty of Science and Engineering, Waseda University, Tokyo, 169-8555, Japan

R. STEPHEN BERRY, Department of Chemistry, The University of Chicago, Chicago, Illinois 60637, USA

JENS BREDENBECK, Max-Planck-Institüt für Strömungsforschung, D-37073 Göttingen, Germany. *Present address*: Physikalisch-Chemisches Institüt, Universität Zürich, CH-8057 Zürich, Switzerland

LINTAO BU, Department of Chemistry, Boston University, Boston, Massachusetts, 02215, USA

MASSIMO CENCINI, Dipartimento di Fisica, Università di Roma ''la Sapienza'' and Center for Statistical Mechanics and Complexity INFM UdR Roma 1 Piazzale Aldo Moro 5, I-00185 Roma, Italy

STAVROS C. FARANTOS, Institute of Electronic Structure and Laser Foundation for Research and Technology, Hellas, Greece; and Department of Chemistry, University of Crete, Iraklion 711 10, Crete, Greece

HIROSHI FUJISAKI, Department of Chemistry, Boston University, Boston, Massachusetts, 02215, USA

JIANGBIN GONG, Department of Chemistry and The James Franck Institute, The University of Chicago, Chicago, Illinois 60637 USA

SERGY YU. GREBENSHCHIKOV, Max-Planck-Institüt für Strömungsforschung, D-37073 Göttingen, Germany

HIROSHI H. HASEGAWA, Department of Mathematical Sciences, Ibaraki University, Mito, 310-8512, Japan; and Center for Studies in Statistical Mechanics and Complex Systems, The University of Texas at Austin, Austin, Texas 78712, USA

SEIICHIRO HONJO, Department of Basic Science, Graduate School of Arts and Sciences, University of Tokyo, Komaba, Meguro-ku, Tokyo, 153-8902, Japan

KYOKO HOSHINO, Nonlinear Science Laboratory, Department of Earth and Planetary Sciences, Faculty of Science, Kobe University, Nada, Kobe, 657-8501, Japan

KENSUKE S. IKEDA, Department of Physical Sciences, Faculty of Science and Engineering, Ritsumeikan University, Kusatsu, 525-8577, Japan

CHARLES JAFFÉ, Department of Chemistry, West Virginia University, Morgantown, West Virginia 26506-6045, USA

MARC JOYEUX, Laboratoire de Spectrométrie Physique (CNRS UMR 5588), Université Joseph Fourier, Grenoble 1, F-38402 St. Martin d'Hères Cedex, France

KUNIHIKO KANEKO, Department of Basic Science, College of Arts and Sciences, University of Tokyo, Komaba, Meguro-ku, Tokyo, 153-8902, Japan

SHINNOSUKE KAWAI, Department of Chemistry, Graduate School of Science, Kyoto University, Kyoto, 606-8502, Japan

TAIZO KOBAYASHI, Department of Physical Sciences, Ritsumeikan University, Kusatsu, 525-8577, Japan

TAMIKI KOMATSUZAKI, Nonlinear Science Laboratory, Department of Earth and Planetary Sciences, Faculty of Science, Kobe University, Nada, Kobe, 657-8501, Japan

TETSURO KONISHI, Department of Physics, Nagoya University, Nagoya, 464-8602, Japan

DAVID M. LEITNER, Department of Chemistry and Chemical Physics Program, University of Nevada, Reno, Nevada 89557, USA

YASUHIRO MATSUNAGA, Nonlinear Science Laboratory, Department of Earth and Planetary Sciences, Faculty of Science, Kobe University, Nada, Kobe, 657-8501, Japan

TAKAYUKI MIYADERA, Department of Information Sciences, Tokyo University of Science, Noda City, 278-8510, Japan

TERUAKI OKUSHIMA, Department of Physics, Tokyo Metropolitan University, Minami-Ohsawa, Hachioji, Tokyo, 192-0397, Japan

YOSHIKAZU OHTAKI, Department of Mathematical Sciences, Ibaraki University, Mito, 310-8512, Japan

YOSHITSUGU OONO, Department of Physics, University of Illinois at Urbana-Champaign, Urbana, Illinois, 61801-3080, USA

JESÚS PALACIÁN, Departamento de Matemática e Informática, Universidad Pública de Navarra, 31006 Pamplona, Spain

STUART A. RICE, Department of Chemistry and The James Franck Institute, The University of Chicago, Chicago, Illinois 60637 USA

SHINJI SAITO, Department of Chemistry, Nagoya University, Furo-cho, Chikusa-ku, Nagoya, 464-8602, Japan

MITSUSADA M. SANO, Graduate School of Human and Environmental Studies, Kyoto University, Sakyo, Kyoto, 606-8501, Japan

SHIN'ICHI SAWADA, School of Science and Technology, Kwansei Gakuin University, Sanda, 669-1337, Japan

REINHARD SCHINKE, Max-Planck-Institüt für Strömungsforschung, D-37073 Göttingen, Germany

NORIHIRO SHIDA, Omohi College, Graduate School of Engineering, Nagoya Institute of Technology, Gokiso-cho, Showa-ku, Nagoya, 466-8555, Japan

YASUSHI SHIMIZU, Department of Physical Sciences, Ritsumeikan University, Kusatsu, 525-8577, Japan

AKIRA SHUDO, Department of Physics, Tokyo Metropolitan University, Minami-Ohsawa, Hachioji, Tokyo, 192-0397, Japan

JOHN E. STRAUB, Department of Chemistry, Boston University, Boston, Massachusetts, 02215, USA

Y-H. TAGUCHI, Department of Physics, Faculty of Science and Technology, Chuo University, Bunkyo-ku, Tokyo, 112-8551, Japan; and Institute for Science and Technology, Chuo University, Bunkyo-ku, Tokyo, 112-8551, Japan

KIN'YA TAKAHASHI, The Physics Laboratories, Kyushu Institute of Technology, Iizuka, 820-8502, Japan

TOSHIYA TAKAMI, Institute for Molecular Science, Okazaki, 444-8585, Japan

KAZUO TAKATSUKA, Department of Basic Science, Graduate School of Arts and Sciences, University of Tokyo, Komaba, 153-8902, Tokyo, Japan

MIKITO TODA, Physics Department, Nara Women's University, Nara, 630-8506, Japan

TURGAY UZER, Center for Nonlinear Science, School of Physics, Georgia Institute of Technology, Atlanta, GA 30332-0430, USA

DAVIDE VERGNI, Istituto Applicazioni del Calcolo, CNR Viale del Policlinico 137, I-00161 Roma, Italy

ANGELO VULPIANI, Dipartimento di Fisica, Università di Roma ''la Sapienza'' and Center for Statistical Mechanics and Complexity INFM UdR Roma 1 Piazzale Aldo Moro 5, I-00185 Roma, Italy

LAURENT WIESENFELD, Laboratoire d'Astrophysique, Observatoire de Grenoble, Université Joseph-Fourier, BP 53, F-38041 Grenoble Cédex 9, France

YOSHIYUKI Y. YAMAGUCHI, Department of Applied Mathematics and Physics, Kyoto University, 606-8501, Kyoto, Japan

TOMOHIRO YANAO, Department of Complex Systems Science, Graduate School of Information Science, Nagoya University, 464-8601, Nagoya, Japan

PATRICIA YANGUAS, Departamento de Matemática e Informática, Universidad Pública de Navarra, 31006 Pamplona, Spain

MEISHAN ZHAO, Department of Chemistry and The James Franck Institute, The University of Chicago, Chicago, Illinois, 60637 USA

INTRODUCTION

Few of us can any longer keep up with the flood of scientific literature, even in specialized subfields. Any attempt to do more and be broadly educated with respect to a large domain of science has the appearance of tilting at windmills. Yet the synthesis of ideas drawn from different subjects into new, powerful, general concepts is as valuable as ever, and the desire to remain educated persists in all scientists. This series, *Advances in Chemical Physics*, is devoted to helping the reader obtain general information about a wide variety of topics in chemical physics, a field that we interpret very broadly. Our intent is to have experts present comprehensive analyses of subjects of interest and to encourage the expression of individual points of view. We hope that this approach to the presentation of an overview of a subject will both stimulate new research and serve as a personalized learning text for beginners in a field.

STUART A. RICE

PREFACE

The study of chemical reactions covers a variety of phenomena, ranging from the microscopic mechanisms of reaction processes through structural changes involving macromolecules such as proteins, to biochemical networks within cells. One common question concerning these seemingly diverse phenomena is how we can understand the temporal development of the system based on its dynamics.

At the microscopic level, chemical reactions are dynamical phenomena in which nonlinear vibrational motions are strongly coupled with each other. Therefore, deterministic chaos in dynamical systems plays a crucial role in understanding chemical reactions. In particular, the dynamical origin of statistical behavior and the possibility of controlling reactions require analyses of chaotic behavior in multidimensional phase space.

In contrast, conventional reaction rate theory replaces the dynamics within the potential well by fluctuations at equilibrium. This replacement is made possible by the assumption of local equilibrium, in which the characteristic time scale of vibrational relaxation is supposed to be much shorter than that of reaction. Furthermore, it is supposed that the phase space within the potential well is uniformly covered by chaotic motions. Thus, only information concerning the saddle regions of the potential is taken into account in considering the reaction dynamics. This approach is called the transition state theory.

Recently, however, experimental studies have cast a doubt on this assumption (see Ref. 1 for a review). For example, spectroscopic studies reveal hierarchical structures in the spectra of vibrationally highly excited molecules [2]. Such structures in the spectra imply the existence of bottlenecks to intramolecular vibrational energy redistribution (IVR). Reactions involving radicals also exhibit bottlenecks to IVR [3]. Moreover, time-resolved measurements of highly excited molecules in the liquid phase show that some reactions take place before the molecules relax to equilibrium [4]. Therefore, the assumption that local equilibrium exists prior to reaction should be questioned. We seek understanding of reaction processes where the assumption does not hold.

The problem requires analyses of phase-space structures in systems with many degrees of freedom. In particular, appreciating the global structure of the phase space becomes essential for our understanding of reactions under nonequilibrium conditions. In order to make this point clear, we briefly summarize the present status of the study.

Since the 1980s, concepts and results from nonlinear physics have been incorporated into studies of unimolecular reactions. (For a review, see Rice and co-workers' contribution in this volume.) In particular, concepts established for systems with two degrees of freedom have played an important role in defining the reaction rate based on dynamics [5]. The concept of transition state has been examined from the standpoint of dynamical system theory, and reformulated in terms of normally hyperbolic invariant manifolds (NHIMs). While transition states in the conventional sense are situated in configuration space, NHIMs corresponding to saddles are structures in phase space. In order to formulate transition states as dividing surfaces, we have to resort to NHIMs and their stable and unstable manifolds. These phase space structures enable us to avoid the so-called recrossing problem. Moreover, Lie perturbation theory makes it possible to calculate the dividing surfaces at least locally near the NHIMs (see Ref. 6 for a review).

However, in systems with more than two degrees of freedom, the dividing surfaces do not generally exist globally in phase space [7,8]. Thus, the attempt to define the reaction rate based on dynamics has not been successful for systems with many degrees of freedom. Instead, global features of the phase space, such as the network of reaction paths, emerge as crucial ingredients in studying reactions from the dynamical point of view.

The reason why the dividing surfaces do not generally exist globally is because intersections between the stable and unstable manifolds of NHIMs sometimes involve tangency. This tangency reveals that branching structures exist in the network of reaction paths. Moreover, combining these branching structures with the Arnold web in the potential well, the global aspects of the phase space offer rich possibilities for nonergodic behavior for reactions in systems with many degrees of freedom. Implications of this possibility are to be sought in reactions under nonequilibrium conditions.

Thus, we shift our attention from quantities related to local equilibrium, notably reaction rate constants, to nonequilibrium aspects of reaction processes. In particular, we list the following three closely related questions as most important.

First, do dynamical correlations exist in processes involving multiple saddles, such as structural changes of macromolecules in clusters and proteins? In the conventional theory, it is supposed that consecutive processes of going over saddles take place independent of one another. In other words, the system loses its memory of the past immediately, since the vibrational relaxation within a well is assumed to be much faster than the escape from it and multistep processes are conventionally assumed to be Markov processes. To the contrary, when the characteristic time scale of IVR is comparable to that of the reaction, the system can keep dynamical correlations as it goes over successive saddles.

These correlations result in (a) acceleration of reactions for some initial conditions and (b) deceleration for others. This approach will shed new light on problems such as why reactions proceed on multibasin energy landscapes without being trapped in deep minima [9], why proteins fold so effectively, how enzymes help specific reactions to take place, and so on.

Second, how we can characterize nonequilibrium reactions using a dynamical viewpoint? Since the conventional concepts are not sufficient here, we need new ideas that relate measurable quantities to reaction dynamics. In particular, for reactions involving structural changes of macromolecules, collective variables will be necessary to describe processes, and the degrees of freedom that compose collective variables will change as the reaction proceeds over multiple saddles. Furthermore, dynamical correlations are likely to play important roles. Then, we need methods that answer the following questions: What degrees of freedom are necessary to describe reaction dynamics, in what way do they evolve and vary during the processes, and how we can extract information on their dynamics from measurements?

Third, what is the dynamical origin of Maxwell's demon? As is well known since the work of Maxwell, Szilard, and Brillouin, nonequilibrium conditions are necessary for systems to do information processing. Therefore, in studying biochemical reactions, we are interested in how nonequilibrium conditions are maintained at the molecular level. From the viewpoint of dynamics, in particular, the following problem stands out as crucial: Does any intrinsic mechanism of dynamics exist which helps to maintain nonequilibrium conditions in reaction processes? In other words, are there any reactions in which nonergodicity plays an essential role for systems to exhibit functional behavior?

Keeping these subjects in perspective, we organized a conference entitled ''Geometrical Structures of Phase Space in Multidimensional Chaos—Applications to Chemical Reaction Dynamics in Complex Systems'' from 26th October to 1st November, 2003, at the Yukawa Institute for Theoretical Physics, Kyoto University, Kyoto, Japan. A pre-conference was also held at Kobe University from 20th to 25th October.

This conference was interdisciplinary, where researchers from physics (including astrophysics), biophysics, physical chemistry, and nonlinear science gathered to discuss a wide range of problems in reaction dynamics with the common theme that chaos in dynamical systems plays a crucial role in studying chemical reactions. Furthermore, we argue that reactions involving macromolecules such as clusters, liquids, and proteins are important examples of dynamical systems with many degrees of freedom. Thus, we expect that studies of these reactions from a dynamics point of view will shed new light on phenomena such as phase transitions in clusters, slow relaxation in liquids, and

the efficiency of protein folding, as well as in seeking the possibility of manipulating these reactions.

In particular, in the Conference we focused our attention on the following topics.

1. Transition state theory revisited from the dynamical point of view, including a historical perspective of the study.
2. Phase-space structure of Hamiltonian systems with multiple degrees of freedom—in particular, normally hyperbolic invariant manifolds (NHIMs), intersections between their stable and unstable manifolds, and the Arnold web.
3. Analyses of reaction processes based on the phase space structure of the system.
4. Quantum aspects of chaos and how we can control them.
5. Nonstatistical properties, such as nonstationary behavior and multiple scales of time and distance for evolution, in systems of many degrees of freedom.
6. Dynamical understanding of reaction processes in macromolecules and liquids, such as phase transitions, fast alloying, energy redistribution, and structural changes in clusters and proteins.
7. Data mining to extract information on dynamics from time series data from experiments and simulations of molecular dynamics.
8. Dynamical insights into reactions at the macroscopic level, including chemical networks in cells and their evolution.

Here, in this volume, we have collected contributions from the invited speakers, from poster presentations that received the best poster awards (Yanao, Honjo, and Okushima), and from poster presentations chosen to cover topics that were not treated by the invited speakers. The best poster awards were decided based on a jury vote by the invited speakers and a popular vote by all the participants. Note, however, that there were many other posters that also deserved inclusion here.

In the following, we give a brief overview of the content of this volume. The volume consists of the following three parts:

I. Phase-space geometry of multidimensional dynamical systems and reaction processes.
II. Complex dynamical behavior in clusters and proteins, and data mining to extract information on dynamics.
III. New directions in multidimensional chaos and evolutionary reactions.

In the first part, our aim is to discuss how we can apply concepts drawn from dynamical systems theory to reaction processes, especially unimolecular reactions of few-body systems. In conventional reaction rate theory, dynamical aspects are replaced by equilibrium statistical concepts. However, from the standpoint of chaos, the applicability of statistical concepts itself is problematic. The contribution of Rice's group gives us detailed analyses of this problem from the standpoint of chaos, and it presents a new approach toward unimolecular reaction rate theory.

In statistical reaction rate theory, the concept of transition state plays a key role. Transition states are supposed to be the boundaries between reactants and products. However, the precise formulation of the transition state as a dividing surface is only possible when we consider ''transition states'' in phase space. This is the place where the concepts of normally hyperbolic invariant manifolds (NHIMs) and their stable and unstable manifolds come into play.

The contributions of Komatsuzaki and Berry, and of Uzer's group, discuss these manifolds, and they present their calculations using Lie perturbation theory methods. The contribution of Wiesenfeld discusses these manifolds in reaction processes involving angular momenta, and the contribution by Joyeux et al. shows applications of the perturbation theory method to reactions involving Fermi resonance. The contribution of Sano discusses invariant manifolds in the Coulomb three-body problem.

The importance of NHIMs, and their stable and unstable manifolds is shared strikingly between chemical reactions and astrophysics. Therefore in the conference at Kyoto, Koon, from Caltech, discussed controlling an orbiter in astrophysics, and Uzer presented his study of asteroids near Jupiter, where analyses of these manifolds were essential.

In reaction processes for which there is no local equilibrium within the potential well, global aspects of the phase space structure become crucial. This is the topic treated in the contribution of Toda. This work stresses the consequences of a variety of intersections between the stable and unstable manifolds of NHIMs in systems with many degrees of freedom. In particular, ''tangency'' of intersections is a feature newly recognized in the phase space structure. It is a manifestation of the multidimensionality of the system, where reaction paths form a network with branches.

Here, we also include the contributions related to quantum mechanics: The chapter by Takami et al. discusses control of quantum chaos using coarse-grained laser fields, and the contribution of Takahashi and Ikeda deals with tunneling phenomena involving chaos. Both discuss how chaos in classical behavior manifests itself in the quantum counterpart, and what role it will play in reaction dynamics.

In the second part, we collect contributions concerning dynamical processes in complex systems such as clusters and proteins. Here, we also include those ideas related to data mining, since this topic is an indispensable part of the studies on dynamics of macromolecules.

The contribution of Berry presents an overview of the study of clusters as vehicles for investigating complex systems. The study of clusters has given birth to a variety of new ideas which turned out to be fruitful in other complex systems such as proteins. The contribution of Takatsuka discusses dynamical and statistical aspects of phase transitions in clusters, and the contribution of Yanao and Takatsuka studies the gauge structure arising from the dynamics of floppy molecules. Shida's contribution presents an important issue related to saddles of index of two or more, and shows their role in the phase transitions of clusters. Another interesting phenomenon of clusters is fast alloying, discussed in the contribution of Shimizu et al. from the standpoint of reaction dynamics.

Liquids and proteins are complex systems for which the study of dynamical systems has wide applicability. In the conference, relaxation in liquids (ε-entropy by Douglas at the National Institute of Standards and Technology, nonlinear optics by Saito, and energy bottlenecks by Shudo and Saito), energy redistribution in proteins (Leitner and Straub et al.), structural changes in proteins (Kidera at Yokohama City University), and a new formulation of the Nosé-Hoover chain (Ezra at Cornell University) were discussed. Kidera's talk discussed time series analyses in molecular dynamics, and it is closely related to the problem of data mining. In the second part of the volume, we collect the contributions by Leitner and by Straub's group, and the one by Shudo and Saito in the third part.

The contribution by Komatsuzaki's group bridges the two research fields—that is, dynamics in complex systems and data mining. They apply to a model of proteins the methods of embedding and Allan variance, both of which have been developed in dynamical system theory. Their results reveal, using the Allan variance, nonstationary behavior in protein dynamics, and they show, by embedding, how many degrees of freedom are necessary to describe this dynamics. Thus, this contribution indicates a crucial role for the methods of data mining in the study of processes involving macromolecules.

Therefore, contributions to methods of data mining are included here. It is uncommon to discuss this topic in the context of reaction processes. However, as we have already discussed, data mining becomes ever more important in analyzing experiments and simulations. In conventional data analyses, the concepts of equilibrium statistical physics have been routinely applied. To the contrary, in situations in which local equilibrium breaks down, established methods do not exist to analyze experiments and simulations. Thus, data mining

to extract information on dynamics is crucial here. In the conference, several methods were discussed (Broomhead at Manchester University on embedding, Vulpiani on finite-size Lyapunov exponents, Taguchi on nonmetric methods, and Hasegawa on inductive thermodynamics approach from time series). Here we include the contributions by Taguchi and Oono and by Hasegawa and Ohtaki.

In the third part, those contributions are collected which discuss nonergodic and nonstationary behavior in systems with many degrees of freedom, and seek new possibilities to describe complex reactions, including even the evolution of living cells.

Conventional theory supposes that statistical ideas would be more applicable to systems of many degrees of freedom than to few-body systems. To the contrary, in these systems, new kinds of behavior such as multiergodicity, nonstationarity, and an anomalous approach to equilibrium can emerge. Consequently, their implications for reaction dynamics should be explored, especially in those cases where biological functions are involved.

Thus, the contribution of Shudo and Saito starts by presenting the problem concerning the relation between nonergodicity and $1/f$ noise. For systems with two degrees of freedom, the dynamical origin of $1/f$ noise is attributed to the hierarchical structures of resonant tori (Aizawa). However, for systems with many degrees of freedom, this relationship is not well understood. This discussion goes on to systems with a gap in the spectrum of characteristic time scales and nonergodic behavior, based on the studies of the Italian group (Benettin et al.). The contributions of Aizawa and of Yamaguchi also discuss these problems in the context of cluster formation (Aizawa) and of an approach to equilibrium (Yamaguchi). These features will become important in understanding reaction processes in complex systems such as protein folding and slow relaxation in complex liquids.

Nonlinear resonances are important factors in reaction processes of systems with many degrees of freedom. The contributions of Konishi and of Honjo and Kaneko discuss this problem. Konishi analyzes, by elaborate numerical calculations, the so-called Arnold diffusion, a slow movement along a single resonance under the influence of other resonances. Here, he casts doubt on the usage of the term ''diffusion.'' In other words, ''Arnold diffusion'' is a dynamics completely different from random behavior in fully chaotic regions where most of the invariant structures are lost. Hence, understanding ''Arnold diffusion'' is essential when we go beyond the conventional statistical theory of reaction dynamics. The contribution of Honjo and Kaneko discusses dynamics on the network of nonlinear resonances (i.e., the Arnold web), and stresses the importance of resonance intersections since they play the role of the hub there.

Here we also include the contribution of Okushima, in which the concept of the Lyapunov exponents is extended to orbits of finite duration. The mathematical definition of the Lyapunov exponents requires ergodicity to ensure convergence of the definition. On the other hand, various attempts have been made to extend this concept to finite time and space, to make it applicable to nonergodic systems. Okushima's idea is one of them, and it will find applications in nonstationary reaction processes.

The contributions of Vulpiani's group and of Kaneko deal with reactions at the macroscopic level. The contribution of Vulpiani's group discusses asymptotic analyses to macroscopic reactions involving flows, by presenting the mechanism of front formation in reactive systems. The contribution of Kaneko deals with the network of reactions within a cell, and it discusses the possibility of evolution and differentiation in terms of that network. In particular, he points out that molecules that exist only in small numbers can play the role of a switch in the network, and that these molecules control evolutionary processes of the network. This point demonstrates a limitation of the conventional statistical quantities such as density, which are obtained by coarse-graining microscopic quantities. In other words, new concepts will be required which go beyond the hierarchy in the levels of description such as micro and macro.

We hope that the contributions collected in this volume convey the stimulating and interdisciplinary atmosphere of the conference. We also expect that the results and discussions in these contributions form a first and decisive step toward understanding reaction processes from the standpoint of dynamics.

The conference was supported by the following grants and institute. We greatly appreciate these organizations for their financial support.

- Japan Society for Promotion of Science, Japan–U.S. Cooperative Science Program.
- The Inoue Foundation for Science.
- Yukawa Institute for Fundamental Physics, Kyoto University.
- Grant-in-Aid for Scientific Research on Priority Areas ''Control of Molecules in Intense Laser Fields'' from the Ministry of Education, Science, Sports, and Culture.

References

1. M. Toda, *Adv. Chem. Phys.* **123**, 3643 (2000).
2. K. Yamanouchi, N. Ikeda, S. Tsuchiya, D. M. Jonas, J. K. Lundberg, G. W. Adamson, and R. W. Field, *J. Chem. Phys*. **95**, 6330 (1991).
3. T. Shibata, H. Lai, H. Katayanagi, and T. Suzuki, *J. Phys. Chem*. **A102**, 3643 (1998).

4. S. L. Schultz, J. Qian, and J. M. Jean, *J. Phys. Chem*. **A101**, 1000 (1997).
5. M. J. Davis and S. K. Gray, *J. Chem. Phys*. **84**, 5389 (1986).
6. T. Komatsuzaki and R. S. Berry, *Adv. Chem. Phys.* **123**, 79 (2002).
7. R. E. Gillilan and G. S. Ezra, *J. Chem. Phys*. **94**, 2648 (1991).
8. S. Wiggins, *Physica* **D44**, 471 (1990).
9. L. Sun, K. Song, and W. L. Hase, *Science* **296**, 875 (2002).

Spring 2004

M. TODA
T. KOMATSUZAKI
T. KONISHI
R. S. BERRY
S. A. RICE

YITP International Symposium on Geometrical Structures of Phase Space in Multidimensional Chaos—Applications to Chemical Reaction Dynamics in Complex System, October 26–November 1, 2003, at the Yukawa Institute for Theoretical Physics, Kyoto University, Kyoto, Japan.

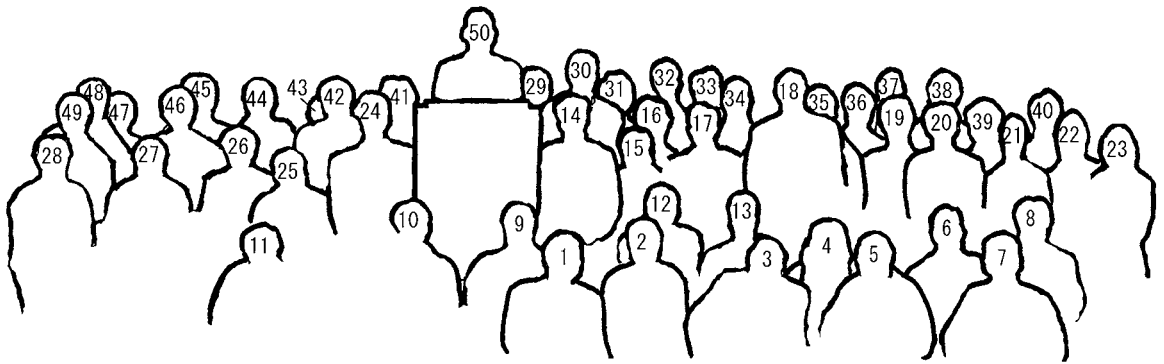

(1) Tamiki Komatsuzaki (2) Gregory Ezra (3) R. Stephen Berry (4) Charles Jaffé (5) Angelo Vulpiani (6) Yoji Aizawa (7) Mikito Toda (8) Masanori Shimono (9) Dave F. Broomhead (10) Shinichiro Goto (11) Yoshihiro Taguchi (12) Shinji Saito (13) David M. Leitner (14) Laurent Wiesenfeld (15) Koji Hotta (16) Seiichiro Honjo (17) Wang Sang Koon (18) Stuart A. Rice (19) Akinori Kidera (20) Toshiya Takami (21) Kyoko Hoshino (22) Ayako Nozaki (23) Yoko K. Ueno (24) Kazuo Takatsuka (25) Yasushi Shimizu (26) Kin'ya Takahashi (27) Mitsusada M. Sano (28) Hiroshi H. Hasegawa (29) Koichi Fujimoto (30) Turgay Uzer (31) Tetsuro Konishi (32) Hidetoshi Morita (33) Yoshiyuki Y. Yamaguchi (34) John E. Straub (35) Hiroshi Fujisaki (36) Mitsunori Takano (37) Sotaro Fuchigami (38) Jack F. Douglas (39) Kazuo Kuwata (40) Taku Mizukami (41) Teruaki Okushima (42) Kim Kyeon-deuk (43) Norihiro Shida (44) Akira Shudo (45) Takefumi Yamashita (46) Kunihiko Kaneko (47) Youhei Koyama (48) Marc Joyeux (49) Lintao Bu (50) Statue of Hideki Yukawa (Nobel Prize Laureate (Physics) 1949)

CONTENTS PART A

PART I PHASE-SPACE GEOMETRY OF MULTIDIMENSIONAL DYNAMICAL SYSTEMS AND REACTION PROCESSES 1

CHAPTER 1 CLASSICAL, SEMICLASSICAL, AND QUANTUM MECHANICAL UNIMOLECULAR REACTION RATE THEORY 3
By Meishan Zhao, Jiangbin Gong, and Stuart A. Rice

CHAPTER 2 REGULARITY IN CHAOTIC TRANSITIONS ON TWO-BASIN LANDSCAPES 143
By Tamiki Komatsuzaki and R. Stephen Berry

CHAPTER 3 A NEW LOOK AT THE TRANSITION STATE: WIGNER'S DYNAMICAL PERSPECTIVE REVISITED 171
By Charles Jaffé, Shinnosuke Kawai, Jesús Palacián, Patricia Yanguas, and Turgay Uzer

CHAPTER 4 GEOMETRY OF PHASE-SPACE TRANSITION STATES: MANY DIMENSIONS, ANGULAR MOMENTUM 217
By Laurent Wiesenfeld

CHAPTER 5 INTRAMOLECULAR DYNAMICS ALONG ISOMERIZATION AND DISSOCIATION PATHWAYS 267
By Marc Joyeux, Sergy Yu. Grebenshchikov, Jens Bredenbeck, Reinhard Schinke, and Stavros C. Farantos

CHAPTER 6 CLASSICAL COULOMB THREE-BODY PROBLEM 305
By Mitsusada M. Sano

CHAPTER 7 GLOBAL ASPECTS OF CHEMICAL REACTIONS IN MULTIDIMENSIONAL PHASE SPACE 337
By Mikito Toda

CHAPTER 8 CLASSICAL MECHANISM OF MULTIDIMENSIONAL BARRIER TUNNELING 401
By Kin'ya Takahashi and Kensuke S. Ikeda

Chapter 9 Coarse-Grained Picture for Controlling Quantum Chaos 435
By Toshiya Takami, Hiroshi Fujisaki, and Takayuki Miyadera

Author Index 459

Subject Index 487

CONTENTS PART B

PART II COMPLEX DYNAMICAL BEHAVIOR IN CLUSTERS AND PROTEINS, AND DATA MINING TO EXTRACT INFORMATION ON DYNAMICS 1

CHAPTER 10 ATOMIC CLUSTERS: POWERFUL TOOLS TO PROBE COMPLEX DYNAMICS 3
By R. Stephen Berry

CHAPTER 11 TEMPERATURE, GEOMETRY, AND VARIATIONAL STRUCTURE IN MICROCANONICAL ENSEMBLE FOR STRUCTURAL ISOMERIZATION DYNAMICS OF CLUSTERS: A MULTICHANNEL CHEMICAL REACTION BEYOND THE TRANSITION-STATE CONCEPT 25
By Kazuo Takatsuka

CHAPTER 12 EFFECTS OF AN INTRINSIC METRIC OF MOLECULAR INTERNAL SPACE ON CHEMICAL REACTION DYNAMICS 87
By Tomohiro Yanao and Kazuo Takatsuka

CHAPTER 13 ONSET DYNAMICS OF PHASE TRANSITION IN Ar_7 129
By Norihiro Shida

CHAPTER 14 RAPID ALLOYING IN BINARY CLUSTERS: MICROCLUSTER AS A DYNAMIC MATERIAL 155
By Yasushi Shimizu, Taizo Kobayashi, Kensuke S. Ikeda, and Shin'ichi Sawada

CHAPTER 15 VIBRATIONAL ENERGY RELAXATION (VER) OF A CD STRETCHING MODE IN CYTOCHROME c 179
By Hiroshi Fujisaki, Lintao Bu, and John E. Straub

CHAPTER 16 HEAT TRANSPORT IN MOLECULES AND REACTION KINETICS: THE ROLE OF QUANTUM ENERGY FLOW AND LOCALIZATION 205
By David M. Leitner

CHAPTER 17 REGULARITY IN CHAOTIC TRANSITIONS ON MULTIBASIN LANDSCAPES 257
By Tamiki Komatsuzaki, Kyoko Hoshino, and Yasuhiro Matsunaga

Chapter 18 Nonmetric Multidimensional Scaling as a Data-Mining Tool: New Algorithm and New Targets 315
By Y-H. Taguchi and Yoshitsugu Oono

Chapter 19 Generalization of the Fluctuation–Dissipation Theorem for Excess Heat Production 353
By Hiroshi H. Hasegawa and Yoshikazu Ohtaki

PART III NEW DIRECTIONS IN MULTIDIMENSIONAL CHAOS AND EVOLUTIONARY REACTIONS 373

Chapter 20 Slow Relaxation in Hamiltonian Systems with Internal Degrees of Freedom 375
By Akira Shudo and Shinji Saito

Chapter 21 Slow Dynamics in Multidimensional Phase Space: Arnold Model Revisited 423
By Tetsuro Konishi

Chapter 22 Structure of Resonances and Transport in Multidimensional Hamiltonian Dynamical Systems 437
By Seiichiro Honjo and Kunihiko Kaneko

Chapter 23 Multiergodicity and Nonstationarity in Generic Hamiltonian Dynamics 465
By Yoji Aizawa

Chapter 24 Relaxation and Diffusion in a Globally Coupled Hamiltonian System 477
By Yoshiyuki Y. Yamaguchi

Chapter 25 Finite-Time Lyapunov Exponents in Many-Dimensional Dynamical Systems 501
By Teruaki Okushima

Chapter 26 The Role of Chaos for Inert and Reacting Transport 519
By Massimo Cencini, Angelo Vulpiani, and Davide Vergni

Chapter 27 On Recursive Production and Evolvability of Cells: Catalytic Reaction Network Approach 543
By Kunihiko Kaneko

Author Index 599

Subject Index 627

PART I

PHASE-SPACE GEOMETRY OF MULTIDIMENSIONAL DYNAMICAL SYSTEMS AND REACTION PROCESSES

CHAPTER 1

CLASSICAL, SEMICLASSICAL, AND QUANTUM MECHANICAL UNIMOLECULAR REACTION RATE THEORY

MEISHAN ZHAO, JIANGBIN GONG, and STUART A. RICE

Department of Chemistry and The James Franck Institute, The University of Chicago, Chicago, Illinois 60637, USA

CONTENTS

I. Introduction
II. Phase-Space Structure of Molecular Dynamics
  A. Canonical Transformation
  B. Invariant Measure
  C. Action and Angle Variables
  D. KAM Theorem
  E. Poincaré Surface of Section
  F. Stability Analysis
  G. Bottlenecks in Few-Dimensional Systems
  H. Bottlenecks in Many-Dimensional Systems
  I. Normally Hyperbolic Invariant Manifold
III. Mapping Models of Unimolecular Fragmentation
  A. Two-Dimensional Free Particle in a Morse-like Kicking Field
  B. Four-Dimensional Free Rotor in a Morse-like Kicking Field
IV. Theory of Unimolecular Predissociation
  A. Davis–Gray Analysis
  B. The Gray–Rice–Davis ARRKM Theory
  C. The Zhao–Rice Approximation (MRRKM)
    1. An Approximate Dividing Surface for the Separatrix
    2. An Approximate Dividing Surface for Intramolecular Bottlenecks
    3. A Zeroth-Order Calculation of the Rate Constant for Crossing Intramolecular Bottlenecks
    4. The Rate Constant for Crossing the Separatrix
  D. The Reaction Path Analysis

Geometric Structures of Phase Space in Multidimensional Chaos: A Special Volume of Advances in Chemical Physics, Part A, Volume 130, edited by M. Toda, T Komatsuzaki, T. Konishi, R.S. Berry, and S.A. Rice. Series editor Stuart A. Rice.
ISBN 0-471-70527-6

E. XI_2 Predissociation
1. HeI_2
2. NeI_2 and ArI_2
F. XCl_2 and XICl Predissociation
1. $HeCl_2$ and $NeCl_2$
2. HeICl and NeICl
V. Theory of Isomerization
A. Gray–Rice Theory
B. Zhao–Rice Approximation
C. Reactive Island Theory
D. Gray–Rice Theory Versus Reactive Island Theory
E. Isomerization in Double-Well Systems
F. Isomerization in a Triple-Well System
G. Isomerization of 3-Phospholene
H. Isomerization of HCN → CNH
I. Isomerization of Cyclobutanone (C_4H_6O)
VI. Quantum and Semiclassical Approaches
A. The Wigner Function and Weyl's Rule
B. Quantum Scars in Phase-Space
C. Quantizing the ARRKM Theory
D. Rigorous Quantum Rate Theory Versus the Quantized ARRKM Theory
E. A Semiclassical Approximation to the Rigorous Quantum Rate Theory
F. Effective Hamiltonian Approach to Unimolecular Dissociation
G. Wave Packet Dynamics Approach
VII. Quantum Transport in Classically Chaotic Systems
A. Quantum Transport Through Cantori
B. Quantum Suppression of Arnold Diffusion
C. Faster-than-Classical Quantum Anomalous Diffusion
VIII. Concluding Remarks
Acknowledgment
References

I. INTRODUCTION

Studies of the rate of a unimolecular reaction have been central to the development of our understanding of reaction dynamics for almost a century. In the early 1900s such reactions appeared mysterious, since the source of the energy required for reaction to occur was not immediately apparent. Indeed, it took careful experimental work to demonstrate that thermal unimolecular reactions were induced by collisions and not by absorption of ambient radiation and that the observed unimolecular kinetics held in only a limited pressure range. Once the phenomenological description of unimolecular reaction kinetics was established, attention turned to the development of a molecular description of the reaction rate. It was understood from the beginning of these studies that a detailed description of the nonlinear dynamical evolution of an energized molecule is extraordinarily difficult. A key breakthrough occurred when it was

realized that for many purposes a statistical description of the energy distribution in the excited molecule suffices. Indeed, statistical theories of molecular energy distribution have been central to our understanding of the kinetics and dynamics of unimolecular reactions.

The beauty of statistical treatments of chemical reaction dynamics lies in their simplicity and universality. Rice, Ramsberger, and Kassel (RRK) [1,2], building on the earlier work of Lindemann and Hinshelwood, developed a statistical theory of unimolecular reaction rate based on the assumption that complete intramolecular energy transfer precedes reaction. Under this assumption, detailed information regarding the excitation step of a unimolecular reaction is irrelevant, and the reaction rate depends only upon the energy of a molecule. The RRK theory is based on classical mechanics. Marcus recast and further developed the RRK theory in the 1950s [3,4] by taking into account the major elements of the energy state structure of the molecule imposed by quantum mechanics. The resultant RRKM statistical theory of unimolecular reaction rate is, by any measure, one of the great successes of chemical physics; it is widely applicable and provides an excellent description of the experimental data in the overwhelming majority of cases [5,6]. There are, however, some instances in which the RRKM theory gives inaccurate or unphysical predictions. In many of these instances the failure of the RRKM theory can be traced to a breakdown of the assumption that the rate of intramolecular energy transfer is greater than the rate of reaction and/or that all states of the molecule are accessible for energy transfer. Typically, analysis of these cases has retained the conceptual framework of the theory and merely modified some of the analysis associated with the intramolecular energy transfer step.

The success of a statistical theory of the overall dynamical evolution of an isolated molecule relies largely on the intrinsic stochasticity of the internal motions—that is, on the existence of deterministic dynamical chaos. As such, studies of the rate of a chemical reaction have become interdisciplinary, and they involve significant overlap with the field of nonlinear dynamics and deterministic chaos [7]. The renaissance in the development of classical unimolecular reaction rate theory has been motivated by the recognition that cantori, remnants of invariant phase space curves with highly irrational winding numbers, constitute bottlenecks to chaotic transport between disjoint phase space regions [8,9,10]. In particular, in treating model molecular systems with two degrees of freedom (DOFs) Davis and Gray [11] replaced the RRKM transition state, which is defined in configuration space, by an exact separatrix that is defined in phase space. The separatrix defines the boundary in phase space between products and reactants—for example, the boundary between bounded motion and unbounded motion in a fragmentation reaction. Davis and Gray also incorporated the bottlenecks to intramolecular energy transfer into their reaction rate theory. This modified statistical theory accurately predicts, for

example, the decay rate of a simplified classical model of He-I_2; that decay rate is overestimated by conventional RRKM theory by at least an order of magnitude. The work of Davis and Gray demonstrated the potential for accurate prediction of unimolecular fragmentation rate constants inherent in statistical theories that account for highly inhomogeneous energy transport. The Davis–Gray theory was later simplified by Gray, Rice, and Davis [12] by replacing the exact separatrix with an approximate phase-space dividing surface, and it was further modified by Zhao and Rice [13–16] to account for some effects of vibrational and rotational motion in both reactants and products and to develop approximations for analytical treatments of intramolecular energy flow. The several reported tests of the Zhao–Rice version of unimolecular reaction rate theory (identified by the acronym MRRKM) are in good, but not perfect, agreement with classical simulations and actual experimental results.

Developing a reaction rate theory for realistic polyatomic systems requires significant extensions of the Davis–Gray theory. One might intuitively expect that the higher the system dimension, the better a statistical description. But this is not the case, and a rigorous extension of the Davis–Gray theory to many-dimensional systems is challenging. For example, identifying the bottlenecks to energy flow in systems with three or more DOFs is far from trivial, since there are no invariant phase-space structures that can separate the energy shell into disjoint regions. Many of the extant approaches, including the MRRKM theory, have either demonstrated or assumed the importance of pairwise frequency ratios, and much work along this direction remains to be done. Furthermore, because of so-called homoclinic tangency [17], a concept further discussed below, the usefulness of a many-dimensional analog of the exact separatrix in the Davis–Gray theory is unclear. Indeed, in a study of a model van der Waals molecule fragmentation reaction, Gillilan and Ezra [18] observed that a two-dimensional projection of a many-dimensional separatrix associated with the fixed point at infinity may or may not resemble the separatrix of a two-dimensional system, implying that this high-dimensional separatrix is unsuitable for determining the flux that crosses from the molecular complex region to the free fragments region of phase space. Of course, this result does not preclude the existence of a well-behaved separatrix associated simultaneously with several fixed points.

In a study of the rate of isomerization of HCN to CNH, Rice and co-workers [19] suggested exploiting a reaction path Hamiltonian as a device to permit extension of classical statistical reaction rate theory from few-dimensional to many-dimensional systems. In that approach the dynamics of the reacting molecule is reduced to that of a system with a complicated but one-dimensional reactive DOF coupled with other effective DOFs. Although their calculations based on this approach yield an accurate description of the isomerization rate as

a function of energy, the reaction path treatment cannot be immediately rationalized because the implicit coupling between the complicated reaction coordinate and the other DOFs, via the definition of the reaction coordinate, obscures the meaning of the two-dimensional mapping that is exploited. Recent advances in chaotic transport in many-dimensional systems, and particularly the Wiggins theory of normally hyperbolic invariant manifolds (NHIM) in dynamical systems [20,21], offer new opportunities to refine classical reaction rate theories. For example, instead of using a reaction path Hamiltonian, Wiggins et al. [22] proposed to transform the system Hamiltonian by a sequence of local and nonlinear canonical transformations to a particular form, which then allows for explicit construction of an exact many-dimensional separatrix and straightforward calculation of the flux across that separatrix. This novel methodology, although based on a local picture of the reaction dynamics, is expected to greatly deepen our understanding of the similarities and differences between many-dimensional and few-dimensional reacting systems.

A successful reaction rate theory cannot completely ignore some of the important features of the reaction dynamics. Reacting molecular systems cannot be truly ergodic, and this ''order in chaos'' is precisely why statistical theories must be rather sophisticated. The importance of this point can be appreciated, for example, from examination of the reactive islands theory (RIT) [23–25] of the rate of unimolecular isomerization. Incorporated into RIT is a high degree of phase space structure associated with the chaotic dynamics of isomerization. More significantly, Komatsuzaki and Berry [26] have presented a systematic approach to identifying local regularities embedded in the chaotic dynamics of many-dimensional systems. The key element in their approach is the use of Lie canonical perturbation theory to rotate away the irregular behavior particularly associated with the motion along the reaction coordinate, and then to identify local constants of the motion. Since the frequency associated with the reactive mode is imaginary, they show that at least one local approximate constant of motion exists even when the dynamics of the transition state becomes manifestly chaotic. This important result makes it possible to construct a local multidimensional separatrix and has provided new perspectives into chemical reaction dynamics.

With this brief overview of classical theories of unimolecular reaction rate, one might wonder why classical mechanics is so useful in treating molecular systems that are microscopic, and one might question when a classical statistical theory should be replaced by a corresponding quantum theory. These general questions bring up the important issue of quantum-classical correspondence in general and the field of quantum chaos [27–29] (i.e., the quantum dynamics of classically chaotic systems) in particular. For example, is it possible to translate the above classical concepts (e.g., phase space separatrix, NHIM, reactive islands) into quantum mechanics, and if yes, how? What is the consequence of

quantization for energy transport in chaotic systems? Anticipating its importance to chemical reaction rate theory, we shall also review some recent results from the relatively young field of quantum chaos.

Recent years have also witnessed exciting developments in the active control of unimolecular reactions [30,31]. Reactants can be prepared and their evolution interfered with on very short time scales, and coherent light sources can be used to imprint information on molecular systems so as to produce more or less of specified products. Because a well-controlled unimolecular reaction is highly nonstatistical and presents an excellent example in which any statistical theory of the reaction dynamics would terribly fail, it is instructive to comment on how to view the vast control possibilities, on the one hand, and various statistical theories of reaction rate, on the other hand. Note first that a controlled unimolecular reaction, most often subject to one or more external fields and manipulated within a very short time scale, undergoes nonequilibrium processes and is therefore not expected to be describable by any unimolecular reaction rate theory that assumes the existence of an equilibrium distribution of the internal energy of the molecule. Second, strong deviations from statistical behavior in an uncontrolled unimolecular reaction can imply the existence of ''order in chaos'' and thus more possibilities for inexpensive active control of product formation. Third, most control scenarios rely on quantum interference effects that are neglected in classical reaction rate theory. Clearly, then, studies of controlled reaction dynamics and studies of statistical reaction rate theory complement each other.

This review chapter, intended to be self-contained and reasonably focused on the work developed in our group, is organized as follows. We begin with introducing some basic but important concepts in classical mechanics and chaotic transport, including canonical transformations, the KAM theorem, bottlenecks to chaotic transport in both few-dimensional and many-dimensional systems, normally hyperbolic invariant manifolds, and more. These concepts are strengthened, in Section III, by presenting some simple mapping models for unimolecular fragmentation. Then, in Section IV, we review a number of classical theories of unimolecular predissociation reaction rate, with detailed comparisons between different theories and between theoretical and experimental results. This is followed, in Section V, by a review of unimolecular isomerization rate theories and their application to various model systems. In Section VI we describe some standard quantum and semiclassical approaches to unimolecular reaction rate theory, with emphasis placed on their connections to classical approaches. Finally, Section VII contains a brief survey of some recent results concerning quantum transport in classically chaotic systems; how these results are expected to influence our understanding of quantum effects in unimolecular reaction dynamics is also discussed. Section VIII contains some concluding remarks and speculations.

II. PHASE-SPACE STRUCTURE OF MOLECULAR DYNAMICS

A. Canonical Transformation

In classical mechanics the state of a system with n DOFs is represented by a vector $(q_1, q_2, \ldots, q_n; p_1, p_2, \ldots, p_n) \equiv (\mathbf{q}, \mathbf{p})$ in a $2n$-dimensional phase space, whose evolution is governed by Hamilton's equations of motion

$$\frac{d\mathbf{q}}{dt} = \frac{\partial H}{\partial \mathbf{p}}, \qquad \frac{d\mathbf{p}}{dt} = -\frac{\partial H}{\partial \mathbf{q}} \tag{1}$$

where $\mathbf{q}$ represents the configuration coordinates, $\mathbf{p}$ represents the conjugate momenta, and $H = H(\mathbf{q}, \mathbf{p})$. Although time-dependent systems such as periodically kicked systems will also be discussed in this review, here we restrict ourselves to time-independent systems. Then the energy of the system, denoted by E, is conserved, and the time-evolving trajectories are necessarily restricted to a $(2n-1)$-dimensional hypersurface.

There exists a special type of coordinate transformation in phase space, called a *canonical* transformation, which transforms the original system variables $(\mathbf{q}, \mathbf{p})$ to new system variables $(\mathbf{q}', \mathbf{p}') \equiv (q_1', q_2', \ldots, q_n'; p_1', p_2', \ldots, p_n')$ while retaining the structure of Hamilton's equations of motion, that is,

$$\frac{d\mathbf{q}'}{dt} = \frac{\partial H'}{\partial \mathbf{p}'}, \qquad \frac{d\mathbf{p}'}{dt} = -\frac{\partial H'}{\partial \mathbf{q}'} \tag{2}$$

where $H' = H'(\mathbf{q}', \mathbf{p}') = H(\mathbf{q}, \mathbf{p})$. A canonical transformation can be generated by requiring $\mathbf{p} \cdot d\mathbf{q} - \mathbf{p}' \cdot d\mathbf{q}'$ to be a complete differential dF. For example, if $F = F(\mathbf{q}, \mathbf{q}')$, then one needs

$$\mathbf{p} = \frac{\partial F_1}{\partial \mathbf{q}}, \qquad \mathbf{p}' = -\frac{\partial F_1}{\partial \mathbf{q}'} \tag{3}$$

to realize the canonical transformation. Of particular importance is the case in which F can be written as $F_2(\mathbf{q}, \mathbf{p}') - \mathbf{p}' \cdot \mathbf{q}'$. One then obtains

$$\mathbf{p} = \frac{\partial F_2}{\partial \mathbf{q}}, \qquad \mathbf{q}' = \frac{\partial F_2}{\partial \mathbf{p}'} \tag{4}$$

where $\mathbf{q}'$ should be regarded as a function of $\mathbf{q}$ and $\mathbf{p}'$. Due to energy conservation, Eq. (4) directly leads to the Hamilton–Jacobi equation:

$$H\left(\mathbf{q}, \frac{\partial F_2}{\partial \mathbf{q}}\right) = E \tag{5}$$

Solving this partial differential equation, which is required to construct the canonical transformation, is in general as difficult as solving Eq. (1). However, Eq. (5) is very useful in obtaining approximate solutions using, for example, perturbation theory.

An alternative procedure to generate a canonical transformation is to use the Hamiltonian flow itself. Consider an arbitrary Hamiltonian system of the same dimension as the original system. The associated functional dependence of the final state at $t = t_f$ on the initial state at $t = t_i$ can be represented by

$$\mathbf{q}(t_i) \to \mathbf{q}(t_f) = \mathbf{q}[\mathbf{q}(t_i), \mathbf{p}(t_i)]; \qquad \mathbf{p}(t_i) \to \mathbf{p}(t_f) = \mathbf{p}[\mathbf{q}(t_i), \mathbf{p}(t_i)] \tag{6}$$

Since both initial and final states satisfy the same equations of motion, the transformation of Eq. (6) is a natural canonical transformation. This kind of canonical transformation is a basic tool in the so-called Lie canonical perturbation theory for obtaining approximate constants of the motion.

B. Invariant Measure

A classical statistical theory is concerned with an ensemble of classical trajectories. Denote the kth evolving trajectory in an ensemble by $[\mathbf{q}_k(t), \mathbf{p}_k(t)]$. Then the ensemble average of a physical observable $A(\mathbf{q}, \mathbf{p})$ is given by

$$\bar{A}(t) = \lim_{n\to\infty} \frac{1}{n} \sum_{k=1}^{n} A[\mathbf{q}_k(t), \mathbf{p}_k(t)] \tag{7}$$

Consider now a trajectory density function $D(\mathbf{q}, \mathbf{p}, t)$, defined by

$$D(\mathbf{q}, \mathbf{p}, t) = \lim_{n\to\infty} \frac{1}{n} \sum_{k=1}^{n} \delta[\mathbf{q} - \mathbf{q}_k(\mathbf{t})]\delta[\mathbf{p} - \mathbf{p}_k(\mathbf{t})] \tag{8}$$

$D(\mathbf{q}, \mathbf{p})$ thus defined is evidently normalized, that is,

$$\int D(\mathbf{q}, \mathbf{p}, t) d\mathbf{q} d\mathbf{p} = 1 \tag{9}$$

The ensemble average $\bar{A}(t)$ can be expressed as

$$\bar{A}(t) = \int A(\mathbf{q}, \mathbf{p}) D(\mathbf{q}, \mathbf{p}, t)\, d\mathbf{q}\, d\mathbf{p} \tag{10}$$

Invariant measure on classical phase space is an important concept in statistical theory. Suppose that there is an arbitrary phase space volume $V(t)$ at time t, which evolves to $V'(t')$ at time t'. An invariant measure,

denoted by μ_i, has the property that it gives the same measure for $V(t)$ and $V'(t')$. That is,

$$\mu_i[V(t)] = \mu_i[\mathrm{V}'(t')] \tag{11}$$

Because the transformation from $[\mathbf{q}(t), \mathbf{p}(t)]$ to $[\mathbf{q}(t'), \mathbf{p}(t')]$ is canonical, an almost trivial example of invariant measure in its differential form is given by

$$d\mu_i = d\mathbf{q}\, d\mathbf{p} \tag{12}$$

The energy of a time-independent Hamiltonian system is a conserved quantity. In this case an invariant measure can be constructed on the energy shell $H(\mathbf{q}, \mathbf{p}) = E$, that is,

$$d\mu_i = N\delta(H - E)d\mathbf{p}\, d\mathbf{q} \tag{13}$$

where N is a normalization constant. Similarly, if taking into account the total angular momentum J_{total} that is conserved at J, an invariant measure can be constructed through

$$d\mu_i = N\delta(H - E)\delta(J_{\text{total}} - J)d\mathbf{p}\, d\mathbf{q} \tag{14}$$

C. Action and Angle Variables

For a completely separable Hamilton–Jacobi equation, one can always derive n constants of motions for a system with n DOFs. It is illustrative to consider a simple case in which $H = \sum_j H_j(q_j, p_j)$ and therefore $H_j(q_j, p_j)$ is conserved. The corresponding Hamilton–Jacobi equation can be readily solved by requiring $F_2 = \sum_j g_j(q_j, \boldsymbol{\alpha})$, where $\boldsymbol{\alpha} \equiv (\alpha_1, \alpha_2, \ldots, \alpha_n)$, and

$$H_j\left(q_j, \frac{\partial g_j}{\partial q_j}\right) = \alpha_j, \qquad j = 1, 2, \ldots, n \tag{15}$$

where the α_j are constants of motion with $\sum_j \alpha_j = E$. Consider now n new variables $(I_1, I_2, \ldots, I_n)$, each of which is defined by

$$I_j = \frac{1}{2\pi}\oint p_j\, dq_j = \frac{1}{2\pi}\oint \frac{\partial g_j(q_j, \boldsymbol{\alpha})}{\partial q_j} dq_j, \qquad j = 1, 2, \ldots, n \tag{16}$$

where $\oint$ denotes the integration over one period of the oscillation in q_j. Equation (16) defines the so-called *action* variables. These action variables can

be regarded as new momentum variables, and they are new constants of motion since they depend on $\boldsymbol{\alpha}$ only:

$$I_j = I_j(\boldsymbol{\alpha}), \qquad j = 1, 2, \ldots, n \tag{17}$$

Inverting Eq. (17) yields α_j as functions of $I_1, I_2, \ldots, I_n$, which further gives the dependence of g_j on $I_1, I_2, \ldots, I_n$:

$$g_j = g_j[q_j, \boldsymbol{\alpha}(I_1, I_2, \ldots, I_n)] \tag{18}$$

The new coordinate variables ϕ_j that are conjugate to I_j are called *angle* variables. The transformation from $(\mathbf{q}, \mathbf{p})$ to $(\phi_1, \phi_2, \ldots, \phi_n)$ can be obtained from

$$\phi_j = \frac{\partial g_j[q_j, \boldsymbol{\alpha}(I_1, I_2, \ldots, I_n)]}{\partial I_j} \tag{19}$$

Using the action and angle variables, Hamilton's equations of motion take the following simple form:

$$\frac{d\phi_j}{dt} = \frac{\partial \alpha_j}{\partial I_j} = \omega_j(I_j), \qquad j = 1, 2, \ldots, n \tag{20}$$

$$\frac{dI_j}{dt} = -\frac{\partial \alpha_j}{\partial \phi_j} = 0, \qquad j = 1, 2, \ldots, n \tag{21}$$

Equation (20) indicates that ϕ_j assumes a linear time dependence. Furthermore, using Eqs. (16) and (19), one finds that over one oscillation period, the change in ϕ_j is given by

$$\oint d\phi_j = \oint d \frac{\partial g_j[q_j, \boldsymbol{\alpha}(I_1, I_2, \ldots, I_n)]}{\partial I_j} = \frac{\partial \oint p_j \, dq_j}{\partial I_j} = 2\pi \tag{22}$$

Equation (21) makes it clear that the action-angle variable representation directly addresses the oscillation frequencies without looking into the details of the dynamics. Indeed, as shown below, the action-angle variable representation plays a key role in understanding important qualitative features of Hamiltonian dynamics.

D. KAM Theorem

Consider a two-DOF system with the following Hamiltonian:

$$H = H_0(J_1, J_2) + \epsilon H_1(J_1, J_2, \phi_1, \phi_2) \tag{23}$$

Here J_1, J_2 and ϕ_1, ϕ_2 are action and angle variables, $H_0(J_1, J_2)$ is the zeroth-order Hamiltonian, and $\epsilon H_1(J_1, J_2, \phi_1, \phi_2)$ represents a perturbing Hamiltonian in a general form. The motion associated with $H_0(J_1, J_2)$ can be easily obtained; it is

$$J_1 = \text{constant}, \qquad J_2 = \text{constant} \tag{24}$$

$$\phi_i = \phi_{0,i} + \omega_i(J_1, J_2)t, \qquad \omega_i \equiv \partial H_0/\partial J_i, \qquad i = 1, 2 \tag{25}$$

The corresponding trajectories can be best visualized as motion restricted to a two-dimensional torus, as shown in Fig. 1. If the frequency ratio, or the winding number ω_1/ω_2, is a rational number, the two DOFs are in resonance and an individual trajectory will close on itself on the torus. By contrast, if ω_1/ω_2 is an irrational number, then as time evolves a single trajectory will eventually cover the torus. The motion in the latter case is called conditionally periodic.

Kolmogoroff, Arnold, and Moser (KAM) established a theorem regarding the qualitative features of a perturbed Hamiltonian system. The KAM theorem states that, under small perturbation and for an analytical $H_1(J_1, J_2, \phi_1, \phi_2)$ in a

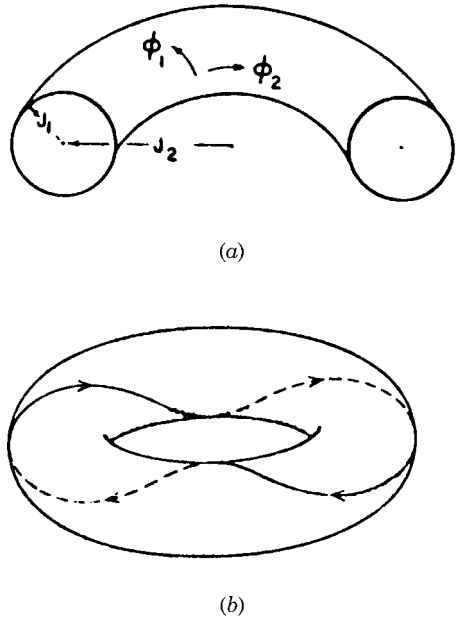

(*a*)

(*b*)

Figure 1. (*a*) Angle-action variables $(\phi_1, \phi_2, J_1, J_2)$ and the invariant torus for a two-oscillator system. (*b*) A periodic trajectory on the torus.

certain domain, classical trajectories display two kinds of motion. One is topologically the same as for $H_0(J_1, J_2)$, while the other can be chaotic—that is, extremely sensitive to slight changes in the initial condition. Specifically, the KAM theorem demonstrates that (a) with "sufficiently small" ϵ and

$$\frac{\partial(\omega_1, \omega_2)}{\partial(J_1, J_2)} \neq 0 \tag{26}$$

most of the unperturbed tori bearing conditionally periodic motion persist, but slightly perturbed by $\epsilon H_1(J_1, J_2, \phi_1, \phi_2)$; and (b) tori bearing motion with rational or almost rational frequency ratios are either drastically deformed or destroyed. Moreover, although the unperturbed tori with rational frequency ratios are everywhere, the majority (in the sense of measure theory) of initial conditions are shown to be restricted to deformed tori bearing conditionally periodic motion.

Hence, for small perturbations the system is nearly integrable: Most classical trajectories are restricted to two-dimensional phase-space structures that are often called "KAM tori." Since two classical trajectories cannot cross each other, a torus such as shown in Fig. 1 is in fact an impenetrable phase-space structure, dividing the three-dimensional energy shell into disjoint regions. With stronger perturbations, more KAM tori are expected to be destroyed and therefore more trajectories become chaotic.

E. Poincaré Surface of Section

The classical dynamics of a system can also be analyzed on the so-called Poincaré surface of section (PSS). Hamiltonian flow in the entire phase space then reduces to a Poincaré map on a surface of section. One important property of the Poincaré map is that it is area-preserving for time-independent systems with two DOFs. In such systems Poincaré showed that all dynamical information can be inferred from the properties of trajectories when they cross a PSS. For example, if a classical trajectory is restricted to a simple two-dimensional torus, then the associated Poincaré map will generate closed KAM curves, an evident result considering the intersection between the torus and the surface of section. If a Poincaré map generates highly erratic points on a surface of section, the trajectory under study should be chaotic. The Poincaré map has been a powerful tool for understanding chemical reaction dynamics in few-dimensional systems.

Here we show several examples of PSS using realistic molecular systems. In particular, Fig. 2 shows a PSS of a model T-shaped HeI_2 molecule undergoing unimolecular dissociation, with a total energy of $E = -2662$ cm^{-1}. Figure 3 depicts the PSS of a model T-shaped $HeBr_2$ molecule with the initial vibrational energy of the Br–Br bond chosen to be the same as that of the 15th quantum

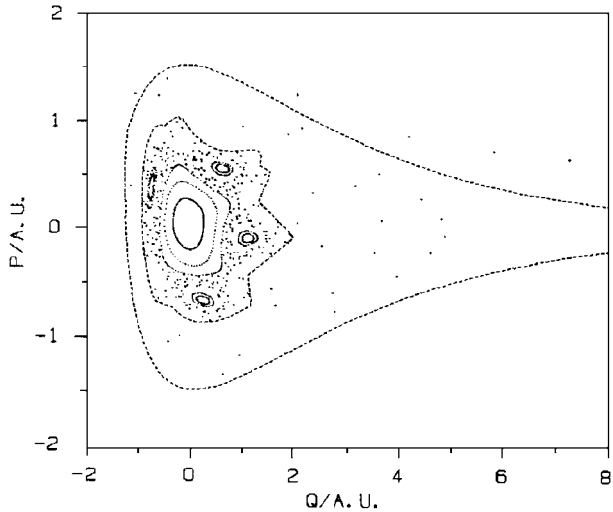

Figure 2. Poincaré surface of section of the T-shaped HeI_2 with a total energy -2662 cm^{-1}. $Q = R - R_0$, where R is the He–I_2 bond length and R_0 is its equilibrium value. P is the momentum conjugate to R. [From S. K. Gray, S. A. Rice, and M. J. Davis, *J. Phys. Chem.* **90**, 3470 (1986).]

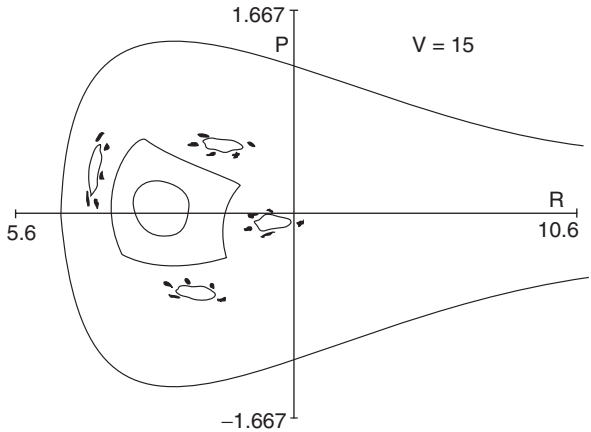

Figure 3. Poincaré surface of section of the T-shaped $HeBr_2$ at the Br–Br vibrational state $v = 15$, showing a 4:1 resonance. [From A. A. Granovsky et al., *J. Chem. Phys.* **108**, 6282 (1998).]

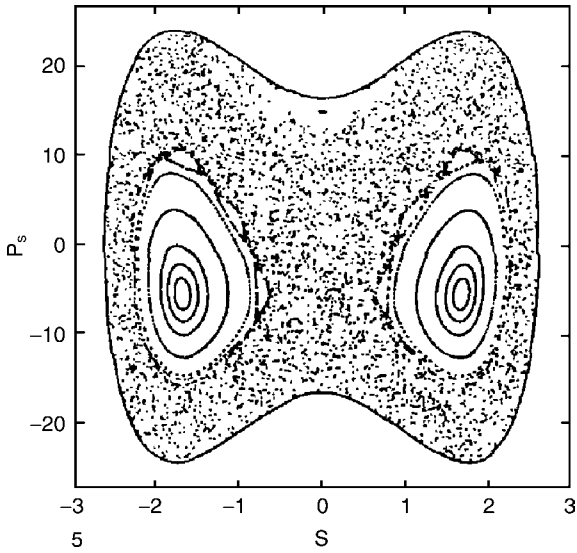

Figure 4. Poincaré surface of section of molecular isomerization of cyclobutanone (C_4H_6O) for the total reaction energy $E = 0.01$a.u, showing a 3:1 resonance.

vibrational state. Shown in Fig. 4 is a PSS associated with the molecular isomerization of cyclobutanone (C_4H_6O) at a total reaction energy of $E = 0.01$ a.u. The reaction coordinate of the isomerization reaction is given as $s = r\phi$, where r is the C=O bond distance and ϕ is the C=O wagging angle.

These examples indicate that the PSS associated with reacting moecular systems typically displays both regular and irregular structures. In particular, the random looking splatter of points on the PSS is generated by a single trajectory, and trajectories with initial conditions that are only slightly different would yield similar patterns. In contrast, there are also smooth KAM curves that occupy significant portions of the PSS. Clearly, trajectories associated with regular structures give no contribution to reaction and only chaotic trajectories, which wander over the entire PSS generate reaction. Also seen is that there often exists a chain of islands between the regular and chaotic regions. For example, in Fig. 2 there are four islands surrounding the closed curves at their centers. Trajectories initiated from these islands cannot escape; they consecutively revisit them. That is, a classical trajectory intersects the PSS four times before visiting all the islands and thus completing a ''rotation'' on the PSS. This suggests that this chain of islands is the new phase-space structure associated with a zeroth-order torus of a $4:1$ resonance. These important features of the PSS can be found in virtually all two-DOF Hamiltonian systems that are neither totally separable nor strongly chaotic.

F. Stability Analysis

Further insights into reaction dynamics can be obtained by analyzing the stability of classical trajectories. Presumably, stable periodic orbits will be restricted to KAM tori and therefore be nonreactive; and unstable periodic orbits will provide information about the location of resonances and therefore some qualitative features of the intramolecular energy flow.

As an example, consider a two-dimensional dynamical mapping with the simplest periodic orbit—that is, a fixed point at (q_0, p_0). Suppose that the initial condition (q_0', p_0') is only infinitesimally shifted from (q_0, p_0) with $q_0' - q_0 = dq$; $p_0' - p_0 = dp$. With one iteration of the map, (q_0, p_0) evolves to (q_1, p_1), and the initial "errors" dq and dp are propagated to δq and δp, which is given by

$$\begin{pmatrix} \delta q \\ \delta p \end{pmatrix} = \mathbf{M} \begin{pmatrix} dq \\ dp \end{pmatrix} \tag{27}$$

where the Jacobi transformation matrix $\mathbf{M}$, usually called the monodromy matrix, is given by

$$\mathbf{M} = \begin{pmatrix} \dfrac{\partial q_1}{\partial q_0} & \dfrac{\partial q_1}{\partial p_0} \\ \dfrac{\partial p_1}{\partial q_0} & \dfrac{\partial p_1}{\partial p_0} \end{pmatrix} \equiv \begin{pmatrix} M_{11} & M_{12} \\ M_{21} & M_{22} \end{pmatrix} \tag{28}$$

For an area-preserving map, such as the Poincaré map, one has

$$\det(\mathbf{M}) = M_{11}M_{22} - M_{12}M_{21} = 1 \tag{29}$$

This leads to a simple relationship between the two eigenvalues of the $\mathbf{M}$ matrix. Indeed, directly solving

$$\det(\mathbf{M} - \lambda \mathbf{I}) = 0 \tag{30}$$

one finds that the eigenvalues are given by

$$\begin{aligned} \lambda_{\pm} &= \frac{M_{11} + M_{22}}{2} \pm \left[\frac{(M_{11} + M_{22})^2}{4} - 1 \right]^{1/2} \\ &= \frac{M_{11} + M_{22}}{2} \pm i \frac{1}{2} \left[4 - (M_{11} + M_{22})^2 \right]^{1/2} \end{aligned} \tag{31}$$

with $\lambda_+ \lambda_- = 1$.

For stable periodic trajectories the two eigenvalues $\lambda_\pm$ are complex numbers conjugate to each other, and the corresponding eigenvectors correspond to a simple rotation around the fixed point (q_0, p_0). By contrast, provided that

$$\frac{(M_{11} + M_{22})^2}{4} > 1 \tag{32}$$

the eigenvalues $\lambda_\pm$ are real and one of them (say λ_+) must be larger than 1. In this case periodic orbits are unstable: A small error in initial conditions along the direction of the λ_+ eigenvector will be amplified by a factor of λ_+ for each iteration of the map, a clear example of the exponential sensitivity of chaotic trajectories. The Lyapunov exponent, which is defined by the exponential divergence rate of two nearby trajectories, is then given by $\ln \lambda_+$. Thus there is an unstable manifold associated with the unstable fixed point. However, if *dq* and *dp* are precisely along the direction of the λ_- eigenvector associated with the same unstable fixed point, the displacement between two nearby trajectories exponentially contracts rather than expands, as is clear from the fact $\lambda_- = 1/\lambda_+ < 1$. Hence there is also a stable manifold associated with an unstable fixed point. This result holds for any area-preserving map. The marginal case $\lambda_+ = \lambda_- = 1$ is indicative of the onset of chaos. A more detailed and extensive discussion of stability analysis can be found in the excellent book *Regular and Chaotic Dynamics* by Lichtenberg and Lieberman [7].

The basic picture discussed above is quite general in Hamiltonian systems. Of particular importance is the concept of stable and unstable manifolds associated with unstable periodic orbits. Trajectories along the stable manifold will be mapped toward the periodic orbit, whereas trajectories along the unstable manifold will be mapped away from the periodic orbit. It turns out that the union of segments of the stable and unstable manifolds is very useful in defining the reaction separatrix and calculating the flux crossing the separatrix in few-dimensional systems.

G. Bottlenecks in Few-Dimensional Systems

The KAM theorem demonstrates the existence of KAM tori when the perturbations to the motion are small. What happens when a nearly integrable Hamiltonian is strongly perturbed? For example, with increasing perturbation strength, what is the last KAM torus to be destroyed and how should we characterize the phase space structures when all KAM tori are destroyed? Using simple dynamical mapping systems, which can be regarded as Poincaré maps in Hamiltonian systems with two DOFs, MacKay, Meiss, and Percival [8,9] and Bensimon and Kadanoff [10] showed that the most robust KAM curve

against perturbation has a winding number associated with the golden mean, that is,

$$\frac{\omega_1}{\omega_2} = (1 + g) \tag{33}$$

where ω_1 and ω_2 are the frequencies, and

$$g = \frac{1}{2}(\sqrt{5} - 1) = \frac{1}{1 + \frac{1}{1 + \frac{1}{1 + \cdots}}} = 0.61803398\ldots \tag{34}$$

More importantly, they showed that even after the most robust KAM curve is destroyed, its remnants display highly fractal structures characteristic of a cantorus, thereby constituting strong bottlenecks to phase space transport. That is, although a classical trajectory is extremely sensitive to slight changes in its initial condition, this trajectory may still find it difficult to go from one phase space region to another through the cantorus. Qualitatively, this is because the exponential sensitivity of chaotic motion is a local property, whereas transport between disjoint phase space regions is a nonlocal phenomenon.

The existence of bottlenecks to Hamiltonian transport suggests that intramolecular energy flow can be highly nonergodic. Thus, accounting for the bottlenecks should greatly improve chemical reaction rate theories. For example, for the 4:1 resonance shown in Figs. 2 and 3, the intramolecular bottleneck should be located at

$$\frac{\omega_1}{\omega_2} = 4 + g \tag{35}$$

For the case in Fig. 4 the intramolecular bottleneck is expected to be associated with

$$\frac{\omega_1}{\omega_2} = 3 + g \tag{36}$$

H. Bottlenecks in Many-Dimensional Systems

In exact dynamics simulations the main difference between many-dimensional and few-dimensional systems is the requirement for computational resources. However, in the context of reaction rate theory the most relevant issue is how to understand and describe the qualitative differences between a few-dimensional topological structure and its many-dimensional analog. For example, given that the PSS in few-dimensional systems provides a powerful tool with which to analyze reaction dynamics, can we utilize the PSS in many-dimensional

systems? The answer is no, because in many-dimensional systems a Poincaré map on a surface of section is no longer an area-preserving map. Hence, it is unclear how to visualize and effectively analyze classical trajectories in a system with many DOFs.

It was shown above that KAM tori can separate a three-dimensional energy surface into disjoint regions. Trajectories on one side of a torus can never reach the other side. This simple picture does not hold in many-dimensional systems. To see this more clearly, consider a nearly integrable system with n DOFs. Its energy surface has dimension $2n - 1$. Thus any phase space structure that can separate this energy surface into two disconnected pieces must have a dimension of $2n - 2$. On the other hand, from the above-mentioned action-angle variable analysis, one sees that each KAM torus is characterized by n actions, so that they have dimension $2n - n = n$, far smaller than $2n - 2$ if $n \geq 3$. As such, KAM tori in many-dimensional systems no longer present structural barriers that restrict chaotic trajectories from visiting almost the entire energy surface. This phenomenon is called Arnold diffusion.

Arnold diffusion is typically slow if the system is not strongly chaotic, a case relevant to many unimolecular reactions. In this sense, although KAM tori no longer divide the energy surface into disjoint regions, their very existence still generates effective bottlenecks to phase-space transport. Furthermore, recent studies of many-dimensional reacting systems suggest that the golden mean cantori (taken in the sense of pairwise frequency ratios) continue to be strong bottlenecks to phase space transport. For example, Tersigni and Rice [32] examined the robustness of cantori in a system with two DOFs perturbed by a third DOF and found that the golden mean cantorus defined in terms of the first two DOFs remains a significant bottleneck in the full system. With a local frequency analysis approach, Martens, Davis, and Ezra [33] analyzed a three-DOF model of the OCS molecule and noticed the importance of the ratio between the O–C and C–S vibrational frequencies, shedding light on the slow chaotic transport observed in the same molecule [34]. Assuming that the most effective bottleneck is associated with a highly irrational pairwise frequency ratio, Zhao and Rice also considered a three-dimensional system and obtained fairly good results that will be reviewed later.

I. Normally Hyperbolic Invariant Manifold

An unstable periodic orbit is one-dimensional, being of dimension two less than the energy surface in systems with two DOFs. In an n-DOF system the energy surface is of dimension $2n - 1$. In such systems, Wiggins showed that the analog of unstable periodic orbits is the so-called ''normally hyperbolic invariant manifold'' (NHIM) of dimension $2n - 3$ [20,21]. Trajectories slightly displaced from an NHIM can be analyzed using a many-dimensional stability analysis. The

expansion and contraction rates normal to an NHIM will dominate those tangent to it. Wiggins demonstrated that an NHIM, if it exists, is structurally stable—that is, robust against perturbations. Wiggins further proved that there always exist NHIMs associated with each individual many-dimensional resonance condition, that is,

$$\mathbf{m} \cdot \boldsymbol{\omega} = m_1\omega_1 + m_1\omega_2 + \cdots + m_n\omega_n = 0 \tag{37}$$

where the m_i are integers not all of which are zero, and ω_i is the frequency associated with the ith DOF.

Similar to unstable periodic orbits, an NHIM has stable and unstable manifolds that are of dimension $2n-2$ and are also structurally stable. Note that a union of the segments of the stable and unstable manifolds is also of dimension $2n-2$, which is only of dimension one less than the energy surface. Hence, as far as dimensionality is concerned, it is possible for a combination of the stable and unstable manifolds of an NHIM to divide the many-dimensional energy surface so that reaction flux can be defined. However, unlike the few-dimensional case in which a union of the stable and unstable manifolds necessarily encloses a phase space region, a combination of the stable and unstable manifolds of an NHIM may not do so in a many-dimensional system. This phenomenon is called "homoclinic tangency," and it is extensively discussed in a recent review article by Toda [17].

To be more specific, consider a system with the following Hamiltonian:

$$\begin{aligned} H = {} & \sum_{i=1}^{n-1} \frac{\omega_i}{2}(p_i^2 + q_i^2) + \lambda q_n p_n + f_1(q_1, q_2, \ldots, q_{n-1}, p_1, p_2, \ldots, p_{n-1}, q_n p_n) \\ & + f_2(q_1, q_2, \ldots, q_{n-1}, p_1, p_2, \ldots, p_{n-1}) \end{aligned} \tag{38}$$

where q_i and p_i are conjugate canonical variables, and

$$f_1(q_1, q_2, \ldots, q_{n-1}, p_1, p_2, \ldots, p_{n-1}, 0) = 0 \tag{39}$$

Wiggins et al. [22] pointed out that one can always locally transform a Hamiltonian to the form of Eq. (1.38) if there exists a certain type of saddle point. Examination of the associated Hamilton's equations of motion shows that $q_n = p_n = 0$ is a fixed point that defines an invariant manifold of dimension $2n-2$. This manifold intersects with the energy surface, creating a $(2n-3)$-dimensional invariant manifold. The latter invariant manifold of dimension $2n-3$ is an excellent example of an NHIM. More interesting, in this case the stable and unstable manifolds of the NHIM, denoted by W^s and W^u,

respectively, can be explicitly constructed by a simple stability analysis. One finds

$$W^s: \quad \sum_{i=1}^{n-1} \frac{\omega_i}{2}(p_i^2 + q_i^2) + f_2 = \text{constant} > 0, \qquad q_n = 0 \tag{40}$$

$$W^u: \quad \sum_{i=1}^{n-1} \frac{\omega_i}{2}(p_i^2 + q_i^2) + f_2 = \text{constant} > 0, \qquad p_n = 0 \tag{41}$$

It should always be remembered that this representation is a local picture of the dynamics. A general way of constructing an NHIM is still unknown and may not exist at all.

III. MAPPING MODELS OF UNIMOLECULAR FRAGMENTATION

A. Two-Dimensional Free Particle in a Morse-like Kicking Field

Gaspard and Rice [35] were the first to use simple mapping models to simulate the dynamics of molecular fragmentation. Consider first a model describing a free particle periodically kicked by a Morse-like potential. The Hamiltonian is given by

$$H = \frac{P^2}{2m} + TG(X) \sum_{n=-\infty}^{\infty} \delta(t - nT) \tag{42}$$

where the kicking potential is given by

$$G(X) = D[1 - \exp(-\alpha X)^2] \tag{43}$$

with

$$\lim_{X \to \infty} \frac{dG(X)}{dX} = 0 \tag{44}$$

This choice of $G(X)$ is designed to mimic some aspects of a molecular process. The classical phase space is two-dimensional. Let (X_n, P_n) be the position and momentum of the particle just before the nth kick. Then the kicking field induces an area-preserving map

$$P_{n+1} = P_n - T\frac{dG(X_n)}{dX_n} \tag{45}$$

$$X_{n+1} = X_n + \frac{T}{m}P_{n+1} \tag{46}$$

To simplify the matter, the scaling transformation

$$p_n = \frac{\alpha T}{m} P_n, \qquad q_n = \alpha X_n \tag{47}$$

is introduced, resulting in the difference equations

$$p_{n+1} = p_n + d[\exp(-2q_n) - \exp(-q_n)] \tag{48}$$

$$q_{n+1} = q_n + p_{n+1} \tag{49}$$

It is seen that after the scaling the map from (p_n, q_n) to (p_{n+1}, q_{n+1}) depends on only one parameter, $d = 2\alpha^2 T^2 D/m$. To be as realistic as possible, we assume $d > 0$.

The map of Eqs. (48) and (49) has two fixed points: $(q,p) = (0,0)$ and $(q,p) = (\infty, 0)$. Their stabilities are determined by the eigenvalues Λ of the linearized mapping, which are given by

$$\det(\mathbf{J} - \Lambda \mathbf{I}) = 0 \tag{50}$$

where $\mathbf{J}$ is the Jacobian of the mapping. At the fixed point $(q,p) = (0,0)$ the eigenvalues are

$$\Lambda_{\pm} = \frac{1}{2}\left[2 - d \pm \sqrt{d(d-4)}\right] \tag{51}$$

When $0 < d < 4$, these two eigenvalues can be written as

$$\Lambda_{\pm} = \exp(\pm i 2\pi\rho) \tag{52}$$

with $d = 2 - 2\cos(2\pi\rho)$. Suppose now ρ can be expressed as the ratio of two integer numbers, say, m_1/m_2. Then after m_2 iterations of this map one has $(\Lambda_{\pm})^{m_2} = 1$. That is, after m_2 rotations on the two-dimensional plane a small change in the initial condition returns exactly to its starting value. As such, this new expression for $\Lambda_{\pm}$ is indicative of resonances. These resonances are arranged in the parameter space in a monotone sequence between $\rho = 1/\infty$ and $\rho = 1/2$. Of particular importance are the low-order resonances associated with $d = 2$ and $d = 3$.

In most cases of $0 < d < 4$, there are a set of bounded trajectories surrounding the stable fixed point and forming the main quasi-periodic islands. These regular trajectories are bounded by the largest invariant island. Outside the largest island there also exist smaller quasi-periodic islands, forming an invariant set of positive Lebesgue measure in the two-dimensional phase space. Besides, there exists a Cantor-like invariant set of unstable trajectories

wandering between these small quasi-periodic islands. This latter set is the repellor of the system that controls the escape dynamics.

By plotting only the trajectories that remain at a finite distance over long times, the global invariant set can be constructed, as shown in Fig. 5 for different values of d. Seen in Fig. 5a are large regular islands around $p = q = 0$ for $d = 1.8$. Then, for the case of $d = 2$ shown in Fig. 5b, there is a catastrophic collapse of the global invariant set when the center $p = q = 0$ undergoes a low-order resonance. A large island reappears as the value of d further increases, as shown in Fig. 5c.

Also interesting is the dynamical behavior associated with the fixed point at infinity, that is, $(q, p) = (\infty, 0)$. Here we introduce the concept of homoclinic orbit, which is a trajectory that goes to an unstable fixed point in the past as well as in the future. A homoclinic orbit thus passes the intersection between the unstable and stable manifolds of a particular fixed point. Indeed, as shown in Fig. 6, these manifolds generate a so-called homoclinic web. In particular, Fig. 6a displays a Smale horseshoe giving a two-symbol subdynamics, indicating that the fixed point $(\infty, 0)$ is not a saddle. Nevertheless, it is still unstable with distinct stable and unstable manifolds, with its dynamics much slower than that for a saddle. Figure 6b shows an example of a numerical plot of the stable and unstable manifolds.

Gaspard and Rice also considered a kicking field with several minima and maxima such that the mapping has several bottlenecks, with each bottleneck associated with particular fixed points. The existence of several bottlenecks allows their model to better mimic some properties of intramolecular energy flow. Specifically, they chose

$$\frac{dg}{dq} = -de^{-q}(e^{-q} - r)(e^{-q} - s)(e^{-q} - w) \tag{53}$$

In this case, there are four fixed points, located at $(\infty, 0)$, $(-\ln r, 0)$, $(-\ln s, 0)$, $(-\ln w, 0)$, respectively. One example of such a map is given by

$$p_{n+1} = p_n + de^{-q_n}(e^{-q_n} - 1)(e^{-q_n} - 1/2)(e^{-q_n} - 1/4) \tag{54}$$

$$q_{n+1} = q_n + p_{n+1} \tag{55}$$

with the two stable fixed points $(0, 0)$ and $(\ln 4, 0)$ and the intermediate saddle point $(\ln 2, 0)$. The number of fixed pointed can be reduced by one if we choose, for example, $w = 0$ instead of $w = 1/4$. Then the following map is obtained:

$$p_{n+1} = p_n + de^{-2q_n}(e^{-q_n} - 1)(e^{-q_n} - 1/2) \tag{56}$$

$$q_{n+1} = q_n + p_{n+1} \tag{57}$$

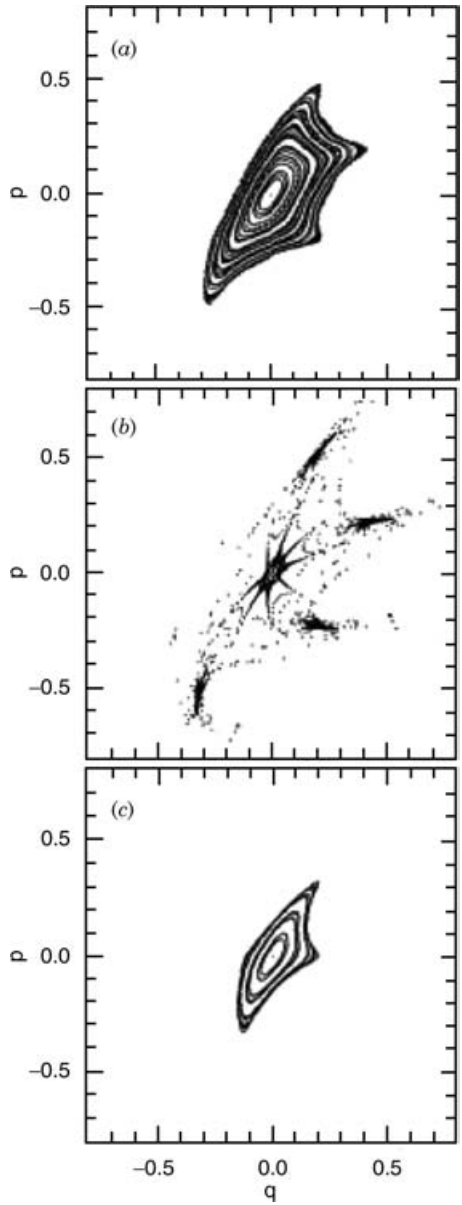

Figure 5. Phase portrait of the Gaspard–Rice two-dimensional mapping with the two fixed points at $(0, 0)$ and $(\infty, 0)$. (*a*) The portrait is obtained with 54 trajectories and 400 iterations; $d = 1.8$. (*b*) Same as in (*a*) except for $d = 2$ with 48 trajectories. (*c*) Same as in (*a*) except for $d = 2.2$ with 22 trajectories. [From P. Gaspard and S. A. Rice, *J. Phys. Chem.* **93**, 6947 (1989).]

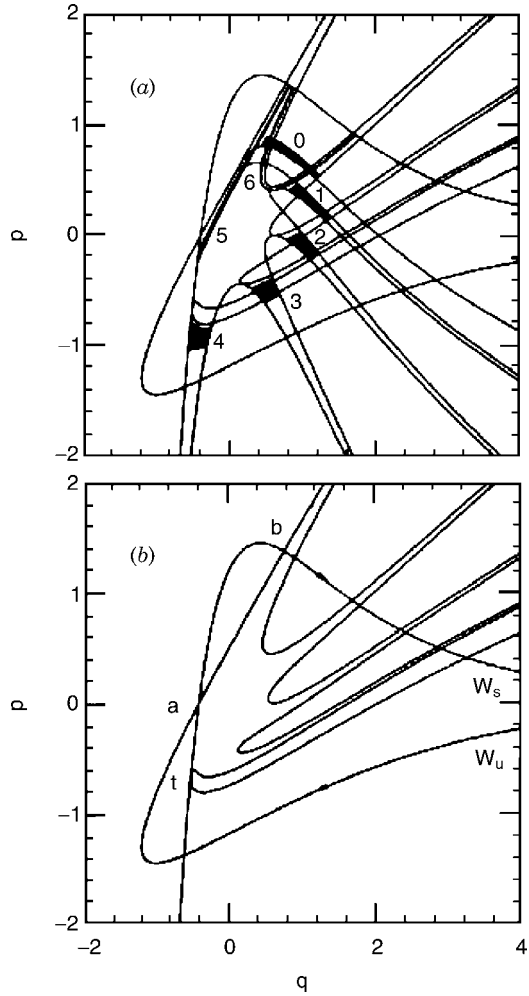

Figure 6. (*a*) Formation of a Smale horseshoe after six iterations starting from the domain labeled 0 under the Gaspard–Rice two-dimensional mapping with $d = 1.8$ and two fixed points at $(0, 0)$ and $(\infty, 0)$. The curves are the stable and unstable manifolds forming the homoclinic web. (*b*) The stable manifold W_s and the unstable manifold W_u. Their intersections a and b define two distinct homoclinic orbits. Another homoclinic orbit is defined by the point t where W_s is tangent to W_u. [From P. Gaspard and S. A. Rice, *J. Phys. Chem.* **93**, 6947 (1989).]

with one stable fixed point at $(0, 0)$ and one saddle point at $(\ln 2, 0)$ for $0 < d < 8$. A standard homoclinic structure can be linked with this saddle, and it mimics an intramolecular bottleneck. Also observed are resonances associated with the center point $(0, 0)$, catastrophic collapses of the invariant sets, and a

period-doubling bifurcation at $d = 8$ that generates a period-2 orbit of the center type. The phase space structures for the various cases are shown in Fig. 7.

B. Four-Dimensional Free Rotor in a Morse-like Kicking Field

Gaspard and Rice [35] also proposed a four-dimensional map in order to study Hamiltonian systems with Arnold diffusion. The model Hamiltonian is a free rotor in a Morse-like kicking field and takes the following form:

$$H = \frac{L^2}{2I} + \frac{P^2}{2m} + TG(\theta, X) \sum_{n=-\infty}^{\infty} \delta(t - nT) \tag{58}$$

The kick amplitude $G(\theta, X)$ is assumed to vanish at large distance X. Note that the rotor may escape from the kicking field. Gaspard and Rice studied a kicking field defined by

$$G(\theta, X) = D\left[(1 + g\cos\theta)e^{-2\alpha X} - 2e^{-\alpha X}\right] \tag{59}$$

with $D > 0$ and $|g| < 1$ in order for the motion be stable in the repulsive part of the field. With a proper scaling one obtains

$$l_{n+1} = l_n + c\sin\theta_n e^{-2q_n} \tag{60}$$

$$\theta_{n+1} = \theta_n + l_{n+1} \tag{61}$$

$$p_{n+1} = p_n + d\left[(1 + g\cos\theta_n)e^{-2q_n} - 2e^{-q_n}\right] \tag{62}$$

$$q_{n+1} = q_n + p_{n+1} \tag{63}$$

as a four-dimensional map induced by Hamilton's equations of motion. This map is pseudosymplectic in the sense that

$$\mathbf{J}^{\mathrm{t}}\boldsymbol{\omega}\mathbf{J} = \boldsymbol{\omega} \tag{64}$$

where $\mathbf{J}$ is the Jacobian

$$\mathbf{J} = \frac{\partial(l_{n+1}, p_{n+1}, \theta_{n+1}, q_{n+1})}{\partial(l_n, p_n, \theta_n, q_n)} \tag{65}$$

and the $\boldsymbol{\omega}$ matrix is given by

$$\boldsymbol{\omega} = \begin{pmatrix} 0 & 0 & \alpha & 0 \\ 0 & 0 & 0 & \beta \\ -\alpha & 0 & 0 & 0 \\ 0 & -\beta & 0 & 0 \end{pmatrix} \tag{66}$$

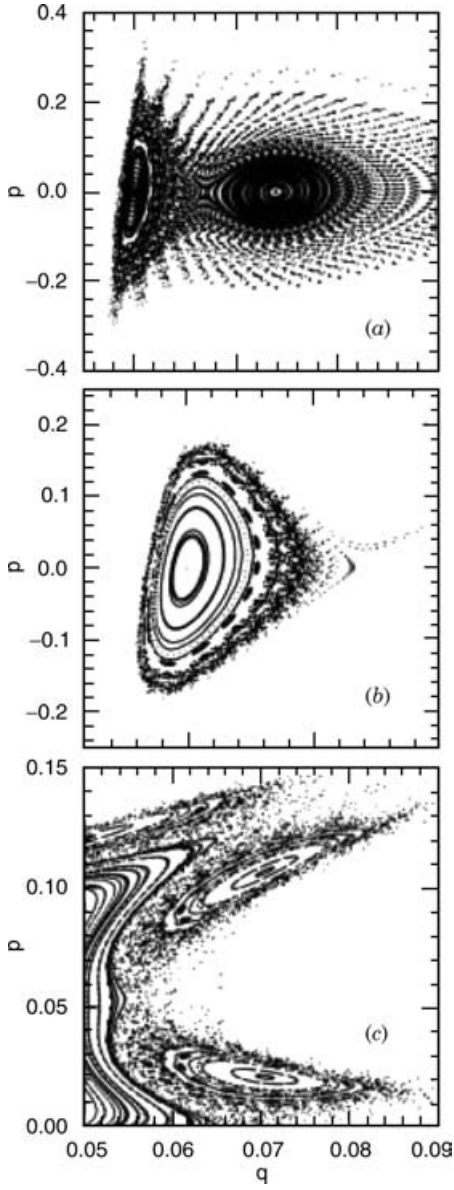

Figure 7. Phase portrait of the Gaspard–Rice two-dimensional mapping model. (*a*) The mapping has two stable fixed points at $(0, 0)$ and $(\ln 4, 0)$ and one intermediate saddle point at $(\ln 2, 0)$; $d = 2$. (*b*) The mapping has one stable fixed point at $(0, 0)$ and one saddle point at $(\ln 2, 0)$; $d = 1$. (*c*) The mapping has one stable fixed point at $(0, 0)$ and one saddle point at $(\ln 2, 0)$; $d = 5$. [From P. Gaspard and S. A. Rice, *J. Phys. Chem.* **93**, 6947 (1989).]

with $2c\alpha = dg\beta$. Of course, this map preserves the phase space volume, as is evident from $\det(\mathbf{J}) = 1$.

There are two fixed points at a finite distance. The first one is at $l = 0$, $\theta = 0$, $p = 0$, $q = \ln(1 + g)$, where the four stability eigenvalues are

$$\Lambda_{1,2} = 1 + \frac{c}{2(1+g)^2} \pm \left(\frac{c}{(1+g)^2} \left[1 + \frac{c}{4(1+g)^2} \right] \right)^{1/2} \tag{67}$$

$$\Lambda_{3,4} = 1 - \frac{d}{2(1+g)} \pm \left(\frac{d}{1+g} \left[\frac{d}{4(1+g)} - 1 \right] \right)^{1/2} \tag{68}$$

with

$$\Lambda_1 \Lambda_2 = 1, \qquad \Lambda_3 \Lambda_4 = 1 \tag{69}$$

The second one is at $l = 0$, $\theta = 0$, $p = 0$, $q = \ln(1 - g)$, where the four stability eigenvalues are

$$\Lambda_{1,2} = 1 - \frac{c}{2(1+g)^2} \pm \left(\frac{c}{(1-g)^2} \left[\frac{c}{4(1-g)^2} - 1 \right] \right)^{1/2} \tag{70}$$

$$\Lambda_{3,4} = 1 - \frac{d}{2(1+g)} \pm \left(\frac{d}{1-g} \left[\frac{d}{4(1-g)} - 1 \right] \right)^{1/2} \tag{71}$$

The decay dynamics of this map is intended to mimic the process of molecular fragmentation. Gaspard and Rice calculated the decay of an ensemble of particles for varying values of d. Figure 8 shows the escape time as a function

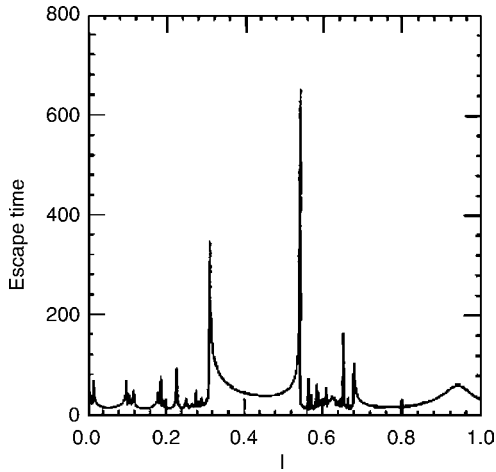

Figure 8. Escape time function as a function of l in the Gaspard–Rice four-dimensional mapping for $d = 3$, $c = g = 0.1$, with the initial condition $p = q = 0$ and $\theta = 1$. [From P. Gaspard and S. A. Rice, *J. Phys. Chem.* **93**, 6947 (1989).]

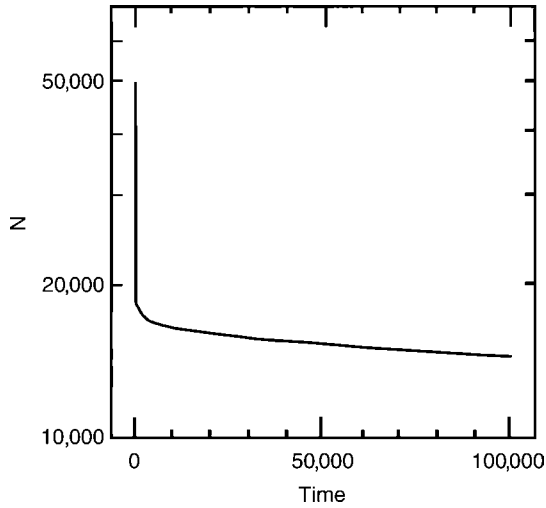

Figure 9. Population decay of an ensemble of 50,000 particles under the four-dimensional mapping with $d = 2$ and $c = g = 0.1$. The initial ensemble is uniformly distributed in the rectangle ($\theta_1 = -1.0$, $\theta_2 = 1.0$, $I_1 = 0.0$, $I_2 = 2.0$) of the $q = p = 0$ plane. [From P. Gaspard and S. A. Rice, *J. Phys. Chem.* **93**, 6947 (1989).]

of I in the four-dimensional mapping for $d = 3$. The decay is seen to be rather fast and the escape time as a function of I displays regular peaks. However, for some other values of d (e.g., $d = 2$) the decay is much slower, and the escape time is a highly irregular function of initial conditions. This can be explained in terms of the slow depletion of the quasi-invariant set. Indeed, as shown in Fig. 9 the decay dynamics was found to occur over two different time scales and could be approximated by a bi-exponential curve for intermediate times. This suggests the existence of long-time correlations in the dynamics of molecular fragmentation. However, it is possible that long-time correlations do not play an important role in a classical reaction rate theory because the subtle dynamical behavior on the long-time scale will also be strongly affected by collisions, emission of radiation, and probably quantum interference effects.

IV. THEORY OF UNIMOLECULAR PREDISSOCIATION

A. Davis–Gray Analysis

The most important element of the Davis–Gray theory of unimolecular reaction rate is the identification of bottlenecks to intramolecular energy flow and the intermolecular separatrix to molecular fragmentation. Davis and Gray's work was motivated by the discovery of bottlenecks in chaotic transport by MacKay, Meiss, and Percival [8,9] and by Bensimon and Kadanoff [10].

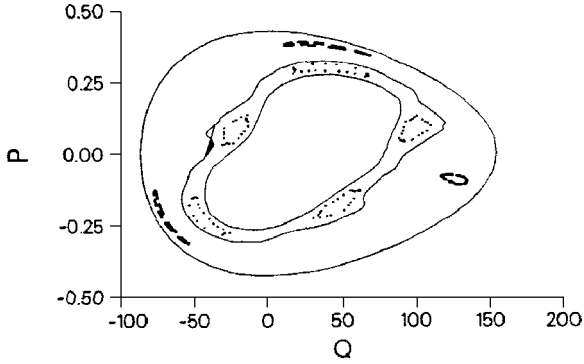

Figure 10. Poincaré surface of section for collinear OCS relaxation at $E = 20{,}000\ \text{cm}^{-1}$. It shows three major quasi-periodic regions, the resonance islands, the location of the dividing surface for intramolecular energy transfer, and a typical turnstile. [From M. J. Davis, *J. Chem. Phys.* **83**, 1016 (1985).]

The first application of transport bottlenecks to a molecular system was in the study of vibrational relaxation of a model OCS molecule with two DOFs. Davis [36] found that the correct location of the bottleneck requires finding a set of unstable orbits that have a set of resonance conditions

$$\frac{\omega_{CO}}{\omega_{CS}} = \frac{3}{1}, \frac{5}{2}, \frac{8}{3}, \frac{13}{5}, \frac{21}{8}, \frac{34}{13}, \ldots \tag{72}$$

This series of resonance conditions converges to $2.618\ldots$, implying that the most important bottleneck to intramolecular energy transfer is determined by a golden mean cantorus, that is,

$$\omega_{CO} = (2 + g)\omega_{CS} = 2.618\ldots\omega_{CS} \tag{73}$$

where ω_{CO} and ω_{CS} are the frequencies of the CO and CS stretches. The phase space structure of this OCS bottleneck on a PSS is shown in Fig. 10.

The bottleneck effects can be better understood by visualizing the PSS at different times, as shown in Fig. 11. Seen there are three disjoint regions separated by closed curves. The middle curve is approximately the last KAM curve separating two primary resonance zones. The randomly positioned dots shown in Fig. 11a represent an ensemble of classical trajectories that are completely located at the outermost region, called region I. At a later time the trajectories pass a barrier separating region I and region II and enter region II. Since the most inner part is associated with purely regular motion, the trajectories will never get into that region.

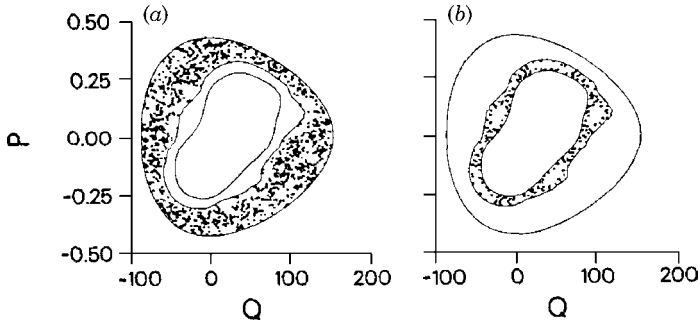

Figure 11. Poincaré surfaces of section for collinear OCS relaxation at $E = 20{,}000\ \text{cm}^{-1}$ at two different times. [From M. J. Davis, *J. Chem. Phys.* **83**, 1016 (1985).]

After properly locating the exact dividing surface, Davis used the following equations to describe the population transfer between the two regions:

$$\frac{dN_1}{d\tau} = -\kappa_1 N_1 + \kappa_2 N_2 \tag{74}$$

$$\frac{dN_2}{d\tau} = \kappa_1 N_1 - \kappa_2 N_2 \tag{75}$$

where N_1 and N_2 refer to the populations in region I and region II, and κ_1 and κ_2 are given by the ratios

$$\kappa_1 = \frac{A_t}{A_1}, \qquad \kappa_2 = \frac{A_t}{A_2} \tag{76}$$

where A_t is the flux in or flux out, and A_1 and A_2 represent the areas of region I and region II, respectively. The flux can be exactly calculated by examining the area of the so-called turnstile, a phase space structure that will be explained in detail below. The total population N is the sum of the populations in the two regions

$$N = N_1 + N_2 \tag{77}$$

Equations (74) and (75) can be easily solved to yield

$$\frac{N_1}{N} = \frac{1}{k}\left(k_1 e^{-kt} + k_2\right) \tag{78}$$

$$\frac{N_2}{N} = \frac{k_1}{k}\left(1 - e^{-kt}\right) \tag{79}$$

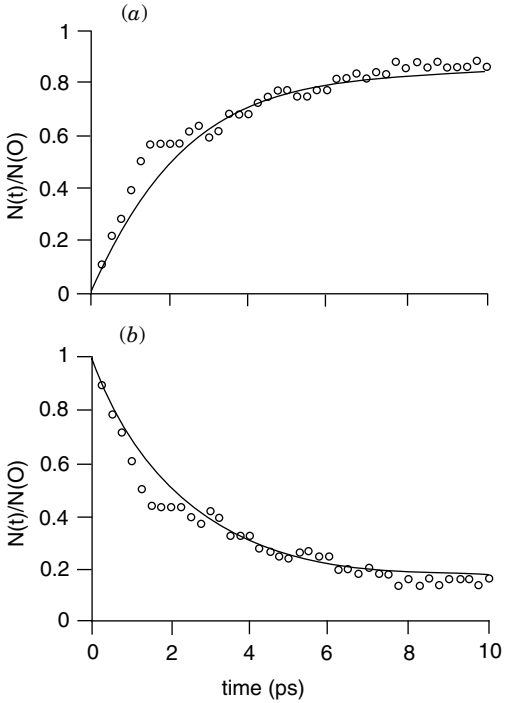

Figure 12. Population relaxation of linear OCS with energy $E = 20,000\ \text{cm}^{-1}$. The circles are the results of numerical simulation and the solid line represents the results of the theoretical kinetics model. The initial population is assumed to be in region II. The top panel is the population versus time in region I, and the lower panel is the population versus time in region II. [From M. J. Davis, *J. Chem. Phys.* **83**, 1016 (1985).]

where k_1, k_2, and k are

$$k_1 = \frac{\kappa_1}{\tau_1}, \qquad k_2 = \frac{\kappa_2}{\tau_2}, \qquad k = \frac{\kappa_1 + \kappa_2}{\tau_1 + \tau_2} \tag{80}$$

The time scales characterized by τ_1 and τ_2 give the mean passage time through the dividing surface. Figure 12 shows the time-dependent populations of regions I and II for OCS relaxation. The circles denote the numerical results and the solid line is given by the above kinetics model. The initial population is assumed to be in region II. The top panel is the population versus time in region I, and the lower panel is the population versus time in region II. These comparisons demonstrate that the Davis–Gray kinetics model is very successful.

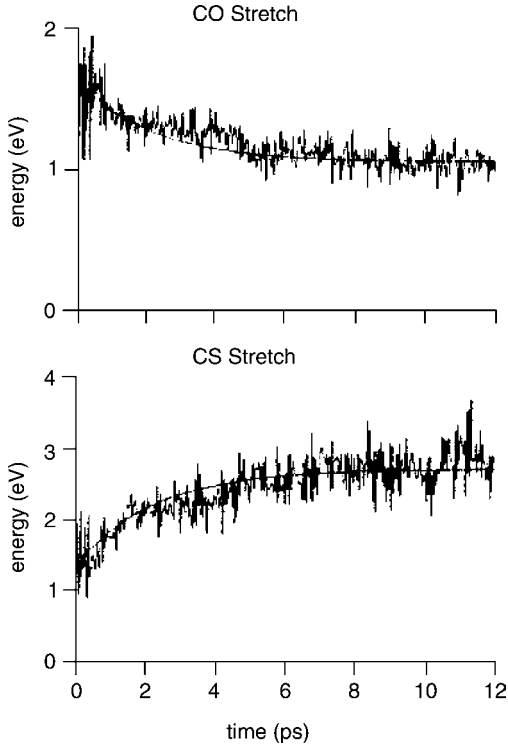

Figure 13. Energy relaxation of linear OCS at $E = 20{,}000\ \text{cm}^{-1}$. The top panel is for region I, and the lower panel is for region II. The smooth line is from the theoretical model calculation. [From M. J. Davis, *J. Chem. Phys.* **83**, 1016 (1985).]

The energy relaxation associated with each of the regions can also be predicted, and the results are displayed in Fig. 13 in a comparison with numerical experiments. Again, there is impressive agreement between the numerical results and the theoretical calculations.

Davis and Gray then successfully extended Davis's analysis to van der Waals molecule predissociation reactions such as

$$\text{HeI}_2(v) \rightarrow \text{He} + \text{I}_2(v' < v) \tag{81}$$

As is typical for van der Waals molecules, there is a very large difference between the I_2 and He–I_2 stretching frequencies. Depending upon the vibrational energy associated with I_2, the effective frequency of He–I_2 stretching is about four to five times smaller than that of I_2. A discrepancy in vibrational frequencies of this magnitude greatly inhibits intramolecular energy transfer and is expected

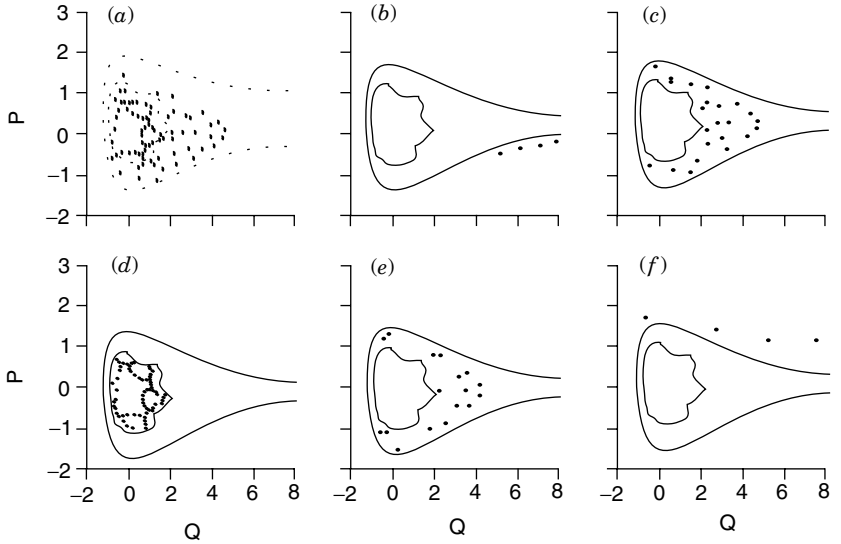

Figure 14. An HeI_2 surface of section for an unstable trajectory which forms a collision complex. The total energy is $-2661.6\ cm^{-1}$. Also shown are the reaction separatrix and the intramolecular bottleneck. (*a*) Graph showing the full dynamics of the trajectory. (*b*)–(*f*) Graphs illustrating the trajectory over five consecutive time ranges. These graphs are arranged to demonstrate the manner in which the trajectory moves with respect to the bottleneck and the separatrix. [From M. J. Davis and S. K. Gray, *J. Chem. Phys.* **84**, 5389 (1986).]

to lead to a breakdown of the RRKM assumption of fast energy randomization. This is indeed the case for the predissociation of HeI_2. To simplify the analysis of the nonlinear dynamics, Davis and Gray [11] adopted a simple model of the molecule. Specifically, they assumed that the equilibrium geometry of HeI_2 is T-shaped and that the I–I and He–I_2 stretches describe all the vibrational motion. The rotation of the molecule, along with its influence on the fragementation kinetics, is neglected. Davis and Gray then located the dividing surface for fragmentation and the bottlenecks to intramolecular energy flow, and they calculated the fluxes across these surfaces using this model Hamiltonian. Both the dividing surface for fragmentation and the bottleneck to energy transfer on a PSS are shown in Fig. 14.

Davis and Gray also demonstrated the existence of a series of intramolecular energy transfer bottlenecks, each corresponding to the breakup of a KAM torus. For example, for I_2 in the vibrational state $v = 20$ they found intramolecular bottlenecks associated with frequency ratios equal to $(3 + g)$ and up. However, Davis and Gray found that the last "golden mean torus" to be broken up is the most effective bottleneck to intramolecular energy transfer and is therefore

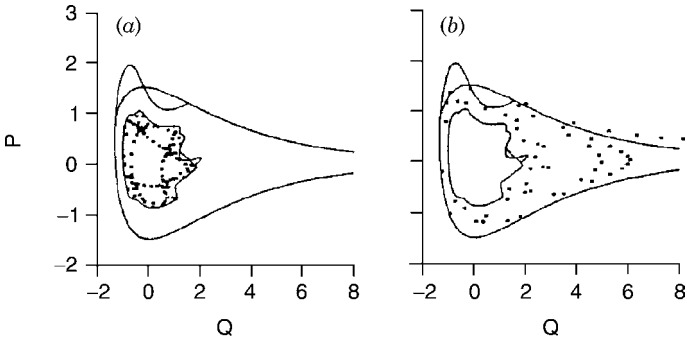

Figure 15. A trajectory that undergoes predissociation with the total energy of the system $E = -2661.6\ \text{cm}^{-1}$. In (*a*) the trajectory is trapped inside an intramolecular bottleneck and escapes in (*b*) and finally dissociates. [From M. J. Davis and S. K. Gray, *J. Chem. Phys.* **84**, 5389 (1986).]

the only one that needs to be considered to model intramolecular relaxation. Figure 15 illustrates the most significant intramolecular bottleneck, the turnstile used for calculating the flux, and a trajectory undergoing predissociation, with the initial vibrational state of I_2 given by $v = 20$ and the total energy $E = -2661.6\ \text{cm}^{-1}$.

With only the most effective intramolecular energy transfer bottleneck accounted for, a simple kinetics model describing the dynamics of He–I_2 predissociation can be defined:

$$\frac{dN_1}{dt} = -k_1 N_1 \tag{82}$$

$$\frac{dN_2}{dt} = k_1 N_1 - k_2 N_2 \tag{83}$$

Here N_1 is the population of region I—that is, outside the regions of quasi-periodic motion but inside the bottleneck to intramolecular energy transfer; k_1 is the rate constant for trajectories that leave region I; N_2 is the population of region II—that is, outside the bottleneck but inside the reaction separatrix; and k_2 is the corresponding escape rate constant. Integrating Eqs. (82) and (83) gives the time dependence of the populations:

$$\frac{N_1(t)}{N_T} = f_1 e^{-k_1 t} + f_q \tag{84}$$

$$\frac{N_2(t)}{N_T} = \frac{1}{k_d}\left[k_1 f_1 e^{-k_1 t} + (k_d f_2 + k_1 f_1) e^{-k_2 t}\right] \tag{85}$$

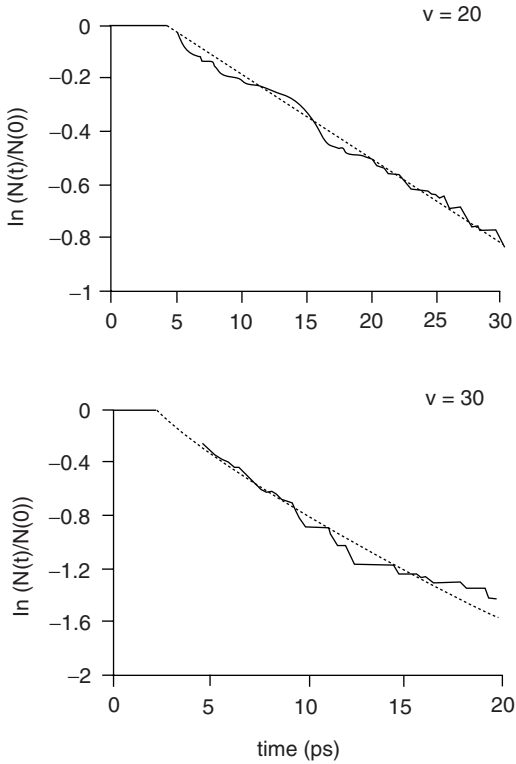

Figure 16. The T-shaped HeI_2 vibrational predissociation time dependence with the initial vibrational state of I_2 given by $v = 20$ and $v = 30$. $N = N_1 + N_2$. The dashed lines represent results from theoretical kinetics calculations, and the solid lines represent results from trajectory calculations. [From M. J. Davis and S. K. Gray, *J. Chem. Phys.* **84**, 5389 (1986).]

where N_T is the total number of trajectories, f_1 is the fraction of phase space points that start in region I at $t = 0$, f_2 is the fraction of phase space points that start in region II at $t = 0$, f_q is the fraction of phase space points corresponding to quasi-periodic motion, and

$$k_d = k_2 - k_1 \tag{86}$$

This kinetics model was tested against the numerically exact classical trajectory calculations for two initial vibrational states of I_2, namely, $v = 20$ and $v = 30$. The results are shown in Fig. 16. In particular, in the case of $v = 20$ the theoretical result fits the numerical data extremely well.

It is worth mentioning that Davis and Gray also found that at low energy, for example, when I_2 is initially in a vibrational state with $v < 5$, no classical dissociation occurs. Furthermore, if I_2 is initially in a vibrational state with $20 > v > 5$, the dynamics appears to be so complicated that including only one intramolecular bottleneck does not suffice. Indeed, in the case of $v = 10$ Davis and Gray used two intramolecular bottlenecks to model the HeI_2 fragmentation reaction. The two bottlenecks on a PSS are illustrated in Fig. 17. It is seen that

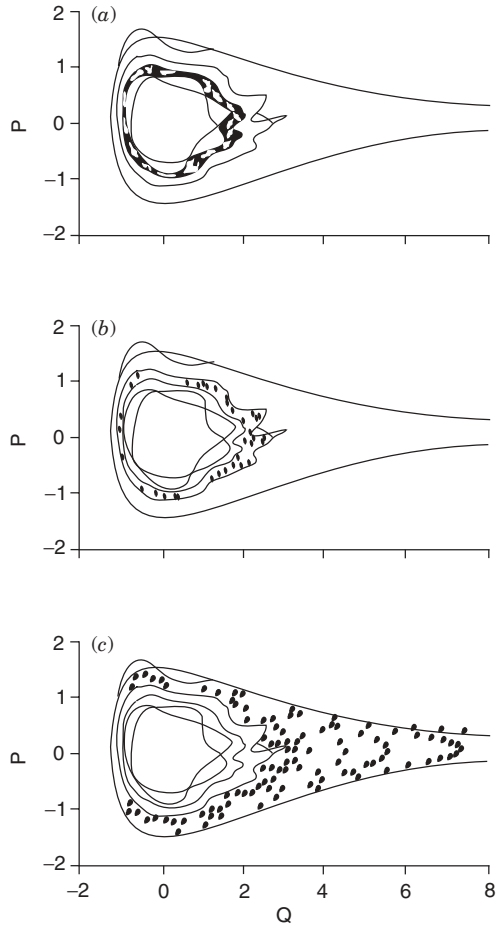

Figure 17. The Poincaré surface of section for T-shaped HeI_2 with the initial vibrational state of I_2 given by $v = 10$. Two bottlenecks to intramolecular energy transfer are shown, together with a 5:1 resonance zone and the dissociation dividing surface. From top to bottom the figures show how trajectories escape the first and then the second intramolecular bottlenecks. The bottom panel shows trajectories passing the separatrix for dissociation. [From M. J. Davis and S. K. Gray, *J. Chem. Phys.* **84**, 5389 (1986).]

trajectories have to escape the first and then the second intramolecular bottleneck before passing the dividing surface for dissociation.

B. The Gray–Rice–Davis ARRKM Theory

The Davis–Gray theory teaches us that by retaining the most important elements of the nonlinear reaction dynamics it is possible to accurately locate the intramolecular bottlenecks and to have an exact phase space separatrix as the transition state. Unfortunately, even for systems with only two DOFs, there may be considerable technical difficulties associated with locating the exact bottlenecks and the separatrix. Exact calculations of the fluxes across these phase space structures present more problems. For these reasons, further development of unimolecular reaction rate theory requires useful approximations.

Gray, Rice, and Davis [12] developed an alternative RRKM (ARRKM) theory in an attempt to simplify the Davis–Gray theory for van der Waals predissociation reactions. Specifically, they replaced the exact separatrix with an approximate phase space dividing surface by dropping a number of small terms in the system Hamiltonian, and they replaced the exact mapping that defines the flux across the true separatrix with an analytic treatment of the flux across the approximate separatrix. This simplification is schematically presented in Fig. 18.

In addition, the ARRKM theory is restricted to the energy regime in which the initial energy of the diatom is large (corresponding to a high-lying vibrational state). Hence, it can be assumed that the rates of crossing the cantori are much greater than that of crossing the separatrix. This separation of time scales being the case, the rate of fragmentation is solely determined by the rate of crossing the separatrix.

Briefly, the ARRKM theory represents the microcanonical rate constant in the form

$$k(E) = \frac{1}{N_S} \int d\mathbf{q} \int d\mathbf{p}\, \delta(S) \dot{S} \theta(S) \delta(E - H) \tag{87}$$

where

$$N_S = \int d\mathbf{q} \int d\mathbf{p}\, \theta[-S(x,p)] \delta(E - H) \tag{88}$$

Here H is the full system Hamiltonian, E is the system energy, $S(\mathbf{q}, \mathbf{p}) = 0$ defines the separatrix, $\dot{S}$ denotes the time derivative on the separatrix, $\delta(E - H)$ defines the surface of constant energy, and $\theta(S)$ is the Heaviside step function. Note that in essence the ARRKM theory belongs to the class of generalized variational transition state theories. Indeed, if the separatrix is chosen to be the conventional dividing surface in the configuration space, then the ARRKM theory reduces to RRKM theory. However, the phase space separatrix defined in

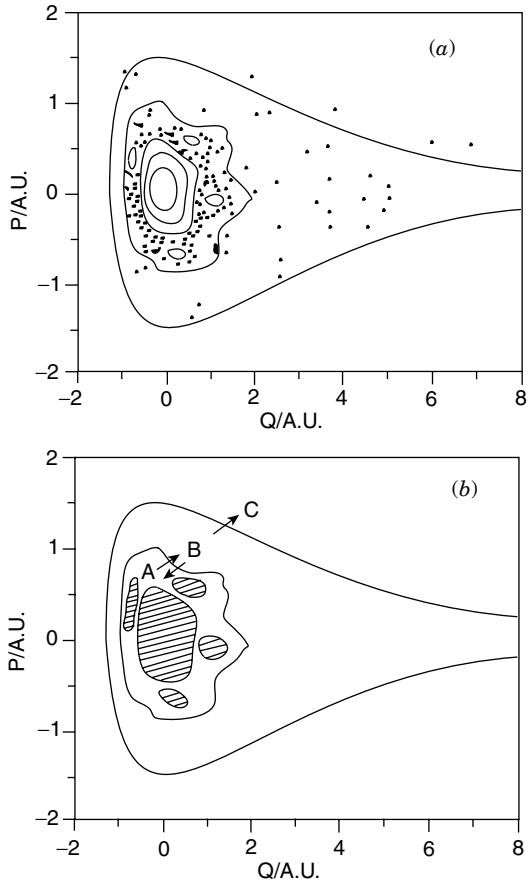

Figure 18. (*a*) A schematic composite surface of section for nonrotating T-shaped HeI_2. (*b*) Idealization of surface of section indicating flow out of various phase-space regions. The hatched areas represent regions of quasi-periodic motion. [From S. K. Gray, S. A. Rice, and M. J. Davis, *J. Phys. Chem.* **90**, 3470 (1986).]

the ARRKM theory does not necessarily pass through the conventional configuration space transition state.

To be more specific, consider again the two-DOF, nonrotating, T-shaped model van der Waals molecule HeI_2 studied by Davis and Gray. The system Hamiltonian is

$$H = \frac{P^2}{2\mu} + \frac{p^2}{2m} + V(R, r) \tag{89}$$

with

$$V(R, r) = 2V_{\text{He–I}}(R_{\text{He–I}}) + V_{\text{I–I}}(r) \tag{90}$$

and

$$R_{\text{He–I}} = \sqrt{(R^2 + r^2/4)} \tag{91}$$

where R is the van der Waals bond length (also the reaction coordinate), r is the I–I bond length, $V_{\text{He–I}}(R_{\text{He–I}})$ is the potential for the He–I interaction, and $V_{\text{I–I}}(r)$ is the I_2 stretching potential, both taken to be Morse functions. The ARRKM theory uses the following zeroth-order phase space separatrix

$$S(R, P) = \frac{P^2}{2\mu} + V_R(R) = 0 \tag{92}$$

With this simplification, Gray, Rice, and Davis obtained reasonably accurate values for the predissociation rate constant as a function of initial vibrational excitation. The rate constant thus obtained is larger than that from exact trajectory calculations by about a factor of two. By contrast, the RRKM theory would give a rate constant that is about three orders of magnitude larger than is observed.

As expected, if the initial vibrational energy of I_2 is not large, then the rates at which trajectories cross intramolecular bottlenecks will be comparable to the rate of crossing the separatrix. In these cases the accuracy of the ARRKM predictions decreases. In addition, when applied to a similar system with three DOFs to include the orbital angular momentum of the separating fragments, the AKKRM theory does not yield satisfactory results. This should not be discouraging, considering the previously mentioned fundamental differences between few-dimensional and many-dimensional systems.

C. The Zhao–Rice Approximation (MRRKM)

In this subsection we describe the Zhao–Rice approximation [13,14] to the Davis–Gray theory. The approximations introduced by Zhao and Rice concern the calculation of the locations of, and the fluxes of phase-space points across, the separatix to fragmentation and the bottlenecks to intramolecular energy transfer. The dividing surface for fragment separation is represented by a vibration–rotation state-dependent separatrix, whose approximation is similar to but extends and improves the approximation for the separatrix introduced by Gray, Rice, and Davis. The novel feature in Zhao and Rice's theory is the representation of the bottlenecks to intramolecular energy transfer as dividing surfaces in phase space. The locations of these dividing surfaces are determined

by the same conditions that are used to locate the remnants of robust tori with frequency ratios related to the golden mean. The flux of phase-space points across both the separatrix and the intramolecular bottlenecks is calculated with an analytic representation instead of a stroboscopic mapping. The rate of unimolecular reaction is identified with the net rate at which phase-space points escape from the region of bounded motion to the region of free fragment motion by consecutively crossing the dividing surfaces for intramolecular energy exchange and the separatrix. The Zhao–Rice approximation to the intramolecular and intermolecular flow in systems with higher dimensionality has been named the modified RRKM theory (MRRKM). The MRRKM theory gives predictions of the rates of predissociation of van der Waals molecules that are in very good agreement with available experimental data.

Zhao and Rice started their analysis by defining a Hamiltonian for a model system designed to mimic a van der Waals complex of the diatom BC and the atom X. The full classical Hamiltonian for that system can be represented, as a function of the variables $\{\mathbf{P}, \mathbf{p}, \mathbf{l}, \mathbf{j}, \mathbf{R}, \mathbf{r}, q_l, q_j\}$, in the form

$$H = \frac{\mathbf{P}^2}{2\mu} + \frac{\mathbf{p}^2}{2m} + \frac{\mathbf{l}^2}{2\mu\mathbf{R}^2} + \frac{\mathbf{j}^2}{2m\mathbf{r}^2} + V(\mathbf{R}, \mathbf{r}, \gamma) \tag{93}$$

where the effective masses in the Hamiltonian are

$$m = \frac{m_B m_C}{m_B + m_C} \tag{94}$$

and

$$\mu = \frac{m_X(m_B + m_C)}{m_X + m_B + m_C} \tag{95}$$

$\mathbf{r}$ is the vector connecting the two atoms in the diatom BC, $\mathbf{R}$ is the vector from the center of mass of BC to X, and $\mathbf{P}$ and $\mathbf{p}$ are the corresponding conjugate momenta. Here $\mathbf{l}$ is the orbital angular momentum

$$\mathbf{l} = \mathbf{R} \times \mathbf{P} \tag{96}$$

and $\mathbf{j}$ is the diatom rotational angular momentum

$$\mathbf{j} = \mathbf{r} \times \mathbf{p} \tag{97}$$

Note that the total angular momentum $\mathbf{J} = \mathbf{j} + \mathbf{l}$ is conserved. For convenience we denote $|\mathbf{X}|$ by X and adopt here the convention $\hbar = 1$. The angle between the

vectors **R** and **r** is given by γ, which can be written in terms of the angle variables q_l and q_j as

$$\cos(\gamma) = -\cos(q_l)\cos(q_j) + \left[(l^2 + j^2 - J^2)/(2lj)\right]\sin(q_l)\sin(q_j) \tag{98}$$

The potential function appearing in the Hamiltonian can only depend on the magnitudes of R and r and the angle γ. Zhao and Rice chose the potential energy surface for the model van der Waals molecule to be a combination of Morse functions such that

$$V(\mathbf{R}, \mathbf{r}, \gamma) = V(\mathbf{r}) + W(\mathbf{R}, \mathbf{r}, \gamma) \tag{99}$$

$$W(\mathbf{R}, \mathbf{r}, \gamma) = \sum_{i=1}^{2} V(x_i) \tag{100}$$

where

$$V(x) = D[\exp[-2\alpha(x - \bar{x})] - 2\exp[-\alpha(x - \bar{x})]] \tag{101}$$

is a Morse potential with parameters D, α, and $\bar{x}$. If the molecular fragment BC is homonuclear then

$$x_1 = \left[R^2 + r^2/4 + Rr\cos(\gamma)\right]^{1/2} \tag{102}$$

$$x_2 = \left[R^2 + r^2/4 - Rr\cos(\gamma)\right]^{1/2} \tag{103}$$

while for the heteronuclear case

$$x_1 = \left[R^2 + r_1^2/4 + Rr_1\cos(\gamma)\right]^{1/2} \tag{104}$$

$$x_2 = \left[R^2 + r_2^2/4 - Rr_2\cos(\gamma)\right]^{1/2} \tag{105}$$

with

$$\mathbf{r}_1 = \frac{m_B}{(m_B + m_C)}\mathbf{r} \tag{106}$$

$$\mathbf{r}_2 = \frac{m_C}{(m_B + m_C)}\mathbf{r} \tag{107}$$

Note also that parity conservation can be used to decouple the Hamiltonian for the model system into four equivalent parts. Indeed, either of the substitutions $q_l \rightarrow q_l + \pi$ and $q_j \rightarrow q_j + \pi$ generates the exchanges $x_1 \rightarrow x_2$ and $x_2 \rightarrow x_1$.

These substitutions leave the potential function, and therefore also the Hamiltonian, unchanged. This property of the Hamiltonian simplifies the integration over phase-space.

The system Hamiltonian can be approximated, as in the ARRKM theory, by decoupling the diatom vibrational motion from overall rotational motion of the molecule and from the van der Waals bond stretching. With this approximation,

$$H_0 = H_0^1(p, r) + H_0^2(P, j, l, R, \gamma) \tag{108}$$

where

$$H_0^1(p, r) = \frac{p^2}{2m} + V(r) \tag{109}$$

and

$$H_0^2(P, j, l, R, \gamma) = \frac{P^2}{2\mu} + \frac{l^2}{2\mu R^2} + \frac{j^2}{2m\bar{r}^2} + W(R, \bar{r}, \gamma) \tag{110}$$

with $\bar{r}$ being the equilibrium internuclear separation in the diatom. Given this approximate three-body Hamiltonian, the energy is well approximated to first order in the vibrational anharmonicity by

$$E = E_D + E_r(v) + E_R(n) + E_\gamma(j, l) \tag{111}$$

with

$$E_D = -(D_{XB} + D_{XC} + D_{BC}) \tag{112}$$

$$E_r(v) = \left(v + \frac{1}{2}\right)\omega_r - \left(v + \frac{1}{2}\right)^2 \chi_r \tag{113}$$

$$E_R(n) = \left(n + \frac{1}{2}\right)\omega_R - \left(n + \frac{1}{2}\right)^2 \chi_R \tag{114}$$

and $E_\gamma(j, l)$ given by

$$E_\gamma(j, l) = \left(j + \frac{1}{2}\right)\omega_j + \left(l + \frac{1}{2}\right)\omega_\ell - \left(j + \frac{1}{2}\right)^2 \chi_j - \left(l + \frac{1}{2}\right)^2 \chi_l \tag{115}$$

in the case of $J > 0$ and

$$E_\gamma(j, l) = \left(l + \frac{1}{2}\right)\omega_\gamma - \left(l + \frac{1}{2}\right)^2 \chi_\gamma \tag{116}$$

for $J = 0$ and $j = l$.

Suppose that the system is prepared in a specified vibrational state of the diatom with a vibrational quantum number v, while the van der Waals bond is maintained in its ground vibrational state $(n = 0)$. The several frequencies appeared in the preceding equations, corresponding to motion along the several coordinates, are defined by

$$\omega_x = \left[\frac{1}{M_x}\frac{d^2H}{dx^2}\right]^{1/2}_{x=\bar{x}}, \qquad \chi_x = \frac{\omega_x^2}{4D_x} \tag{117}$$

where $x = R, r, \gamma$; $M_x = \mu, m, I(\bar{R}, \bar{r})$.

1. An Approximate Dividing Surface for the Separatrix

For a given diatom vibrational state with classical vibrational action v, Zhao and Rice defined a vibrational-state-dependent separatrix function by

$$S_{\text{Sep}} = \frac{P^2}{2\mu} + \frac{l^2}{2\mu R^2} + \frac{j^2}{2m\bar{r}^2} + W(R, \bar{r}, \gamma) - \varepsilon_{R,\gamma}(0) - \varepsilon(v) \tag{118}$$

where $\varepsilon(v)$ is the energy that can be transferred from the diatom vibrational mode to the van der Waals stretching and bending modes. The definition of S_{Sep} is motivated by considerations based on the conservation of energy. The total energy of the system is given by

$$\begin{aligned} &\frac{P^2}{2\mu} + \frac{l^2}{2\mu R^2} + \frac{j^2}{2m\bar{r}^2} + W(R, \bar{r}, \gamma) + \left[\frac{p^2}{2m} + V(r)\right] \\ &= \frac{P^2}{2\mu} + \frac{l^2}{2\mu R^2} + \frac{j^2}{2m\bar{r}^2} + W(R, \bar{r}, \gamma) + E_r(v' < v) \\ &\approx \varepsilon_{R,\gamma}(0) + E_r(v) \end{aligned} \tag{119}$$

so that

$$\begin{aligned} S_{\text{Sep}} &= \frac{P^2}{2\mu} + \frac{l^2}{2\mu R^2} + \frac{j^2}{2m\bar{r}^2} + W(R, \bar{r}, \gamma) - \varepsilon_{R,\gamma}(0) - [E_r(v) - E_r(v' < v)] \\ &\approx 0 \end{aligned} \tag{120}$$

which is just the definition for S_{Sep}. For a T-shaped nonrotating model the dependences of S_{Sep} on j, l, and γ are eliminated.

The inclusion of $\varepsilon(v)$ in the definition of separatrix involves the assumption that, as in adiabatic variational transition state theory, the diatom remains in the same vibrational state throughout the slow van der Waals bond stretching and breaking process. That is, the vibrational quantum number v of the diatom in the

van der Waals molecule is invariant throughout the bond-breaking process. However, the frequency of the diatom vibration with quantum number v is a function of the length of the van der Waals bond, and it is not constant throughout the bond-breaking process. That frequency is obtained from

$$\omega(v) = \frac{d}{dv} E_r(v) \tag{121}$$

which yields

$$\omega(v) = \omega_r - (2v + 1)\chi_r \tag{122}$$

The active part of the vibrational energy is defined by the relation

$$\varepsilon(v) = E_r(v) - E_r(v' < v) \approx v \frac{d}{dv} [E_r(v) - E_r(v' < v)] \tag{123}$$

which leads to

$$\varepsilon(v) = v\omega(v) \tag{124}$$

and

$$S_{\text{Sep}} = \frac{P^2}{2\mu} + \frac{l^2}{2\mu R^2} + \frac{j^2}{2m\bar{r}^2} + W(R, \bar{r}, \gamma) - \varepsilon_{R,\gamma}(0) - v\omega(v) \tag{125}$$

In a classical treatment, any fraction of the energy deposited in the diatom vibration can be transferred to the van der Waals stretching and bending modes. However, there is a penalty associated with transferring energy in excess of that needed to break the van der Waals bond, so one expects to find that the average energy transferred is much less than the total diatom vibrational energy.

2. An Approximate Dividing Surface for Intramolecular Bottlenecks

Zhao and Rice then developed an approximation to locate the intramolecular bottlenecks and calculate the associated flux. There are two principal motivations for the development of such an approximation. These are, first, the need to simplify the very complicated mapping-based calculation of the flux crossing a cantorus so as to make the calculation practical in systems with many DOFs and, second, the desirability of having a simple representation of the intramolecular energy transfer barrier in terms of molecular properties.

Imagine that a dividing surface is drawn around the cantorus. Since the cantorus lies entirely inside the separatrix, the dividing surface that just contains it will correspond to a bound state of the molecule—that is, one with negative

energy. In this region of phase-space the maximum kinetic energy that can be accumulated in the van der Waals bond of the molecule can be estimated from

$$\omega_R(n) = \frac{\omega_r(v)}{(N+g)} \tag{126}$$

with the local frequency $\omega_R(n)$ given by

$$\omega_R(n) = \frac{d}{dn}E_R(n) = \omega_R - (2n+1)\chi_R \tag{127}$$

A simple rearrangement yields

$$n = -\frac{1}{2} + \frac{[\omega_R - \omega_R(n)]}{2\chi_R} \tag{128}$$

which gives

$$\begin{aligned} E_R(n) &= \frac{\left[\omega_R^2 - \omega_R^2(n)\right]}{4\chi_R} \\ &= \frac{1}{4\chi_R}\left[\omega_R^2 - \frac{\omega_r^2(v)}{(N+g)^2}\right] \end{aligned} \tag{129}$$

This is the maximum kinetic energy accessible to the van der Waals bond when motion is limited to the interior of the dividing surface that just contains the contorus.

To locate the intramolecular bottleneck, it is assumed that there is no energy transfer to the van der Waals stretching motion or to rotational motion, so the energy in all other DOFs is conserved. This energy is negative, corresponding to bounded motion, and is given by

$$\frac{P^2}{2\mu} + \frac{l^2}{2\mu R^2} + \frac{j^2}{2m\bar{r}^2} + W(R,\bar{r},\gamma) \approx -D_{XB} - D_{XC} + E_R(n) + E_\gamma(j,l) \tag{130}$$

which leads to the following definition of the dividing surface that represents the intramolecular bottleneck:

$$\begin{aligned} S_{\text{intra}} = &\frac{P^2}{2\mu} + \frac{l^2}{2\mu R^2} + \frac{j^2}{2m\bar{r}^2} + W(R,\bar{r},\gamma) \\ &+ \left[D_{XB} + D_{XC} - E_R(n) - E_\gamma(j,l)\right] \end{aligned} \tag{131}$$

Again, for a T-shaped nonrotating model molecule the dependence of S_{intra} on j, l, and γ can be eliminated and we find

$$S_{\text{intra}} = \frac{P^2}{2\mu} + W(R, \bar{r}) + D_{XB} + D_{XC} - \frac{1}{4\chi_R}\left[\omega_R^2 - \frac{\omega_r^2(v)}{(N+g)^2}\right] \tag{132}$$

When applied to a particular case, N is chosen using the prescription introduced by Davis and Gray. For example, in HeI_2 the frequency of the van der Waals bond is $26.4\,\text{cm}^{-1}$ and the diatom vibrational state with $v = 20$ has a local frequency $\omega_r(v) = 93.81\,\text{cm}^{-1}$, implying that $4 < N < \infty$.

As shown before, in a system with two DOFs the bottlenecks to intramolecular energy transfer appear in those regions of phase-space where the nonlinear oscillators have the most difficulty driving each other—that is, regions where the ratio of frequencies is irrational. For the three-body system here, Zhao and Rice selected for consideration only the *pairwise* resonances, assuming that these dominate the system dynamics. This assumption is consistent with the numerical results of the dynamics of model systems with four DOFs studied by Gillilan and Ezra [18]. The most important of the pairwise resonances is that involving coupling of the diatom vibration and the van der Waals bond vibration. In this case the local frequencies associated with the other degrees of freedom are not constrained. Let

$$\omega_r(v)/\omega_R(n) = R_f \tag{133}$$

and, for simplicity, we assume $j = 0$ and $l = 0$. Then

$$E_R(n) = \frac{1}{4\chi_R}\left[\omega_R^2 - \frac{\omega_r^2(v)}{R_f^2}\right] \tag{134}$$

and the intramolecular bottleneck dividing surface takes the form

$$S_{\text{intra}} = \frac{P^2}{2\mu} + W(R, \bar{r}, \gamma) + D_{XB} + D_{XC} - \frac{1}{4\chi_R}\left[\omega_R^2 - \frac{\omega_r^2(v)}{R_f^2}\right] \tag{135}$$

3. A Zeroth-Order Calculation of the Rate Constant for Crossing Intramolecular Bottlenecks

It is instructive to examine a zeroth-order calculation of intramolecular energy transfer in a model molecule in which the energies of the vibrational and rotational modes are conserved separately, in which the initial excitation of the van der Waals stretching mode is zero ($n = 0$), and in which the initial values of

the molecular and orbital angular momenta are zero ($j = l = 0$). During the intramolecular vibrational relaxation process the maximum kinetic energy in the van der Waals mode cannot exceed the initial energy, so

$$\frac{P^2}{2\mu} \leq E_R(n = 0) \tag{136}$$

and

$$\frac{j^2}{2}\left(\frac{1}{\mu R^2} + \frac{1}{mr^2}\right) \approx E_\gamma(j = l = 0) \tag{137}$$

Given these constraints the intramolecular rate constant can be rewritten as

$$k_{\text{intra}} = \frac{1}{N_A}\int dP\, dp\, dR\, dr\, d\gamma \dot{S}\theta(\dot{S})\delta(S)\delta(E - H)\theta\left[E_R(0) - \frac{P^2}{2m}\right] \tag{138}$$

Integration over the momenta yields

$$k_{\text{intra}} = \frac{\mu}{N_A}\int dR\, dr\, d\gamma \sum_{i=1}^{2} \frac{\dot{S}\theta(\dot{S})\theta(2\mu E_R(0) - P_i^2)}{\sqrt{P_i^2(A^2 - P_i^2)}} \tag{139}$$

with

$$A^2 = 2\mu\left[E - E_\gamma(j = l = 0) - V(R, r, \gamma)\right] \tag{140}$$

$$P_1 = +\sqrt{2\mu[E_R(n) - D_{\text{X}B} - D_{\text{X}C} - W(R, \bar{r}, \gamma)]} \tag{141}$$

and

$$P_2 = -\sqrt{2\mu[E_R(n) - D_{\text{X}B} - D_{\text{X}C} - W(R, \bar{r}, \gamma)]} \tag{142}$$

To calculate the normalization constant N_A in k_{intra} Zhao and Rice proceeded as follows. Assuming that the system is prepared in a state with all the phase-space points inside the intramolecular bottleneck dividing surface, then the density of these phase-space points can be written as

$$\rho(p, x) = F_S(p, x)\delta(E - H) \tag{143}$$

One can also assume that after the intramolecular vibrational relaxation process is completed the phase-space points are uniformly distributed inside the system

separatrix. The zeroth-order approximation to that region then defines the constraint

$$\frac{P^2}{2\mu} + W(R, \bar{r}, \gamma) \; < 0 \tag{144}$$

and

$$N_A = \int dP\, dp\, dR\, dr\, d\gamma \theta(-F)\delta(E - H) \tag{145}$$

with

$$F = \frac{P^2}{2\mu} + W(R, \bar{r}, \gamma) \tag{146}$$

After integration over momentum, one finds

$$N_A = 2 \int dR\, dr\, d\gamma \arcsin \left(\frac{P}{A}\right)_{\min} \tag{147}$$

with

$$P_{\min} = \min\left[\sqrt{-2\mu W(R, \bar{r}, \gamma)}, A\right] \tag{148}$$

4. The Rate Constant for Crossing the Separatrix

One still has to carry out calculations for the rate constant k_{Sep} of crossing the separatrix S_{Sep} defined above. According to the ARRKM theory, for particular total angular momentum J one has

$$k_{\text{Sep}}(J) = \frac{1}{N_A(J)} \int dP\, dp\, dj\, dl\, dr\, dq_j\, dq_l \dot{S} \theta(\dot{S}) \delta(S) \delta(E - H) \tag{149}$$

where

$$N_A(J) = \int dP\, dp\, dj\, dl\, dr\, dq_j\, dq_l \theta(-S) \delta(E - H) \tag{150}$$

with the values for j and l constrained by angular momentum conservation.

The integrals in Eqs. (149) and (150) can be evaluated as follows. We slightly deviate from a strictly classical analysis by quantizing the orbital angular momentum l and the diatom rotational angular momentum j. That is, we assign

j and l integer values, which procedure reduces the dimensionality of the integrations by two and thereby reduces the difficulty of subsequent numerical evaluation by the Monte Carlo method. For any given value of J, j and l are related by

$$l = |J-j|,\ |J-j+1|, \ldots, |J+j-1|,\ |J+j| \tag{151}$$

so that $k(J)$ and $N_A(J)$ reduce to

$$k_{\mathrm{Sep}}(J) = \frac{1}{N_A(J)} \sum_{j=0}^{j_{\max}} \sum_{l=|J-j|}^{|J+j|} \int dP\, dp\, dR\, dr\, dq_j\, dq_l \dot{S} \theta(\dot{S}) \delta(S) \delta(E-H) \tag{152}$$

$$N_A(J) = \sum_{j=0}^{j_{\max}} \sum_{l=|J-j|}^{|J+j|} \int dP\, dp\, dR\, dr\, dq_j\, dq_l \theta(-S) \delta(E-H) \tag{153}$$

The integration over p yields

$$k_{\mathrm{inter}}(J) = \frac{\sqrt{2m}}{N_A(J)} \sum_{j=0}^{j_{\max}} \sum_{l=|J-j|}^{|J+j|} \int \frac{dP\, dR\, dr\, dq_j\, dq_l \dot{S}_{\mathrm{Sep}} \theta(\dot{S}_{\mathrm{Sep}}) \delta(S_{\mathrm{Sep}})}{\sqrt{E - \frac{P^2}{2\mu} - \frac{l^2}{2\mu R^2} - \frac{j^2}{2mr^2} - V(R,r,\gamma)}} \tag{154}$$

$$N_A(J) = \sum_{j=0}^{j_{\max}} \sum_{l=|J-j|}^{|J+j|} \int \frac{dP\, dR\, dr\, dq_j \sqrt{2m} \theta(-S_{\mathrm{Sep}})}{\sqrt{E - \frac{P^2}{2\mu} - \frac{l^2}{2\mu R^2} - \frac{j^2}{2mr^2} - V(R,r,\gamma)}} \tag{155}$$

The time derivative of the separatrix

$$\dot{S}_{\mathrm{Sep}} = \frac{d}{dt} S_{\mathrm{Sep}}(P,R,j,l,\gamma) \tag{156}$$

can be evaluated from its Poisson bracket with the Hamiltonian

$$\begin{aligned} \dot{S}_{\mathrm{Sep}} = {} & \frac{\partial S_{\mathrm{Sep}}}{\partial R}\frac{\partial H}{\partial P} - \frac{\partial S_{\mathrm{Sep}}}{\partial P}\frac{\partial H}{\partial R} \\ & + \frac{\partial S_{\mathrm{Sep}}}{\partial q_l}\frac{\partial H}{\partial l} - \frac{\partial S_{\mathrm{Sep}}}{\partial l}\frac{\partial H}{\partial q_l} + \frac{\partial S_{\mathrm{Sep}}}{\partial q_j}\frac{\partial H}{\partial j} - \frac{\partial S_{\mathrm{Sep}}}{\partial j}\frac{\partial H}{\partial q_j} \end{aligned} \tag{157}$$

Then it is followed by integration over P, leading to

$$k_{\mathrm{Sep}}(J) = \frac{\sqrt{4\mu m}}{N_A(J)} \sum_{j=0}^{j_{\max}} \sum_{l=|J-j|}^{|J+j|} \sum_{i=1}^{2} \int \frac{dR\, dr\, dq_j\, dq_l\ \mu \dot{S}_{\mathrm{Sep}} \theta(\dot{S}_{\mathrm{Sep}})}{\sqrt{P_i^2 (A^2 - P_i^2)}} \tag{158}$$

with

$$P_1 = +\sqrt{2\mu\left[\varepsilon_{R,\gamma}(0) + v\omega(v) - \frac{l^2}{2\mu R^2} - \frac{j^2}{2m\bar{r}^2} - w(R,\bar{r},\gamma)\right]} \tag{159}$$

$$P_2 = -\sqrt{2\mu\left[\varepsilon_{R,\gamma}(0) + v\omega(v) - \frac{l^2}{2\mu R^2} - \frac{j^2}{2m\bar{r}^2} - w(R,\bar{r},\gamma)\right]} \tag{160}$$

and

$$A = \sqrt{2\mu\left[E - \frac{l^2}{2\mu R^2} - \frac{j^2}{2m\bar{r}^2} - w(R,\bar{r},\gamma)\right]} \tag{161}$$

The step function sets the limit for the integration range of P, namely,

$$-\mid P_i(l,j,R,q_l,q_j) \mid \leq P \leq \mid P_i(l,j,R,q_l,q_j) \mid, \qquad i = 1,2 \tag{162}$$

After carrying out the integration over P, one finds

$$k_{\text{Sep}} = \frac{1}{N_A(J)} \sum_{j=0}^{j_{\max}} \sum_{l=|J-j|}^{|J+j|} \sum_{i=1}^{2} \int \frac{dR\, dr\, dq_j\, dq_l \mu \dot{S}_{\text{Sep}} \theta(\dot{S}_{\text{Sep}})}{\sqrt{P_i^2(A^2 - P_i^2)}} \tag{163}$$

$$N_A(J) = 2 \sum_{j=0}^{j_{\max}} \sum_{l=|J-j|}^{|J+j|} \int dP\, dR\, dr\, dq_j\, dq_l \arcsin\left[\frac{P_{\min}(l,j,R,r,q_l,q_j)}{A(l,j,R,r,q_l,q_j)}\right] \tag{164}$$

with

$$P_{\min} = \min\{P_i(l,j,R,r,q_l,q_j),\, A(l,j,R,r,q_l,q_j)\} \tag{165}$$

The total rate constant is determined by the sum over contributions from all $k_{\text{inter}}(J)$, that is,

$$k_{\text{Sep}} = \lim_{J_{\max} \to +\infty} \sum_{J=0}^{J_{\max}} k_{\text{Sep}}(J) \tag{166}$$

The model of van der Waals fragmentation used by Zhao and Rice, like that of Davis and Gray from which it is derived, assumes that the crossings of the several bottlenecks in the phase-space of the molecule are independent. A

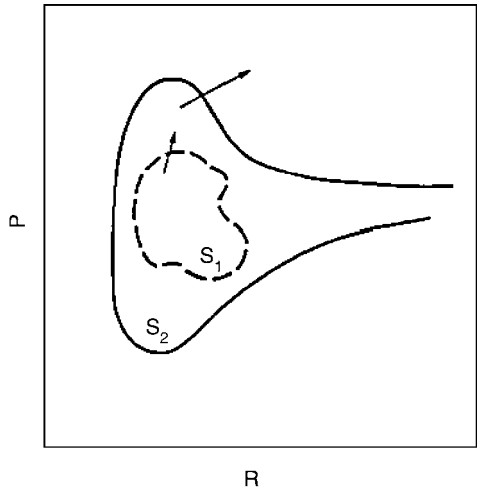

Figure 19. A schematic plot of the ideal bottlenecks on the Poincaré surface of section for van der Waals molecule predissociation. R is the van der Waals bond length and P is the conjugate momentum. S_1 is the intramolecular bottleneck dividing surface and S_2 is the intermoleculear bottleneck dividing surface.

schematic bottleneck on a PSS is shown in Fig. 19. Then the observed rate of fragmentation is described by the set of kinetic equations

$$\frac{dN_1}{dt} = -k_{\text{intra}} N_1 \tag{167}$$

$$\frac{dN_2}{dt} = k_{\text{intra}} N_1 - k_{\text{Sep}} N_2 \tag{168}$$

where N_1 and N_2 are the populations of phase-space points inside and outside the intramolecular energy transfer dividing surface. The solution to this set of equations is

$$N_1(t) = N_1(0) e^{-k_{\text{intra}} t} \tag{169}$$

$$N_2(t) = N_2(0) e^{-k_{\text{Sep}} t} + \frac{N_1(0) k_{\text{intra}}}{k_{\text{Sep}} - k_{\text{intra}}} \left[e^{-k_{\text{intra}} t} - e^{-k_{\text{Sep}} t} \right] \tag{170}$$

and the total number of points inside the separatrix is

$$\begin{aligned} N(t) &= N_1(t) + N_2(t) \\ &= \frac{N_1(0)}{k_{\text{Sep}} - k_{\text{intra}}} \left[k_{\text{Sep}} e^{-k_{\text{intra}} t} - k_{\text{intra}} e^{-k_{\text{Sep}} t} \right] \\ &\quad + N_2(0) e^{-k_{\text{Sep}} t} \end{aligned} \tag{171}$$

The separation of the phase-space inside the separatrix into a region inside and a region outside the intramolecular energy transfer dividing surface defines the initial conditions $N_1(0)$ and $N_2(0)$, and leads us to write

$$N_1(0) = f_1 N(0) \tag{172}$$

$$N_2(0) = f_2 N(0) \tag{173}$$

$$f_1 + f_2 = 1 \tag{174}$$

so that total population as a function of time is given by

$$\frac{N(t)}{N(0)} = \frac{f_1}{k_{\text{Sep}} - k_{\text{intra}}} \left[k_{\text{Sep}} e^{-k_{\text{intra}} t} - k_{\text{intra}} e^{-k_{\text{Sep}} t} \right] + f_2 e^{-k_{\text{Sep}} t} \tag{175}$$

Zhao and Rice have calculated the fragmentation rate constant k by fitting the numerical simulation data from the time at which dissociation first starts to the time when

$$\ln\left(\frac{N(t)}{N(0)}\right) = -1 \tag{176}$$

This method of calculating the fragmentation rate constant gives good agreement with the rate constants determined by trajectory calculations.

D. The Reaction Path Analysis

In this section we discuss the use of the Miller–Handy–Adams reaction path formalism [37] so that the dynamics of a seemingly complicated system can be better understood and analyzed. For example, if, with that formalism, the dynamics of a system can be reasonably reduced to only two or three DOFs, then it is expected that one can directly apply the above various statistical theories for few-dimensional systems. In the reaction path formalism the reactive trajectory is determined by the minimum energy path with small displacements from that path.

The Hamiltonian for an N-particle molecular system is, in Cartesian coordinates, given by

$$H(\mathbf{p}, \mathbf{x}) = \sum_{i=1}^{3N} \frac{P_i^2}{2m_i} + V(\mathbf{x}) \tag{177}$$

where $\mathbf{x}$ is the $3N$-dimensional coordinate vector and P_i $(i = 1 - 3N)$ are the conjugate momenta. Let $\mathbf{a} = (a_1, \ldots, a_{3N})$ be a vector on the reaction path. Then

the potential energy function $V(\mathbf{x})$ can be expanded near the reaction path in powers of $(\mathbf{x} - \mathbf{a})$. To second-order, one has

$$V(\mathbf{x}) \approx V(\mathbf{a}) + \nabla V(\mathbf{a}) \cdot (\mathbf{x} - \mathbf{a}) + \frac{1}{2}(\mathbf{x} - \mathbf{a}) \cdot \mathbf{F} \cdot (\mathbf{x} - \mathbf{a}) \tag{178}$$

where $\mathbf{F}$ is the force constant matrix. Because the displacement vector $(\mathbf{x} - \mathbf{a})$ is orthogonal to the reaction path in the $3N$-dimensional space, the linear term in the preceding equation vanishes. The motions associated with the overall rotation and the translation of the center of mass are not of interest and can be removed by use of the projected force constant matrix

$$\mathbf{F}^P = (1 - P^{RT}) \cdot \mathbf{F} \cdot (1 - P^{RT}) \tag{179}$$

where P^{RT} is the projection operator for the overall translational and rotational motion. Following the application of the projector P^{RT}, a normal mode analysis can be carried out for vibrational motion.

For a polyatomic reactant with many DOFs, the scale of numerical calculations required to execute this approach can be prohibitively large. The simplest approximation that reduces the scale of numerical calculations is to neglect some subset of the internal molecular motions. However, this approximation usually leads to considerable error. A more sophisticated and intuitively reasonable approximation is to reduce the system dimensionality by placing constraints on the values of the internal molecular coordinates (instead of omitting them from the analysis). It is this approximation that we now consider.

Assuming that most of the atomic displacements in the reactant molecule are small, the most obvious choices for constraints on the internal coordinates not directly participating in the reaction are fixed values of the bond lengths and bond angles. To represent the fixed bond length between atoms A and B, denoted by d_{AB}, a unit vector is introduced, the components of which are

$$e_{A\alpha}^{(AB)} = \frac{(r_{A\alpha} - r_{B\alpha})}{\sqrt{2}d_{AB}}, \qquad e_{B\alpha}^{(AB)} = -\frac{(r_{A\alpha} - r_{B\alpha})}{\sqrt{2}d_{AB}}, \qquad \alpha = x, y, z \tag{180}$$

These components are combined to form the vector

$$\mathbf{u}_{(AB)}^T = \left(0, \ldots, 0, e_{Ax}^{(AB)}, e_{Ay}^{(AB)}, e_{Az}^{(AB)}, 0, \ldots, 0, e_{Bx}^{(AB)}, e_{By}^{(AB)}, e_{Bz}^{(AB)}, 0, \ldots, 0\right) \tag{181}$$

To represent the fixed angle between atoms M, O, and N, with O at the vertex position, we introduce the following two unit vectors:

$$e_{N\alpha}^{(MON)} = \frac{\lambda}{d_{NO}\sin\theta_{MON}}\left[\frac{(r_{N\alpha}-r_{O\alpha})}{d_{NO}}\cos\theta_{MON} - \frac{(r_{M\alpha}-r_{O\alpha})}{d_{MO}}\right] \tag{182}$$

$$e_{O\alpha}^{(MON)} = -\left(e_{M\alpha}^{(MON)} + e_{N\alpha}^{(MON)}\right), \qquad \alpha = x, y, z \tag{183}$$

where λ is a normalization constant, and the bond angle θ_{MON} is defined by

$$\cos\theta_{MON} = \frac{(\mathbf{r}_M - \mathbf{r}_O)\cdot(\mathbf{r}_N - \mathbf{r}_O)}{d_{MO}\, d_{NO}} \tag{184}$$

These vector components are combined to form the unit vector

$$\begin{aligned}\mathbf{u}_{(MON)}^T = \big[&0,\ldots,0,e_{Mx}^{(MON)},e_{My}^{(MON)},e_{Mz}^{(MON)}\\ &0,\ldots,0,e_{Ox}^{(MON)},e_{Oy}^{(MON)},e_{Oz}^{(MON)}\\ &0,\ldots,0,e_{Nx}^{(MON)},e_{Ny}^{(MON)},e_{Nz}^{(MON)},0,\ldots,0\big]\end{aligned} \tag{185}$$

To construct the projection operators corresponding to the constraints, the subspace unit vectors representing different constraints must be independent. As shown by Miller et al., this can be affected by Gram–Schmidt orthogonalization that yields a set of orthogonal unit vectors:

$$\mathbf{u}_k' = N_k\left[1 - \sum_{j=1}^{k-1}\mathbf{u}_j\mathbf{u}_j^T\right]\mathbf{u}_k \tag{186}$$

where N_k is the normalization constant. The projection operator is then given by

$$P^C = \sum_{k=1}^{f}\mathbf{u}_k'\mathbf{u}_k'^T \tag{187}$$

where the prime indicates orthogonalized unit vectors and f is the total number of constraints (the same as number of DOFs reduced). The use of P^C yields

$$\mathbf{F}_{\text{final}} = (\mathbf{1} - P^C - P^{RT})\cdot\mathbf{F}\cdot(\mathbf{1} - P^C - P^{RT}) \tag{188}$$

A normal mode representation of the Hamiltonian for the reduced system involves the diagonalization of the projected force constant matrix $\mathbf{F}_{\text{final}}$, which

in turn generates a reduced-dimension potential energy surface in terms of the mass-weighted coordinates of the reaction path:

$$V(s, Q_1, \ldots, Q_{3N-f-7}) = V(s) + \sum_{k=1}^{3N-f-7} \tfrac{1}{2}\omega_k^2(s) Q_k^2 \tag{189}$$

The coordinates $\{Q_k,\ k = 1, 2, \ldots, (3N - f - 7)\}$ are the normal mode coordinates and $\omega_k(s)$, $k = 1, 2, \ldots, (3N - f - 7)$, are the corresponding normal mode frequencies. The kinetic energy is then given by

$$T = \sum_{k=1}^{3N-f-7} \tfrac{1}{2}P_k^2 + \frac{\left[p_s - \sum_{k=1,\ell=1}^{3N-f-7} Q_k B_{k\ell}(s) P_\ell\right]^2}{2\left(1 + \sum_{k=1}^{3N-f-7} Q_k B_{k,3N-f-6}\right)^2} \tag{190}$$

where the $B_{k\ell}(s)$ describe the Coriolis coupling between the normal modes and the $B_{k,3N-f-6}(s)$ originate from the curvature of the reaction path.

Further reduction of the constrained reaction path model is possible. Here we adopt a system-bath model in which the reaction path coordinate defines the system and all other coordinates constitute the bath. The use of this representation permits the elimination of the bath coordinates, which then increases the efficiency of calculation of the motion along the reaction coordinate. In particular, Miller showed that a canonical transformation of the reaction path Hamiltonian $(T + V)$ yields [38]

$$\begin{aligned} H = {} & \tfrac{1}{2}\frac{p_s^2}{\left[1 + \sum_{k=1}^{3N-f-7} Q_k \tilde{B}_{k,3N-f-6}\right]^2} + V(s) \\ & + \sum_{k=1}^{3N-f-7} \tfrac{1}{2}P_k^2 + \sum_{k=1}^{3N-f-7} \tfrac{1}{2}\tilde{\omega}_k^2(s) Q_k^2 + \sum_{k,\ell=1\ k\neq\ell}^{3N-f-7} Q_k \tilde{B}_{k\ell}(s) Q_\ell \end{aligned} \tag{191}$$

where $\tilde{B}_{k\ell}(s)$ and $\tilde{B}_{k,3N-f-6}$ are related to $B_{k\ell}(s)$ and $B_{k,3N-f-6}$ via a unitary transformation, and the $\tilde{\omega}_k$ are the normal mode frequencies in the new representation. If we expand the first term of Eq. (191) such that

$$\begin{aligned} & \frac{1}{\left[1 + \sum_{k=1}^{3N-f-7} Q_k \tilde{B}_{k,3N-f-6}\right]^2} \\ & = 1 - 2\sum_{k=1}^{3N-f-7} Q_k \tilde{B}_{k,3N-f-6} + 3\sum_{k=1}^{3N-f-7} Q_k^2 \tilde{B}_{k,3N-f-6}^2 + \cdots \end{aligned} \tag{192}$$

then

$$H = \frac{p_s^2}{2} + V(s) - \frac{p_s^2}{2}\left[2\sum_{k=1}^{3N-f-7} Q_k \tilde{B}_{k,3N-f-6} - 3\sum_{k=1}^{3N-f-7} Q_k^2 \tilde{B}_{k,3N-f-6}^2 + \cdots\right] + \sum_{k=1}^{3N-f-7} \tfrac{1}{2}P_k^2 + \sum_{k=1}^{3N-f-7} \tfrac{1}{2}\tilde{\omega}_k^2(s) Q_k^2 + \sum_{k,\ell=1\, k\neq\ell}^{3N-f-7} Q_k \tilde{B}_{k\ell}(s) Q_\ell \tag{193}$$

For consistency with the quadratic approximation used in the potential expansion, the above expression for H has been truncated at the quadratic term; the higher-order and off-diagonal terms in the expansion can be treated as perturbations. Then, the approximate effective Hamiltonian for the reaction dynamics can be written in the form

$$H_{\text{eff}}(s, \{Q_k\}) = \frac{p_s^2}{2} + \sum_{k=1}^{3N-f-7} \tfrac{1}{2}P_k^2 + V(s) + \sum_{k=1}^{3N-f-7} \tfrac{1}{2}\Omega_k^2(s) Q_k^2 - 2E_a(s) \sum_{k=1}^{3N-f-7} Q_k \tilde{B}_{k,3N-f-6}(s) \tag{194}$$

where $E_a(s) \equiv p_s^2/2$ and $\Omega_k^2(s)$ is given by

$$\Omega_k^2(s) = \tilde{\omega}_k^2(s) + 6E_a(s)\tilde{B}_{k,3N-f-6}^2(s) \tag{195}$$

We note that this effective Hamiltonian $H_{\text{eff}}(s, \{Q_k\})$ treats the bath as a set of linearly shifted harmonic oscillators, that is,

$$H_{\text{eff}}(s, \{Q_k\}) = \frac{p_s^2}{2} + \sum_{k=1}^{3N-f-7} \tfrac{1}{2}P_k^2 + U(s) + \sum_{k=1}^{3N-f-7} \tfrac{1}{2}\Omega_k^2(s) \times \left[Q_k - \frac{2E_a(s)_k \tilde{B}_{k,3N-f-6}(s)}{\Omega_k(s)}\right]^2 \tag{196}$$

where $U(s)$ serves as the effective energy barrier and is given by

$$U(s) = V(s) - \sum_{k=1}^{3N-f-7} 2\left[\frac{E_a(s)_k \tilde{B}_{k,3N-f-6}(s)}{\Omega_k(s)}\right]^2 \tag{197}$$

One way of eliminating the harmonic bath coordinates is to use the vibrational adiabatic approximation, which leads to

$$H_{\text{ad}} = \frac{p_s^2}{2} + U(s) + \sum_{k=1}^{3N-f-7} \varepsilon_{\text{vib}}(n_k, s) \tag{198}$$

with

$$\varepsilon_{\text{vib}}(n_k, s) = \left(n_k + \frac{1}{2}\right)\hbar\Omega_k(s) \tag{199}$$

where the zero-point vibrational motion has been accounted for.

E. XI_2 Predissociation

The van der Waals molecules XI_2 (X = He, Ne, Ar) are the primitive systems for testing the various theories described in the preceding subsections. The unimolecular reactions are

$$XI_2(v) \rightarrow X + I_2(v' < v) \tag{200}$$

These reactions have played a significant role in understanding unimolecular predissociation. The potential parameters relevant to the calculations reviewed below are listed in Table I.

1. HeI_2

The predissociation of HeI_2 has been extensively studied, both experimentally and theoretically. Davis and Gray [11] carried out a detailed analysis of the classical mechanics of predissociation of a nonrotating T-shaped model of HeI_2. Gray, Rice, and Davis [12] evaluated the predissociation rate using their ARRKM theory and explored the associated PSS for various initial vibrational states. For the same system, Zhao and Rice studied both the intramolecular bottleneck and intermolecular dividing surface using their MRRKM theory.

We consider first the simplest model of the HeI_2 predissociation, namely the one that restricts the geometry to a T-shape and that excludes rotation. The calculated rate constant for crossing the separatrix from the MRRKM theory, as

TABLE I
Morse Potential Parameters for Triatomic van der Waals Molecules

Diatomic	D (cm)	$\alpha(a_0^{-1})$	$\bar{x}(a_0^{-1})$
I–I	4911	0.9380	5.6994
Cl–Cl	3145	1.2450	4.5610
I–Cl	1270	2.0955	5.0267
I–Ar	122	0.7000	9.4500
I–Ne	26	0.9525	10.2045
I–He	18	0.6033	7.5589
Ne–Cl	39	0.9525	6.9920
He–Cl	14	0.8467	6.8030

TABLE II
Rate Constants (in cm^{-1}) for Crossing the Separatrix in the Case of a T-Shaped HeI_2 Molecule[a]

v	Davis–Gray	MRRKM	ARRKM
10	0.186	0.140	0.52
20	0.374	0.393	0.80
30	0.626	0.679	1.09
50	1.295	1.22	1.89

[a]The initial vibrational state of I_2 is represented by v.

a function of initial vibrational excitation, is displayed in Table II along with the exact calculations of the same rate constant by Davis and Gray [11] and the approximate ARRKM calculations by Gray, Rice, and Davis [12]. It is seen that the rate constants obtained from MRRKM theory are in satisfactory agreement with the results of Davis and Gray over the range $v = 10$–50. Also evident is that the MRRKM rates are significantly better than those from ARRKM, which is, after all, based upon a zeroth-order approximation to the phase space separatrix. It should be stressed that thus far all these calculations omit the effect of nonstatisitical intramolecular energy transfer, and hence give results that are too large by more than a factor of 2 for $v = 20$ and about a factor of 20 for $v = 10$.

When the effect of intramolecular energy transfer is taken into account, more accurate rate constants can be obtained. We first compare the rate constants associated with the intramolecular bottleneck from the MRRKM theory with those from the Davis–Gray turnstile approach. As seen in Table III, they are in reasonable agreement. Hence, the Davis–Gray theory and the MRRKM theory predict similar overall reaction rates. This is demonstrated in Table IV. Table IV also shows that the predissociation rate constants would have been overestimated by a factor more than 100 if the RRKM theory were to be directly applied.

TABLE III
Intramolecular Bottleneck Predissociation Rate Constants (in cm^{-1}) for the T-Shaped HeI_2 Molecule[a]

v	Davis–Gray	MRRKM
10	0.121	0.16
20	0.216	0.27
30	0.273	0.43
50	—	0.60

[a]The initial vibrational state of I_2 is represented by v.

TABLE IV
The Overall Predissociation Rate Constant (in cm^{-1}) for the T-Shaped HeI_2 Molecule, with Intramolecular Bottlenecks Considered[a]

v	Davis–Gray	MRRKM	ARRKM	RRKM
10	0.083	0.076	0.52	66.0
20	0.17	0.24	0.80	110.5
30	0.56	0.56	1.09	135.7
50	1.57	1.22	1.89	128.0

[a] The initial vibrational state of I_2 is represented by v.

A more complicated model of the van der Waals molecule allows for considerations of diatom rotation and the orbital angular momentum of the separating fragments, subject to the constraint that the total angular momentum is zero $(J = 0, j = l)$. The theoretical rate constants for this model, with or without considering intramolecular bottleneck effects, are compared to the experimental data of Levy and co-workers [39,40] in Table V for $v = 5$ to $v = 35$. As expected, the calculated fragmentation rate constants without intramolecular bottleneck effects are larger than the observed fragmentation rate constants by a considerable amount, namely a factor of 12 when $v = 5$, decreasing to a factor of 2 when $v = 20$. However, the overall reaction rates from the MRRKM theory are seen to be in rather good agreement with the experimental data.

2. *NeI_2 and ArI_2*

Experimental results for the predissociation of NeI_2 are available from the work of Zewail and co-workers [41]. Since the frequency of the NeI_2 van der Waals

TABLE V
Predissociation Rate Constant of the MRRKM Theory (in cm^{-1}) for a Three-Dimensional Model of the HeI_2 Molecule, Compared to the Available Experiment Observations[a]

v	k_{Sep}	k_{intra}	k	Experiment
5	0.039	0.018	0.013	0.0032
10	0.068	0.034	0.028	0.015
15	0.10	0.044	0.047	0.034
20	0.13	0.086	0.086	0.070
25	0.15	0.15	0.13	0.12
30	0.22	0.34	0.22	0.19
35	0.25	—	0.25	—

[a]The initial vibrational state of I_2 is represented by v.

TABLE VI
Predissociation Rate Constants of the MRRKM Theory (in cm^{-1}) for a Three-Dimensional Model of the NeI_2 Molecule, Compared to the Available Experiment Data[a]

v	k_{Sep}	k_{intra}	k	Experiment
10	0.019	0.016	0.011	—
13	0.046	0.0096	0.020	0.025
14	0.051	0.011	0.025	0.027
15	0.063	0.025	0.038	0.029
16	0.064	0.031	0.043	0.033
17	0.067	0.031	0.048	0.042
18	0.074	0.027	0.056	0.050
19	0.073	0.043	0.060	0.061
20	0.082	0.048	0.073	0.062
21	0.085	0.073	0.081	0.077
22	0.10	0.11	0.10	0.092
23	0.11	0.28	0.11	0.10
25	0.13	—	0.13	—

[a]The initial vibrational state of I_2 is represented by v.

bond is much larger than that in HeI_2, we expect the contribution of flux across the intramolecular energy transfer dividing surface to the rate of predissociation to be smaller than in HeI_2. The calculated k_{Sep} as a function of initial vibrational excitation from $v = 10$ to $v = 25$ is compared with the experimental data in Table VI. It is seen that the neglect of the influence of intramolecular vibrational relaxation on the predissociation process does lead to an overestimate of the fragmentation rate, but the discrepancy is much smaller than in the HeI_2 case. Indeed, for NeI_2 we find reasonable agreement between the calculated k_{Sep} and the observed rate constants for $v > 18$, and the error is less than a factor of 2 for $v < 18$. The MRRKM calculations of the rate of predissociation of NeI_2, which include the rate of intramolecular energy transfer and allow for nonzero diatom and fragment orbital angular momenta (subject to the total angular momentum being zero, $J = 0$, $j = l$) are also shown in Table VI. Comparison to experimentally observed predissociation lifetimes for NeI_2 shows that the agreement between the MRRKM theory and experiment is satisfactory.

Zewail and co-workers [42] made a few measurements of the rate of predissociation of ArI_2 but only the ratios of the rate constants for different initial vibrational excitation were reported. The predissociation of ArI_2 was also experimentally studied by Levy co-workers [39,40]. The experimental data—for example, the ratio $k(v = 21)/k(v = 18)$—again support the MRRKM theory. In this particular application, the MRRKM calculations were based on a three-dimensional model in which both diatom and fragment orbital angular

TABLE VII
Predissociation Rate Constant of the MRRKM Theory (in cm^{-1}) for the Three-Dimensional ArI_2 Molecule[a]

v	k_{Sep}	k_{intra}	k
15	0.020	0.0048	0.0088
16	0.034	0.0082	0.016
17	0.047	0.0098	0.024
18	0.045	0.015	0.027
19	0.059	0.021	0.038
20	0.063	0.026	0.045
21	0.071	0.033	0.054
22	0.085	0.069	0.071
25	0.089	0.073	0.085
30	0.12	0.018	0.012

[a]The initial vibrational state of I_2 is represented by v.

TABLE VIII
The Rate Constant Ratio $k(v = 21)/k(v = 18)$ for Three-Dimensional ArI_2 Predissociation

Levy and co-workers	Beswick and Jortner	Zewail and co-workers	MRRKM
2.2	2.5	2.9	2.0

momentum are nonzero (again subject to the total angular momentum being zero, $J = 0, j = l$). The corresponding MRRKM rates are shown in Table VII. A comparison between the MRRKM result, the theoretical result of Beswick and Jortner [43], and the observed data for the rate-constant ratio $k(v = 21)/k(v = 18)$ is shown in Table VIII. The agreement between calculated and observed ratios of reaction rate constants is modestly good.

F. XCl_2 and XICl Predissociation

1. $HeCl_2$ and $NeCl_2$

Cline and co-workers [44–46] carried out experiments on the rates of predissociation of both $HeCl_2$ and $NeCl_2$, with the initial vibrational state of Cl_2 in a certain range. The calculated fragmentation rates of $HeCl_2$ as a function v are listed in Table IX along with the available experimental data. For the same molecule, Table X displays a comparison of the MRRKM calculated lifetimes and the experimental predissociation lifetimes by Cline and co-workers. Similar comparsions are made for $NeCl_2$ in Table XI and Table XII.

TABLE IX
Predissociation Rate Constants from the MRRKM Theory (in cm^{-1}) for the Three-Dimensional $HeCl_2$ Molecule Compared to the Available Experiment Observations[a]

v	k_{Sep}	k_{intra}	k	Experiment
6	0.123	0.0086	0.0080	—
7	0.135	0.012	0.011	—
8	0.150	0.023	0.020	0.011
9	0.172	0.032	0.027	0.019
10	0.183	0.016	0.033	0.030
11	0.187	0.038	0.065	0.055
12	0.216	0.070	0.099	0.101
13	0.277	0.088	0.14	—
14	0.284	0.056	0.17	—
15	0.295	0.069	0.18	—

[a]The initial vibrational state of Cl_2 is represented by v.

TABLE X
Predissociation Lifetime (in ps) for the Three-Dimensional $HeCl_2$ Molecule[a]

v	MRRKM	Cline (QM)	Cline (Expt.)	Zhang	Gray
8	271	311	506	245	240
9	198	231	275	180	—
10	160	131	179	180	—
11	82	75	97	100	—
12	53	71	52	66	—
13	—	44	—	33	—

[a]The initial vibrational state of Cl_2 is represented by v.

TABLE XI
Predissociation Rate Constant from the MRRKM Theory (in cm^{-1}) for the Three-Dimensional $NeCl_2$ Molecule Compared to the Available Experiment Observations[a]

v	k_{Sep}	k_{intra}	k	Experiment
6	0.096	0.0045	0.0043	—
7	0.125	0.0157	0.013	—
8	0.147	0.025	0.021	—
9	0.174	0.034	0.028	0.022
10	0.178	0.022	0.040	0.029
11	0.200	0.043	0.071	0.053
12	0.226	0.032	0.075	0.081
13	0.244	0.076	0.12	0.16
14	0.287	0.079	0.15	—
15	0.295	0.069	0.16	—

[a]The initial vibrational state of Cl_2 is represented by v.

TABLE XII
Predissociation Lifetime (in ps) for the Three-Dimensional $NeCl_2$ Molecule[a]

v	MRRKM	Cline (Expt.)	Gray	Gray (QM)
9	192	240	—	310
10	131	180	—	—
11	75	100	150	120
12	71	66	—	—
13	44	33	44	40
20	10	—	4.5	—

[a]The initial vibrational state of Cl_2 is represented by v.

Wozny and Gray [47] reported classical trajectory calculations of the rate of predissociation of $NeCl_2$ for $v = 11, 13$, and 20. Their results are also compared with MRRKM calculations in Table XII. In particular, in the case of $v = 13$, Wozny and Gray's trajectory calculation and MRRKM calculation give the same lifetime of 44 ps. However, for $v = 11$ and $v = 20$ the MRRKM theory gives lifetimes of 75 ps and 10 ps, respectively, whereas the classical trajectory calculations yield the values 150 ps and 4.5 ps. These differences are, of course, a measure of the accuracy of the approximations used in the MRRKM theory.

The excellent agreement between the MRRKM theory and the experimental results shown above is not totally expected. After all, the MRRKM theory is an approximate and classical statistical theory. As such, it is interesting to actually compare the MRRKM results with fully quantum mechanical calculations for the same systems using the same potential energy surface. Some such quantum calculations are available. In particular, Cline et al. [48] carried out time-independent quantum mechanical calculations of the rates of predissociation of $HeCl_2$ and $NeCl_2$. For the same molecules, Gray and Wozny [49] also carried out time-dependent wave packet dynamics calculations of the rates of predissociation, and Zhang and Zhang [50] reported quantum mechanical golden-rule-approximation calculations of the rates of predissociation of $HeCl_2$ for $v = 8$ to $v = 13$. The results of these calculations have also been listed in Table X and Table XII.

Clearly, quantum mechanical calculations in many cases yield better agreement with experimental data than do the classical theory calculations. Indeed, Gray, Rice, and Noid [51], and Davis and Gray [11] discussed the low-energy limit for the rate of predissociation of HeI_2 and demonstrated that for initial energies lower than a certain value classical theories will predict a zero rate constant while quantum mechanically the rate constant is never zero due to tunneling. These observations indicate that, in some cases—for example, when high accuracy of a theoretical prediction is needed or tunneling effects are important—classical unimolecular reaction rate theory may have to be replaced

TABLE XIII
Predissociation Lifetime (in ps) for a Three-Dimensional HeICl or NeICl Molecule

System	MRRKM	Experiment	Gray
HeICl (v=3)	557	550	1000
NeICl (v=5)	116	—	160
NeICl (v=10)	43	50	—

by a quantum theory. However, Table X also shows that for $HeCl_2$ the predictions of the MRRKM theory are rather close to the results of quantum mechanical calculations, the deviation being, typically, less than 40 ps for all the initially excited states in the energy range studied. It is also interesting to note that even quantum mechanical calculations are not in perfect agreement with the experimental data. This discrepancy could be linked to a number of sources, amongst which are the accuracy of the potential energy surface, the difference between reduced-dimension and full-dimension descriptions, uncertainties in an experimental setup, and so on.

2. HeICl and NeICl

Experimental studies of the fragmentation of HeICl and NeICl by Skene and coworkers [52–54] are restricted to the region of low-lying initial vibrational states of ICl, that is, $v = 3$–10. The classical trajectory calculations of Gray and Wozny [49], the MRRKM calculations [16] and the experimental results are listed in Table XIII for comparison. Once again there is reasonable agreement between MRRKM, direct trajectory calculations, and experimental data.

V. THEORY OF ISOMERIZATION

A. Gray–Rice Theory

Gray and Rice [55] developed a theory of the rate of isomerization that differs in several important aspects from the conventional RRKM theory. In addition to applying the ideas introduced by Davis and Gray—that is, identifying the exact phase-space separatrix for reaction—Gray and Rice proposed a three-state model for the process of isomerization. This proposal was motivated by the observation that as long as the molecule remains intact, there must be, in addition to the states we identify with isomers *A* and *B*, a third state, denoted by *C*, with energy in excess of the barrier to isomerization, which is neither *A* or *B*. The existence of these three states can be clearly seen in trajectory studies of an isomerizing molecule.

The original Gray–Rice theory of isomerization was developed from a two-DOF model in which the potential energy surface displays a double well when

cut along the reaction coordinate. The model potential energy surface they used is defined by the sum of a fourth-order polynomial in the y-coordinate (the reaction coordinate), a Morse potential in the orthogonal coordinate x, and a coupling potential between the two DOFs. The Hamiltonian has the form

$$H(x, y, p_x, p_y) = \frac{p_x^2}{2m_x} + \frac{p_y^2}{2m_y} + V_x + V_y + W(x, y) \tag{201}$$

where

$$V_x = D(1 - e^{-\alpha x})^2 \tag{202}$$

$$V_y = 4y^2(y^2 - 1) + \varepsilon_b \tag{203}$$

$$W(x, y) = 4y^2(y^2 - 1)(1 - e^{-z\alpha x}) \tag{204}$$

Here ε_b is the barrier height of the potential energy surface; D, α, and z are potential parameters, and $m_x = m_y$ is the mass factor.

Clearly, the A and B isomer states should be inside the separatrix, and the state C should be in the phase-space region outside of the separatrix but inside the energy boundary. A schematic diagram of this three-state isomerization model is presented in Fig. 20. From the results of previous analyses of predissociation we expect that within the A and B domains there are, in general, intramolecular bottlenecks to energy transfer. However, these bottlenecks are

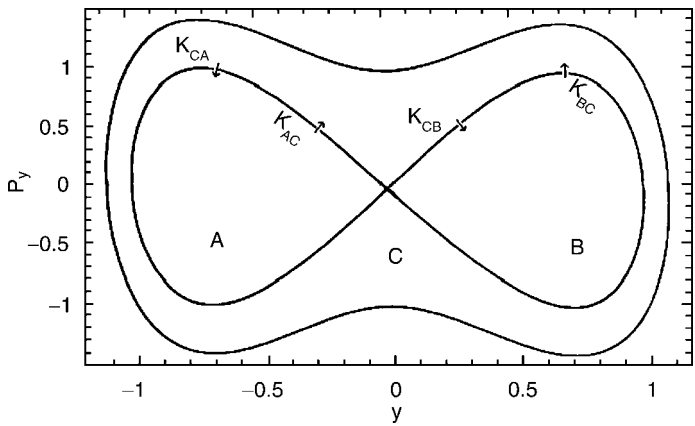

Figure 20. Schematic surface of section in modeling the Gray–Rice theory of isomerization, showing the separatrix and the phase regions A, B, and C, which are the generalized states of the system.

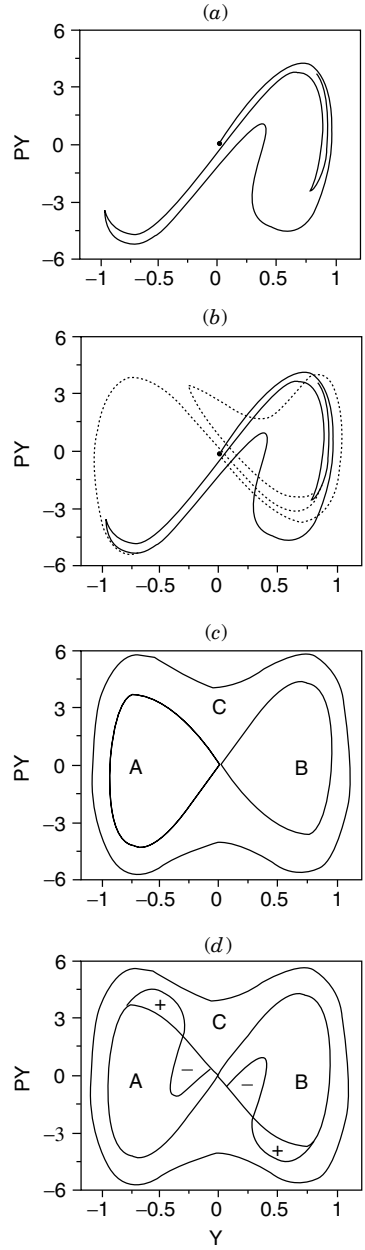

Figure 21. Construction of the exact separatrix on the surface of section for a symmetric double-well model potential. (*a*) The unstable manifold; (*b*) Superposition of the stable (dashed) and unstable (solid) manifolds. (*c*) The exact separatrix, which is a union of portions of the above manifolds. (*d*) Turnstiles superimposed on the separatrix. [From S. K. Gray and S. A. Rice, *J. Chem. Phys.* **86**, 2020 (1987).]

not considered in the original Gray–Rice theory of isomerization because, for the potential parameters and energies studied, the motion in their model system is dominantly chaotic.

Gray and Rice extended the Davis–Gray method of locating a predissociation separatrix to the case of isomerization. That is, they generated the stable and unstable manifolds associated with the saddle point of isomerization and then defined the separatrix as a union of the segments of the generated stable and unstable manifolds. The flux crossing the separatrix can then be calculated by one iteration of the separatrix on the PSS. This is illustrated in Fig. 21. In particular, superimposing the iterated separatrix on the original separatrix yields ''lobes,'' and trajectories are seen to leave the inside of the separatrix only through the small areas labeled ''+'' and enter the separatrix through the areas labeled ''−''. Each ''+'' or ''−'' pair seen in Fig. 21 is called a turnstile.

The time dependences of the populations of the A, B, and C states are then given by the three-state scheme

$$\frac{dA}{dt} = -k_{AC}A + k_{CA}C \tag{205}$$

$$\frac{dB}{dt} = -k_{BC}B + k_{CB}C \tag{206}$$

$$\frac{dC}{dt} = -(k_{CA} + k_{CB})C + k_{AC}A + k_{BC}B \tag{207}$$

where A, B, and C represent the respective populations, k_{AC} is the rate constant associated with phase-space points that cross from A to C, k_{CB} is the rate constant associated with phase space points that cross from C to B, and so on. The normalization condition is $A + B + C = 1$. Furthermore, for a symmetric double well potential one has $k_{AC} = k_{BC}$, $k_{CA} = k_{CB}$. With the initial condition

$$A(0) = 1,\ B(0) = C(0) = 0 \tag{208}$$

the time dependences of the populations are given by

$$A(t) = A_e + \left(\tfrac{1}{2} - A_e\right)e^{-\lambda_1 t} + \tfrac{1}{2}e^{-\lambda_2 t} \tag{209}$$

$$B(t) = B_e + \left(\tfrac{1}{2} - B_e\right)e^{-\lambda_1 t} - \tfrac{1}{2}e^{-\lambda_2 t} \tag{210}$$

$$C(t) = 1 - A(t) - B(t) \tag{211}$$

where $\lambda_1 = k_{AC} + 2k_{CA}$, $\lambda_2 = k_{AC}$, and

$$A_e = B_e = \frac{k_{CA}}{k_{AC} + 2k_{CA}} \tag{212}$$

Gray and Rice also proposed an approximate analytical treatment for locating the separatrix for isomerization, the use of which leads to an overestimate of the rate constants by about a factor of two relative to the values obtained from direct trajectory studies.

B. Zhao–Rice Approximation

Zhao and Rice extended the above-sketched Gray–Rice theory to include the effects of intramolecular energy transfer, using analytical approximations for various quantities [15]. Because this extension is in the same spirit as in the case of unimolecular predissociation, the Zhao–Rice approximation presented here is still called the MRRKM theory. Zhao and Rice employed a model double-well potential similar to that used by Gray and Rice, but parameterized to have greater flexibility. Specifically, the three terms in the potential of Eq. (201) are taken to have the following form:

$$V_x = D(1 - e^{-\alpha x})^2 \tag{213}$$

$$V_y = \epsilon y^2 (y - a)(y - b) + \varepsilon_b \tag{214}$$

$$W(x, y) = \eta \epsilon y^2 y^2 (y - a)(y - b)(1 - e^{-z\alpha x}) \tag{215}$$

where $a, b, \epsilon, m_x, m_y, D, \varepsilon_b, z$, and η are parameters. When $a = b$, the potential function has a symmetric double well; when $a \neq b$, the potential function has an asymmetric double well.

Zhao and Rice adopted the same three-state model for isomerization as introduced by Gray and Rice. Assuming that there are no direct transitions from A to B, the elementary rate constant in the three-state model is given by $k_{AC} = F_{AC}/N_{A,}\ k_{CA} = F_{CA}/N_{C,}$ where N_A and N_C are normalization factors, and $F_{AC} = F_{BC}$ (for the symmetric double-well case) is the flux of phase space points from region A to region C. According to the ARRKM theory one has

$$F_{AC} = \int dx\, dy\, dp_x\, dp_y \delta(S_{\text{Sep}}) \dot{S}_{\text{Sep}} \theta(\dot{S}_{\text{Sep}}) \delta(E - H) \tag{216}$$

where S_{Sep} is the phase-space separatrix dividing region A from region C. Zhao and Rice defined an approximate separatrix by

$$S_{\text{Sep}} = \frac{p_y^2}{2m_y} + V_y + W(\bar{x}, y) - \Delta\varepsilon \tag{217}$$

where $\bar{x}$ is a fixed value of the x-coordinate, and $\Delta\varepsilon$ is given below. Use of S_{Sep} and integrating over p_x and p_y yields

$$F_{AC} = \int \frac{dx\, dy \sqrt{2m_x} \theta(y^\ddagger - y)}{\sqrt{E + V_y + W(\bar{x}, y) - \Delta\varepsilon - V(x, y)}} \left| \frac{\partial[W(x, y) - W(\bar{x}, y)]}{\partial y} \right| \tag{218}$$

where $y^{\ddagger} = 0$ for the case of a symmetric potential energy surface and if the dividing surface defined by $S_{\text{Sep}} = 0$ is the exact separatrix. The normalization constants for regions A and C are calculated from

$$N_A = 4\sqrt{m_x m_y} \int dx\, dy \theta(y^{\ddagger} - y) \arcsin\left(\frac{P_{\min}}{G}\right) \tag{219}$$

$$N_C = 4\sqrt{m_x m_y} \int dx\, dy \theta(y^{\ddagger} - y) \theta[E - V(x,y)] \left[\pi - 2\arcsin\left(\frac{P_{\min}}{G}\right)\right] \tag{220}$$

with

$$G = \sqrt{E - V(x,y)} \tag{221}$$

$$P_{\min} = \min\left[G, \sqrt{\Delta\varepsilon - V_y - W(\bar{x},y)}\right] \tag{222}$$

The Zhao–Rice approximation for obtaining S_{Sep} is based on the following considerations. First, there is a maximum kinetic energy (denoted by ε_b) associated with the motion along the reaction coordinate y and within the separatrix that defines one geometric isomer. They defined the dividing surface to exclude the trajectories for which the kinetic energy along y exceeds this value because such trajectories generate direct conversion of A to B, which is omitted in the Gray–Rice three-state model of isomerization. Second, on the transition state dividing surface the x-component of the energy is defined to be

$$\frac{p_x^2}{2m_x} + V_x = \varepsilon_x \tag{223}$$

Thus, by conservation of energy, one has

$$\frac{p_y^2}{2m_y} + V_y + W(\bar{x},y) = \Delta\varepsilon \tag{224}$$

where $\Delta\varepsilon = E - \varepsilon_x$. Equation (224) is identical to the above definition of S_{Sep} since

$$S_{\text{Sep}} = \frac{p_y^2}{2m_y} + V_y + W(\bar{x},y) - \Delta\varepsilon = 0 \tag{225}$$

Thus, assuming $\Delta\varepsilon = \varepsilon_b$, Zhao and Rice obtained an approximate separatrix, denoted S_{Sep}^A and given by

$$S_{\text{Sep}}^A = \frac{p_y^2}{2m_y} + V_y + W(\bar{x},y) - \varepsilon_b \tag{226}$$

To include some bottleneck effects in intramolecular energy flow, Zhao and Rice defined a second dividing surface drawn around a region of quasi-periodic motion of isomer A. This dividing surface lies inside the separatrix. To so do, they considered the case when the initial state of the system has all of the energy in the x-DOF and only zero-point energy $E_y(0)$ in the y-DOF. By analogy with the construction of S^A_{Sep}, they proposed the following intramolecular energy transfer dividing surface

$$S^A_{\text{intra}} = \frac{p_y^2}{2m_y} + V_y + W(\bar{x}, y) - E_y(0) \tag{227}$$

Note that, although their analysis is based on classical mechanics, the zero-point energy in the y-DOF was taken into account to better approximate the partitioning of the energy between different DOFs. When the motion in the y-DOF is confined to the vicinity of the isomer geometry minimum, the harmonic approximation should be valid. Then

$$E_y(n) = \left(n + \tfrac{1}{2}\right)\hbar\omega_y \tag{228}$$

with

$$\omega_y = \left(\frac{1}{m_y}\frac{\partial^2 H(x,y)}{\partial y^2}\right)^{1/2}_{x=x_0, y=y_0} \tag{229}$$

Inserting this expression into S^A_{intra} yields

$$S^A_{\text{intra}} = \frac{p_y^2}{2m_y} + V_y + W(\bar{x}, y) - \tfrac{1}{2}\hbar\omega_y \tag{230}$$

The corresponding rate constant associated with S^A_{intra} can be calculated in the same way as in the case of S^A_{Sep}.

A simple kinetics model of the three-state mechanism that takes into account bottlenecks to intramolecular energy transfer can be developed by splitting the phase space region A into the quasi-periodic motion region A_1 and the highly chaotic region A_2, with $A = A_1 + A_2$. Such a kinetics model is presented in Fig. 22. Let $k_{A_1A_2}$ be the rate constant for flow of phase space points from A_1 into

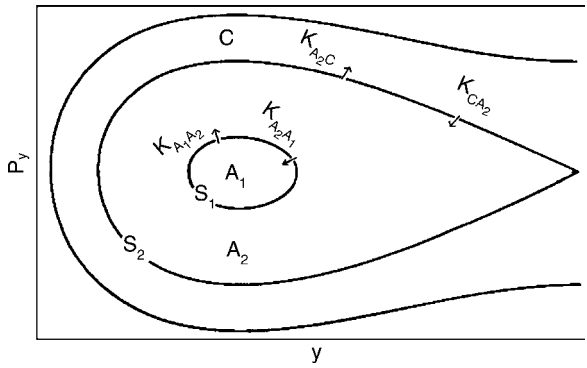

Figure 22. Schematic mechanism of reaction including intramolecular energy transfer. The phase-space of state A is partitioned into A_1 and A_2. S_1 is a representation of an intramolecular energy transfer dividing surface, and S_2 is the A-state separatrix.

A_2, and let $k_{A_2A_1}$ be the back flow rate from A_2 to A_1. Then, with obvious notation one obtains

$$\frac{dA_1}{dt} = -k_{A_1A_2}A_1 + k_{A_2A_1}A_2 \tag{231}$$

$$\frac{dA_2}{dt} = k_{A_1A_2}A_1 - (k_{A_2A_1} + k_{A_2C})A_2 + k_{CA_2}C \tag{232}$$

$$\frac{dB_1}{dt} = -k_{B_1B_2}B_1 + k_{B_2B_1}B_2 \tag{233}$$

$$\frac{dB_2}{dt} = k_{B_1B_2}B_1 - (k_{B_2B_1} + k_{B_2C})B_2 + k_{CB_2}C \tag{234}$$

$$\frac{dC}{dt} = k_{A_2C}A_2 + k_{B_2C}B_2 - (k_{CB_2} + k_{CA_2})C \tag{235}$$

This set of first-order linear differential equations can be formally solved to yield the populations as functions of time for the various regions in phase space.

Based on the Gray–Rice assumption that dynamical chaos is fully developed before the isomerization reaction occurs, crossing the intramolecular bottleneck can be considered to be independent of crossing the intermolecular dividing surface. Then the rate constant for the transfer of phase space points from region A to C, as observed by Gray and Rice, can be described by only using Eqs. (231) and (232) with $k_{CA_2} = 0$. Hence

$$A_1(t) = Q_1 e^{-\lambda_1 t} + \frac{Q_2 k_{A_2A_1}}{k_{A_2A_1} - \lambda_2} e^{-\lambda_2 t} \tag{236}$$

$$A_2(t) = \frac{Q_1 k_{A_1A_2}}{k_{A_2A_1} + k_{A_2C} - \lambda_1} e^{-\lambda_1 t} + Q_2 e^{-\lambda_2 t} \tag{237}$$

where

$$\lambda_1 = \tfrac{1}{2}\left[k_t + \sqrt{k_t^2 - 4k_{A_1A_2}k_{A_2C}}\right] \tag{238}$$

$$\lambda_2 = \tfrac{1}{2}\left[k_t - \sqrt{k_t^2 - 4k_{A_1A_2}k_{A_2C}}\right] \tag{239}$$

$$k_t = k_{A_1A_2} + k_{A_2A_1} + k_{A_2C} \tag{240}$$

$$Q_1 = A_1(0) - \frac{Q_2 k_{A_2A_1}}{k_{A_1A_2} - \lambda_2} \tag{241}$$

$$Q_2 = \left[A_2(0) - \frac{A_1(0)k_{A_1A_2}}{k_{A_2A_1} + k_{A_2C} - \lambda_1}\right] \times \left[1 - \frac{k_{A_1A_2}k_{A_2A_1}}{(k_{A_1A_2} - \lambda_2)(k_{A_2A_1} + k_{A_2C} - \lambda_1)}\right]^{-1} \tag{242}$$

The population inside the A-separatrix $A(t) = A_1(t) + A_2(t)$ is given by

$$A(t) = Q_1\left(1 + \frac{k_{A_1A_2}}{k_{A_2A_1} + k_{A_2C} - \lambda_1}\right)e^{-\lambda_1 t} + Q_2\left(1 + \frac{k_{A_2A_1}}{k_{A_2A_1} - \lambda_2}\right)e^{-\lambda_2 t} \tag{243}$$

The above result can also rewritten as

$$\frac{A(t)}{A(0)} = \bar{Q}_1\left(1 + \frac{k_{A_1A_2}}{k_{A_2A_1} + k_{A_2C} - \lambda_1}\right)e^{-\lambda_1 t} + \bar{Q}_2\left(1 + \frac{k_{A_2A_1}}{k_{A_2A_1} - \lambda_2}\right)e^{-\lambda_2 t} \tag{244}$$

with

$$\bar{Q}_1 = f_1 - \frac{\bar{Q}_2 k_{A_2A_1}}{k_{A_2A_1} - \lambda_2} \tag{245}$$

$$\bar{Q}_2 = \left[f_2 - \frac{f_1 k_{A_1A_2}}{k_{A_2A_1} + k_{A_2C} - \lambda_1}\right] \times \left[1 - \frac{k_{A_1A_2}k_{A_2A_1}}{(k_{A_1A_2} - \lambda_2)(k_{A_2A_1} + k_{A_2C} - \lambda_1)}\right]^{-1} \tag{246}$$

and

$$f_1 = \frac{A_1(0)}{A(0)}, f_2 = \frac{A_2(0)}{A(0)} \tag{247}$$

Assuming that the effective rate constant k_{AC} is equivalent to that determined from trajectory studies and also assuming that

$$A(t) = A(0)e^{-k_{AC}t} \tag{248}$$

for short time, Zhao and Rice evaluated k_{AC} by fitting the numerical simulation data. Specifically, this fitting was carried out by setting

$$\ln\left[\frac{A(\tau_{AC})}{A(0)}\right] = -1 \tag{249}$$

with $k_{AC} = 1/\tau_{AC}$. In essence, this procedure assumes that relaxation in region A is fully developed before the transition from A to C occurs, and thus the contribution from $k_{A_2A_1}$ is negligible. The initial conditions are chosen so that f_1 is approximated by the fraction of quasi-periodic region on the PSS within the isomer A region. Once the rate constant k_{AC} is known, k_{CA} can be determined from

$$k_{CA} = \frac{k_{AC}k_{CA_2}}{k_{A_2C}} \tag{250}$$

If the A to C and C to B transitions are independent processes, then a simple approximation to the effective isomerization lifetime τ can be made:

$$\tau = \frac{1}{k} = \frac{1}{k_{CA}} + \frac{1}{k_{AC}} \tag{251}$$

C. Reactive Island Theory

A beautiful classical theory of unimolecular isomerization called the reactive island theory (RIT) has been developed by DeLeon and Marston [23] and by DeLeon and co-workers [24,25]. In RIT the classical phase-space structures are analyzed in great detail. Indeed, the key observation in RIT is that different cylindrical manifolds in phase space can act as mediators of unimolecular conformational isomerization. Figure 23 illustrates homoclinic tangling of motion near an unstable periodic orbit in a system of two DOFs with a fixed point τ, and it applies to a wide class of isomerization reaction with two stable isomer

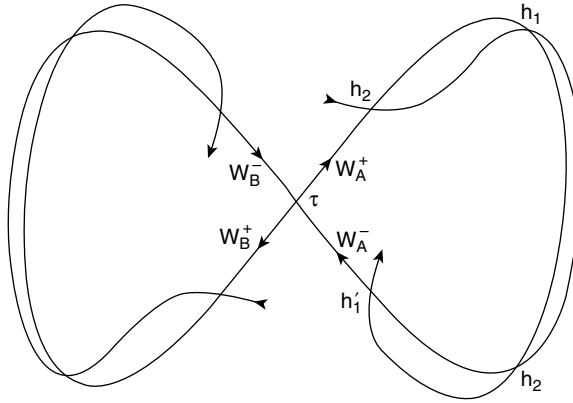

Figure 23. Homoclinic tangling of motion near an unstable periodic orbit in a system of two degrees of freedom at a fixed point τ. [From A. M. O. De Almeida et al. , *Physica D* **46**, 265 (1990).]

states (A and B), represented by two wells in the potential energy surface. Furthermore, the existence of a homoclinic orbit guarantees that on a particular surface of section the Poincaré map always has the structure shown in Fig. 23.

As is clear from the previously discussed properties of unstable periodic orbits and NHIM, there are both stable (W_A^-, W_B^-) and unstable manifolds (W_A^+, W_B^+) associated with the unstable fixed point shown in Fig. 23. These manifolds are called stable and unstable cylinders in RIT. The intersection of the cylinders with a surface of section generates the so-called reactive islands (RI). Specifically, RIs can be constructed for a given dynamical system by propagating ensembles of trajectories along the stable and unstable branches of a reactive periodic orbit, the propagation being in negative and positive time, respectively. Figure 24 presents Poincaré maps for an isomerization system on two different surfaces, showing W^+ and W^- RI structures.

For a system with two DOFs, both the cylinder and the surface of section (denoted Σ) are of dimension two and embedded within the three-dimensional energy shell. Their intersection is therefore generically along lines. There are three major possibilities: (i) The intersection is a line of infinite length; (ii) the intersection is a reducible closed curve on the cylinder; and (iii) the intersection is an irreducible closed curve on the cylinder. Figure 25 shows a schematic drawing of a surface Σ intersecting a W^- cylinder. In Fig. 25A (one orbit) and Fig. 25B (several orbits) the surface intersects W^- tangentially forming a reducible curve. In Fig. 25C the surface intersects W^- transversely, forming an irreducible curve (which is identified to be an RI in RIT). Figure 26 shows a schematic surface Σ intersecting a W^- cylinder both transversely and tangentially, demonstrating how a discontinuous Poincaré map can be obtained.

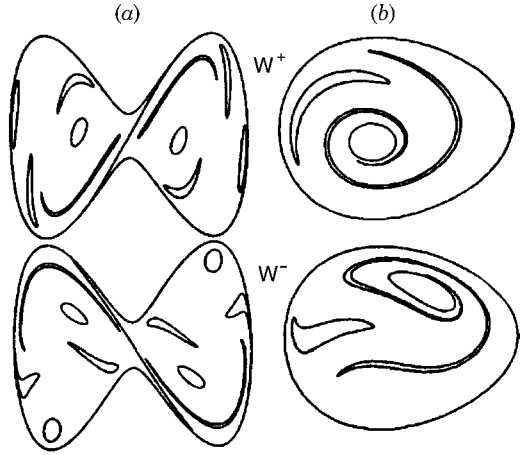

Figure 24. Reactive island structure for a two-well potential isomerization model, generated from the stable and unstable branches of the transition state fixed point. (a) Stable branch structure. (b) Unstable branch structure. [From A. M. O. De Almeida et al., *Physica D* **46**, 265 (1990).]

The RIs display a number of interesting mathematical and physical properties. To briefly introduce these properties, we define the RIs generated from the same branch (either the stable or the unstable branch) to be of the same family. We also denote by RI_{j+1} the reactive island generated from a further iteration of the reactive island RI_j. That is, the area of RI_j will, upon one positive or negative time iteration, map onto RI_{j+1} or RI_{j-1} within the same family. It

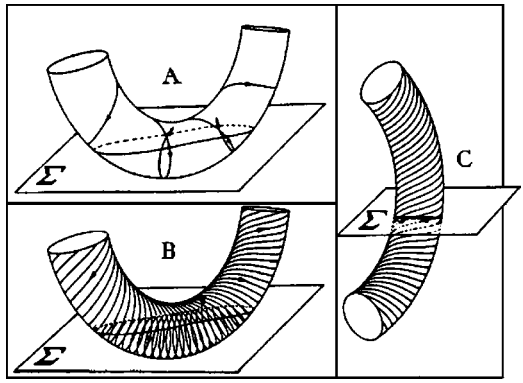

Figure 25. Schematic drawing of a surface Σ intersecting a cylinder. (A, one orbit; B, several orbits) Σ intersects the cylinder tangentially, forming a reducible curve. (C) Σ intersects the cyclinder transversally, forming an irreducible curve—that is, a reactive island. [From A. M. O. De Almeida, et al. , *Physica D* **46**, 265 (1990).]

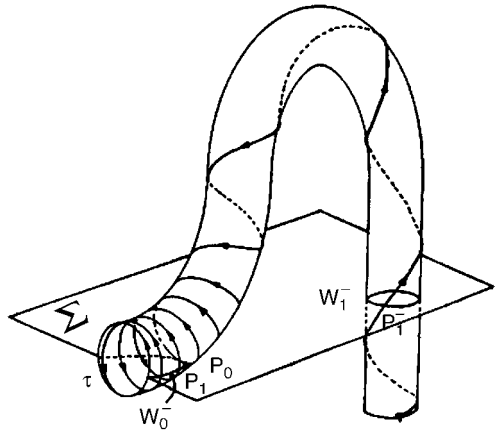

Figure 26. A schematic presentation of a surface Σ intersecting with a W^- cylinder both transversally and tangentially, and how a discontinuous Poincaré map is obtained. [From A. M. O. De Almeida et al., *Physica D* **46**, 265 (1990).]

can be shown that: (i) All reactive islands within a family have the same area. (ii) The area of an RI is equal to the action over one period of motion of the transition state periodic orbit. Consequently, the area of an RI from a stable branch family will be equal to the area of an RI from an unstable branch family. (iii) Reactive islands from the same family cannot intersect one another. (iv) The intersection of two RIs from different families generates four lobes and an overlap region. Four homoclinic points will be generated by the peripheries of the two intersecting RIs. The four lobes pair into two sets of equal area lobes. Those lobes generated from the stable branch bound reactive dynamics in positive time, whereas those lobes generated from the unstable branch bound reactive dynamics in negative time. The overlap region is reactive in both positive and negative time. These properties of RIs make it clear that the probabilities associated with isomerization reaction, trapping, and back reaction are entirely determined by the overlap between stable and unstable branches of RIs. (v) Reactive to trapped motion will proceed through the RIs generated from the unstable branch, whereas trapped to reactive motion will proceed through the RIs generated from the stable branch. The last member of a family of RIs from the stable branch constitutes the bottleneck to reaction.

Figure 27 illustrates reactive motion through cylindrical manifolds and construction of the manifolds. It shows that a trajectory initially trapped in conformer A eventually enters the interior of the cylinder W_A^-. By going through W_A^-, it reacts, and it goes to conformer B by entering manifold W_B^+. The cylinder W_A^- mediates all pre-reactive motion $A \rightarrow B$, and the cylinder W_B^- mediates all

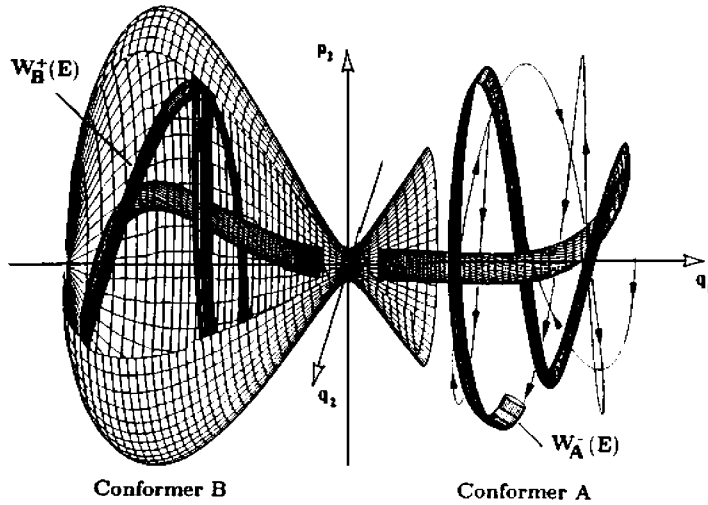

Figure 27. An example of cylindrincal manifolds in a system with two DOFs. A trajectory is initially trapped in conformer A and eventually enters the interior of the cylinder W_A^-. By going through W_A^-, it reacts, and it goes to conformer B by entering the manifold W_B^+. [From N. De Leon, M. A. Mehta, and R. Q. Topper, *J. Chem. Phys.* **94**, 8310 (1991).]

pre-reactive motion $B \to A$. Due to time-reversal symmetry, W_A^+ and W_B^+ mediate all post-reactive motion. Therefore, the four cylinders, particularly their overlaps in phase space, mediate all the details of the kinetics of isomerization—for example, how flux moves back and forth between the two isomer states.

A detailed discussion of RIT is beyond the scope of this chapter. Here we confine ourselves to the first-order kinetics obtained from RIT. Since RIT shows that all forward reactions must occur by passing through the interior of W_A^-, and all backward reactions must occur by passing through the interior of W_B^-, the simplest reaction mechanism predicted by RIT takes into account only direct recrossing—that is, recrossing motion within one oscillation of the reaction coordinate. The kinetics associated with this simplest case can be represented by

$$\begin{aligned} A &\xrightarrow{\delta} W_A^- \xrightarrow{\gamma} W_B^+ \xrightarrow{\beta} B \\ B &\xrightarrow{\delta} W_B^- \xrightarrow{\gamma} W_A^+ \xrightarrow{\beta} A \end{aligned} \tag{252}$$

In addition, RIT introduces a common rate constant α associated with the transitions $W_A^+ \to W_A^-$ and $W_B^+ \to W_B^-$. Then the population dynamics is

given by

$$\frac{dA(t)}{dt} = \beta W_A^+(t) - \delta A(t) \tag{253}$$

$$\frac{dW_A^+(t)}{dt} = \gamma W_B^-(t) - (\alpha + \beta) W_A^+(t) \tag{254}$$

$$\frac{dW_A^-(t)}{dt} = \alpha W_A^+(t) + \delta A(t) - \gamma W_A^-(t) \tag{255}$$

$$\frac{dB(t)}{dt} = \beta W_B^+(t) - \delta B(t) \tag{256}$$

$$\frac{dW_B^+(t)}{dt} = \gamma W_A^-(t) - (\alpha + \beta) W_B^+(t) \tag{257}$$

$$\frac{dW_B^-(t)}{dt} = \alpha W_B^+(t) + \delta B(t) - \gamma W_B^-(t) \tag{258}$$

Here $A(t)$, $B(t)$, $W_A^+(t)$, $W_A^-(t)$, $B(t)$, $W_B^+(t)$, and $W_B^-(t)$ are the populations of the respective phase space regions, and the rate constants α, β, γ, and δ are explicitly given by RIT by calculating the areas of overlap regions and the density of states. The overall isomerization rate constant can be obtained by solving the preceding set of equations. Assuming a set of eigenvalues $\{\lambda\}$ associated with the kinetic equations, RIT takes $k_{\mathrm{RIT}} = \inf(\lambda)$ to be the reaction rate constant of isomerization.

As an application of RIT, consider the following Hamiltonian system

$$H = \frac{1}{2\mu}(p_1 + p_2) + D[1 - \exp(-\lambda q_2)] + 4q_1^2\left(q_1^2 - 1\right)\exp(-z\lambda q_2) \tag{259}$$

where the parameters have the values $\mu = 8.0$, $D = 10.0$, $z = 2.3$, and $\lambda = 1.95$. The Hamiltonian is symmetric with respect to the reaction coordinate q_1. The dynamics of this specific system is classically chaotic, the potential energy barrier is at $E = 0$, and there exists a family of periodic orbits along q_2 at $q_1 = 0$ for energies greater than zero. Figures 28 and 29 present reactive island structure on a surface of section and kinetics data for this symmetric model Hamiltonian with energies $E = 1.0$ and 3.0, respectively, compared to the result from a purely random model (PR) and to that of classical trajectory calculations.

D. Gray–Rice Theory Versus Reactive Island Theory

It is interesting and important to note that the conceptual structure of the lowest-order application of RIT is similar to the Gray–Rice three-state model of

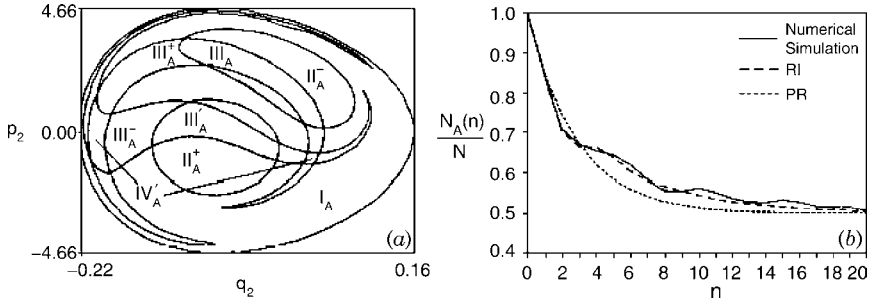

Figure 28. Reactive island structure on a surface of section and kinetics data for the symmetric model Hamiltonian for $E = 1.0$. (*a*) The reactive island structure. (*b*) The population decay of isomer *A* from different calcualtions. [From A. M. O. De Almeida et al., *Physica D* **46**, 265 (1990).]

isomerization. Let us first recall that the mechanism of the Gray–Rice three-state model can be summarized in the form

$$[A] \underset{k_{CA}}{\overset{k_{AC}}{\rightleftarrows}} [C] \underset{k_{CB}}{\overset{k_{BC}}{\rightleftarrows}} [B] \tag{260}$$

where A and B are the stable isomer states, and C is the intermediate state. The three state kinetics equations are

$$\frac{dA}{dt} = -k_{AC}A + k_{CA}C \tag{261}$$

$$\frac{dB}{dt} = -k_{BC}B + k_{CB}C \tag{262}$$

$$\frac{dC}{dt} = -(k_{CA} + k_{CB})C + k_{AC}A + k_{BC}B \tag{263}$$

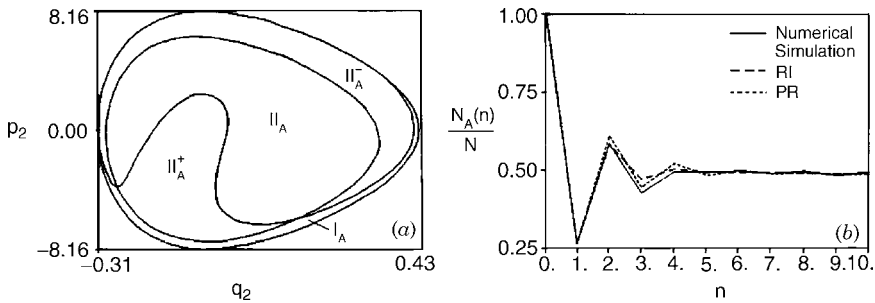

Figure 29. Reactive island structure on a surface of section and kinetics data for the symmetric model Hamiltonian for $E = 3.0$. (*a*) The reactive island structure. (*b*) The population decay of isomer *A* from different calcualtions. [From A. M. O. De Almeida et al., *Physica D* **46**, 265 (1990).]

A special solution with the initial conditions $A(0) = 1$, $B(0) = C(0) = 0$ is

$$A(t) = A_e + \left(\tfrac{1}{2} - A_e\right)e^{-\lambda_1 t} + \tfrac{1}{2}e^{-\lambda_2 t} \tag{264}$$

$$B(t) = B_e + \left(\tfrac{1}{2} - B_e\right)e^{-\lambda_1 t} - \tfrac{1}{2}e^{-\lambda_2 t} \tag{265}$$

$$C(t) = 1 - A(t) - B(t) \tag{266}$$

where

$$A_e = B_e = \frac{k_{CA}}{k_{AC} + 2k_{CA}} \tag{267}$$

and the two exponents are $\lambda_1 = k_{AC} + 2k_{CA}$, $\lambda_2 = k_{AC}$.

Consider first the case where all the three states are taken into account and $\lambda_2 < \lambda_1$. Then the isomerization rate from the Gray–Rice theory is characterized by the decay rate constant $\lambda_2 = k_{AC}$. This is a general result from the three-state mechanism. Consider a second case in which the third intermediate state C vanishes from the mechanism by setting $C = 0$. Then the reaction mechanism becomes

$$[A] \underset{k_{BA}}{\overset{k_{AB}}{\rightleftarrows}} [B] \tag{268}$$

for which the reaction rate constant must be $(k_{AB} + k_{BA}) = 2k_{AB}$ for the symmetric double-well potential. This result can be derived from the Gray–Rice theory by setting $C = 0$. In doing so, the equilibrium concentrations of A and B are $A_e = 1/2$, and $B_e = 1/2$ for any symmetric double-well potential. Then from Eq. (267) one has

$$A_e = B_e = \frac{k_{CA}}{k_{AC} + 2k_{CA}} = \tfrac{1}{2} \tag{269}$$

which gives

$$k_{AC} + 2k_{CA} = 2k_{CA} \tag{270}$$

or

$$k_{AC} = 0 \tag{271}$$

This is true, since the C state does not exist. Hence, if the system goes to the B state from C, it must come from A, and vice versa. This implies that

$$k_{CB} \rightarrow k_{AB},\ k_{CA} \rightarrow k_{BA} \tag{272}$$

and

$$\lambda_1 = k_{AC} + 2k_{CA} = 2k_{BA} = 2k_{AB} \tag{273}$$

$$\lambda_2 = k_{AC} = 0 \tag{274}$$

Therefore, the reaction rate constant is now $\lambda_1 = 2k_{AB}$, which is exactly the RRKM rate constant.

To consider the relationship between RIT and the Gray–Rice theory, we reexpress the simplest reaction mechanism of RI T in the form

$$\begin{array}{ccccc} & & W_{AB} & & \\ & \delta \nearrow & & \searrow \beta & \\ A & & \alpha \Updownarrow \alpha & & B \\ & \beta \nwarrow & & \swarrow \delta & \\ & & W_{BA} & & \end{array} \tag{275}$$

where W_{AB} is comprised of W_A^- and W_B^+ and W_{BA} is comprised of W_B^- and W_A^+. Clearly, Eq. (275) indicates that between state A and state B there are the intermediate states W_{AB} and W_{BA}. Identifying the intermediate states W_{AB} and W_{BA} with the state C in the Gray–Rice theory, one sees that (first-order) RIT and the Gray–Rice theory are based upon the same reaction mechanism. Specifically, for the case of a symmetric double-well potential, RIT yields the rate constant [56]

$$k_{\mathrm{RIT}} = \frac{4F(E)}{N_T}\left(\frac{1-Z}{1+Z}\right) \tag{276}$$

where $F(E)$ is the flux from A to B in the two-state mechanism (i.e., $C = 0$), N_T is the population trapped in the whole phase space, and Z is the fraction of recrossing motion. Assuming that N_A is the population of the A state in the Gray–Rice theory, we have

$$k_{\mathrm{RIT}} = \frac{2F(E)}{N_A}\left(\frac{1-Z}{1+Z}\right) \tag{277}$$

Since the flux $F_{\mathrm{GR}}(E)$ in the Gray–Rice theory is defined by the flux crossing the separatrix from the trapped A state to state $C = C_A + C_B$, we have

$$2F(E) \approx F_{\mathrm{GR}}(E) \tag{278}$$

and

$$k_{\mathrm{RIT}} = \frac{F_{\mathrm{GR}}(E)}{N_A}\left(\frac{1-Z}{1+Z}\right) \tag{279}$$

Equation (279) suggests that in the $Z = 0$ limit,

$$k_{\mathrm{RIT}} = \frac{F_{\mathrm{GR}}(E)}{N_A} = k_{\mathrm{GR}} \tag{280}$$

This important similarity between the first-order RIT and the Gray–Rice theory was also analyzed by Deleon and Ling [56] with, however, different conclusions.

The difference between the Gray–Rice theory and RIT in its general form is evident. In the Gray–Rice theory the chaotic dynamics of isomerization is assumed to be fully developed. This is why the flux across the reaction separatix can be calculated knowing only the properties of the separatrix and the density of phase space points in the chaotic domain. By contrast, RIT shows that there is substructure to the chaotic dynamics in that trajectories that lead to isomerization pass through RIs which are distinct regions embedded in the chaotic domain. Such substructure in phase space exposes the detailed dynamics of isomerization which is not considered by the Gray–Rice theory. However, since the area of reactive islands is preserved under the stroboscopic mapping and the area of the PSS is finite, successive mappings of a reactive island will eventually cover the surface of section. As such, the area of intersection of two reactive islands from different branches decreases as the stage of mapping increases, and the locations of intersections are apparently randomly distributed on the PSS. This implies that contributions to the rate of isomerization come from all over the surface of section, a fact that is consistent with the Gray–Rice analysis.

E. Isomerization in Double-Well Systems

Consider the rate constants for isomerization in symmetric and asymmetric double-well systems predicted by the several theories discussed above. The two-well potential for coupled x and y DOFs is given by

$$\begin{aligned} V(x,y) = {} & D(1-e^{-\alpha x})^2 + \epsilon y^2(y-a)(y-b) + \varepsilon_b \\ & + \eta\epsilon y^2 y^2 (y-a)(y-b)(1-e^{-z\alpha x}) \end{aligned} \tag{281}$$

where $a, b, \epsilon, m_x, m_y, D, \varepsilon_b, z$, and η are parameters. The potential is symmetric for $a = b$ and asymmetric for $a \neq b$. In all the systems studied below $m_x = m_y = 8.0$, $D = 10.0$, $\varepsilon_b = 1.0$, $\epsilon = 4$. Different choices of the other parameters, listed in Table XIV, give rise to different systems. A schematic plot of both the symmetric and the asymmetric potentials is given in Fig. 30.

TABLE XIV
The System Parameters for a Number of Model Double-Well Potentials[a]

System No.	z	α	Energy (E)	a	b	η
1	1.0	1.50	1.25	1.0	1.0	1.0
			2.00	1.0	1.0	1.0
			3.00	1.0	1.0	1.0
			6.00	1.0	1.0	1.0
2	2.3	2.10	1.05	1.0	1.0	−1.0
3	1.9	1.95	1.20	1.0	1.0	−1.0
4	2.3	1.95	2.00	1.0	1.0	−1.0
5	1.7	2.00	2.00	1.0	1.0	−1.0
6	1.8	2.10	2.50	1.0	1.0	−1.0
7	2.3	1.95	1.05	1.1	0.9	−1.0
8	2.3	1.95	1.50	1.1	0.9	−1.0

[a] Note that the potential is symmetric for $a = b$ and asymmetric for $a \neq b$.

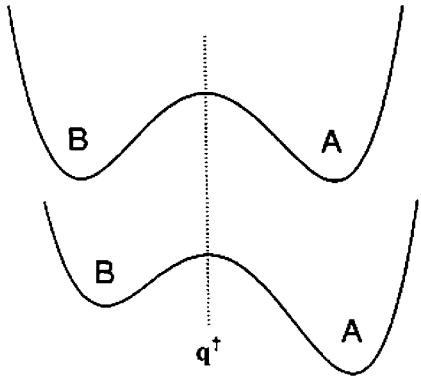

Figure 30. A schematic presentation of the symmetric and asymmetric double-well potentials.

System No. 1 describes a symmetric double-well potential that was studied by Gray and Rice. A PSS for this system is displayed in Fig. 31. For this system the MRRKM results [15] are presented in Table XV, compared to the exact trajectory calculations by Gray and Rice [55]. It is seen that for all the energies considered, the predicted rate constants are in good agreement with Gray and Rice's results except for $E = 3.00$, for which the MRRKM theory overestimates the rate constant by a factor of 1.25. It is plausible that a principal component of this difference arises from uncertainty in the value of f_{QP}—that is, the fraction of quasi-periodic motion on the PSS. Indeed, a small change in that value will bring the calculated and exact values into agreement to the same accuracy as for the other energies considered. Clearly, the Zhao–Rice approximations to the

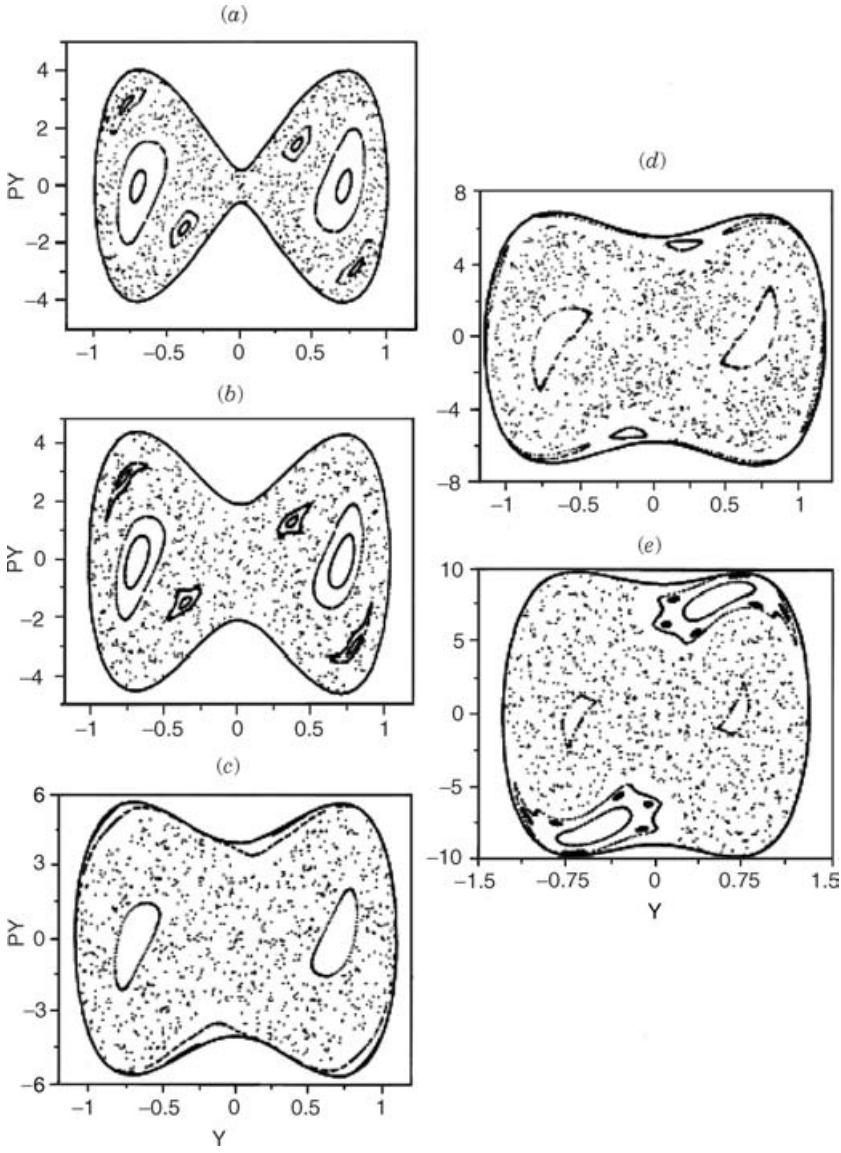

Figure 31. Poincaré surfaces of section for a symmetric double-well potential with parameters given in Table I. (*a*) $E = 1.02$, (*b*) $E = 1.25$, (*c*) $E = 2.0$, (*d*) $E = 3.0$, and (*e*) $E = 6.0$. [From S. K. Gray and S. A. Rice, *J. Chem. Phys.* **86**, 2020 (1987).]

TABLE XV
Comparison of Elementary Rate Constants Calculated from the MRRKM Theory to Those Obtained by Gray and Rice's Exact Trajectory Calculations [55] for System No. 1

E	f_{QP}	k_{intra}	k_{Sep}	k_{AC}	Gray–Rice
1.25	0.24	0.055	0.025	0.022	0.026
2.00	0.099	0.085	0.054	0.050	0.048
3.00	0.058	0.107	0.075	0.071	0.057
6.00	0.038	0.125	0.097	0.094	0.100

separatrix and to the rate of intramolecular energy transfer yield a significant improvement in the predicted isomerization rate constants relative to the predictions of the earlier theory of Gray and Rice (which gives an error of a factor around 2.0).

Systems No. 2 to No. 6 defined in Table XIV were studied by De Leon and coworkers using RIT [23,57]. They reported that these systems are primarily chaotic. Their theoretical results are compared, in Table XVI, to their trajectory calculations, the RRKM results, the MRRKM calculations, and the results based on a reaction path Hamiltonian analysis by Jang and Rice [58]. The entries in Table XVI show that the MRRKM theory yields rate constants that are in excellent agreement with direct trajectory calculations for almost all the cases. By contrast, the RRKM results overestimate the isomerization rate constants by a factor of around 4.0. The MRRKM theory does give an erroneous prediction for system No. 2, which has a very low excess energy $E = 1.05$. In such cases one may have to consider more than one intramolecular bottleneck to make more accurate calculations of the isomerization rate. Note that RIT seems to give the best result. This is understandable because RIT takes into account more information concerning the reaction dynamics. Note also that, at least for these model systems, the reaction path approach of Jang and Rice is successful. This suggests that although, as shown by Gray and Rice, a large fraction of the trajectories that contribute to the isomerization process depart considerably from the minimum energy path through the saddle region, the reaction path

TABLE XVI
Isomerization Rate Constants for Symmetric Double-Well Potential Systems Defined in Table XIV

System No.	RRKM	MRRKM	Trajectory	Reaction-Path	RIT
2	0.0084	0.0069	0.0023	0.011	0.0023
3	0.031	0.015	0.014	0.018	0.015
4	0.073	0.029	—	0.029	0.027
5	0.096	0.023	0.020	0.020	0.020
6	0.120	0.026	0.031	0.021	0.029

TABLE XVII
Isomerization Rate Constants for Systems No. 7 and No. 8 Obtained from Trajectory Calculations, RIT, the Transition State Theory (TST), and the MRRKM Theory

System No.	Trajectory	RIT	TST	MRRKM
7	0.04	0.0614	0.089	0.089
8	0.27	0.312	0.626	0.31

formalism does capture some contributions from these trajectories via the self-consistent inclusion of the averaged motion perpendicular to the reaction coordinate.

Comparison between the MRRKM theory and RIT [59] in the case of asymmetric double-well potentials—that is, systems No. 7 and No. 8—is made in Table XVII. There the transition state theory (TST) results reported by De Leon et al. [59] are also given. The MRRKM results were obtained by ignoring the effects of intramolecular energy transfer, and they are seen to be in good agreement with those from RIT and from direct numerical simulations. It is also seen that both the MRRKM theory and RIT considerably overestimate the rate constant for system No. 7. Again this is possibly due to the presence of intramolecular energy transfer bottlenecks.

F. Isomerization in a Triple-Well System

Jang, Zhao, and Rice [60] also examined the rate of isomerization in a model system that supports three stable isomers, denoted by B, A and B', and a bound state denoted by C, which is distinct from all the isomeric states. A schematic plot of the triple-well potential and a phase-space contour plot is presented in Fig. 32.

For simplicity we assume that the following: (i) Isomers B and B' have the same energy, as displayed in Fig. 32. (ii) Isomer A has an energy that is higher than that of B and B'. (iii) The bound state C corresponds to all system conformations with energies in excess of the barrier energies separating B, A and B'. (iv) The potential wells corresponding to the several isomers are linearly distributed along the reaction coordinate in the sequence B', A, B. While both the direct conversion

$$B \rightarrow C \rightarrow B' \tag{282}$$

and the indirect conversion

$$B \rightarrow C \rightarrow A \rightarrow C \rightarrow B' \tag{283}$$

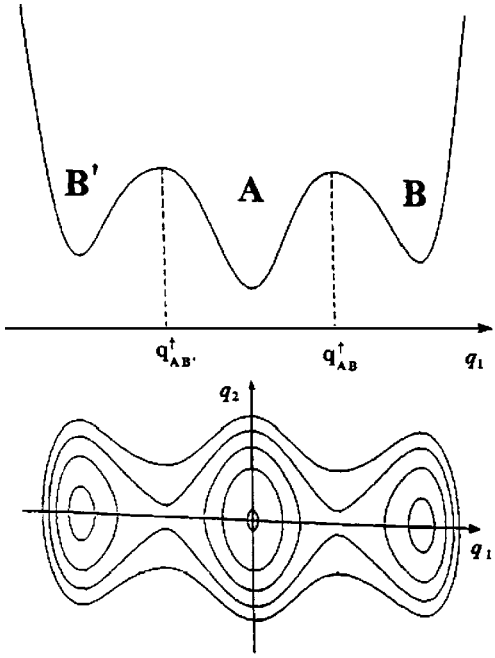

Figure 32. A three-well potential modeling unimolecular isomerization between three isomers, denoted by B, A, and B'.

are allowed in the considerations, we neglect conversions of the type $B \rightarrow A$ and $A \rightarrow B$. The main interest is with the extent to which the presence of the intermediate isomeric state A modifies the flux from B to B', hence also the rate of that isomerization.

The model triple-well potential surface is defined by the sum of a sixth-order polynomial in the displacement of y-coordinate, a Morse potential in the orthogonal x-coordinate, and a potential describing the coupling between x and y:

$$V(x, y) = V_x + V_y + W(x, y) \tag{284}$$

where

$$V_x = D(1 - e^{-\alpha x})^2 \tag{285}$$

$$V_y = \epsilon y^2 \left(y^2 - a^2\right)\left(y^2 - b^2\right) \tag{286}$$

$$W(x, y) = \eta\epsilon y^2 \left(y^2 - a^2\right)\left(y^2 - b^2\right)(1 - e^{-z\alpha x}) \tag{287}$$

TABLE XVIII
Elementary Rate Constants and Lifetimes from the MRRKM Theory for a Model Triple-Well Potential

E	k_{AC}	k_{BC}	k_{CA}	k_{CB}	k	τ
0.58	0.066	0.028	0.034	0.024	0.016	62
0.70	0.20	0.086	0.063	0.049	0.047	21
0.75	0.24	0.11	0.067	0.054	0.055	18
0.80	0.27	0.12	0.071	0.057	0.063	16
0.85	0.31	0.14	0.074	0.059	0.071	14
0.90	0.34	0.15	0.075	0.061	0.076	13
0.95	0.36	0.16	0.077	0.063	0.082	12
1.00	0.39	0.17	0.079	0.064	0.087	11

and the parameters $m_x, m_y, D, \epsilon, \alpha, z, \eta, a, b$ take the following values:

$$\begin{aligned} m_x &= 8.0, \quad & m_y &= 8.0, \quad & D &= 5.00 \\ \epsilon &= 10.00, \quad & \alpha &= 1.95, \quad & \eta &= -1.00 \\ z &= 5.00, \quad & a &= 0.90, \quad & b &= 1.00 \end{aligned}$$

The saddle point between isomer B and isomer A is represented by $y_1^\ddagger = q_{AB}^\ddagger$, and the saddle point between isomer B' and isomer A is represented by $y_2^\ddagger = q_{AB'}^\ddagger$. As in the case of double-well potentials, the MRRKM theory defines isomerization separatrix surfaces for the three isomer states B, A and B' by

$$S_{\text{Sep}} = \frac{p_y^2}{2m_y} + V_y + W(\bar{x}, y) - \varepsilon_b = \begin{cases} S_B, & y \geq y_1^\ddagger \\ S_A, & y_1^\ddagger \leq y \leq y_2^\ddagger \\ S_{B'}, & y \leq y_2^\ddagger \end{cases} \tag{288}$$

where $\bar{x}$ is a fixed point in x. Using this definition for the separatrix, the MRRKM calculations can be carried out. We also define, solely for convenience of discussion, the "isomerization rate constants" $k = 1/\tau$, where τ is the "relaxation lifetime." The MRRKM results for this system, as a function of energy, are displayed in Table XVIII.

A few of these cases were studied within the framework of RIT by DeLeon et al. [59] for energy $E = 0.58$, 0.75, and 1.00. The "isomerization rate constants" calculated from the MRRKM theory are in very good agreement with those obtained from trajectory calculations and with those calculated from RIT. This comparison is given in Table XIX. Interestingly, both the MRRKM theory and RIT more or less overestimate the rate of isomerization when compared to the trajectory calculations.

TABLE XIX
The Isomerization Rate Constants in a Model Three-Well Potential, Obtained from MRRKM, Trajectory Calculations, and RIT

E	Trajectory	RIT	MRRKM
0.58	0.015	0.019	0.016
0.75	0.047	0.049	0.055
1.00	0.085	0.091	0.087

G. Isomerization of 3-Phospholene

Isomerization of 3-phospholene is of considerable interest for two reasons. First, the potential energy surface for the isomerization reaction coordinates is well known due to the spectroscopic studies of Harthcock and Laane [61,62]. Second, its Hamiltonian has important off-diagonal kinetic energy coupling terms, which provide a different test of the accuracy of the approximations used in the MRRKM theory than posed by previous applications.

Let x be the ring-puckering coordinate and y the PH inversion coordinate in 3-phospholene (see Fig. 33). The dynamics of isomerization in this molecule is assumed to be adequately described by these coupled two DOF's without need for consideration of other DOFs. Under this assumption, the Harthcock–Laane potential energy surface consists of a fourth-order polynomial in x, a fourth-order polynomial in y, and a sixth-order polynomial coupling x and y. With molecular rotation neglected, the model Hamiltonian for 3-phospholene is given by

$$H = \tfrac{1}{2} P^T \cdot G \cdot P + V(x, y) \tag{289}$$

where

$$V_x = a_1 x^4 + b_1 x^2 \tag{290}$$

$$V_y = a_2 y^4 + b_2 y^2 \tag{291}$$

$$W(x, y) = \sum_{m=1}^{5} \sum_{n=1}^{5} c_{mn} x^m y^n \tag{292}$$

$$V(x, y) = V_x + V_y + W(x, y) \tag{293}$$

Here P^T is the transpose of the momentum vector P. As indicated above, the kinetic energy is not diagonal in either x or y. The 2×2 kinetic energy matrix,

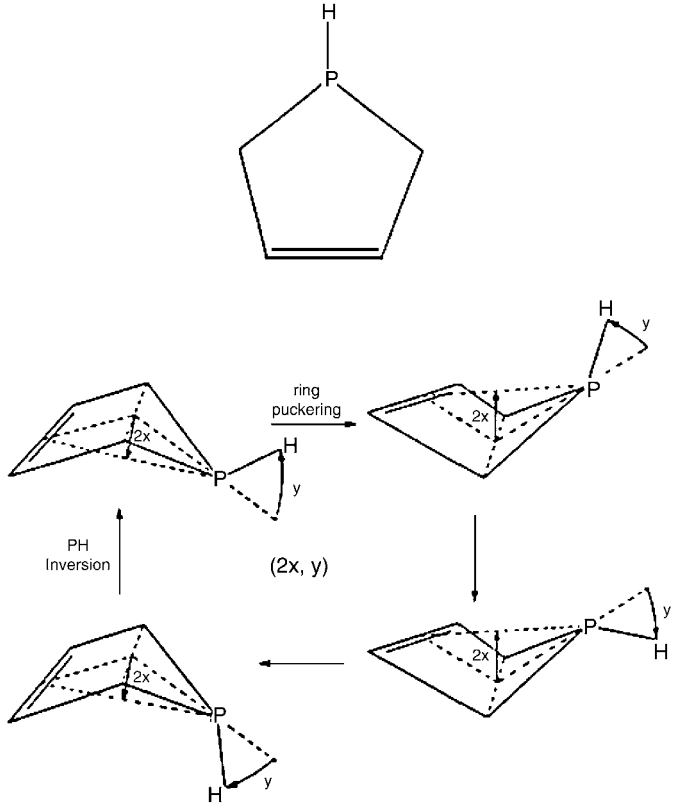

Figure 33. The conformation interconversion of 3-phospholene, associated with the ring pucking coordinate x and the PH inversion coordinate y. [From M. S. Zhao and S. A. Rice, *J. Chem. Phys.* **98**, 2837 (1993).]

denoted by $G(x, y)$, is a slowly varying function of x and y with its matrix elements given by

$$g_{11}(x, y) = \sum_{m=1}^{6} \sum_{n=1}^{6} d_{xx}(m, n) x^m y^n \tag{294}$$

$$g_{12}(x, y) = \sum_{m=1}^{6} \sum_{n=1}^{6} d_{xy}(m, n) x^m y^n \tag{295}$$

$$g_{22}(x, y) = \sum_{m=1}^{6} \sum_{n=1}^{6} d_{yy}(m, n) x^m y^n \tag{296}$$

$$g_{21}(x, y) = g_{12}(x, y) \tag{297}$$

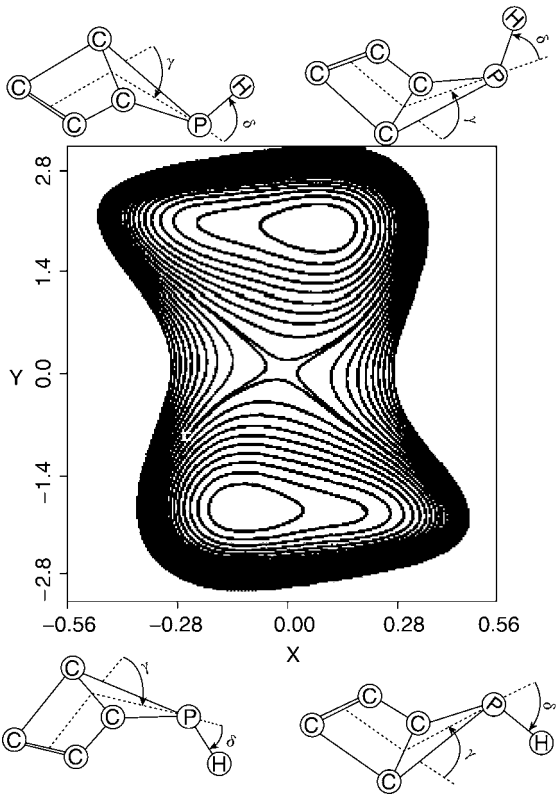

Figure 34. Contour plot of the potential energy surface for the isomerization of 3-phospholene. x is the ring pucking coordinate and y is the PH inversion coordinate. [From C. C. Marston and N. De Leon, *J. Chem. Phys.* **91**, 3392 (1989).]

The contours of the potential function are shown in Fig. 34. Numerical values of the parameters a_i, b_i, c_{ij} are given by (in a.u.)

$$a_1 = 1.22 \times 10^{-1}, \qquad a_2 = 1.136 \times 10^{-4}$$
$$b_1 = 3.317 \times 10^{-2}, \qquad b_2 = -3.139 \times 10^{-3}$$

and

$$c_{11} = -7.043 \times 10^{-3}, \quad c_{13} = 5.288 \times 10^{-4}, \quad c_{15} = -1.541 \times 10^{-5}$$
$$c_{22} = -4.859 \times 10^{-3}, \quad c_{24} = 1.681 \times 10^{-4}, \quad c_{31} = 1.904 \times 10^{-2}$$
$$c_{33} = 3.502 \times 10^{-4}, \quad c_{42} = -5.213 \times 10^{-4}, \quad c_{51} = -1.291 \times 10^{-3}$$

All other c_{ij} are zero. The nonzero $d(i,j)$ coefficients are given by the following (also in a.u.):

(i,j)	$d_x(i,j)$	$d_y(i,j)$	$d_{xy}(i,j)$
(0,0)	5.74556×10^{-6}	-1.44334×10^{-5}	6.30483×10^{-4}
(0,2)	-2.75898×10^{-9}	2.72180×10^{-7}	-3.97533×10^{-6}
(0,4)	1.10125×10^{-10}	7.62182×10^{-8}	9.79076×10^{-8}
(0,6)	-1.20461×10^{-12}	2.40922×10^{-12}	-1.03596×10^{-9}
(1,1)	1.02878×10^{-8}	-1.47638×10^{-6}	3.37376×10^{-6}
(1,3)	-4.85666×10^{-10}	2.33670×10^{-8}	-4.39208×10^{-8}
(2,0)	-3.83084×10^{-6}	3.97712×10^{-6}	1.20922×10^{-5}

The 3-phospholene potential energy surface has an energy barrier between isomers with height $\varepsilon_b = 5083\ \text{cm}^{-1}$. Results from direct trajectory calculations by De Leon and Marston [23,63] are available for one energy, namely, $5133\ \text{cm}^{-1}$. The PSS for this energy is shown in Fig. 35. It is seen that although overall the system displays characteristics of chaotic motion, a considerable portion of the PSS supports quasi-periodic motion.

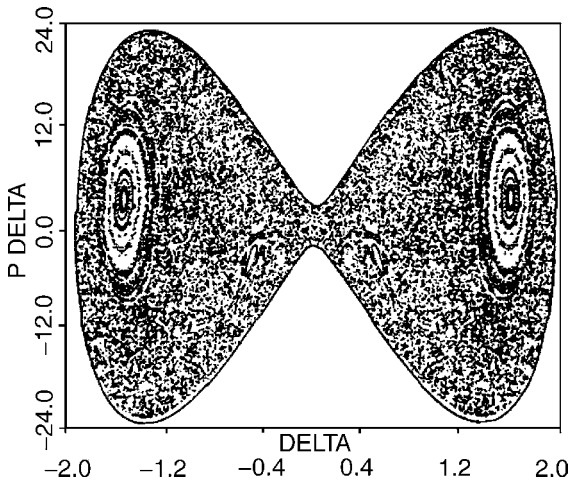

Figure 35. Poincaré surface of section of 3-phospholene at $E = 5133\ \text{cm}^{-1}$, showing chaotic motion and embedded regions of quasi-periodic motion. [From C. C. Marston and N. De Leon, *J. Chem. Phys.* **91**, 3392 (1989).]

This same energy was assumed in an application of the MRRKM theory [64]. In doing so, one can adopt the separatrix

$$S_{\text{Sep}} = \tfrac{1}{2} g_{22}(\bar{x}, y) p_y^2 + g_{12}(\bar{x}, y) p_x p_y + V_y + W(\bar{x}, y) - \Delta\varepsilon = \begin{cases} S_{\text{Sep}}^A, & y \le y^\ddagger \\ S_{\text{Sep}}^B, & y \ge y^\ddagger \end{cases} \tag{298}$$

where $\bar{x}$ is a fixed point. To account for the periodic motion, the initial conditions for the isomerization kinetics are determined by setting $A_1(0)$ equal to the fraction of the PSS for isomer A that supports quasi-periodic motion [see Eqs. (231) and (232)]. To account for intramolecular bottleneck effects, Zhao and Rice defined an intramolecular dividing surface that has the same form as the intermolecular separatrix, but with negative energy appropriate to its location—that is, with $\Delta\varepsilon$ replaced by the local zero point energy of the *PH* inversion motion, denoted by $E_y(0)$. Assuming that the small amplitude *PH* inversion motion is harmonic, one has

$$E_y(0) = \tfrac{1}{2}\hbar\omega_y \tag{299}$$

with the local frequency

$$\omega_y = \left[g_{22}(x, y) \frac{\partial^2 H(x, y)}{\partial y^2} \right]^{1/2}_{x=x_0, y=y_0} \tag{300}$$

where $x_0 = -0.209277$ a.u., $y_0 = -3.71661$ a.u. are the coordinates of the local minimum of the potential energy surface. Equation (300) also indicates that ω_y depends on $g_{22}(x, y)$, which is a function of x and y. However, because $g_{22}(x, y)$ is a slowly varying function, it is approximated by a constant—that is, $g_{22} = 1.1493$ a.m.u.$^{-1}$, where a.m.u. is the atomic mass unit. Then $E_y(0) = 307$ cm^{-1}.

Table XX displays a comparison of the rates of isomerization of 3-phospholene with excess energy 50 cm^{-1} over the reaction barrier as calculated from the

TABLE XX
Isomerization Rate Constants of 3-Phospholene at $E = 5133$ cm^{-1} [a]

Model No.	Trajectory	RI	MRRKM	RRKM
1	0.0083	0.0124	0.0078	0.0304
2	0.0083	0.0088	0.0064	—

[a] In model No. 1 only the intermolecular dividing surface is considered. Model No. 2 includes bottleneck effects in intramolecular energy transfer.

MRRKM theory, from RIT, from direct trajectory simulations, and, for reference purposes, from the RRKM theory. In particular, a test of the effect of the RRKM choice of transition state on the predicted rate of isomerization is made by neglecting the contribution of intramolecular energy transfer (Model No. 1). It is seen that the RRKM choice of transition state leads to considerable error; the isomerization rate constant predicted is greater than those from the MRRKM theory and RIT by as much as a factor of 4. With intramolecular bottlenecks taken into account, both RIT and the MRRKM theory agree well with trajectory calculations.

H. Isomerization of HCN → CNH

The potential energy surface for the isomerization reaction HCN → CNH used below was proposed by Murrell, Carter, and Halonen [65]. A contour plot of this potential energy surface is presented in Fig. 36. The two local minima correspond clearly to HCN and CNH. Although there are quantitative differences between this potential energy surface and others, all of the surfaces are sufficiently similar that the qualitative character of the classical dynamics that each surface supports is the same.

The classical Hamiltonian of the HCN system is given by

$$H(\mathbf{P},\mathbf{p},\mathbf{l},\mathbf{j},\mathbf{R},\mathbf{r}) = \frac{\mathbf{P}^2}{2\mu} + \frac{\mathbf{p}^2}{2m} + \frac{\mathbf{l}^2}{2\mu R^2} + \frac{\mathbf{j}^2}{2mr^2} + V(\mathbf{R},\mathbf{r},\gamma) \tag{301}$$

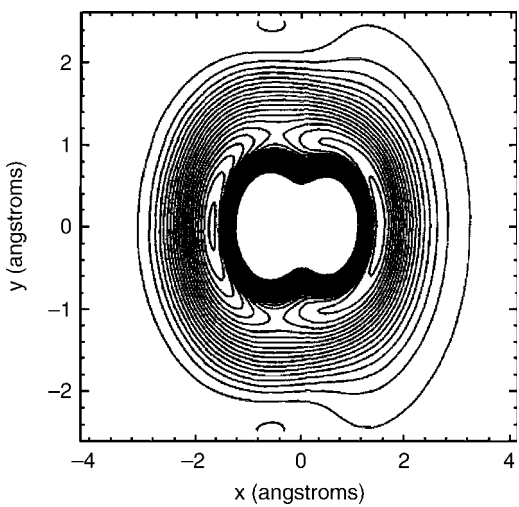

Figure 36. Contour plot of the potential surface for HCN isomerization with $J = 0$. [From H. Tang, S. M. Jang, M. S. Zhao, and S. A. Rice, *J. Chem. Phys.* **101**, 8737 (1994).]

where the effective masses are

$$\mu = \frac{m_H(m_C + m_N)}{m_H + m_C + m_N}, \qquad m = \frac{m_C m_N}{m_C + m_N} \tag{302}$$

r is the bond length vector for the diatom CN, **R** is the position vector from the center of mass of CN to H, and **p** and **P** are the corresponding canonical conjugate momenta. The angle between the vectors **r** and **R** is γ. **l** is the orbital angular momentum of H relative to CN, with its magnitude denoted by l, and **j** is the rotational angular momentum of the diatom, with its magnitude denoted by j. The total angular momentum is restricted to zero so that $l = j$. Thus molecular motion is confined to a plane fixed in configuration space, giving rising to a three-DOF model. Although unnecessary when applying the MRRKM theory [19], a two-DOF model of isomerization can be constructed by freezing the CN bond at $r = r_0$, the equilibrium position. Specifically, the two-dimensional model Hamiltonian is given by

$$H = \frac{p_x^2}{2\mu} + \frac{p_y^2}{2\mu} + \frac{j^2}{2mr_0^2} + V(x, y) \tag{303}$$

with the model potential energy surface $V(x, y)$ already shown in Fig. 36. Figure 37 is a PSS associated with the HCN isomerization; it supports both chaotic motion and quasi-periodic motion.

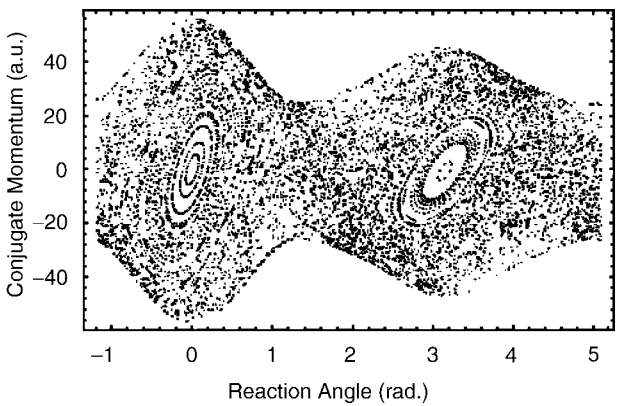

Figure 37. Poincaré surface of section for HCN isomerization, showing both chaotic motion and quasi-periodic motion.

The MRRKM theory defines the separatrix with respect to the reaction coordinate γ by the relation

$$S_{\text{Sep}} = \frac{j^2}{2I(\bar{R}, r_0)} + V(\bar{R}, r_0, \gamma) - \varepsilon_b \tag{304}$$

where

$$\frac{1}{I(R, r)} = \frac{1}{2\mu R^2} + \frac{1}{2mr^2} \tag{305}$$

The vibrational-state-dependent intramolecular dividing surface can be defined by

$$S_{\text{intra}} = \frac{j^2}{2I(\bar{R}, r_0)} + V(\bar{R}, r_0, \gamma) - \varepsilon_\gamma(n) \tag{306}$$

Furthermore, with the harmonic approximation one has

$$\varepsilon_\gamma(n) = \left(n + \tfrac{1}{2}\right)\hbar\omega_\gamma \tag{307}$$

where

$$\omega_\gamma = \left[\frac{1}{I(\bar{R}, r_0)} \frac{\partial^2 V(\bar{R}, r_0, \gamma)}{\partial \gamma^2}\right]^{1/2} \tag{308}$$

The derivative is evaluated at the well minimum, where $\gamma = 0$ for HCN and $\gamma = \pi$ for CNH. The frozen CN bond length was chosen to be the average of the CN bond lengths in HCN (1.153) and in CNH (1.165).

The HCN well depth is -13.589 eV, the CNH minimum lies 0.484 eV above the HCN minimum, the isomerization barrier height energy is at -12.08 eV, and the saddle point angle is at $\gamma = 67^\circ$. For the two-DOF model, the values of $\bar{R}$ for defining the separatrices [see Eq. (304)] were chosen to correspond to the atomic configurations of the isomer equilibrium states, namely 1.690 for HCN and 1.528 for CNH. For the three-DOF case the values of $\bar{R}$ and r_0 in Eq. (306) are $\bar{R} = 1.687$ and $r_0 = 1.153$ for HCN and $\bar{R} = 1.532$ and $r_0 = 1.165$ for CNH.

The rate constants calculated for the reactions HCN $\rightarrow$ CNH $(A \rightarrow B)$ and CNH $\rightarrow$ HCN $(B \rightarrow A)$ from the MRRKM theory [19] are listed in Tables XXI and XXII, for the two-DOF and three-DOF models, respectively. Interestingly, the results in Table XXI are almost the same as those in Table XXII. This supports the validity of the frozen bond approximation. That is, in applying

TABLE XXI
Rate Constants (10^{-3} a.u.) of HCN $\rightleftharpoons$ CNH Isomerization Obtained from the MRRKM Theory Using a two-DOF Model

E(eV)	k_{AC}	k_{CA}	k_{BC}	k_{CB}
−11	0.429	0.146	0.545	0.133
−10	0.647	0.157	0.768	0.143
−9	1.046	0.202	1.054	0.182
−8.5	1.018	0.188	0.911	0.170

TABLE XXII
Rate Constants (10^{-3} a.u.) of HCN $\rightleftharpoons$ CNH Isomerization, Obtained from the MRRKM Theory Using a Three-DOF Model

E(eV)	k_{AC}	k_{CA}	k_{BC}	k_{CB}
−11	0.197	0.139	0.310	0.147
−10	0.415	0.186	0.599	0.190
− 9	0.735	0.250	1.016	0.258
− 8.5	0.826	0.251	1.064	0.250

statistical theories it is possible to first reduce the dimension of a reacting system.

Table XXIII displays the rate constants obtained from the MRRKM theory and the reaction path analysis. It is seen that the former are about a factor of two smaller, and the latter about a factor of two larger, than those derived from direct trajectory calculations. We infer that, since both the RRKM and the MRRKM calculated rate constants are smaller than that calculated from trajectory calculations, there is a nonstatistical contribution to the isomerization rate that is not captured by the MRRKM theory.

The comparison between the MRRKM and reaction-path rate constants and the rate constants obtained from trajectory calculations is subject to the

TABLE XXIII
Rate Constant (10^{-3} a.u.) of HCN $\rightarrow$ CNH Isomerization from Various Theories

E(eV)	Trajectory	MRRKM	Reaction Path
−11.5	0.146	—	0.207
−11.0	0.179	0.095	0.395
−10.5	0.216	—	0.461
−10.0	0.261	0.142	0.513

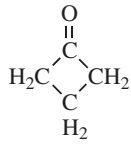

Figure 38. The structure of the cyclobutanone C_4H_6O molecule.

uncertainty associated with the dynamical differences between a three-state model (MRRKM and reaction path analyses) and a two-state model, the latter of which was used to extract a rate constant from the trajectory studies. Nevertheless, accepting the trajectory study rate constants as guideline values, the agreement with the rate constants derived from the reaction path analysis is quite good. We attribute the deviations to a breakdown of the harmonic approximation used to define the reaction path Hamiltonian. It remains to further apply the reaction path approach to other systems with more than two DOFs, particularly in the energy range where the harmonic approximation is valid.

I. Isomerization of Cyclobutanone (C_4H_6O)

The Hamiltonian for the model study of isomerization of cyclobutanone was derived by Zhang, Chiang, and Laane [66], by fitting the experimental data obtained from fluorescence excitation spectra. The structure of the cyclobutanone (C_4H_6O) molecule is shown in Fig. 38.

This molecule has a large number of DOFs, so that a reduction of the system dimensionality is required. The model used here assumes that by ignoring the minor corrections from other DOFs, the dynamics of the isomerization process is dominated by the coupling between C=O "wagging" and "ring-puckering." Let s be the coordinate representing the out-of-plane carbonyl C=O wagging, and let x be the coordinate representing the ring-puckering motion. The system Hamiltonian for the model cyclobutanone has the form

$$H(x,s) = \frac{1}{2}g_1(s)p_s^2 + \frac{1}{2}g_2(x)p_x^2 + V(x,s) \tag{309}$$

where the kinetic energy coefficients can be expanded as

$$g_1(s) = g_1^{(0)} + g_1^{(2)}s^2 + g_1^{(4)}s^4 + g_1^{(6)}s^6 \tag{310}$$

$$g_2(x) = g_2^{(0)} + g_2^{(2)}x^2 + g_2^{(4)}x^4 + g_2^{(6)}x^6 \tag{311}$$

and p_s and p_x are the conjugate momenta to the s and x coordinates. The potential energy surface is given by

$$V(x,s) = V_1(s) + V_2(x) + U(x,s) \tag{312}$$

with $V_1(s) = a_1 s^4 + b_1 s^2$, $V_2(x) = a_2 x^4 + b_2 x^2$, and $U(x,s) = csx^3$. The values of the parameters are chosen to be

$$\begin{aligned}
g_1^{(0)} &= 135.00 \times 10^3\,\mathrm{u}^{-1}, & g_1^{(2)} &= -17.69 \times 10^3\,\mathrm{u}^{-1-2} \\
g_1^{(4)} &= 2.562 \times 10^3\,\mathrm{u}^{-1-4}, & g_1^{(6)} &= -0.237 \times 10^3\,\mathrm{u}^{-1-6} \\
g_2^{(0)} &= 5.24 \times 10^3\,\mathrm{u}^{-1}, & g_2^{(2)} &= -4.16 \times 10^3\,\mathrm{u}^{-1-2} \\
g_2^{(4)} &= -27.76 \times 10^3\,\mathrm{u}^{-1-4}, & g_2^{(6)} &= 34.69 \times 10^3\,\mathrm{u}^{-1-6}
\end{aligned}$$

and

$$\begin{aligned}
a_1 &= 3.34 \times 10^3\,\mathrm{cm}^{-1-4}, & a_2 &= 1.3 \times 10^7\,\mathrm{cm}^{-1-4} \\
b_1 &= -5.26 \times 10^3\,\mathrm{cm}^{-1-2}, & b_2 &= -2.65 \times 10^4\,\mathrm{cm}^{-1-2} \\
c &= -5.0 \times 10^5 \mathrm{cm}^{-1-4}
\end{aligned}$$

where u is the atomic mass unit. The potential function $V_1(s)$ along the reaction coordinate is plotted in Fig. 39. The barrier height energy is 0.00094 a.u. Figure 40 shows the contours of the potential energy surface.

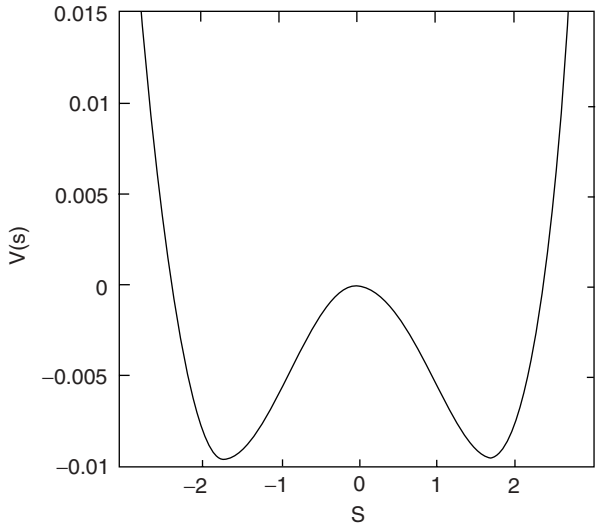

Figure 39. The potential energy of isomerization of cyclobutanone C_4H_6O along the reaction coordinate. [From H. Tang, S. M. Jang, M. S. Zhao, and S. A. Rice, *Chem. Phys. Lett.* **285**, 143 (1998).]

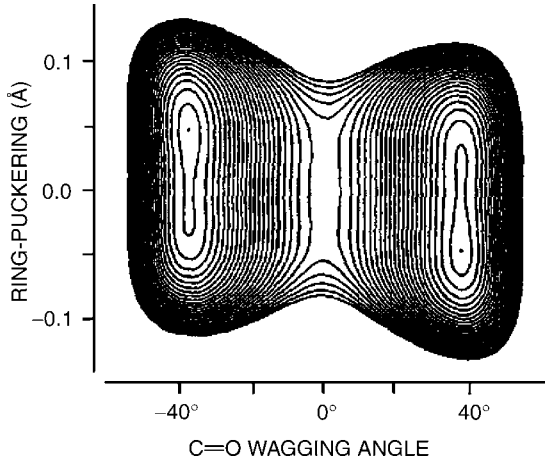

Figure 40. The potential energy contours of cyclobutanone C_4H_6O. [From J. Zhang, W. Chiang, and J. Laane, *J. Chem. Phys.* **100**, 3455 (1994).]

The phase space structures on a PSS are also shown in Fig. 41 for different energies. Clearly, a considerable portion of the PSS is occupied by quasi-periodic motion. The two elliptic fixed points are separated by the point $(s = 0, p_s = 0)$. Trajectories started on any of the closed curves evolve forever on KAM tori. The four cases are for (a) $E = 0.0025$, (b) $E = 0.005$, (c) $E = 0.0075$, and (d) $E = 0.01$, all in unit of a.u. Case (c) shows a $4:1$ resonance, whereas case (d) shows a $3:1$ resonance. As stressed before, in the neighborhoods of the resonance islands there are cantori, remnants of broken KAM tori.

Gray and Rice used a zeroth-order analytic approximation to the separatrix with respect to the reaction coordinate. For the model cyclobutanone it is defined by

$$S_{\text{Sep}}(p_s, s, \bar{x}) = \tfrac{1}{2} g_1(s) p_s^2 + V(s) + U(\bar{x}, s) \tag{313}$$

where $\bar{x}$ is a fixed value of x and is normally chosen to be at the saddle point of the potential energy surface. In an effort to further improve the Gray–Rice approach, the MRRKM theory also considers additionally the nth intramolecular bottleneck

$$S_{\text{intra}}(p_s, s, \bar{x}) = \tfrac{1}{2} g_1(s) p_s^2 + V(s) + U(\bar{x}, s) - E_s(n) \tag{314}$$

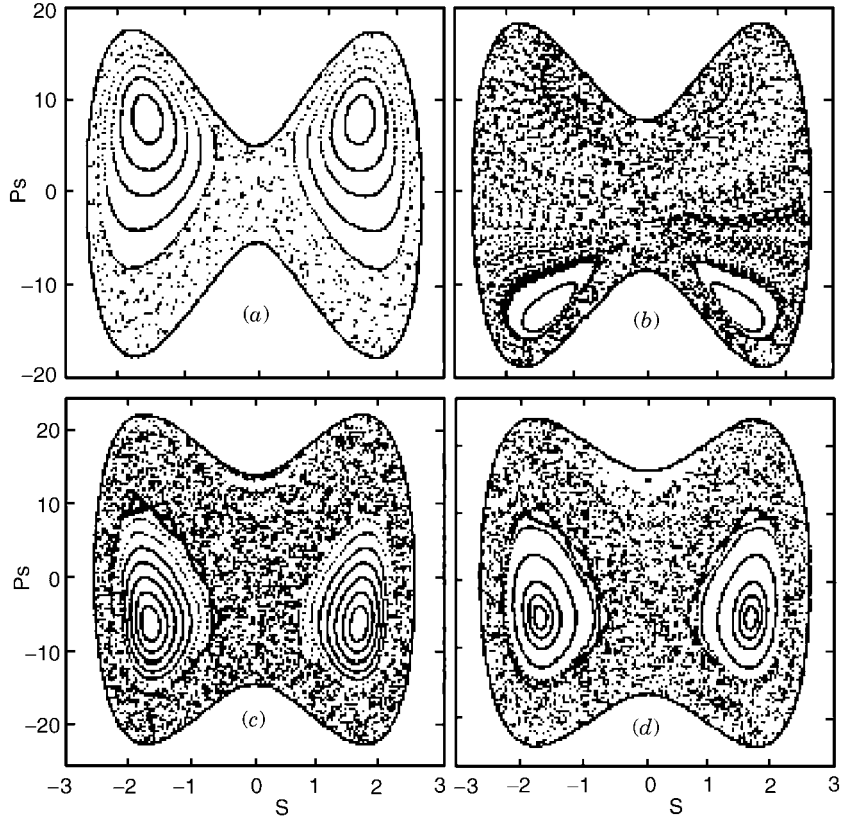

Figure 41. Poincaré surfaces of section associated with the isomerization of cyclobutanone for energies (*a*) $E = 0.0025$ a.u., (*b*) $E = 0.0050$ a.u., (*c*) $E = 0.0075$ a.u., and (*d*) $E = 0.01$ a.u.

As in other applications, the motion in s is assumed to be confined to the vicinity of the isomer equilibrium value so that a harmonic approximation can be used. This assumption yields

$$E_s(n) = \left(n + \tfrac{1}{2}\right)\hbar\omega_s \tag{315}$$

with

$$\omega_s = \left[g_1(s)\frac{\partial^2 V(x,s)}{\partial s^2}\right]^{1/2}_{s=s_0,x=x_0} \tag{316}$$

TABLE XXIV
The Classical Isomerization Rate Constants of Cyclobutanone from the RRKM Theory, Gray–Rice theory, MRRKM Theory, and Trajectory Calculations (in 10^{-4} a.u.)

E	RRKM	Gray–Rice	MRRKM	Trajectory
25	0.71	0.067	0.031	0.078
50	0.95	0.073	0.035	0.081
75	1.14	0.076	0.037	0.111
100	1.31	0.079	0.039	0.156

where the derivative is evaluated at the potential well minimum. For the model of cyclobutanone considered, the potential minimum appears at $s_0 = 1.68$ a.u. and $x_0 = 0$. The isomerization rate constants from the RRKM theory [67], Gray–Rice theory, MRRKM theory, and trajectory calculations are presented in Table XXIV. The entries in this table show that for this model system the RRKM theory gives about an order of magnitude overestimate of the reaction rate constants. Both the Gray–Rice and MRRKM theories predict rate constants with about the correct magnitude but with an energy dependence that is too weak. Overall, the MRRKM rate constants agree within a factor of three with those derived from the trajectory calculations. This discrepancy is also subject to the uncertainty associated with the difference between the rate constants extracted from the three-state MRRKM model and the two-state model used to analyze the trajectory studies.

VI. QUANTUM AND SEMICLASSICAL APPROACHES

A. The Wigner Function and Weyl's Rule

The phase space structure of classical molecular dynamics is extensively used in developing classical reaction rate theory. If the quantum reaction dynamics can also be viewed from a phase-space perspective, then a quantum reaction rate theory can use a significant amount of the classical language and the quantum-classical correspondence in reaction rate theory can be closely examined. This is indeed possible by use of, for example, the Wigner function approach. For simplicity let us consider a Hamiltonian system with only one DOF. Generalization to many–dimensional systems is straightforward. The Wigner function associated with a density operator $|\psi\rangle\langle\psi|$ is defined by

$$W(q,p) = \frac{1}{2\pi\hbar}\int dx \left\langle q + \frac{x}{2}|\psi\right\rangle \left\langle \psi|q - \frac{x}{2}\right\rangle \exp\left(-\frac{ixp}{\hbar}\right) \tag{317}$$

The Wigner function thus defined has the following property [68]:

$$\text{Trace}[|\psi\rangle\langle\psi| \exp(ia\hat{q} + ib\hat{p})] = \int dq \int dp W(p,q) \exp(iaq + ibp) \tag{318}$$

where $[\hat{q}, \hat{p}] = -i\hbar$. As seen from Eq. (318), the value of the quantum observable $\exp(ia\hat{q} + ib\hat{p})$ can be obtained by evaluating the average value of the phase-space function $\exp(iaq + ibp)$ with the "weight function" $W(q,p)$, without dealing with the noncommuting operators $\hat{q}$ and $\hat{p}$. Clearly then, the Wigner function $W(q,p)$ is a quantum analog of the classical phase-space density function.

Within the Wigner function framework the operator $\exp(ia\hat{q} + ib\hat{p})$ is associated with the phase-space function $\exp(iaq + ibp)$. This particular association between a phase-space function and a function of noncommuting operators is an example of "Weyl's rule" [69]. Indeed, by generalizing Eq. (1.317) one obtains the Weyl transform $A_W(q,p)$ of an arbitrary operator $A(\hat{q}, \hat{p})$,

$$A_W(q,p) = \int dx \left\langle q + \frac{x}{2} \middle| A(\hat{q}, \hat{p}) \middle| q - \frac{x}{2} \right\rangle \exp\left(-\frac{ixp}{\hbar}\right) \tag{319}$$

with the desired property

$$\text{Trace}[|\psi\rangle\langle\psi| A(\hat{q}, \hat{p})] = \int dq \int dp W(p,q) A_W(q,p) \tag{320}$$

Furthermore, inverting Eq. (319) yields Weyl's rule for quantizing a classical phase-space function $f(q,p)$, that is,

$$f(q,p) \rightarrow \hat{f}_W(\hat{q}, \hat{p}) \tag{321}$$

where

$$\hat{f}_W(\hat{q}, \hat{p}) = \frac{1}{8\pi^3\hbar} \int dq \int dp \int da \int db\, f(q,p) \exp(iaq + ibp) \exp(-ia\hat{q} - ib\hat{p}) \tag{322}$$

The matrix elements of $\hat{f}_W(\hat{q}, \hat{p})$ in the q-representation are given by

$$\langle q | \hat{f}_W(\hat{q}, \hat{p}) | q' \rangle = \frac{1}{2\pi\hbar} \int dp \exp\left[\frac{ip(q - q')}{\hbar}\right] f\left(\frac{q' + q}{2}, p\right) \tag{323}$$

For example, if $f(q,p) = g(q)$ (independent of p), then $\hat{f}_W(\hat{q}, \hat{p}) = g(\hat{q})$; if $f(q,p) = qp$, then $\hat{f}_W(\hat{q}, \hat{p}) = (\hat{q}\hat{p} + \hat{p}\hat{q})/2$. Weyl's rule introduced above

provides a specific and convenient method of quantizing classical phase-space functions.

The Wigner function has the valuable property that the time evolution equation for the quantum dynamics in the Wigner representation resembles that for the classical Liouville dynamics. Specifically, the Schrödinger equation can be transformed to [70]

$$\frac{\partial W_t(q,p)}{\partial t} = \frac{2}{\hbar}\sin\left[\frac{\hbar}{2}\left(\frac{\partial}{\partial q_1}\frac{\partial}{\partial p_2} - \frac{\partial}{\partial q_2}\frac{\partial}{\partial p_1}\right)\right]_{q_1=q_2=q,\ p_1=p_2=p} H_W(q_1,p_1)W_t(q_2,p_2) \tag{324}$$

where H_W is the Weyl transform of the Hamiltonian and W_t is the Wigner function associated with the time-evolving quantum state. If $H = \hat{p}^2/2 + V(\hat{q})$, one has $H_W = p^2/2 + V(q)$ and Eq. (324) reduces to

$$\frac{\partial W_t(q,p)}{\partial t} = \left(\frac{\partial V(q)}{\partial q}\frac{\partial W_t(q,p)}{\partial p} - p\frac{\partial W_t(q,p)}{\partial q}\right) + \sum_{l=1}^{+\infty}\left(\frac{\hbar}{2i}\right)^{2l}\frac{1}{(2l+1)!}\frac{\partial^{(2l+1)}V(q)}{\partial q^{(2l+1)}}\frac{\partial^{(2l+1)}W_t(q,p)}{\partial p^{(2l+1)}} \tag{325}$$

Note that the right-hand side of Eq. (325) consists of the classical Poisson bracket between $H_W(q,p)$ and $W_t(q,p)$, plus a series of additional terms that depend on $\hbar$. This makes it clear that the time-evolving Wigner function is the quantum analog of the time-evolving classical Liouville density function.

B. Quantum Scars in Phase-Space

Considerable effort has been devoted to examining the properties of the Wigner function. Of particular relevance to unimolecular reaction rate theory is the behavior of the Wigner function in classically chaotic systems. For example, the ''semiclassical eigenfunction hypothesis'' [71] asserts that if the underlying classical dynamics is completely chaotic, then the Wigner function associated with a quantum eigenstate can be approximated by a delta function concentrated on the energy surface. That is, in this case the Wigner function collapses to $W(\mathbf{q},\mathbf{p}) \sim \delta[E - H(\mathbf{q},\mathbf{p})]$, which is analogous to the classical microcanonical density in phase-space. However, this enlightening qualitative picture has been found to be oversimplified, because individual periodic trajectories, which are invariant sets of measure zero, can also strongly influence the behavior of the Wigner function in chaotic systems. In particular, the Wigner function can display highly nonstatistical behavior by building up additional strength, called

"quantum scars" [72–74]. Thus, in the neighborhood of classical periodic trajectories the Wigner function should be described by

$$W(\mathbf{q},\mathbf{p}) \sim \delta[E - H(\mathbf{q},\mathbf{p})] + W_{\text{scar}}(\mathbf{q},\mathbf{p}) \tag{326}$$

Note that the periodic trajectories embedded in a chaotic domain must have neutral stability or be unstable.

Using semiclassical techniques Berry obtained the following representation for $W_{\text{scar}}(\mathbf{q},\mathbf{p})$ [73]:

$$W_{\text{scar}}(q,p) = \sum_j W_{\text{scar},j}(\mathbf{x},E,\varepsilon) \tag{327}$$

where each index j labels the contributing classical periodic trajectories and $W_{\text{scar},j}(\mathbf{x},E,\varepsilon)$ is given by

$$\begin{aligned} W_{\text{scar},j}(\mathbf{x},E,\varepsilon) = {} & \frac{2^n}{\sqrt{|\det(\mathbf{M}+\mathbf{I})|}} \exp\left(-\frac{\varepsilon T}{\hbar}\right) \\ & \times \cos\left\{\frac{1}{\hbar}\left[S(E) - \mathbf{X}\frac{\mathbf{J}(\mathbf{M}-\mathbf{I})}{\mathbf{M}+\mathbf{I}}\mathbf{X}^t\right] + \gamma_j\right\} \\ & \times \frac{2}{\left(\hbar^2|\ddot{\mathbf{x}}\times\dot{\mathbf{x}}|\right)^{1/3}} \text{Ai}\left\{-\frac{2[H(\mathbf{x})-E]}{\left(\hbar^2|\ddot{\mathbf{x}}\times\dot{\mathbf{x}}|\right)^{1/3}}\right\} \end{aligned} \tag{328}$$

Here $S(E)$ is the classical action at the energy E, $\mathbf{x} = (\mathbf{q},\mathbf{p})$, $\mathbf{X} = (\mathbf{Q},\mathbf{P})$ represent the coordinates transverse to the trajectory on a PSS, $\mathbf{M}$ is the mapping matrix on the same PSS, $\mathbf{I}$ is a unit matrix, n is the dimensionality of the system, $\mathbf{J}$ is the $2(n-1)$ by $2(n-1)$ unit matrix, ε is a spectral parameter that will eventually be set to zero, T is the period of the periodic trajectory, $\text{Ai}(x)$ is the Airy function, and the phase factor γ_j is a multiple of $\pi/4$ determined by the focusing behavior of classical trajectories close to the jth periodic orbit. Note that on the closed periodic trajectory we have $\mathbf{X} = 0$. In the semiclassical limit i.e., $(\hbar \to 0)$, these scar terms reduce to

$$\begin{aligned} W_{\text{scar},j}(\mathbf{x},E,\varepsilon) = {} & \frac{2^n}{\sqrt{|\det(\mathbf{M}+\mathbf{I})|}} \exp\left(-\frac{\varepsilon T}{\hbar}\right) \\ & \times \cos\left(\frac{S(E)}{\hbar} + \gamma_j\right)\delta[E - H(\mathbf{x})]\delta(\mathbf{X}) \end{aligned} \tag{329}$$

The properties of the unstable periodic trajectories can be described in terms of Lyapunov exponents. That is,

$$\frac{1}{\sqrt{|\det(\mathbf{M}+\mathbf{I})|}} \sim \exp\left(-\tfrac{1}{2}\sum_{\lambda_i>0}\lambda_i\right) \tag{330}$$

where the λ_i are Lyapunov exponents. With Eq. (330) one may further simplify Eq. (329) and obtain

$$W_{\text{scar},j}(\mathbf{x}, E, \varepsilon) = 2\hbar^{n-1} \exp\left[-\left(\frac{\varepsilon}{\hbar} + \tfrac{1}{2}\sum_{\lambda_i>0}\lambda_i\right)T\right] \times \cos\left(\frac{S(E)}{\hbar} + \gamma_j\right)\delta[E - H(\mathbf{x})]\delta(\mathbf{X}) \tag{331}$$

Three observations can be made from Eq. (331). First, the least unstable trajectories—that is, the trajectories with the smallest positive Lyapunov exponents—contribute most to $W_{\text{scar},j}(\mathbf{x}, E, \varepsilon)$. Second, if

$$\cos\left(\frac{S}{\hbar} + \gamma_j\right) = 1 \tag{332}$$

then $W_{\text{scar},j}(\mathbf{x}, E, \varepsilon)$ is maximal, giving rise to the most significant scar contributions. Third, if

$$\cos\left(\frac{S}{\hbar} + \gamma_j\right) = 0 \tag{333}$$

then $W_{\text{scar},j}(\mathbf{x}, E, \varepsilon) = 0$. In the third case there is no influence from the unstable periodic trajectory and the associated Wigner function should display more ergodic behavior.

The fact that classical unstable periodic trajectories can manifest themselves in the Wigner function implies that nonstatistical behavior in the quantum dynamics can be intimately related to the phase-space structure of the classical molecular dynamics. Consider, for example, the bottlenecks to intramolecular energy flow. Since the intramolecular bottlenecks are caused by remnants of the most robust tori, they are presumably related to the least unstable periodic trajectories. Hence quantum scars, being most significant in the case of the least unstable periodic trajectories, are expected to be more or less connected with intramolecular bottlenecks. Indeed, this observation motivated a recent proposal [75] to semiclassically locate quantum intramolecular bottlenecks. Specifically, the most robust intramolecular bottlenecks are associated with the least unstable periodic trajectories for which Eq. (332) holds, that is,

$$S = -\gamma_j\hbar + 2m\pi\hbar, \qquad m = 1, 2, \ldots \tag{334}$$

C. Quantizing the ARRKM Theory

The fundamental difference between the ARRKM theory and the traditional RRKM theory is that the former utilizes a phase-space separatrix rather than a

dividing surface in the configuration space. This suggests that in quantizing the ARRKM theory the phase-space formulation of quantum molecular dynamics will be an indispensable tool. By use of Weyl's rule, we present below a simple approach to the quantization of the ARRKM theory.

Let us first recall the following reaction rate expression from the ARRKM theory:

$$k(E) = \frac{1}{N_s}\int d\mathbf{q}\int d\mathbf{p}\delta(S)\dot{S}\theta(\dot{S})\delta(E-H) \tag{335}$$

where the normalization constant N_s is given by

$$N_s = \int d\mathbf{q}\int d\mathbf{p}\theta[-S(\mathbf{q},\mathbf{p})]\delta(E-H) \tag{336}$$

$H(\mathbf{q},\mathbf{p})$ is the Hamiltonian, $S(\mathbf{q},\mathbf{p})=0$ defines the phase space separatrix, and the time derivative of the phase-space dividing surface $\dot{S}$ is given by

$$\begin{aligned}\dot{S} &= \frac{\partial S}{\partial q_1}\frac{dq_1}{dt}+\frac{\partial S}{\partial q_2}\frac{dq_2}{dt}+\cdots+\frac{\partial S}{\partial p_1}\frac{dp_1}{dt}+\frac{\partial S}{\partial p_2}\frac{dp_2}{dt}+\cdots \\ &\equiv \boldsymbol{\nabla} S\cdot\mathbf{v}\end{aligned} \tag{337}$$

Note that, for an n-dimensional system, the $2n$-dimensional "velocity vector" $\mathbf{v}$ defined above is also a function of $(\mathbf{q},\mathbf{p})$ since

$$\begin{aligned}\mathbf{v} &\equiv \left(\frac{dq_1}{dt},\frac{dq_2}{dt},\ldots,\frac{dp_1}{dt},\frac{dp_2}{dt},\ldots\right) \\ &= \left(\frac{\partial H}{\partial p_1},\frac{\partial H}{\partial p_2},\ldots,-\frac{\partial H}{\partial q_1},-\frac{\partial H}{\partial q_2},\ldots\right)\end{aligned} \tag{338}$$

With Eq. (337) the ARRKM rate constant can be written as

$$k(E) = \frac{1}{N_s}\int d\mathbf{q}\int d\mathbf{p}F(\mathbf{q},\mathbf{p})\theta(\boldsymbol{\nabla}S\cdot\mathbf{v})\delta(E-H) \tag{339}$$

where

$$F(\mathbf{q},\mathbf{p}) \equiv \delta(S)(\boldsymbol{\nabla}S\cdot\mathbf{v}) \tag{340}$$

The quantization of the ARRKM theory can be carried out with the following two steps:

(a) Classical phase-space functions such as $F(\mathbf{q},\mathbf{p})$, $\theta(\boldsymbol{\nabla}S\cdot\mathbf{v})$, $\theta(-S)$, and $H(\mathbf{q},\mathbf{p})$ are transformed to operators $\hat{F}_W$, $\hat{\theta}_W(\boldsymbol{\nabla}S\cdot\mathbf{v})$, $\hat{\theta}_W(-S)$, and $\hat{H}_W$ using

Weyl's rule [Eq. (322)], with their matrix elements in the **q**-representation given by

$$\langle \mathbf{q}|\hat{F}_W|\mathbf{q}'\rangle = \frac{1}{(2\pi\hbar)^n}\int d\mathbf{p}\exp\left[\frac{i\mathbf{p}\cdot(\mathbf{q}-\mathbf{q}')}{\hbar}\right]F\left(\frac{\mathbf{q}'+\mathbf{q}}{2},\mathbf{p}\right) \tag{341}$$

$$\langle \mathbf{q}|\hat{\theta}_W(\boldsymbol{\nabla}S\cdot\mathbf{v})|\mathbf{q}'\rangle = \frac{1}{(2\pi\hbar)^n}\int d\mathbf{p}\exp\left[\frac{i\mathbf{p}\cdot(\mathbf{q}-\mathbf{q}')}{\hbar}\right] \times \theta\left[\boldsymbol{\nabla}S\left(\frac{\mathbf{q}'+\mathbf{q}}{2},\mathbf{p}\right)\cdot\mathbf{v}\left(\frac{\mathbf{q}'+\mathbf{q}}{2},\mathbf{p}\right)\right] \tag{342}$$

$$\langle \mathbf{q}|\hat{\theta}_W(-S)|\mathbf{q}'\rangle = \frac{1}{(2\pi\hbar)^n}\int d\mathbf{p}\exp\left[\frac{i\mathbf{p}\cdot(\mathbf{q}-\mathbf{q}')}{\hbar}\right]\theta\left[-S\left(\frac{\mathbf{q}'+\mathbf{q}}{2},\mathbf{p}\right)\right] \tag{343}$$

$$\langle \mathbf{q}|\hat{H}_W|\mathbf{q}'\rangle = \frac{1}{(2\pi\hbar)^n}\int d\mathbf{p}\exp\left[\frac{i\mathbf{p}\cdot(\mathbf{q}-\mathbf{q}')}{\hbar}\right]H\left(\frac{\mathbf{q}'+\mathbf{q}}{2},\mathbf{p}\right) \tag{344}$$

(b) The classical phase-space average $\int d\mathbf{q}\int d\mathbf{p}$ is tranformed to a quantum mechanical trace operation, that is,

$$\int d\mathbf{q}\int d\mathbf{p}\{\cdots\} \rightarrow \text{Trace}\{\cdots\} \tag{345}$$

The resultant quantized ARRKM theory gives

$$k(E) = \frac{1}{N_s}\text{Trace}\left[\hat{F}_W(\hat{\mathbf{q}},\hat{\mathbf{p}})\hat{\theta}_W(\boldsymbol{\nabla}S\cdot\mathbf{v})\delta(E-\hat{H}_W)\right] \tag{346}$$

with the normalization constant N_s given by

$$N_s = \text{Trace}\left[\hat{\theta}_W(-S)\delta(E-\hat{H}_W)\right] \tag{347}$$

It is also interesting to consider the thermally averaged rate constant $k(T)$, which can be obtained from

$$k(T) = \frac{1}{\Phi_r}\int_0^{+\infty}\exp\left(\frac{-E}{k_BT}\right)\rho(E)k(E)\,dE \tag{348}$$

where Φ_r, the reactant partition function per unit volume, is given by

$$\Phi_r = \int_0^{+\infty}\exp\left(\frac{-E}{k_BT}\right)\rho(E)\,dE \tag{349}$$

and $\rho(E)$ is the density of states per unit energy per volume. Substituting Eqs. (346) and (347) into Eq. (348) one has

$$k(T) = \frac{\int_0^{+\infty} dE \exp\left(\frac{-E}{k_B T}\right) \text{Trace}\left[\hat{F}_W \hat{\theta}_W (\nabla S \cdot \mathbf{v}) \delta(E - \hat{H}_W)\right]}{\int_0^{+\infty} dE \exp\left(\frac{-E}{k_B T}\right) \text{Trace}\left[\hat{\theta}_W (-S) \delta(E - \hat{H}_W)\right]}$$
$$= \frac{\text{Trace}\left[\exp(-\beta \hat{H}_W) \hat{F}_W \hat{\theta}_W (\nabla S \cdot \mathbf{v})\right]}{\text{Trace}\left[\exp(-\beta \hat{H}_W) \hat{\theta}_W (-S)\right]} \tag{350}$$

where $\beta = 1/k_B T$. Equation (350) can be rewritten as

$$k(T) = \frac{1}{\Phi_r} \text{Trace}\left[\exp(-\beta \hat{H}_W) \hat{F}_W \hat{\theta}_W (\nabla S \cdot \mathbf{v})\right] \tag{351}$$

where

$$\Phi_r = \text{Trace}\left[\exp(-\beta \hat{H}_W) \hat{\theta}_W (-S)\right] \tag{352}$$

Just like other attempts to quantize the classical transition state theory [70,77], quantizing the ARRKM theory is not free of all ambiguity. This is largely because the result of quantizing the product of two classical phase-space functions may differ from the product of the two operators quantized from the same classical phase-space functions. For example, we propose to first obtain $\delta(S)(\nabla S \cdot \mathbf{v})$ and $\theta(\nabla S \cdot \mathbf{v})$ as two functions of $\mathbf{q}$ and $\mathbf{p}$ and then quantize these individual phase-space functions using Weyl's rule. However, using other procedures, such as quantizing the product of $\delta(S)(\nabla S \cdot \mathbf{v})$ and $\theta(\nabla S \cdot \mathbf{v})$ using Weyl's rule, may give slightly different results. Nevertheless, the quantization procedure described above is the first attempt to directly quantize the ARRKM theory that is formulated in terms of a phase-space dividing surface.

D. Rigorous Quantum Rate Theory Versus the Quantized ARRKM Theory

The quantum flux–flux autocorrelation formalism, developed by Miller, Schwartz, and Tromp [78] and by Yamamoto [79], represents an exact quantum mechanical expression for a chemical reaction rate constant. According to the flux–flux autocorrelation formalism, the thermally averaged rate constant $k(T)$ is given by

$$k(T) = \frac{1}{\Phi_r} \int_0^{+\infty} dt C_f(t) \tag{353}$$

where Φ_r again denotes the reactant partition function per unit volume, and the thermally averaged flux–flux autocorrelation function $C_f(t)$ takes the following form:

$$C_f(t) = \text{Trace}\left[\hat{F}\exp\left(\frac{i\hat{H}t}{\hbar}\right)\exp\left(\frac{-\beta\hat{H}}{2}\right)\hat{F}\exp\left(\frac{-\beta\hat{H}}{2}\right)\exp\left(-\frac{i\hat{H}t}{\hbar}\right)\right] \quad (354)$$

Here $\hat{H}$ is the Hamiltonian operator, and $\hat{F}$ is defined by

$$\hat{F} = \frac{i}{\hbar}\left[\hat{H},\, \theta[S(\mathbf{q})]\right] \quad (355)$$

and represents the operator associated with the quantum flux across the dividing surface $S(\mathbf{q})$ embedded in an n-dimensional configuration space. Also of interest to unimolecular reaction rate theory is the microcanonical rate constant $k(E)$, which is given by

$$k(E) = \frac{\pi\hbar}{\rho(E)}\text{Trace}[\hat{F}\delta(E-H)\hat{F}\delta(E-H)] \quad (356)$$

To make connections to classical reaction rate theory and to the quantized ARRKM theory discussed above, we turn to an alternative expression of the flux–flux autocorrelation formalism. Defining the time-dependent projection operator

$$\hat{P}(t) \equiv \exp\left(\frac{i\hat{H}t}{\hbar}\right)\theta[S(\mathbf{q})]\exp\left(-\frac{i\hat{H}t}{\hbar}\right) \quad (357)$$

and using

$$\frac{d}{dt}\hat{P}(t) = \exp\left(\frac{i\hat{H}t}{\hbar}\right)\hat{F}\exp\left(-\frac{i\hat{H}t}{\hbar}\right) \quad (358)$$

one finds that the thermally averaged rate constant $k(T)$ is given by [80]

$$k(T) = \frac{1}{\Phi_r}\lim_{t\to+\infty}\text{Trace}\left[\exp(-\beta\hat{H})\hat{F}\hat{P}(t)\right] \quad (359)$$

If $\hat{P}(t)$ is understood to be an operator in the Heisenberg representation, then in the classical limit, Eq. (359) becomes [80]

$$k^{\text{CL}}(T) = \frac{1}{(2\pi\hbar)^n\Phi_r}\lim_{t\to+\infty}\int d\mathbf{q}_0\int d\mathbf{p}_0\exp[-\beta H(\mathbf{q}_0,\mathbf{p}_0)]F(\mathbf{q}_0,\mathbf{p}_0)\theta[S(\mathbf{q}_t)] \quad (360)$$

where $F(\mathbf{q}_0, \mathbf{p}_0)$ is the classical flux. Similarly, in the microcanonical case, one has

$$k(E) = \frac{1}{2\pi\hbar\rho(E)} \lim_{t\to+\infty} \text{Trace}\left[\hat{F}\hat{P}(t)\delta(E-\hat{H})\right] \tag{361}$$

whose classical limit is given by

$$k^{\text{CL}}(E) = \frac{1}{(2\pi\hbar)^{n+1}\rho(E)} \lim_{t\to+\infty} \int d\mathbf{q}_0 \int d\mathbf{p}_0 \delta[E - H(\mathbf{q}_0, \mathbf{p}_0)] F(\mathbf{q}_0, \mathbf{p}_0) \theta[S(\mathbf{q}_t)] \tag{362}$$

Equations (359) and (361) indicate that the reason that the flux–flux autocorrelation formalism gives exact quantum reaction rate constants is simply that all the dynamical information from time zero to time infinity has been included. Indeed, as shown by Eqs. (360) and (362), in the classical limit the flux–flux autocorrelation formalism requires us to follow all classical trajectories until $t = +\infty$ so as to rigorously tell which trajectory is reactive and which trajectory is nonreactive. Evidently, then, the flux–flux autocorrelation formalism is not a statistical reaction rate theory insofar as no approximation to the reaction dynamics is made.

To gain more insight into quantum reaction rate theory, we below make a detailed comparison between the rigorous quantum rate theory and the quantized ARRKM theory. It is significant that the rigorous quantum results [Eqs. (359) and (361)] are very similar to the results from the quantized ARRKM theory [Eqs. (346) and (351)]. In particular, with the three assumptions

$$\text{(a)}\ \hat{H}_W \to \hat{H} \tag{363}$$

$$\text{(b)}\ \hat{F}_W \to \hat{F} \tag{364}$$

$$\text{(c)}\ \hat{\theta}_W(\nabla S \cdot \mathbf{v}) \to \lim_{t\to+\infty} \hat{P}(t) \tag{365}$$

Eq. (351) can be transformed to Eq. (359). Further identifying N_s with $2\pi\hbar\rho(E)$, Eq. (346) becomes identical with Eq. (361). Hence, under certain circumstances the quantized ARRKM theory is equivalent to the rigorous quantum reaction rate theory. A number of remarks are in order. First, assumption (a) is automatically satisfied by definition. Second, assumption (b) implies that $\hat{F}_W$ in the quantized ARRKM theory be the direct analog of the quantum flux operator in the flux–flux autocorrelation formalism. Third, assumption (c) requires that the action of the operator $\hat{\theta}_W(\nabla S \cdot \mathbf{v})$ at any particular time, say at time zero, is equivalent to the action of the projector $\hat{P}(t)$ at time infinity. Regarding $\hat{\theta}_W(\nabla S \cdot \mathbf{v})$ as the analog

of $\hat{P}(0)$, one sees that assumption (c) is equivalent to the requirement that the zero time quantum dynamics already suffices to rigorously determine whether the quantum flux leads to reactants or products. This is the case if the separatrix for reaction is exact—that is, a true dividing surface with no return.

It should be stressed that the quantized ARRKM theory is a statistical reaction rate theory while the flux–flux autocorrelation formalism is not. In addition to this, there are other conceptual differences between the quantized ARRKM theory and the rigorous quantum rate theory. Consider first the microcanonical density assumption. In the former case the microcanonical density $\delta(E - \hat{H}_W)$ can be rationalized by the fact that dynamical chaos is fully developed before reaction occurs. This may not be true when, for example, quantum scars or intramolecular bottleneck effects are significant. By contrast, in the latter case the microcanonical density $\delta(E - \hat{H})$ is due to the existence of thermal equilibrium. Note also that in a rigorous quantum rate theory there is no need to construct a phase-space separatrix, whereas in the quantized ARRKM theory a dividing surface defined in the phase-space (rather than in the configuration space) is necessary in order to remove recrossing trajectories seen in the configuration space. Thus, only in cases for which an appropriate phase-space separatrix is defined can the approximation

$$\lim_{t \to +\infty} \hat{P}(t) \approx \hat{\theta}_W(\nabla S \cdot \mathbf{v}) \tag{366}$$

be made, and the quantized ARRKM theory is then expected to be a very useful quantum statistical reaction rate theory.

E. A Semiclassical Approximation to the Rigorous Quantum Rate Theory

Since the flux–flux autocorrelation formalism requires extensive dynamical calculations, it is of limited use in actually calculating exact quantum reaction rate constants. Nevertheless, the rigorous quantum rate theory constitutes a firm starting point from which a number of approximations can be made. For example, one may treat some DOFs including the reaction coordinate rigorously and the remaining DOFs approximately. One may also use a quantum-classical hybrid approach—that is, treating the most important DOFs quantum mechanically and other background DOFs classically. Here we do not aim to give a complete list of all the useful approximations to the rigorous quantum rate theory that have been suggested. Rather, we choose to introduce in detail one particular approximate quantum reaction rate theory that treats all DOFs in the same manner and allows for a closer examination of the quantum-classical correspondence. The approximation is based on the so-called semiclassical "initial value representation" (IVR) approach [81–83].

With the IVR approach the quantum mechanical propagator can be semiclassically approximated by a phase-space average that involves all possible initial conditions for the classical trajectories. Consider a simple version of IVR—that is, the so-called coordinate space IVR. In this case the quantum propagator is given by

$$\exp\left(\frac{-i\hat{H}t}{\hbar}\right) = \int d\mathbf{q}_0 \int d\mathbf{p}_0 C_t(\mathbf{q}_0, \mathbf{p}_0) \exp\left[\frac{iS_t(\mathbf{q}_0, \mathbf{p}_0)}{\hbar}\right] |\mathbf{q}_t\rangle\langle\mathbf{q}_0| \tag{367}$$

where $\mathbf{q}_t$ denotes the coordinate at time t in an n-dimensional configuration space with the initial condition given by $(\mathbf{q}_0, \mathbf{p}_0)$, $|\mathbf{q}\rangle$ represents the usual Dirac coordinate eigenstate, $S_t(\mathbf{q}_0, \mathbf{p}_0)$ is the classical action integral (the time integral of the Lagrangian) associated with the initial condition $(\mathbf{q}_0, \mathbf{p}_0)$, and the prefactor $C_t(\mathbf{q}_0, \mathbf{p}_0)$ is given by

$$C_t(\mathbf{q}_0, \mathbf{p}_0) = \left[\left(\frac{1}{2\pi i\hbar}\right)^n \left|\frac{\partial \mathbf{q}_t(\mathbf{q}_0, \mathbf{p}_0)}{\partial \mathbf{p}_0}\right|\right]^{1/2} \tag{368}$$

Substituting the semiclassical propagator of Eq. (367) into Eq. (359), one obtains the following semiclassical reaction rate constant [80]:

$$\begin{aligned} k^{\mathrm{SC}}(T) = \frac{1}{\Phi_r} \lim_{t\to+\infty} \int d\mathbf{q}_0 \int d\mathbf{p}_0 \int d\mathbf{p}_0' \theta[S(\mathbf{q}_0)] \langle \mathbf{q}_t | \hat{F}(\beta) | \mathbf{q}_t' \rangle C_t(\mathbf{q}_0, \mathbf{p}_0) \\ \times \left[C_t(\mathbf{q}_0, \mathbf{p}_0')\right]^* \exp\left[\frac{iS_t(\mathbf{q}_0, \mathbf{p}_0)}{\hbar} - \frac{iS_t(\mathbf{q}_0, \mathbf{p}_0')}{\hbar}\right] \end{aligned} \tag{369}$$

where $\mathbf{q}_t'$ is associated with the initial condition $(\mathbf{q}_0, \mathbf{p}_0')$, and

$$\hat{F}(\beta) = \exp\left[-\frac{\beta\hat{H}}{2}\right] \hat{F} \exp\left[-\frac{\beta\hat{H}}{2}\right] \tag{370}$$

Equation (369) indicates that to obtain the semiclassical reaction rate constant $k^{\mathrm{SC}}(T)$ one needs to carry out the multidimensional phase-space average for a sufficiently long time. This is far from trivial, since the integrand in Eq. (369) is highly oscillatory due to quantum interference effects between the sampling classical trajectories. The use of some filtering methods to dampen the oscillations in the integrand may improve the accuracy of the semiclassical calculation.

A further analytical approximation to Eq. (369), proposed by Miller and coworkers [84–86], demonstrates how the above semiclassical reaction rate theory approaches a quasi-classical reaction rate theory. Specifically, consider the

following drastic approximation:

$$S_t(\mathbf{q}_0, \mathbf{p}_0) - S_t(\mathbf{q}_0, \mathbf{p}_0') \approx \frac{\partial S_t(\mathbf{q}_0, \bar{\mathbf{p}}_0)}{\partial \bar{\mathbf{p}}_0}(\mathbf{p}_0 - \mathbf{p}_0') \tag{371}$$

where $\bar{\mathbf{p}}_0 = (\mathbf{p}_0 + \mathbf{p}_0')/2$. With this approximation and some manipulation, Miller and co-workers showed that Eq. (369) reduces to

$$k^{\mathrm{SC}}(T) \approx \frac{1}{(2\pi\hbar)^n \Phi_r} \lim_{t\to+\infty} \int d\mathbf{q}_0 \int d\mathbf{p}_0 \theta[S(\mathbf{q}_t)] F_W(\beta)(\mathbf{q}_0, \mathbf{p}_0) \tag{372}$$

where $F_W(\beta)$ is the Weyl transform of $\hat{F}(\beta)$. This expression is quasi-classical insofar as it is very similar to the classical result of Eq. (360), the only difference being that the product of the Boltzmann factor $\exp[-\beta H(\mathbf{q}_0, \mathbf{p}_0)]$ and the flux function $F(\mathbf{q}_0, \mathbf{p}_0)$ in Eq. (360) is replaced by $F_W(\beta)$.

Since $k^{\mathrm{SC}}(T)$ given by Eq. (372) is essentially a classical result, it may be well approximated by a statistical theory without referring to the detailed dynamics of the system. That is, if an appropriate phase space separatrix $S(\mathbf{q}, \mathbf{p})$ can be constructed, then the approximation

$$\lim_{t\to+\infty} \theta[S(\mathbf{q}_t)] \approx \theta(\boldsymbol{\nabla} S \cdot \mathbf{v}) \tag{373}$$

can be made and we obtain

$$k^{\mathrm{SC}}(T) \approx \frac{1}{(2\pi\hbar)^n \Phi_r} \int d\mathbf{q}_0 \int d\mathbf{p}_0 \theta(\boldsymbol{\nabla} S \cdot \mathbf{v}) F_W(\beta)(\mathbf{q}_0, \mathbf{p}_0) \tag{374}$$

Equation (374) can be regarded as a quasi-classical extension of classical reaction rate theory.

F. Effective Hamiltonian Approach to Unimolecular Dissociation

In an effort to understand the intramolecular dynamics in unimolecular dissociation, Remacle and Levine [87] used an effective Hamiltonian approach that can account for different time scales associated with unimolecular reaction. In doing so, they assumed that a dense set of energy levels lies above the dissociation barrier and that the barrier is sufficiently high that the number of states from which dissociation occurs is small compared to the number of bound states.

The full system Hamiltonian is given by

$$\hat{H} = \hat{H}_0 + \hat{V} + \hat{U} \tag{375}$$

where $\hat{H}_0$ is the zeroth-order Hamiltonian of the bound states that cannot couple to the continuum, and $\hat{V}$ and $\hat{U}$ are the bound–bound and bound–continuum

coupling potentials. Let $\hat{P}$ and $\hat{Q} = 1 - \hat{P}$ denote the projectors onto the open- and bound-state subspaces, respectively. Then the effective Hamiltonian for the bound-state subspace can be written as

$$\hat{H}_{\text{eff}} = \hat{Q}H\hat{Q} + \hat{Q}(\hat{V} + \hat{U})\hat{P}(E - \hat{P}\hat{H}\hat{P})^{-1}\hat{P}(\hat{V} + \hat{U})\hat{Q} \tag{376}$$

The coupling to the continuum is implicitly contained in the second term in Eq. (376). The decay of the population in the bound state subspace is due to the imaginary part of $\hat{P}(E - \hat{P}\hat{H}\hat{P})^{-1}\hat{P}$. The contribution from the real part of $\hat{P}(E - \hat{P}\hat{H}\hat{P})^{-1}\hat{P}$, the so-called "level shift" due to the coupling to the continuum, can be neglected, if the energy dependence of the coupling term $\hat{Q}\hat{H}\hat{P}$ is weak. In this case the second term in Eq. (376) can be regarded as a purely anti-Hermitian operator, and the effective Hamiltonian reduces to

$$\hat{H}_{\text{eff}} = \hat{Q}(\hat{H} - i\hat{\Gamma})\hat{Q} \tag{377}$$

where $\hat{\Gamma}$ is given by

$$\hat{\Gamma} = \pi\hat{Q}\hat{H}\hat{P}\delta(E - \hat{P}\hat{H}\hat{P})\hat{P}\hat{H}\hat{Q} \tag{378}$$

The key element in the effective Hamiltonian approach is the determination of the eigenvalues of the effective Hamiltonian $\hat{H}_{\text{eff}}$. Consider first a limiting case in which the bound states are not coupled by intramolecular interactions, that is,

$$\hat{H}_{\text{eff}} = \hat{Q}(\hat{H}_0 - i\hat{\Gamma})\hat{Q} \tag{379}$$

where $\hat{Q}\hat{H}_0\hat{Q}$ and $\hat{Q}\hat{\Gamma}\hat{Q}$ can be simultaneously diagonalized. Suppose that among the N states under study there are K quasi-bound states ($K<N$) and $(N - K)$ purely bound states that will never decay. Then the eigenvalue equation for $\hat{H}_{\text{eff}}$ gives

$$\hat{H}_{\text{eff}}|\varphi_\ell\rangle = \begin{array}{ll} (E_\ell - i\Gamma_\ell)|\varphi_\ell\rangle, & \ell = 1, 2, \ldots, K \\ E_\ell|\varphi_\ell\rangle, & \ell = K+1, \ldots, N \end{array} \tag{380}$$

For an arbitrary initial superposition state $|\phi_0\rangle = \sum_{\ell=0}^{N} c_\ell^{(0)}|\varphi_\ell\rangle$, where the $c_\ell^{(0)}$ are the expansion coefficients, the time-evolving state can be described by

$$|\phi(t)\rangle = \exp\left(-\frac{i}{\hbar}\hat{H}_{\text{eff}}t\right)|\phi_0\rangle = \sum_{\ell=1}^{K} c_\ell^{(0)} \exp\left[-\frac{i}{\hbar}(E_\ell - i\Gamma_\ell)t\right]|\varphi_\ell\rangle + \sum_{\ell=K+1}^{N} c_\ell^{(0)} \exp\left(-\frac{i}{\hbar}E_\ell t\right)|\varphi_\ell\rangle \tag{381}$$

In the more general case that allows for intramolecular energy flow, the effective Hamiltonian must include another perturbation term $\hat{H}_1$ so that

$$\hat{H}_{\text{eff}} = \hat{Q}(\hat{H}_0 - i\hat{\Gamma} + \hat{H}_1)\hat{Q} \tag{382}$$

One way of treating the $\hat{H}_1$ term is to use perturbation theory to eliminate the effect of intramolecular coupling in successive orders. Alternatively, one may numerically diagonalize the matrix of the effective Hamiltonian in the representation of $\{|\varphi_\ell\rangle\}$. That is, with the expansion

$$|\Phi_m\rangle = \sum_{\ell=1}^{K} c_\ell^{(m)}|\varphi_\ell\rangle + \sum_{\ell=K+1}^{N} c_\ell^{(m)}|\varphi_\ell\rangle, \quad m = 1, 2, \ldots \tag{383}$$

one solves the eigenvalue equation

$$\hat{Q}(\hat{H}_0 - i\hat{\Gamma} + \hat{H}_1)\hat{Q}|\Phi_m\rangle = \lambda_m|\Phi_m\rangle, \quad m = 1, 2, \ldots \tag{384}$$

where the eigenvalue $\lambda_m = E'_m - i\Gamma'_m$ is complex in general.

For an arbitrary initial state that is a linear combination of the eigenstates $\{|\Phi_m\rangle\}$, that is,

$$|\psi(0)\rangle = \sum_{m=1}^{N} a_m|\Phi_m\rangle \tag{385}$$

the time evolution is given by

$$\begin{aligned} |\psi(t)\rangle &= \exp\left(-\frac{i}{\hbar}\hat{H}_{\text{eff}}t\right)|\psi(0)\rangle \\ &= \sum_{m=1}^{N} a_m|\Phi_m\rangle \exp\left(-\frac{i}{\hbar}\lambda_m t\right) \end{aligned} \tag{386}$$

which leads to the time autocorrelation function

$$C(t) = \langle\psi(0)|\psi(t)\rangle = \sum_{m=1}^{N}|a_m|^2 \exp\left(-\frac{i}{\hbar}\lambda_m t\right) \tag{387}$$

Note that $|C(t)|^2$ gives the "survival probability" of the initial state. Furthermore, the probability of finding the system still in the bound-state subspace is given by

$$P(t) = \langle\psi(t)|\psi(t)\rangle = \sum_{n=1}^{N}\sum_{m=1}^{N} a_n^* a_m \langle\Phi_n|\Phi_m\rangle \exp\left[-\frac{i}{\hbar}(\lambda_m - \lambda_n)t\right] \tag{388}$$

To examine the dynamics in more detail one can partition the bound-state subspace by a set of projectors $\{\hat{Q}_j\}$ such that

$$\hat{Q} = \sum_j \hat{Q}_j \tag{389}$$

For example, one may choose

$$\hat{Q}_j = \sum_{\ell=\ell_j+1}^{\ell_j+N_j} |\varphi_\ell\rangle\langle\varphi_\ell| \tag{390}$$

where $|\varphi_\ell\rangle$ is the zeroth-order eigenstate of $\hat{H}_0 - i\hat{\Gamma}$, and N_j is the number of states in the jth sub-subspace. The probability of finding the system in the bound-state sub-subspace associated with $\hat{Q}_j$ is given by

$$P_j(t) = \langle\psi(t)|\hat{Q}_j|\psi(t)\rangle = \sum_{n=1}^{N}\sum_{m=1}^{N}\left[\sum_{\ell=\ell_j+1}^{\ell_j+N_j}\langle\Phi_n|\varphi_\ell\rangle\langle\varphi_\ell|\Phi_m\rangle\right] \times a_n^* a_m \exp\left[\frac{i}{\hbar}(\lambda_m - \lambda_n)t\right] \tag{391}$$

The effective Hamiltonian analysis makes evident the existence of different time scales in unimolecular decay. Consider first the zeroth-order states $|\varphi_\ell\rangle$ with $\ell = 1, 2, \ldots, K$. Each of these states decays with a lifetime $1/\Gamma_\ell$, even in the absence of intramolecular coupling. These states are called "prompt" states. Their average lifetime defines the average prompt lifetime $\langle\tau_p\rangle$. The intramolecular coupling will affect the decay behavior of the prompt states, but only perturbatively. By contrast, the decay of the zeroth-order states $|\varphi_\ell\rangle$ with $\ell = K, K+1, \ldots, N$ is induced entirely by the perturbation $\hat{H}_1$. Presumably, the weaker the perturbation is, the slower the decay will be. This second class of states is defined as the set of "delayed" states. Their average lifetime defines the average delayed lifetime $\langle\tau_d\rangle$.

Figure 42 displays a computational example of $P(t)$ (solid line) and the survival probability $|C(t)|^2$ (dashed line) as a function of the total number of states N and the number of the prompt states K. The initial state is taken to have uniform weights for either the K prompt states or the $N - K$ delayed states. It is seen that with fixed K and increasing N the decay of the initial delayed state is shifted to much longer time, whereas the decay of the initial prompt state changes little.

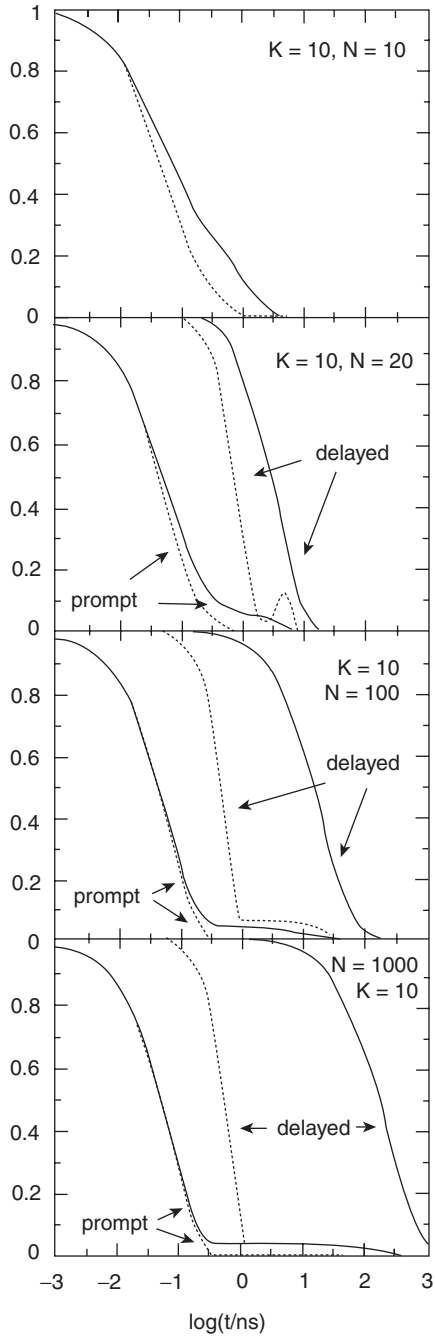

Figure 42. A computational example of $P(t)$ (solid line) and the survival probability $|C(t)|^2$ (dashed line) as a function of the total number of states N and the number of prompt states K. [From F. Remacle and R. D. Levine, *J. Phys. Chem.* **100**, 7962 (1996).]

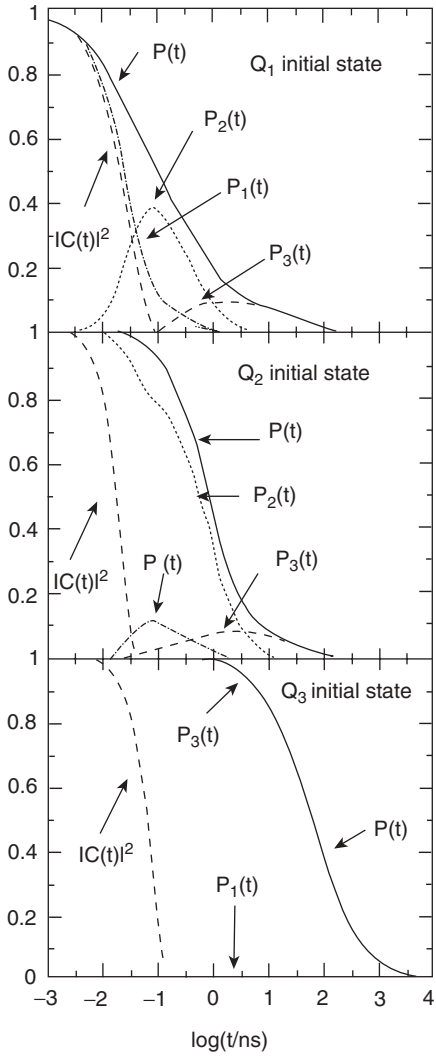

Figure 43. A computational example of $P(t)$, $P_j(t)$, and $|C(t)|^2$, for three different initial states taken to be uniformly weighted in three different sub-subspaces (denoted by Q_1, Q_2, and Q_3) of the bound-state subspace. Note that there is coupling between the three sub-subspaces. [From F. Remacle and R. D. Levine, *J. Phys. Chem.* **100**, 7962 (1996).]

Figure 43 shows a computational example of $P(t)$, $P_j(t)$, and $|C(t)|^2$, for three different initial states associated with three different sub-subspaces Q_1, Q_2 and Q_3, The Q_1 sub-subspace is made up of 20 prompt states, and the Q_2 and Q_3 sub-subspaces are made up of delayed states, being of dimension 100 and 1000,

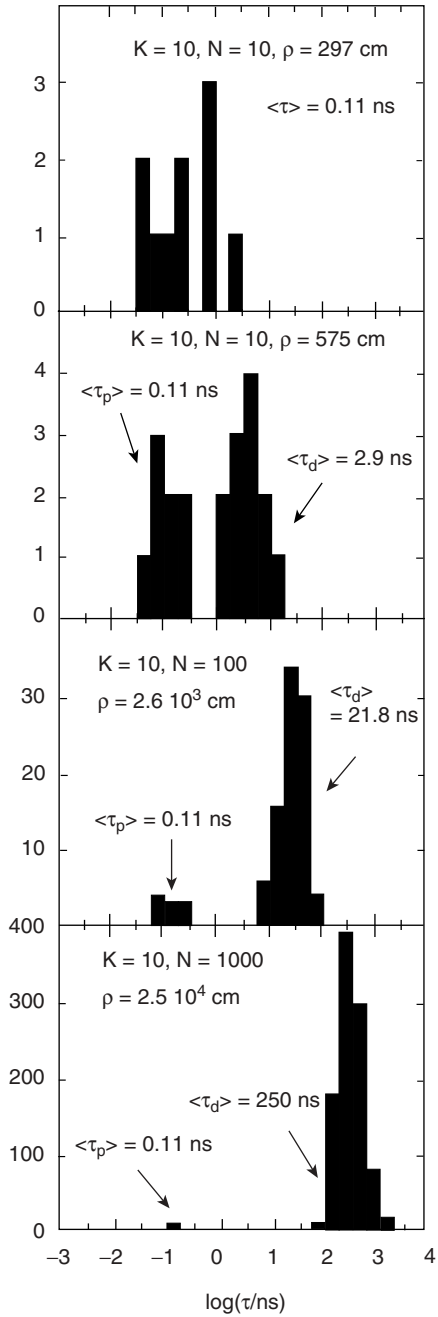

Figure 44. A computational example of the bifurcation of the decay lifetimes into a prompt and a delayed branch as a function of the density of states ρ. The number of prompt states is denoted by K, and the number of delayed states is denoted by $(N - K)$. [From F. Remacle and R. D. Levine, *J. Phys. Chem.* **100**, 7962 (1996).]

respectively. Because the Q_1 initial state is a prompt state, the major part of its decay takes place in the prompt time regime. However, due to the coupling between the three sub-subspaces, there is significant population transfer to the Q_2 and Q_3 sub-subspaces, which results in different decay behavior at later times. For the Q_2 and Q_3 initial states that are delayed states, the population transfer is seen to be much less significant.

The dependence of $\langle \tau_p \rangle$ and $\langle \tau_d \rangle$ on the density of states can also be examined. The density of states can be obtained from

$$\rho = \left[\frac{1}{N-1} \sum_{n=1}^{N-1} (E_{n+1} - E_n) \right]^{-1} \tag{392}$$

where the $\{E_n\}$ are the real parts of the eigen-energies of the effective Hamiltonian. In the case shown in Fig. 44, $\langle \tau_p \rangle$ is almost independent of ρ while $\langle \tau_d \rangle$ decreases as $1/\rho$.

The effective Hamiltonian approach clearly shows the important role of intramolecular energy flow in the quantum dynamics of unimolecular dissociation. It suggests that unless intramolecular energy flow is dominantly rapid, there exist two drastically different time scales in the reaction dynamics. This is consistent with the classical concept that nonstatistical behavior in intramolecular energy flow, such as bottleneck effects, can dramatically alter the kinetics of unimolecular reaction.

G. Wave Packet Dynamics Approach

In the wave packet dynamics approach to unimolecular predissociation, the quantum dynamics is studied by directly propagating quantum wave packets. After numerically propagating the quantum wave packets, all the detailed information about the reaction dynamics can, in principle, be extracted from the numerical results.

Consider the formal solution of the time-dependent Schrödinger equation

$$|\psi(t)\rangle = \exp\left(-\frac{i}{\hbar} \hat{H} t \right) |\psi(0)\rangle \tag{393}$$

where $|\psi(0)\rangle$, the initial wave packet at $t = 0$, is typically a combination of quasi-bound states in the case of unimolecular predissociation. As is consistent with the results from the effective Hamiltonian approach, the time-evolving wave packet can be described by

$$|\psi(t)\rangle = \sum_j a_j |\phi_j\rangle \exp\left(-\frac{i}{\hbar} E_j t \right) \exp\left(-\frac{\Gamma_j}{2\hbar} t \right) \tag{394}$$

where a_j is an expansion coefficient, and $|\phi_j\rangle$ is the jth quasi-bound state with resonance energy E_j and decay width Γ_j. This general representation of $|\psi(t)\rangle$ suggests that the time autocorrelation function is given by

$$C(t) = \langle\psi(0)|\psi(t)\rangle = \sum_j |a_j|^2 \exp\left(-\frac{i}{\hbar}E_j t\right)\exp\left(-\frac{\Gamma_j}{2\hbar}t\right) \tag{395}$$

and that its norm takes the following form:

$$N(t) = \langle\psi(t)|\psi(t)\rangle = \sum_j |a_j|^2 \exp\left(-\frac{\Gamma_j}{\hbar}t\right) \tag{396}$$

Given the formal time dependences of $C(t)$ and $N(t)$ shown in Eqs. (395) and (396), one may fit the results from numerically propagated wave packets so as to extract E_j and Γ_j. The resonance lifetime τ_j and fragmentation rate constant k_j can then be determined from $\tau_j = \hbar/\Gamma_j$ and $k_j = 1/\tau_j$.

One attractive feature of the wave packet dynamics approach is that it makes it possible to visualize the quantum reaction dynamics in phase-space by examining the time-evolving Wigner function. Consider a two-DOF system for which the time-evolving quantum wave packet is a function of two coordinates R and r, where R denotes the reaction coordinate. To focus on the R-coordinate, one may construct the following "half" Wigner transformation:

$$W(R,P,r,t) = \frac{1}{2\pi\hbar}\int dx\langle R+\frac{x}{2},r,t|\psi\rangle\langle\psi|R-\frac{x}{2},r,t\rangle\exp\left(-\frac{ixP}{\hbar}\right) \tag{397}$$

which leaves the r-DOF intact. The Wigner function $W(R,P,r,t)$ at a given time t can then be visualized on a surface of section (i.e., for fixed r) and compared to the classical phase-space distribution function.

To be specific, let us consider again the predissociation of the T-shaped HeI_2 molecule [88]. The Hamiltonian operator is given by

$$\hat{H} = -\frac{\hbar^2}{2\mu}\frac{\partial^2}{\partial R^2} - \frac{\hbar^2}{2m}\frac{\partial^2}{\partial r^2} + V_{\mathrm{I-I}}(r) + 2V_{\mathrm{He-I}}[R_{\mathrm{He-I}}(R,r)] \tag{398}$$

where the potential terms are the same as in Eq. (90). The numerical propagation of the quantum wave packet can be carried out, for example, in the standard discrete variable representation (DVR) [89]. In the DVR approach the coordinate space is discretized by defining the following grid points:

$$r_i = r_{\min} + i\Delta r, \qquad i = 1,2,\ldots,N_r \tag{399}$$

$$R_j = R_{\min} + j\Delta R, \qquad j = 1,2,\ldots,N_R \tag{400}$$

where

$$\Delta r = \frac{r_{\max} - r_{\min}}{N_r + 1}, \qquad \Delta R = \frac{R_{\max} - R_{\min}}{N_R + 1} \tag{401}$$

and $(r_{\min}, r_{\max})$ and $(R_{\min}, R_{\max})$ obviously define the region that is occupied by the grid points. The basis set for expanding the time-evolving quantum state is chosen to be

$$|\varphi_1(r_i)\rangle|\varphi_2(R_j)\rangle = \sum_{n_r=1}^{N_r} \sum_{n_R=1}^{N_R} |\varphi_1(r_i, n_r)\rangle|\varphi_2(R_j, n_R)\rangle \tag{402}$$

where

$$|\varphi_1(r_i, n_r)\rangle = \left(\frac{2}{r_{\max} - r_{\min}}\right)^{1/2} \sin\left(\frac{r_i - r_{\min}}{r_{\max} - r_{\min}} n_r \pi\right) \tag{403}$$

$$|\varphi_2(R_j, n_R)\rangle = \left(\frac{2}{R_{\max} - R_{\min}}\right)^{1/2} \sin\left(\frac{R_j - R_{\min}}{R_{\max} - R_{\min}} n_R \pi\right) \tag{404}$$

In the representation of $|\varphi_1(r_i)\rangle|\varphi_2(R_j)\rangle$, the matrix elements of $V_{\text{I-I}}$ and $V_{\text{He-I}}$ are automatically diagonalized, and the kinetic energy operator in Eq. (398) can also be evaluated straightforwardly. Hence numerically propagating the quantum wave packets reduces to a linear algebra routine. Figure 45 displays the calculated quantum wave packets $|\psi(R, r, t)\rangle$ at three different times. The initial vibrational state of I_2 is taken to be $v = 20$.

To extract various decay rates from $|\psi(R, r, t)\rangle$, the time dependence of the norm $\langle\psi(R, r, t)|\psi(R, r, t)\rangle$ is fit to three exponential terms such that

$$\langle\psi(R, r, t)|\psi(R, r, t)\rangle = N_1 \exp(-k_1 t) + N_2 \exp(-k_2 t) + N_3 \exp(-k_3 t) \tag{405}$$

The results are as follows:

$$\begin{aligned} N_1 &= 0.0057, & k_1 &= 2.8982 \times 10^{-4}\text{a.u.} \\ N_2 &= 0.2409, & k_2 &= 4.9849 \times 10^{-7}\text{a.u.} \\ N_3 &= 0.7549, & k3 &= 4.7361 \times 10^{-7}\text{a.u.} \end{aligned}$$

with $N_1 + N_2 + N_3 = 1$. The very fast decay characterized by the rate constant k_1 can be attributed to the dephasing of the initially prepared wave packet. However, since the magnitude of N_1 is small this fast decay does not contribute significantly to the vibrational predissociation. The rate constants k_2 and k_3 are almost equal in magnitude, but their corresponding coefficients N_2 and N_3 are different. The overall predissociation rate constant obtained from the wave

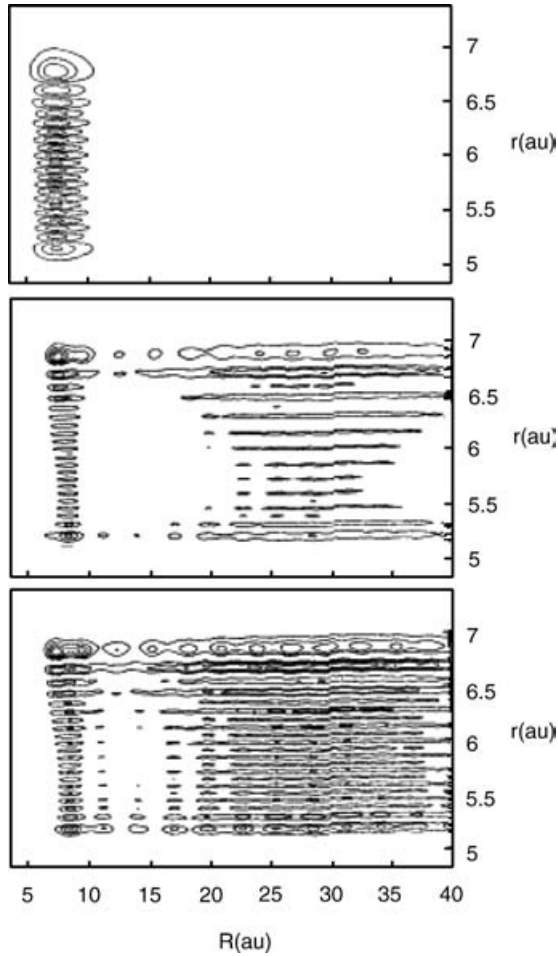

Figure 45. Contour plot of the wavefunction for the T-shaped HeI_2 molecule with the initial vibrational state of I_2 given by $v = 20$. Shown from top to bottom panels are three wavefunctions at $t = 0$, $t = 9\tau$, and $t = 10\tau$, where $\tau = 14{,}700$ a.u. is approximately the virbrational period of I_2.

packet dynamics approach is found to be 0.113 cm^{-1}, which is about one-half of the MRRKM result (see Table IV).

To visualize the time-evolving Wigner function associated with the reaction coordinate, we choose $r = 5.70$ a.u., which is close to the minimum of the I_2 potential energy curve. The Wigner functions at four different times are displayed in Fig. 46. From Fig. 46 it is seen that as time evolves, more and more phase space flux flows out of the original support of the Wigner function. Also

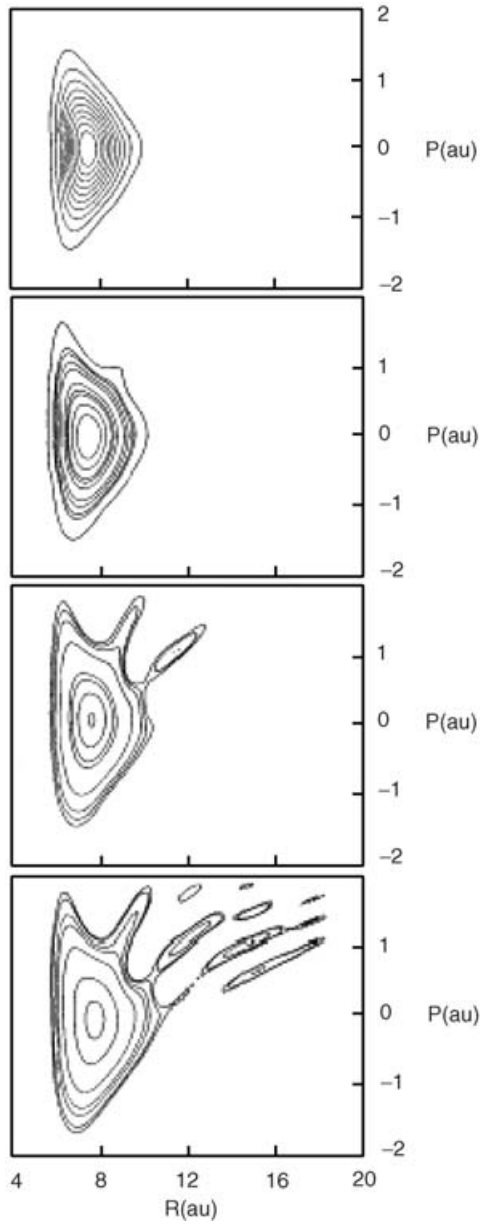

Figure 46. The time-evolving Wigner functions for the T-shaped HeI_2 molecule with the initial state of I_2 given by $v = 20$. Shown from top to bottom panels are Wigner functions at $t = 0, \tau, 3\tau, 5\tau$, where $\tau = 14{,}700$ a.u. is approximately the vibrational period of I_2. The contours from innermost to the outermost correspond to: at $t = 0$, $W = 0.30, 0.25, 0.20, 0.18, 0.15, 0.10, 0.05, 0.04, 0.03, 0.02$; at $t = \tau$, $W = 0.30, 0.25, 0.20, 0.18, 0.15, 0.10, 0.05, 0.04, 0.03, 0.02$; at $t = 3\tau$, $W = 0.18, 0.15, 0.10, 0.08, 0.06, 0.05, 0.02, 0.01, 0.007, 0.005$; at $t = 5\tau$, $W = 0.18, 0.15, 0.10, 0.08, 0.06, 0.05, 0.02, 0.01, 0.004, 0.003$.

seen is a pattern of ''finger formation,'' with the number of fingers closely related to the propagation time measured by the vibrational period of I_2. The finger patterns can be regarded as quantum mechanical realizations of the underlying classical phase-space structure that evolves from the classical exact separatrix. Indeed, further comparisons between the Wigner functions and the classical phase-space density functions show that they are in agreement, suggesting that in this case quantum-classical correspondence is excellent

As mentioned earlier, Gray and Wozny [97] studied the predissociation of three-dimensional models of the molecules $HeCl_2$ and $NeCl_2$ using the wave packet dynamics approach. Their results are close to classical results. Quéré and Gray [90] further applied the wave packet dynamics approach to other three-DOF model systems such as He_2Cl_2 and Ne_2Cl_2 and obtained results that are in reasonable agreement with experiment. However, we do not expect the wave packet dynamics approach to be generally feasible in many-dimensional systems, primarily because the quantum calculations can be prohibitively expensive if the number of DOFs is much larger than three.

VII. QUANTUM TRANSPORT IN CLASSICALLY CHAOTIC SYSTEMS

As shown above, classical unimolecular reaction rate theory is based upon our knowledge of the qualitative nature of the classical dynamics. For example, it is essential to examine the rate of energy transport between different DOFs compared with the rate of crossing the intermolecular separatrix. This is also the case if one attempts to develop a quantum statistical theory of unimolecular reaction rate to replace exact quantum dynamics calculations that are usually too demanding, such as the quantum wave packet dynamics approach, the flux–flux autocorrelation formalism, and others. As such, understanding quantum dynamics in classically chaotic systems in general and quantization effects on chaotic transport in particular is extremely important.

There have been numerous studies of quantization effects on chaotic transport. For example, it has been long known that a cantorus in the classical phase-space comprise a strong barrier to transport when $\pi\hbar$ is larger than the classical flux across the cantorus [91,92]. In this case, the fractal structure of the cantorus, which slows down but still allows for classical transport, cannot be resolved by quantum dynamics and therefore behaves more or less the same as a closed phase-space curve in the quantized system. A second important example is ''dynamical localization'' [28], which was first discovered in the so-called ''standard map'' (introduced below) generated by a one-dimensional kicked-rotor system. There, although the classical system continuously diffuses in the energy space as a manifestation of classical chaos, quantum interference effects quickly saturate the energy diffusion.

Here we review some recent results concerning quantum transport in classically chaotic systems, including new results on suppressed quantum transport through cantori, quantum suppression of Arnold diffusion, and faster-than-classical quantum anomalous diffusion.

A. Quantum Transport Through Cantori

Recently, Maitra and Heller reexamined quantum transport through cantori [93], including the cases in which $\pi\hbar$ is actually smaller than the classical flux crossing a particular cantorus. In doing so, they used the Whisker map, which can describe the motion within a chaotic layer near a separatrix in a typical nonintegrable system. The Whisker map is given by

$$I_{n+1} = I_n - k \sin \phi_n \tag{406}$$

$$\phi_{n+1} = \phi_n + \lambda \ln \left| \frac{c}{I_{n+1} - I_0} \right| \tag{407}$$

where (I_n, ϕ_n) are action and angle variables before the $(n+1)$th mapping, and the parameters k and λ determine the phase space structure. Typically, there are several cantori within the chaotic layer, corresponding to irrational winding numbers that are given by $r \pm (1-g)$, where r is an integer and g is the golden mean previously defined. The flux F across a cantorus can be estimated from

$$F \approx \exp\left(\frac{0.7c \exp\{-2\pi[r \pm (1-g)]/\lambda\}}{\lambda} \right) (\lambda k_c \exp\{2\pi[r \pm (1-g)]/\lambda\} - k_c)^{3.01} \tag{408}$$

where $k_c = 0.9716$.

Quantizing the action and angle variables, one obtains the following quantum map:

$$U = \exp\left[\frac{-i\lambda(\hat{I} - I_0)(\ln|\frac{c}{\hat{I}-I_0}| + 1)}{\hbar} \right] \exp\left[\frac{ik \cos\phi}{\hbar} \right] \tag{409}$$

where $\hat{I}$ and ϕ should be understood as operators in the Hilbert space. The eigenstate of the action $\hat{I}$ with eigenvalue I is denoted by $|I\rangle$. The diffusion in action space can be studied using the time-averaged probability $P(I_f, I_i)$ of being in the final state $|I_f\rangle$ starting from the initial state $|I_i\rangle$. $P(I_f, I_i)$ is given by

$$P(I_f, I_i) = \lim_{N\to\infty} \frac{1}{N} \sum_{n=0}^{N} |\langle I_f | U^n | I_i \rangle|^2 \tag{410}$$

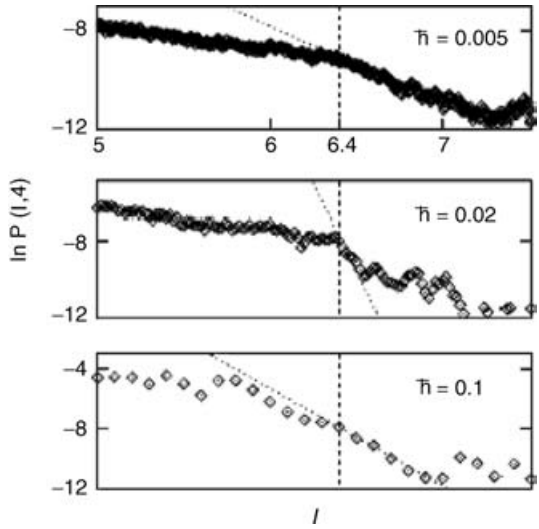

Figure 47. Quantum transport suppressed by the cantorus. Shown here is the logarithm of $P(I, I_i)$ versus I, with the initial state given by $I_i = 4$. The winding number of the cantorus is given by $2 - g$. From top to bottom the dotted lines have the slopes 3.2, 18, and 6.5, respectively. [From N. T. Maitra and E. J. Heller, *Phys. Rev. E* **61**, 3620 (2000).]

We consider below a case in which the cantorus is at $I \sim 6.4$, with the winding number given by $2 - g$, and the classical flux F through the cantous given by $\sim 0.01\pi$. Figure 47 shows $\ln[P(I, I_i = 4)]$ versus I, with the initial state at $|I_i = 4\rangle$, and $\hbar = 0.005$, 0.02 or 0.1. For all the cases shown it is seen that $P(I, I_i = 4)$ decays exponentially, implying that the cantorus presents a strong barrier to quantum transport. A linear fit of the results in the neighborhood of the cantorus can be carried out, giving a slope S as a fitting parameter. The inverse of the slope thus obtained (i.e., $1/S$) is indicative of the extent to which the quantum state can penetrate into the cantorus. Specifically, S is found to be 3.2, 18, and 6.5, for the three values of $\hbar$, respectively. Thus, as $\pi\hbar$ increases from below the classical flux, S increases; but then decreases as $\pi\hbar$ gets larger than the classical flux. This clearly demonstrates the existence of different mechanisms that account for the suppressed quantum transport.

When $\pi\hbar$ is larger than the classical flux, the mechanism of suppression is well known; that is, the quantum state cannot get through the fractal structure of the cantorus, and as a result the associated quantum transport is due entirely to tunneling. What is most interesting is that quantum transport is still suppressed, as seen in the decay behavior of $P(I_f, I_i)$, even when $\pi\hbar$ is considerably smaller than the classical flux. To demonstrate that this suppression is uniquely related

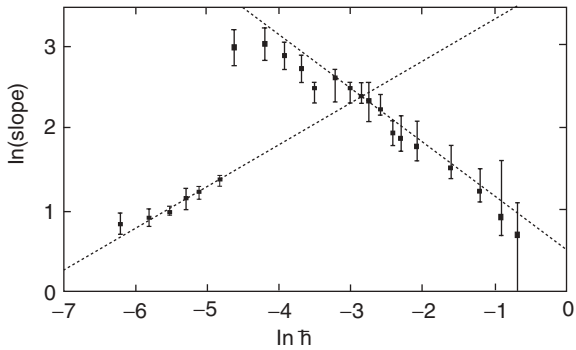

Figure 48. The dependence of $\ln S$ on $\ln \hbar$. The dashed lines indicate that S scales with $\hbar^{0.5}$ if $\pi\hbar$ is smaller than the classical flux and that S scales with $\hbar^{-0.66}$ if $\pi\hbar$ is larger than the classical flux. [From N. T. Maitra and E. J. Heller, *Phys. Rev. E* **61**, 3620 (2000).]

to the cantorus, Maitra and Heller further showed that S scales with $\hbar^{\alpha}$ with $\alpha \sim 0.5$. This result is shown in Fig. 48. Note that in the case of quantum suppression of chaotic transport due to dynamical localization, one has that S scales with $\hbar$. As such, for sufficiently small $\hbar$ the quantum suppression effect on chaotic transport due to a cantorus is always much larger than that due to dynamical localization.

This finding concerning quantum transport in classically chaotic systems sheds new light on quantum effects in unimolecular reaction dynamics. For example, one expects that intramolecular bottlenecks associated with cantori, if treated quantum mechanically, would be more effective than in a classical statistical theory even when $\pi\hbar$ is smaller than the reaction flux crossing the intramolecular dividing surface. Clearly, it would be interesting to examine realistic molecular systems in a similar fashion.

B. Quantum Suppression of Arnold Diffusion

Given the important role of Arnold diffusion in understanding chaotic transport in many-dimensional systems, it is quite surprising that a study of the quantization effect on Arnold diffusion was not carried out until very recently [94–96]. In particular, Izrailev and co-workers are the first to carefully examine quantum manifestations of Arnold diffusion in a well-studied model system. The model system is comprised of two coupled quartic oscillators, one of which driven by a two-frequency field. Its Hamiltonian is given by

$$H = H_1^0 + H_2^0 - \mu xy - fx[\cos(\omega_1 t) + \cos(\omega_2 t)] \tag{411}$$

where

$$H_1^0 = \frac{p_x^2}{2} + \frac{x^4}{4} \tag{412}$$

$$H_2^0 = \frac{p_y^2}{2} + \frac{y^4}{4} \tag{413}$$

with all variables in dimensionless units. In particular, p_x, p_y, x, and y are momentum and position variables, μ is the coupling constant between the two DOFs, f is the amplitude of the driving field, and ω_1 and ω_2 are the two frequencies of the driving field.

For nonzero f the separatrix associated with the main $1:1$ resonance in the undriven system is destroyed and a chaotic layer that allows for Arnold diffusion can be induced. Note that using two driving frequencies is not essential to induce Arnold diffusion. However, with two commensurate driving frequencies the Arnold diffusion would be much more homogeneous, thus simplifying the analytical considerations in obtaining the Arnold diffusion coefficient. To quantize the system, one simply sets $[p_x, x] = [p_y, y] = -i\hbar_0$, where $\hbar_0$ should be regarded as a dimensionless effective Planck constant of the system, such as the ratio of $\hbar$ to the characteristic action of the system. The quantum dynamics can be examined by direct propagation of quantum wave packets. For the results discussed below, the system parameters were chosen as follows: $f/\mu = 0.01$, $\hbar_0 \approx 1.77 \times 10^{-5}$, $10\pi/\omega_1 = 12\pi/\omega_2 = T = 150$.

Figure 49 shows the energy variance (denoted by Δ_q and in unit of $[\hbar_0^2(\omega_1 + \omega_2)^2/4]$) versus time (denoted by N and in units of T), for three different initial states—that is, below, above, and within the chaotic layer that is responsible for Arnold diffusion. Clearly, the quantum transport depends strongly on the location of the initial quantum state. In particular, with the initial state below or above the chaotic layer (curve 1 or curve 2), Δ_q quickly saturates; whereas with the initial state inside the chaotic layer, after a transient period Δ_q keeps increasing for a long time in a more or less linear fashion. The average linear rate of increase of Δ_q gives the quantum diffusion coefficient.

To further demonstrate that the quantum transport of curve 3 in Fig. 49 is intrinsically related to Arnold diffusion, Izrailev and co-workers compared the μ-dependence of the quantum diffusion coefficient to that of the Arnold diffusion coefficient. This comparison is shown in Fig. 50. It is seen that the quantum result resembles the classical result. That is, roughly speaking, in either case the logarithm of the diffusion coefficient decreases linearly with increasing $1/\sqrt{\mu}$. This makes it clear that quantum manifestations of Arnold diffusion are indeed observed.

Figure 50 also shows that quantum effects strongly suppress Arnold diffusion (note the logarithmic scale). The suppression effect for very small μ is

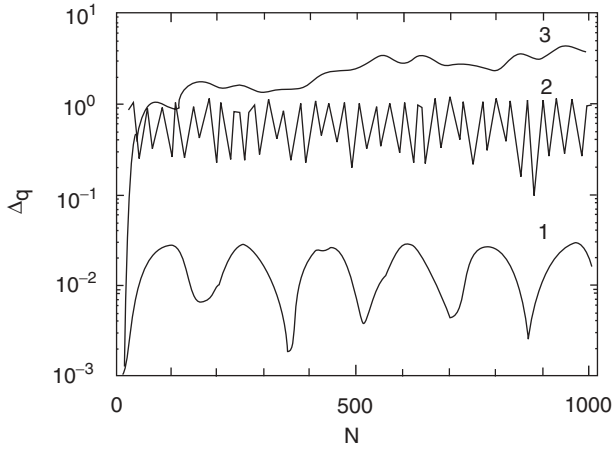

Figure 49. The energy variance Δ_q (in units of $[\hbar_0^2(\omega_1+\omega_2)^2/4]$) versus the time variable N (in units of T). The system parameters are chosen as $f/\mu = 0.01$, $\hbar_0 \approx 1.77 \times 10^{-5}$, $10\pi/\omega_1 = 12\pi/\omega_2 = T = 150$. The three curves correspond to three initial states, i.e., below, above, or within the separatrix associated the Arnold diffusion. [From V. Ya Demikhovskii, F. M. Izrailev, and A. I. Malyshev, *Phys. Rev. Lett.* **88**, 154101 (2002).]

understandable because the thin chaotic layer can only support very few quantum eigenstates. However, as estimated by Izrailev and co-workers, for $\mu > 1.25 \times 10^{-4}$, which is true for most cases shown in Fig. 50, the number of quantum states that can be supported by the chaotic layer should be larger

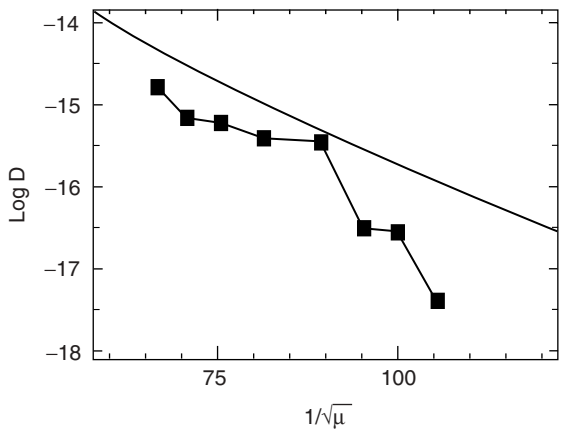

Figure 50. Quantum and classical Arnold diffusion constants versus $1/\sqrt{\mu}$. [From V. Ya Demikhovskii, F. M. Izrailev, and A. I. Malyshev, *Phys. Rev. Lett.* **88**, 154101 (2002).]

than 10. This being the case, we see that quantum effects can strongly suppress Arnold diffusion even when the system is not in the deep quantum regime.

It remains to examine whether or not the results of Izrailev and co-workers are general. In particular, since the Gaspard–Rice four-dimensional mapping model introduced above can mimic the Arnold diffusion in unimolecular predissociation, the corresponding quantum dynamics is of considerable interest.

C. Faster-than-Classical Quantum Anomalous Diffusion

As seen throughout this chapter, for most Hamiltonian systems regular regions coexist with chaotic regions in phase-space. The boundary between a regular region and a chaotic region is complicated, due to, for example, the fractal structures of cantori. As such, in many cases there are strong correlations in the dynamics, and chaotic diffusion in energy space is not a random walk. To see this more clearly, consider the standard map (defined below) as an example. Assuming that the system is strongly chaotic, one expects that the average energy of a classical ensemble should increase linearly with time, with the chaotic diffusion coefficient well-predicted by a statistical approach. However, in many cases this is not true. Instead, the system may display anomalous diffusion: that is, the average energy of the system may increase as $\sim t^{\alpha}$, where t is the time variable, and $1 < \alpha < 2$. Note that in this case the average energy of the system increases much faster than for the normal diffusion case in which $\alpha = 1$.

To date there are only a few studies of the quantum dynamics associated with classical anomalous diffusion. We consider here a recent study by Brumer and co-workers, who showed that quantum effects can further accelerate classical anomalous diffusion [97]. This is highly counterintuitive, since people tend to believe that in all cases quantum effects suppress classical chaotic transport. The system they studied is a modified kicked rotor system, whose Hamiltonian is given by

$$H(\hat{L}, \theta, t) = \hat{L}^2/2I + \lambda \cos(\theta) \sum_n f(n) \delta\left(\frac{t}{T} - n\right) \tag{414}$$

where $f(n) = 1$ if $n = 4j + 1$ or $4j + 2$, $f(n) = -1$ if $n = 4j + 3$ or $4j + 4$, $\hat{L}$ is the angular momentum operator, θ is the conjugate angle, I is the moment of inertia, λ is the strength of the kicking field, and T is the time interval between kicks. The basis states of the Hilbert space are given by $|m\rangle$, with $\hat{L}|m\rangle = m\hbar|m\rangle$. The quantum dynamics depends on the dimensionless parameters $k = \lambda T/\hbar$ and the effective Planck constant $\tau = \hbar T/I$. The underlying classical dynamics depends only on one parameter, $\kappa \equiv k\tau$, and takes the form

$$\tilde{L}_{n+1} = \tilde{L}_n + \kappa f(n) \sin(\theta_n), \;\; \theta_{n+1} = \theta_n + \tilde{L}_{n+1} \tag{415}$$

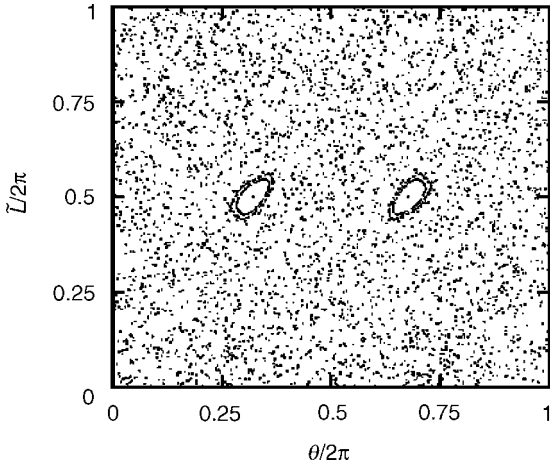

Figure 51. Classical phase-space structures of a modified kicked rotor system. Note that the regular islands are transporting islands. [From J. B. Gong, H. J. Wörner, and P. Brumer, *Phys. Rev. E.* **68**, 026209 (2003).]

where $\tilde{L} \equiv L\tau/\hbar$ is the scaled c-number angular momentum and $(\tilde{L}_n,\ \theta_n)$ represents the phase-space location of a classical trajectory at $(n + 1 - 0^+)T$. If $f(n)$ is replaced by a constant, then Eq. (415) defines the standard map. The introduction of $f(n)$ is used to magnify the effects discussed below.

For $\kappa = (2l_2 + 1)\pi$, the classical map of Eq. (415) has the marginally stable points $\tilde{L} = (2l_1 + 1)\pi, \theta = \pm\pi/2$, where l_1 and l_2 are integers. These points are shifted by a constant value $(\pm(2l_2 + 1)\pi)$ in $\tilde{L}$ after each kick. Around these stable points are regular phase-space structures, called ''transporting regular islands.'' These islands are structurally stable insofar as they persist as long as κ is close to $(2l_2 + 1)\pi$. Any trajectory launched from the transporting regular islands will consecutively jump to other similar islands located in adjacent phase-space cells, resulting in an energy increase that is quadratic with time. For trajectories initially outside the transporting regular islands, the stickiness of the boundary between the transporting regular islands and the chaotic sea induces classical anomalous diffusion. Figure 51 displays both the transporting regular islands and the chaotic sea on the PSS for $\kappa = 3.5$.

Figure 52 displays a quantum-classical comparison of energy diffusion $\kappa = 3.5$, in terms of the dimensionless scaled energy averaged over the quantum and classical ensemble, denoted by $\tilde{E}_q \equiv \langle \hat{L}^2 \rangle \tau^2/2\hbar^2$ and $\tilde{E}_c \equiv \langle \tilde{L}^2 \rangle/2$, respectively. The effective Planck constant τ is chosen to be 0.1, a value far from the semiclassical limit but relatively small compared to the area of the transporting islands shown in Fig. 51. Furthermore, this value of τ ensures that

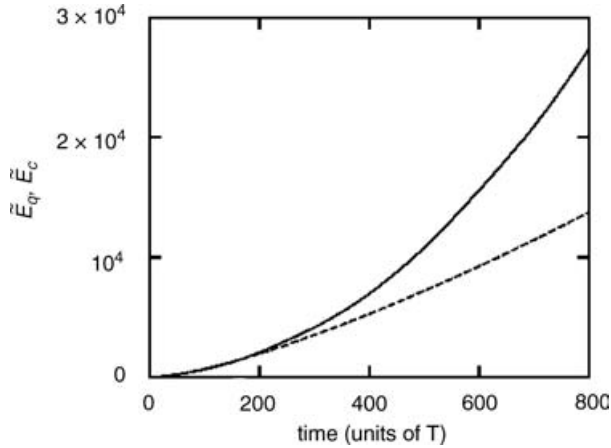

Figure 52. Quantum and classical anomalous diffusion in a modified kicked rotor system. Shown here is the time dependence of the average scaled rotational energy, denoted as $\tilde{E}_q$ (solid line) and $\tilde{E}_c$ (dashed line) for the quantum and classical ensembles, respectively. Note that the quantum result is well above the classical result. [From J. B. Gong, H. J. Wörner, and P. Brumer, *Phys. Rev. E* **68**, 026209 (2003).]

the nongeneric behavior associated with quantum resonances (i.e., $\tau = 2\pi l_1/l_2$) is avoided. The initial quantum state is chosen to be $|0\rangle$, which does not overlap with the transporting regular islands. The corresponding classical initial state is given by $\tilde{L} = 0$ with θ uniformly distributed in $[0, 2\pi]$. It is seen that energy increases nonlinearly with time in both quantum and classical cases. The quantum-classical break time is at $t_b \sim 200T$. An excellent log–log linear fit of the results after t_b gives $\tilde{E}_q \propto N^{1.85}$ (solid line) and $\tilde{E}_c \propto N^{1.36}$ (dashed line), where N is the number of kicks. Hence, both quantum and classical dynamics display characteristics of anomalous diffusion, and, more significantly, the quantum anomalous diffusion is much faster than classical anomalous diffusion. Brumer and co-workers also studied other cases with much smaller τ and found that quantum anomalous diffusion indeed approaches the underlying classical anomalous diffusion from above rather than from below as the effective Planck constant goes to zero. Note also that quantum anomalous diffusion will saturate eventually, due to dynamical localization.

Brumer and co-workers qualitatively explained the observed faster-than-classical quantum anomalous diffusion in terms of strong quantum tunneling between the transporting regular islands and the chaotic sea. If this is correct, then the notion that quantum states are primarily located on either chaotic or regular regions does not apply to the case of transporting regular islands embedded in a chaotic sea. This is consistent with a recent study by Hufnagel

et al. [98], who observed that quantum states can indeed ignore regular or chaotic phase-space structures.

VIII. CONCLUDING REMARKS

In this chapter we have reviewed the development of unimolecular reaction rate theory for systems that exhibit deterministic chaos. Our attention is focused on a number of classical statistical theories developed in our group. These theories, applicable to two- or three-dimensional systems, have predicted reaction rate constants that are in good agreement with experimental data. We have also introduced some quantum and semiclassical approaches to unimolecular reaction rate theory and presented some interesting results on the quantum-classical difference in energy transport in classically chaotic systems. There exist numerous other studies that are not considered in this chapter but are of general interest to unimolecular reaction rate theory.

There are a number of open issues associated with statistical descriptions of unimolecular reactions, particularly in many-dimensional systems. One fundamental issue is to find a qualitative criterion for predicting if a reaction in a many-dimensional system is statistical or nonstatistical. In a recent review article, Toda [17] discussed different aspects of the ''Arnold web''—that is, the network of nonlinear resonances in many-dimensional systems. Toda pointed out the importance of analyzing the qualitative features of the Arnold web—for example, how different resonance zones intersect and how the intersections further overlap with one another. However, as pointed out earlier, even in the case of fully developed global chaos it remains challenging to define a nonlocal reaction separatrix and to calculate the flux crossing the separatrix in a many-dimensional phase-space.

Recent studies of intramolecular energy transfer in organic molecules [99,100] suggest that it is rare to see a dense Arnold web in many-dimensional molecular systems. It is observed that even in large molecules, energy transport may be still governed by local phase space structures. Thus, an initial vibrational state typically undergoes relaxation on a manifold whose dimension is much smaller than that predicted by global chaos. This is confirmed by recent experimental results [100], which indicate that the slow energy transport in large molecules could manifest itself as the reaction rate becomes larger—for example, when the energy of the reacting system increases. The general observation of slow energy transport in large molecule systems brings up two new directions for investigation. First, the slow energy transport indicates that the dynamics of intramolecular energy transport is weakly chaotic. Hence, as pointed out by Gruebele [100], active control of molecular dynamics in large molecular systems, such as reversing the intramolecular energy transport, is very possible. Second, it is necessary to develop a new statistical reaction rate

theory (classical and quantum mechanical) that can first model and then incorporate slow energy transport in a many-dimensional system.

As mentioned earlier, Komatsuzaki and Berry [26] have recently developed a promising approach to analyzing many-dimensional reacting systems. By seeking appropriate canonical transformations that yield local approximate constants of motion associated with the reactive mode, they were able to transform the conventional dividing surface in configuration space to a many-dimensional separatrix in phase-space. Specifically, suppose the original phase-space variables are denoted by $(\mathbf{q}, \mathbf{p}) = (q_1, q_2, \ldots, q_n; p_1, p_2, \ldots, p_n)$, the conventional dividing surface is located at $q_1 = 0$, and the required approximate canonical transformation to a certain order is given by

$$(\mathbf{q}, \mathbf{p}) \rightarrow [\mathbf{q}'(\mathbf{q}, \mathbf{p}), \mathbf{p}'(\mathbf{q}, \mathbf{p})] \tag{416}$$

where $(\mathbf{q}', \mathbf{p}') = (q_1', q_2', \ldots, q_n'; p_1', p_2', \ldots, p_n')$, and $q_1' = q_1'(\mathbf{q}, \mathbf{p})$ is the new reactive mode "dressed" by $(q_2, \ldots, q_n; p_1, p_2, \ldots, p_n)$. As is forced by the construction of the canonical transformation, this dressed reactive mode $q_1'(\mathbf{q}, \mathbf{p})$ is approximately and locally separable from $(q_2', \ldots, q_n'; p_2', \ldots, p_n')$. Hence, the approximate dividing surface

$$q_1'(\mathbf{q}, \mathbf{p}) = 0 \tag{417}$$

defined in the original phase-space, is in fact an approximate many-dimensional phase-space separatrix and can be close to an exact separatrix insofar as trajectories will not recross it, provided that the approximate constants of motion persist long enough that the final state of the saddle crossings can be determined. Recalling that the key element in the ARRKM theory is to seek an approximate phase-space separatrix, one sees that the Komatsuzaki–Berry approach is, in essence, a many-dimensional extension of the ARRKM theory by use of canonical transformations. Indeed, identifying the $q_1'(\mathbf{q}, \mathbf{p})$ in Eq. (417) with the phase-space separatrix $S(\mathbf{q}, \mathbf{p})$ in the ARRKM theory [see Eq. (87)], one obtains the following microcanonical reaction rate constant:

$$k(E) = \frac{1}{N_S} \int d\mathbf{q} \int d\mathbf{p} \delta[q_1'(\mathbf{q}, \mathbf{p})] p_1'(\mathbf{q}, \mathbf{p}) \theta[p_1'(\mathbf{q}, \mathbf{p})] \delta(E - H) \tag{418}$$

where N_S is a normalization constant and H is the system Hamiltonian. However, since such an extension of the ARRKM theory does not account for the peculiarity of intramolecular energy transfer in many-dimensional systems, the predicted rate constant $k(E)$ is not expected to be very useful, particularly when the initial state is far away from the dividing surface $q_1'(\mathbf{q}, \mathbf{p}) = 0$.

Having recognized a similarity between the ARRKM theory and the Komatsuzaki–Berry approach, we now comment on the difference between

them. First, Komatsuzaki and Berry have carefully investigated the dynamical behavior of the classical trajectories that recross the conventional dividing surface $q_1 = 0$. For example, they have vividly demonstrated that the trajectories recrossing $q_1 = 0$ can indeed avoid recrossing the phase-space separatrix $q_1'(\mathbf{q}, \mathbf{p}) = 0$. In contrast, in developing the ARRKM theory and its various extensions in few-dimensional systems, Rice et al. focused their attention on the reaction rate constant and did not examine in detail to what extent the approximate phase-space separatrix can rotate away the recrossing trajectories. The results of Rice et al. suggest that the calculation of the approximate reaction rate constant within—for example, a factor of two or three—is insensitive to the fine structure of the separatrix and therefore does not need a more formal approach, such as the Lie canonical perturbation theory. Second, there exists a natural many-dimensional extension of the ARRKM theory based on the reaction path formalism. In particular, with Eqs. (189) and (190), one may intuitively use (with somewhat different notation from above)

$$\frac{\left[p_s - \sum_{k=1,\ell=1}^{3N-f-7} Q_k B_{k\ell}(s) P_\ell\right]^2}{2\left(1 + \sum_{k=1}^{3N-f-7} Q_k B_{k,3N-f-6}\right)^2} + V(s) - E_s = 0 \tag{419}$$

as an approximate phase-space separatrix, where s is the reaction coordinate, E_s is the saddle point energy, and Q_k and P_ℓ represent the coordinates and momenta of other DOFs. It would be of great interest to compare this approximate many-dimensional phase-space separatrix, constructed by physical intuition, with that obtained by the Komatsuzaki–Berry approach. It is plausible that they are different in their capabilities for removing recrossing trajectories, but could give similar reaction rate constants such as $k(E)$ in Eq. (418). Note that in the adiabatic limit—that is, when the motion associated with the DOFs other than the reactive mode is much faster than the reaction—the dynamics of the reactive mode is entirely determined by an effective potential [see Eq. (198)]. As such, the constant of motion associated with the reactive mode—for example, the adiabatic Hamiltonian itself [see Eq. (198)]—indeed exists. This suggests that the difference between the many-dimensional extension of the ARRKM theory based upon the reaction path formalism [see Eq. (419)] and the Komatsuzaki–Berry result should diminish as the reaction becomes slower.

Throughout this chapter we have been concerned with statistical approaches applied to isolated molecules. Since most (unimolecular) reactions occur in an environment comprised of other molecules, it is important to examine the effects of molecule–molecule interaction on the kinetics and dynamics of unimolecular reactions. Take the difference between quantum and classical transport as an example. Based on recent studies of quantum-classical

correspondence in open systems [101–103], it is reasonable to expect that molecule–molecule collisions may introduce decoherence to reacting systems to such a degree that predictions from the quantum dynamics become even closer to that from a classical theory. Of course, when molecule–molecule interactions are no longer perturbative—for example, in a liquid—then a unimolecular reaction rate theory that is based on phase-space structures of isolated molecular systems does not apply, and the models that we have discussed need significant extension.

Acknowledgment

This work was supported by the National Science Foundation.

References

1. O. K. Rice, H. C. Ramsperger, *J. Am. Chem. Soc.* **49**, 1616 (1927); **50**, 617 (1928).
2. L. S. Kassel, *J. Phys. Chem.* **32**, 225 (1928).
3. R. A. Markus, O. K. Rice, *J. Phys. Colloid. Chem.* **55**, 894 (1951).
4. R. A. Markus, *J. Chem. Phys.* **20**, 359 (1952); **43**, 2658 (1965).
5. W. Frost, *Theory of Unimolecular Reactions*, Wiley-Interscience, London, 1972.
6. T. Baer and W. L. Hase, *Unimolecular Reaction Dynamics: Theory and Experiments*, Oxford University Press, New York, 1996.
7. A. J. Lichtenberg and M. A. Lieberman, *Regular and Chaotic Dynamics*, 2nd ed., Springer-Verlag, New York, 1992.
8. R. MacKay, J. D. Meiss, and I. C. Percival, *Physica D* **13**, 55 (1984).
9. R. MacKay, J. D. Meiss, and I. C. Percival, *Physica D* **27**, 1 (1987).
10. D. Bensimon and L. P. Kadanoff, *Physica D* **13**, 82 (1984).
11. M. J. Davis and S. K. Gray, *J. Chem. Phys.* **84**, 5389 (1986).
12. S. K. Gray, S. A. Rice, and M. J. Davis, *J. Phys. Chem.* **90**, 3470 (1986).
13. M. S. Zhao and S. A. Rice, *J. Chem. Phys.* **96**, 3542 (1992).
14. M. S. Zhao and S. A. Rice, *J. Chem. Phys.* **96**, 6654 (1992).
15. M. S. Zhao and S. A. Rice, *J. Chem. Phys.* **97**, 943 (1992).
16. M. S. Zhao and S. A. Rice, *J. Chem. Phys.* **96**, 7483 (1992).
17. M. Toda, *Adv. Chem. Phys.* **123**, 153 (2002).
18. R. E. Gillilan and G. S. Ezra, *J. Chem. Phys.* **94**, 2648 (1991).
19. H. Tang, S. Jang, M. Zhao, and S. A. Rice, *J. Chem. Phys.* **101**, 8737 (1994).
20. S. Wiggins, *Normally Hyperbolic Invariant Manifolds in Dynamcial Systems*, Springer-Verlag, New York, 1994.
21. S. Wiggins, *Chaotic Transport in Dynamcial Systems*, Springer-Verlag, New York, 1992.
22. S. Wiggins, L. Wiesenfeld, C. Jaffe, and T. Uzer, *Phys. Rev. Lett.* **86**, 5478 (2001).
23. N. De Leon and C. C. Marston, *J. Chem. Phys.* **91**, 3405 (1989).
24. N. De Leon, M. A. Mehta, and R. Q. Topper, *J. Chem. Phys.* **94**, 8310 (1991).
25. A. M. O. De Almeida, N. De Leon, M. A. Mehta, and C. C. Marston, *Physica D* **46**, 265 (1990).
26. T. Komatsuzaki and R. S. Berry, *Adv. Chem. Phys.* **123**, 79 (2002).

27. M. C. Gutzwiller, *Chaos in Classical and Quantum Mechanics*, Springer-Verlag, New York, 1990.
28. G. Casati and B. Chirikov, *Quantum Chaos: Between Order and Disorder*, Cambridge University Press, New York, 1995.
29. F. Haake, *Quantum Signatures of Chaos*, Springer-Verlag, New York, 1991.
30. S. A. Rice and M. S. Zhao, *Optical Control of Molecular Dynamics*, John Wiley & Sons, New York, 2000.
31. M. Shapiro and P. Brumer, *Principles of the Quantum Control of Molecular Processes*, John Wiley & Sons, New York, 2003.
32. S. H. Tersigni and S. A. Rice, *Ber. Bunseges. Phys. Chem.* **92**, 227 (1988).
33. C. C. Martens, M. J. Davis, and G. S. Ezra, *Chem. Phys. Lett.* **142**, 519 (1987).
34. D. Carter and P. Brumer, *J. Chem. Phys.* **77**, 4208 (1982); **78**, 2104E (1983).
35. P. Gaspard and S. A. Rice, *J. Phys. Chem.* **93**, 6947 (1989).
36. D. J. Davis, *J. Chem. Phys.* **83**, 1016 (1985).
37. W. H. Miller, N. C. Handy, and J. E. Adams, *J. Chem. Phys.* **72**, 99 (1980).
38. W. H. Miller, *Potential Energy Surfaces and Dynamics Calculations*, D. G. Truhlar, ed., Plenum, New York, 1981, p. 265.
39. K. E. Johnson, L. Wharton, and D. H. Levy, *J. Chem. Phys.* **69**, 2719 (1978).
40. J. E. Kenny, K. E. Johnson, W. Shafin, and D. H. Levy, *J. Chem. Phys.* **72**, 1109 (1980).
41. D. M. Willberg, M. Gutmann, J. J. Breen, and A. H. Zewail, *J. Chem. Phys.* **96**, 198 (1992).
42. J. J. Breen, D. M. Willberg, M. Gutmann, and A. H. Zewail, *Chem. Phys. Lett.* **93**, 9180 (1990).
43. J. A. Beswick and J. Jortner, *Mol. Phys.* **39**, 1137 (1980).
44. J. I. Cline, D. D. Evard, F. Thommen, and K. C. Janda, *J. Chem. Phys.* **84**, 1165 (1986).
45. D. D. Evard, F. Thommen, J. I. Cline, and K. C. Janda, *J. Phys. Chem.* **91**, 2508 (1987).
46. J. I. Cline, N. Sivakumer, D. D. Evard, and K. C. Janda, *J. Chem. Phys.* **86**, 1636 (1987).
47. C. E. Wozny and S. K. Gray, *Ber. Bunsenges. Phys. Chem.* **92**, 236 (1988).
48. J. I. Cline, B. P. Reid, D. D. Evard, N. Sivakumer, N. Halberstadt, and K. C. Janda, *J. Chem. Phys.* **89**, 3535 (1988).
49. S. K. Gray and C. E. Wozny, *J. Chem. Phys.* **94**, 2816 (1991).
50. D. H. Zhang and J. Z. H. Zhang, *J. Chem. Phys.* **95**, 6449 (1991).
51. S. K. Gray, S. A. Rice, and D. W. Noid, *J. Chem. Phys.* **84**, 3745 (1986).
52. J. M. Skene, J. C. Drobits, and M. I. Lester, *J. Chem. Phys.* **85**, 2329 (1986).
53. R. L. Waterland, J. M. Skene, and M. I. Lester, *J. Chem. Phys.* **89**, 7277 (1988).
54. J. M. Skene and M. I. Lester, *Chem. Phys. Lett.* **116**, 93 (1985).
55. S. K. Gray and S. A. Rice, *J. Chem. Phys.* **86**, 2020 (1987).
56. N. De Leon and S. Ling, *J. Chem. Phys.* **101**, 4790 (1994).
57. N. De Leon, *J. Chem. Phys.* **96**, 285 (1992).
58. S. M. Jang and S. A. Rice, *J. Chem. Phys.* **99**, 9585 (1993).
59. N. De Leon, M. A. Mehta, and R. Q. Topper, *J. Chem. Phys.* **94**, 8329 (1991).
60. S. M. Jang, M. S. Zhao, and S. A. Rice, *J. Chem. Phys.* **97**, 8188 (1992).
61. M. A. Harthcock and J. Lanne, *J. Mol. Spectrosc.* **91**, 300 (1982).
62. M. A. Harthcock and J. Lanne, *J. Chem. Phys.* **79**, 2103 (1983).
63. C. C. Marston and N. De Leon, *J. Chem. Phys.* **91**, 3392 (1989).

64. M. S. Zhao and S. A. Rice, *J. Chem. Phys.* **98**, 2837 (1993).
65. J. N. Murrell, S. Carter, and L. O. Halonen, *J. Mol. Spectrosc.* **93**, 307 (1982).
66. J. Zhang, W. Chiang, and J. Laane, *J. Chem. Phys.* **100**, 3455 (1994).
67. H. Tang, S. M. Jang, M. S. Zhao, and S. A. Rice, *Chem. Phys. Lett.* **285**, 143 (1998).
68. H. W. Lee, *Phys. Rep.* **259**, 147 (1995).
69. H. Weyl, *Z. Phys.* **46**, 1 (1927).
70. J. E. Moyal, *Proc. Cambridge Philos. Soc.* **45**, 99 (1949).
71. M. V. Berry, in *Chaotic Behavior of Deterministic Systems*, G. Iooss, R. H. G. Helleman, and R. Stora, eds., North-Holland, Amsterdam, pp. 171–271.
72. E. J. Heller, *Phys. Rev. Lett.* **53**, 1515 (1984).
73. M. V. Berry, *Proc. R. Soc. Lond. A* **423**, 219 (1989).
74. E. B. Bogomolny, *Physica D* **31**, 169 (1988).
75. S. M. Jang, M. S. Zhao, and S. A. Rice, *Chem. Phys.* **230**, 237 (1998).
76. W. H. Miller, *J. Chem. Phys.* **61**, 1823 (1970).
77. K. G. Kay, *J. Chem. Phys.* **65**, 3813 (1976).
78. W. H. Miller, S. D. Schwartz, and J. W. Tromp, *J. Chem. Phys.* **79**, 4889 (1983).
79. T. Yamamoto, *J. Chem. Phys.* **33**, 281 (1960).
80. W. H. Miller, *Faraday Discuss.* **110**, 1 (1998).
81. W. H. Miller, *J. Chem. Phys.* **53**, 3578 (1970).
82. K. G. Kay, *J. Chem. Phys.* **100**, 4377 (1994); **100**, 4432 (1994).
83. G. Campolieti and P. Brumer, *J. Chem. Phys.* **96**, 5969 (1992).
84. X. Sun and W. H. Miller, *J. Chem. Phys.* **106**, 916 (1997).
85. H. Wang, X. Sun, and W. H. Miller, *J. Chem. Phys.* **108**, 9726 (1998).
86. X. Sun, H. Wang, and W. H. Miller, *J. Chem. Phys.* **109**, 4190 (1998).
87. F. Remacle and R. D. Levine, *J. Phys. Chem.* **100**, 7962 (1996).
88. M. S. Zhao, S. M. Jang, and S. A. Rice, *Int. J. Chem.* **2**, art. no. 1 (1999).
89. J. C. Light and T. Carrington, *Adv. Chem. Phys.* **114**, 263 (2000).
90. F. Le Quéré and S. K. Gray, *J. Chem. Phys.* **98**, 5396 (1993).
91. R. C. Brown and R. E. Wyatt, *Phys. Rev. Lett.* **57**, 1 (1986).
92. G. Radons, T. Geisel, and J. Rubner, *Phys. Rev. Lett.* **57**, 2883 (1986); **58**, 2506 (1987).
93. N. T. Maitra and E. J. Heller, *Phys. Rev. E* **61**, 3620 (2000).
94. D. M. Leitner and P. G. Wolynes, *Phys. Rev. Lett.* **79**, 55 (1997).
95. V. Ya. Demikhovskii, F. M. Izrailev, and A. I. Malyshev, *Phys. Rev. Lett.* **88**, 154101 (2002).
96. V. Ya. Demikhovskii, F. M. Izrailev, and A. I. Malyshev, *Phys. Rev. E.* **66**, 036211 (2002).
97. J. B. Gong, H. J. Wörner, and P. Brumer, *Phys. Rev. E.* **68**, 026209 (2003).
98. L. Hufnagel, R. Ketzmerick, M. F. Otto, and H. Schanz, *Phys. Rev. Lett.* **89**, 154101 (2002).
99. M. Gruebele and R. Bigwood, *Int. Rev. Phys. Chem.* **17**, 91 (1998).
100. M. Gruebele, *Theor. Chem. Acc.* **109**, 53 (2003).
101. D. Giulini, E. Joos, C. Kiefer, J. Kupsch, I. O. Stamatescu, and H. D. Zeh, *Decoherence and the Appearance of a Classical World in Quantum Theory*, Springer-Verlag, New York, 1996.
102. S. Habib, K. Shizume, and W. H. Zurek, *Phys. Rev. Lett.* **80**, 4361 (1998).
103. J. B. Gong and P. Brumer, *Phys. Rev. E* **60**, 1643 (1999).

CHAPTER 2

REGULARITY IN CHAOTIC TRANSITIONS ON TWO-BASIN LANDSCAPES

TAMIKI KOMATSUZAKI

Nonlinear Science Laboratory, Department of Earth and Planetary Sciences, Faculty of Science, Kobe University, Nada, Kobe, 657-8501, Japan

R. STEPHEN BERRY

Department of Chemistry, The University of Chicago, Chicago, Illinois 60637, USA

CONTENTS

I. Introduction
II. Dynamical Regularity in the Region of Saddles
III. Geometric Aspects of the Phase Space
IV. Kramers–Grote–Hynes Theory Revisited
V. Stochasticity of Saddle Crossings
VI. Concluding Remarks and Future Prospects
Acknowledgments
References

I. INTRODUCTION

Let us begin with a simple, but still unresolved question, that is, ''Why can a reacting system climb through the saddle from a basin to one another?'' Figure 1 schematically shows representative reactive and nonreactive, saddle crossing trajectories that were initiated from the reactant well. Although both trajectories have sufficient total energy larger than the saddle point energy, one will climb

Geometric Structures of Phase Space in Multidimensional Chaos: A Special Volume of Advances in Chemical Physics, Part A, Volume 130, edited by M. Toda, T Komatsuzaki, T. Konishi, R.S. Berry, and S.A. Rice. Series editor Stuart A. Rice.
ISBN 0-471-70527-6

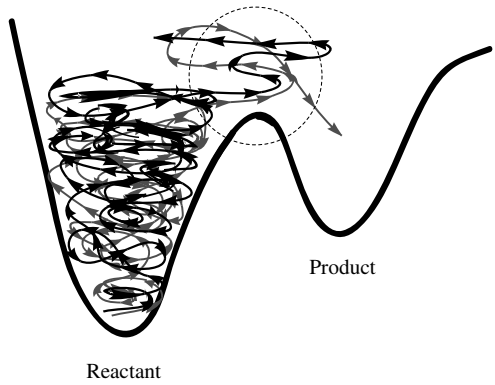

Figure 1. Reactive and nonreactive saddle crossing trajectories on a potential energy surface.

through to the product well but the other will go back to the original, reactant well. This implies for classical systems that the condition for the reacting systems to possess a total energy larger than the saddle point energy is only necessary and not sufficient. Then, what are the necessary and sufficient conditions for a reacting system to climb through from one basin to another? This is one of the central issues we want to focus on in the present chapter.

Dynamics on two-basin potential energy surfaces has been extensively explored in the context of chemical reactions over the past several decades [1–14]. Transition state theories (TST), first developed by Eyring [3] and Evans [4] and by Wigner [5] in the 1930s, have had great success in elucidating absolute reaction rates of chemical reactions. All the various forms of (classical) TST are based on two fundamental assumptions:

No-Return Assumption. A dividing hypersurface—that is, the transition state (TS)—exists (generally in phase space) through which a reacting species should pass only once on the way from the reactants to the products before being ''captured'' in the products. Note that this implicitly requires that the hypersurface can decompose the space into two distinct regions, reactant and product. This, in turn, implies that for Hamiltonian systems with n degrees of freedom, the TS must be of co-dimension one—that is, $(2n-2)$ dimension—on the $(2n-1)$-dimensional equienergy hypersurface of the chosen $2n$-dimensional phase space $\mathbb{R}^{2n}$ [15].

Local Equilibrium Assumption. There exists a quasi-equilibrium between the reactant and *a system crossing the TS* from the reactant to the product. This precise representation was taken from an insightful article on the observability of the invariant of motion in the transition state by Marcus [16]: The motions along the reaction coordinate at the transition state was

postulated in the original TST to be one-dimensional, translational motions. This implies that the reactive degree of freedom is assumed to be dynamically separable from the other degrees of freedom *at* the transition state. Although many literatures have often described to assume the quasi-equilibrium as ''occurring between the reactant and *the TS itself*,'' rigorously speaking, there is no source to yield a quasi-equilibrium between the reactant and a *dynamically separable*, elusive state. In the other words, the reacting systems move about ''ergodically'' within the reactant well more quickly than finding *en route* to the TS. (Readers will see in this chapter that this is a generic consequence inherent to the first-rank saddles up to moderately high energies if the TS is defined not in the configurational space but in the phase space.)

However, few theories have clarified the physical conditions needed to validate these fundamental assumptions—that is, the necessary and sufficient conditions to use this description for a reacting species climbing through the saddle from the reactant to the product well. This is one of the most elusive aspects in justifying the application of TST to a multitude of reacting systems. In practice, one has often defined the TS in configurational space with an *ad hoc* correction factor, called the transmission coefficient κ, to take into account that the system of interest actually makes more than one crossing of the surface presumed either to be the desired dividing surface or one that the system finds en route to the TS without moving about ''ergodically'' in the reactant well.

In the developments [17–24] of classical unimolecular reaction rate theories, there has been a great improvement of our understanding of the definability of such a general, no-return dividing hypersurface from the viewpoint of the geometric structure of the phase space in chemical reactions. Davis and Gray [17] first showed in the late 1980s that in Hamiltonian systems with two degrees of freedom (DOFs), a TS *always* free from recrossings can be defined as the separatrix in the Poincaré section formed by taking the union of segments of the stable and unstable manifolds, and the transport across the TS is interpreted as mediated through the turnstile lobes bounded by two homoclinic intersection points. Gillilan and Ezra [20] analyzed the predissociation of van der Waals complex He–I_2 with three DOFs—that is, the four-dimensional Poincaré section. They demonstrated, as predicted by Wiggins [21], that the occurrence of homoclinic tangency inherent to higher-dimensional systems ($>$two) hampers the construction of the hypersurface dividing the bound complex reactant region from unbound trajectories. Toda [22–24] noticed that the homoclinic tangency leads to a bifurcation of the phase-space reaction path with a transition between two topologically distinct chaotic regimes. Thus, the Davis–Gray separatrix transition state depends crucially on the Poincaré section having only two

dimensions. No general, *no-return* dividing hypersurface has been found yet for systems of higher dimensionality. In other words, it is still an unresolved open problem to determine the circumstances in which such a hypersurface would persist, if it exists, or would be ruined in the chaotic thermal bath of multidimensional systems.

Focusing on regulation of trajectories in the vicinity of the saddle points on potential energy surfaces, several theoretical and experimental developments have shed light on mechanics of passage through the region of a potential saddle for higher-dimensional systems. Indicative symptoms of local regularity near the saddles appeared in theoretical studies of small atomic clusters by Berry and co-workers [25–31] that compared local Liapunov functions and Kolmogorov entropies in saddle regions with those in other regions of potential surfaces. Evidence appeared also in experiments by Lovejoy and co-workers [32,33] on decomposition of vibrationally excited ketene that showed rates with quantized steps; Marcus suggested that this could be a signature of existence of approximate invariants of motion in the TS [16].

De Leon and co-workers [34–37] established an elegant reaction theory for a system with two DOFs, the so-called reactive island theory to mediate reactions through cylindrical manifolds apart from the saddles. Their original algorithm depends crucially on the existence of *pure* unstable periodic orbits in the nonreactive DOFs in the region of the saddles and did not extend to systems with many DOFs.

Recently, Komatsuzaki and Berry revealed [38–45] using classical isomerization of a 6-atom Lennard-Jones cluster that at least three distinct energy regimes of dynamical behavior, so-called *quasi-regular*, *semi-chaotic*, and *fully developed chaotic* regimes, exist in the region of a saddle of strongly coupled, many particle Hamiltonian systems. These are distinguished by the extent of regularity of their dynamics. Up to energies high enough to make the system manifestly chaotic, approximate invariants of motion associated with a reaction coordinate in the phase space imply a multidimensional dividing hypersurface that is free from recrossings occurring in that regime even in a sea of chaos. Their technique relies on the application of Lie canonical perturbation theory [46,47] (with algebraic quantization [48–50], if necessary), a classical analog of Van Vleck perturbation theory [51,52], for the region of potential saddles. This provides us with the natural reformulation [38,39] of the conventional TST based on that hypersurface in multidimensional phase space, which gives us better classical reaction rates of multidimensional systems. They presented a practical algorithm to visualize the dividing hypersurface in the multidimensional phase space of a given system [40,41], illuminated a new type of phase space bottleneck that emerges as the total energy and mode-coupling increase, which keeps a reacting system increasingly trapped in the region of a saddle [42,43], and established a strong propensity rule and corresponding

formula for transitions of chemical reactions which enables us to predict *a priori* whether the system climbs through the saddle to the product or returns to its original state [45].

The earlier work of Wiggins [21,53] provides a firm mathematical framework for many-dimensional phase space transport, based on the notion of a normally hyperbolic invariant manifold (NHIM) and its stable and unstable manifolds as the appropriate generalization of the concept of ''saddle'' and ''separatrices'' on a multidimensional phase space. However, the major technical obstacle preventing its implementation has been the lack of an algorithm for searching arbitrary NHIMs in realistic multidimensional systems. As shown by Komatsuzaki and Berry, Lie transforms provide one of the most powerful techniques to extract a NHIM at least in the region of saddles from many-dimensional phase space. Recently, Uzer et al. [54] applied the Lie transformation to the vicinity of a saddle for a hydrogen atom in crossed electric and magnetic fields containing significant Coriolis interactions (a 3-DOFs system) and provided a detailed description of the (local) geometric structure of chemical reactions in multidimensional phase space. Wiggins et al. [15] presented a mathematical foundation of the robust persistence, in each order, of the invariant of motion along the phase-space reaction coordinate.

In this chapter, we briefly survey our recent findings on the mechanism for a reacting species to climb through the saddle and its relevance to the underlying geometric structure of the phase space. We focus on describing the concept, sacrificing mathematical rigor. (Readers can refer to our recent review article [41] for the mathematical description and also the articles by others [55–58] in this volume of *Advances in Chemical Physics*.) In another article in this volume [59], one of the authors reviews several kinds of strange, cooperative dynamical behavior observed through structural transitions on multibasin landscapes for liquid water and proteins and discusses how such a regulatory structure through a ''reaction bottleneck'' may be generic irrespective of the size of the systems and ''ruggedness'' of potential energy surfaces.

II. DYNAMICAL REGULARITY IN THE REGION OF SADDLES

Suppose that Hamiltonian $H(\mathbf{p}, \mathbf{q})$ is expressed in a region around a saddle point of interest as an expansion in a small parameter ϵ, so that the zero-order Hamiltonian H_0 is regular in that region; specifically, it is written as a sum of harmonic-oscillator Hamiltonians. Such a zero-order system is a function of action variables $\mathbf{J}$ of H_0 only, and it does not depend on the conjugate angle variables $\boldsymbol{\Theta}$. The higher-order terms of the Hamiltonian are expressed as sums of

cubic, quartic, and so on, terms in the normal coordinates of the system, at its saddle [9,38,39].

$$H = H_0 + \sum_{n=1}^{\infty} \epsilon^n H_n \tag{1}$$

$$H_0 = \tfrac{1}{2} \sum_j (p_j^2 + \omega_j^2 q_j^2) = H_0(\mathbf{J}) \tag{2}$$

$$\sum_{n=1}^{\infty} \epsilon^n H_n = \epsilon \sum_{j,k,l} C_{jkl} q_j q_k q_l + \epsilon^2 \sum_{j,k,l,m} C_{jklm} q_j q_k q_l q_m + \cdots = \sum_{n=1}^{\infty} \epsilon^n H_n(\mathbf{J}, \boldsymbol{\Theta}) \tag{3}$$

Here, q_j and p_j are the jth normal coordinate and its conjugate momentum, respectively; ω_j and C_{jkl}, $C_{jklm}, \ldots$ are, respectively, the frequency of the jth mode, the coupling coefficient among q_j, q_k, and q_l and that among q_j, q_k, q_l, and q_m, and so forth. We denote hereinafter a reactive DOF, ''1'', whose fundamental frequency ω_1 is pure imaginary, while the frequencies $\boldsymbol{\omega}_B$ of the other ''bath'' modes B are real. An early insight by Hernandez and Miller [60] in their semiclassical theory based on Van Vleck perturbation theory and recent classical chemical reaction theory based on Lie canonical perturbation theory by Komatsuzaki and Berry [38–45] show that there robustly exists an invariant of (classical) action associated with the phase-space reaction coordinate buried in a sea of chaos for strongly coupled many-body systems in the region of the first-rank saddles. This is due to the generic fact that an arbitrary combination of modes cannot satisfy the resonance conditions if one mode has an imaginary frequency, included in the combination, that is,

$$\left| \sum_{k=1} n_k \omega_k \right| \geq |\omega_1| > O(\epsilon^n) \tag{4}$$

for arbitrary integers n_k with $n_1 \neq 0$. This implies that one can generally find a nonlinear, canonical transformations of the coordinates to transform nonintegrable Hamiltonian $H(\mathbf{p}, \mathbf{q})$ into a new form:

$$\bar{H}(\bar{\mathbf{p}}, \bar{\mathbf{q}}) = \bar{H}_0(\bar{\mathbf{J}}) + \sum_{n=1} \epsilon^n \bar{H}_n(\bar{J}_1, \bar{\boldsymbol{\xi}}_B) \tag{5}$$

in the vicinity of the saddles up to arbitrarily high order [15,44,45,54]. Here $(\bar{\mathbf{p}}, \bar{\mathbf{q}})$ are new canonical variables, $(\bar{\mathbf{J}}, \bar{\boldsymbol{\Theta}})$ their action-angle variables, and $\bar{\boldsymbol{\xi}}_{\mathbf{B}}$

represents those of bath modes $(\bar{\mathbf{J}}_B, \bar{\mathbf{\Theta}}_B)$, collectively. The phase-space reaction coordinate $\bar{q}_1$ and momentum $\bar{p}_1$ obeys

$$\ddot{\bar{q}}_1(\mathbf{p},\mathbf{q}) + \bar{\omega}_1^2 \bar{q}_1(\mathbf{p},\mathbf{q}) = \Gamma, \qquad \bar{p}_1(\mathbf{p},\mathbf{q}) = \frac{\omega_1}{\bar{\omega}_1}\dot{\bar{q}}_1(\mathbf{p},\mathbf{q}) \tag{6}$$

in the region of any first-rank saddle [44], where

$$\Gamma \equiv \frac{\dot{\bar{\omega}}_1}{\bar{\omega}_1}\dot{\bar{q}}_1(\mathbf{p},\mathbf{q}) \qquad \bar{\omega}_1 = \bar{\omega}_1(\bar{J}_1, \bar{\boldsymbol{\xi}}_B) = \frac{\partial \bar{H}(\bar{J}_1, \bar{\boldsymbol{\xi}}_B)}{\partial \bar{J}_1} \tag{7}$$

($\dot{x}$ and $\ddot{x}$ represent the first and second derivatives of x with respect to time t.) The $\bar{\omega}_1(\bar{J}_1, \bar{\boldsymbol{\xi}}_B)$ depends on time t only through bath modes $\bar{\boldsymbol{\xi}}_B(t)$ because $\bar{J}_1$ is independent of t by Eq.(5). If all the actions $\bar{\mathbf{J}}$ approximately persist as invariants of motion in the region of the saddles—that is, $\bar{H}(\bar{\mathbf{p}}, \bar{\mathbf{q}}) = \bar{H}(\bar{\mathbf{J}})$—then $\Gamma = 0$. Even while all or most of all the actions no longer retain their invariance, the exception being the phase space reaction coordinate, i.e., $\bar{H}(\bar{\mathbf{p}}, \bar{\mathbf{q}}) = \bar{H}(\bar{J}_1, \bar{\boldsymbol{\xi}}_B)$ [Eq. (5)], still $\Gamma \sim \mathcal{O}(\epsilon^2)$ in the vicinity of the saddles. The former case generally holds at an energy regime slightly above the threshold saddle point energy in the region of (first-rank) saddles, where the saddle crossing process is fully deterministic spanning all the degrees of freedom with a strong dynamical correlation between incoming and outgoing trajectories to and from the saddle. We referred to this energy regime as the *quasi-regular* region [38]. The latter case holds up to moderately high energies above the threshold thanks to Eq. (4), where the full dynamics of the saddle crossing process is unpredictably "stochastic," but the motion *along* the phase space reaction coordinate can still be predicted, with a weak (but nonzero!) dynamical correlation between the wells. We referred to this energy regime as the *intermediate*, *semi-chaotic* region [38].

As shown in Figure 2, Eq. (6) tells us that even if reaction transition processes look to be "diffusive stochastic" processes in the configurational space, they can always be represented in the phase space as ballistic dynamical processes decoupled from all the other parts of the bath space if the action associated with (at least) the phase space reaction coordinate $\bar{q}_1$ maintains its invariance long enough to determine the final state of the reactions [38]. From the projection of a nonreactive "recrossing" trajectory onto the configurational space and the phase space in Figure 3, one can deduce one very important clue for what the necessary and sufficient conditions must be for the system to climb through one basin to another. That is, all nonreactive recrossing trajectories in the configurational space are transformed to nonreactive, nonrecrossing trajectories over the phase-space dividing surface $S(\bar{q}_1(\mathbf{p},\mathbf{q}) = 0)$, if the invariants of action persist locally, for the phase-space reaction coordinate $\bar{q}_1$. This is because decoupling the motion along $\bar{q}_1$ removes all forces that would return the system back across the dividing surface [38].

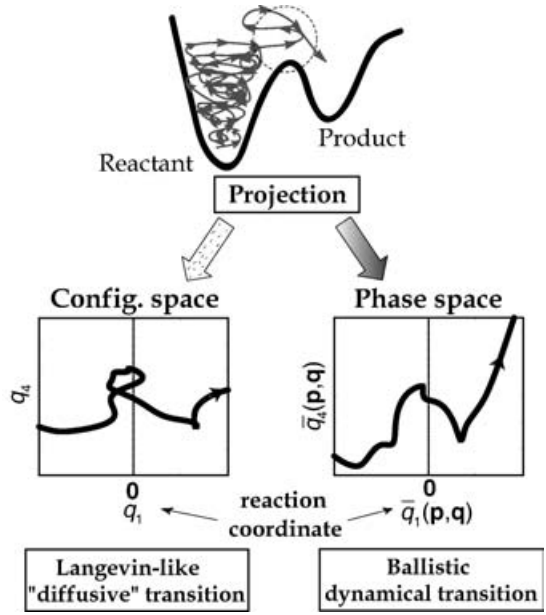

Figure 2. The projections of a reactive, ''recrossing'' trajectory onto the configurational space and the phase space (see text for details).

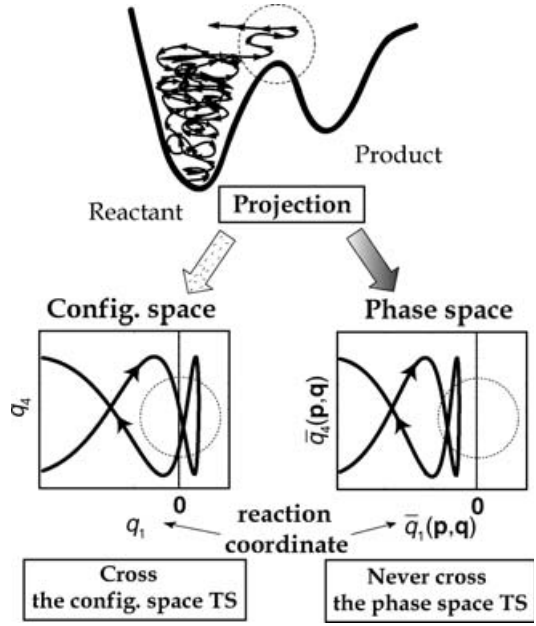

Figure 3. The projection of a nonreactive ''recrossing'' trajectory onto the configurational space and the phase space (see text for details).

We derived a dynamical propensity rule for transitions as follows: From Eq. (6), one can derive an approximate analytical form for $\bar{q}_1(\mathbf{p},\mathbf{q})$ [44,45];

$$\bar{q}_1(\mathbf{p}(t),\mathbf{q}(t)) = \frac{\alpha}{2} e^{\int^t |\bar{\omega}_1(t')|dt'} + \frac{\beta}{2} e^{-\int^t |\bar{\omega}_1(t')|dt'} \tag{8}$$

$$\simeq \frac{\alpha}{2} e^{|\bar{\omega}_1|t} + \frac{\beta}{2} e^{-|\bar{\omega}_1|t} \tag{9}$$

$$\alpha = \bar{q}_1(t_0) + \frac{\bar{p}_1(t_0)}{|\omega_1|}, \qquad \beta = \bar{q}_1(t_0) - \frac{\bar{p}_1(t_0)}{|\omega_1|} \tag{10}$$

where constant coefficients α and β can be estimated from $\bar{q}_1(\mathbf{p}(t_0),\mathbf{q}(t_0))$ and $\bar{p}_1(\mathbf{p}(t_0),\mathbf{q}(t_0))$ at any arbitrary time t_0 in the region of the saddle. This enables us to predict *a priori* whether the system climbs through the saddle to the product, or returns to its original state, and tell us the physical foundation of why and how the system traverses the saddles from reactant to product states; if the trajectories have crossed a configurational dividing surface $S(q_1 = 0)$ at time t_0 with $\alpha > 0$, the final state has already been determined at "the time t_0 when the system has just left the $S(q_1 = 0)$" to be a stable state directed by $\bar{q}_1 > 0$ (let us denote that state as the product state). Similarly, from only the phase-space information at $t = t_0$ (the sign of β), one can infer whether the system on $S(q_1 = 0)$ at time t_0 has climbed from either stable state—that is, reactant or product.

The dynamical propensity rule for (forward) transitions is derived as

$$\text{"If } \bar{q}_1(t_0) > -\frac{\bar{p}_1(t_0)}{|\omega_1|} \left(\bar{q}_1(t_0) < -\frac{\bar{p}_1(t_0)}{|\omega_1|} \right) \tag{11}$$

the system will go through to the product (return to the reactant)"

III. GEOMETRIC ASPECTS OF THE PHASE SPACE

Figure 4 shows a schematic portrait of the phase space flows (denoted by arrows) in the $(\bar{q}_1(\mathbf{p},\mathbf{q}),\bar{p}_1(\mathbf{p},\mathbf{q}))$ plane and the caricature of the corresponding

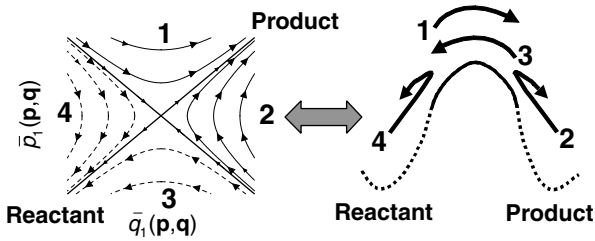

Figure 4. A schematic portrait of the stable and unstable invariant manifolds and the phase-space flows on $(\bar{q}_1(\mathbf{p},\mathbf{q}),\bar{p}_1(\mathbf{p},\mathbf{q}))$.

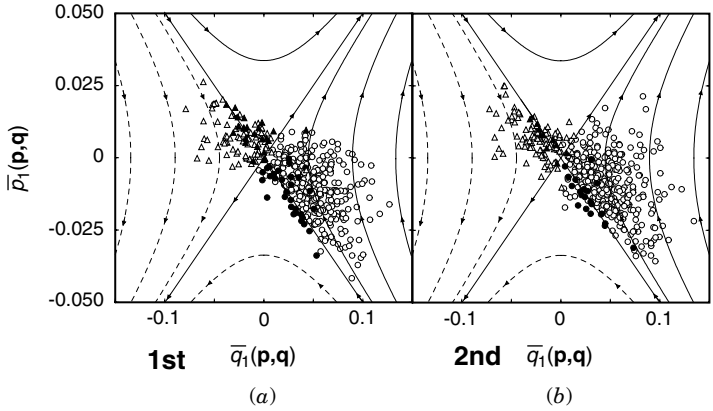

Figure 5. The distributions of the recrossing trajectories over configurational surface $S(q_1 = 0)$ at time $t = 0$ on the *phase*-space planes $(\bar{p}_1^{i\text{th}}(\mathbf{p}, \mathbf{q}), \bar{q}_1^{i\text{th}}(\mathbf{p}, \mathbf{q}))$ at $E = 0.5\varepsilon$, where *most modes are strongly chaotic—except* $\bar{q}_1(\mathbf{p}, \mathbf{q})$. (*a*) First and (*b*) second orders: The circle and triangle symbols denote the system trajectories having negative and positive incident momenta $p_1(t = 0)$ on the $S(q_1 = 0)$, and the open and filled symbols denote those whose final states were predicted correctly and falsely by Eq. (11), respectively [45].

trajectories on the potential energy surfaces. Eq. (11) tells us that if one divides the phase space into four domains using the stable and unstable invariant manifolds to and from the unstable fixed point $\bar{q}_1 = \bar{p}_1 = 0$, all the system trajectories classified at any time (e.g., $t = 0$), into the domains **1** and **2** should eventually go into the product state, and those classified into the domains **3** and **4** go into the reactant state. While the former and latter domains could be regarded, respectively, as "reactive" and "nonreactive" in elucidating the fate of reactions after the system leaves $S(q_1 = 0)$, all the system trajectories classified in domain **2** or domain **4** never cross through the phase-space dividing hypersurface $S(\bar{q}_1(\mathbf{p}, \mathbf{q}) = 0)$; that is, these trajectories do not correspond to reactions.

Up to moderately high energy ($\sim$179%) of the activation barrier for reactant $\rightarrow$ product in the Ar_6 isomerization reaction, the fates of most trajectories can be predicted more accurately by Eq. (11) as the order of perturbation calculation increases, except just in the vicinity of the (approximate) stable invariant manifolds (e.g., see Fig. 5), and that the transmission coefficient κ observed in the configurational space can also be reproduced by the dynamical propensity rule without any elaborate trajectory calculation (see Fig. 6). Our findings indicate that almost all observed deviations from unity of the *conventional* transmission coefficient κ may be due to the choice of the reaction coordinate whenever the κ arises from the recrossings, and most transitions in chemical

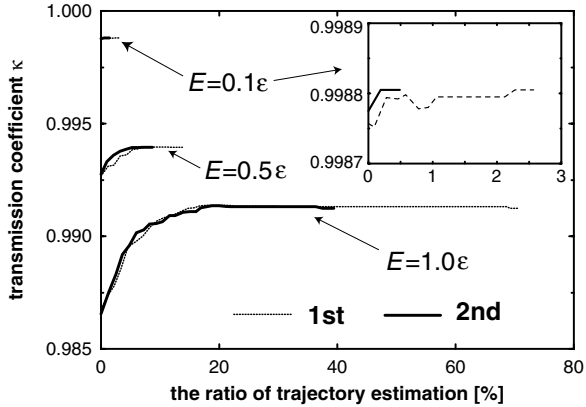

Figure 6. The transmission coefficients across the conventional dividing surface $S(q_1 = 0)$, κ, at $E = 0.1, 0.5$, and 1.0ε above the saddle point energy. The activation barrier height is about 0.633ε. The fates of the reactions were estimated both by Eq. (11) and by direct molecular dynamics (MD) simulations: if the system falls outside/inside a sensitive band defined vertical to the (approximate) stable invariant manifolds on the $(\bar{p}_1, \bar{q}_1)$ plane, we estimated the final state by use of Eq. (11)/direct MD simulations. In the figure, the sensitive band is set for each order by changing the size of the band from 0 to a number so large that the estimated κ's converge to those evaluated by the *full* MD estimation. Here, the abscissa gives the ratio of the number of those whose fates were estimated correctly by MD calculations to the total number of trajectories; that is, 0% implies that the fates of all the reactions were estimated solely by Eq. (11). The ratios of the trajectory calculations in evaluating κ to yield the convergence to the exact values are 2.4%(1), 0.6%(2) at 0.1ε; 12.1%(1), 7.1%(2) at 0.5ε; and 69.2%(1), 37.5%(2) at 1.0ε. (The numbers in the parentheses are the orders of the perturbative calculations we performed.) [Reprinted with permission from Ref. 45. Copyright © 2002, American Chemical Society.]

reactions must not take place in *fully* stochastic fashion but in some predictable, dynamical fashion.

Then, how can one "capture" the global aspects of the phase-space geometry from the geometric structure of the phase space in that *local* region? One can find an essential clue from an insightful classical theory for isomerization reactions composed of two DOFs, so-called reactive island theory (RIT) developed by De Leon, Marston, Mehta, and Ozorio De Almeida [34–37] (see also Ref. 55).

Let us begin with the following system with two DOFs, which we shall henceforth call a 2-DOFs system, in this case with a Hamiltonian for a double-well potential:

$$H = \tfrac{1}{2}(p_1^2 + p_2^2) - q_1^2 + q_1^4 + q_2^2 \tag{12}$$

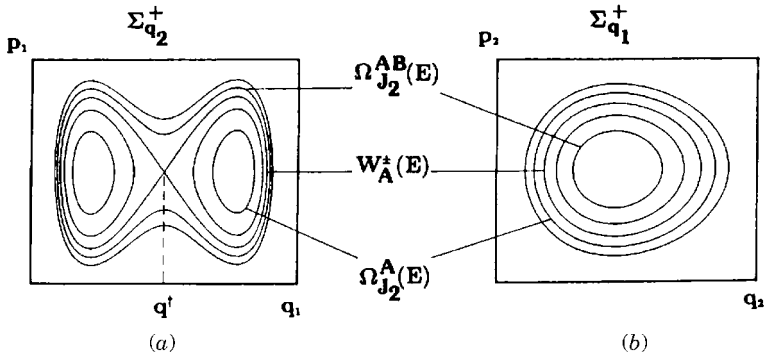

Figure 7. The two Poincaré sections. (*a*) $\Sigma^+_{q_2}$ and (*b*) $\Sigma^+_{q_1}$ at a total energy E for an uncoupled bound two-mode system, Eq. (12). The region where $q_1 > q^\dagger$ is referred as to region A, and that where $q_1 < q^\dagger$ as region B hereinafter. $W^+_A(E)$ $(W^-_A(E))$ denotes unstable (stable) invariant cylinder manifold asymptotically departing from (approaching toward) the unstable periodic orbit at the fixed point $q_1 = p_1 = 0$ to (from) the region A at total energy E. $\Omega^{AB}_{J2}(E)$ and $\Omega^{A}_{J2}(E)$ denote, respectively, the invariant cylinder manifold on which all "reactive" rotational motions, both A $\rightarrow$ B and A $\leftarrow$ B, lie with a constant action $J2$ in the q_2 mode, and that on which librational motions lie inside region A. [Reprinted with permission from N. De Leon, M. A. Mehta, and R. Q. Topper, *J. Chem. Phys.* **94**, 8310 (1991), Copyright © 1991, American Institute of Physics.]

where there is no coupling between reactive DOF (p_1, q_1) and the other bath DOFs (p_2, q_2). Now, consider the following two Poincaré sections $\Sigma^+_{q_2}$ and $\Sigma^+_{q_1}$.

$$\Sigma^+_{q_2} = \{(\mathbf{p}, \mathbf{q}) | q_2 = q^0_2, p_2 > 0\} \tag{13}$$

$$\Sigma^+_{q_1} = \{(\mathbf{p}, \mathbf{q}) | q_1 = q^0_1 (> q^\dagger = 0), p_1 > 0\} \tag{14}$$

Here, $q^\dagger$ is the position of the saddle point in q_1, and q^0_1 and q^0_2 are some fixed values of q_1 and q_2, respectively. The geometrical structure of the stable and unstable invariant manifolds $W^-_A(E)$ and $W^+_A(E)$ is the direct product of the one-dimensional circular space S^1_E composed of q_2 and p_2 on the three-dimensional equienergy hypersurface embedded in the phase space $\mathbb{R}^4$ and the linear space $\mathbb{R}^1$ associated with the unbound, reactive degree of freedom q_1—that is, two-dimensional cylindrical topology. As interpreted from Fig. 7, all the "reactive" crossing trajectories occur through the interior of the cylinder whose boundary consists of the stable and unstable invariant manifolds $W^-_A(E)$ and $W^+_A(E)$. (Note that the system is bounded by an equienergy hypersurface in the phase space at total energy E.) If the system resides on the *boundary* of the cylinder, it never crosses the saddle although it approaches asymptotically to the unstable periodic orbit at the unstable fixed point, referred as to $\tau(E)$ hereinafter, in the infinite future or past. If and only if the system resides *interior* of the cylinder, can it cross through the saddle.

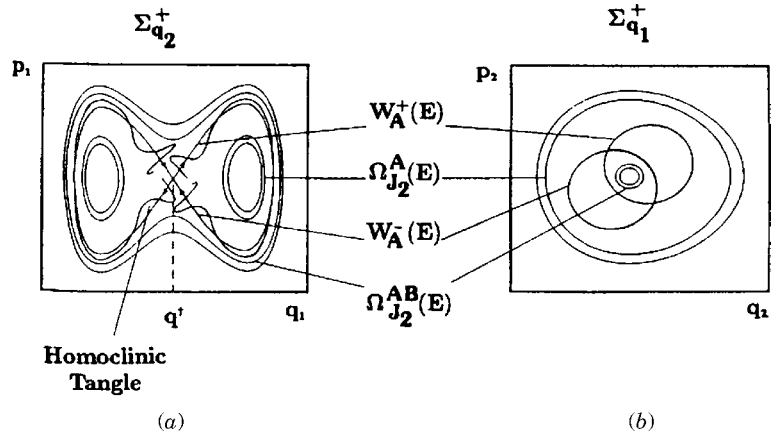

Figure 8. The two Poincaré sections. (*a*) $\Sigma^+_{q_2}$ and (*b*) $\Sigma^+_{q_1}$ at a total energy E same as Fig. 7 except the two modes are coupled. Note that $W^-_A(E)$ and $W^+_A(E)$ partially overlap on $\Sigma^+_{q_1}$, corresponding to the appearance of homoclinic tangle on $\Sigma^+_{q_2}$. [Reprinted with permission from N. De Leon, M. A. Mehta, and R. Q. Topper, *J. Chem. Phys.* **94**, 8310 (1991). Copyright © 1991, American Institute of Physics.]

However, we lose the concept of *reaction* itself for systems being integrable because all the "reactive" trajectories eternally rotate between regions A and B and can never be "captured" by either A or B. Figure 8 shows the corresponding Poincaré section structures when the two modes are weakly coupled each other. Under the perturbation, it is well known that the unstable and stable invariant manifolds $W^+_A(E)$ and $W^-_A(E)$ in the phase space no longer connect smoothly, but generically intersect each other with a finite angle on $\Sigma^+_{q_2}$, resulting in a tangled structure due to the infinite number of the intersections between $W^+_A(E)$ and $W^-_A(E)$ at homoclinic points on that surface of section [47]. (This intersection occurring between *one*-dimensional "curves" arising from the *two*-dimensional invariant cylinders $W^+_A(E)$ and $W^-_A(E)$ on the *two*-dimensional Poincaré section $\Sigma^+_{q_2}$ is generically *zero*-dimensional (i.e., point) and referred to as *homoclinic point*, because it connects outgoing and incoming "curves" of the topologically *same* hyperbolic, unstable fixed point.) As $W^+_A(E)$ and $W^-_A(E)$ extend away from the unstable periodic orbit at the unstable fixed point, their *initial* intersections across the $\Sigma^+_{q_1}$ may give rise to an overlap between them on that section. Note that $W^+_A(E)$ and $W^-_A(E)$ never overlap themselves, and the areas closed by them on $\Sigma^+_{q_1}$ are conserved as the same because each reaches the same unstable periodic orbit in the infinite past and future.

Invariant tori $\Omega^A_{J2}(E)$ and $\Omega^{AB}_{J2}(E)$ may exist in the phase space, resulting in librational motions within the potential well and rotational motions across the saddle, respectively, although their measure of the phase space should depend

on both the strength of nonlinear coupling among modes and total energy E. The invariant cylinder manifolds $W_{\mathrm{A}}^{+}(E)$ and $W_{\mathrm{A}}^{-}(E)$ wander about in a sea of chaos (between these invariant tori) in an indefinite complicated fashion. However, the manner in which the cylinders overlap one another in the phase space mediates the reactions: All the reactive trajectories from A to B are mediated through the *interior* of the cylinder, the so-called *reactive island* (RI), bounded by the stable invariant manifold $W_{\mathrm{A}}^{-}(E)$ from the unstable periodic orbit at the unstable fixed point, $\tau(E)$. Similarly, all the back reactions from B to A are mediated through the *interior* of the RI bounded by the unstable invariant manifold $W_{\mathrm{A}}^{+}(E)$.

A very insightful picture is shown in Fig. 9 of the RIs at a Poincaré surface of section with the corresponding "semi-global" dynamics in region A. In the figure, $\mathrm{II}_{\mathrm{A}}^{+}$ and $\mathrm{II}_{\mathrm{A}}^{-}$ represent the regions that contain the set of all points (p_2, q_2) on the $\Sigma_{q_1}^{+}$ within the RIs bounded by W_{A}^{+} and W_{A}^{-}, respectively. (Hereinafter, for the sake of simplicity, we omit any notation of their E dependence, although they all depend on total energy E.) The overlap "hatched" region is denoted by

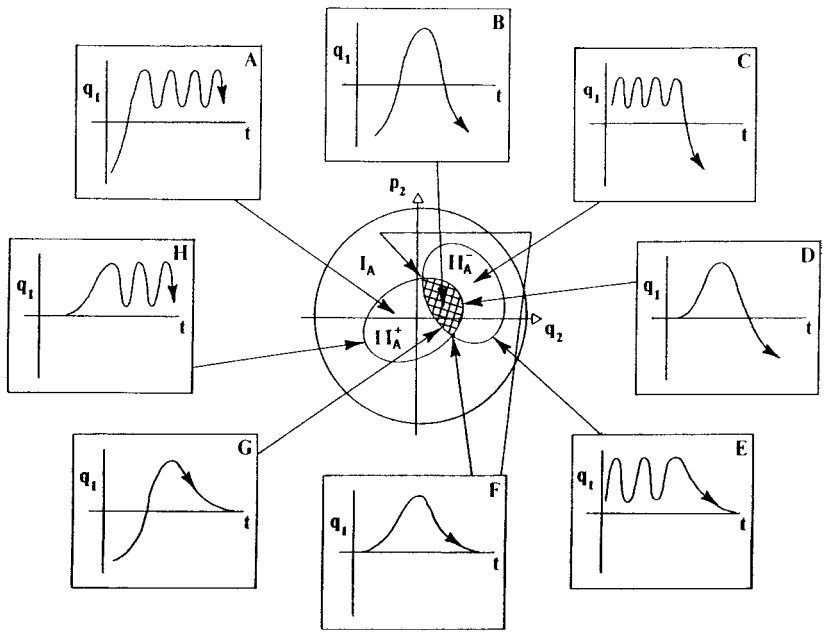

Figure 9. Schematic picture of the reactive island structure on $\Sigma_{q_1}^{+}$ and the corresponding dynamics in the reaction coordinate q_1. See text for detail discussions. [Reprinted with permission from A. M. Ozorio de Almeida, N. De Leon, M. A. Mehta, and C. C. Marston, *Physica D* **46**, 265 (1990). Copyright © 1990, Elsevier Science Publishers, North-Holland.]

$\mathrm{II}_\mathrm{A}(=\mathrm{II}_\mathrm{A}^+ \cap \mathrm{II}_\mathrm{A}^-)$. The consequent semi-global dynamics belonging to each region on the Poincaré section $\Sigma_{q_1}^+$ composed of overlapped two RIs can be well interpreted as follows:

A: All B $\rightarrow$ A trajectories (passing from B to A) which will be "captured" in A ($\sim$ at least more than one oscillation in q_1) must go through the interior of $\mathrm{II}_\mathrm{A}^+ - \mathrm{II}_\mathrm{A}$.

B: All B $\rightarrow$ A trajectories which will go back to B immediately ($\sim$ in one oscillation in q_1) must go through the interior of II_A.

C: All A $\rightarrow$ B trajectories which had temporarily been "captured" in A ($\sim$ at least more than one oscillation in q_1) must go through the interior of $\mathrm{II}_\mathrm{A}^- - \mathrm{II}_\mathrm{A}$.

D: All A $\rightarrow$ B trajectories which were originally initiated from the unstable periodic orbit $\tau(E)$ as $t \rightarrow -\infty$ without returning to A must lie along the part of the boundary of II_A^+ within the interior of II_A^-.

E: All trajectories which had temporarily been "captured" in A ($\sim$ at least more than one oscillation in q_1) and will be asymptotic to $\tau(E)$ without visiting B must lie along the part of the boundary of II_A^- exterior to II_A^+.

F: Homoclinic trajectories asymptotic to $\tau(E)$ as $t \rightarrow \pm\infty$ lie on the intersection of the boundary of II_A^+ and II_A^-.

G: B $\rightarrow$ A trajectories which will be asymptotic to $\tau(E)$ as $t \rightarrow \infty$ without returning to B must lie along the part of the boundary of II_A^- within the interior of II_A^+.

H: All trajectories which will be "captured" in A ($\sim$ at least more than one oscillation in q_1) which were initiated from $\tau(E)$ as $t \rightarrow -\infty$ without visiting B must lie along the part of the boundary of II_A^+ exterior to II_A^-.

I: All trajectories temporarily captured in A that are neither pre-, post-reactive to B nor asymptotic to $\tau(E)$ must lie in a region exterior to both II_A^+ and II_A^-, $\mathrm{I}_\mathrm{A}(=\mathrm{II}_\mathrm{A}^+ \cup \mathrm{II}_\mathrm{A}^-)$ (of course, it is possible for the system belonging to I_A to enter the interior of II_A^- and go through to B).

The stable and unstable invariant cylinders intersect this section infinitely often, preserving each area bounded by the closed curve of W_A^- and W_A^+, although it will become indefinitely deformed due to their homoclinic tangles. However, one of the most striking consequences deduced from the analyses of the *initial* intersection of the invariant cylinder manifolds at a certain Poincaré section defined in region A is this: If and only if the system lies in the interior of $\mathrm{II}_\mathrm{A}^- - \mathrm{II}_\mathrm{A}$, the system can climb through from A to B whenever wandering in the region of A for at least more than one oscillation in q_1.

Figure 10 shows a representative trajectory passing through the two Poincaré sections Σ_A and Σ_B defined in both the regions of A and B, where $\Sigma_\mathrm{A} = \Sigma_\mathrm{A}^+$

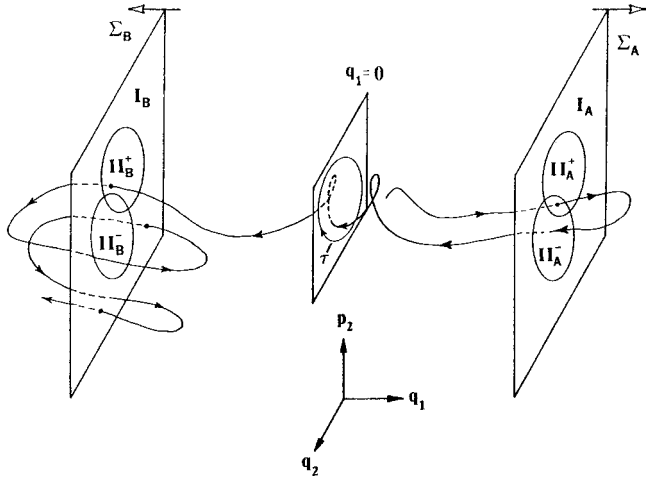

Figure 10. A representative reactive trajectory intersecting two Poincaré sections Σ_A and Σ_B defined in both the regions of A and B through the reactive island at $q_1 = 0$. Note that the passing through the interior of $\mathrm{II}_\mathrm{A}^- - \mathrm{II}_\mathrm{A}$ will never occur in that direct back reaction on Σ_A^+ after passing through the interior of II_A, although it is depicted so for the sake of simplicity. [Reprinted with permission from A. M. Ozorio de Almeida, N. De Leon, M. A. Mehta, and C. C. Marston, *Physica D* **46**, 265 (1990). Copyright © 1990, Elsevier Science Publishers, North-Holland.]

[Eq. (14)] and $\Sigma_\mathrm{B} = \{(\mathbf{p}, \mathbf{q}) | q_1 = q_1^0 (< q^\dagger = 0), p_1 < 0\}$. Note here that W_A^- may intersect with W_A^+ or W_B^+, but it never does with W_B^- and W_A^- itself, and all the reactions will occur through the interior of the invariant cylinders. By assuming that successive intersections of the reactive islands will eventually cover both surfaces of section (faster than a characteristic time scale of the reaction), a simple first-order kinetics can be formulated, taking into account the direct back reaction (recrossing motion within one oscillation in q_1):

$$\mathrm{I}_\mathrm{B}^- \xrightarrow{\alpha_\mathrm{B}} \mathrm{II}_\mathrm{B}^- \xrightarrow{\beta_\mathrm{A}} \mathrm{I}_\mathrm{A}^-, \qquad \mathrm{I}_\mathrm{A}^- \xrightarrow{\alpha_\mathrm{A}} \mathrm{II}_\mathrm{A}^- \xrightarrow{\beta_\mathrm{B}} \mathrm{I}_\mathrm{B}^-, \qquad \mathrm{II}_\mathrm{A}^- \underset{\gamma_\mathrm{A}}{\overset{\gamma_\mathrm{B}}{\rightleftharpoons}} \mathrm{II}_\mathrm{B}^- \tag{15}$$

where I_A^- and I_B^- are the regions exterior to II_A^- and II_B^-, respectively, and each rate constant α, β, γ is, respectively,

$$\alpha_\mathrm{A} = \frac{\mathrm{Area}(\mathrm{II}_\mathrm{A}^- - \mathrm{II}_\mathrm{A})}{\mathrm{Area}(\mathrm{I}_\mathrm{A}^-)} \tag{16}$$

$$\beta_\mathrm{A} = \frac{\mathrm{Area}(\mathrm{II}_\mathrm{A}^+ - \mathrm{II}_\mathrm{A})}{\mathrm{Area}(\mathrm{II}_\mathrm{A}^+)} \tag{17}$$

$$\gamma_\mathrm{A} = \frac{\mathrm{Area}(\mathrm{II}_\mathrm{A})}{\mathrm{Area}(\mathrm{II}_\mathrm{A}^+)} = 1 - \beta_\mathrm{A} \tag{18}$$

Similar equations hold for α_B, β_B, and γ_B.

Then, the population kinetics can be written with respect to the "mapping time" n;

$$\begin{aligned}
\mathrm{II}_{\mathrm{A}}^{-}(n) &= \alpha_{\mathrm{A}}\mathrm{I}_{\mathrm{A}}^{-}(n-1) + \gamma_{\mathrm{A}}\mathrm{II}_{\mathrm{B}}^{-}(n-1) \\
\mathrm{I}_{\mathrm{A}}^{-}(n) &= (1-\alpha_{\mathrm{A}})\mathrm{I}_{\mathrm{A}}^{-}(n-1) + \beta_{\mathrm{A}}\mathrm{II}_{\mathrm{B}}^{-}(n-1) \\
\mathrm{II}_{\mathrm{B}}^{-}(n) &= \alpha_{\mathrm{B}}\mathrm{I}_{\mathrm{B}}^{-}(n-1) + \gamma_{\mathrm{B}}\mathrm{II}_{\mathrm{A}}^{-}(n-1) \\
\mathrm{I}_{\mathrm{B}}^{-}(n) &= (1-\alpha_{\mathrm{B}})\mathrm{I}_{\mathrm{B}}^{-}(n-1) + \beta_{\mathrm{B}}\mathrm{II}_{\mathrm{A}}^{-}(n-1)
\end{aligned}$$

The population of A can be obtained as $N_{\mathrm{A}}(n) = \mathrm{I}_{\mathrm{A}}^{-}(n) + \mathrm{II}_{\mathrm{A}}^{-}(n)$ and the asymptotic (exponential) decay rate of $N_{\mathrm{A}}(n)$, k^{RI}, is given by

$$k^{\mathrm{RI}} = -\ln|\lambda^{\max}| \tag{19}$$

Here $\lambda^{\max}$ is the eigenvalue with the largest norm, which can be obtained by diagonalization of the above discretized master equation (the corresponding, continuous master equation formulation with respect to the *real* time domain can be found in Ref. 36).

De Almeida et al. [34] applied the RIT to the following 2-DOFs Hamiltonian:

$$H = \frac{1}{\mu}(p_1^2 + p_2^2) + 4q_1^2(q_1^2 - 1)\exp(-z\lambda q_2) + D[1 - \exp(-\lambda q_2)]^2 \tag{20}$$

where $\mu = 8.0$, $z = 2.3$, $\lambda = 1.95$, and $D = 10.0$. The point $q_1 = 0$ corresponds to the saddle point, and the potential energy surface is symmetric with respect to the reaction coordinate q_1. Figure 11 shows the RI structure on Σ_{A}^{+} at three distinct energies above the saddle point energy. Note that, as the total energy becomes higher above the barrier, the system undergoes more direct back reactions (the area of the overlap region between $\mathrm{II}_{\mathrm{A}}^{+}$ and $\mathrm{II}_{\mathrm{A}}^{-}$ increases) and the population of A becomes more "oscillatory" in converging to an equilibrium value. On the other hand, at a total energy just slightly above the barrier, there exists no overlap region between the first intersections of the cylinder manifolds bounded by W_{A}^{+} and W_{A}^{-}, resulting in no direct back reaction occurring in one oscillation in q_1 as Fig. 12**A** $\rightarrow$ Fig. 12**B**.

These observations coincide with our naive intuition that we have had no means to quantify so far; that is, the closer is the total energy to the energy barrier, the more difficult it becomes for the system that had passed through the saddle to go back to the original state due to the "dissipation" of the energy accumulated for climbing in the reactive DOF (p_1, q_1) to the "bath." This indicates that there exists one possible diagnosis to address the question, "What is the condition that enables us to assume local equilibrium in the reactants, in

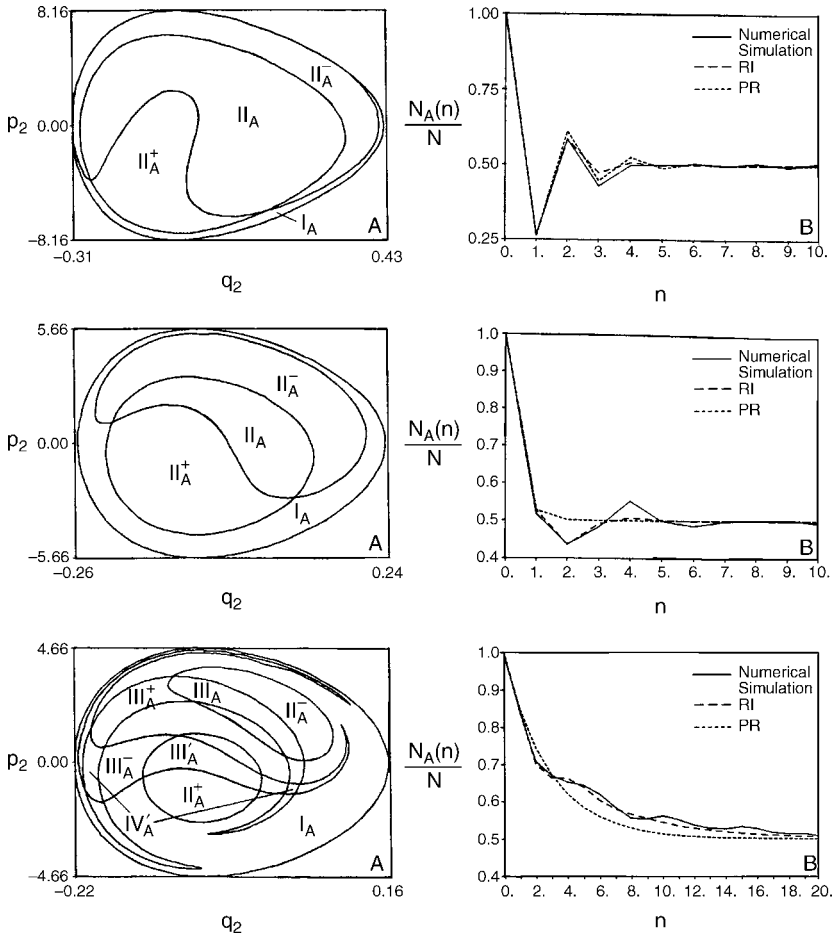

Figure 11. Reactive island structures on the Poincaré section Σ_A at $q_1^0 = 1/\sqrt{2}$ and the kinetic data for the symmetrical Hamiltonian in Eq. (20) at an excess energy of $\Delta E = 3.0$ (upper), $\Delta E = 1.0$ (middle), and $\Delta E = 0.2$ (bottom). (**A**) The reactive island structure. (**B**) The population decay results of A using three different methods: trajectory calculation by preparing 4000 points uniformly distributed above the barrier and mapping them numerically (bold line), RIT (dashed line), and "purely random" (PR) model that does not explicitly take into account direct back reaction—that is, ignoring the overlap region of the direct back route (dotted line). At $\Delta E = 0.2$, III_A^+ and III_A^- denote the next intersections of II_A^+ and II_A^-, respectively. III_A (III'_A) denotes the overlap region between II_A^- and III_A^+ (II_A^+ and III_A^-), resulting from the next intersection of III'_A, and IV'_A denotes the overlap region between III_A^+ and III_A^-. III_A and IV'_A yields two and three oscillations in q_1 prior to return to B after crossing the saddle from B to A. [Reprinted with permission from A. M. Ozorio de Almeida, N. De Leon, M. A. Mehta, and C. C. Marston, *Physica D* **46**, 265 (1990). Copyright © 1990, Elsevier Science Publishers, North-Holland.]

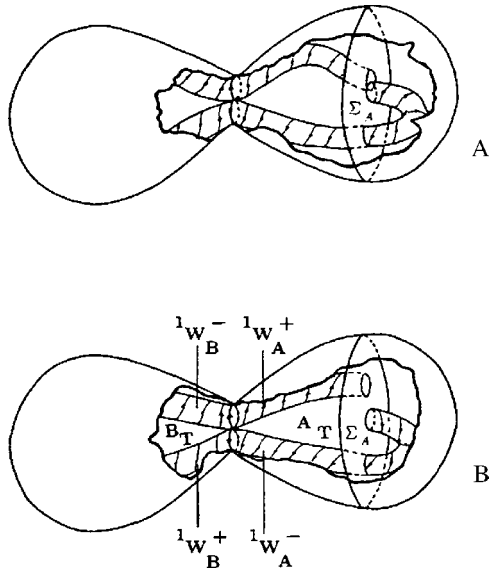

Figure 12. Caricatures of the cylinders as they wind about the phase space volume. All the surfaces and volumes are embedded in four-dimensional phase space $\mathbb{R}^4$. (**A**) The cylinders W_A^+ and W_A^- overlap one another at Σ_A^+, resulting in direct back reactions. (**B**) These two cylinders do not overlap one another. [Reprinted with permission from N. De Leon, *J. Chem. Phys.* **96**, 285 (1992). Copyright © 1992, American Institute of Physics.]

terms of the topological character of the reactive islands on the Poincaré surface of section defined in the reactant domain?''

If the coupling between the two modes is sufficiently strong, W^+ and W^- will be discontinuous on the Euclidean mapping plane $\Sigma_{q_2}^+$, because they can wander away from the mapping plane before intersecting it again [34]. This implies that the turnstile transition state developed by Davis and Gray in terms of surface of section $\Sigma_{q_2}^+$ for a 2-DOFs reacting system may be very difficult to apply, in practise, for strongly coupled, 2-DOFs systems. On the other hand, the RIT usually requires only the first few intersections of W^+ and W^- from the unstable periodic orbit $\tau(E)$ at the Poincaré section ''perpendicular to'' the reaction coordinate. These intersections will give rise to discontinuous island structures, and hence RIT may be more applicable, in practice, at least for a general class of systems with 2 DOFs.

Why has this elegant reaction theory not been applied to general reactive systems with many DOFs? It was because their algorithm depends crucially on finding *pure* unstable periodic orbits in the nonreactive degrees of freedom. As pointed out previously [44], it is always possible to find this regulatory object in

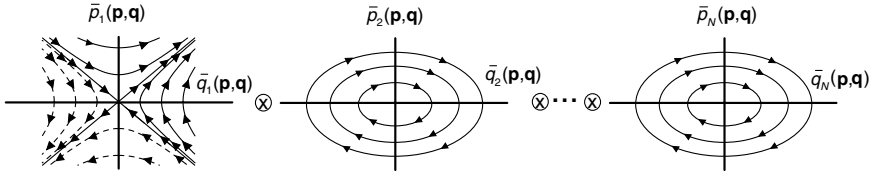

Figure 13. The phase-space portrait of N-DOF saddle Hamiltonian.

any 2-DOFs system irrespective of the kind of system and the value of total energy the system possesses, because there is no source to yield resonance by a single imaginary-frequency mode and a single real-frequency mode. Systems of many DOFs are no longer integrable in the saddles except at energies just slightly above the threshold energy because of resonances amongst the nonreactive modes that spoil any unstable, regular, periodic orbits.

Readers may easily notice that the application of Lie transforms to the vicinity of the first rank saddles [49] has a great potential for revisiting this classic theory that enables us to capture the semi-global, multidimensional substructure in a sea of chaos. Figure 13 shows the phase space portrait of an N degrees of freedom (N-DOFs) Hamiltonian in the region of the first-rank saddles at the quasi-regular regime where almost of all actions behave as approximate invariants. In this energy regime, the geometric structure of the stable and unstable invariant manifolds W_{A}^{-} and W_{A}^{+} is the direct product of the $(2N-2)$-dimensional spherical space S^{2N-2} composed of the $(N-1)$-uncoupled bath modes $(\bar{p}_k(\mathbf{p},\mathbf{q}),\bar{q}_k(\mathbf{p},\mathbf{q}))$ $(1 < k \leq N)$ and the interval $\mathbb{R}^1$ associated with the unbound, reactive DOF. As discussed by Uzer et al. [54], this leads to $(2N-2)$-dimensional, stable and unstable, invariant spherical cylinder manifolds $S_E^{2N-3}\times\mathbb{R}^1$ on the $(2N-1)$-dimensional equienergy hypersurface at total energy E in the $2N$-dimensional phase space $\mathbb{R}^{2N}$.

The trajectories inside these spherical cylinders look like "regular flows," and their projections onto a two-dimensional space spanned by any two bath modes $\bar{q}_k(\mathbf{p},\mathbf{q})$ result in a Lissajous figure as depicted in Fig. 2.6a in Ref. 44. As the total energy increases, the bath DOFs no longer retain their invariants of action and they become coupled with one another. However, as shown previously [38–45] as far as belonging to the semi-chaotic energy regime, the reactive DOF $\bar{q}_1(\mathbf{p},\mathbf{q})$ can be well uncoupled from all the other chaotic, bath DOF. Here, one might regard $W_{\mathrm{A}}^{-}(E)$ and $W_{\mathrm{A}}^{+}(E)$ as $(2N-2)$-dimensional, stable and unstable, invariant "deformed" spherical cylinders on the equienergy hypersurface. The trajectories inside these "deformed" spherical cylinders look like "chaotic flows," and their projections onto a two-dimensional space spanned by any two bath modes $\bar{q}_k(\mathbf{p},\mathbf{q})$ result in a chaotic dynamics as depicted in Fig. 2.6b in Ref. 44.

Recently, Wiggins et al. [15] provided a firm mathematical foundation of the robust persistence of the invariant of motion associated with the phase-space reaction coordinate in a sea of chaos. The central component in RIT that is, unstable periodic orbits, are naturally generalized in many DOFs systems in terms of so-called normally hyperbolic invariant manifold (NHIM). The fundamental theorem on NHIMs, denoted here by $\mathscr{M}$, ensures [21,53] that NHIMs, if they exist, survive under arbitrary perturbation with the property that the stretching and contraction rates under the linearized dynamics transverse to $\mathscr{M}$ dominate those tangent to $\mathscr{M}$. Note that NHIM only requires that instability in either a forward or backward direction in time transverse to $\mathscr{M}$ is much stronger than those tangential directions of $\mathscr{M}$, and hence the concept of NHIM can be applied to any class of continuous dynamical systems. In the case of the vicinity of saddles for Hamiltonian problems with many DOFs, the NHIM is expressed by a set of all $(\mathbf{p}, \mathbf{q})$ satisfying both $\bar{q}_1 = \bar{p}_1 = 0$ and $\bar{H}_0(\bar{\mathbf{J}}_\mathbf{B}) + \sum_{n=1} \epsilon^n \bar{H}_n\ (\bar{\mathbf{J}}_B, \bar{\mathbf{\Theta}}_B) = E$, that is,

$$\begin{aligned} \mathscr{M} = \{(\bar{q}_1, \bar{p}_1, \ldots, \bar{q}_N, \bar{p}_N) | \bar{q}_1(\mathbf{p}, \mathbf{q}) = \bar{p}_1(\mathbf{p}, \mathbf{q}) = 0, \\ \bar{H}_0(\bar{\mathbf{J}}_\mathbf{B}) + \sum_{n=1} \epsilon^n \bar{H}_n(\bar{\mathbf{J}}_B, \bar{\mathbf{\Theta}}_B) = E\} \end{aligned} \tag{21}$$

with $(2N-3)$ dimensionality on the $(2N-1)$-dimensional equienergy hypersurface. One of the big differences between the unstable *regular* periodic orbits RIT requires and NHIM is that the motions inside the NHIM can even be *chaotic* (although a straightforward extension of the concept of unstable periodic orbits to n degrees of freedom systems should possess n unstable, *regular*, periodic orbits), and the NHIMs retain their invariance robustly against perturbation with the stable and unstable *invariant* manifolds. So, at a wide range of energies above the barrier, the RIT can be generalized and applied, in principle, to a wide class of chemical reaction systems with many DOFs; if one brings about the backward calculations (to the reactant domain) initiated from the interior of the phase space bounded by the NHIM at the saddle, one may reveal what kinds of initial conditions one must prepare to obtain fast transitions from the reactant to the product.

IV. KRAMERS–GROTE–HYNES THEORY REVISITED

Two approaches to overcome the recrossing problem have been variational TST [8,10,61], which optimizes a configurational dividing surface by minimizing the number of recrossings, or by (generalized) Langevin formalism of Kramers [6] and Grote and Hynes [11], which regards the recrossings as arising from

"(molecular) friction" by the "bath" DOFs. Zwanzig [62] proved that the following class of Hamiltonians, that is,

$$H(\mathbf{p},\mathbf{q}) = \frac{p_1^2}{2\mu} + V(q_1) + \sum_{i=1}\left[\frac{p_{Bi}^2}{2m_i} + \frac{m_i\omega_1^2}{2}\left(q_{Bi} - \frac{c_i q_1}{m_i\omega_i^2}\right)^2\right] \tag{22}$$

can be reformulated by a generalized Langevin formalism,

$$\mu\ddot{q}_1 = -\frac{\partial V}{\partial q_1} - \mu\int_0^t \dot{q}_1(t')\zeta(t-t')dt' + R(t) \tag{23}$$

$$\langle R(0)R(t)\rangle = k_B T\zeta(t) \tag{24}$$

where, for example

$$\zeta(t) = \sum_i \frac{c_i^2}{m_i\omega_i^2}\cos\omega_i t \tag{25}$$

Here, q_1, p_1 are the "system" coordinate and momentum; and q_{Bi}, p_{Bi} are the ith "bath" variables with mass m_i and frequency ω_i. c_i is the coupling constant of the ith "bath" oscillator with the "system." μ is the mass of the "system" and k_B Boltzmann constant, and the average $\langle\rangle$ is over the "thermal bath" at temperature T.

van der Zwan and Hynes [63] and later Pollak [64] showed that the reaction rate of the Grote–Hynes formulation with the reaction coordinate q_1 is exactly equivalent to that of the transition state theory if the reaction coordinate is chosen as an unstable normal coordinate $\tilde{q}_1$ composed of the total system (= "system q_1" + "bath $\mathbf{q}_B$") (see also Fig. 14).

However, their arguments have been often criticized because of the simplicity of its Hamiltonian class (it's integrable!). Our recent findings suggest that nevertheless their equivalence arguments may be made much more general and applicable to a wider range of Hamiltonian classes, even when the system is almost chaotic. This stimulates us to reconsider a fundamental question of what constitutes the "thermal bath" for reacting systems. One may anticipate that reactions take place along a *ballistic* path composed of the *total* system in the thermal fluctuation, at least, in the region of saddles. The "thermal bath" for reactions, simply defined thus far as all the rest of the atoms or molecules except the reacting system, does not necessarily retard the reactive trajectories; rather, such a "bath" might control and assist the reactants to climb and go through the saddles. In the context of protein folding, Plotkin and Wolynes [65] addressed how the inclusion of the other degrees of freedom into the reaction coordinate is essential for obtaining the optimal dividing surface for protein folding. Still, the

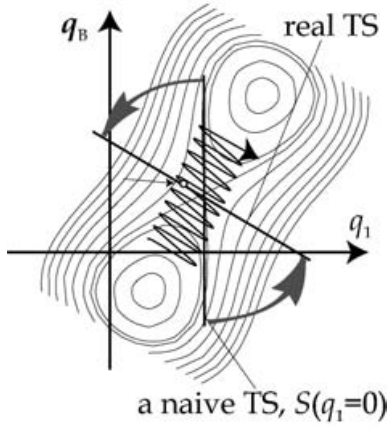

Figure 14. A schematic picture of how a reactive recrossing trajectory passing through a naive TS, $S(q_1 = 0)$, on a double-well Hamiltonian, Eq. (21), is rotated away to a single crossing through a real TS, $S(\tilde{q}_1(q_1, \mathbf{q}_B) = 0)$. The open circle denotes the point where the trajectory crosses the real TS only once.

questions, ''What is the dynamical role of water molecules surrounding the protein system?'' [66,67] and ''What should be regarded as the system and the thermal bath during the dynamical evolution of structural transitions?'' have been nontrivial, open subjects in many disciplinary fields in sciences.

V. STOCHASTICITY OF SADDLE CROSSINGS

The classical canonical perturbation calculation at the region of a saddle provides us with interesting *local* information of the original system at a finite low order up to which the series of the transformation are expected to be less affected by the ultimate divergence arising from the characteristics of the whole phase space. The *local* region in which the invariants of motion persist at least along the reaction coordinate should cover an entire saddle region that the system explores prior to being ''captured'' in either reactant or product state, in order to predict the termini of the trajectories. In other terms, energy regimes in which all or most of all the recrossing events occur within such a locality can be classified into *quasi-regular*, or *semi-chaotic* regimes. The more the total energy increases, the more the broadening of the excursion regime competes with the shrinkage of the ''convergence radius'' in which an approximate invariant of the action exists at least for the phase-space reaction coordinate. It is expected that, in an extremely high-energy regime, most recrossing events would take place outside of the ''region of invariance'' and the saddle crossing motions are entirely stochastic in

nature, irrespective of any choice of reaction coordinate, and dynamical correlation between outgoing and incoming trajectories to and from the saddle is completely lost. Such an energy regime may be regarded as *stochastic (= fully developed chaotic)* regime [38]. However, there is no mathematical framework yet that shows how the breakup of the normal hyperbolicity for the NHIMs affects the crossing trajectories over the region of the saddles. Komatsuzaki and Berry found [42,43] that the approximant of the NHIM at a finite order implies that a reacting system be substantially trapped as the total energy of the system increases from the ''semi-chaotic'' regime. It may lead a conjecture that a ''vague NHIM'' makes a reacting system increasingly trapped as vague tori do [68,69]. A new mathematical foundation is apparently required to inquire further into the question. Note, in addition, that, especially at high energies, the system may also pass over higher-rank saddles, and we encounter many new, untouched subjects—for example, definability of transition state and the role of resonance in the imaginary ω-plane for the bifurcation.

VI. CONCLUDING REMARKS AND FUTURE PROSPECTS

The robust existence of a *skeleton* composed of a NHIM and its spherical invariant cylinders in the phase space should play their essential roles not only to help us understand the physical origin of observed nonstatistical, dynamical behavior but also to provide us with a new scope to control chemical reaction dynamics in terms of geometrical feature of the phase space. Here, let us articulate some of the subjects we have to confront in the immediate future:

1. It is ensured that the NHIMs, $\mathcal{M}$, if they exist, survive under arbitrary perturbation to maintain the property that the stretching and contraction rates under the linearized dynamics transverse to $\mathcal{M}$ dominate those tangent to $\mathcal{M}$. In practice, we could compute the $\mathcal{M}$ only approximately with a finite-order perturbative calculation. Therefore, the robustness of the NHIM against perturbation (referred as to *structurally stable* [21,53]) is expected to provide us with one of the most appropriate descriptions of a ''phase-space bottleneck'' of reactions, if such an approximation of the $\mathcal{M}$ due to a finite order of the perturbative calculation can be regarded as a ''perturbation.'' One of the questions arising is, ''How can the NHIMs composed of a reacting system in solutions survive under the influence of solvent molecules?'' (This is closely relevant to the subject of how the ''system'' and ''bath'' should be identified in many-body systems.)
2. In two-mode [17] and three-mode [20] systems it was shown that dynamical bottlenecks exist to intramolecular energy transfer; that is, cantori are buried in the reactant basin, which form partial barriers between irregular regions of phase space. This brought about multiply

exponential decay on a wide range of time scales of the reaction. There exists no general algorithm for locating arbitrary NHIMs, while the stable and unstable manifolds of some of them may represent the multidimensional generalization of the partial barrier associated with a periodic orbit approximant to a cantorus [70]. An analysis of pairwise local frequency ratios would be useful to search the intramolecular bottlenecks, at least, for 3-mode systems [71–73]. However, it would be a very difficult task to deal with higher-dimensional systems.

3. One can visualize the NHIM and its stable and unstable invariant manifolds by the projections of those objects onto the original space by inverting all the transformed new coordinates and momenta into the original ones in the *quasi-regular* region, in which all actions persist approximately as the local invariants. However, although the motions inside the NHIM and its invariant manifolds can be chaotic in the *semi-chaotic* region, the inverse of $(\bar{\mathbf{p}}, \bar{\mathbf{q}})$ into the original $(\mathbf{p}, \mathbf{q})$ should become rather problematic because of the divergence of most terms in the generating functions. The partial normalization in which Lie transform applies only to the reactive DOF is required to capture these abstract invariant objects in the original coordinate space in the *semi-chaotic* region.
4. There exists no mathematically rigorous framework for describing the mechanism of the breakup of NHIM. There exists only a conjecture that a ''vague NHIM'' might act as a new bottleneck in the phase space transport [42,43].
5. The computer algorithm for Lie canonical transformation technique has not been improved essentially after Dragt and Finn [74,75]. It would be almost impossible to apply this beyond a few tens DOFs even to a fairly low order by using modern computational facilities. In this regard, the development of a means for coarse-graining multimode systems to a reduced set of DOFs is quite a challenge for further applications to *rugged*, multibasin dynamics [76].
6. There are great potentialities to explore multibasin chemical reaction theory based on the geometric structure of the phase space for multibasin transitions: By identifying each first-rank (and higher-rank if necessary) saddle linking the distinct energy minima (or lower-rank saddle), one can apply a Lie transform to the regions in the vicinity of each fixed point and extract the normally hyperbolic invariant manifolds (NHIM) and its stable and unstable invariant manifolds from the state space. The intersection phenomena between the stable cylinder approaching one NHIM associated with one saddle and the unstable cylinder departing from another NHIM with another saddle can tell us how a bundle of trajectories

passing through different saddles are dynamically correlated. In the case of gas-phase multibasin reactions, to elucidate the mechanism of the intersection provides us with a clue to establish the control of sequential chemical reactions. Consider a system of n DOFs. The NHIM is a topologically $(2n-3)$-dimensional (''deformed'' in the semi-chaotic regime) sphere, S_E^{2n-3}, and the stable and unstable invariant manifolds are the $(2n-2)$-dimensional (''deformed'' in the semi-chaotic regime) spherical cylinder topologies, $S_E^{2n-3} \times \mathbb{R}^1$, on the $(2n-1)$-dimensional equienergy hypersurface at total energy E in the phase space $\mathbb{R}^{2n}$. The dimensionality of an intersection manifold (if it exists for $n > 2$) is $2n-3$. It is expected that there would be strong dependency on the initial condition ''interior of NHIM'' to bring the system either to another NHIM or back to the same NHIM. That is, to understand the *skeleton* of the phase space composed of the cylinder invariant manifolds provides us with not only a new insight to control the dynamical correlations but also the rigorous reaction pathways of multibasin chemical reactions [77–79].

These are some of several challenging, but very fascinating, subjects for the forthcoming future for two-basin chemical reactions.

Acknowledgments

We thank Professors Mikito Toda, Stephen Wiggins, and Laurent Wiesenfeld for their valuable discussions and criticisms. Parts of this work were supported by the Japan Society for the Promotion of Science, Grant-in-Aid for Research on Priority Areas ''Genome Information Science'' and ''Control of Molecules in Intense Laser Fields'' of the Ministry of Education, Science, Sports and Culture of Japan. We also thank Sumitomo Foundation of Science, Inoue Foundation of Science, Hyogo Science Foundation and 21st century COE (Center of Excellence) of ''Origin and Evolution of Planetary Systems (Kobe University),'' MEXT, and the National Science of Foundation.

References

1. O. K. Rice and H. C. Ramsperger, *Am. Chem. Soc. J.* **50**, 617 (1928).
2. L. S. Kassel, *J. Phys. Chem.* **32**, 1065 (1928).
3. H. Eyring, *J. Chem. Phys.* **3**, 107 (1935).
4. M. G. Evans and M. Polanyi, *Trans. Faraday Soc.* **31**, 875 (1935).
5. E. Wigner, *J. Chem. Phys.* **5**, 720 (1938).
6. H. A. Kramers, *Physica* **7**, 284 (1940).
7. R. A. Marcus, *J. Chem. Phys.* **20**, 359 (1952).
8. J. C. Keck, *Adv. Chem. Phys.* **13**, 85 (1967).
9. W. H. Miller, *Faraday Discussions Chem. Soc.* **62**, 40 (1977).
10. D. G. Truhlar and B. C. Garrett, *Acc. Chem. Res.* **13**, 440 (1980)
11. R. F. Grote and J. T. Hynes, *J. Chem. Phys.* **73**, 2715 (1980).
12. B. J. Berne, M. Borkovec, and J. E. Straub, *J. Phys. Chem.* **92**, 3711 (1988).

13. T. Seideman and W. H. Miller, *J. Chem. Phys.* **95**, 1768 (1991).
14. D. G. Truhlar, B. C. Garrett, and S. J. Klippenstein, *J. Phys. Chem.* **100**, 12771 (1996).
15. S. Wiggins, L. Wiesenfeld, C. Jaffé, and T. Uzer, *Phys. Rev. Lett.* **86**, 5478 (2001).
16. R. A. Marcus, *Science* **256**, 1523 (1992).
17. M. J. Davis and S. K. Gray, *J. Chem. Phys.* **84**, 5389 (1986).
18. S. K. Gray and S. A. Rice, *J. Chem. Phys.*, **87**, 2020 (1987).
19. M. Zhao and S. A. Rice, *J. Chem. Phys.* **96**, 6654 (1992).
20. R. E. Gillian and G. S. Erza, *J. Chem. Phys.* **94**, 2468 (1991).
21. S. Wiggins, *Physica D* **44**, 471 (1990).
22. M. Toda, *Phys. Rev. Lett.* **74**, 2670 (1995).
23. M. Toda, *Phys. Lett. A* **227**, 232 (1997).
24. M. Toda, *Adv. Chem. Phys.* **123**, 153 (2002).
25. D. J. Wales and R. S. Berry, *J. Phys. B* **24**, L351 (1991).
26. C. Amitrano and R. S. Berry, *Phys. Rev. Lett.* **68**, 729 (1992).
27. C. Amitrano and R. S. Berry, *Phys. Rev. E* **47**, 3158 (1993).
28. R. J. Hinde and R. S. Berry, *J. Chem. Phys.* **99**, 2942 (1993).
29. R. S. Berry, *Chem. Rev.* **93**, 2379 (1993).
30. R. S. Berry, *Int. J. Quantum. Chem.* **58**, 657 (1996).
31. R. S. Berry, *Adv. Chem. Phys.* **0**, 0 (0).
32. E. R. Lovejoy, S. K. Kim, and C. B. Moore, *Science* **256**, 1541 (1992).
33. E. R. Lovejoy and C. B. Moore, *J. Chem. Phys.* **98**, 7846 (1993).
34. A. M. Ozorio De Almeida, N. De Leon, M. A. Mehta, and C. C. Marston, *Physica D* **46**, 265 (1990).
35. N. De Leon, M. A. Mehta, and R. Q. Topper, *J. Chem. Phys.* **94**, 8310 (1991).
36. N. De Leon, *J. Chem. Phys.* **96**, 285 (1992).
37. N. De Leon and S. Ling, *J. Chem. Phys.* **101**, 4790 (1994).
38. T. Komatsuzaki and R. S. Berry, *J. Chem. Phys.* **110**, 9160 (1999).
39. T. Komatsuzaki and R. S. Berry, *J. Chem. Phys.* **116**, 862 (2002).
40. T. Komatsuzaki and R. S. Berry, *Phys. Chem. Chem. Phys.* **1**, 1387 (1999).
41. T. Komatsuzaki and R. S. Berry, *J. Mol. Struct. (Thiochem)* **506**, 55 (2000).
42. T. Komatsuzaki and R. S. Berry, *Proc. Natl. Acad. Sci. USA* **78**, 7666 (2001).
43. T. Komatsuzaki and R. S. Berry, *J. Chem. Phys.* **115**, 4105 (2001).
44. T. Komatsuzaki and R. S. Berry, *Adv. Chem. Phys.* **123**, 79 (2002).
45. T. Komatsuzaki and R. S. Berry, *J. Phys. Chem. A* **106**, 10945 (2002).
46. J. R. Carry, *Phys. Rep.* **79**, 130 (1981).
47. A. J. Lichtenberg and M. A. Lieberman, *Regular and Chaotic Dynamics*, 2nd ed., Springer, New York, 1992.
48. L. E. Fried and G. S. Erza, *J. Chem. Phys.* **90**, 6378 (1989).
49. T. Komatsuzaki and M. Nagaoka, *J. Chem. Phys.* **105**, 10838 (1996).
50. T. Komatsuzaki and M. Nagaoka, *Chem. Phys. Lett.* **265**, 91 (1997).
51. R. Hernandez and W. H. Miller, *Chem. Phys. Lett.* **214**, 129 (1993).
52. R. Hernandez, *J. Chem. Phys.* **101**, 9534 (1994).

53. S. Wiggins, *Normally Hyperbolic Invariant Manifolds in Dynamical Systems*, Springer-Verlag, New York, 1991.
54. T. Uzer, C. Jaffé, J. Palacián, P. Yanguas, and S. Wiggins, *Nonlinearity* **15**, 957 (2002).
55. M. Zhao, J. Gong, and S. A. Rice, *Adv. Chem. Phys. Part A* **130**, 3 (2005).
56. M. Toda, *Adv. Chem. Phys. Part A* **130**, 337 (2005).
57. L. Wiesenfeld, *Adv. Chem. Phys. Part A* **130**, 217 (2005).
58. T. Uzer, C. Jaffe, S. Kawai, J. Palacian, and P. Yanguas, *Adv. Chem. Phys. Part A* **130**, 171 (2005).
59. T. Komatsuzaki, K. Hoshino, and Y. Matsunaga, *Adv. Chem. Phys. Part B* **130**, 257 (2005).
60. R. Hernandez and W. H. Miller, *Chem. Phys. Lett.* **214**, 129 (1993).
61. J. Villa and D. G. Truhlar, *Theor. Chem. Acc.* **97**, 317 (1997).
62. R. Zwanzig, *J. Stat. Phys.* **9**, 215 (1973).
63. G. van der Zwan and J. T. Hynes, *J. Chem. Phys.* **78**, 4174 (1983).
64. E. Pollark, *Chem. Phys. Lett.* **127**, 178 (1986).
65. S. S. Plotkin and P. G. Wolynes, *Phys. Rev. Lett.* **80**, 5015 (1998).
66. J. Higo, M. Sasai, H. Shirai, H. Nakamura, and T. Kugimiya, *Proc. Natl. Acad. Sci. USA* **98**, 5961 (2001).
67. T. Yokomizo, S. Yagihara, and J. Higo, *Chem. Phys. Lett.* **374**, 453 (2003).
68. R. B. Shirts and W. P. Reinhardt, *J. Chem. Phys.* **77**, 5204 (1982).
69. R. B. Shirts and W. P. Reinhardt, *J. Chem. Phys.* **79**, 3173 1983).
70. L. Wiesenfeld, *J. Phys. A: Math. Gen.* **37**, 143 (2004).
71. C. C. Martens, M. J. Davis, and G. S. Ezra, *Chem. Phys. Lett.* **142**, 519 (1987).
72. J. C. Losada, J. M. Estebaranz, and R. M. Benito, *J. Chem. Phys.* **108**, 63 (1998).
73. L. V. Vela-Arevalo and S. Wiggins, *Int. J. Bifurc. Chaos* **11**, 1359 (2001).
74. A. J. Dragt and J. M. Finn, *J. Math. Phys.* **17**, 2215 (1976).
75. A. J. Dragt and J. M. Finn, *J. Math. Phys.* **20**, 2649 (1979).
76. T. Komatsuzaki, K. Hoshino, Y. Matsunaga, G. J. Rylance, R. L. Johnston, and D. J. Wales, submitted for publication.
77. S. Jang, M. Zhao, and S. A. Rice, *J. Chem. Phys.* **97**, 8188 (1992).
78. W. S. Koon, M. W. Lo, J. E. Marsden, and S. D. Ross, *Chaos* **10**, 427 (2000).
79. L. Sun, K. Song, and W. L. Hase, *Science* **296**, 875 (2002).

CHAPTER 3

A NEW LOOK AT THE TRANSITION STATE: WIGNER'S DYNAMICAL PERSPECTIVE REVISITED

CHARLES JAFFÉ

Department of Chemistry, West Virginia University, Morgantown, West Virginia 26506-6045, USA

SHINNOSUKE KAWAI

Department of Chemistry, Graduate School of Science, Kyoto University, Sakyo-ku, Kyoto 606-8502, Japan

JESÚS PALACIÁN and PATRICIA YANGUAS

Departamento de Matemática e Informática, Universidad Pública de Navarra, 31006, Pamplona, Spain

TURGAY UZER

Center for Nonlinear Sciences, School of Physics, Georgia Institute of Technology, Atlanta, GA 30332-0430, USA

CONTENTS

I. Introduction: Wigner's "Three Threes"
II. Brief History of Transition State Theory
III. Saddles in Energy Landscapes
    A. Phase Space Versus Coordinate Space
    B. Stability

Geometric Structures of Phase Space in Multidimensional Chaos: A Special Volume of Advances in Chemical Physics, Part A, Volume 130, edited by M. Toda, T Komatsuzaki, T. Konishi, R.S. Berry, and S.A. Rice. Series editor Stuart A. Rice.
ISBN 0-471-70527-6

C. Energy Landscapes in Phase Space
IV. Phase-Space Structure Around a Simple (Rank-One) Saddle
A. Justification of the *n*-Degree-of-Freedom Hamiltonian
B. Finding the "Apt" Coordinates Around a Saddle Using a Normal Form
C. Normally Hyperbolic Invariant Manifolds (NHIMs) and Their Stable and Unstable Manifolds
D. The Transition State
E. Searching for the Transition State and Other Phase-Space Structures
F. Flux Through the Transition State
V. Normalization by Lie Transformations
A. Lie Transformations
B. Dynamics Near the Transition State Using the Normal-Form Coordinates
VI. The Isomerization of HCN
A. The Model System
B. The Hamiltonian
C. Points of Stationary Flow
D. Preparation for Transformation to the Normal Form
E. Transformation to the Normal Form
F. Visualization of the HCN Dynamics
G. The Quantization of the Nonreactive Degrees of Freedom
VII. Summary and Outlook
Acknowledgments
References

I. INTRODUCTION: WIGNER'S "THREE THREES"

The proper departure point for a discussion of the transition state (TS) are the proceedings of the lively 67th General Discussion of the Faraday Society [1]. In his admirable summary of this Discussion, given during the Spiers Memorial Lecture of the 110th Faraday Discussion of 1998 [2], W. H. Miller recounts how two distinct points of view emerged on rates of chemical reaction from the discussions of the 67th meeting: Eyring's thermodynamic picture and Wigner's dynamical perspective, which, in the decades between the 1930s and 1970s was buried by the enormous numbers of applications of the thermodynamic picture [3]. In his perceptive article [4], Wigner gave a clear outline of the subject in terms of his "Three Threes" [2]. First there were the three steps in the theory of kinetics: (1) constructing the potential energy surface, (2) calculating the rates of elementary reactions, and (3) combining many elementary reactions into a complex reaction mechanism. Next came the three groups of elementary reactions, and finally there were the three assumptions of Transition State Theory (TST): (1) no electronically nonadiabatic transitions, (2) validity of classical mechanics for the nuclear motion, and (3) the existence of a dividing surface, separating the reactants and products, that no classical trajectory passes through more than once. Wigner noted that the failure of the last assumption will lead, in

general, to values of the reaction rate that are too large. Wigner's formulation quickly leads to the recognition that the TS is actually a general property of all dynamical systems, provided that they evolve from ''reactants'' to ''products.'' The TS, therefore, is not confined to chemical reaction dynamics [2], but it also controls rates in a multitude of interesting systems, including, for example, the rearrangements of clusters [5], the ionization of atoms [6,7], conductance due to ballistic electron transport through microjunctions [8], diffusion jumps in solids [9], and statistical rates of asteroid capture [10]. With the reemergence of Wigner's dynamical approach to TST [4,11,12], the search for these no-recrossing surfaces has been pursued vigorously, leading researchers to dynamical systems theory [13,14] through the intermediate stages of variational TST [15] and PODS [16,17]. Despite this effort, the no-recrossing rule has been ''more honored in its breach than its observance.'' The formalism presented here addresses this issue by constructing the dynamically correct higher-dimensional geometrical structures in phase space that regulate transport between qualitatively different states (''reactants'' and ''products''). The salient features of this new formulation are as follows:

- It is a phase space rather than configuration space theory, so it can treat Hamiltonian systems containing unconserved angular momenta like Coriolis interactions which prevent the Hamiltonian from being written as a sum of the kinetic and potential energies [6,18]. The resulting hypersurfaces are dynamical in that they involve momenta as well as coordinates.
- It is designed for multidimensional systems. This is a qualitative difference from the existing formulations which attempt to extrapolate to three or more degrees of freedom (DOF) geometrical methods that work for systems with two DOFs.
- The TS it produces is locally a surface of no return.
- It identifies impenetrable barriers [19] which, by acting as phase-space ''scissors'' [20], cut phase space into hypervolumes of initial conditions that are destined to react and those which cannot.
- It is a ''top-down'' approach in providing explicit recipes for all these geometrical structures, and it is presumably equivalent to the ''bottom-up'' approach of working through their manifestations in terms of ensembles of trajectories [5].

Details of our approach, which is reviewed in Sections IV and V, can be found in the original article [21]. Two of the most striking features of our solution, namely the recrossing-free TS and the identification and construction of the multidimensional separatrices, are illustrated in Figs. 1, 2, and 3.

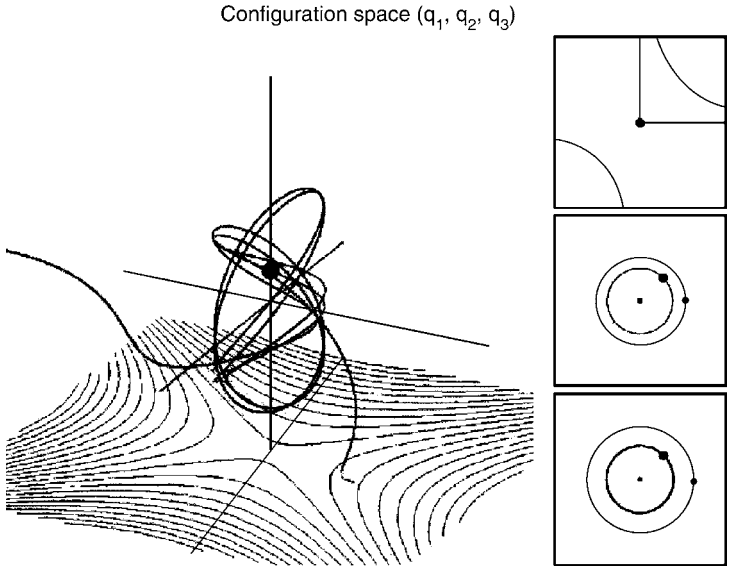

Figure 1. (The color version is available from the authors.) The trajectory of an electron ionizing under the influence of crossed electric and magnetic fields [18,21]. The line passing through the saddle point shows the projection of the conventional transition state, which is a vertical plane. Of course the trajectory can cross this plane many times. We cannot display our true TS, which is a complicated four-dimensional object, but we note that it is intersected only once, namely at the dot. The right-hand panels show the same trajectory in the three normal-form coordinates (see Section F).

This account is organized as follows: After briefly reviewing the history of TST, we present a pedagogical discussion of the geometry of the TS. This is followed by the rigorous mathematical theory of the geometry of higher-dimensional saddles and their associated separatrices in the context of the theory of normally hyperbolic invariant manifolds (NHIMs) [22]. We begin by showing that near an equilibrium point consisting of a reactive direction and several nonreactive (''bath'') directions (technically of the saddle $\otimes$ center $\otimes \cdots \otimes$ center stability type) the Hamiltonian can be transformed to a normal form [13] from which the NHIM, its stable and unstable manifolds, and the TS are straightforward to obtain analytically. Moreover, if the center (or bath) vibrations are nonresonant, the normal form, truncated at any finite order, is integrable. The theory leads to an algorithm for identifying the TS (and other geometrical structures) analytically. Finally, we apply this formalism to the isomerization of HCN. In this process we identify the center manifold as the activated complex and demonstrate how it can be quantized to obtain the quantized thresholds first discussed by Chatfield et al. [23] and subsequently observed [24,25].

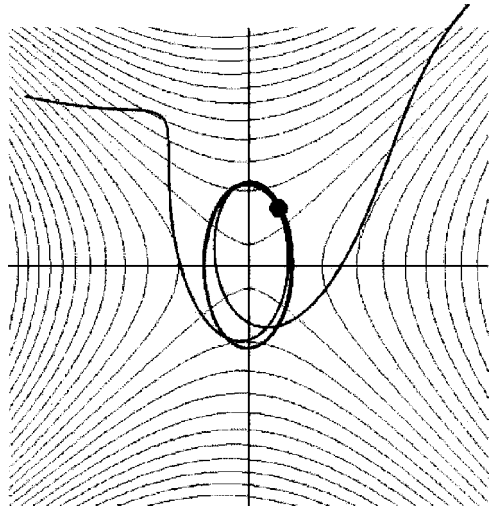

Figure 2. (The color version is available from the authors.) Two-dimensional configuration-space projection of the trajectory of the previous figure. The projection of the conventional TS in configuration space is the vertical axis. The trajectory crosses it many times. Our new TS is intersected only once, namely at the dot in the upper right-hand side of the ellipse.

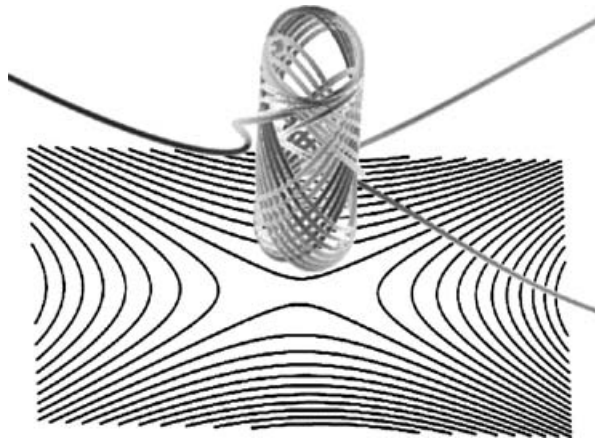

Figure 3. (The color version is available from the authors.) Two electron trajectories, so close in phase space that they appear as one, approach the ionization saddle [6] from the top right. After some complex dynamics at the saddle point, one reacts (by crossing the TS at the dot in the upper left-hand corner of the bundle) and goes off to the top left, and the nonreactive one returns to the bottom right. We engineered this outcome by selecting their initial conditions on opposite sides of the impenetrable phase-space barrier (one of the ''scissors'' [20]) between ionizing and nonionizing hypervolumes.

II. BRIEF HISTORY OF TRANSITION STATE THEORY

The idea of the existence of a boundary between ''reactants'' and ''products'' can be traced to the scientific memoirs of Marcelin published in 1915 [26]. It was not until 1931 that this idea began to percolate into the thinking of the chemistry community. In that year Eyring and Polanyi published their seminal article on the calculation of the absolute reaction rate for the collinear $H + H_2$ reaction [27]. It was in this article, which must be viewed as the origin of the modern theory of chemical reactions, that the concept of a TS separating reactants from products is first quantified. They defined it in terms of the morphology of the potential energy surface.

The impact of this idea was immense. Six years later, the 67th General Discussion of the Faraday Society addressed this subject under the guise of Reaction Kinetics [1]. This Discussion, which has been alluded to above, set the stage for the further development of these ideas and the general acceptance of them by the chemistry community at large. By this point, two distinct approaches to TST had developed. The first one, primarily due to Eyring [3,28], was based in thermodynamics. Here the idea was to develop the quantities of interest from a thermodynamic perspective and then to evaluate the thermodynamic quantities in terms of simple molecular models. The second approach, advocated by Wigner [4,11,12,29], was to calculate quantities of interest directly from the dynamics. When properly implemented, both approaches are expected to be equivalent.

In the decades following this Discussion, the majority of the progress made in the development and application of TST followed the thermodynamic path [30,31]. To a large extent, this was due to the nature of the difficulties encountered when following the dynamical path. The first of these was the fact that the technology needed to numerically investigate the dynamics simply did not exist. Furthermore, the theory of dynamical systems, despite the efforts of Poincaré [32], was still in a primitive state. In the early 1970s, when interest in the classical mechanics was rekindled by the quest for quantum chaos [33,34], attention was again focused upon the dynamical version of TST. The variational TST together with the identification of the ''periodic orbit dividing surfaces'' or PODS (both singular and plural) [16,17,35–37] were just the initial steps in this reawakening of interest.

The central idea in the variational treatment of TST [15,38,39] is to consider all possible dividing surfaces that partition coordinate space into two separate regions, one associated with reactants and the other with products. One then considers the flux across each of these surfaces and chooses the surface with the minimum flux as the TS. The logic is as follows: We are interested in the rate at which states cross the TS. If, during the course of a reaction, the trajectory of each initial reactant state only crosses the TS once, then the rate of reaction can

be determined by simply counting the number of crossings of the TS—that is, the flux across the TS. However, if there are recrossings of the TS, then simply counting the number of crossings will overestimate the true rate.

Pechukas argued that there exists a set of periodic orbits whose projections into coordinate space, which he calls PODS, are solutions to the variational problem [35,36,40]. The projections of these orbits touch the equipotentials of the potential energy at two different points. At each of these points the trajectory is reflected and retraces its path in coordinate space. Pechukas recognized that the principle of least action for such a periodic orbit implied that it was a solution to the variational TS problem. Pechukas' work is particularly significant, despite shortcomings due to the formulation of the variational principle in coordinate space, since it refocused attention on the dynamical aspect of TST. The shortcomings of Pechukas' approach are reflections of problems with the formulation of variational principle. The most fundamental of these is that the TS is defined in coordinate space and not in the state space, that is, phase space. While this does not pose significant difficulties for systems having just two DOFs, it has prevented the extension of Pechukas' results to higher-dimensional systems. Recently, Jaffé et al. [6,18] have shown how to apply Pechukas' approach to the ionization of hydrogen atom in crossed static electric and magnetic fields. Due to the presence of the magnetic field, the Hamiltonian of this system cannot be divided into the kinetic and potential energy, and consequently it would appear that Pechukas' formalism, which requires the existence of a potential energy, will fail. However, Jaffé et al. [6,18] show that in this case Pechukas' approach works provided the dynamics are projected into a different (two-dimensional) plane.

In the 1970s with the introduction of more sophisticated computer technology, one of the primary difficulties facing the scientist wishing to investigate the dynamics of realistic model systems vanished. It now became possible not only to investigate numerically the dynamics of reactive systems, but it also become possible to implement a number of important tools such as Poincaré's surface of section. This set the stage for the next development, that of the advancement of the theory of dynamical systems. Many examples can be cited. Of particular interest is the work of MacKay, Meiss, and Percival [41] concerning the existence of cantori acting as space barriers in the vicinity of the last surviving torus. Davis and co-workers applied these ideas to chemical reactions [42–44]. Similarly, Tiyapan and Jaffé [45–47] demonstrated that in the formation of complexes, the homoclinic tangle associated with the periodic orbit defining the TS imposes an invariant fractal structure upon the energy shell and that the asymptotic scaling laws of this fractal are related to the long time behavior. Unfortunately, these, and many other efforts, rely heavily on techniques only applicable to systems with two DOFs and consequently are not readily extendable to systems with more DOFs.

Despite these difficulties, significant progress was made. In particular, it was observed that something remarkable happens to the dynamics near a saddle. No matter how complicated the motion is leading up to the saddle, at the saddle it becomes simpler only to become more complicated once more as the system leaves the saddle region. The reason for this striking simplification has been explained by Miller [48]: Simply put, at a saddle, the potential consists of an inverted parabola in the reaction coordinate and ordinary parabolas in the bath directions. Technically speaking, the frequency is imaginary in the reactive direction and real in the bath directions, and since there cannot be a resonance between imaginary and real frequencies, whatever couplings there may be cannot be effective, thereby isolating the reactive direction from the bath modes and, in simple cases, making the dynamics in the reaction direction integrable [48–51].

The dynamics near the TS have been the subject of many theoretical [52–66] and experimental [24,25] investigations. The experiments of Lovejoy and co-workers [24,25] see the TS via the photofragment excitation spectra for unimolecular dissociation of excited ketene. They have shown that, in the vicinity of the barrier, the reaction rate is controlled by the flux through quantized thresholds. The observability of quantized thresholds in the TS was first discussed by Chatfield et al. [23]. Marcus pointed out that this indicates that the transverse vibrational quantum numbers might indeed be approximate constants of the motion in the saddle region [60].

During the same period, Berry and co-workers were exploring the non-uniformity of the dynamical properties of Hamiltonian systems representing atomic clusters with up to 13 atoms. In particular, they explored how regular and chaotic behavior may vary locally with the topography of the potential energy surfaces (PES) [53,54,57,58,61–63,65,66]. By analyzing local Lyapunov functions and Kolmogorov entropies, they showed that when systems have just enough energy to go through the TS, the system's trajectories become collimated and regularized through the TS regions, developing approximate local invariants of the motion different from those in the potential well. This happens even though the dynamics in the potential well is fully chaotic under these conditions. They also showed that at higher energies above the threshold, intermode mixing wipes out these approximate invariants of the motion even in the region of the TS [5].

Recently, Komatsuzaki and co-workers have investigated regularity observed in the vicinity of the TS in many-body systems [5,67–74]. They used Lie transformations [75,76] together with microcanonical molecular dynamics simulations of the region near a potential energy saddle point. They construct a nonlinear transformation that ''rotates away'' the recrossings and irregular behavior. Using the intramolecular proton transfer reaction in malonaldehyde [67,68] and the isomerization of a simple cluster of six argon

atoms [69–73], they showed that this separation of the dynamical modes persists up to energies well above the onset of chaos in the TS. In other words, they observed that the action associated with the reaction coordinate remains an approximate invariant of the motion throughout the region of the TS. Moreover, they demonstrated that it is possible to choose a multidimensional phase-space dividing surface satisfying the dynamical requirement of TST [69]. They ''visualized'' the dividing surface in phase space by constructing the projections onto smaller subspaces, revealing how the shape of the reaction bottleneck depends on the energy of the system and the passage velocity through the TS and how the complexity of the recrossings emerges over the saddle in the configuration space [70,71]. Using this visualization, they further showed that changing the energy of the dynamics results in the dividing surfaces ''migrating'' just as the PODS do.

We have taken the opposite, top-down approach by asking what the structures based on a simple rank-one saddle look like for a general Hamiltonian. Indeed, in the early 1990s the Wiggins group [14,22] investigated the geometry associated with certain types of stationary points in phase space. They proved the existence of NHIMs in the vicinity of these stationary points. With these results and with the technology of Lie–Deprit transforms [75,76], we have been able to reformulate the definition of the TS in terms of the geometrical objects that lie in the vicinity of the phase-space barrier or saddle. A consequence of the phase space geometry in the vicinity of the stationary point is that the Hamiltonian can be transformed into a known normal form. It is this normal form that is responsible for the separation between the dynamics in the reactive mode from those in the internal modes. This is reflected in the equations of motion when they transformed into the normal-form variables. There are classical trajectories that remain in the vicinity of the stationary point for all time. These trajectories lie on a $(2n-2)$-dimensional invariant manifold called the center manifold. This manifold is of fundamental importance in the phase-space formulation of TST because it corresponds to the activated complex.

Moreover, the intersection of the center manifold with an energy shell yields an NHIM. The NHIM, which is a $(2n-3)$-dimensional hypersphere, is the higher-dimensional analog of Pechukas' PODS. Because this manifold is normally hyperbolic, it will possess stable and unstable manifolds. These manifolds are the $(2n-2)$-dimensional analogs of the separatrices. The NHIM is the edge of the TS, which is a $(2n-2)$-dimensional hemisphere.

In the next two sections we will review the mathematical foundations of the phase space formalism. This is followed in Section V by a discussion of how the Hamiltonian is transformed into normal form; finally in the last section, in order to illustrate these concepts, we quantize semiclassically the TS for the isomerization of HCN.

III. SADDLES IN ENERGY LANDSCAPES

Our intuition in the study of reaction dynamics is largely based upon our understanding of the "geography" of simple two-dimensional potential energy surfaces. While this basis has proven very useful, it also has produced a false sense of security. The very simplicity of the geometry a two-dimensional potential energy surface can lead one into difficulties that only arise in higher-dimensional systems. Similar problems are encountered in 2-DOF systems. The ionization of Rydberg atoms in the presence of external electromagnetic fields provides an excellent example [6,18]. The complication that occurs is that in the presence of the electromagnetic fields the Hamiltonian can no longer be partitioned into the kinetic and potential energies. Consequently, it is not possible to define the TS in terms of the morphology potential energy surfaces, but instead must be defined in terms of the geometry of the total energy surface.

The difficulty is that we have trained ourselves to think of potential energy surfaces defined on n-dimensional coordinate spaces. Instead we should be thinking of the total energy defined on the $2n$-dimensional phase space. The method of analysis for the total energy is essentially the same as is used for the potential energy surface. The first step is to identify the stationary points (extrema) and their linear stabilities. Once these points are found and characterized, the machinery of geometrical mechanics can be applied to obtain the invariant manifolds and their stable and unstable manifolds associated with the stationary points. Using these geometrical constructs, phase space can be partitioned into reactive and nonreactive regions, and such physically interesting properties as the rate of reaction or branching ratios can be obtained from the geometry.

Finding and characterizing the stationary states of systems with more than two DOFs is an unsolved problem. Isolated stationary points are the best known of these manifolds. In systems with two DOFs, in addition to isolated stationary points, it is also possible to find a closed loop of stationary points [77]. These are associated with parabolic resonances. More complicated manifolds will exist in systems having more than two DOFs. In the present discussion we will focus on the consequences of the existence of isolated points of stationary flow in phase space.

A. Phase Space Versus Coordinate Space

In the coordinate-space treatment of TST, certain assumptions must be made concerning the nature of the Hamiltonian of the system. First, it must be assumed that it can be partitioned into the sum of two terms, the kinetic and the potential energy. Furthermore, one must also assume that the kinetic energy is positive definite and is quadratic in the momenta. With these assumptions, then the point of stationary flow in phase space and the saddle point of the potential energy

coincide. That is, the conditions placed on the kinetic energy guarantee that the momenta characterizing the point of stationary flow are equal to zero; consequently, the coordinate space configuration of this point must be such that the various forces are balanced. In other words, that it is extremum of the potential energy.

A major difference between phase and coordinate space is that phase space is a state space; that is, each point corresponds to a unique state of the system, whereas a point in coordinate space determines only the physical configuration of the system. Mathematical consequences of this seemingly small difference are remarkable. First, the metric in phase space corresponds to a volume. The physical interpretation of this volume as the number of states follows from the fact that phase space is a state space. On the other hand, in the coordinate space treatment, the metric provides us with a way of measuring the ''distance'' between two physical configurations. This difference in the metric results in a significant difference in the nature of the questions that can be addressed. In the phase-space treatment we construct probabilities that certain events occur by considering ratios of phase-space volumes. The rates at which these events occur are readily obtained as fluxes across boundaries between phase-space volumes. And in coordinate space one focuses primarily on the rate at which the coordinate space configuration changes.

The coordinate space approach to TST encounters a number of significant problems. The most serious of these concerns the definition of the TS. A ''rigorous'' definition of the TS only exists for systems with two DOFs. Efforts at extending this definition to systems with three or more DOFs have not been successful. A similar difficulty occurs when the distinction between the kinetic and potential energy is lost. Jaffé et al. [6,18] have shown that this particular difficulty can be avoided by the judicious choice of a different coordinate space. They argue that the TS must be defined in phase space and that if this object is projected into the appropriate coordinate space, then the coordinate space formalism can be applied. From this the origin of these difficulties becomes apparent: The coordinate-space objects are shadows (projections) of the phase-space objects. Seen from this point of view, it is not surprising that difficulties are encountered when trying to extend the coordinate space formalism to systems with more than two DOFs.

B. Stability

The analysis of the stability of isolated stationary points is different in the phase-space treatment from that in the coordinate space treatment. In the coordinate space treatment the slope of the potential energy surface gives the forces exerted on the system. Stationary points occur at extrema of the potential energy. Their stability is determined by the eigenvalues of the matrix of second derivatives evaluated at the extremum. Assuming the system has n DOFs, it will possess n

eigenvalues. The stability of the extremum is determined by the number of eigenvalues greater than or less than zero. If all of the eigenvalues are positive, then the extremum is a minimum and it is stable against all perturbations. In contrast, when all of the eigenvalues are negative, then the extremum corresponds to a maximum and all perturbations are unstable. Clearly, the extremum can be characterized by the number of positive and negative eigenvalues it possesses. If it possesses m negative eigenvalues, it is said to be a rank-m saddle—that is, it is unstable in m DOFs and stable in the remaining $n - m$ DOFs.

In the analogous analysis in the phase-space treatment, one examines the stability matrix

$$\begin{pmatrix} \dfrac{\partial \dot{\boldsymbol{q}}}{\partial \boldsymbol{q}} & \dfrac{\partial \dot{\boldsymbol{q}}}{\partial \boldsymbol{p}} \\ \dfrac{\partial \dot{\boldsymbol{p}}}{\partial \boldsymbol{q}} & \dfrac{\partial \dot{\boldsymbol{p}}}{\partial \boldsymbol{p}} \end{pmatrix} = \begin{pmatrix} \dfrac{\partial^2 H}{\partial \boldsymbol{q} \partial \boldsymbol{p}} & \dfrac{\partial^2 H}{\partial^2 \boldsymbol{p}} \\ -\dfrac{\partial^2 H}{\partial^2 \boldsymbol{q}} & -\dfrac{\partial^2 H}{\partial \boldsymbol{q} \partial \boldsymbol{p}} \end{pmatrix}$$

evaluated at the point of stationary flow. The eigenvalues of this matrix occur in n pairs of numbers being either real or imaginary. A pair of imaginary eigenvalues corresponds to a stable DOF (elliptical), and a pair of real eigenvalues corresponds to an unstable DOF (hyperbolic). When both treatments are both valid, the eigenvalues of the coordinate treatment are equal to minus the square of eigenvalues of the corresponding phase-space treatment (assuming mass weighted coordinates).

The case when the eigenvalues are equal to zero is special and must be treated separately. One is tempted to assume that such cases are rare. In fact these cases occur when the manifolds of stationary flow are not isolated points. The simplest of these cases give rise to parabolic resonances [77]; however, they are beyond the scope of this review. These resonances have been observed in some of the simplest reactive systems [78].

C. Energy Landscapes in Phase Space

In the coordinate space formulation, one investigates the geometry of the potential energy surface, which is defined on the n-dimensional coordinate space. On this surface the minima are called potential wells. In turn, each of these wells are separated from each other by a rank-one saddle. The transport from one potential well to the next must pass over the saddle that separates them. The rate of a reaction is formulated in terms of the flux across the saddle. In systems with more than two DOFs, higher rank saddles occur. These occur when the boundaries of more than three or more potential wells coincide.

In the phase-space treatment the situation is very similar. However, rather than study the morphology of the potential energy surface, we must focus on the total energy surface. The geometry of this surface, which is defined on phase space instead of coordinate space, can also be characterized by its stationary points and their stability. In this treatment, the rank-one saddles play a fundamental result. They are, in essence, the traffic barriers in phase space. For example, if two states approach such a point and one passes on one side and the other passes on the other side, then one will be reactive and the other nonreactive. Once the stationary points are identified, then the boundaries between the reactive and nonreactive states can be constructed and the dynamical structure of phase space has been determined. As in the case of potential energy surfaces, saddles with rank greater than one occur, especially in systems with high symmetry between outcomes, as in the dissociation of ozone.

In the next section we will review the mathematical foundations of the phase space formalism.

IV. PHASE-SPACE STRUCTURE AROUND A SIMPLE (RANK-ONE) SADDLE

In this section we will develop the phase-space structure for a broad class of n-DOF Hamiltonian systems that are appropriate for the study of reaction dynamics through a rank-one saddle. For this class of systems we will show that on the energy surface there is always a higher-dimensional version of a ''saddle'' (an NHIM [22]) with codimension one (i.e., with dimensionality one less than the energy surface) stable and unstable manifolds. Within a region bounded by the stable and unstable manifolds of the NHIM, we can construct the TS, which is a dynamical surface of no return for the trajectories. Our approach is algorithmic in nature in the sense that we provide a series of steps that can be carried out to locate the NHIM, its stable and unstable manifolds, and the TS, as well as describe all possible trajectories near it.

A. Justification of the n-Degree-of-Freedom Hamiltonian

Consider a Hamiltonian of the following form:

$$\begin{aligned} H = &\sum_{i=1}^{n-1} \frac{\omega_i}{2}\left(p_i^2 + q_i^2\right) + \lambda q_n p_n + f_1(q_1, \ldots, q_{n-1}, p_1, \ldots, p_{n-1}, \mathscr{I}) \\ &+ f_2(q_1, \ldots, q_{n-1}, p_1, \ldots, p_{n-1}), \\ &(q_1, \ldots, q_n, p_1, \ldots, p_n) \in \mathbb{R}^{2n} \end{aligned} \tag{1}$$

Here $\mathscr{I} \equiv p_n q_n$ and f_1, f_2 are at least of third order; that is, they are responsible for the nonlinear terms, and $f_1(q_1, \ldots, q_{n-1}, p_1, \ldots, p_{n-1}, 0) = 0$. In the language

of reaction dynamics, the coordinates (q_n, p_n) are the reaction coordinates and the remaining coordinates are referred to as the bath coordinates. The corresponding Hamiltonian vector field is given by

$$\begin{aligned}
\dot{q}_i &= \frac{\partial H}{\partial p_i} = \omega_i p_i + \frac{\partial f_1}{\partial p_i} + \frac{\partial f_2}{\partial p_i} \\
\dot{p}_i &= -\frac{\partial H}{\partial q_i} = -\omega_i q_i - \frac{\partial f_1}{\partial q_i} - \frac{\partial f_2}{\partial q_i}, \qquad i = 1, \ldots, n-1 \\
\dot{q}_n &= \frac{\partial H}{\partial p_n} = \lambda q_n + \frac{\partial f_1}{\partial \mathscr{I}} q_n \\
\dot{p}_n &= -\frac{\partial H}{\partial q_n} = -\lambda p_n - \frac{\partial f_1}{\partial \mathscr{I}} p_n
\end{aligned} \tag{2}$$

Most realistic Hamiltonians with simple saddles do not appear in this form. In what follows, we show how to transform such a Hamiltonian into this form using Normal-Form theory [13]. The phase-space structures that form the subject of this review will then be expressed in terms of the normal-form coordinates $(q_1, \ldots, q_n, p_1, \ldots, p_n)$. Therefore, before analyzing Eq. (2) we show that any Hamiltonian vector field in the neighborhood of an equilibrium point of saddle $\otimes$ center $\otimes \cdots \otimes$ center type can be transformed to the form of Eq. (2).

B. Finding the "Apt" Coordinates Around a Saddle Using a Normal Form

Finding a coordinate system that minimizes the coupling between the DOFs has always been a natural aspiration in theoretical chemistry. The so-called reaction-path formalism is just such a procedure, as is the use of Normal-Form theory [13], which is our method of choice. Normal-Form theory gives us sufficient conditions for a Hamiltonian to be transformed into the form of Eq. (1) in the neighborhood of an equilibrium point of center $\otimes \cdots \otimes$ center $\otimes$ saddle type. This result is well known (see, e.g., Ref. 13). To summarize, first we perform a Taylor expansion of the Hamiltonian [Eq. (1)]:

$$H = H_2 + H_3 + H_4 + \cdots \tag{3}$$

where H_k is a homogeneous polynomial of degree k in q_1-$\cdots$-q_n-p_1-$\cdots$-p_n.

The quadratic part of the Hamiltonian, H_2, is given by

$$H_2 = \sum_{i=1}^{n-1} \frac{\omega_i}{2} (q_i^2 + p_i^2) + \lambda q_n p_n \tag{4}$$

We then transform the nonhyperbolic part of H_2 into complex coordinates:

$$z_j = q_j + ip_j, \qquad \bar{z}_j = q_j - ip_j, \quad j = 1, \ldots, n-1$$

In these coordinates H_2 becomes

$$H_2 = \sum_{j=1}^{n-1} \frac{\omega_j}{2} |z_j|^2 + \lambda q_n p_n \tag{5}$$

Moreover, H_k is made up of linear combinations of terms of the form

$$z_1^{k_1} \cdots z_{n-1}^{k_{n-1}} q_n^{k_n} \bar{z}_1^{\ell_1} \cdots \bar{z}_{n-1}^{\ell_{n-1}} p_n^{\ell_n} \tag{6}$$

where k_i, $\ell_i \geq 0$ and $k_1 + \cdots + k_n + \ell_1 + \cdots + \ell_n = k$.

The Poisson bracket between two scalar-valued functions, F and G, in these variables is given by

$$\{ F, G \} \equiv 2i \sum_{j=1}^{n-1} \left(\frac{\partial F}{\partial \bar{z}_j} \frac{\partial G}{\partial z_j} - \frac{\partial F}{\partial z_j} \frac{\partial G}{\partial \bar{z}_j} \right) + \frac{\partial F}{\partial q_n} \frac{\partial G}{\partial p_n} - \frac{\partial F}{\partial p_n} \frac{\partial G}{\partial q_n} \tag{7}$$

Now the map

$$\mathrm{ad}_{H_2}(\cdot) \equiv \{ \cdot, H_2 \} \tag{8}$$

is a linear map of the space of homogeneous polynomials of degree k into itself. Normal-Form theory [13] tells us that the only terms that cannot be removed from Eq. (3) at order k are those in the kernel of $\mathrm{ad}_{H_2}(\cdot)$. A simple calculation shows that

$$\begin{aligned} &\mathrm{ad}_{H_2} \left(z_1^{k_1} \cdots z_{n-1}^{k_{n-1}} q_n^{k_n} \bar{z}_1^{\ell_1} \cdots \bar{z}_{n-1}^{\ell_{n-1}} p_n^{\ell_n} \right) \\ &\quad = \left(i \sum_{j=1}^{n-1} \omega_j (k_j - \ell_j) + \lambda(\ell_n - k_n) \right) z_1^{k_1} \cdots z_{n-1}^{k_{n-1}} q_n^{k_n} \bar{z}_1^{\ell_1} \cdots \bar{z}_{n-1}^{\ell_{n-1}} p_n^{\ell_n} \end{aligned} \tag{9}$$

So we see that $z_1^{k_1} \cdots z_{n-1}^{k_{n-1}} q_n^{k_n} \bar{z}_1^{\ell_1} \cdots \bar{z}_{n-1}^{\ell_{n-1}} p_n^{\ell_n}$ is an eigenvector for $\mathrm{ad}_{H_2}(\cdot)$ with eigenvalue $i \sum_{j=1}^{n-1} \omega_j (k_j - \ell_j) + \lambda(\ell_n - k_n)$. Therefore terms of the form (6) cannot be removed if

$$i \sum_{j=1}^{n-1} \omega_j (k_j - \ell_j) + \lambda(\ell_n - k_n) = 0 \tag{10}$$

That we have arrived at the desired coordinate system in which q_n and p_n appear only as a product of each other in the Hamiltonian follows immediately from Eq. (10) since if that quantity is zero, then both the real and imaginary parts must be zero. The real part being zero implies that $k_n = \ell_n$. Therefore, from Eq. (6), the power on the q_n and p_n coordinates must be the same at any order. Note, however, that this argument merely shows that such a coordinate system exists which brings the Hamiltonian into the form of Eq. (1) *order by order*. Actually computing this coordinate transformation, which would bring an arbitrary Hamiltonian into the form of Eq. (1), is an additional technical problem that needs to be solved on each problem at hand. Note also that this is a local result valid in the neighborhood of the equilibrium point of center $\otimes \cdots \otimes$ center $\otimes$ saddle type. However, once the phase-space structure is established locally, it can be continued numerically outside of the local region.

It is well known (see, e.g., Ref. 13) that the normal form transformations do not converge in the sense that normalization to all orders generally does not yield a meaningful result. However, this is of no consequence for our purposes. We view the technique more as the input to a numerical method for realizing the NHIM, its stable and unstable manifolds, and the TS. In this sense the limitations of machine precision make normalization beyond a certain finite order meaningless. This is a local result valid in the neighborhood of the equilibrium point of center $\otimes \cdots \otimes$ center $\otimes$ saddle type. However, once the phase-space structure is established locally, it can be numerically continued outside of the local region.

If the $n-1$ frequencies ω_i are nonresonant, then the truncated normal form (at any order) is integrable. That is, the quantities $J_i = \frac{1}{2}\left(p_i^2 + q_i^2\right)$, $i = 1, \ldots, n-1$, and $\mathscr{I} = p_n q_n$ are integrals of the truncated normal form, and the Hamiltonian can be written as a function of these integrals. In these coordinates the quantity $\partial f_1 / \partial \mathscr{I}$ becomes a constant and the q_n-p_n component of Hamilton's equations becomes a simple, 2-DOF saddle. This implies that actions remain constant while passing through the saddle region—a situation that has been numerically observed in realistic examples [63,69].

C. Normally Hyperbolic Invariant Manifolds (NHIMs) and Their Stable and Unstable Manifolds

In the 2-DOF case, it is well known that the motion in the direction transverse to the reaction direction takes place on a periodic orbit, and this orbit forms the boundary of the PODS [17]. Beyond 2 DOF, the periodic orbit does not have the right dimensionality to be the boundary of the TS, and the NHIM takes its place. Normal hyperbolicity means that, under the linearized dynamics, the growth and decay rates of tangent vectors normal to the manifold (the "reaction") dominates the growth and decay of tangent vectors tangent to the manifold. Hence, NHIMs are higher-dimensional analogs of saddle points ("saddle spheres").

The dynamics occurs on the $(2n-1)$-dimensional energy surface given by

$$\mathscr{E}_h^{2n-1} = \Bigg\{ (q_1, \ldots, q_n, p_1, \ldots, p_n) \;\Bigg|\; \sum_{i=1}^{n-1} \frac{\omega_i}{2} \left(p_i^2 + q_i^2\right) + \lambda q_n p_n + f_1(q_1, \ldots, q_{n-1}, p_1, \ldots, p_{n-1}, \mathscr{I}) + f_2(q_1, \ldots, q_{n-1}, p_1, \ldots, p_{n-1}) = h = \text{constant} > 0 \Bigg\} \tag{11}$$

When $q_n = p_n = 0$ in Eq. (2), $\dot{q}_n = \dot{p}_n = 0$. Therefore $q_n = p_n = 0$ is a $(2n-2)$-dimensional invariant manifold for this problem. Its intersection with the $(2n-1)$-dimensional energy surface, denoted $\mathscr{M}_h^{2n-3}$, is given by

$$\mathscr{M}_h^{2n-3} = \Bigg\{ (q_1, \ldots, q_n, p_1, \ldots, p_n) \;\Bigg|\; q_n = p_n = 0, \sum_{i=1}^{n-1} \frac{\omega_i}{2} \left(p_i^2 + q_i^2\right) + f_2(q_1, \ldots, q_{n-1}, p_1, \ldots, p_{n-1}) = h = \text{constant} > 0 \Bigg\} \tag{12}$$

This is also the Hamiltonian of the activated complex. We will encounter it in Eq. (23) with the customary symbol $H^{\ddagger}$. Regardless of its stability properties or the size of the nonlinearity, Eq. (12) is always an invariant manifold. However, we are interested in the case when it is of the saddle type with stable and unstable manifolds. If the physical Hamiltonian is of the form of Eq. (1), then a preliminary, local transformation is not required. The manifold (12) is invariant regardless of the size of the nonlinearity. Moreover, it is also of saddle type with respect to stability in the transverse directions. This can be seen by examining Eq. (1). On $q_n = p_n = 0$ the transverse directions, (i.e., q_n and p_n), are still of saddle type (more precisely, they grow and decay exponentially).

Normally, hyperbolic invariant manifolds persist under perturbation [22]. If we are in the setting where the form of Eq. (1) must first be obtained by applying Normal Form theory, then we are restricted to a sufficiently small neighborhood of the equilibrium point. In this case the nonlinear terms are much smaller than the linear terms. Therefore, the sphere present in the linear problem becomes a deformed sphere for the nonlinear problem and still has $(2n-2)$-dimensional stable and unstable manifolds in the $(2n-1)$-dimensional energy surface since normal hyperbolicity is preserved under perturbations.

In the q_n-p_n phase portrait the trajectories that go from $p_n > q_n > 0$ (respectively $p_n < q_n < 0$) to $q_n > p_n > 0$ (respectively $q_n < p_n < 0$) are said to be the trajectories that undergo reaction (see Fig. 4). [Keep in mind that for nonlinear Hamiltonian systems this is a local picture valid near Eq. (12), that is,

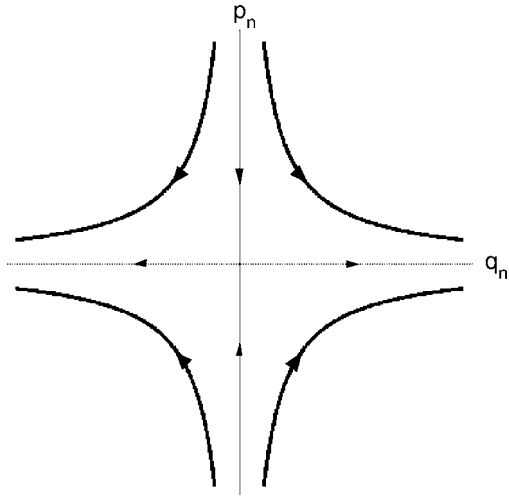

Figure 4. (The color version is available from the authors.) The projection of the reactive and nonreactive trajectories into the q_n-p_n plane near $q_n = p_n = 0$.

$q_n = p_n = 0$.] These are the trajectories with $q_n p_n > 0$ in Fig. 4. We can see from Fig. 4 that there are two types of *reactive trajectories*: those with q_n, $p_n > 0$, which are referred to as the *forward reactive trajectories*, and those with q_n, $p_n < 0$, which are referred to as the *backward reactive trajectories*. Notice that the q_n and p_n components of a reactive trajectory cannot change sign during their evolution. The trajectories with $q_n p_n < 0$ are referred to as *nonreactive trajectories*.

A key advantage of the normal form is that the stable and unstable manifolds of $\mathcal{M}_h^{2n-3}$ are known explicitly. These are the impenetrable barriers and act as phase-space "scissors." Their effect was illustrated in Fig. 3. They are given by

$$\begin{aligned} W^s\left(\mathcal{M}_h^{2n-3}\right) = \Bigg\{ & (q_1, \ldots, q_n, p_1, \ldots, p_n) \,\Big|\, q_n = 0, \\ & \sum_{i=1}^{n-1} \frac{\omega_i}{2}\left(p_i^2 + q_i^2\right) + f_2(q_1, \ldots, q_{n-1}, p_1, \ldots, p_{n-1}) \\ & = h = \text{constant} > 0 \Bigg\} \\ W^u\left(\mathcal{M}_h^{2n-3}\right) = \Bigg\{ & (q_1, \ldots, q_n, p_1, \ldots, p_n) \,\Big|\, p_n = 0, \\ & \sum_{i=1}^{n-1} \frac{\omega_i}{2}\left(p_i^2 + q_i^2\right) + f_2(q_1, \ldots, q_{n-1}, p_1, \ldots, p_{n-1}) \\ & = h = \text{constant} > 0 \Bigg\} \end{aligned} \tag{13}$$

Hence, the stable and unstable manifolds of the sphere have the structure of $\mathcal{M}_h^{2n-3} \otimes \mathbb{R}$.

In the language of dynamical systems theory, both the stable and unstable cylinders have two "branches" corresponding to $p_n > 0$ and $p_n < 0$, related to the forward and backward reactions.

The forward stable manifold of $\mathcal{M}_h^{2n-3}$ is given through

$$W_f^s(\mathcal{M}_h^{2n-3}) = \left\{ (q_1, \ldots, q_n, p_1, \ldots, p_n) \,\middle|\, q_n = 0,\ p_n > 0,\ \sum_{i=1}^{n-1} \frac{\omega_i}{2}(p_i^2 + q_i^2) + f_2(q_1, \ldots, q_{n-1}, p_1, \ldots, p_{n-1}) = h = \text{constant} > 0 \right\} \tag{14}$$

The backward stable manifold of $\mathcal{M}_h^{2n-3}$ is defined by

$$W_b^s(\mathcal{M}_h^{2n-3}) = \left\{ (q_1, \ldots, q_n, p_1, \ldots, p_n) \,\middle|\, q_n = 0,\ p_n < 0,\ \sum_{i=1}^{n-1} \frac{\omega_i}{2}(p_i^2 + q_i^2) + f_2(q_1, \ldots, q_{n-1}, p_1, \ldots, p_{n-1}) = h = \text{constant} > 0 \right\} \tag{15}$$

The forward unstable manifold of $\mathcal{M}_h^{2n-3}$ is

$$W_f^u(\mathcal{M}_h^{2n-3}) = \left\{ (q_1, \ldots, q_n, p_1, \ldots, p_n) \,\middle|\, q_n > 0,\ p_n = 0,\ \sum_{i=1}^{n-1} \frac{\omega_i}{2}(p_i^2 + q_i^2) + f_2(q_1, \ldots, q_{n-1}, p_1, \ldots, p_{n-1}) = h = \text{constant} > 0 \right\} \tag{16}$$

The backward unstable manifold of $\mathcal{M}_h^{2n-3}$ is given by

$$W_b^u(\mathcal{M}_h^{2n-3}) = \left\{ (q_1, \ldots, q_n, p_1, \ldots, p_n) \,\middle|\, q_n < 0,\ p_n = 0,\ \sum_{i=1}^{n-1} \frac{\omega_i}{2}(p_i^2 + q_i^2) + f_2(q_1, \ldots, q_{n-1}, p_1, \ldots, p_{n-1}) = h = \text{constant} > 0 \right\} \tag{17}$$

The stable and unstable manifolds of $\mathscr{M}_h^{2n-3}$ are indeed the natural higher-dimensional analogs of the 2-DOF "cylinder manifolds" described in Ref. 79.

D. The Transition State

There is some latitude in defining the TS. We obtain it by setting $q_n = p_n$. On the energy surface this gives

$$\begin{aligned}\mathscr{T}_h^{2n-2} = \Bigg\{ (q_1,\ldots,q_n,p_1,\ldots,p_n) \;\Bigg|\; & q_n = p_n, \\ & \sum_{i=1}^{n-1} \frac{\omega_i}{2}\left(p_i^2+q_i^2\right) + \lambda p_n^2 + f_1(q_1,\ldots,q_{n-1},p_1,\ldots,p_{n-1},p_n^2) \\ & + f_2(q_1,\ldots,q_{n-1},p_1,\ldots,p_{n-1}) = h = \text{constant} \Bigg\} \end{aligned} \tag{18}$$

This $(2n-2)$-dimensional surface is divided into two halves ($p_n > 0$ and $p_n < 0$) by $p_n = 0$, which corresponds to the invariant manifold $\mathscr{M}_h^{2n-3}$. If we are close to the equilibrium point so that the nonlinearity is small, then the transition state is a deformed $(2n-2)$-dimensional sphere. It can be proven that (18) is *locally* a surface of no return for the trajectories of Hamilton's equations given in Eq. (2). "Locally" it refers to a neighborhood of Eq. (18) such that trajectories starting on Eq. (18) (except those starting on the $(2n-3)$-dimensional invariant manifold (12)) must leave before they can possibly re-intersect Eq. (18) because the $(2n-2)$-dimensional invariant manifold in the energy surface is defined by $q_n = p_n$. If we examine Hamilton's equations (2), we see that the vector field is not tangent to Eq. (18). Moreover, the vector field is not zero on Eq. (18). Therefore trajectories starting on Eq. (18) always leave Eq. (18). By continuity of solutions with respect to initial conditions, they must leave a neighborhood of Eq. (18) before possibly returning.

The $(2n-2)$-dimensional $W^s\left(\mathscr{M}_h^{2n-3}\right)$ and $W^u\left(\mathscr{M}_h^{2n-3}\right)$ bound a region in the $(2n-1)$-dimensional energy surface that is divided into two components by the TS. All reacting trajectories start in one component, cross the TS, then enter the other component. On a fixed energy surface with energy value $h = \text{constant} > 0$, the reactant segments of the forward reactive trajectories are contained in the region

$$0 < \sum_{i=1}^{n-1} \frac{\omega_i}{2}\left(p_i^2+q_i^2\right) + f_2(q_1,\ldots,q_{n-1},p_1,\ldots,p_{n-1}) < h, \quad p_n > q_n > 0 \tag{19}$$

and the reactant segments of the backward reactive trajectories are contained in the region

$$0 < \sum_{i=1}^{n-1} \frac{\omega_i}{2}\left(p_i^2 + q_i^2\right) + f_2(q_1, \ldots, q_{n-1}, p_1, \ldots, p_{n-1}) < h, \quad p_n < q_n < 0 \tag{20}$$

In Fig. 5 we illustrate a forward and backward reacting trajectory. Besides, in Fig. 6 we illustrate just the reactant segment of the forward and backward reacting trajectory shown in Fig. 5, whereas in Fig. 7 we illustrate the product segments of the forward and backward reacting trajectory shown in Fig. 5.

Now consider a forward reacting trajectory (i.e., $p_n > 0,\ q_n > 0$). It follows, by examining the q_n–p_n phase portrait in Fig. 5, that the p_n component of the trajectory decreases. It touches the line $q_n = p_n$, at which point it has reached the TS as defined in Eq. 18. It then crosses the TS.

E. Searching for the Transition State and Other Phase-Space Structures

As mentioned above, we can obtain all these phase-space structures in explicit form following these steps:

1. For a given Hamiltonian, find an equilibrium point for which the linearization about the equilibrium point yields the form described in

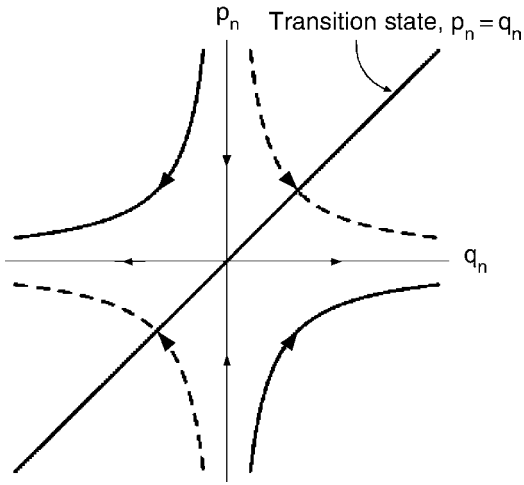

Figure 5. (The color version is available from the authors.) The projection of a forward and backward reactive and nonreactive trajectories into the q_n–p_n plane.

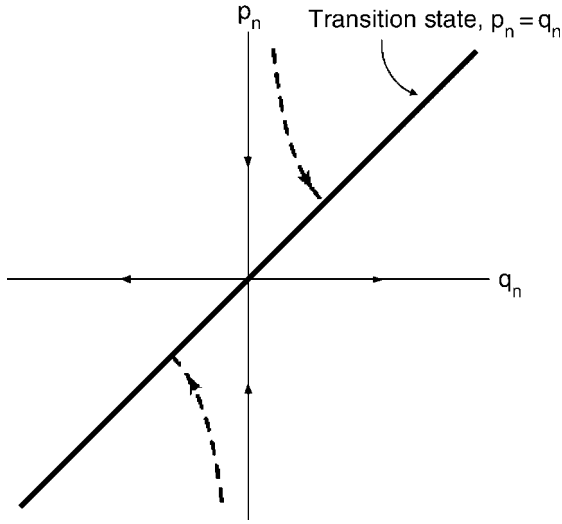

Figure 6. (The color version is available from the authors.) The projection of the reactant segment of the forward and backward reactive trajectory shown in Fig. 5 into the q_n–p_n plane.

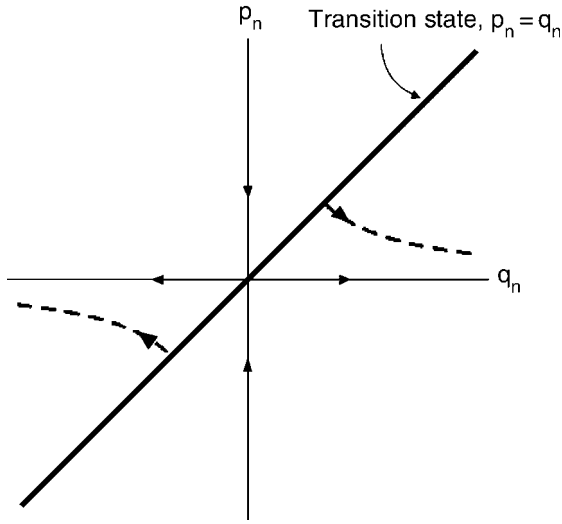

Figure 7. (The color version is available from the authors.) The projection of the product segment of the forward and backward reactive trajectories shown in Fig. 5 into the q_n–p_n plane.

Eq. (4). We have not yet developed the theory for saddles higher than rank one.

2. Transform the Hamiltonian to the normal form described above up to the desired degree of accuracy using a symbolic manipulator. The Hamiltonian is now in a new coordinate system that we will call the "normal form coordinates."
3. Identify the TS [Eq. (18)] and the higher-dimensional analogs of the stable and unstable manifolds that describe the reaction in the normal-form coordinates.
4. These structures can be visualized in the original coordinates by operating the normal-form transformations in reverse.
5. Integrals of flux across the TS can be computed in the normal-form coordinates since the transformation between the original coordinates and the normal-form coordinates is symplectic, hence volume preserving.

F. Flux Through the Transition State

The flux through the TS is important in reaction dynamics since the reaction rate can be obtained by dividing this flux by the appropriate partition function [35]. Specifically, the classical canonical reaction rate is given by [80]

$$k_{\mathrm{cl}}(T) = Q_{\mathrm{r}}(T)^{-1}(2\pi\hbar)^{-n}\int d\mathbf{p}\, d\mathbf{q}\, \mathrm{e}^{-\beta H(\mathbf{p},\mathbf{q})}F(\mathbf{p},\mathbf{q})P_{\mathrm{r}}(\mathbf{p},\mathbf{q}) \tag{21}$$

where $(\mathbf{p},\mathbf{q})$ are the totality of the phase-space coordinates [i.e., $\mathbf{q} = (q_1,\ldots,q_n)$ and $\mathbf{p} = (p_1,\ldots,p_n)$], and $F(\mathbf{p},\mathbf{q})$ is the flux factor across TS—that is, the rate at which trajectories cross the dividing surface [80], specified in our case by $s(\mathbf{p},\mathbf{q}) = p_n + q_n$. The term $P_{\mathrm{r}}(\mathbf{p},\mathbf{q})$ selects the forward reactive trajectories. To work on the energy surface, we rewrite the integral slightly to read

$$k_{\mathrm{cl}}(T) = Q_{\mathrm{r}}(T)^{-1}(2\pi\hbar)^{-n}\int dE\, \mathrm{e}^{-\beta E}\int d\mathbf{p}\, d\mathbf{q}\, \delta(H(\mathbf{p},\mathbf{q}) - E)F(\mathbf{p},\mathbf{q})P_{\mathrm{r}}(\mathbf{p},\mathbf{q}) \tag{22}$$

where the inner integral is the flux of energy surface volume across the forward TS. This flux through the TS turns out to be equal to the flux across its boundary [81], which is the NHIM. In practical terms, this means that δ function only contributes when the Hamiltonian H is evaluated at $\mathscr{I} = 0$, namely when it becomes the Hamiltonian [Eq. (12)] of the activated complex, $H = h =$ constant. If we use the symbol $H^{\ddagger}$ for the Hamiltonian function of the activated complex,

the partition function is

$$Q^{\ddagger}(T) = (2\pi\hbar)^{-(n-1)} \int d\mathbf{p}'\, d\mathbf{q}'\, \mathrm{e}^{-\beta H^{\ddagger}(\mathbf{p}',\mathbf{q}')} \tag{23}$$

(where the primed quantities exclude the reaction coordinates p_n, q_n) and the conventional TST result for the rate constant [35]

$$k_{\mathrm{cl}}(T) = \frac{kT}{(2\pi\hbar)} \frac{Q^{\ddagger}(T)}{Q_r(T)} \tag{24}$$

is recovered.

V. NORMALIZATION BY LIE TRANSFORMATIONS

A. Lie Transformations

Briefly, the aim of Lie transformations in Hamiltonian theory is to generate a symplectic (that is, canonical) change of variables depending on a small parameter as the general solution of a Hamiltonian system of differential equations. The method was first proposed by Deprit [75] (we follow the presentation in Ref. 76) and can be stated as follows.

We start with an analytic Hamiltonian function depending on a small parameter ε:

$$\mathscr{H}(\mathbf{x};\varepsilon) = \sum_{i=0}^{\infty} \frac{\varepsilon^i}{i!} \mathscr{H}_i(\mathbf{x})$$

where the Hamiltonians $\mathscr{H}_i(\mathbf{x})$ are analytic functions in the variable $\mathbf{x} = (x_1, \ldots, x_n, x_{n+1}, \ldots, x_{2n})$. Here x_i, $1 \le i \le n$ represent the coordinates whereas x_i, $n+1 \le i \le 2n$, are their conjugate momenta. Hamiltonian $\mathscr{H}$ is transformed into another Hamiltonian

$$\mathscr{K}(\mathbf{y};\varepsilon) = \sum_{i=0}^{\infty} \frac{\varepsilon^i}{i!} \mathscr{K}_i(\mathbf{y}) \equiv \sum_{i=0}^{\infty} \frac{\varepsilon^i}{i!} \mathscr{H}_0^{(i)}(\mathbf{y})$$

and $\mathbf{y} = (y_1, \ldots, y_n, y_{n+1}, \ldots, y_{2n})$ (where y_i, $1 \le i \le n$, refers to the transformed coordinates and y_i, $n+1 \le i \le 2n$, refers to the transformed conjugate momenta), through a generating function

$$\mathscr{W}(\mathbf{x};\varepsilon) = \sum_{i=0}^{\infty} \frac{\varepsilon^i}{i!} \mathscr{W}_{i+1}(\mathbf{x})$$

according to the recursion formula

$$\mathscr{H}_i^{(j)} = \mathscr{H}_{i+1}^{(j-1)} + \sum_{k=0}^{i} \binom{i}{k} \left\{ \mathscr{H}_{i-k}^{(j-1)}, \mathscr{W}_{k+1} \right\} \tag{25}$$

with $i \geq 0, j \geq 1$ and $\mathscr{H}_i^{(0)} = \mathscr{H}_i$ and $\{\cdot, \cdot\}$ denotes the Poisson bracket of two scalar fields; for example, given $\mathscr{P}$ and $\mathscr{Q}$ the Poisson bracket is defined over an open domain of $\mathbb{R}^{2n}$ as the quantity

$$\{\mathscr{P}, \mathscr{Q}\} = \sum_{i=1}^{n} \left(\frac{\partial \mathscr{P}}{\partial x_i} \frac{\partial \mathscr{Q}}{\partial x_{n+i}} - \frac{\partial \mathscr{P}}{\partial x_{n+i}} \frac{\partial \mathscr{Q}}{\partial x_i} \right)$$

or equivalently in terms of the variables $y_1, \ldots, y_{2n}$. We emphasize that $\mathscr{W}(\mathbf{x}; \varepsilon)$ is conserved under the transformation, and thus it can also be expressed as $\mathscr{W}(\mathbf{y}; \varepsilon)$. The recursion process can be summarized in the so-called Lie triangle (see Fig. 8).

Hence, Eq. (25) yields now the partial differential identity

$$\mathscr{K}_i - \mathrm{ad}_{\mathscr{H}_0}(\mathscr{W}_i) = \tilde{\mathscr{H}}_i \tag{26}$$

where $\tilde{\mathscr{H}}_i$ collects all the terms known from order $i-1$ and is computed using the recursive formula (25). In identity (26), called the homology equation, $\mathscr{W}_i$ and $\mathscr{K}_i$ must be determined according to the specific requirements of the Lie transformation that one performs.

$\mathcal{K}_0$		$\mathcal{K}_1$		$\mathcal{K}_2$		$\mathcal{K}_3$		$\mathcal{K}_4$	...
$\Vert$		$\Vert$		$\Vert$		$\Vert$		$\Vert$	...
$\mathcal{H}_0^{(0)}$		$\mathcal{H}_0^{(1)}$		$\mathcal{H}_0^{(2)}$		$\mathcal{H}_0^{(3)}$		$\mathcal{H}_0^{(4)}$	...
$\uparrow$	$\swarrow$	$\uparrow$	$\swarrow$	$\uparrow$	$\swarrow$	$\uparrow$	$\swarrow$	...	...
$\mathcal{H}_1^{(0)}$		$\mathcal{H}_1^{(1)}$		$\mathcal{H}_1^{(2)}$		$\mathcal{H}_1^{(3)}$	...	...	..
$\uparrow$	$\swarrow$	$\uparrow$	$\swarrow$	$\uparrow$	$\swarrow$	...	...	...	...
$\mathcal{H}_2^{(0)}$		$\mathcal{H}_2^{(1)}$		$\mathcal{H}_2^{(2)}$	...	..	...	...	..
$\uparrow$	$\swarrow$	$\uparrow$	$\swarrow$	...	..	...	...	...	...
$\mathcal{H}_3^{(0)}$		$\mathcal{H}_3^{(1)}$	...	..	...	...	...	...	...
$\uparrow$	$\swarrow$	...	...	...	...	...	...	..	...
$\mathcal{H}_4^{(0)}$	...	...	...	...	...	...	...	...	...

Figure 8. At each order $i \geq 1$ of the process, the diagonal $\mathscr{H}_j^{(k)}$ with $j + k = i$ is built starting with $\mathscr{H}_{i-1}^{(1)}$ and finishing with $\mathscr{H}_1^{(i-1)}$. Note that $\mathscr{H}_0^{(i)}$ cannot be determined unless $\mathscr{W}_i$ is previously known.

The transformation $\mathbf{x} = \mathbf{X}(\mathbf{y}; \varepsilon)$ relates the "old" variables $\mathbf{x}$ with the "new" ones $\mathbf{y}$ and is a near-identity change of variables. The direct change is given by

$$\mathbf{x} = \mathbf{y} + \sum_{i=1}^{\infty} \frac{\varepsilon^i}{i!} \mathbf{y}_0^{(i)} \tag{27}$$

The coordinates $\mathbf{y}_0^{(i)}$, $i \geq 1$ are calculated recursively with the aid of

$$\mathbf{y}_i^{(j)} = \mathbf{y}_{i+1}^{(j-1)} + \sum_{k=0}^{i} \binom{i}{k} \left\{ \mathbf{y}_k^{(j-1)}, \mathscr{W}_{i+1-k} \right\} \tag{28}$$

with $i \geq 0$, $j \geq 1$ and $\mathbf{y}_i^{(0)} \equiv 0$ for $i \geq 1$ and $\mathbf{y}_0^{(0)} \equiv \mathbf{y}$. Consequently, Eq. (27) gives the set of coordinates $\mathbf{x}$ in terms of $\mathbf{y}$ with the use of the generating function $\mathscr{W}$.

Similar formulae can be used to obtain the inverse transformation $\mathbf{y} = \mathbf{Y}(\mathbf{x}; \varepsilon)$, which explicitly reads as

$$\mathbf{y} = \mathbf{x} + \sum_{i=1}^{\infty} \frac{\varepsilon^i}{i!} \mathbf{x}_i^{(0)} \tag{29}$$

Now $\mathbf{x}_0^{(0)} \equiv \mathbf{x}$ and for $i \geq 1$ coordinates $\mathbf{x}_i^{(0)}$ are calculated recursively by means of

$$\mathbf{x}_i^{(j)} = \mathbf{x}_{i-1}^{(j+1)} - \sum_{k=0}^{i-1} \binom{i-1}{k} \left\{ \mathbf{x}_{i-k-1}^{(j)}, \mathscr{W}_{k+1} \right\} \tag{30}$$

with $i \geq 1$, $j \geq 0$. This time $\mathbf{x}_0^{(i)} \equiv 0$ for $i \geq 1$ and the Jacobians appearing in the operators of (30) are computed with respect to $\mathbf{x}$, and $\mathscr{W}_{k+1}$ is also written in $\mathbf{x}$.

Note that Eq. (27) can be used to transform any function expressed in the old variables $\mathbf{x}$ as a function of the new variables $\mathbf{y}$. Similarly, Eq. (29) is used to transform any function in $\mathbf{y}$ by a function of $\mathbf{x}$. In this respect we can compute a formal integral of the original system by going back to the departure system. Specifically if the normal form calculations have been carried out to an order $M > 1$, then we determine $T^*(\mathbf{x}; \varepsilon)$ as

$$T^*(\mathbf{x}; \varepsilon) = T(\mathbf{x}) + \sum_{i=1}^{M} \frac{\varepsilon^i}{i!} T(\mathbf{x})_i^{(0)} \tag{31}$$

where $T(\mathbf{x})_i^{(0)}$ are calculated using

$$T(\mathbf{x})_i^{(j)} = T(\mathbf{x})_{i-1}^{(j+1)} - \sum_{k=0}^{i-1} \binom{i-1}{k} \left\{ T(\mathbf{x})_{i-k-1}^{(j)}, \mathscr{W}_{k+1} \right\} \tag{32}$$

with $i \geq 1$ and $j \geq 0$. Now $T(\mathbf{x})_0^{(0)} \equiv T(\mathbf{x})$ and for $i \geq 1$, $T(\mathbf{x})_0^{(i)} \equiv 0$. Then $T^*(\mathbf{x}; \varepsilon)$ is an asymptotic integral of H in some domain, that is, $\{H, T^*\} = \mathcal{O}(\varepsilon^{M+1})$. Details can be found in Ref. 76.

The above method is formal in the sense that the convergence of the various series is not discussed. Indeed, the series diverge for many applications. However, the lower orders of the transformed system can give interesting information, and the process can be stopped at a certain order M. This means that these terms of the series are useful to construct both the transformed Hamiltonian and the generating function, since they are unaffected by the ultimately divergent character of the whole process.

Once $\mathscr{W}$ has been determined, we can calculate the new coordinates (or any function of them) as functions of the old ones and vice versa.

B. Dynamics Near the Transition State Using the Normal-Form Coordinates

Using normal-form coordinates helps in the understanding and description of the motion near the saddle. If the $n-1$ frequencies ω_i are nonresonant, then the truncated normal form (at any order) is integrable. That is, the quantities $J_i = \frac{1}{2}(p_i^2 + q_i^2)$, $i = 1, \ldots, n-1$, and $\mathscr{I} = p_n q_n$ are integrals of the truncated normal form, and the truncated Hamiltonian can be written as a function of these integrals. To illustrate it, take the simplest possible case, namely a 3-DOF system with nonresonant frequencies:

$$K = K(J_1, J_2, \mathscr{I}) \tag{33}$$

Working in the space of integrals, which is a three-dimensional space with coordinates J_1–J_2–$\mathscr{I}$, brings advantages to computation and visualization. Since these integrals are constant on trajectories, a trajectory in this space corresponds to a point.

- **Energy Surface.** This is given by:

$$K(J_1, J_2, \mathscr{I}) = h = \text{constant} \tag{34}$$

  This will typically be a two-dimensional surface in the J_1–J_2–$\mathscr{I}$ space, for each fixed h.

- **The NHIM and Its Stable and Unstable Manifolds.** In the normal-form coordinates the NHIM is given by $q_3 = p_3 = 0$, the stable manifold of the

NHIM is given by $q_3 = 0$, and the unstable manifold of the NHIM is given by $p_3 = 0$. In the J_1–J_2–$\mathscr{I}$ space these are all given by $\mathscr{I} = 0$. In other words, the NHIM and its stable and unstable manifolds are all identified with

$$K(J_1, J_2, 0) = h = \text{constant}$$

which is typically a curve in J_1–J_2–$\mathscr{I}$ space.

- **The Transition State.** In the normal-form coordinates this is given by $q_3 = p_3$; hence $\mathscr{I} \geq 0$. Therefore the TS is given by

$$K(J_1, J_2, \mathscr{I} \geq 0) = h = \text{constant}$$

In this representation the TS is a portion of the energy surface.

In order to construct the change of coordinates back to the original coordinates, we make use of the generating function $\mathscr{W}$. Indeed we simply have to evaluate Poisson brackets but without solving any partial differential equations. Therefore the computational effort is much smaller than the one corresponding to the calculation of the normal-form Hamiltonian and the generating function.

Using (33) and the chain rule, Hamilton's equations can be written in terms of the integrals. It is important to note that $\partial K/\partial J_i$, $i = 1, 2, 3$, are constants on trajectories. Hence, once the initial condition of a trajectory is chosen, evolution of the trajectory is given by a linear system whose coefficients are constant, but depend on the trajectory.

This simple form of Hamilton's equations in the normal-form coordinates near the TS enables us to construct trajectories showing any possible behavior near the transition state. These trajectories can then be visualized in the original coordinates (see Section VI.F). An example on the isomerization of HCN follows.

VI. THE ISOMERIZATION OF HCN

This section presents a discussion of the treatment outlined above applied to a realistic molecular reaction. For simplicity we have chosen the isomerization of hydrogen cyanide (HCN) to form hydrogen isocyanide (HNC) because it is commonly used as model system in the study of isomerization reactions. This reaction, which has been the subject of innumerable studies, is excellent for our purposes. While the system is small (only three atoms) it does possess sufficient complexity to be an excellent test case. The importance of this system as a test case, both experimentally and theoretically, is demonstrated by the size of the literature [82,83–141]. This list is by no means exhaustive, nor particularly representative.

In the present work we use the potential of Murrell, Carter, and Halonen (MCH) [142]. Despite the fact that it is known to be inaccurate at energies at which the isomerization occurs, because the majority of previous investigations of the classical dynamics of the isomerization of HCN/HNC have used this potential. In the present study it is not our goal to calculate chemical rates for comparison with experimental results but rather to illustrate a new approach to the calculation of such rates.

A. The Model System

The hydrogen cyanide molecule is a linear triatomic molecule and, consequently, is described by nine DOFs. Three of these represent the center of mass and can immediately be separated. Of the remaining six DOFs, two can taken to be the total angular momentum and the projection of the total angular momentum along a space-fixed axis. The remaining four DOFs are the internal degrees of freedom. Three of these we take to be the Jacobi coordinates that are shown in Fig. 9 and discussed below. The fourth DOF will be taken to be the projection of the angular momentum about the axis defined by the smallest moment of inertia. Taking this quantity to be equal to zero allows the motion to be viewed as taking place in a plane. Care must be taken in this reduction because the Hamiltonian is singular in these coordinates when the three atoms are collinear.

We define the Jacobi coordinates r, R, and γ as the interatomic CN distance, the distance from the hydrogen atom to the center of mass of the CN bond, and the angle between the hydrogen atom, the center of mass of the CN

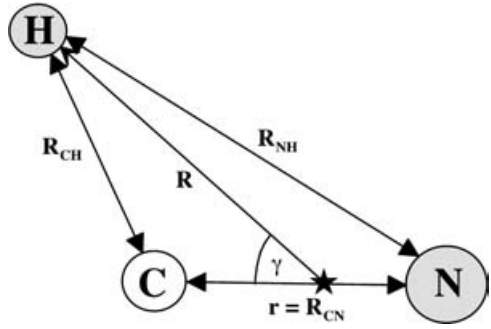

Figure 9. The Jacobi coordinates for HCN. The potential energy is constructed as a sum of three two-body interactions plus a three-body term. These terms are functions of the distances between the bodies, R_{CN}, R_{CH}, R_{NH}. R_{CN} is taken to be r, and R_{CH} and R_{NH} are expressed as functions of R and γ.

bond, and the carbon atom (see Fig. 9). In these variables the interatomic distances are given by

$$R_{CN} = r$$

$$R_{CH} = \sqrt{\left(\frac{m_N}{m_C + m_N}\right)^2 r^2 + R^2 - 2\left(\frac{m_N}{m_C + m_N}\right) rR\cos\gamma}$$

$$R_{NH} = \sqrt{\left(\frac{m_C}{m_C + m_N}\right)^2 r^2 + R^2 + 2\left(\frac{m_C}{m_C + m_N}\right) rR\cos\gamma}$$

where m_C and m_N are the masses of carbon and nitrogen, respectively.

Phase space is spanned by the Jacobi coordinates and their conjugate momenta. The dimensionality of the various geometrical object that we are interested in are as follows: Phase space is six-dimensional. The energy shell is five-dimensional. The TS, which is a codimension-one surface that partitions the energy shell, is four-dimensional. The boundary or edge of the four-dimensional TS, which is an NHIM, will be three-dimensional. Our goal in this section is to illustrate how to construct representations of these various geometrical objects. We will accomplish this in the course of investigating the flow of states in phase space.

B. The Hamiltonian

The Hamiltonian has the form

$$H = T\big(p_r, p_R, p_\gamma, r, R\big) + V(r, R, \gamma)$$

where $T\big(p_r, p_R, p_\gamma, r, R\big)$ is the kinetic energy and $V(r, R, \gamma)$ is the MCH potential [142]. The kinetic energy has the form

$$T\big(p_r, p_R, p_\gamma, r, R\big) = \frac{1}{2\mu}p_r^2 + \frac{1}{2m}p_R^2 + \tfrac{1}{2}\left(\frac{1}{\mu r^2} + \frac{1}{mR^2}\right)p_\gamma^2$$

where μ is the reduced mass of the CN diatom, that is, $\mu = m_C m_N/(m_C + m_N)$, and m corresponds to the reduced mass of the full system, that is, $m = m_H(m_C + m_N)/(m_H + m_C + m_N)$. As before, m_C and m_N are the masses of carbon and nitrogen, and m_H is the mass of hydrogen. It is crucial to observe at this junction that kinetic energy is positive definite. This has important consequences that we will discuss shortly.

The MCH potential [142] is given as sum of four terms. The first three are two-body interactions between the three atoms. Each of these take the form

$$V_2(q) = -D_e \mathrm{e}^{-a_1(q-q^0)} \sum_{k=0}^{n} a_k \big(q - q^0\big)^k$$

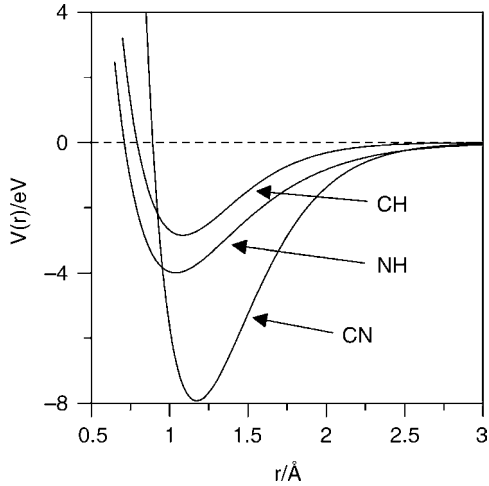

Figure 10. The potential energies for the three two-body potentials are shown in this figure. The three-body potential is a minor perturbation. Note that the CN potential is much deeper and narrower than the other two potentials. This DOF is often decoupled from the other two dynamical DOFs.

where q is one of the three distances between two atoms, namely q is either R_{CN}, R_{CH}, or R_{NH}. The constant q^0 is the distance between the atoms at equilibrium, that is, it belongs to $\{R^0_{CN}, R^0_{CH}, R^0_{NH}\}$. Moreover, D_e is the binding energy of the two-body interactions, thus it is either D_e^{CN}, D_e^{CH}, or D_e^{NH}. The coefficients a_i are also constant terms. These three two-body interactions are shown in Fig. 10. Finally, in our simulations we have taken $n = 3$ for the interactions between the carbon and hydrogen and between the carbon and the nitrogen and $n = 1$ for the interaction between hydrogen and nitrogen.

The fourth term is a three-body interaction term. It is the product of three terms

$$V_3(R_{CN}, R_{CH}, R_{NH}) = V_I^0 \mathscr{S}(\mathscr{R}) \mathscr{P}(\mathscr{R})$$

Here, $\mathscr{R}$ refers to the three interatomic distances collectively. The first factor in of V_3 is a constant and can be interpreted as the strength of the three-body interaction. The second factor is a product of three switching functions

$$\mathscr{S}(\mathscr{R}) = \prod_{CN,\, CH,\, NH} \left(1 - \tanh \frac{\Gamma_i (R_i - S_i)}{2}\right)$$

where the constants S_i and Γ_i are to be interpreted as the range over which the three-body interaction is felt and the range over which the interaction is

switched. The last factor, $\mathscr{P}(\mathscr{R})$, is a polynomial of the form

$$\mathscr{P}(\mathscr{R}) = 1 + \sum_i c_i s_i + \sum_{j \le i} c_{ij} s_i s_j + \cdots$$

where

$$s_i = \sum_{j = CN,\ CH,\ NH} \varepsilon_i^j \left(R_j - S_j\right)$$

where c_i, c_{ij} and ε_i^j are fixed parameters. The values of these constants can be found in Murrell et al. [142]. In our simulations, $\mathscr{P}$ is truncated at degree five in s_i. It should be noted that distances are given in units of angstroms, energies in units of electron volts, and masses in units of atomic mass units. These are the units in which the original potential was developed.

We have included this discussion of the functional form of the potential energy in order to clearly illustrate complexity of the Hamiltonian function.

C. Points of Stationary Flow

As we noted above, the kinetic energy is positive definite. Furthermore, it is quadratic in the momenta. As a consequence, we can reduce the search for points of stationary flow in phase space to one of finding the stationary points of the potential energy surface. To see how this comes about, consider the Hamilton's equations for the three velocities

$$\dot{r} = \frac{\partial H}{\partial P_r}$$

$$\dot{R} = \frac{\partial H}{\partial P_R}$$

$$\dot{\gamma} = \frac{\partial H}{\partial P_\gamma}$$

Setting the velocities equal to zero and using the Hamiltonian given above to evaluate the derivatives yields

$$\frac{1}{\mu} p_r = 0$$

$$\frac{1}{m} p_R = 0$$

$$\left(\frac{1}{\mu r^2} + \frac{1}{mR^2}\right) p_\gamma = 0$$

TABLE I
The Positions of the Five Equilibrium Points of the Murrell, Carter, and Halonen Potential Energy Surface[a]

	r	R	γ
HCN	1.15321621033313359	1.6864160898153111	0.0
HNC	1.16451121001722257	1.53121204160717798	π
Saddle	1.1394029718182721	1.20844255384653775	1.16823395477807734
Barrier 2	1.14781465664160409	1.19699789318508864	2.15136248734495216
Well 2	1.13654692030783732	1.11615395989081878	1.99142694984300057

[a]The first two are the minima of the HCN and HNC potential wells. The third is the saddle point separating these two wells. The final two points are associated with a very shallow well within the HNC well. There are included here for the sake of completeness. The distances are given in angstroms.

From this we see that the only solution corresponds to the three momenta equaling zero, $p_r = p_R = p_\gamma = 0$. The remaining three equations of motion in essence, require that the forces exerted on the system be equal to zero. This occurs at the extremum, or equilibrium, points of the potential energy.

The MCH potential energy surface has five equilibrium points in the energy regime of interest in the present study. These are given in Table I.

The conjugate momenta of these fixed points are given by $p_r = 0$, $p_R = 0$, and $p_\gamma = 0$. The energies of these equilibrium points appear in Table II.

The stability of the equilibrium points can be determined in either of two ways. We can evaluate the eigenvalues of the matrix of second derivatives of the potential energy surface, or we can evaluate the eigenvalues of the stability matrix again evaluated. In either case we evaluate the matrices at the equilibrium points. These eigenvalues are given, respectively, in Tables III and IV.

The first two equilibrium points are stable in all three DOFs and occur at the bottom of the two major potential wells. The first corresponds to the hydrogen cyanide equilibrium configuration, while the second corresponds to the

TABLE II
The Energies of the Five Fixed Points

	Energy	Relative to HCN	Relative to HNC
HCN	−13.5914	0.0	−0.4849
HNC	−13.1065	0.4849	0.0
Saddle	−12.0827	1.5087	1.0238
Barrier 2	−12.7174	0.8739	0.3890
Well 2	−12.7217	0.8697	0.3848

TABLE III
The Force Constant for the Normal Modes at the Equilibrium Points of the Potential Energy Surface[a]

	κ_1	κ_2	κ_3
HCN	134.43	33.9942	4.11204
HNC	125.485	41.3439	1.6211
Saddle	134.193	31.8395	−5.48101
Barrier 2	128.109	41.2462	−0.746732
Well 2	139.425	38.0718	0.844229

[a]Observe that, since all three force constants are positive, the motion will be oscillatory in the neighborhood of the first two and fifth equilibrium points.

hydrogen isocyanide equilibrium configuration. The third equilibrium point is a rank-one saddle; that is, it is stable in two DOFs and unstable in last DOF. It corresponds to the saddle point that separates the two major wells. The fourth and fifth equilibrium points are associated with a very shallow well that lies within much larger and deeper hydrogen isocyanide well. These two points will not play a role in our analysis and are mentioned here only for completeness reasons.

The eigenvalues of the matrix of second derivative of the potential energy surface are equal to the force (or spring) constants of the normal modes at the equilibrium points. Examining the values of these constants, which are given in Table III, we see that, in the neighborhood of the first and second equilibrium points, the motion will be oscillatory in all three DOFs. The eigenvalues of the stability matrix, which are given in Table IV, have a similar interpretation. They

TABLE IV
The Eigenvalues of the Stability Matrix at the Five Fixed Points in Phase Space[a]

	λ_1	λ_2	λ_3
HCN	6.61679i	4.07866i	1.40293i
HNC	7.27826i	3.95081i	0.94732i
Saddle	5.99066i	4.28245i	2.1828
Barrier 2	6.95079i	4.14571i	0.881658
Well 2	6.76476i	4.32309i	0.865383i

[a]The eigenvalues occur as complex conjugate pairs. The imaginary eigenvalues correspond to stable modes, and the magnitude of the eigenvalues are equal to the frequencies. Note that the frequencies of the two stable modes at the saddle are not in resonance. Consequently, good quantum numbers can be defined for the activated complex.

are, in essence, rate constants. That is, they are a measure of the length of time required for a system to escape from the neighborhood of the equilibrium point. When these constants take imaginary values, it implies that the system is oscillating in the neighborhood of the equilibrium point with a frequency equal to the magnitude of the eigenvalue.

D. Preparation for Transformation to the Normal Form

Once the rank-one saddles in phase space have been identified, it is, in principle, straightforward to prepare the Hamiltonian for transformation into normal form (for a detailed example, see Ref. 21). This process involves three steps. First the origin of phase space is transformed to the desired stationary point. In the present case, a simple translation of the origin of coordinate space accomplishes this shift of the origin of phase space to the location of the third point of stationary flow—that is, to the saddle point lying between the two major potential wells. The second step identifies the normal modes of the Hamiltonian and transforms to the corresponding set of variables. This is accomplished by the symplectic diagonalization on the quadratic part of the initial Hamiltonian. The third and final step involves expanding the Hamiltonian into a Taylor series about the desired saddle point. While this step is not conceptually difficult, in actual practice accomplishing this step can be very time-consuming and can require significant computer resources.

E. Transformation to the Normal Form

We apply the Lie transformation to the Hamiltonian $H = \sum_{n=2}^{8} H_n$, where H_2 is given by

$$H_2 = \lambda_1 x_1 x_4 + \lambda_2 x_2 x_5 + \lambda_3 x_3 x_6$$

and the frequencies λ_i are the ones corresponding to the saddle point (see Table IV). Each H_n for $2 < n \leq 8$ is a homogeneous polynomial of degree n in the complex coordinates $\mathbf{x}$ obtained from the potential V after passing from the coordinates (r, R, γ) to the variables $\mathbf{x}$. Thus, we plan to carry out the calculations up to polynomials of degree eight—i.e., up to sixth order in the normal-form construction. In this way, we build a change of variables from the old ones $\mathbf{x} = (x_1, x_2, x_3, x_4, x_5, x_6)$ to the new ones $\mathbf{y} = (y_1, y_2, y_3, y_4, y_5, y_6)$.

We start by identifying H_2 with $\mathscr{H}_0$ and each H_{n+2} with $\mathscr{H}_n/n!$, $2 < n \leq 6$. Then, we must recall that terms belonging to $\tilde{\mathscr{H}}_n$ are monomials in $\mathbf{x}$ of degree $n+2$ with real or complex coefficients c.

As the operator ad_{H_2} is diagonal, we can proceed by examining if a simple monomial will be included in the normal-form Hamiltonian or not. Specifically, a monomial of degree $n+2$,

$$m_n = c x_1^{j_1} x_2^{j_2} x_3^{j_3} x_1^{k_1} x_2^{k_2} x_3^{k_3}$$

such that $\sum_{l=1}^{3}(j_l + k_l) = n + 2$, belongs to the kernel of ad_{H_2} (i.e., it satisfies $\{ m_n , H_2 \} = 0$), and therefore it must be incorporated to the new Hamiltonian if and only if $j_1 = k_1$, $j_2 = k_2$ and $j_3 = k_3$. Otherwise its contribution to the new Hamiltonian K is zero, and the part corresponding to the generating function $\mathscr{W}_n$ becomes

$$\frac{m_n}{\lambda_3 (k_3 - j_3) + \lambda_1 (k_1 - j_1) + \lambda_2 (k_2 - j_2)}$$

Note that this denominator does not vanish since the eigenvalues λ_2 and λ_3 correspond to nonresonant normal modes. This is the key point in solving the homology equation (26) at each order n.

We rescale the coordinates, say $\mathbf{x}^* \to \varepsilon \mathbf{x}$, to introduce the small parameter ε and adopt then the formulae of Section V.A. Afterwards we set $\varepsilon = 1$ and drop the star to simplify our notation further. We call the normal form $K = \sum_{n=2}^{8} K_n$, and in complex coordinates (the transformed ones $\mathbf{y}$) it reads as follows:

$$K(\mathbf{y}) = \sum_{0 \le i+j+k \le 4} \bar{a}_{ijk} (y_1 y_4)^i (y_2 y_5)^j (y_3 y_6)^k \tag{35}$$

where the sum goes over all i, j, and k with $0 \le i + j \le 4$ and the coefficients $\bar{a}_{ijk}$ are real or complex. In particular,

$$K_2 = \lambda_1 y_1 y_4 + \lambda_2 y_2 y_5 + \lambda_3 y_3 y_6$$

The Hamiltonian K can be split into Hamiltonians K_n for $2 \le n \le 8$. Each K_n is a homogeneous polynomial of degree n. The generating function is also a polynomial in $\mathbf{x}$ (or in $\mathbf{y}$) of degree eight, but it is too long display here. Specifically, $\mathscr{W} = \sum_{n=1}^{6} \mathscr{W}_n / n!$ is written as $W = \sum_{n=3}^{8} W_n$ where each W_n is also a homogeneous polynomial in $\mathbf{x}$ of degree n.

Once W has been determined, we can calculate the new variables (or any function of them) as functions of the old ones and vice versa, by means of Eqs. (27) and (29). In particular, the use of the direct change which makes explicitly $\mathbf{x}$ as polynomials of $\mathbf{y}$ of degree eight will be crucial to obtain the expressions of the NHIM, the TS and the other structures in terms of the original coordinates (r, R, γ) and momenta (p_r, p_R, p_γ).

Next, it is straightforward to use action-angle variables, with the aim of writing K as the normal form

$$K(I_1, I_2, I_3) = \sum_{0 \le i+j+k \le 4} a_{ijk} I_1^i I_2^j I_3^k$$

TABLE V
Values of the Coefficients of the Normal-Form Hamiltonian

a_{000}	−12.08270621909487		
a_{100}	0.954905129358249	a_{301}	0.0005856303577910487
a_{200}	−0.03806852708896476	a_{011}	−0.003100813333260371
a_{300}	0.0027310729862473205	a_{111}	−0.003222234665742905
a_{400}	0.00003034242269138 6055	a_{211}	0.0013154465433325067
a_{010}	0.6784357290530834	a_{021}	−0.00029536597940468037
a_{110}	−0.03634032763273621	a_{121}	−0.00009307509500353229
a_{210}	0.005010467124410658	a_{031}	−0.00016681125684889185
a_{310}	0.000521036141694136	a_{002}	0.0167902092282642
a_{020}	−0.015100569431461403	a_{102}	−0.001920402152291333
a_{120}	0.0007005897422981253	a_{202}	0.00038444427179500226
a_{220}	0.0018285195757281284	a_{012}	−0.0006592352377808216
a_{030}	−0.0007327257466574936	a_{112}	0.00002943000778286972
a_{130}	1.4149150136276378	a_{022}	−0.0002881442069027329
a_{040}	0.00003581710535858259	a_{003}	−0.0013124004701446804
a_{001}	0.34527320408687906	a_{103}	0.00006355693478722243
a_{101}	−0.01911783201950005	a_{013}	−0.00002306758498780 7643
a_{201}	0.0004324327528662697	a_{004}	0.0002690597101034 8154

where the sum goes over all i, j, and k such that $0 \leq i + j \leq 4$ and the first two constants of the motion, $I_1 = iy_1y_4$ and $I_2 = iy_2y_5$, are the classical action variables associated with the two nonreactive DOFs. The first I_1 is associated with the vibrational motion of the hydrogen atom, while the second is associated with the CN stretching motion. The third constant of the motion, $I_3 = y_3y_6$ is the action associated with the reactive coordinate. The coefficients in the above Hamiltonian are given in Table V.

F. Visualization of the HCN Dynamics

It is possible to introduce a new set of normal-form variables, related to the coordinates (y_1, y_2, y_3) and momenta (y_4, y_5, y_6). We introduce Cartesian variables $(q'_1, q'_2, q'_3, p'_1, p'_2, p'_3)$ through

$$\begin{aligned} y_1 &= q'_3, \qquad y_2 = \frac{1}{\sqrt{2}}(q'_2 + ip'_2), \qquad y_3 = \frac{1}{\sqrt{2}}(q'_1 + ip'_1) \\ y_4 &= p'_3, \qquad y_5 = \frac{1}{\sqrt{2}}(iq'_2 + p'_2), \qquad y_6 = \frac{1}{\sqrt{2}}(iq'_1 + p'_1) \end{aligned} \tag{36}$$

The variables $(q'_1, q'_2, q'_3,\ p'_1, p'_2, p'_3)$ can be mapped back to the Cartesian coordinates previous to the normal-form process—that is, to the variables $(q_1, q_2, q_3, p_1, p_2, p_3)$ by means of the direct change of the Lie transformation, using the generating function W written in terms of the q'_i and p'_i.

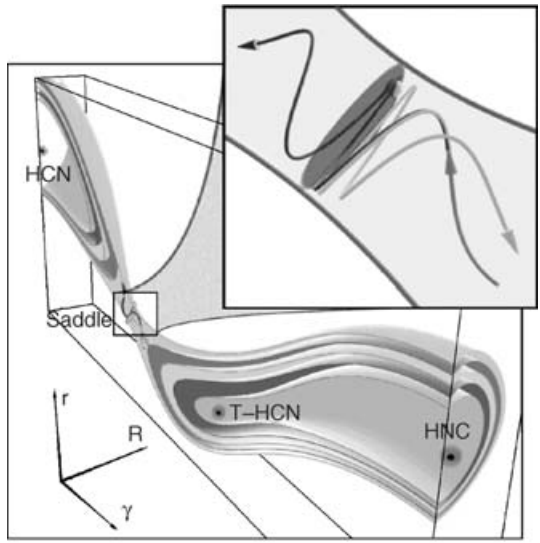

Figure 11. (The color version is available from the authors.) A picture of the three-dimensional PES of isomerizing HCN. At the saddle (the bottleneck of the large figure), we show a pair of close-by trajectories, one reactive and one nonreactive, very much like in Fig. 3. The saddle region is magnified in the inset. The gray ellipse around the saddle is the configuration-space projection of the four-dimensional TS.

Next we put into effect the visualization techniques we discussed in Section V.B. Our purpose is to show how the complex dynamics of the pair of trajectories in Figs. 11 and 12 is simplified by the normal-form transformation.

In the following figures the reader can see the three uncoupled motions that make up the complex motions depicted in the previous two figures—that is, single trajectories in the saddle plane (see Fig. 13), in the center plane (see Fig. 14), and in the other center plane (see Fig. 15), respectively, depicted in the normal-form variables q'_i, p'_i. Note that the TS is denoted by the diagonal line, $q'_3 = p'_3$, in the saddle plane as it appears in Fig. 13. The NHIM is given by $q'_3 = p'_3 = 0$, and the stable and unstable manifolds of the NHIM are given by $q'_3 = 0$ and $p'_3 = 0$, respectively. Thus, a forward reactive trajectory requires $q'_3 > 0$ and a forward nonreactive trajectory requires $q'_3 < 0$. The rest of the coordinates of the trajectory can be chosen arbitrarily (but respecting energy conservation). In each figure, the ball indicates the point of passage through the TS. The curves (outermost circles) indicate the boundary of the energy surface. Once the two trajectories are chosen in the normal-form variables, they

Figure 12. (The color version is available from the authors.) Two trajectories, so close in phase space that they appear as one, approach the saddle from the lower right, as in Fig. 3. After some complex dynamics around the saddle point, one reacts (crosses the TS at the dot) and goes off to the top left, and the nonreactive one returns to the lower right. We engineered this outcome by selecting their initial conditions on opposite sides of the impenetrable phase-space barrier (one of the ''scissors'' [20]) between reacting and nonreacting hypervolumes.

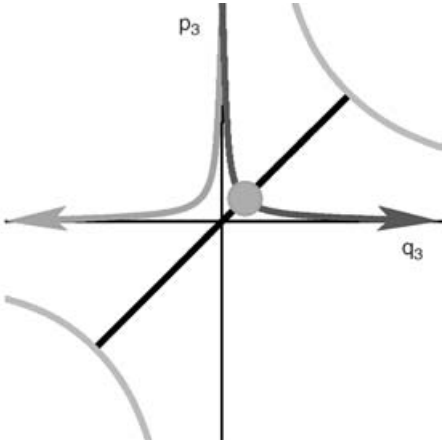

Figure 13. (The color version is available from the authors.) The previous pair of trajectories as seen in the normal-form coordinates in the hyperbolic direction. The complicated dynamics at the saddle has been smoothed out. The two trajectories approach from the top. Note how the p_3 axis acts as a separatrix between them. The reactive one intersects the TS (the diagonal) at the dot. Compare this with Figs. 5, 6, and 7. Primes on q_3' and p_3' (see the text) have been dropped.

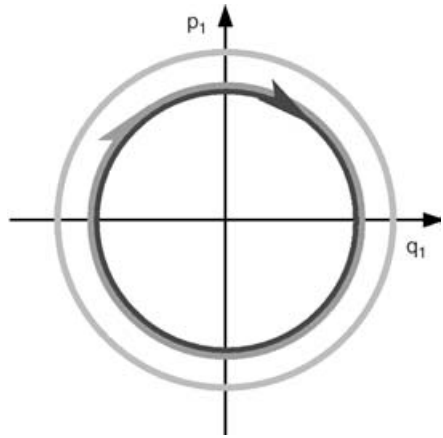

Figure 14. (The color version is available from the authors.) The same pair of trajectories in one of the bath mode normal-form variables. The outer circle is determined by the total energy. Primes on q_1' and p_1' have been dropped.

are mapped back into the original variables. Moreover, all of the other explicitly known geometrical structures in normal-form coordinates relevant to the reaction—the TS, the NHIM, and its stable and unstable manifolds (which define the boundaries of the reaction channels)—can be mapped back into the original variables.

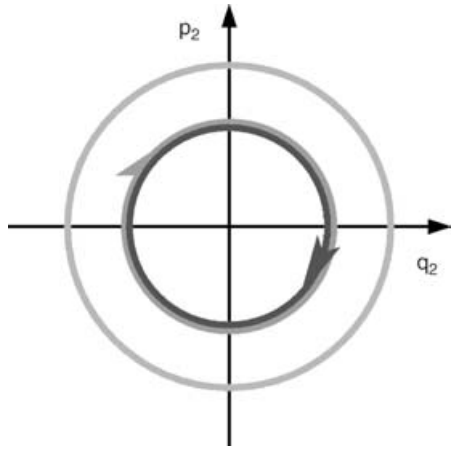

Figure 15. (The color version is available from the authors.) The same pair of trajectories in the other bath mode's normal-form variables. Primes on q_2' and p_2' have been dropped.

G. The Quantization of the Nonreactive Degrees of Freedom

Once the Hamiltonian has been transformed into normal form, the quantization of the nonreactive DOFs is straightforward. While complications can occur, the present example is free of the worst of these. The vibrational modes normal to the reactive coordinate are not in resonance. Consequently, the quantization is straightforward and accomplished by quantizing the classical action variables

$$I_1 = \left(n_r + \frac{1}{2}\right)\hbar$$
$$I_2 = \left(n_R + \frac{1}{2}\right)\hbar$$

for $n_r = 0, 1, 2 \ldots$ and $n_R = 0, 1, 2 \ldots$. This results in an expression for the total energy in terms of the quantum numbers for the internal DOFs and the action in the reactive mode.

At the barrier height, the action in the reactive mode is equal to zero. Setting it to zero yields an expression for the energies of the quantized states sitting above the barrier. These are the ''gateway'' states. This expression is given by

$$E^{TS}_{n_r,n_R} = \sum_{0 \le i+j \le 4} b_{ij}\, n_r^i\, n_R^j$$

where the sum goes over all i and j such that $0 \le i + j \le 4$ and the coefficients b_{ij} are given in Table VI. The difference between the coefficients b_{00} and a_{000} gives the zero-point energy associated with the lowest quantized TS, $E^0_{TS} = 0.79546447$. The quantized energy levels are given in Table VII.

TABLE VI
Values of the Coefficients of the Normal Form Hamiltonian: $\hbar = 0.0646541478$

b_{00}	−11.287241748006593	b_{31}	0.000521036141694136
b_{10}	0.9041762942583398	b_{02}	−0.014657625171057372
b_{20}	0.030573263413148734	b_{12}	0.0038908742325688573
b_{30}	0.003052275902477161	b_{22}	0.0018285195757281284
b_{40}	0.00003034242269138 6055	b_{03}	−0.0002071698977594 6035
b_{01}	0.6470989723404712	b_{13}	0.0009078432763617361
b_{11}	−0.027729091626757386	b_{04}	0.0000358171053585 8259
b_{21}	0.007620540912679991		

TABLE VII
The Energies of the Quantized Transition States[a]

n_r	n_R	E
0	0	−12.0300
0	1	−11.9863
1	0	−11.9687
0	2	−11.9428
1	1	−11.9251
2	0	−11.9076

[a]The energy is given in units of electron volts (eV). These energies correspond to the quantized threshold energies discussed in Ref. 23.

VII. SUMMARY AND OUTLOOK

The Normal Form approach can give the researcher an analytical tool for finding phase-space geometrical objects such as normally hyperbolic invariant manifolds (NHIMs), and, of even greater interest to a chemist, the transition state (TS) [19,21]. In this review, we illustrated the procedure on the isomerization of HCN. Concretely, we showed how to determine the TS analytically. We constructed the three asymptotic integrals of the original Hamiltonian by inverting the normal-form transformations. The same procedure led to the NHIM and its stable and unstable manifolds. We also computed trajectories that start on the NHIM on the five-dimensional energy surface, as well as in the forward and backward stable and unstable manifolds associated with the NHIM. It is straightforward to choose and run these trajectories from the normal-form vector field. The normal-form transformation then allows us to obtain them in the original coordinates. We projected these phase-space objects into configuration space by computer visualization. In short, we showed the degree of control and knowledge of the exact dynamical trajectories near the TS in a system with three DOFs. The procedure is designed to work similarly well in arbitrary numbers of dimensions. We hope that the theory explained here will help in the solutions of problems more complex than those in small isolated molecules.

Acknowledgments

We are grateful to S. Wiggins and A. Burbanks for their help at various stages of this work and for some of the figures. One of us (TU) is grateful to the United States National Science Foundation for the support of this research. The work of JP and PY has been partially supported by Project #BFM2002-03157 of Ministerio de Ciencia y Tecnologia (Spain).

References

1. *Trans. Faraday Soc. London*, **34**, 1938.
2. W. H. Miller, *Faraday Discuss. Chem. Soc. Lond.*, **110**; 1 (1998).
3. H. Eyring, J. Walter, and G. E. Kimball, *Quantum Chemistry*, Wiley, New York, 1944.
4. E. P. Wigner, *Trans. Faraday Soc.* **34**, 29 (1938).
5. T. Komatsuzaki and R. S. Berry, *Adv. Chem. Phys.* **123**, 79 (2002).
6. C. Jaffé, D. Farrelly, and T. Uzer, *Phys. Rev. Lett.* **84**, 610 (2000).
7. C. Jaffé and T. Uzer, *J. Phys. Chem. A* **105**, 2783 (2001).
8. B. Eckhardt, *J. Phys. A: Math. Gen.* **28**, 3469 (1995).
9. M. Toller, G. Jacucci, G. DeLorenzi, and C. P. Flynn, *Phys. Rev. B* **32**, 2082 (1985).
10. C. Jaffé, S. D. Ross, M. W. Lo, J. E. Marsden, D. Farrelly, and T. Uzer, *Phys. Rev. Lett.* **89**, 11101 (2002).
11. E. P. Wigner, *J. Chem. Phys.* **5**, 720 (1937).
12. E. P. Wigner, *J. Chem. Phys.* **7**, 646 (1939).
13. V. I. Arnol'd, V. V. Kozlov, and A. I. Neishtadt, *Mathematical Aspects of Classical and Celestial Mechanics*, Springer-Verlag, New York, 1988.
14. S. Wiggins, *Chaotic Transport in Dynamical Systems*. Springer-Verlag, New York, 1992.
15. J. C. Keck, *Adv. Chem. Phys.* **13**, 85 (1967).
16. P. Pechukas and F. J. McLafferty, *J. Chem. Phys.* **58**, 1622 (1973).
17. E. Pollak and P. Pechukas, *J. Chem. Phys.* **69**, 1218 (1978); P. Pechukas and E. Pollak, *J. Chem. Phys.* **71**, 2062 (1979).
18. C. Jaffé, D. Farrelly, and T. Uzer, *Phys. Rev. A* **60**, 3833 (1999).
19. S. Wiggins, L. Wiesenfeld, C. Jaffé, and T. Uzer, *Phys. Rev. Lett.* **86**, 5478 (2001).
20. We owe this terminology to Prof. Carles Simó.
21. T. Uzer, C. Jaffé, J. Palacián, P. Yanguas, and S. Wiggins, *Nonlinearity* **15**, 957 (2002).
22. S. Wiggins, *Normally Hyperbolic Invariant Manifolds in Dynamical Systems*, Springer-Verlag, New York, 1994.
23. D. C. Chatfield, R. S. Friedman, D. G. Truhlar, B. C. Garrett, and D. W. Schwenke, *J. Am. Chem. Soc.* **113**, 486 (1991).
24. E. R. Lovejoy, S. K. Kim, and C. B. Moore, *Science* **256**, 1541 (1992).
25. E. R. Lovejoy and C. B. Moore, *J. Chem. Phys.* **98**, 7846 (1993).
26. A. Marcelin, *Ann. Chim. Phys.* **3**, 158 (1915).
27. H. Eyring and M. Polanyi, *Z. Physik. Chem. B* **12**, 279 (1931).
28. M. G. Evans and M. Polanyi, *Trans. Faraday. Soc.* **31**, 875 (1935).
29. J. O. Hirschfelder and E. Wigner, *J. Chem. Phys.* **7**, 616 (1939).
30. W. Forst, *The Theory of Unimolecular Reactions*, Academic, New York, 1973.
31. P. J. Robinson and K. A. Holbrook, *Unimolecular Reactions*, Wiley, New York, 1992.
32. H. Poincaré, *New Methods of Celestial Mechanics, Part 3*, American Institute of Physics, New York, 1993.
33. A. J. Lichtenberg and M. A. Lieberman, *Regular and Chaotic Dynamics*, Springer, New York, 1992.
34. M. C. Gutzwiller, *Chaos in Classical and Quantum Mechanics*, Springer-Verlag, New York, 1990.

35. P. Pechukas, Statistical Approximations in Collision Theory, in *Dynamic of Molecular Collisions, Part 3*, Plenum, New York, p. 269, 1976.
36. P. Pechukas, *Annu. Rev. Phys. Chem.* **32**, 159 (1981).
37. E. Pollak and M. S. Child, *J. Chem. Phys.* **72**, 1669 (1980).
38. J. Horiuti, *Bull. Chem. Soc. Japan* **13**, 210 (1937).
39. G. W. Koeppl, *J. Am. Chem. Soc.* **96**, 6539 (1974).
40. E. Pollak, Periodic orbits and the theory of chemical reactions, in *Theory of Chemical reaction Dynamics*, Vol. III, M. Baer, ed., CRC Press, Boca Raton, FL, 1985, p. 123.
41. R. S. MacKay, J. D. Meiss, and I. C. Percival, *Physica D* **13**, 55 (1984); D. Bensimon and L. D. Kadanoff, *Physica D* **13**, 82 (1984); R. S. MacKay, J. D. Meiss, and I. C. Percival, *Physica D* **27**, 1 (1987), I. Dana, N. V. Murray, and I. C. Percival, *Phys. Rev. Lett.* **62**, 233 (1988).
42. M. J. Davis, *J. Chem. Phys.* **86**, 3978 (1987).
43. M. J. Davis and S. K. Gray, *J. Chem. Phys.* **84**, 5389 (1986).
44. M. J. Davis, *J. Phys. Chem.* **92**, 3124 (1988).
45. A. Tiyapan and C. Jaffé, *J. Chem. Phys.* **99**, 2765 (1993).
46. A. Tiyapan and C. Jaffé, *J. Chem. Phys.* **101**, 10393 (1994).
47. A. Tiyapan and C. Jaffé, *J. Chem. Phys.* **103**, 5499 (1995).
48. W. H. Miller, *Faraday Discuss. Chem. Soc. Lond.* **62**, 40 (1977).
49. R. Hernandez and W. H. Miller, *Chem. Phys. Lett.* **214**, 129 (1993).
50. S. Keshavamurthy and W. H. Miller, *Chem. Phys. Lett.* **205**, 96 (1993).
51. R. Hernandez, *J. Chem. Phys.* **101**, 9534 (1994).
52. S. K. Gray and S. A. Rice, *J. Chem. Phys.* **87**, 2020 (1987).
53. T. L. Beck, D. M. Leitner, and R. S. Berry, *J. Chem. Phys.* **89**, 1681 (1988).
54. D. J. Wales and R. S. Berry, *J. Phys. B* **24**, L351 (1991).
55. R. E. Gillilan and G. S. Ezra, *J. Chem. Phys.* **94**, 2648 (1991).
56. N. DeLeon, *J. Chem. Phys.* **96**, 285 (1992).
57. R. J. Hinde, R. S. Berry, and D. J. Wales, *J. Chem. Phys.* **96**, 1376 (1992).
58. C. Amitrano and R. S. Berry, *Phys. Rev. Lett.* **68**, 729 (1992).
59. M. Zhao and S. A. Rice, *J. Chem. Phys.* **96**, 6654 (1992).
60. R. A. Marcus, *Science* **256**, 1523 (1992).
61. C. Amitrano and R. S. Berry, *Phys. Rev. E* **47**, 3158 (1993).
62. R. S. Berry, *Chem. Rev.* **93**, 237 (1993).
63. R. J. Hinde and R. S. Berry, *J. Chem. Phys.* **99**, 2942 (1993).
64. J. R. Fair, K. R. Wright, and J. S. Hutchinson, *J. Phys. Chem.* **99**, 14707 (1995).
65. R. S. Berry, *Int. J. Quantum Chem.* **58**, 657 (1996).
66. S. K. Nayak, P. Jena, K. D. Ball, and R. S. Berry, *J. Chem. Phys.* **108**, 234 (1998).
67. T. Komatsuzaki and M. Nagaoka, *J. Chem. Phys.* **105**, 10838 (1996).
68. T. Komatsuzaki and M. Nagaoka, *Chem. Phys. Lett.* **265**, 91 (1997).
69. T. Komatsuzaki and R. S. Berry, *J. Chem. Phys.* **110**, 9160 (1999).
70. T. Komatsuzaki and R. S. Berry, *Phys. Chem. Chem. Phys.* **1**, 1387 (1999).
71. T. Komatsuzaki and R. S. Berry, *J. Mol. Struct. (Theochem)* **506**, 55 (2000).
72. T. Komatsuzaki and R. S. Berry, *Proc. Nat–. Acad. Sci. USA* **78**, 7666 (2001).

73. T. Komatsuzaki and R. S. Berry, *J. Chem. Phys.* **115**, 4105 (2001).
74. T. Komatsuzaki and R. S. Berry, *J. Phys. Chem. A* **106**, 10945 (2002).
75. A. Deprit, *Celestial Mech.* **1**, 12 (1969).
76. J. Palacián and P. Yanguas, *Nonlinearity* **13**, 1021 (2000).
77. A. Litvak-Hinenzon and V. Rom-Kedar, *Nonlinearity* **15**, 1149 (2000).
78. C. Jaffé and T. Uzer, unpublished.
79. A. M. Ozorio de Almeida, N. de Leon, M. A. Mehta, and C. C. Marston, *Physica D* **46**, 265 (1990).
80. W. H. Miller, *J. Phys. Chem. A* **102**, 793 (1998).
81. R. S. MacKay, *Phys. Lett. A* **145**, 425 (1990); *Nonlinearity* **4**, 155 (1991).
82. R. J. Wolf and W. L. Hase, *J. Chem. Phys.* **73**, 3779 (1980).
83. B. A. Waite and W. H. Miller, *J. Chem. Phys.* **73**, 3713 (1980).
84. B. A. Waite, *J. Phys. Chem.* **88**, 5076 (1984).
85. D. Farrelly and W. P. Reinhardt, *J. Chem. Phys.* **78**, 606 (1983).
86. S. C. Ross and P. R. Bunker, *J. Mol. Spectrosc.* **101**, 199 (1983).
87. K. K. Lehmann, G. J. Scherer, and W. Klemperer, *J. Chem. Phys.* **76**, 6441 (1982).
88. K. K. Lehmann, G. J. Scherer, and W. Klemperer, *J. Chem. Phys.* **77**, 2853 (1982).
89. K. K. Lehmann, G. J. Scherer, and W. Klemperer, *J. Chem. Phys.* **78**, 608 (1983).
90. S. K. Gray, W. H. Miller, Y. Yamaguchi, and H. F. Schaefer III, *J. Chem. Phys.* **73**, 2733 (1980).
91. S. K. Gray, S. A. Rice, and M. J. Davis, *J. Phys. Chem.* **90**, 3470 (1986).
92. S. K. Gray and S. A. Rice, *J. Chem. Soc. Faraday Discuss.* **82**, 307 (1986).
93. S. K. Gray and S. A. Rice, *J. Chem. Phys.* **86**, 2020 (1987).
94. M. J. Davis, *J. Chem. Phys.* **83**, 1016 (1985).
95. M. J. Davis and S. K. Gray, *J. Chem. Phys.* **84**, 5389 (1986).
96. T. A Holme and J. S. Hutchinson, *J. Chem. Phys.* **83**, 2860 (1985).
97. R. S. Smith, R. B. Shirts, and C. W. Patterson, *J. Chem. Phys.* **86**, 4452 (1987).
98. R. S. Smith and R. B. Shirts, *J. Chem. Phys.* **89**, 2948 (1988).
99. M. Founargiotakis, S. C. Farantos, and J. Tennyson, *J. Chem. Phys.* **88**, 1598 (1988).
100. J. M. Gomez Llorente, S. C. Farantos, O. Hahn, and H. S. Taylor, *J. Opt. Soc. Am. B Opt. Phys.* **7**, 1851 (1990).
101. S. C. Farantos, J. M. Gomez Llorente, O. Hahn, and H. S. Taylor, *J. Chem. Phys.* **93**, 76 (1990).
102. S. C. Farantos, J. M. Gomez Llorente, O. Hahn, and H. S. Taylor, *Chem. Phys. Lett.* **166**, 71 (1990).
103. S. C. Farantos and M. Founargiokis, *Chem. Phys.* **142**, 345 (1990).
104. S. C. Farantos, J. M. Gomez Llorente, O. Hahn, and H. S. Taylor, *J. Chem. Phys.* **94**, 2376 (1991).
105. P. R. Fleming and J. S. Hutchinson, *J. Chem. Phys.* **90**, 1735 (1989).
106. M. Mladenovic and Z. Bacic, *J. Chem. Phys.* **93**, 3039 (1990).
107. V. Szalay, *J. Chem. Phys.* **92**, 3633 (1990).
108. W. Quapp, *J. Mol. Struct.* **218**, 261 (1990).
109. W. Quapp, M. Hirsch, O. Imig, and D. Heidrich, *Journal of Computational Chemistry* **19**, 1087 (1998).
110. S. Carter, N. C. Handy, and I. M. Mills, *Philos. Trans. R. Soc. Lond., Ser. A* **332**, 309 (1990).

111. A. B. McCoy and E. L. Sibert III, *J. Chem. Phys.* **95**, 3488 (1991).
112. A. B. McCoy and E. L. Sibert III, *J. Chem. Phys.* **95**, 3476 (1991).
113. B. Gazdy and J. M. Bowman, *J. Chem. Phys.* **95**, 6309 (1991).
114. J. A. Bentley, J. M. Bowman, B. Gazdy, T. J. Lee, and C. E. Dateo, *Chem. Phys. Lett.* **198**, 563 (1992).
115. B. L. Lan and J. M. Bowman, *J. Phys. Chem.* **97**, 12535 (1993).
116. T. J. Lee, C. E. Dateo, B. Gadzy, and J. M. Bowman, *J. Phys. Chem.* **97**, 8937 (1993).
117. B. L. Lan and J. M. Bowman, *J. Chem. Phys.* **101**, 8564 (1994).
118. J. M. Bowman and B. Gazdy, *J. Phys. Chem. A* **101**, 6384 (1997).
119. K. M. Christoffel and J. M. Bowman, *J. Chem. Phys.* **112**, 4496 (2000).
120. J. A Bentley, C. M. Huang, and R. E Wyatt, *J. Chem. Phys.* **98**, 5207 (1993).
121. S. A. Kulkarni and S. R. Gadre, *J. Am. Chem Soc.* **115**, 7434 (1993).
122. H. Tang, S. Jang, M. Zhao, and S. A. Rice, *J. Chem. Phys.* **101**, 8737 (1994).
123. S. A. Rice and M. Zhao, *Int. J. Quant. Chem.* **58**, 593 (1996).
124. S. P. Shah and S. A. Rice, *Faraday Discuss.* **113**, 319 (1999).
125. S. P. Shah and S. A. Rice, *J. Chem. Phys.* **113**, 6536 (2000).
126. V. Kurkal and S. A. Rice, *Chem. Phys. Lett.* **344**, 125 (2001).
127. N. DeLeon and S. Ling, *J. Chem. Phys.* **101**, 4790 (1994).
128. S. Ling, *J. Chem. Phys.* **100**, 8554 (1994).
129. W.-T. Chan, D. Shen, and H. O. Pritchard, *J. Chem. Soc. Faraday Trans.* **91**, 1717 (1995).
130. D. Talbi and Y. Ellinger, *Chem. Phys. Lett.* **263**, 385 (1996).
131. V. S. Rao, A. Vijay, and A. K. Chandra, *Can. J. Chem.* **74**, 1072 (1996).
132. A. K. Chandra and T. Uchimaru, *J. Phys. Chem. A* **105**, 3578 (2001).
133. Y. Justum, F. Gatti, and X. Chapuisat, *THEOCHEM* **453**, 131 (1998).
134. Y. Justum, F. Gatti, D. Lauvergnat, A. Nauts, and X. Chapuisat, *Spectrochim. Acta, Part A* **58A**, 649 (2002).
135. J. H. Kiefer, P. S. Mudipalli, A. F. Wagner, and L. Harding, *J. Chem. Phys.* **105**, 8075 (1996).
136. C. M. Dion, S. Chelkowski, A. D. Bandrauk, H. Umeda, and Y. Fujimura, *J. Chem. Phys.* **105**, 9083 (1996).
137. Y. Fujimura, L. Gonzalez, K. Hoki, J. Manz, Y. Ohtsuki, and H. Umeda, *Advances in Multi-Photon Processes and Spectroscopy*, **14**, 30 (2001).
138. K. M. Westerberg and C. A. Floudas, *J. Chem. Phys.* **110**, 9259 (1999).
139. P. P. Schmidt, *Int. J. Quant. Chem.* **72**, 473 (1999).
140. Y. Kumeda, Y. Minami, K. Takano, T. Taketsugu, and T. Hirano, *THEOCHEM* **458**, 285 (1999).
141. D. Sugny, M. Joyeux, and E. L. Sibert III, *J. Chem. Phys.* **113**, 7165 (2000).
142. J. N. Murrell, S. Carter, and L. O. Halonen, *J. Mol. Spectrosc.* **93**, 307 (1982).

CHAPTER 4

GEOMETRY OF PHASE-SPACE TRANSITION STATES: MANY DIMENSIONS, ANGULAR MOMENTUM

LAURENT WIESENFELD

Laboratoire d'Astrophysique, Observatoire de Grenoble, Université Joseph-Fourier, BP 53, F-38041 Grenoble Cédex 9, France

G stands for Geometry, the art of measuring things.
Anonymous, 18th century

CONTENTS

I. Introduction
II. Hamiltonian Dynamics
  A. General Equations
  B. Dimensions
III. Geometry in Simpler Cases
  A. One Degree of Freedom
    1. Linear Case, Linearization
    2. Nonlinearities
    3. Some Remarks on 1-DOF Hamiltonians
  B. Two Degrees of Freedom: PODS and Beyond
    1. Linear Theory
    2. Periodic Orbit Dividing Surfaces
IV. General Transition States in n Degrees of Freedom
  A. Dimensions and NHIM
    1. Linear Regime
    2. Description of the Geometry
  B. Some Examples
    1. A Three-Dimensional Version of Hénon–Heiles Potential
    2. Dynamics of Three Identical Atoms, Zero Angular Momentum
V. Angular Momentum
  A. Dynamics in the Rotating Frame

Geometric Structures of Phase Space in Multidimensional Chaos: A Special Volume of Advances in Chemical Physics, Part A, Volume 130, edited by M. Toda, T Komatsuzaki, T. Konishi, R.S. Berry, and S.A. Rice. Series editor Stuart A. Rice.
ISBN 0-471-70527-6

1. Relative Equilibrium
2. An Example: A Rotating van der Waals Complex
B. Some Results in Astrophysics
1. General Considerations
2. Inelastic Scattering
VI. Conclusion
Acknowledgments
References

I. INTRODUCTION

Transition State theory (TST) is an extremely successful theory for chemical physics. It is simple to understand in its elementary versions and is appealing for its intuitiveness. It has been developed over the years into a whole series of theories or branches of theories, in order to make it more apt to calculate and predict kinetic factors of various chemical reactions or half reactions. Very many references appeared, dealing with transition state theories, in its many variants, and some of the articles in this series of reviews contain many of those. In particular, unimolecular decays are treated here in great detail by Rice [1]. A general review, exhaustive at its time of appearance, is Ref. 2. Some particularly stimulating references may be found in the work by Gaspard [3].

As stated earlier by Komatsuzaki and Berry [4], it is a common intuition that there should exist somewhere in phase space a surface (a manifold) that would separate the regions of reactants from the region of products. For obvious reasons, this surface has been named a transition state, or dividing surface. It has to be crossed by the system in order for it to be transported from reactants to products. For many reasons, finding this surface proved to be much more elusive than anticipated years ago. Also, it must be stated at once that such a concept is essentially a classical one. Still, three problems make the definition of a transition state far from obvious:

1. Quantum mechanics does not define easily a surface. There have been many attempts to properly define a quantum transition state [5]. While a purely quantum view is difficult, semiclassical insights are awaited [6,7].
2. Because of the prevalence of Hamiltonian chaos, trajectories may cross the dividing surface and than cross it back and forth a certain amount time, even an indefinite one. While this is impossible at the linear level, one has to resort to perturbation theory to overcome this drawback.
3. The third problem is a problem of dimensionalities. While it is easy to visualize dynamics with few degrees of freedom and/or zero angular momentum, the situation may be far from obvious with angular momentum and/or many dimensions. Some steps towards this understanding will be presented here.

In this chapter, I do not wish to enter into a review of all those variants of TST, nor into many actual chemical applications. My goal is more pedagogical. I wish to try to describe how it is possible, in general, to define a classical transition state for a n degrees of freedom system, which includes chemical reactions and/or angular momentum. Because geometry is our main theme here, much of the chapter is restricted to linear Hamiltonians. Indeed, those linear (or linearized) Hamiltonians are a good base for discussion of the topological structure of phase space near a transition state. The linearized Hamiltonian is easy to understand and allows for exact calculations and representations, yet captures some of the most important concepts. Furthermore, it serves as a basis for a perturbation theory, which deals with the extremely serious problem of nonlinearities (the *recrossing problem*, point 2 above). These canonical perturbation theories, in their various variants, have been described in great detail recently [4,8–12] and I do not wish do go into that subject. Rather, when presenting actual examples, I will present purely numerical support for the generalization of linear analysis toward the fully nonlinear case. It is hoped that this approach will help the reader in devising another approach to the problem of nonlinearities in TST.

As this book shows, TST is becoming more and more of a multidisciplinary endeavor. Some new applications may be found outside the realm of chemical physics. In particular, Marsden and co-workers [13] applied those concepts to celestial mechanics of small bodies, while the general theory of the Keplerian three-body problem makes use of TST, even if in a highly singular case [14,15]. Much work remains to be done outside of chemical physics types of dynamics. I come back to this question in the conclusion.

The outline of this chapter is as follows. We begin by putting forward some elementary properties of Hamiltonian dynamics and defining linearization processes (Section II). Then, we describe one and two degree of freedom dynamics, having in mind our next generalization to n-degree-of-freedom dynamics (Section III). All other necessary tools having been described, we proceed to the two new cases, n degrees of freedom and nonzero angular momentum. Examples are proposed in this part (Section IV). We end with a short conclusion.

II. HAMILTONIAN DYNAMICS

A. General Equations

To begin with, it is useful to recall some elementary properties of dynamics in phase space [16]. Let a classical Hamiltonian be written as

$$H = H(p_i, q_i), \qquad i = 1, \ldots, n \tag{1}$$

In Eq. (1), q_i are the generalized coordinates, p_i, their conjugate generalized momenta and n is the number of coordinates necessary to fully describe the

system; n is called the number of degrees of freedom (DOFs). In short we speak of H (Eq. (1)) as an n-DOF Hamiltonian. Throughout this article we explicitly exclude time dependent Hamiltonians, since very little is known in terms of time-dependent transition state (TS).

Let us note in passing that we do not restrain to Hamiltonians of the form:

$$H = T(p_i) + V(q_i) \tag{2}$$

where T and V would be respectively kinetic and potential energies. While this situation often occurs, it is not so realistic in molecular physics. Hamiltonians we have to deal with become easily rather involved, all the more if angular momentum comes into play. In particular, H involving both angular momentum and deformation in molecular systems is by no means trivial [17–19].

Let us recall also the equation of motion (the dot denotes derivatives with time, $\dot{a} \equiv da/dt$):

$$\begin{aligned} \dot{q}_i &= +\frac{\partial H}{\partial p_i} \\ \dot{p}_i &= -\frac{\partial H}{\partial q_i} \end{aligned} \tag{3}$$

In more mathematical contexts, it is customary to write down these equations in a more compact way, that readily extends towards n-DOF Hamiltonians. Let $x = \{q_i, p_i\}$, where x is a vector. x denotes collectively all coordinates and momenta, emphasizing their possible combination in canonical transformations. Then $H = H(x)$ and equations (3) become

$$\dot{x} = \mathsf{J}\nabla H(x) \tag{4}$$

where $\nabla H \equiv \partial H/\partial x$ and J is the so-called symplectic matrix:

$$\mathsf{J} = \begin{pmatrix} 0 & I \\ -I & 0 \end{pmatrix}, \qquad I = \delta_{ij}, i, j = 1, \ldots, n \tag{5}$$

I is the $n \times n$ identity matrix. Let us recall here that the classical equations of motion, Eq. (4), is an ordinary differential equation (ODE), as opposed to the Schrödinger equation, which is a partial differential equation. Being an ODE, even if nonlinear, the solution of Eq. (4), $x(t)$, is *uniquely* defined by the initial conditions $x(t = 0)$.

An equilibrium point, in general, is defined as a point for which $\dot{x} = 0$ ($\dot{p}_i = \dot{q}_i = 0$). Looking at Eqs. (3 and 4), this amounts to stating that a certain point P is an equilibrium point if the gradient $\nabla H = 0$. This definition is general

for true (absolute) equilibrium points. It can be readily extended to relative equilibria (see Section V). On the other hand, if we restrict the form of H to

$$H = \sum_i \frac{p_i^2}{2m} + V(q_i)$$

where m is the mass of the system, then $p_i = m\dot{q}_i$. The equilibrium points are found at the usual conditions

$$\dot{q}_i = 0; \qquad \frac{\partial V}{\partial q_i} = 0 \tag{6}$$

Hamiltonian dynamical system theory is the mathematical framework on which TST rests; many textbooks, of various mathematical sophistication, describe this branch of pure/applied mathematics. Some of the various flavors are [20–24]. Very little of this vast information will be needed here, and we shall try to be as self-consistent as possible.

B. Dimensions

In order to understand the problem of finding TS with three or more DOFs, it is useful to address the question of dimensionalities, in configuration and phase space. In classical, Hamiltonian dynamics, transition states are grounded on the idea that certain surfaces (more precisely, certain manifolds) act as barriers in phase space. It is possible to devise barriers in phase space, since in phase space, in contrast to configuration space, two trajectories never cross [uniqueness of solutions of ODEs, see Eq. (4)]. In order to construct a barrier in phase space, the first step is to construct a manifold $\mathcal{W}$ that is made of a set of trajectories [8].

1. $\mathcal{W}$ is said to be "invariant under the flow generated by the Hamiltonian H."
2. $\mathcal{W}$ is codimension 1 in the phase space ϕ or its restriction to a particular energy, $\phi(E)$.

Point 2 means that (D is a dimension)

$$D^{(\mathcal{W})} = D^{(\phi)} - 1 \quad \text{or} \quad D^{(\mathcal{W})}(E) = D^{(\phi)}(E) - 1 \tag{7}$$

With these properties, $\mathcal{W}$ locally separates phase space, as illustrated in the scheme (Figure 1). It is very important to note that even if $\mathcal{W}$ has codimension 1 and is locally a separatrix, it does mean in n DOFs that $\mathcal{W}$ neither has a simple geometry, because it is subject to stretching and folding because of chaos [24–26], nor separates globally (see Ref. 27). Let us now make a summary of the

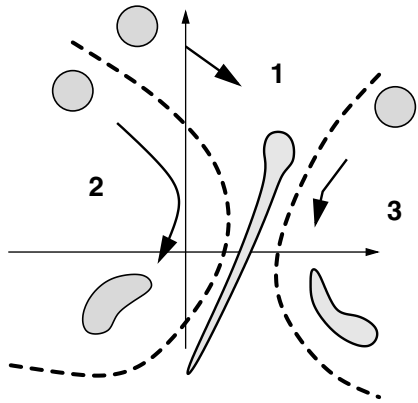

Figure 1. A scheme of separatrices. Ensemble of trajectories are schematized by gray sets. The three sets of trajectories, 1,2,3, evolute but never cross the separatrices represented by dashed lines.

dimensionalities for several values of n (Table I). Examination of Table I shows that three different types of dynamics occur.

1. $n = 1$. The energy level is made of trajectories. Separatrices are identified with some particular trajectories (see Section III.A).
2. $n = 2$. Poincaré surface of section is of dimension 2, as are stable and unstable manifolds of periodic orbits. Hence, the huge simplicity of $n = 2$ is that:
   (a) Poincaré sections may be drawn on a sheet of paper or on a computer screen, allowing easy exploration of $\phi(E)$.
   (b) Stable/unstable manifolds of periodic orbits are separatrices. This is the departure point of many studies of transport in phase space, based on lobe dynamics seen one way or another [28–33].

TABLE I
Dimensions of Various Objects of n-DOF Hamiltonian System[a]

n	1	2	3	N
ϕ, phase space	2	4	6	$2N$
$\phi(E)$, energy level	1	3	5	$2N-1$
Trajectory	1 *(0)*	1 *(2)*	1 *(4)*	1 *(2N − 2)*
(Un)stable manifold of trajectory	—	2 *(1)*	2 *(3)*	2 *(2N − 3)*
Poincaré section	—	2 *(1)*	4 *(1)*	*2N − 2 (1)*

[a]When relevant, codimensions are mentioned in italics.

3. $n \geq 3$. All the nice features disappear. It is impossible to draw Poincaré sections easily because periodic orbits have large codimensions, as have their stable/unstable manifolds.

Point 3 is developed fully in Section IV, especially in Section IV.A.

III. GEOMETRY IN SIMPLER CASES

A. One Degree of Freedom

While the one-dimensional case may seem too simple, even trivial, it presents a good opportunity to put forward some very general concepts. These concepts, like the existence of barriers in phase space and the stable/unstable manifolds theorem, are best introduced here, having in mind that most interesting applications will come later on. Also, the one-dimensional case has been employed in less trivial ways, by reducing all rapid DOFs to some adiabatic approximation allowing nonlinear one-dimensional TST to be applied [34].

1. Linear Case, Linearization

To begin our discussion of geometry, let us restrict ourselves to 1-DOF systems,

$$H = H(p, q) \tag{8}$$

This system is too simple to display a proper TS, but is good enough to begin with and shows some interesting features. Let us simplify dynamics as much as possible and write

$$H = \frac{p^2}{2} + V(q) \tag{9}$$

Mass is set to 1 without loss of generality, for all Hamiltonians definition, except where explicitly needed.

Equation (6) tells us that an equilibrium point may be found for Hamiltonian (9) at points such that $\mathrm{d}V/\mathrm{d}q = 0$ (Fig. 2). The linear stability of the equilibrium points is easily found by examining the sign of the second derivative:

$$\text{Stable:} \quad \frac{\partial^2 V}{\partial q^2} > 0 \qquad \text{Unstable:} \quad \frac{\partial^2 V}{\partial q^2} < 0 \tag{10}$$

Marginally stable equilibrium points are such that $\partial^2 V/\partial q^2 = 0$. The stability is then determined by the nonlinearity of the force $-\partial V/\partial q$. In the 1-DOF case, this is easily extended to the general Hamiltonian (8). An equilibrium point is such that $\partial H/\partial p = \partial H/\partial q = 0$. The linear stability proceeds as follows,

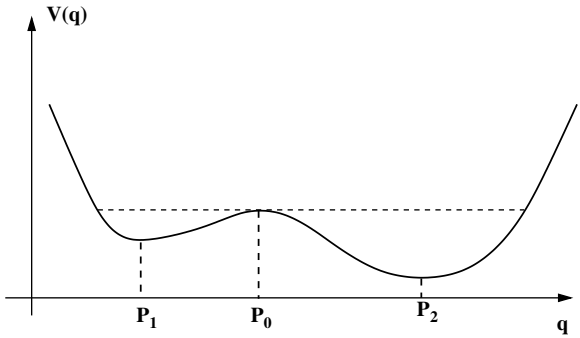

Figure 2. A one-dimensional potential, with three equilibrium points: P_0, P_1, P_2.

which is readily generalizable to more DOFs. Let the Hessian of Hamiltonian H be defined as

$$\mathrm{Hess}(H) = \begin{pmatrix} \dfrac{\partial^2 H}{\partial p^2} & \dfrac{\partial^2 H}{\partial p \partial q} \\ \dfrac{\partial^2 H}{\partial p \partial q} & \dfrac{\partial^2 H}{\partial q^2} \end{pmatrix} \tag{11}$$

Since we are interested in motion nearby the equilibrium point, let us make the following expansion. Let the coordinates of P be x_P and define $x = x_P + \delta x$. Setting without loss of generality $x_P = 0$, we have in first order in δx the following matrix equation:

$$\dot{\delta} x = \mathsf{J}\,\mathrm{Hess}(H)\,\delta x = \mathsf{M}\,\delta x \tag{12}$$

Restricting to one DOF, equation (12) reads

$$\begin{pmatrix} \dot{\delta} p \\ \dot{\delta} q \end{pmatrix} = \begin{pmatrix} \dfrac{\partial^2 H}{\partial p \partial q} & \dfrac{\partial^2 H}{\partial q^2} \\ -\dfrac{\partial^2 H}{\partial p^2} & -\dfrac{\partial^2 H}{\partial p \partial q} \end{pmatrix} \begin{pmatrix} \delta p \\ \delta q \end{pmatrix} \tag{13}$$

In order to find the linear stability of P, let us look at the eigenvalues of the matrix in (13). We have

$$\lambda_{1,2} = \pm \left[\left(\frac{\partial^2 H}{\partial p \partial q} \right)^2 + \frac{\partial^2 H}{\partial q^2} \frac{\partial^2 H}{\partial p^2} \right]^{1/2} \tag{14}$$

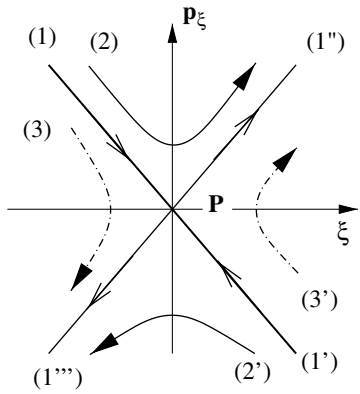

Figure 3. Phase portrait of a hyperbolic fixed point, for a 1-DOF linear Hamiltonian.

If the square root is real, it is possible to put Hamiltonian (8) in the following linearized form in the vicinity of P:

$$H_{\text{lin}} = \frac{1}{2}p_\xi^2 - \frac{1}{2}\lambda_{1,2}^2\xi^2 \tag{15}$$

where (p_ξ, ξ) is the eigenvector of the matrix (14). This is the equation of an *anti-harmonic* oscillator. Its well-known phase-space portrait is depicted Fig. 3. A linearly unstable equilibrium point is called a hyperbolic equilibrium point. In some contexts, the point P is called a critical point; an unstable equilibrium is a saddle critical point; a stable equilibrium point is called a center critical point. Coordinates ξ, p_ξ are called *reaction coordinate and momentum*. Likewise, if $\lambda_{1,2}$ is imaginary, we have

$$H_{\text{lin}} = \frac{1}{2}p_y^2 + \frac{1}{2}\lambda_{1,2}^2 y^2 \tag{16}$$

where (p_y, y) are the eigenvector of the matrix (14). This is the equation of a *harmonic* oscillator, and its phase-space portrait is depicted in Fig. 4. In Fig. 2, points P_1 and P_2 are elliptic and point P_0 is hyperbolic.

Let us examine in some detail what Fig. 3 tell us about the different possible motions. Since H, Eq. (15) is a 1-DOF H, each energy (except $E = 0$) is represented by only two trajectories. Let $p_x i < 0$ be called the reactant region and let $\xi > 0$ be called the product region.

1. $E < 0$, trajectories (3) and (3′). Only nonreactive trajectories are possible, without change of $\xi(t)$.

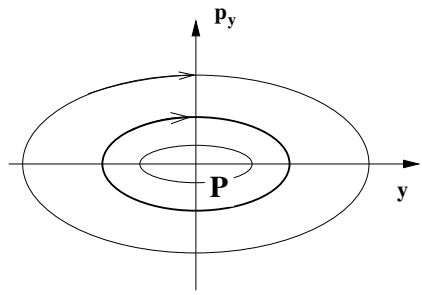

Figure 4. Phase portrait of an elliptic fixed point, for a 1-DOF linear Hamiltonian.

2. $E > 0$, trajectories (2) and $(2')$. Only reactive trajectories are possible, from product to reactants ($p_\xi > 0$) or from reactants to products ($p_\xi < 0$).
3. $E = 0$, two types of solution:
   (a) the unstable equilibrium point P
   (b) the stable and unstable lines (called manifolds) that come from $(1'')$–$(1''')$ or go to (1)–$(1')$ point P.

Trajectories $(1) \rightarrow (1''')$ are called separatrices. They separate reactive parts of phase space from nonreactive parts, since trajectories never cross. Also, the amount of time necessary to go from any point to/from P on the separatrices is infinite. This is necessary because of the unicity of solution at point P (one can also consider this infinite time as a consequence of continuity of classical mechanics).

Trajectories $(1) \rightarrow (3)$ may also be depicted in a more usual way, in the energy/coordinate plane (Fig. 5). Note that some authors, drawing from Figs. 5 and 3, have long ago extended trajectories into the complex domain, thereby allowing for tunneling. In this context, powerful methods were developed,

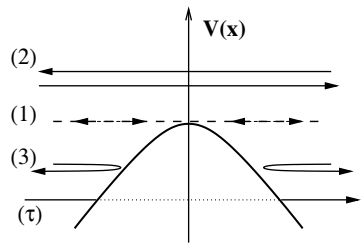

Figure 5. Energy/coordinate scheme of the trajectories of Fig. 3. Trajectory (τ) is a tunneling trajectory.

somehow outside of the scope of this review (see Ref. 35, Chapter 9 for references). Considerable amount of work is performed on this topic, but mainly with more than 1 DOFs (see Sections III.B to IV). Also, instanton-type of approximation belongs to this topic. A recent reference is Ref. 36.

2. *Nonlinearities*

Extension toward the fully nonlinear case is straightforward for 1-DOF Hamiltonians. The energy conservation relation $H(p,q) = E$ allows us to define (explicitly or implicitly) $p = p(q;E)$, thereby reducing the ODE to a simple quadrature. In this procedure there is no problem of principle (unlike the $n \geq 2$-DOF case). It works in practice also, and it is possible to adapt Figs. 3–5 to the nonlinear regime. It must be underlined that besides that simple procedure, we present a theorem in dynamical system theory (containing Hamiltonian dynamics as a particular case). This theorem is valid for n DOFs (hence for $n = 1$); it relates the full dynamics to the linearized dynamics, called tangent dynamics in the mathematical literature.

The *local and global stable/unstable manifold theorems* (see, e.g., Ref. 24, pp. 136–140) tell us the following ($\mathcal{W}^{u,s}$ are the (un)stable manifolds):

1. In the vicinity of P, $\mathcal{W}^{u,s}$ of the full dynamics are tangent to the $\mathcal{W}^{u,s}_L$ of the linearized dynamics (Fig. 6).
2. The extension of $\mathcal{W}^{u,s}$ is infinite. Furthermore, they tend to P as $t \to +\infty(\mathcal{W}^u)$ or $t \to -\infty(\mathcal{W}^s)$.

We see thus that our description of the dynamics in the linearized regime is very general and is transferred readily to the nonlinear regime.

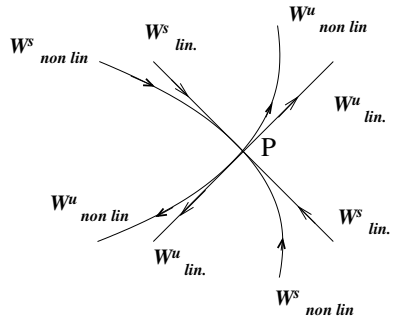

Figure 6. The nonlinear stable/unstable manifolds are tangent to the linearized stable/unstable manifolds.

3. *Some Remarks on 1-DOF Hamiltonians*

While all that material presented in this section looks very elementary, the structure presented thus far is the dynamical system theory basis of the reaction path TS theory. If, in a complicated landscape with many dimensions, we reduce dynamics to following a winding path, the above images are enough for all our purposes. They are also a very good basis in the first approximation of 2-DOF and even n-DOF, if we adiabatically decouple the reaction coordinate and all the other coordinates, which are called bath coordinates.

As a last point, it must be underlined that if the approximation of Hamiltonian dynamics is lifted—that is, if we include dissipation in one way or another—very little is known outside of either strong dissipation or 1-DOF systems. While this is outside of the scope of this review, the interested reader should consult Refs. 37 and 38.

B. Two Degrees of Freedom: PODS and Beyond

While still not very realistic, since they can barely encompass angular momentum, 2-DOF Hamiltonian models for chemical reaction or unimolecular dissociation have a long and rich history. Several reviews exist that underline this history [1,28]. Our purpose here is slightly different. We wish to describe TS in 2 DOFs as an intermediate in complexity between the oversimple 1-DOF TS and the fully complicated story of $n > 2$ DOFs, including possibly angular momentum. On a physical point of view, most of the early studies that appeared up to the late 1970s and early 1980s dealt with the classical dynamics of collinear collisions or dissociation [39], with the following scheme:

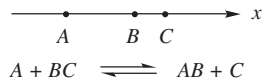

On that system were exact TS discovered [39], the importance of mass mismatch between atoms A, B, C underlined and chaos in reactive scattering described [3, 29,40–42]. It must be underlined that studies in atomic physics and celestial dynamics were decisive in a definition of a TS, with less obvious Hamiltonians, see the chapter by Jaffé et al. in this book.

To begin with, let us suppose that the Hamiltonian may be written as

$$H = \frac{p_1^2}{2m_1} + \frac{p_2^2}{2m_2} + V(q_1, q_2) \tag{17}$$

For three-body collinear systems, various types of coordinate systems allow for this type of kinetic energy (Jacobi type of coordinates).

1. Linear Theory

As before, we begin by organizing dynamics around an equilibrium point P. Because of the form of H, Eq. (17), we have $\nabla V(q_1, q_2)|_P = 0$. We look for the linear stability of this point and find that the tangent flow (see Section II) has two pairs of eigenvalues, $\lambda_{1,2} = \pm i\omega$ and $\lambda_{3,4} = \pm \kappa$, with $\kappa, \omega > 0$. The corresponding eigenvectors pairs are respectively the bath coordinates, y, p_y, and the reaction coordinates, ξ, p_ξ. Then, in the neighborhood of P and setting the origin of energy at P, the linearized Hamiltonian reads, setting masses to unity:

$$H = \frac{1}{2}\left(p_y^2 + p_\xi^2\right) + \frac{\omega^2}{2} y^2 - \frac{\kappa^2}{2}\xi^2 \tag{18}$$

This very simple Hamiltonian is at the basis of the whole TS approach. It generalizes easily into many dimension (Section IV), is a good basis for perturbation theory [4], and is also the basis for numerical schemes, classical and semiclassical. The inclusion of angular momentum implies that some ingredients must be added (see Section V). Let us thus describe how this very simple, linear Hamiltonian supports normally hyperbolic invariant manifolds (NHIMs; see Section IV for a proper discussion) separatrices and a transition state.

The first thing to note is that the linearized Hamiltonian is separable,

$$E = H = H(y) + H(\xi) = \omega_y I_y + H(\xi) \tag{19}$$

Hence, the total energy $H = E$ is split into the energy of the oscillator, H(y), with an action of the oscillator written as I_y and a reaction coordinate part, $H(\xi)$. Furthermore, $I_y \geq 0$ but $H(\xi) \gtrless 0$. In order to have trajectories that react (go from the reactant side to the product side, or vice versa), we must have $H(\xi) > 0$, since at $\xi = 0$, $H(\xi) > 0$ and $H(\xi) = \text{ct}$. There are two important objects here:

$$\text{The periodic orbit } \Gamma: \quad \xi = p_\xi = 0, \quad E > 0 \tag{20a}$$

$$\text{The transition state:} \quad \xi = 0\,, \quad E > 0 \tag{20b}$$

We see that, indeed, Eq. (20b) is a transition state, since

1. It is a dividing surface (codimension 1 in the energy level), its dimension here being indeed 2.
2. It separates products from reactants.
3. Once a trajectory crosses it, it never comes back.

All these properties are more or less obvious in the linear case. However, because of the essentially four-dimensional nature of phase space, it is somewhat difficult to get an intuitive nature of the phase-space structure. This is

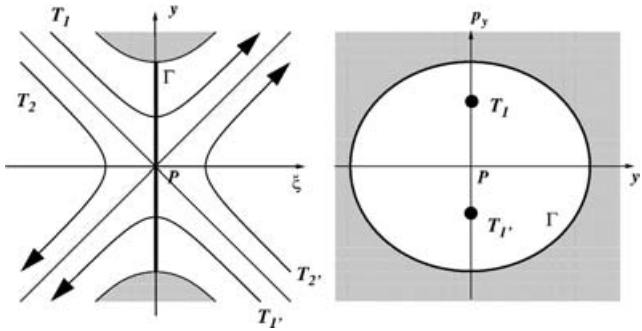

Figure 7. Linearized transition state. **Left panel**: The reaction coordinate part of phase space. **Right panel**: $\xi = 0$ surface of section. The shaded areas are forbidden by energy conservation.

especially true for the transition state, which is *not* made of trajectories, since it crossed by trajectories and should be transverse to the flow. An image of the transition state is given in Fig. 7.

2. *Periodic Orbit Dividing Surfaces*

Description. Among all physically relevant Hamiltonian dynamics, one case is particularly important:

$$H = T(p_1, p_2) + V(q_1, q_2) \tag{21}$$

where $T(p_1, p_2)$ is a positive definite quadratic form. Without loss of generality, we can write

$$H = \frac{p_1^2}{2m_1} + \frac{p_2^2}{2m_2} + V(q_1, q_2) \tag{22}$$

It is very fortunate that in this very important case, it was possible to devise an exact theoretical form of a classical transition state. This theory was discovered in the late 1970s by Pechukas, Child, and Pollak [39] and may be intuitively understood. We wish to replace the linearized motion by an analysis of the full Hamiltonian (21). Let us examine Fig. 8.

If we replace the $\xi = p_\xi = 0$ periodic orbit by the Γ periodic orbit, this p.o. is named a periodic orbit dividing surface (PODS). It has the following properties:

- Γ connects the $V = E$ lines; hence Γ is a periodic orbit that is symmetric under time reversal.

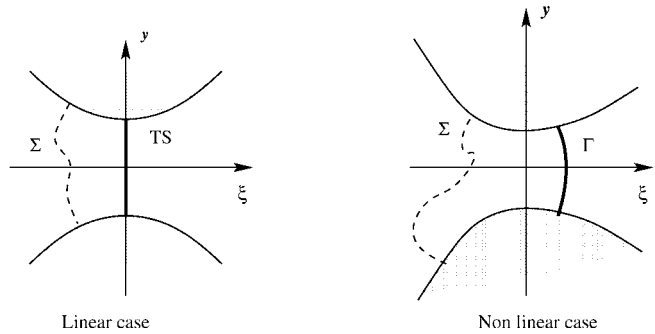

Figure 8. Linear transition state (TS) and nonlinear periodic orbit dividing surface (PODs) Γ.

- Of all possible surface Σ drawn in phase space, whose projection onto configuration space is a line connecting the two $V = 0$ lines, the flux Φ is minimum for $\Sigma = \Gamma$, with

$$\Phi = \int_{\Sigma^+} p\, dq \tag{23}$$

  where the $+$ superscript indicates trajectories going from left to right.
- Γ is an unstable periodic orbit, whose linearization is *direct* hyperbolic. Consequently, all trajectories crossing Σ in configuration space have to leave its neighborhood before possibly returning to Γ. Γ was named a repulsive PODS; we would now call it an NHIM. An image of the situation is shown in Fig. 9.

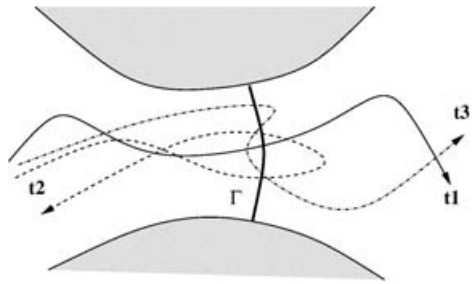

Figure 9. A repulsive pods Γ, with a possible trajectory **t1** and two forbidden ones **t2**, **t3**. **t3** exhibits recrossing of Γ.

Being a repulsive PODS—a fully nonlinearly determined NHIM—the ubiquitous problem of recrossings (trajectory t3 in Fig. 9; see Ref. 6) is totally avoided.

Finding a PODS is a very easy task. Because the system has only two DOFs, the $V = E$ manifolds are simply one-dimensional lines in configuration space, $V(q_1, q_2) = E$. Momentum is zero on those points. Finding the self-retracing p.o. amounts to a very easy one-dimensional search. Once a p.o. is found, a linear stability determination is enough to determine the PODS character of a particular p.o. These properties have been used many times in the literature, in a classical or semiclassical, even quantum, context [6,39,43–45]. The reader is referred to the rich literature for many actual examples. The series of articles by Gaspard and Rice are particularly detailed [46].

Phase Space. The PODS structure is easily lifted into phase space and described in a way very analogous to the linear case. We begin by finding the equilibrium points of the original Hamiltonian. Let P_i be such points. In a general case of chemical relevance, there will be a point P whose linear stability will be of stable/unstable (center/saddle) character. That is,

$$\mathrm{Eig}(\mathsf{M})|_P = \pm\kappa, \pm i\omega \qquad \omega, \kappa > 0 \tag{24}$$

In the neighborhood of P, the Hamiltonian may be written as

$$H = \omega I + \frac{1}{2}\left(p_\xi^2 - \kappa^2 \xi^2\right) + h_{\mathrm{NL}}(I, p_\xi, \xi) \tag{25}$$

with ωI the periodic orbit and p_ξ, ξ, coordinate normal to it. Now, we include the nonlinear terms in the expression. Since I is the exact periodic orbit and p_ξ, ξ determine the true nonlinear stable/unstable manifolds, we have that $h_{\mathrm{NL}} = 0$ if $p_\xi = \xi = 0$. The structure of the dynamics in the neighborhood of Γ is easily approached with Poincaré surfaces of section. Numerous examples exist in the literature; these are essentially equivalent to Fig. 7. However, identifying the surface of section with the orbit Γ has not always been clear, since shadowing problems (pruning) may occur [41,47].

Cylindrical Manifolds. There is one big advantage of looking at 2-DOF TS in phase space: It puts emphasis on the existence of the tubes that determine the transport of classical probability in phase space. Existence of those tubes has been known for a long time [48]. These tubes are the set of trajectories that constitute the stable/unstable manifolds of PODS. Locally, in the vicinity of P, they immediatly generalize to higher dimensions. They are constructed as follows:

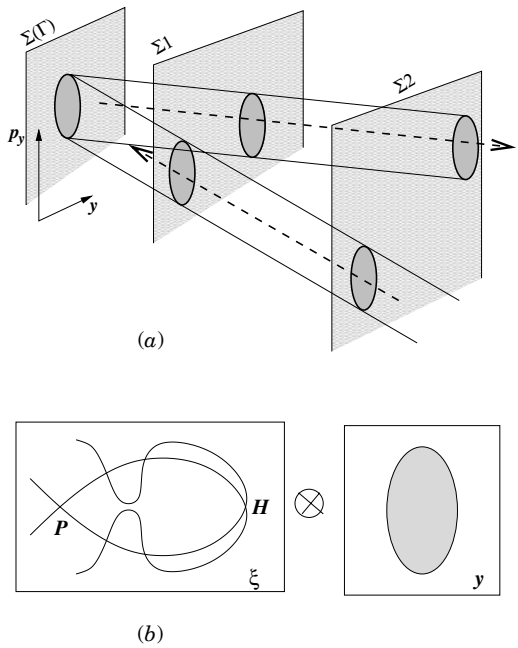

Figure 10. Two views of the tubes. (*a*) Left, a series of Poincaré sections, beginning with the TS, $\Sigma(\Gamma)$. Large arrows denote the sense of trajectories, and gray ellipses denote the density of probability after and before crossing the TS. (*b*) A view of the dynamics in the ξ and y sectors. P is the equilibrium point, and H the homoclinic point.

- Attach to each point of the PODS its stable/unstable directions.
- Integrate the trajectory along this direction; one finds the stable/unstable manifold itself.
- Make a union of all those trajectories; they make up a tube extending in phase space.
- These tubes, being made up of trajectories, must not be crossed by any trajectory, hence by any density of probability.

An illustration is found in Fig. 10.

And finally, the TS itself is found at the intersection of tubes. More precisely, the TS (which is two-dimensional in the three-dimensional energy level) is found at the intersection of the interiors of the two tubes, constituted by the stable/unstable manifolds, at each side of the Γ PODs. A rigorous definition (valid for n DOF) is found in Ref. 9. An illustration may help the intuition (Fig. 11).

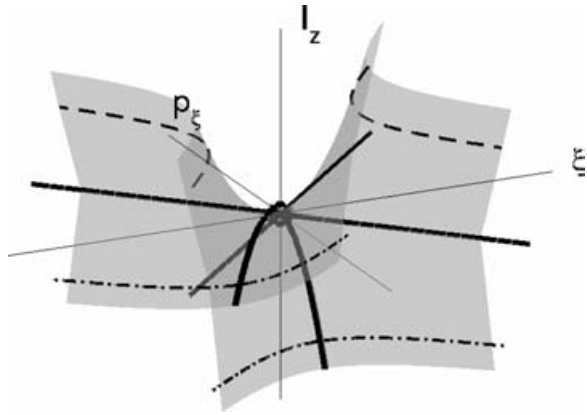

Figure 11. Schematic view of a TS (thick black line), with the same type of view as in Fig. 10. The equilibrium point is in the middle with its stable manifold and unstable manifold extending as straight lines. Trajectories in dot-dashed lines are reactive (inside the tubes) and cross TS; trajectories in dashed lines are not reactive. The whole gray surface is the energy level. For a linear motion, it takes the form of a parabolic hyperboloid.

IV. GENERAL TRANSITION STATES IN *n* DEGREES OF FREEDOM

Several reviews and articles have appeared recently that deal with *n*-DOF transition states [4,8,49,50]. These works come after several pioneering works on the subject, published earlier, that began the generalzation of TS toward a full-fledged phase space theory [13,51]. Since we described in some detail the 2-DOF case in the preceding section, the generalization will come very easily, as far as no angular momentum is involved. However, in Section V we deal with the nonzero angular momentum case in great detail, since it offers new perspectives in the geometry of phase space.

We shall make more use of the notion of normally hyperbolic invariant manifold (NHIM). This invariant surface is the *n*-DOF generalization of the periodic orbit dividing surface, even if originally defined in a much more general framework (a bibliography may be found in Ref. 24). Its correct definition is put forward in Section IV.A and is used in all examples coming thereafter.

A. Dimensions and NHIM

The structures of *n*-DOF TS and their associated NHIM are interesting by themselves, especially because many ideas are already present at the PODS level.

However, some points differ markedly, because of the higher dimensionality of all the objects considered. We shall swiftly describe the overall geometric properties of the NHIM and the TS, and then we will proceed with some examples that clarify the situation. Other examples may be found in Refs. 9 and 52.

1. *Linear Regime*

As in previous simpler cases with fewer DOFs, everything begins with equilibrium points (critical points in mathematical language). We straightforwardly generalize earlier results. Let $H = H(p_1, \ldots, p_n, q_1, \ldots, q_n) = H(x)$ be the Hamiltonian and suppose that P is an equilibrium point, $\nabla H(x) \mid_P = 0$. We linearize motion around P, and we analyze the eigenvalues of the $2n \times 2n$ matrix M, Eq. (4). If we have the following situation:

$$\begin{aligned} \lambda_{i,i+1} &= \pm i\omega_i, \qquad \omega_i > 0 \quad i = 1, 3, \ldots, 2n-3 \\ \lambda_{2n-1,2n} &= \pm\kappa, \qquad \kappa > 0 \end{aligned} \tag{26}$$

then we are able to build a NHIM and a TS in the neighborhood of P. We begin by finding the $n-1$ first eigenvector pairs corresponding to the imaginary eigenvalues of M. Let us call those eigenvectors y_i/p_{y_i}. These are the linear normal modes of the transition states, as is well known in TST. This is always possible if $\omega_i \neq \omega_j$, $\forall i \neq j$. Otherwise, some special treatment is necessary for resonances, if $k_i\omega_i = k_j\omega_j$, with $k_i, k_j = 1, 2, 3$ in practice (any integer k in theory). We call ξ, p_ξ the last two eigenvectors, which constitute the reaction coordinate and associate momentum. As before, we may write a linear Hamiltonian, in the vicinity of P:

$$H = \sum_{i=1,n-1} \tfrac{1}{2}\left(p_{y_i}^2 + \omega_i^2 y_i^2\right) + \tfrac{1}{2}\left(p_\xi^2 - \kappa^2\xi^2\right) \tag{27a}$$

In order to use earlier articles and facilitate contact with perturbation theory, it is useful to make the following change of variables:

$$\eta = \frac{1}{2\kappa}(p_\xi + \kappa\xi)$$
$$p_\eta = \frac{1}{2\kappa}(p_\xi - \kappa\xi)$$

and the Hamiltonian is written as

$$H = \sum_{i=1,n-1} \tfrac{1}{2}(p_{y_i}^2 + \omega_i^2 y_i^2) + \kappa^2\, p_\eta \eta \tag{27b}$$

Again, dynamics generated by Eqs. (27a and 27b) is that of an NHIM and a TS, which are defined as follows:

$$\eta = p_\eta = 0/\xi = p_\xi = 0 \qquad \text{NHIM} \tag{28a}$$

$$\eta = p_\eta \neq 0/\xi = 0 \qquad \text{Transition state} \tag{28b}$$

The nature of the object (28a) is very interesting and new with respect to the 2-DOF case. If we were 2-DOF only, Eq. (28a) would be the equation of a periodic orbit, the PODs of Section III.B.2. This cannot be the case here because of dimensionalities.

2. *Description of the Geometry*

Equation (28a) is in fact the equation of an S_{2n-3} sphere, which is the equivalent for the n-DOF to the periodic orbit: $2n - 3 = 1$, if $n = 2$. Its geometry is easier to apprehend for $n = 3$. The S_3 sphere may be described as a union of T_2 tori. This is easily seen if we switch to action-angle variables:

$$H(I_1, \phi_1, I_2, \phi_2) = \omega_1 I_1 + \omega_2 I_2 \tag{29}$$

where I_i and ϕ_i are actions and associated angles. Each torus is the familiar solution with both $I_1, I_2 \neq 0$. By varying I_1 and I_2 we recover the S_3 sphere, recalling that the angle ϕ_i loses significance if $I_i = 0$ [53]. An abstract image of the NHIM is found in Fig. 12.

In the liner approximation, we see thus that the NHIM is made of periodic/quasi-periodic orbits, organized in the usual tori characteristic of the integrable systems. Because the NHIM is ''normally hyperbolic,'' each point of the sphere has stable/unstable manifolds attached to it. This situation is exactly parallel to the one described earlier for PODS. The equation for it is

$$H = \omega_1 I_1 + \omega_2 I_2 + \frac{1}{2}(p_\xi^2 - \kappa^2 \xi^2) \qquad \text{with} \qquad I_1 = I_1(M), I_2 = I_2(M) \tag{30}$$

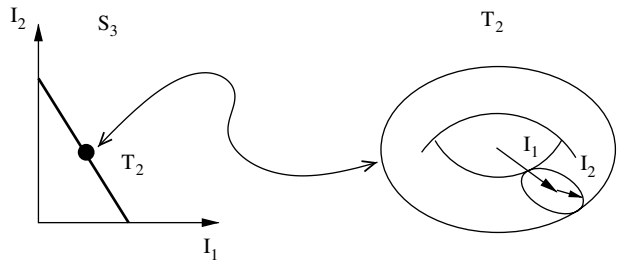

Figure 12. A scheme of the S_3 sphere, built with a foliation of tori. The straight line in the left panel is the image of equation Eq. (29).

where M is any point on the torus. Equation (30) thus defines a one-dimensional motion (the anti-oscillator in ξ, p_ξ) and adds one dimension to S_3, yielding four-dimensional manifolds in the five-dimensional energy level of the phase space. Everything falls thus rightly in place.

It is then possible to have a global picture [9,24,53,54] of what is happening in the whole phase space neighborhood of the equilibrium point P, for $0 \leq E < \bar{E}$:

Center Sector. Corresponding to the $n-1$ pairs of imaginary eigenvalues, it is possible to build a center manifold spanned by the corresponding eigenvectors, of dimension $2n-2$. Its intersection with the energy level $\Phi(E)$ is precisely the NHIM.

Hyperbolic Sector. Corresponding to the real pair of eigenvalues of the linearized motion, there is a hyperbolic sector, consisting of stable and unstable manifolds. These manifolds emanate from the equilibrium point at $E = 0$, with a dimension 1. For $0 < E < \bar{E}$, each point of the center manifold (or at a given E, each point of the NHIM) has a pair of stable/unstable manifolds. Their union makes up separatrices that have codimension 1 in phase space Φ as well as in the energy level $\Phi(E)$. The stable/unstable manifold theorem [23,24] guarantees that in the nonlinear regime, the hyperbolic structure is preserved, tangent to the linearized structure. Furthermore, the stable/unstable manifolds exist with $t \to \pm\infty$.

The whole set is schematized in Fig. 13. It must be emphasized that these manifolds may actually be calculated (see Sections IV.B and V.A.1).

It must be underlined that the central manifold theorem, extending the linear center manifold into the nonlinear regime, is way less powerful than its stable/unstable counterpart. There is no limit $t \to \pm\infty$ and even no unicity of nonlinear center manifolds. Consequently, it is not well known how this whole beautiful structure bifurcates and disappears as $E \geq \bar{E}$. There has been virtually no study of the bifurcation structure (see, however, Ref. 55), and the transition from threshold behavior to far-above-threshold behavior is an open question, as far as I am aware.

The only object that still lacks in Fig. 13 is the TS itself. It lies at the intersection of the interiors of the stable/unstable high-dimensional manifolds. A good numerical study is in Uzer et al. [9], final section.

B. Some Examples

1. A Three-Dimensional Version of Hénon-Heiles Potential

A Simple 3-DOF Hamiltonian. An example that illustrates in a nontrivial way some of the statements above is the three-dimensional Hénon–Heiles potential

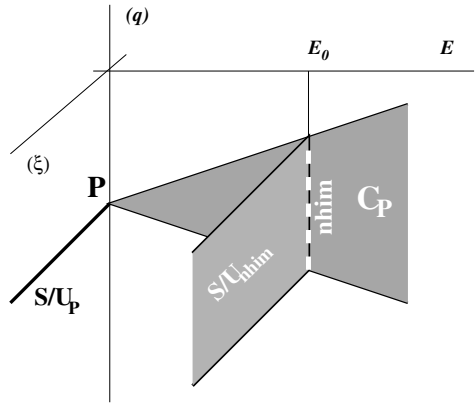

Figure 13. The whole structure of the phase space in a nutshell. P is the equilibrium point, E is the energy, (q) are the collective bath coordinates, and (ξ) is the collective transition coordinates. The cental manifold of P is C_P, and the stable and unstable manifolds are indicated by S/U.

[56]. From a standard two-dimensional Hénon–Heiles Hamiltonian, Ferrer et al. [57] derived some time ago a three-dimensional version. In Cartesian coordinates, this Hamiltonian reads:

$$H = \tfrac{1}{2}(p_x^2 + p_y^2 + p_z^2) + \frac{\omega^2}{2}(x^2 + y^2 + z^2) + \epsilon\omega^2 z\left(x^2 + y^2 - \tfrac{1}{3}z^2\right) \tag{31}$$

Since this Hamiltonian conserves the axial symmetry around the Oz axis, it may also be written in cylindrical coordinates with $\rho^2 = x^2 + y^2$ and the angle ϕ. As usual, the conjugate momentum to ϕ, $\Lambda \equiv p_\phi$ is the angular momentum. In these coordinates, defined for $\rho > 0$, the Hamiltonian reads

$$H = \tfrac{1}{2}\left(p_\rho^2 + p_z^2\right) + \frac{\Lambda^2}{2\rho^2} + \frac{\omega^2}{2}\left(\rho^2 + z^2\right) + \epsilon\omega^2 z\left(\rho^2 - \tfrac{1}{3}z^2\right) \tag{32}$$

with

$$\Lambda = xp_y - yp_x \quad p_\rho = \frac{xp_x + yp_y}{\rho}$$

As is apparent from Eq. (32), besides the total energy $E = H$, the dynamical system has another conserved quantity, the total angular momentum Λ. The angular momentum Λ plays definitely an important role here, but we do not deal yet with relative equilibria, as in Section V. While derivation of the equation of

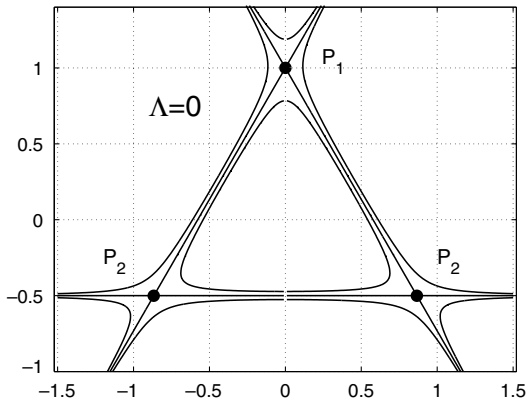

Figure 14. Potential energy surfaces, in two and three DOFs, for the Hénon–Heiles potential, with $\omega = \epsilon = 1$.

motion is trivial, it is still useful to state them explicitly, so that we can refer to them in the sequel.

$$\dot{q} = p_q, \qquad q = x, y, z$$

$$\dot{p}_x = -\omega^2 x - 2\epsilon\omega^2 xz \tag{33a}$$

$$\dot{p}_y = -\omega^2 y - 2\epsilon\omega^2 yz \tag{33b}$$

$$\dot{p}_z = -\omega^2 z - \epsilon\omega^2 (x^2 + y^2 - z^2) \tag{33c}$$

One notices that the $\epsilon = 0$ case corresponds to the linear dynamics.

The potential energy surface associated with the 3-DOF Hamiltonian, Eq. (31), resembles the usual 2-DOF one. In particular, a threshold energy may be defined, $E_t = \omega^2/6\epsilon^2$, below which the motion is bound and above which the motion becomes unbound. At $E = E_t$, configuration space is an equilateral triangle for the 2-DOF version and a cone for the 3-DOF case (see Fig. 14).

As the equations of motion show and as is apparent from the configuration space pictures, two sets of equilibrium points exist at $E = E_t$. The first equilibrium point P_1 is at the summit of the cone, with coordinates

$$P_1: \quad \left\{ E = \frac{\omega^2}{6\epsilon^2}; p_x = p_y = p_z = 0; x = 0, y = 0, z = \frac{1}{\epsilon} \right\} \tag{34}$$

Another set exists at the bottom of the cone, but we shall not deal with it here.

Linearization Around P_1. Let us linearize the motion around the equilibrium point P_1, by means of the following change of coordinates:

$$H' = H - \frac{\omega^2}{6\epsilon^2}$$
$$z' = z - \frac{1}{\epsilon}$$

Other coordinates do not change. The full Hamiltonian in the new coordinates reads

$$H' = \tfrac{1}{2}\left(p_x^2 + p_y^2 + p_z^2\right) + \tfrac{3}{2}\omega^2\left(x^2 + y^2\right) - \frac{\omega^2}{2}z'^2 + \epsilon\omega^2 z'\left(x^2 + y^2 - \tfrac{1}{3}z'^2\right) \quad (35)$$

This yields the following full equations of motion (which are linearized around P_1 setting $\epsilon = 0$):

$$\dot{q} = p_q, \qquad q = x, y, z'$$
$$\dot{p}_x = -3\omega^2 x - 2\epsilon\omega^2 x z' \quad (36a)$$
$$\dot{p}_y = -3\omega^2 y - 2\epsilon\omega^2 y z' \quad (36b)$$
$$\dot{p}_z = \omega^2 z' - \epsilon\omega;^2\left(x^2 + y^2 - z'^2\right) \quad (36c)$$

It is seen by simple inspection that the *linearized* equations of motion in the vicinity of P_1 have the remarkable property to leave invariant the manifold defined by $z' = p_z = 0$. This manifold is a 3-sphere S_3, whose equation is

$$S_3(P_1) = \tfrac{1}{2}(p_x^2 + p_y^2) + \frac{3\omega^2}{2}(x^2 + y^2) = \text{constant} > 0 \quad (37)$$

It must be underlined that the sphere exists only for $H' > 0$. Evidently, $S_3(P_1)$ is the NHIM that is supported by point P_1, with the right geometry, announced in Sections IV.A and IV.A.1.

The eigenvalue/eigenvector structure of the linear part is simple. It consists of a saddle in the $z' p_z$ plane, with eigenvalues $\pm\omega$ and eigenvectors $z' = 1; p_z = \pm 1/\omega$. These directions are transverse to the sphere S_3. The four remaining eigenvalues are $\pm i\,\omega\sqrt{3}$, each twice degenerate. Their eigenvectors span the central manifold $\mathscr{C}(P_1)$, passing through the equilibrium point P_1, at the origin. Intersecting $\mathscr{C}(P_1)$ with the energy level E gives the sphere $H_{S3} = E$. On the sphere, the motion is harmonic, with all trajectories periodic, of period $\omega\sqrt{3}$.

Drawing Linear and Nonlinear NHIM. The equilibrium point P_1 is thus of center/center/saddle type. The linearized motion in the vicinity lends itself to several pictures worth describing here. Let us begin with configuration space. The linearized potential energy may be written as

$$V(x, y, z') = H' - \tfrac{1}{2}(p_x^2 + p_y^2 + p_z^2) = \frac{\omega^2}{2}(3x^2 + 3y^2 - z'^2) \tag{38}$$

Depending on the sign of V, the surface described by Eq. (38) is a hyperboloid with one ($V > 0$) or two sheets ($V < 0$). For $V = 0$, it is a cone, whose apex is precisely the equilibrium point. For $V > 0$, at the waist of the hyperboloid ($z' = 0$) sits a disk invariant in configuration space, whose equation is

$$D_2 : x^2 + y^2 = V(x, y, z = 0)$$

An image of the disk is shown in Fig. 15.

Let us now lift this disk D_2 into phase space. To do so, one must go back to the sphere S_3 equation, Eq. (37). There are several ways of depicting a 3-sphere; one is particularly appropriate here [24]. The S_3 sphere is dynamically composed of two identical harmonic oscillators without explicit coupling, but whose *total* energy is a constant, $h_{S3} > 0$. Let us thus transform the Hamiltonian (37) in action angle variables, where I_x, I_y are the actions of the two oscillators and θ_x, θ_y are the two associated angles. Since

$$h_{S_3} = \omega(I_x + I_y) = \text{constant}$$

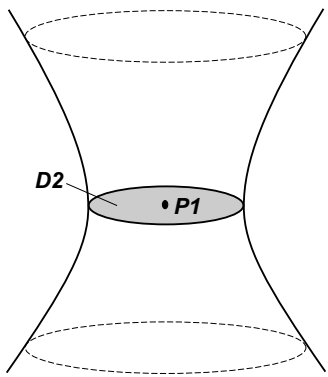

Figure 15. Potential energy surface around the equilibrium point P_1 for $V > 0$, with $\omega = \epsilon = 1$. The disk D_2 is shown at the waist of the hyperboloid.

there is a linear relation between the two actions. The sphere is foliated by a three-parameter family of orbits γ (all periodic): $\gamma(I_x, \theta_x, \theta_y)$. Specifying these three coordinates at time $t = t_0$ specifies a trajectory.

We can construct the representation of the sphere with this parameterization. One must, however, be careful when $I_x = 0$ (resp. $I_y = 0$) since then the corresponding angle θ_x (resp. θ_y) is not defined. The two angles $0 \leq \theta_{x,y} < 2\pi$ specify a 2-torus. To fully foliate the sphere, two distances I_x, I_y, with a linear relation, may be specified. A one-parameter family of tori of varying radii foliates the 3-sphere. Each trajectory is fully specified by a point on these tori.

However, there is another, more specific, yet more interesting, way to portray the sphere. Recalling that not only energy but also angular momentum Λ is conserved, the sphere S_3 is also parameterized with the three quantities $\gamma(I_x, \Lambda, \phi)$, with ϕ the angle conjugated to Λ. This view is particularly useful for the construction of the normally hyperbolic manifolds.

Since ϕ does not appear explicitly in the Hamiltonian, we go one step further, exploiting the other constant of the motion, Λ (rotational invariance of the Hamiltonian). Let us define a torus $T_2 \subset S_3$ in the following way. Since Λ is a conserved quantity, the $\Lambda = \Lambda_0$ surfaces foliate the $S_3(P_1; h_{S_3})$ sphere in a simple way. The two-dimensional manifold resulting in the intersection of $S_3 \cap \{\Lambda = \Lambda_0\}$ may now be characterized. One of its coordinates is the angle $0 \leq \phi < 2\pi$, where ϕ is, as before, the angle conjugate to Λ. The other coordinate is also an angle, $0 \leq \alpha < 2\pi$, that may be obtained for example by solving for ρ, p_ρ in the linearization of Hamiltonian (32). The solution for ρ, p_ρ yields one closed $S_1(P_1; h_{S_3}, \Lambda_0, \phi)$ line in the ρ, p_ρ plane. The angle describing this S_1 manifold is α, which may be understood as the phase of the oscillator in ρ, p_ρ. Because the Hamiltonian is independent of ϕ, the two angles are independent from one another and we see that the figure so constructed is a T_2 torus:

$$T_2(P_1; h_{S3}, \Lambda_0) = S_3(P_1; h_{S_3}) \cap \{\Lambda = \Lambda_0\} \tag{39}$$

$$= S_1(P_1; h_{S_3}, \Lambda_0, \phi) \times \{0 \leq \phi < 2\pi\} \tag{40}$$

The actual trajectories cover this torus, while not following the iso-α or iso-ϕ lines. Another torus is generated for another value of Λ_0; a singularity occurs for $\Lambda_0 = 0$, since then any $\phi = \phi_0$ plane is invariant and the $Oz \equiv Oz'$ axis is no more inaccessible.

A representation of the $S_1(P_1; h_{S_3}, \Lambda_0, \phi)$ circle is given in Fig. 16. The linearized NHIM is also represented. Because of the independence of the z'/p_z motion with respect to the ρ/p_ρ motion as well as the absence of p_z motion, the NHIM appears singularly in Fig. 16.

As explained in Section IV, it is possible to find a fully nonlinear NHIM in the vicinity of the linear NHIM. Now, instead of treating analytically the

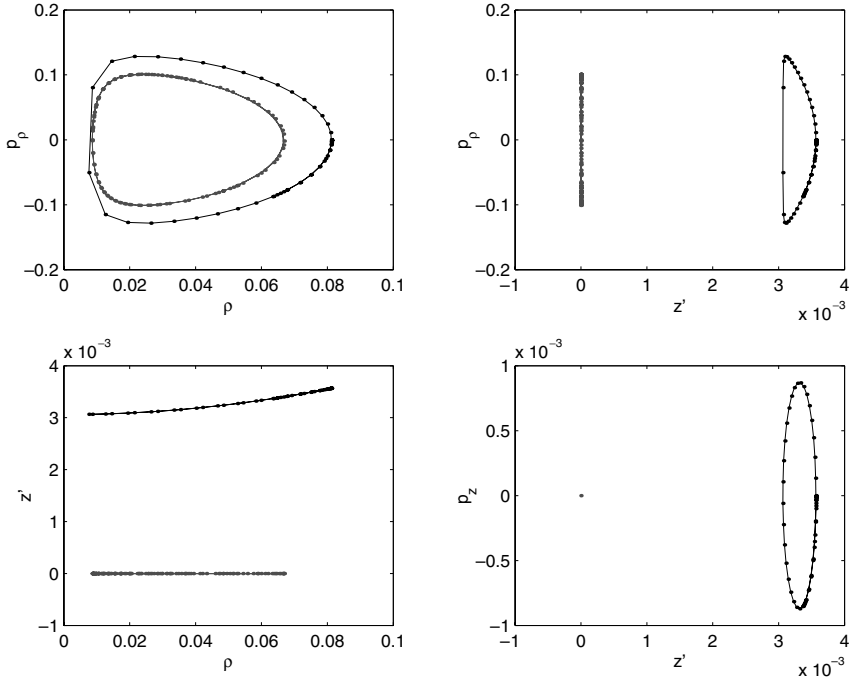

Figure 16. The linear and nonlinear NHIM in the vicinity of the equilibrium point P_1. Cylindrical coordinates, with $z' = z - 1/\epsilon$. Numerical values: $\omega = \epsilon = 1$, $H' = 0.01, \Lambda = 0.001$. Note the degeneracy of the linear NHIM, which is reduced to a single point in the z'/p_z plane and is reduced to a line in the z'/P_ρ and ρ/z' planes.

linearized motion, we integrate numerically the full equations of motion. For moderate energy and angular momentum ($h_{S_3} = 0.01$; $\Lambda = 0.001$), we are able to find the invariant surface

$$S_1(P_1; h_{S_3}, \Lambda_0, \phi): \quad \rho, z', p_\rho, p_z \mapsto S_1(\rho, z', p_\rho, p_z) \tag{41}$$

An image of S_1, Eq. (41), is given in Fig. 16, together with its linear counterpart. It must be noted that now there is no reason for any of the coordinates to be independent of any other one, since the equations of motion couple them all. Also, there is no symmetry in the full Hamiltonian with respect to $z' \leftrightarrow -z'$.

It is interesting to have some representation of the $T_2(P_1; h_{S3}, \Lambda_0)$ torus, Eq. (40). Only a partial representation is possible, since the embedding space is four-dimensional. Two projections are given in Fig. 17. Also, a trajectory originating in the NHIM is shown, numerically showing how the trajectory remains in the invariant submanifold, even in the full, nonlinear case.

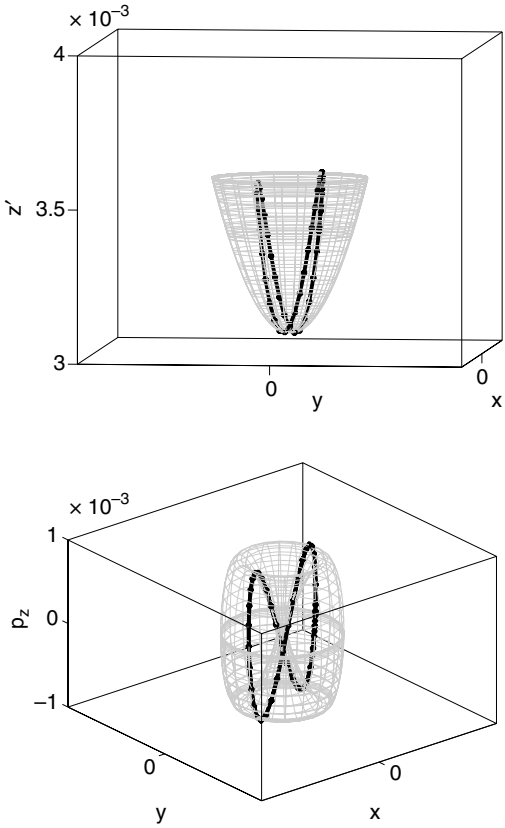

Figure 17. Two views of the nonlinear NHIM in gray. An actual trajectory is also shown (heavy black). It remains inside the nonlinear NHIM. Parameters are in Fig. 16.

2. Dynamics of Three Identical Atoms, Zero Angular Momentum

A problem of great practical importance is the three-body problem with non-Keplerian forces and a repulsive core.[1] The triatomic problem has widespread applications in reactive scattering and triatomic isomerization. There are many studies dealing with experiments and theory. The principal problem for reactive scattering has always been the calculation of a reliable potential function on which the triatomic dynamics takes place. However, quantum dynamics on those

[1]Three body with Keplerian forces or other short-range attractive forces have singular configurations when 2 and 3 bodies collide [14].

surfaces are now more or less routine, at least for moderate angular momenta. However, as always, classical dynamics is very useful for giving us guiding principles or even insights over propensity rules [18,58]. Also, the full understanding of the triatomic problem is the necessary gateway for the partial understanding of four or five colliding bodies, including inelastic scattering [59]. In order to simplify here, we deal only with the very simple case of three identical atoms:

$$A_1A_2 + A_3 \rightleftharpoons A_1A_3 + A_2A_3 + A_1$$

Other cases, which lack symmetry, are also tractable but necessitate some numerical and perturbational work to find the equilibrium points and the associated NHIM. Only one such case has been analyzed, the dynamics of CO_2 in the neighborhood of asymmetric dissociation [55]. However, dynamics in that context reduced essentially to 2-DOF (the bending of CO_2 is essentially a spectator mode).

Hamiltonians adapted to zero and nonzero configurations have been known for long [60,61]. In the case of zero angular momentum, they are particularly simple, once the relevant hyperspherical coordinates have been defined. In order not to burden the reader with unnecessary complications, all definitions are taken from [58,61] and not repeated here.

In order to be specific, we deal here only with the Ar_3 simple cluster, as studied by Yanao and Takatsuka [18] and Kamatsuzaki and Berry [50]. Atoms in the cluster interact via a Morse potential, of form

$$V = \sum_{i<j} \left[\exp -2(r_{ij} - r_0) - 2\exp -(r_{ij} - r_0)\right] \tag{42}$$

We take $r_0 = 0.6$.

It is possible to study stability of equilibrium points for this Hamiltonian [62]. Because of symmetry, we know beforehand that the equilibrium point may exist only at $z = 0$ and either at $x = 0, y = y_e$ or at the two equivalent points turned $\pm 120^\circ$ in the $z = 0$ plane. These three equilibrium configurations correspond to the three situations of Fig. 18.

The next step consists in studying the stability. The Hamiltonian at zero angular momentum, incorporating all possible reductions, may be written in many different ways [18]. We use the following expression, which is generalizable to $J \neq 0$ [61]:

$$H = \frac{1}{2\mu}(4p^2 - 3p_\rho^2) \tag{43}$$

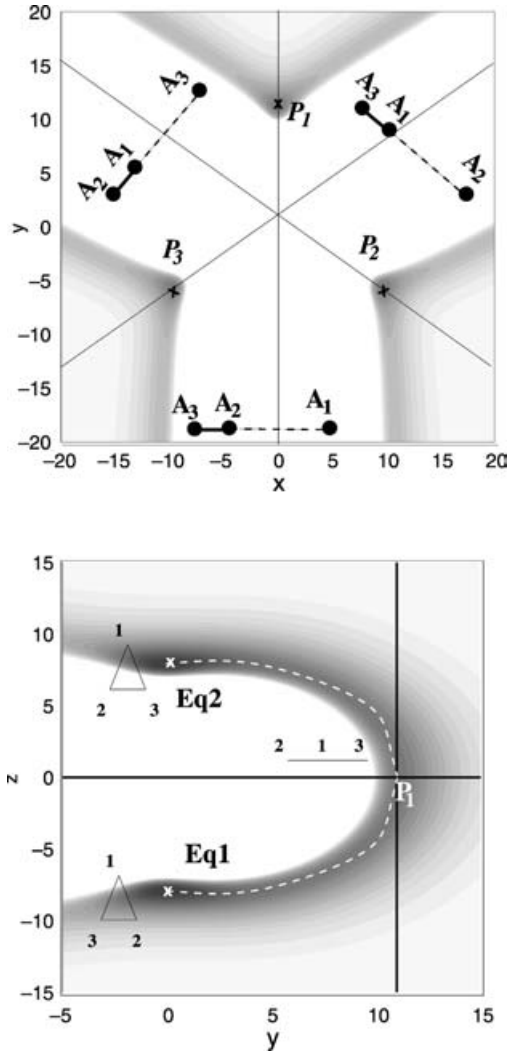

Figure 18. The *Oxy* plane of linear configurations (**above**) and the *Oyz* plane of isoceles configurations in the A–lA_2A_3 problem. The potential function is deeper for darker gray. The lines cross at the center and at the equilibrium points. The white dashed line is the ''reaction path,'' if there were no inertial or nondiagonal kinetic energy effects.

where

$$p_\rho^2 = \frac{xp_x + yp_y + zp_z}{x^2 + y^2 + z^2}$$

The equilibrium point P_1 has coordinate $x = 0, y = y_0, z = 0, p_x = p_y = p_z = 0$, with y_0 found numerically from $\nabla V = 0$. We have to calculate the eigenvalues of the M matrix. With the relevant numbers (see above), we have the z, p_z direction unstable and the xp_x; y, p_y directions stable. The NHIM is thus defined by $z = p_z = 0$. Because of symmetry, this case is rather simplified with respect to the general case; it will be tested for the bifurcation of the NHIM [62]. Also, it provides a very easy case to include angular momentum (see Section V).

V. ANGULAR MOMENTUM

Up to now, we have been concerned essentially with Hamiltonians possessing no angular momentum. Yet, in real situations, the importance of angular momentum is often paramount, dynamically and physically.

Physically first, any scattering experiments involves a nonzero J. Indeed, one may think of the quantum mechanical picture of a scattering experiment as a plane wave colliding with a center. The incoming conditions as well as the outgoing conditions may be expanded in terms of partial waves with varying ℓ, the orbital angular momentum. It is well known that any actual simulations must include high ℓ partial waves, hence nonzero J conditions. In a classical picture, with an impact parameter $b \neq 0$, the nonzero ℓ value is recovered with $b = b\,\bar{P}_{As}$, where $\bar{P}_{As}$ is the incoming asymptotic momentum.

Also, angular momentum is very important in experimental situations when the centrifugal energy is an appreciable part of the total energy. In those situations (generally, low masses and low temperatures), centrifugal barriers may completely or partially block a reaction or an inelastic channel. Also, unimolecular decomposition or chemidesorption from a surface may be very different with varying J. It also may happen that quantum mechanics may have some selection rules pertaining, for example, to odd or even j states, like the familiar ortho- and para-hydrogen molecules. Occurrence of those rules necessitates the inclusion of nonzero total and partial angular momenta.

In some instances, existence of a nonzero angular total angular momentum J dramatically changes the very shape of phase space. For a triatomic molecule, if $J = 0$, the collinear configuration is always possible. If $J \neq 0$, only if J is perpendicular to the plane of the three atoms (planar configurations) is the collinear case still possible. In the spirit of Section IV.B.2, the space of possible configurations is halved, with a $z = 0$ plane that cannot be reached (infinite centrifugal energy). On the other hand, the transition states P_1, P_2, P_3 disappear, since the ''isomerization'' may be obtained by a simple rotation of the molecule.

This change of shapes also happens in other contexts. The three-dimensional Henon–Heiles potential changes with nonzero J (called Λ in Wiesenfeld and Wiggins [56]; see Section IV.B.1). Many nontrivial instances may be found in Cushman [63].

There have been various studies concerning relative equilibria [58,64–66], especiallys so for bound systems. Rotating scattering systems have been much less studied except when the rotating frequency is imposed and constant. Many gravitational N-body problems belong to this class. In particular, some versions of the restricted three-body problem are treated in the rotating frame, where equilibria are actually only relative equilibria. Drift of objects in the solar system has been studied in a well-chosen rotating reference frame [22,67,68]. This approach is similar to ours but is restricted to few DOFs. It also uses the determination of a TS in order to transport in phase-space rates, in way similar to chemical theory. It must be emphasized here that the idea of a relative equilibrium is simple only if the two objects are rigid. Otherwise, the full rotation/vibration/deformation Hamiltonian is much more involved [17,69].

Before going into a detailed description, a mathematical definition of the problem is useful. If we have conserved quantities, like the total angular momentum J and its projection J_z, the eigenvalues of the linearized motion matrix M has now the following eigenvalue structure. Let us have, as usual, n degrees of freedom and $k < n - 2$ conserved quantities. Then we have

$$\begin{aligned} \lambda_{i,i+1} &= \pm i\omega_i, & \omega_i > 0, \quad i &= 1, 3, \ldots, 2n - 2k - 3 \\ \lambda_{2n-1,2n} &= \pm\kappa, & \kappa &> 0 \\ \lambda_{i,i+1} &= 0, & i &= 2n - 2k - 1, 2n - 2k + 1, \ldots, 2n - 3 \end{aligned} \tag{44}$$

For example, if J is the only conserved quantity, we have one pair of zero eigenvalue.

A. Dynamics in the Rotating Frame

The conservation of total angular momentum $\mathbf{J}$ encourages studying dynamics in the rotating frame, thereby hoping to simplify dynamics. This step has been taken a long time ago, in a process called mathematical *reduction* [22]. It is not at all our purpose here to enter this mathematically active field, especially because reduction is much more general, encompassing any type of continuous symmetry, in the same vein as rotations.

Let us just state here that we wish to replace the static equilibria that were the cornerstone of our previous study by equilibria in the rotating frame. In this manner, we should recover the whole set of ideas we had on absolute stability, NHIM and TST, and transport them onto *relative stability*, NHIM and TST.

There have been various studies concerning relative equilibria [58,65,66, 70–72], especially so for bound systems. Rotating scattering systems have been much less studied except when the rotating frequency is imposed and constant. Many gravitational N-body problems belong to this class.

While relative equilibria and relative TS might occur in bound motion (isomerization with nonzero J, we restrict ourselves to scattering situations in all that follows. A generalization of the isomerization for the three-body system, for instance, is still lacking. Also, the very important case of three-body (and four-body) reactive scattering, with angular momentum, is only treated in the literature without explicitly resorting to a TS concept [73–75].

1. Relative Equilibrium

Relative equilibria arise when the shape of the system does not change in time while the object as a whole is rotating. A relative equilibrium (RE) point means that:

1. There is no relative radial speed nor acceleration.
2. The composed body rotates as a whole, at uniform angular speed and zero angular accelerations.

Let us first consider a radial Hamiltonian, with an angular momentum J, reduced mass m, and radial potential V:

$$H = \frac{p_r^2}{2m} + \frac{J^2}{2mr^2} + V(r) \tag{45}$$

An RE occurs when

$$\frac{dV(r)}{dr} - \frac{J^2}{mr^3} = 0$$

This RE is radially unstable if $J^2/(2mr^2) + V(r)$ is a maximum, radially stable if it is a minimum. If an unstable RE occurs, the deflection function $\Theta_f = f(b_i)$, [41,76], displays rainbows (Θ_f is the final angle of exit of the particle in the inertial frame, b_i is the initial impact parameter). The structure of these rainbows is well known in the classical or quantum cases [77]. For such an integrable Hamiltonian like equation (45), there are as many singularities (rainbows) of the deflection function as integer numbers: each singularity is characterized by an increase by 1 of $k = \mathrm{mod}(\Theta_f, 2\pi)$. There is one impact parameter b^* such that

$k \to \infty$. It corresponds to the intersection of the asymptotic condition $r \to \infty$ with the *stable* manifold of the unique RE point.

A general Hamiltonian is more like:

$$H = \frac{p_r^2}{2m} + \frac{J^2}{2mr^2} + V(r, \theta_J) \tag{46}$$

with θ_J conjugated to the total angular momentum J. Motion is vastly more complicated, exhibiting generically regular and chaotic regions in phase space as well as one or several RE points. The dynamically invariant objects in the relative motion frame (RE, periodic orbits, and their high-dimensional analogues, [8,48]) have stable/unstable manifolds. These manifolds create heteroclinic and homoclinic tangles, in a way totally analogous to inertial periodic orbits [26,78,79].

If one considers the whole Hamiltonian H, Eq. (46), including the rotation, the RE point becomes a periodic orbit (p.o.). This periodic orbit has a trivial equation:

$$\begin{aligned} \mathbf{x} &= \mathbf{x}^0, \qquad x \neq \theta_J \\ \theta_J &= \theta_J^0 + \omega t \end{aligned} \tag{47}$$

where superscript 0 denotes initial conditions for the orbit. In the language of linearized motion, the following eigenvalue structure appears for the p.o. [23]:

1. One eigenvalue pair $\lambda_1^{\pm} = 1$, in the J, θ_J plane, corresponding to the conservation of total angular momentum, along the p.o.
2. K pairs of imaginary eigenvalues of modulus one, $\lambda_k^{\pm} = e^{\pm i\omega_k}$.
3. K' pairs of real eigenvalues $\lambda_k'^{\pm} = \kappa_k, 1/\kappa_k$.

We have $1 + K + K' = N$. Please note that this eigenvalue structure is that of a p.o., not of a equilibrium point [24].

Returning to the relative frame, let H' be the Hamiltonian restricted to the relative motion. An RE will occur at points where $\nabla H' = 0$. The linear stability is now defined with respect to the Hessian of H' and no more of H as in Section II. For general relative Hamiltonians, with several rotation-like motions [17], there are in general $m \geq 1$ DOFs that are frozen in the rotating frame. For Hamiltonian (46) as well as for the planar, nondeformable bodies problem that is dealt with in this study, we have $m = 1$: The total angular momentum J and its conjugated angle θ_J. Then, if we have the following structure of eigenvalues for the RE point P [see Eq. (26)]:

$$\lambda_k^{\pm}, k = \mathbf{2}, \ldots N-1 \text{ pure imaginary}; \quad \lambda_N^{\pm} \text{ real} \tag{48}$$

we define in a neighborhood of P a *relative TS*. The first eigenvalue pair does not appear in the relative frame. In a manner totally comparable to the usual TS, we have in relative coordinates and in the linear approximation [see Eq. (44)]

$$H' = \tfrac{1}{2}\sum_{k=2}^{N-1}(p_k^2 + \omega_k^2 q_k^2) + \tfrac{1}{2}(p_\xi^2 - \kappa^2\xi^2) \tag{49}$$

The dynamics across this linearized relative TS is exactly comparable to the dynamics across the linearized usual TS. Like the usual TS, a relative TS defines two regions in phase space: an outer region and an inner region with $\xi > 0$ and $\xi < 0$, for the Hamiltonian equation, Eq. (49)]. However, the full dynamics may be qualitatively different, precisely because of the relative nature of the equilibrium and the occurrence of Coriolis terms in the relative frame.

2. *An Example: A Rotating van der Waals Complex*

Equilibria. As a worked out example, I wish to present here the dynamics and relative TS associated with a very well known system of molecular physics, the van der Waals molecule. Simply stated, a van der Waals molecule AB is bound not by the creation of electronic orbitals extending over both fragments A and B but rather by the attraction due to multipolar electric forces between the two fragments A and B. In addition to this attraction, there also exists a chemical repulsion, responsible for the nonreactivity of A and B. Since the bonding is multipolar, it is weak, of the order of tens to hundreds cm^{-1} (1 atomic unit of energy $\simeq 2.19 \times 10^5\ cm^{-1}$). Because the bonding is so weak, it is to be expected that centrifugal effects will be important, as has often been experimentally and theoretically observed.

We use a very simple example, consisting of a dipolar and quadrupolar molecule interacting with a polarizable atom. The molecule is of cylindrical symmetry yet has the dimensions and the long-range electrical and inertial properties of H_2O; the atom is akin to atomic H. Because of the (supposed) cylindrical symmetry and because of the great simplification it entails, we restrict ourselves to a *planar* problem.

The (planar) Hamiltonian is written in fixed-frame coordinates as

$$H = \frac{p_R^2}{2m} + \frac{\ell^2}{2mR^2} + \frac{j_a^2}{2I_a} + V(R, \chi) \tag{50}$$

where R is the distance from the H atom to the center of mass of the H_2O molecule, P_R is the radial momentum, ℓ is the orbital angular momentum of H, j_a is the rotational angular momentum of H_2O, I_a is its moment of inertia, and χ is the relative angle between the axis of symmetry of H_2O and the direction of H.

The construction of a meaningful potential $V(R, \chi)$ is always a serious matter. Let us, however, describe it cursorily.

1. The short-range potential is exponentially repulsive. The characteristics of the exponential function are chosen to match the high-energy potential calculated for the reaction $H + H_2O \to OH + H_2$, in an averaged isotropic way.
2. The long-range potential is electrostatic. It comprises an isotropic van der Waals $O(R^{-6})$ part, a dipole-induced dipole $O(R^{-6})$ part, and a quadrupole-induced dipole $O(R^{-7})$ part.
3. The joining of the two parts is made by damping the electrostatic potential with an *ad hoc* damping function $d_n(R)$, which proved its usefulness in many other instances; see Toennies et al. [80].

With all these considerations, the potential reads

$$V(R,\chi) = C_1 \exp(-\beta R) + \frac{C_2}{R^6}\, d_6(R) + \frac{C_3}{2R^6}\,(3\cos^2\chi + 1)\, d_6(R) + \frac{C_4}{3R^7}(\cos^3\chi)\, d_7(R) \tag{51}$$

Equipped with this Hamiltonian, it is possible to look for relative equilibria and their linear stability, as a function of total angular momentum J. The full calculations are tedious and need not be reproduced here. In Fig. 19, we plot the energy of the various RE as a function of total angular momentum. We see that they undergo a saddle-node bifurcation for a different, even if similar, value of J. The upper branch has at least one real eigenvalue, and the lower one has at least one imaginary eigenvalue. The main couple, at $\chi = 0$, has its eigenvalues depicted in Fig. 20 (recall that eigenvalues come here in pairs $\lambda^{\pm}$). Finally, the Hamiltonian function with zero momenta and $J = 8$ is depicted in Fig. 21.

Transport. We need now to construct the NHIM, its stable/unstable manifolds, and the center manifold. Let P be the main relative equilibrium point. The first task is to find the short periodic orbits lying above P in energy. These p.o. are unstable. We did so by exploring phase space at energies 4, 10, and 14 cm^{-1} above E^* (1 atomic unit $= 2.194746 \times 10^5\,\mathrm{cm}^{-1}$). It is not possible to go much higher in E, since the center manifold disappears shortly above $E^* + 14\,\mathrm{cm}^{-1}$, because of the structure of the potential energy surface.

By joining corresponding points in the p.o. at successive energies, Fig. 22 is obtained. Note that each p.o., which acts as a NHIM, is by no means plane and its projection onto configuration space does not show its full structure.

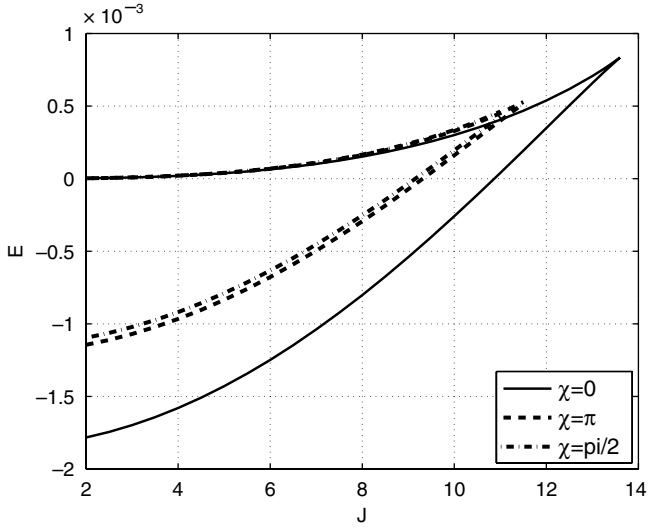

Figure 19. For the value $\chi = 0, \pi/2, \pi$, energy of the relative equilibria as a function of J. Note that the three families undergo a saddle-node bifurcation at different energy each.

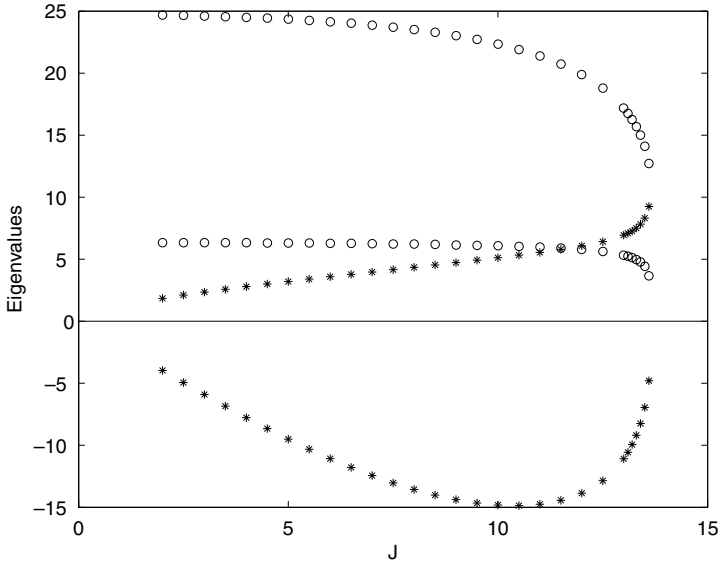

Figure 20. For the value $\chi = 0$, eigenvalues of the relative equilibria as a function of J. Inner point, circles; outer point, crosses. Only positive imaginary and negative real eigenvalues are shown. Note that the equilibria undergo a saddle-node bifurcation at $J \simeq 13.5$.

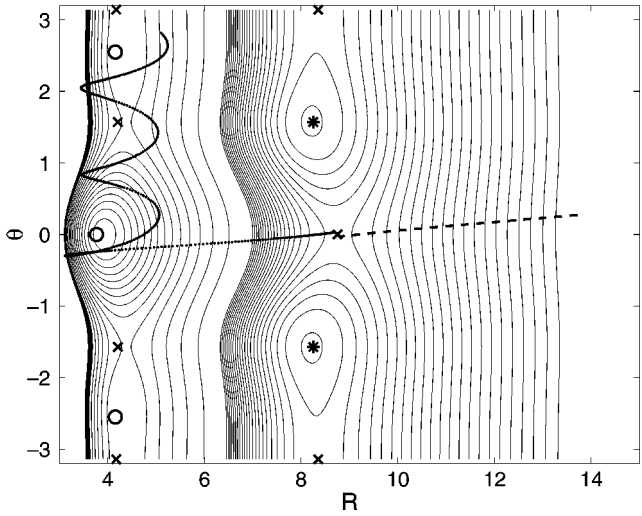

Figure 21. Lines of equal value of the Hamilton function, for $p_R = 0$, $J = 8$, $\delta j = \delta j^*$ for the equilibrium point at $\chi = 0$, $R \simeq 9$. Stability of the various REs of the $J = 8$ foliation is denoted by the following symbols: ∘, stable; ×, saddle; *, unstable. Two trajectories along the stable manifold of the RE are also shown. The levels go up for the $R \to \infty$, and are $-1.e^{-3} \ldots 5.e^{-5} \ldots 1.e^{-4}$, $1.e^{-4} \ldots 3.e^{-6} \ldots 2.e^{-4}$ in atomic unit.

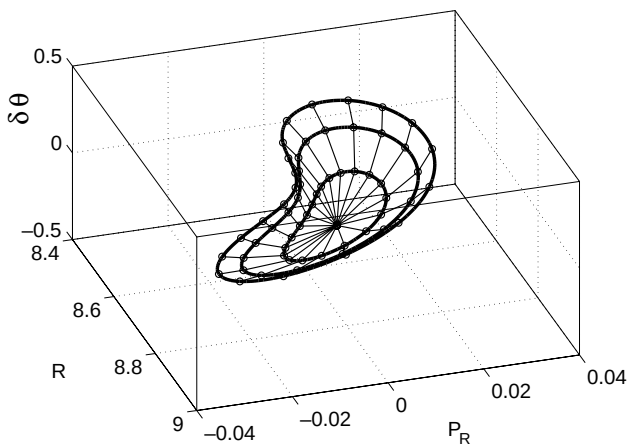

Figure 22. Two views of the stable/unstable manifolds of P, for $J = 8$. The inner part and outer part of phase space are clearly seen. They cross at the TS.

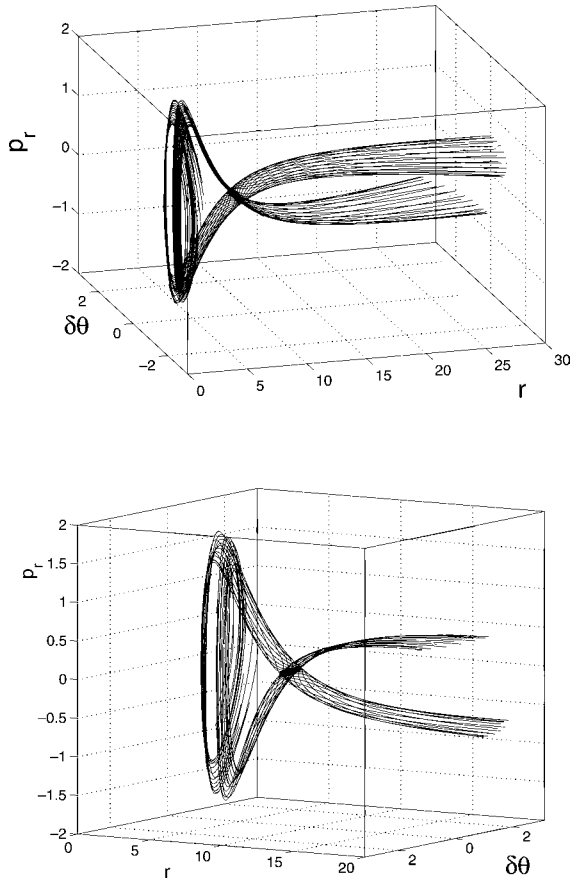

Figure 23. The center manifold of P, for $J = 8$. The thick lines are p. o., and the thin lines serve as a guide for the eyes to visualize the center manifold.

We go on by looking for the transport structure, the stable and unstable manifolds. While in principle, one could look for stable/unstable manifolds for any point of the center manifold of Fig. 22, in practice, it is easier to begin with a p.o. and describe its stable/unstable manifolds. Figure 23 depicts those manifolds. The light gray manifolds extend from the p.o. at the middle toward the inner region. In the relative frame we are (recall that the coordinates are all rotating with Θ, Eq. (50), these tubes are very much alike those of Ozorio et al., with hetero- and homoclinic intersections, responsible for the chaos appearing in the inner region. On the outer side, the situation is different. The black tubes extend readily into the asymptotic region, in a very straight way, undergoing no

hetero- or homoclinic intersection. This may be readily understood by simple inspection of Fig. 21. As soon as $R > R^*$, the angular dependance of the potential energy surface becomes very weak, making the Hamiltonian nearly separable.

The relative TS itself lies in the intersection of the tubes. This TS connects the two regions of the potential, the inner one, organized around the stable van der Waals complex and the outer one, extending toward asymptotic regions.

B. Some Results in Astrophysics

1. General Considerations

One of the incentives for studying transition states including angular momentum comes from molecular astrophysics. Conditions prevailing in interstellar media are such that very clean rotational effects are observed. Many reviews exist describing molecular environments in interstellar media, as well as their chemistry [81,82].

Two main parameters make astrochemistry different from usual laboratory chemistry : low densities ($\rho \lesssim 10^6\,\mathrm{cm}^{-3}$) and low temperatures, depending on the various interstellar media ($10\,\mathrm{K} < T < 300\,\mathrm{K}$, usually). With these energies and densities, it is understandable that (i) reactions usually considered as negligible may acquire a special importance (like neutral–neutral radical chemistry) and (ii) reactions with an appreciable activation energy are of no importance. It must also be underlined that hydrogen is by far (90%) the most abundant element and all hydrogen compounds (for example, $\mathrm{H}, \mathrm{H}_2, \mathrm{H}_2^+, \mathrm{H}_3^+$) are of great importance for all chemical network of reaction.

Because of the low kinetic energy available, it is to be expected that centrifugal forces should be of importance, especially so for neutral–neutral reactions, without any charge/multipole force between the reactants. If ions are present, the Langevin approximation/capture theory is more than enough to calculate most chemical rates [83]. On the contrary, for neutral–neutral reactions the situations are vastly different [84]. In particular, some reaction rates diminish rapidly as temperature increases.

A preliminary study was undertaken without a precise knowledge of the rotational TS [58]. The problem was as follows. We wish to look at the temperature dependence of the reaction

$$\mathrm{CN} + \mathrm{O} \rightarrow \mathrm{CO} + \mathrm{N}$$

at low temperatures. In order to keep everything as simple as possible, elementary interatomic potentials (Lennard-Jones and Morse) were used, with

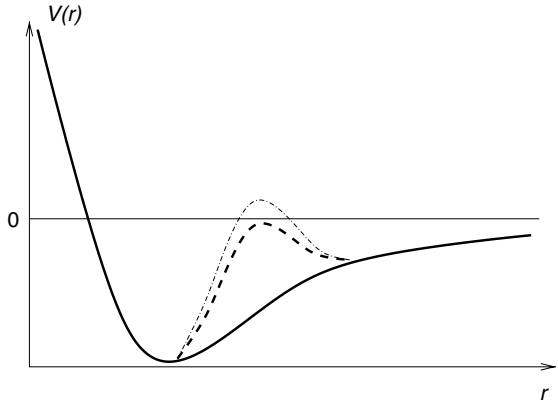

Figure 24. Potential of Lennard-Jones type (full line), with a coral reef (dash) and a entrance barrier (dot-dash).

the possible addition of a weak barrier in the entrance channel. Similar studies have been performed in different context, for the O_3 system [85].

Without an entrance barrier (or a ''coral reef'', which is a bump in the potential below the threshold energy) the centrifugal barrier is not high enough, at any energy, to induce any dynamical effect. However, including a barrier, something new appears. Let us call ℓ the orbital angular momentum and j the angular momentum of CN before reaction. A simple planar model is used, so that the total angular momentum is $J = j \pm \ell$. For low temperatures, only low j states are populated and any effect is weak. If $T \sim 300\,\mathrm{K}$, $|j| < 11$. Counter-rotation is the very different from co-rotation, and evidence for a rotational transition state appear (see Fig. 25). Evidently, more precise work is still needed (see Section V.A).

2. *Inelastic Scattering*

A scheme for inelastic scattering is beginning to emerge mainly from model studies. The inelastic collision

$$H_2O(j) + H_2(j = 0) \rightarrow H_2O(j') + H_2(j'')$$

has been studied in the spirit of TST, in the relative equilibrium framework [59].

The full *planar* Hamiltonian for the collision is written in atomic units as

$$H = \frac{p_R^2}{2m} + \frac{\ell^2}{2mR^2} + \frac{j_{H_2O}^2}{2I_{H_2O}} + \frac{j_{H_2}^2}{2I_{H_2}} + V(R, \theta, \chi_{H_2O}, \chi_{H_2}) \tag{52}$$

where I_a ($a = H_2O$, H_2) denotes a constant of inertia.

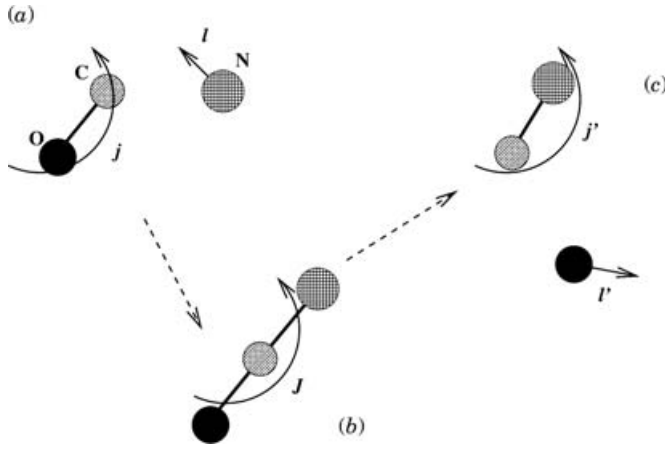

Figure 25. Scheme of the CN + O reaction, co-rotating with an intermediate TS (stage **(B)**).

It must be noticed that H is written in the center-of-mass, laboratory frame. Consequently, the angle conjugated to j_a are $\phi_a = \theta + \chi_a$. An image of the collision is given in Fig. 26. The exact form of the multipolar potential may be found in Ref. 59. It must be noticed that H is written in the center-of-mass, laboratory frame. The number of DOFs of this rotating planar composed

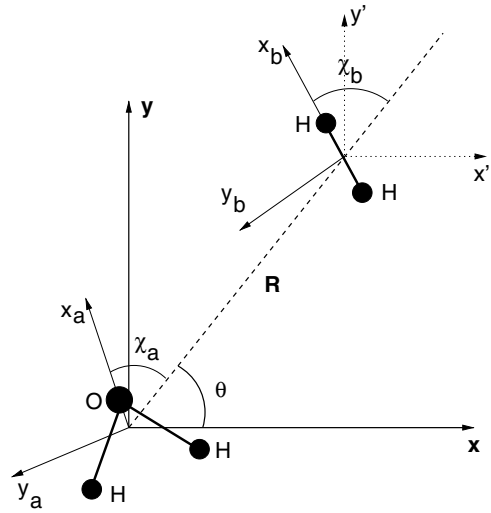

Figure 26. Scheme of the $a \equiv H_2O$ and $b \equiv H_2$ coordinates. x, x', y are lab-fixed frames and the dashed line is the intermolecular axis, with R being the intermolecular distance. The dipole of H_2O is along x_a, and the H–H internuclear axis is oriented along x_b. Angles as shown.

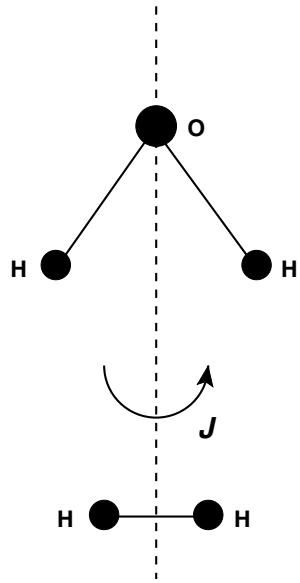

Figure 27. Schematic view of the relative equilibrium.

system is 4, precluding any detailed image of the whole dynamics. The concept of relative motion thus takes a particular importance for such a large system.

Using Hamiltonian (52), it is possible to find REs, by differentiating the Hamiltonian. Recalling the definition of the angles and imposing $\dot{\theta} = \Omega$, the overall angular speed (θ is conjugated with the total angular momentum J), we find various REs. The relative angles are $\chi_{H_2O} = K\pi$ and $\chi_{H_2} = K'\pi/2$. The radius is defined as R_{eq}. Looking for the stability matrix M, one position is a good candidate for the relative TS ($K = 0, K' = 0$) (Fig. 27). A confirmation is found by *numerically* integrating the equations of motion in its neighborhood. The characteristic behavior of a saddle equilibrium point is recovered (Fig. 28).

As a final illustration, it is possible in the context of this RE to have an image of the actual opening of the TS as J decreases for a given energy (this is equivalent in the context of inelastic scattering of varying E at constant J).

While in some analogous works, it was possible to devise surfaces of section or even full representations of phase space; this is hardly thinkable here. Let us recall that an on-shell (or constant energy $H = E = 0.001$ atomic units) Poincaré section would be of dimension $D_\Sigma = D(\text{phasespace}) - 1 - 1 = 6$. Instead we

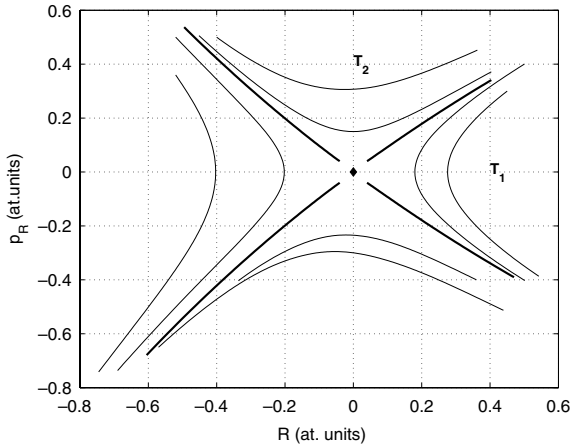

Figure 28. Numerically integrated dynamics around the main RE at $E = 0.001$ atomic units. $R = p_R = 0$ is the RE. The dynamics is projected onto the R, p_R plane. Thick lines represent the stable and unstable manifolds of the RE; thin lines represent several trajectories. T_1 and T_2, nonreactive and reactive trajectories, respectively.

depict the asymptotic conditions, on-shell, for which trajectories enter or do not enter into the inner region. We set the following conditions:

1. The initial conditions for a trajectory are: $R \to \infty$; $j_{H_2O} = j_{H_2} = 0$, in accordance to the RE conditions; $0 \leq \ell = p_R \cdot b \lesssim 27$, where b is the impact parameter and p_R is found by energy conservation.
2. $0 \leq \chi_{H_2O} < 2\pi$, $0 \leq \chi_{H_2} < \pi$: The χ_{H_2O}, χ_{H_2} angles are scanned, since they have no physical meaning. We thus have a *two-dimensional* set of initial conditions.
3. Because the inner part of the potential ($R \ll R_{eq}$) is not very meaningful and because the depth of the potential well in the inner part is not controlled, we monitor only whether or not the trajectory enters the inner region.

With help of all those conditions, we have the results presented in Fig. 29. We see clearly three regimes.

i. For high-ℓ, ($\ell > \ell_{eq}$), the centrifugal barrier is too high and all collisions are quasi-elastic. This has been verified by monitoring the j_{H_2O} values before and after collisions and by founding near-zero changes. In chemical reactions, we would say that we are *below* threshold.

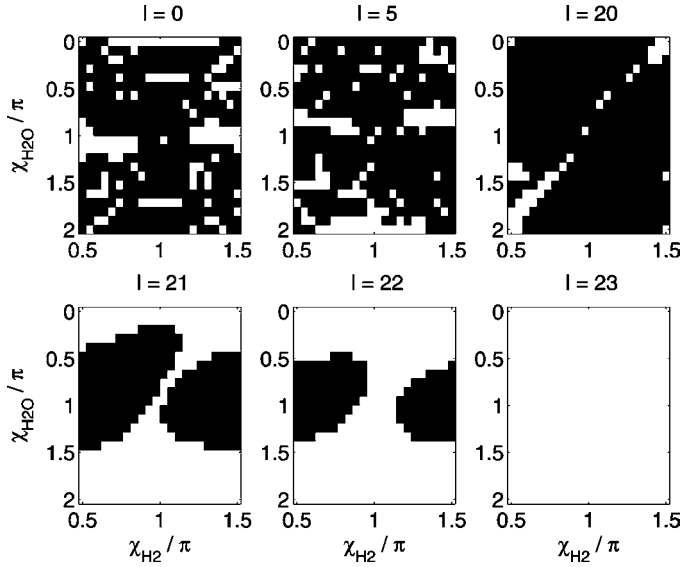

Figure 29. With varying ℓ, at $E = 0.001$ atomic units, sets of trajectories entering (black dot) or not entering (white dot) the inner region.

ii. Around $\ell \lesssim \ell_{\text{eq}} \sim 22$, we open a valley into the inner region. This valley has an image in the asymptotic conditions described above. The transport in the outer region is regular and the valley has an image backwards in time like a simply connected region, centered around the perpendicular RE ($\chi_{H_2O} = 0$, $\chi_{H_2} = \pi/2$). This means also that during the approach part of the trajectory ($R_{\text{asymptotic}} \to R_{\text{eq}}$), the relative positions of the two molecules do not change and no angular momentum is transferred. This is in agreement with the preceding case. In chemical reactions, we would say that we are *at and just above* threshold.

iii. As ℓ diminishes, the valley opens and covers the whole χ_{H_2O} domain. For low values of ℓ ($0 \leq \ell \lesssim 17$), the RE that lies very far in phase space seems to have no influence anymore. The TS is absent and dynamics is dominated by a complex (maybe chaotic) interplay between short-range and long-range potentials. This is analogous to reaction paths *far above threshold*, where details others than TS may determine the output.

It is thus possible to actually see the opening of a TS and its image onto the asymptotic plane. This is a first step toward a theory using this opening of TS as an alternative capture theory.

VI. CONCLUSION

The theory of the classical transition state (classical opposed to quantum) presented thus far shows that the geometrical view gained in the last few years is large. It is nearly complete for practical purposes on several levels:

- The number of DOFs is no longer a main difficulty. While the linear theory is mainly tamed, geometrical representations are still difficult but need not be focused on.
- Numerical definition of TS (or NHIM) seems within reach, at least for a few DOFs. Analysis of the flow of classical density of probability, at least locally, is possible and has been performed at several instances. It should be by now possible to connect these numerical computations with sophisticated classical tools, like Pollicot–Ruelle resonances, in order to find a rate of transition across the TS.
- The classical perturbation theory, which was not discussed here, has made tremendous practical progresses, allowing one to treat intricate Hamiltonians. The presence of complicated kinetic energies or resonances is no longer a hindrance for perturbation theory.
- Angular momentum begins to be included in a meaningful way, yet not complete. This is of particular importance for low-energy processes.

While, at least in this author's opinion, the situation is very satisfactory on the theoretical view, only few applications have up to now taken advantage of the formalism of TS in many dimensions. It is, however, very noticeable that applications that exist already draw from many different fields, as this and all the other chapters of this book emphasize. The convergence between celestial dynamics and atomic/molecular physics is particularly striking.

Several avenues remain for the moment either completely unknown or barely touched upon. While inclusion of many DOFs is possible by now, it is still very unclear how robust the concept of a NHIM is. In particular, inclusion of dissipation might or might not disrupt the very existence of a NHIM. Most probably, different regimes should exist and be explored theoretically and numerically.

Today, it is also unclear as to what is the scenario for the bifurcations of NHIMs as energy increases. In other words, the change from threshold regime to above-threshold regimes remains very unclear. The same is true for the importance of symmetries in the dynamics, especially so for the breaking of some symmetries through bifurcations.

However, the most important drawback for chemical physics is of course the classical nature of the theory. It is possible, however, that quantum or semiclassical theories of reactions [86] might greatly take profit of the images

presented here. The increased sophistication of semiclassical *S*-matrix calculations, their ability to treat many DOFs make those methods good candidates to make the bridge between the very different points of views of classical and quantum mechanics.

Acknowledgments

I wish to thank many colleagues for discussions and insightful remarks or criticisms, spanning many years: Yves Colin de Verdière, Alexandre Faure, Marc Joyeux, Christof Jung, Tamiki Komatsuzaki, Aron Kuppermann, Robert Littlejohn, Maurice Lombardi, Mark Roberts, Mikito Toda, Turgay Uzer, Pierre Valiron, and Stephen Wiggins. Special thanks to John B. Delos and Hicham Wadi, who initiated in their ways this whole story.

Parts of this work were supported by the California Institute of Technology, the Universities of Kobe (21st-century COE of Origin and Evolution of Planetary Systems, MEXT), Nara, and Warwick (MASIE program of the European Union), the NSF/CNRS cooperation program, and the "Physical Chemistry of Interstellar Matter" program of the CNRS. The Laboratoire d'Astrophysique is a common research unit CNRS/Université Joseph-Fourier.

References

1. M. Zhao, J. Gong, and S. A. Rice, *Adv. Chem. Phys*. **130**, 1 (2005).
2. D. G. Truhlar, B. C. Garrett, and S. J. Klippenstein, *J. Phys. Chem.* **100**, 212771 (1996).
3. I. Burghardt and P. Gaspard, *J. Chem. Phys.* **100**, 6395 (1994).
4. T. Komatsuzaki and R. S. Berry, *Adv. Chem. Phys.* **123**, 79 (2002).
5. E. Pollak and Jie-Lou Liao, *J. Chem. Phys.* **108**, 2733 (1998).
6. W. H. Miller, *Faraday Discuss.* **110**, 1 (1998).
7. S. C. Creagh, *J. Phys. A: Math. Gen.* **27**, 4969 (1994).
8. S. Wiggins, L. Wiesenfeld, C. Jaffé, and T. Uzer, *Phys. Rev. Lett* **86**, 5478 (2001).
9. T. Uzer, C. Jaffé, J. Palacián, P. Yanguas, and S. Wiggins, *Nonlinearity* **15**, 957 (2002).
10. M. Joyeux and D. Sugny, *Can. J. Phys.* **80**, 1459 (2002).
11. J. Palacián and P. Yanguas, *Nonlinearity* **13**, 1021 (2000).
12. P. Leboeuf and A. Mouchet, *Ann. Phys. NY* **275**, 54 (1999).
13. C. Jaffé, S. D. Ross, M. W. Lo, J. E. Marsden, D. Farrelly, and T. Uzer *Phys. Rev. Lett.* **89**, 011101-1 (2002) ; W. S. Koon, M. Lo, J. E. Marsden, and S. Ross, *Contemp. Math.* **292**, 129 (2002).
14. G. Tanner, K. Richter, J. M. Rost, *Rev. Mod. Phys.* **72**, 497 (2000).
15. A. Chenciner and R. Montgomery, *Ann. Math.* **152**, 881 (2000); also see references cited herein.
16. An introduction to Hamiltonian dynamics may be found in H. Goldstein, *Classical Mechanics*, Addison-Wesley, Reding, MA, 1964.
17. R. G. Littlejohn and M. Reinsch, *Rev. Mod. Phys*. **69**, 213 (1997).
18. T. Yanao and K. Takatsuka, *Phys. Rev. A* **68**, 032714 (2003).
19. O. L. Polyansky et al., *Science* **299**, 539 (2003). J. Tennyson, J. R. Henderson, and N. G. Fulton, *Computer Phys. Comm.* **30**, 735 (1995).
20. V. I. Arnol'd, *Mathematical Methods in Classical Mechanics*, Springer, Berlin, 1978.
21. V. I. Arnol'd, *Ordinary Differential Equations*, MIT Press, Cambridge, MA, 1973.

22. J. E. Marsden and T. Ratiu *Introduction to Mechanics and Symmetry*, Springer-Verlag, Berlin, 1994; 2nd ed., 1999.
23. S. Wiggins, *Introduction to Applied Nonlinear Dynamical Systems and Chaos*, Springer, Berlin, 2003.
24. K. R. Meyer and Hall, *Introduction to Hamiltonian Dynamical Systems and the N-Body Problem*, Springer, Berlin, 1992.
25. A. M. Ozorio de Almeida, *Hamiltonian Systems: Chaos and Quantization*, Cambridge University Press, Cambridge, England, 1988.
26. Z. Kovács and L. Wiesenfeld, *Phys. Rev. E, Phys. Rev. E* **63**, 056207 (2001).
27. S. Wiggins, *Normally Hyperbolic Invariant Manifolds in Dynamical Systems*, Springer, Berlin, 1990.
28. S. A. Rice and M. Zhao, *Int. J. Quantum Chem.* **58**, 593 (1996) and references cited therein.
29. M. J. Davis and S. K. Gray, *J. Chem. Phys.* **84**, 5389 (1984).
30. T. Uzer and W. H. Miller, *Phys. Rep.* **199**, 73 (1991).
31. R. E. Gillilan and G. S. Ezra, *J. Chem. Phys.* **94**, 2648 (1991).
32. S. Wiggins, *Physica D* **44**, 471 (1990).
33. H. Wadi and L. Wiesenfeld, *Phys. Rev E* **55**, 271 (1997).
34. M. Joyeux et al., *Adv. Chem. Phys. Part A* **130**, 267 (2005).
35. M. S. Child, *Molecular Collision Theory*, Academic Press, London, 1974.
36. A recent reference with a good bibliography is G. V. Mil'Nikov and H. Nakamura, *J. Chem. Phys* **117**, 10081 (2002).
37. P. Hänggi, P. Talkner, and M. Borkovec, *Rev. Mod. Phys.* **62**, 251 (1990) and references cited therein.
38. E. Hershkovitz and L. Wiesenfeld, *J. Chem. Phys.* **113**, 4558 (2000).
39. P. Pechukas and E. Pollak, *J. Chem. Phys.* **71**, 2062 (1979); E. Pollak, M. S. Child, and P. Pechukas, *J. Chem. Phys.* **72**, 1669 (1980).
40. N. De Leon and B. J. Berne, *J. Chem. Phys.* **75**, 3495 (1981).
41. Z. Kovács, and L. Wiesenfeld, *Phys. Rev. E* **51**, 5476 (1995).
42. P. Bhatia, B. Maiti, N. Sathyamurthy, S. Stamatiadis, and S. C. Farantos, *Phys. Chem. Chem. Phys.* **1**, 1105 (1999).
43. A recent example is T. S. van Erp, D. Moroni, and P. G. Bolhuis, *J. Chem. Phys.* **118**, 7762 (2003).
44. R. Sadeghi and R. T. Skodje, *J. Chem. Phys.* **102**, 193 (1995).
45. I. Burghardt and P. Gaspard, *Adv. Chem. Phys.* **101**, 497 (1997).
46. P. Gaspard and S. A. Rice, *J. Chem. Phys.* **90**, 2242 (1989).
47. H. Wadi and L. Wiesenfeld, *Chem. Phys. Lett.* **300**, 36 (1999).
48. A. M. Ozorio de Almeida, N. De Leon, M. A. Mehta, and C. C. Marston, *Physica D* **46**, 265 (1990).
49. M. Toda, *Adv. Chem. Phys.* **123**, 153 (2002).
50. T. Komatsuzaki and R. S. Berry, *J. Chem. Phys.* **110**, 9160 (1999); R. J. Hinde, R. S. Berry, and D. J. Wales, *J. Chem. Phys.* **96**, 1376 (1992).
51. C. Jaffé, D. Farelly, and T. Uzer, *Phys. Rev. A* **60**, 3833 (1999).
52. T. Komatsuzaki and M. Nagaoka, *J. Chem. Phys.* **105**, 10838 (1996).
53. L. Wiesenfeld, *J. Phys. A* **37**, L143–L147 (2004).
54. J. Murdock, *Normal Forms and Unfoldings for Local Dynamical Systems*, Springer, Berlin, 2003.

55. I. Burghardt and P. Gaspard, *Chem. Phys.* **225**, 259 (1997).
56. L. Wiesenfeld and S. Wiggins, 2000, unpublished material.
57. S. Ferrer, M. Lara, J. Placián, J. F. San Juan, A. Viartola, and P. Yanguas, *Int. J. Bifur. Chaos* **8**, 1199 (1998); *Int. J. Bifurc. Chaos* **8**, 1215 (1998).
58. A. Faure, L. Wiesenfeld, and P. Valiron, *Chem. Phys.* **254**, 49 (2000).
59. L. Wiesenfeld, A. Faure, and T. Johann, *J. Phys. B: At. Mol. Opt. Phys.* **36**, 1319 (2003).
60. A. Kuppermann *Chem. Phys. Lett.* **32**, 374 (1975).
61. B. R. Johnson, *J. Chem. Phys.* **79**, 1906 (1983).
62. T. Komatsuzaki, M. Toda, and L. Wiesenfeld, in preparation.
63. R. Cushman, *Global Aspects of Classically Integrable Systems*, Birkhaüser, 1997.
64. I. N. Kozin, R. M. Roberts, and J. Tennyson, *J. Chem. Phys.* **111**, 140 (1999); I. N. Kozin, R. M. Roberts, and J. Tennyson, *Mol. Phys.* **98**, 295 (2000).
65. T. Uzer, F. Lee, and D. Farrelly, *Phys. Rev. A* **58**, 4761 (1998).
66. Ch. van Hecke, D. A. Sadovskií, B. I. Zhilinskií, and V. Boudon, *Eur. Phys. J. D* **17**, 13 (2001).
67. J. Henrard and J. F. Navarro, *Celest. Mech. Dyn. Astron* **79**, 297 (2002).
68. W. S. Koon, M. Lo, J. E. Marsden and S. Ross, *Chaos* **10**, 427 (2000).
69. I. N. Kozin and I. M. Pavlichenkov, *J. Chem. Phys.* **104**, 4105 (1996).
70. I. N. Kozin, R. M. Roberts, and J. Tennyson, *J. Chem. Phys.* **111**, 140, (1999); I. N. Kozin, R. M. Roberts, and J. Tennyson, *Mol. Phys.* **98**, 295 (2000).
71. R. M. Roberts and M. E. R. de Sousa Dias, *Nonlinearity* **10**, 1719 (1997).
72. There is a large body of mathematical and nonlinear control theory literature; an example is: S. M. Jalnapurkar and J. E. Marsden, *IEEE Trans. Automat. Control* **45**, 1483 (2000).
73. M. E. Grice, K. Song, and W. J. Chesnavich, *J. Phys. Chem.* **90**, 3503 (1986).
74. T. W. J. Whiteley, C. Noli, and J. N. L. Connor, *J. Phys. Chem.* **105**, 2792 (2001).
75. P. Larregaray, L. Bonnet, and J. C. Rayez, *Phys. Chem. Chem. Phys.* **4**, 1781 (2002).
76. C. Jung and H. J. Scholz, *J. Phys A: Math. Gen.* **20**, 3607 (1987).
77. E. De Micheli and G. A. Viano, *Phys. Rev. A* **65**, 032728 (2002).
78. N. Meyer, L. Benet, C. Lipp, D. Trautmann, C. Jung, and T. H. Seligman, *J. Phys A: Math. Gen.* **28**, 2529 (1995).
79. C. Jung and T. H. Seligman, *Phys. Rep.* **285**, 77 (1997).
80. K. T. Tang and J. P. Toennies, *J. Chem. Phys.* **80**, 3726 (1984).
81. E. F. Van Dishoek, ed., *Molecules in Astrophysics: Probes and Processes*, International Astronomical Union and Kluwer Academic Publishers, Dordrecht, 1997.
82. E. Herbst, *Annu. Rev. Phys. Chem.* **46**, 27 (1995).
83. G. Winnewisser and E. Herbst, *Rep. Prog. Phys.* **56**, 1209 (1993).
84. A. Faure, C. Rist, and P. Valiron, *Astron. and Astrophys.* **348**, 972 (1999).
85. D. Babikov, B. K. Kendrick, R. B. Walker, R. T. Pack, P. Fleurat-Lesard, and R. Schinke, *J. Chem. Phys.* **119**, 2590 (2003).
86. Many articles are published on the "Initial Value Representation" of the *S*-matrix, see, e.g., Y. Elran and K. G. Kay, *J. Chem. Phys.* **114**, 4362 (2001) and references mentioned therein.

CHAPTER 5

INTRAMOLECULAR DYNAMICS ALONG ISOMERIZATION AND DISSOCIATION PATHWAYS

MARC JOYEUX

Laboratoire de Spectrométrie Physique (CNRS UMR 5588), Université Joseph Fourier, Grenoble 1, F-38402, St. Martin d'Hères Cedex, France

SERGY YU. GREBENSHCHIKOV, JENS BREDENBECK,[1] and REINHARD SCHINKE

Max-Planck-Institut für Strömungsforschung, D-37073 Göttingen, Germany

STAVROS C. FARANTOS

Institute of Electronic Structure and Laser Foundation for Research and Technology, Hellas, Greece; and Department of Chemistry, University of Crete, Iraklion 711 10, Crete, Greece

CONTENTS

I. Introduction
II. Nearly Separable Isomerizing Systems
  A. Application of Canonical Perturbation Theory to Floppy Molecules
  B. Adiabatic Versus Nonadiabatic Delocalization in Isomerizing Systems
III. Resonantly Coupled Isomerizing and Dissociating Systems

[1]*Present Address*: Physikalisch-Chemisches Institut, Universität Zürich, CH-8057 Zürich, Switzerland.

Geometric Structures of Phase Space in Multidimensional Chaos: A Special Volume of Advances in Chemical Physics, Part A, Volume 130, edited by M. Toda, T Komatsuzaki, T. Konishi, R.S. Berry, and S.A. Rice. Series editor Stuart A. Rice.
ISBN 0-471-70527-6

A. Polyad Folding and Saddle-Node Bifurcations
B. Bifurcations at Higher Energies
IV. Summary
References

I. INTRODUCTION

The purpose of this chapter is to review some properties of isomerizing ($ABC \leftrightarrow BCA$) and dissociating ($ABC \rightarrow AB + C$) prototype triatomic molecules, which are revealed by the analysis of their dynamics on precise ab initio potential energy surfaces (PESs). The systems investigated will be considered from all possible viewpoints—quantum, classical, and semiclassical mechanics—and several techniques will be applied to extract information from the PES, such as Canonical Perturbation Theory, adiabatic separation of motions, and Periodic Orbit Theory.

The key quantity in these studies is the strength of the coupling between reactive coordinates and perpendicular ones, where a coordinate is called reactive if it leads from reactants to products. The reactive coordinate is essentially an angle in the case of an isomerizing system and a stretching coordinate in the case of a dissociating system. The strength of the coupling between different degrees of freedom obviously depends on the choice of coordinates. When ''natural'' sets of coordinates, like valence or Jacobi ones, are used, it is rather rare that the couplings remain negligible up to the reaction threshold. In contrast, ''optimized'' sets of coordinates, which minimize the couplings between the various degrees of freedom up to and above the reaction threshold, can be derived rather straightforwardly for a certain number of isomerizing systems, like $HCN \leftrightarrow CNH$ or $LiNC \leftrightarrow NCLi$. Section II describes in detail a procedure based on Canonical Perturbation Theory, which enables near-separation of motions for such isomerizing systems. Section II furthermore discusses vibrationally nonadiabatic tunneling in $HCN \leftrightarrow CNH$, that is, the effect of remaining small couplings below the top of the adiabatic isomerization barrier on the shape of the wavefunctions along the perpendicular degrees of freedom.

For the nearly separable isomerizing systems studied in Section II, it is sufficient to increase the energy in the reactive degree of freedom to let the molecule explore the reaction pathway further and further and eventually react when the deposited energy is larger than the energy of the adiabatic reaction threshold. Recent studies dealing with the vibrational dynamics of small molecules (HCP, HOCl, HOBr...) have shown that this is certainly not the case for systems, which display a pronounced resonance between the reactive degree of freedom and a perpendicular one. Section III is devoted to the description of the subtle pattern of bifurcations, which the molecules mentioned above must

undergo in order to reach the reaction threshold, due to the existence of a 2:1 Fermi coupling between the reactive degree of freedom and perpendicular ones.

II. NEARLY SEPARABLE ISOMERIZING SYSTEMS

This section describes the dynamics of the isomerizing system HCN $\leftrightarrow$ CNH, for which near-separation of the various degrees of freedom can be achieved. It is first shown in Section II.A how Canonical Perturbation Theory (CPT) can be applied to this floppy molecule in order to find ''optimized'' sets of coordinates, which minimize the couplings between the various degrees of freedom. Section II.B further discusses the effects of the remaining small coupling terms on the tunneling between states with different quantum numbers in the perpendicular degrees of freedom.

A. Application of Canonical Perturbation Theory to Floppy Molecules

The basic idea of this section, which collects information scattered in Refs. 1–3, is to apply several unitary (or canonical) transformations to floppy systems initially described by ab initio or fitted potential energy surfaces and exact kinetic energy operators, in order to rewrite their Hamiltonian in terms of, as complete as possible, a set of good quantum numbers (or classical constants of the motion), plus some high-order small coupling terms that are eventually neglected at the end of the procedure. For HCN $\leftrightarrow$ CNH [1,2,4], LiNC $\leftrightarrow$ LiCN [5], and C_3 [6], a complete separation of motions was actually achieved after the high-order small coupling terms were neglected: As will be seen below, the final (or perturbative) Hamiltonian is formally a one-dimensional Hamiltonian in the bending angle, which is parameterized by the stretch quantum numbers.

The possibility of such a separation of motions is not obvious at all when looking at the PES of an isomerizing molecule. Figure 1 (left) shows as an example a two-dimensional cut in the (R, γ) plane of the three-dimensional PES for the HCN $\leftrightarrow$ CNH system obtained by Tennyson and co-workers [7,8]. R is the distance between H and the center of mass G of CN, while γ is the HGC angle ($\gamma = 0$ at the linear HCN configuration). For this figure, the third coordinate—that is, the distance r between C and N—is fixed to the HCN equilibrium value of 1.1528 Å. It is seen that the reaction pathway (or minimum energy path, MEP), which connects the HCN absolute minimum (at $\gamma = 0$) to the CNH relative one (at $\gamma = 180^\circ$) through the saddle (at $\gamma \approx 80^\circ$), displays a very strong curvature in the (R, γ) plane. Consequently, if the Hamiltonian matrix is built in the basis set constructed as the direct products of the one-dimensional functions for each Jacobi coordinate, then the couplings between the vectors of the basis are strong. The first step of the CPT procedure aimed at

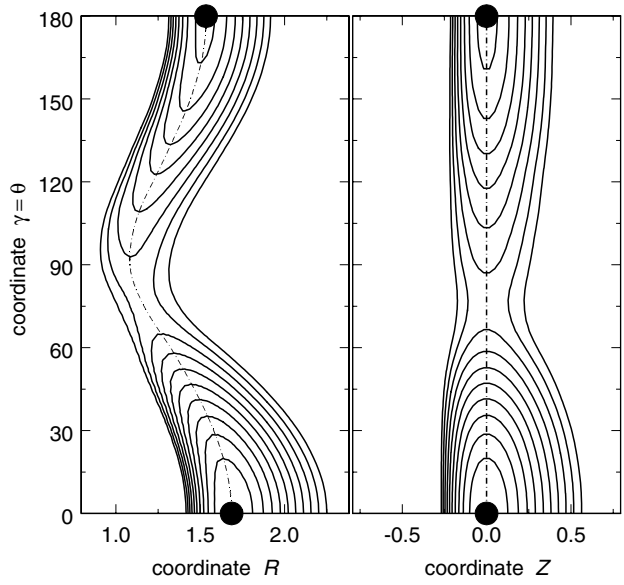

Figure 1. (**Left**) Two-dimensional cut in the (R, γ) plane of the three-dimensional PES for the HCN $\leftrightarrow$ CNH system obtained by Tennyson and co-workers [7,8]. R is the distance in Å between H and the center of mass, G, of CN, while γ is the HGC angle ($\gamma = 0$ at the linear HCN configuration, $\gamma = \pi$ at the linear CNH configuration). For this figure, the third coordinate (i.e., the distance r between C and N) is fixed to the HCN equilibrium value of 1.1528 Å. (**Right**) Same plot, but for coordinates (Z, θ) defined in Eq. (3).

minimizing these couplings consists in developing the initial Hamiltonian in Fourier series with respect to γ along the MEP and in Taylor series with respect to the stretch coordinates perpendicular to the MEP, in order to rewrite it in terms of simple operators.

More precisely, let us suppose that the initial Hamiltonian of the system is written in the form

$$\begin{aligned} H &= T + V(R, r, \gamma) \\ T &= \frac{1}{2\mu_r} p_r^2 + \frac{1}{2\mu_R} p_R^2 + \left(\frac{1}{2\mu_r r^2} + \frac{1}{2\mu_R R^2} \right) p_\gamma^2 \end{aligned} \tag{1}$$

where μ_r and μ_R stand for the reduced masses of C–N and H–CN, respectively, V is the PES expressed in terms of the Jacobi coordinates, and T is the classical expression of the kinetic energy of a triatomic molecule (we temporarily forget the additional term, which arises from the fact that the molecule is linear at equilibrium). Defining a grid γ_i $(i = 1, \ldots, i_{\max})$ of equally spaced points in γ,

such that $\gamma_1 = 0$ and $\gamma_{i_{\max}} = 180^\circ$ ($i_{\max}$ is usually taken in the range 100–200), the MEP is first determined as the set of points $(R_{MEP}(\gamma_i), r_{MEP}(\gamma_i), \gamma_i)$, where $R_{MEP}(\gamma)$ and $r_{MEP}(\gamma)$ are solutions of

$$\left(\frac{\partial V}{\partial R}\right)_{R_{MEP}, r_{MEP}, \gamma} = \left(\frac{\partial V}{\partial r}\right)_{R_{MEP}, r_{MEP}, \gamma} = 0 \tag{2}$$

One also calculates by the method of finite differences the vectors $R'_{MEP}(\gamma_i)$ and $r'_{MEP}(\gamma_i)$ of the derivatives of R_{MEP} and r_{MEP} with respect to γ. For each value γ_i, the Hamiltonian is then rewritten in terms of the new set of conjugate variables

$$\begin{aligned} Z &= R - R_{MEP}(\gamma_i), \qquad & p_Z &= p_R \\ z &= r - r_{MEP}(\gamma_i), \qquad & p_z &= p_r \\ \theta &= \gamma, \qquad & p_\theta &= p_\gamma + R'_{MEP}(\gamma_i) p_R + r'_{MEP}(\gamma_i) p_r \end{aligned} \tag{3}$$

and expanded in Taylor series with respect to the coordinates Z and z. For each value of γ_i one thus obtains a series of the form

$$H(\theta = \gamma_i) = \sum_{\mathbf{m},\mathbf{n},N} h^{(i)}_{\mathbf{mn}N} Z^{m_1} z^{m_2} p_Z^{n_1} p_z^{n_2} p_\theta^N \tag{4}$$

where $\mathbf{m} = (m_1, m_2)$ and $\mathbf{n} = (n_1, n_2)$. By expanding each vector $h^{(i)}_{\mathbf{mn}N}$ ($i = 1, \ldots, i_{\max}$) in Fourier series with respect to $\theta = \gamma$ and rewriting $\cos(n\theta)$ in terms of $(\cos\theta)^n$, and likewise $\sin(n\theta)$ in terms of $(\sin\theta)(\cos\theta)^n$, the initial Hamiltonian H is cast in the form

$$H = \sum_{\mathbf{m},\mathbf{n},M,P,N} h_{\mathbf{mn}MPN} Z^{m_1} z^{m_2} (\cos\theta)^M p_Z^{n_1} p_z^{n_2} (\sin(\theta) p_\theta)^P p_\theta^{2N} \tag{5}$$

where $P = 0$ or $P = 1$. A two-dimensional cut in the (Z, θ) plane of the potential energy part of this expression is plotted in Fig. 1 (right) for $m_1 + m_2 \leq 12$ and $M \leq 24$. Wilson's GF formalism [9] is then applied to Eq. (5), in order to rewrite the Hamiltonian of the system in terms of the dimensionless normal coordinates (p_1, q_1) and (p_3, q_3) for the stretch degrees of freedom (for HCN $\leftrightarrow$ CNH, indexes 1 and 3 stand for the H–CN and C–N stretches, respectively).

At last, a few steps are necessary to make the expansion of Eq. (5) amenable to quantum CPT procedures: The dimensionless normal coordinates for the stretch degrees of freedom are expressed in terms of the ladder operators

$$a_k = \frac{1}{\sqrt{2}}(q_k + \mathrm{i}p_k), \qquad a_k^+ = \frac{1}{\sqrt{2}}(q_k - \mathrm{i}p_k) \tag{6}$$

where $i^2 = -1$ and $k = 1, 3$ (the convention $\hbar = 1$ is assumed throughout the manuscript), while p_θ^2 is replaced by the operator J^2, where

$$J^2 = -\frac{1}{\sin\theta}\frac{\partial}{\partial\theta}\sin\theta\frac{\partial}{\partial\theta} - \frac{1}{(\sin\theta)^2}\frac{\partial^2}{\partial\varphi^2} \tag{7}$$

and φ describes the rotation of the molecule around the axis with the smallest moment of inertia. One obtains

$$H = \sum_{\mathbf{m},\mathbf{n},M,P,N} H_{\mathbf{mn}MPN}(a_1^+)^{m_1}(a_1)^{n_1}(a_3^+)^{m_3}(a_3)^{n_3}(\cos\theta)^M\sigma^P(J^2)^N \tag{8}$$

where σ stands for the differential operator $\sin\theta\partial/\partial\theta$. Note that all of the operators that appear in Eq. (8) have simple matrix elements in the bases of the harmonic oscillator and of the spherical functions. Note also that symmetrization of Eq. (8), which is made necessary by the canonical transformations of Eq. (3), is postponed to an ulterior step (see below).

Following Van Vleck [10] Jordahl [11], and Kemble [12], the CPT procedure itself consists of a series of unitary transformations of increasing order s ($s = 1, 2, 3, \ldots$)

$$K = \exp(S)H\exp(-S) \tag{9}$$

where the initial operator H at order $s = 1$ is the expansion of Eq. (8) and the transformed Hamiltonian K obtained at order s serves as the initial operator H at order $s + 1$. The operator S, which appears in this equation, is anti-Hermitian. Reference to the current perturbation order s (in the form of subscripts or superscripts) will not be used, in order to avoid too complex notations. For the same reason, no artificial small parameter λ is introduced. The basic idea of CPT is to expand, at each order s, H, and K in the form

$$\begin{aligned} H &= \sum_{i=0}^{\infty} H^{(i)} \\ K &= \sum_{i=0}^{\infty} K^{(i)} \end{aligned} \tag{10}$$

where the $H^{(i)}$ and $K^{(i)}$ become smaller and smaller with increasing values of the order i. Actually, the ordering of the successive operators H (at $s > 1$) and K (at $s \geq 1$) is uniquely determined by the ordering of the initial operator H at order $s = 1$—that is, of Eq. (8). The choice of $H^{(0)}$ is particularly important, because the ability to solve the cohomology equation (see below) depends crucially on

this choice. Moreover, the number of terms to handle, and therefore the size of the required computer memory, depends on the ordering of the other $H^{(i)}$'s $(i > 0)$. The best choice consists in retaining in $H^{(0)}$, at first order of the theory, only the sum of the harmonic oscillators for the stretch degrees of freedom, that is,

$$H^{(0)} = \sum_{i=1,3} \omega_i a_i^+ a_i \tag{11}$$

while the terms with $m_1 + m_3 + n_1 + n_3 + P + 2N = k$ are retained in $H^{(k)}$ if $M \neq 0$ and in $H^{(k-2)}$ if $M = 0$. An exception occurs for the pure bending terms in J^2 and $(\cos\theta)^M$, which are retained in $H^{(1)}$ rather than $H^{(0)}$, in order to satisfy Eq. (11). Each term $H^{(k)}$ is then symmetrized independently.

If one further assumes that, at order s of the perturbation procedure, the operator S is of the same order of magnitude as $H^{(s)}$ and $K^{(s)}$, then the relationship between the $K^{(i)}$ and the $H^{(i)}$ is simply obtained by expanding the exponential operators in Eq. (9) and equating the terms of the same order. One gets

$$\begin{aligned} &\text{If } i < s, \qquad K^{(i)} = H^{(i)} \\ &\text{If } i = s, \qquad K^{(s)} = H^{(s)} + [S, H^{(0)}] \\ &\text{If } i > s, \qquad K^{(i)} = H^{(i)} + \sum_m \frac{1}{n!} [\underbrace{S, \ldots [S}_{n \text{ times}}, H^{(m)}] \ldots] \end{aligned} \tag{12}$$

In the last equation, the summation runs over all integers m, for which there exists another integer n larger than or equal to 1, such that $m + ns = i$. The second equation of Eq. (12) is used to determine S by requiring that (at order s of the perturbation procedure) $K^{(s)}$ contains only the "physically important" terms of $H^{(s)}$. In other words, if R contains the terms of $H^{(s)}$, which are *not* wanted in $K^{(s)}$—that is, $R = H^{(s)} - K^{(s)}$—then S is determined by solving the so-called cohomology equation

$$[S, H^{(0)}] = -R \tag{13}$$

Straightforward calculations show that the choice of $H^{(0)}$ in Eq. (11) implies that an operator R of the form

$$R = \sum_{\mathbf{m},\mathbf{n},M,P,N} R_{\mathbf{mn}MPN} (a_1^+)^{m_1} (a_1)^{n_1} (a_3^+)^{m_3} (a_3)^{n_3} (\cos\theta)^M \sigma^P (J^2)^N \tag{14}$$

is canceled from $K^{(s)}$ if S is taken as

$$S = \sum_{\mathbf{m},\mathbf{n},M,P,N} \frac{R_{\mathbf{mn}MPN}}{\Delta_{\mathbf{mn}}} (a_1^+)^{m_1} (a_1)^{n_1} (a_3^+)^{m_3} (a_3)^{n_3} (\cos\theta)^M \sigma^P (J^2)^N \qquad (15)$$

where $\Delta_{\mathbf{mn}} = (m_1 - n_1)\omega_1 + (m_3 - n_3)\omega_3$. The terms of K of order i higher than s are finally obtained from the third equation of Eq. (12) (note that the terms of order i smaller than s are not changed by the transformation at order s). Practically, the only tedious point in setting up a computer program consists in rewriting products of two terms $(a_1^+)^{m_1} (a_1)^{n_1} (a_3^+)^{m_3} (a_3)^{n_3} (\cos\theta)^M \sigma^P (J^2)^N$ as linear combinations of terms of the same form. This is achieved by using Sibert's formula [see Eq. (11) of Ref. 13) for stretch operators and the recurrence relations in Eq. (5) of Ref. 1 for bend operators.

The key of any CPT procedure is actually the choice, at each order s of the theory, of the terms of $H^{(s)}$ to be kept in $K^{(s)}$ and of those to be put in R, so that they are canceled by the unitary transformation at order s. The simplest perturbative Hamiltonian is obtained when only the terms, which are diagonal with respect to the stretch degrees of freedom, are kept in $K^{(s)}$, while all the other ones are assigned to R. In other words, all the terms of $H^{(s)}$ such that $\mathbf{m} \neq \mathbf{n}$ are canceled. When performing s unitary transformations with this criterion for the definition of R and then neglecting the terms $K^{(i)}$ such that $i > s$, one is left with a Hamiltonian of the form

$$K = \sum_{\mathbf{m},M,P,N} K_{\mathbf{m}MPN} (a_1^+)^{m_1} (a_1)^{m_1} (a_3^+)^{m_3} (a_3)^{m_3} (\cos\theta)^M \sigma^P (J^2)^N \qquad (16)$$

which is called the "perturbative Hamiltonian of order s." The most useful expression for this Hamiltonian is obtained by expanding each product $(a_i^+)^{m_i} (a_i)^{m_i}$ in terms of the $(a_i^+ a_i)^{m_i} = v_i^{m_i}$, where the v_i are the stretch quantum numbers. One gets

$$K = \sum_{\mathbf{m},M,P,N} k_{\mathbf{m}MPN} v_1^{m_1} v_3^{m_3} (\cos\theta)^M \sigma^P (J^2)^N \qquad (17)$$

where the $k_{\mathbf{m}MPN}$ are real coefficients. K is formally a one-dimensional Hamiltonian in the bending angle θ and its conjugate momentum. It depends only parametrically on the good quantum numbers for the stretch degrees of freedom.

Figure 2 shows the convergence of the CPT procedure described above, when it is applied to the ab initio surface for HCN $\leftrightarrow$ CNH computed by Tennyson and co-workers [7,8]. This figure indicates, for each order s of the perturbation procedure, the average arithmetic error between the energies of the lowest 101

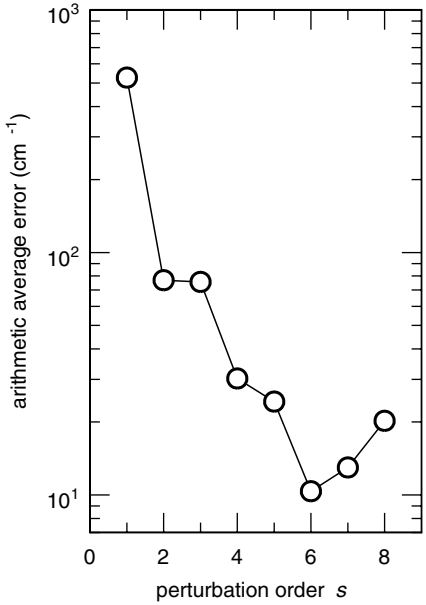

Figure 2. Plot, as a function of the order s of the perturbation procedure, of the average arithmetic error between the energies of HCN ↔ CNH obtained for the ab initio surface of Refs. 7 and 8 and the perturbative Hamiltonian of Eq. (17). The lowest 101 rotationless states of the system are taken into account (see Tables VI and VII of Ref. 7). These states have up to 18 quanta of excitation in the bend degree of freedom and 12,400 cm^{-1} of vibrational energy above the quantum mechanical ground state.

rotationless states reported in Tables VI and VII of Ref. 7 and the corresponding energies computed with the perturbative Hamiltonian of order s [Eq. (17)]. The states taken into account have up to 18 quanta of excitation in the bend degree of freedom and 12,400 cm^{-1} of vibrational energy above the quantum mechanical ground state. Practically, the PES and the kinetic energy operator were initially Fourier expanded up to $(\cos\theta)^{M_{\max}}$ with $M_{\max} = 10$, because expansion to higher orders does not change significantly the results. Note, however, that all the trigonometric terms of higher order, which appear upon application of the CPT procedure, must be taken into account, so that the successive Hamiltonians remain Hermitian [if one orders the initial expansion of Eq. (8) as described in (and below) Eq. (11), then the trigonometric term with highest power one has to consider at order s of the perturbation procedure is $(\cos\theta)^{(s-2)M_{\max}}$]. It is well known that CPT leads to asymptotic series—that is, to series that converge for a certain number of iterations and then fluctuate or diverge. One therefore has to check somehow the convergence of the series of

perturbative Hamiltonians after each canonical transformation. It is seen in Fig. 2 that the best agreement with variational calculations is obtained for the sixth-order perturbative Hamiltonian, for which the average error is as low as about $10\,\mathrm{cm}^{-1}$.

Pseudo-potential energy curves are extracted from the perturbative Hamiltonian of Eq. (17) by retaining only the terms with $P = N = 0$—that is, the terms without differential operator. One obtains a one-dimensional pseudo-potential curve $V_{v_1,v_3}(\theta)$ for each pair of quantum numbers v_1 (H–CN stretch) and v_3 (C–N stretch)

$$V_{v_1,v_3}(\theta) = \sum_{\mathbf{m},M} k_{\mathbf{m}M00} v_1^{m_1} v_3^{m_3} (\cos\theta)^M \tag{18}$$

The lowest 11 pseudo-potential curves are drawn in Fig. 3. These curves can be used to determine, for example, if there is any chance to detect the system in the CNH well following its excitation to a given (v_1, v_2, v_3) state of HCN [14]—that is, if state (v_1, v_2, v_3) lies above or below the isomerization barrier for these values of v_1 and v_3. Figure 3 shows that, for HCN $\leftrightarrow$ CNH, an increase in the

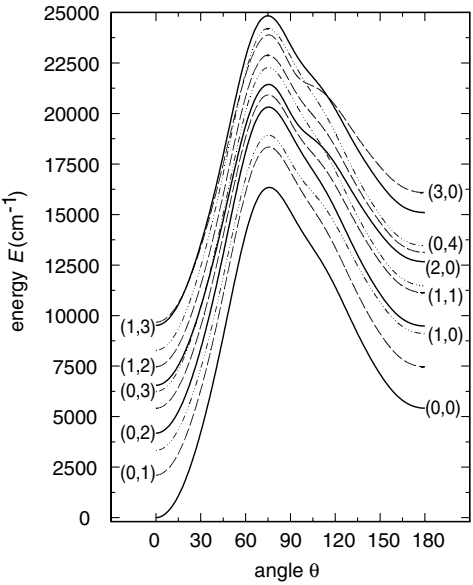

Figure 3. Plot of the lowest 11 pseudo-potential energy curves $V_{v_1,v_3}(\theta)$ obtained by applying sixth-order CPT to the HCN $\leftrightarrow$ CNH surface of Refs. 7 and 8. The stretch quantum numbers v_1 (H–CN stretch) and v_3(C–N stretch) are indicated for each curve as (v_1, v_3).

stretch quantum numbers essentially results in the shift of the energies of the HCN and CNH minima, as well as the isomerization threshold, by the corresponding linear combination of the fundamental frequencies. However, in other systems, like C_3 [6], variations of the stretch quantum numbers have a much more dramatic influence on the pseudo-potential energy curves. Moreover, the tunneling effect, which takes place slightly below the top of the isomerization barrier, is clearly seen when plotting, on the same graph, the wave functions of the states with given values of v_1 and v_3 and the corresponding pseudo-potential energy curve (see Fig. 4). We shall come back to this point in more detail in Section II.B.

Before concluding this section, let us just mention that, while all of the equations above refer explicitly to the Van Vleck quantum procedure [10–12,15], they are most straightforwardly adapted to the classical procedure based on Lie algebra [16–18] by replacing quantum commutators with Poisson brackets. Most of the concepts remain also valid for the classical

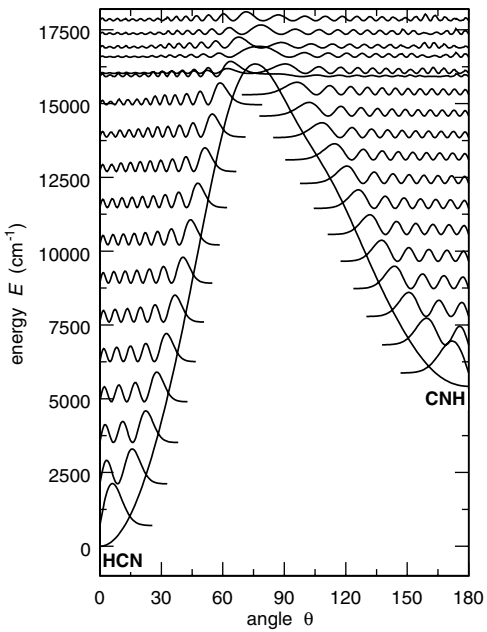

Figure 4. Plot of the pseudo-potential and the probability density for the pure bending states ($v_1 = v_3 = 0$) of the HCN $\leftrightarrow$ CNH system versus bending angle θ. These results were obtained by applying sixth-order CPT to the ab initio surface of Tennyson and co-workers [7,8]. The vertical scale is the same for all probability plots, and the baseline for each plot coincides with the energy of the corresponding state.

Birkhoff–Gustavson procedure [19–21], although Eq. (12) has a slightly different form in this latter case [3].

B. Adiabatic Versus Nonadiabatic Delocalization in Isomerizing Systems

The theory described in Section II.A applies to the progressions of quantum mechanical ''adiabatic'' states. A state is adiabatic in the Ehrenfest sense, if the two perpendicular stretch quantum numbers v_1 and v_3 remain unchanged as the angle θ varies between 0° and 180°. As is known from the quantum mechanical calculations, all localized eigenstates of the non-rotating HCN and CNH molecules, trapped below the barrier on their respective adiabatic pseudo-potential curves (see Figs. 3 and 4), satisfy this definition. Moreover, many delocalized states located above their respective adiabatic barriers $V^+_{v_1,v_3}$ have the same assignment v_1 and v_3 on both HCN and CNH sides. Thus, the adiabatic approximation is realistic for a significant portion of the spectrum, including many of the delocalized states. The states belonging to the HCN and CNH well are usually assigned as $(v_1, v_2, v_3)_{\mathrm{HCN}}$ and $(v_1, v_2, v_3)_{\mathrm{CNH}}$, respectively. Alternatively, one might organize these states into adiabatic progressions $(v_1, v_2, v_3)_{\mathrm{ad}}$, by counting the bending quanta over the whole range of θ between 0° and 180°.

In view of the hitherto unsuccessful experimental search for eigenstates delocalized between the HCN and CNH isomers [14,22–28], the analysis of the mechanisms and spectral signatures of delocalization becomes central to theoretical studies. According to the adiabatic theory presented in Section II.A, states with excitation (v_1, v_3) in the perpendicular stretching coordinates are expected to remain localized even above the lowest adiabatic pseudo-potential barrier $V^+_{0,0}$. Indeed, in the adiabatic picture, these states become delocalized only if they are located close to or above the corresponding adiabatic potential barrier $V^+_{v_1,v_3}$, which can be located far above $V^+_{0,0}$ (see Fig. 3). This might explain the fact that no delocalized states were detected in the experiments that pumped energy in HCN through a combination of the bending and stretching modes [14,23,24]. Figure 5 illustrates more quantitatively the correlation between $V^+_{v_1,v_3}$ and the extent of delocalization. Each eigenstate can be ascribed probability densities in the HCN and CNH wells, P_{HCN} and P_{CNH}, respectively. Delocalization P_{del} of a normalized eigenstate is defined as the lesser of the two probabilities

$$P_{\mathrm{del}} = \min(P_{\mathrm{HCN}}, P_{\mathrm{CNH}}) \tag{19}$$

Figure 5 shows P_{del} for bending states in the pure and several combination progressions as a function of energy. The vertical solid line in each frame marks the position of the adiabatic barrier $V^+_{v_1,v_3}$. It is clear that full delocalization $P_{\mathrm{del}} = 50\%$ is reached only at and above the top of the adiabatic barrier,

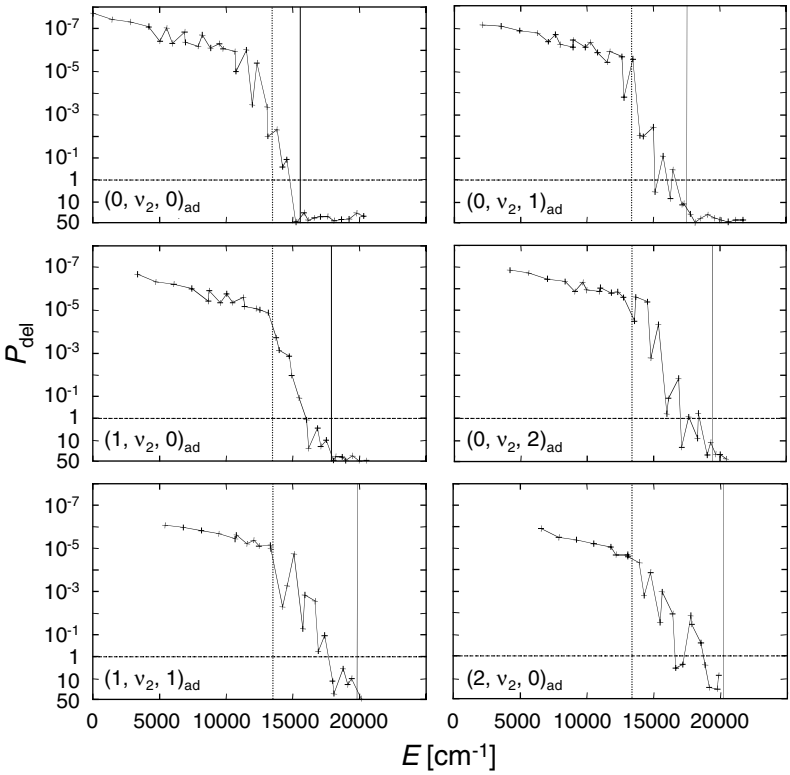

Figure 5. Plot of delocalization P_{del} (in %), defined in Eq. (19), as a function of the energy E above the ground vibrational state, for six bending progressions $(v_1, v_2, v_3)_{\mathrm{ad}}$. The stretching quantum numbers v_1 and v_3 remain constant within each frame. The vertical solid lines indicate the position of the adiabatic barrier, $V^{+}_{v_1,v_3}$, for each progression. The energy of the PES' saddle point, close to $\gamma = 80°$, is marked with vertical dotted lines.

especially for low perpendicular excitations. Note that, due to couplings between the bending mode and the H–CN stretch, the height of the adiabatic barriers $V^{+}_{v_1,0}$ decreases with growing v_1. For example, the barrier $V^{+}_{6,0}$ (measured relative to the CNH minimum on the pseudo-potential curve) is only half as high as the barrier $V^{+}_{0,0}$. The higher the value of v_1, the lower the amount of bending excitation needed to achieve a certain degree of adiabatic delocalization.

At higher energies, it becomes increasingly difficult to organize delocalized eigenstates in adiabatic progressions. Quantum calculations show that, for many states, quantum numbers v_1 and/or v_3 are not conserved along θ. The stretching excitations instead change upon traversing the barrier separating HCN from CNH. Figure 6 illustrates this point. In the left-hand frame, the

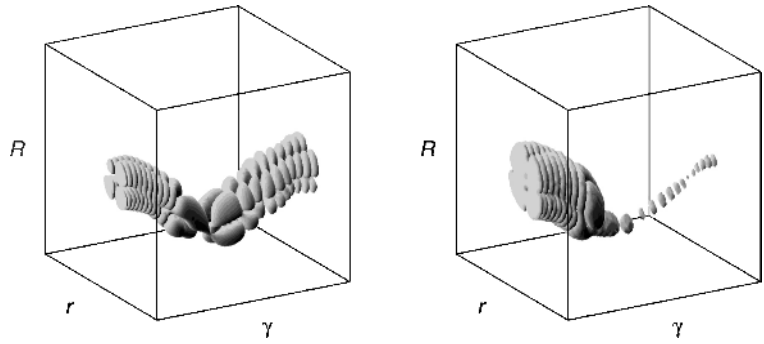

Figure 6. Wavefunctions of states 315 and 206 of the HCN ↔ CNH system, with respective energies $E = 18,069\,\mathrm{cm}^{-1}$ and $E = 15,750\,\mathrm{cm}^{-1}$ above the quantum mechanical ground state. The figures show one particular contour $|\Psi(R,r,\gamma)|^2 = \text{const}$, where (R,r,γ) are the Jacobi coordinates. (**Left**) The adiabatically delocalized state 315, which is assigned as $(1,40,1)_{\mathrm{ad}}$. (**Right**) The nonadiabatically delocalized state 206, which can be assigned as $(1,16,1)_{\mathrm{HCN}}$ but displays the nodal structure of $(0,24,0)_{\mathrm{CNH}}$ on the CNH side.

three-dimensional (3D) wavefunction of an adiabatically delocalized state is shown. It has one quantum of excitation in each perpendicular mode all the way from HCN to CNH. The theory of Section II.A can be applied to it. In the right-hand frame, another delocalized state is shown. On the HCN side, it has the same nodal pattern as the adiabatically delocalized state shown in the left-hand frame of Fig. 6. On the CNH side, the state has instead no node in the stretching coordinates. This is an example of a ''nonadiabatically'' delocalized eigenstate. Note that nonadiabatic delocalization is due to small terms belonging to one of the $K^{(i)}$ $(i > s)$ which, in Section II.A, were neglected after the desired number s of transformations was performed. These small terms therefore do not appear in the expression of the effective Hamiltonian of Eq. (17), so that this Hamiltonian cannot reproduce the nonadiabatic delocalization effect.

In the remainder of this section, we consider the properties of the nonadiabatically delocalized states of HCN ↔ CNH in more detail. We argue that this type of delocalization becomes dominant and responsible for HCN ↔ CNH isomerization above the top of the potential barrier. Our analysis is based on numerically exact quantum mechanical calculations for the HCN ↔ CNH system performed using the PES of Bowman et al. [29], which reproduces the experimental vibration and vibration–rotation eigenenergies to within $60\,\mathrm{cm}^{-1}$ or better even at high energies. For the present study, we calculated the energies of the first 600 states of the nonrotating molecule—that is, up to about $22{,}200\,\mathrm{cm}^{-1}$ above the vibrational ground state—using successive truncation-diagonalization [30,31]. The eigenstates are converged

to within $0.5\,\mathrm{cm}^{-1}$ or better. The first 455 eigenstates and some of the states at higher energies were assigned using visual inspection of their wavefunctions, in order to provide an as complete as possible characterization of the localized and delocalized states.

The correlation between the height of the adiabatic barrier and the onset of delocalization is clearest in the pure bending progression $(0, v_2, 0)$ shown in Fig. 5. Delocalization patterns in other progressions are more involved. An example is provided by the progression $(1, v_2, 0)$, for which full delocalization, $P_{\mathrm{del}} = 50\%$, is achieved only at $E \geq V^{+}_{1,0}$. However, several states below this barrier are also delocalized to some extent, with P_{del} ranging from 1% to 10%. A closer look indicates that the first weakly delocalized states ($P_{\mathrm{del}} = 1.2\%$) appears near the top of the barrier of the lowest adiabatic curve $V^{+}_{0,0}$. In other words, weakly delocalized states in the progression $(1, v_2, 0)$ appear in the vicinity of the fully delocalized states of the progression $(0, v_2, 0)$. A similar behavior is found for other progressions shown in Fig. 5. Visual inspection of the three-dimensional eigenfunctions shows that the majority of the states with $P_{\mathrm{del}} \leq 10\%$ are nonadiabatically delocalized. For these nonadiabatically delocalized states, $v_1(\mathrm{HCN}) \neq v_1(\mathrm{CNH})$ and/or $v_3(\mathrm{HCN}) \neq v_3(\mathrm{CNH})$. Their assignment to pure progressions is based on the nodal structure of the strongest component of the wavefunction.

Visual inspection of the wavefunctions reveals another feature of the nonadiabatically delocalized states, which is crucial for rationalizing the effect and building up a model. Namely, the perpendicular quantum numbers v_1 and v_3 of the weak component of these states systematically coincide with the perpendicular quantum numbers of an adjacent adiabatically delocalized state. This suggests that weak delocalization is induced by coupling between a certain zero-order localized state $|\phi_k\rangle$ and a neighboring adiabatically delocalized state $|\chi_v\rangle$. Suppose that both $|\phi_k\rangle$ and $|\chi_v\rangle$ are known. Then, a nonadiabatically delocalized state $|\Psi_k\rangle$ can be expressed as

$$|\Psi_k\rangle \approx \alpha_k|\phi_k\rangle + \beta_k|\chi_v\rangle \tag{20}$$

where $|\phi_k\rangle$ is assumed to be completely localized in one of the potential wells, while $|\chi_v\rangle$ is delocalized between the HCN and CNH isomers. By construction, one has $P_{\mathrm{del}} = |\beta_k|^2 P_{\mathrm{del}}(\chi_v)$, where $P_{\mathrm{del}}(\chi_v)$ is the probability density of $|\chi_v\rangle$ in the potential well where $|\phi_k\rangle \equiv 0$. The wavefunctions $|\phi_k\rangle$ and $|\chi_v\rangle$ are normalized, but they are in general not orthogonal. Their overlap $S_{kv} = \langle\phi_k|\chi_v\rangle$ controls the coefficients α_k and β_k and, hence, the extent of delocalization P_{del}:

$$\begin{aligned} \alpha_k &= (1 - S_{kv}^2)^{-1/2} \\ \beta_k &= -\alpha_k S_{kv} \\ P_{\mathrm{del}} &= P_{\mathrm{del}}(\chi_v) S_{kv}^2/(1 - S_{kv}^2) \end{aligned} \tag{21}$$

If the zero-order basis is properly chosen, the model of Eq. (20) is a sensitive indicator of those couplings in the molecule that lead to delocalization. This in turn can be used to describe the delocalization mechanisms in HCN $\leftrightarrow$ CNH.

The states $|\phi_k\rangle$ and $|\chi_v\rangle$ in Eq. (20) can be chosen in a variety of ways. For example, the delocalized states calculated in Section II.A using the one-dimensional pseudo-potential curves can in principle be used as functions $|\chi_v\rangle$. The states $|\phi_k\rangle$ localized in each potential well can also be determined using the same pseudo-potential curves (eventual tunneling contributions should be neglected). Unfortunately, the accuracy of the adiabatic pseudo-potentials of Section II.A, although sufficient for predicting the positions of the energy levels to within a few tens of reciprocal centimeters (compared to the variationally calculated energies), is not high enough to describe the subtle effects of weak delocalization. For this reason, it is more appropriate to construct the basis states using three-dimensional quantum mechanical calculations. We define the localized basis states $|\phi_k\rangle$ as solutions of the ''restricted'' Schrödinger equation in the isolated wells. The dividing surface between the HCN and CNH parts of the PES is determined in molecular coordinates. The potential energy along the dividing surface in the restricted calculations is set to some large number which guarantees that wavefunctions are localized in one of the potential wells. Thus, solutions in one well are independent of the solutions in the other and can be used as $|\phi_k\rangle$. Next, this basis is augmented by the adiabatically delocalized eigenstates $|\chi_v\rangle$ of the original unrestricted Schrödinger equation: This is in accord with our conjecture that adiabatically delocalized states are the main perturbers causing weak delocalization.

The wavefunctions $|\phi_k\rangle$ and $|\chi_v\rangle$ solve different Schrödinger equations and therefore are not orthogonal. Since the overlap integrals between them are the measure of nonadiabatic delocalization, one first calculates S_{kv} between all localized and delocalized states. This identifies the most important couplings in the system, as well as the states that can be nonadiabatically delocalized. Next, the weakly delocalized eigenstates are reconstructed using Eq. (20) and compared to the exact results. Note that this procedure is somewhat reminiscent of the well-known tier model widely used in the investigations of intramolecular energy redistribution [32]. State $(2, 16, 0)_{\mathrm{HCN}}$ provides a typical example (see Fig. 7). Its nonadiabatic delocalization is entirely due to the coupling with the adiabatically delocalized state $(0, 56, 0)_{\mathrm{ad}}$, which lies only $11\,\mathrm{cm}^{-1}$ below $(2, 16, 0)_{\mathrm{HCN}}$. This is confirmed by reconstructing the weakly delocalized state using Eq. (20) and comparing the obtained nodal structure with the exact one. The extent of delocalization of the reconstructed wavefunction, $P_{\mathrm{del}} = 3.4\%$, is in excellent agreement with the exact result, $P_{\mathrm{del}} = 3.6\%$. The eigenenergy and the rotational constant of this state are also accurately reproduced within the simple approximation of Eq. (20).

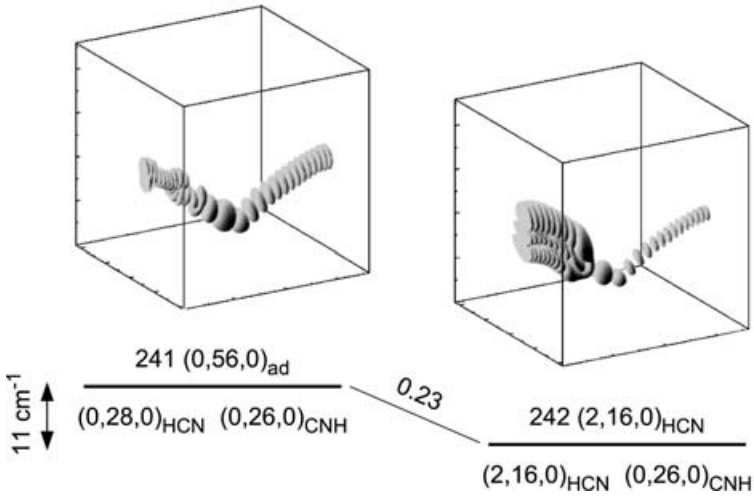

Figure 7. Simple two-state coupling scheme in HCN ↔ CNH, according to Eq. (20). (**Left**) Wavefunction of the adiabatically delocalized state 241 ($E = 16,612\,\mathrm{cm}^{-1}$), which is assigned as $(0,56,0)_{\mathrm{ad}}$. This is state $|\chi_v\rangle$ of Eq. (20). (**Right**) Wavefunction of the resulting nonadiabatically delocalized state 242 ($E = 16,623\,\mathrm{cm}^{-1}$), which can be assigned as $(2,16,0)_{\mathrm{HCN}}$ but displays the nodal structure of $(0,26,0)_{\mathrm{CNH}}$ on the CNH side. This is state $|\Psi_k\rangle$ of Eq. (20). The various assignments refer to the adiabatic description (upper) and to the nodal structures in the isolated wells (lower). The value of the overlap integral S_{kv} is indicated along the line connecting the two states. The wavefunctions are shown in the same representation as in Fig. 6.

Some of the localized basis functions couple to more than one adiabatically delocalized states. In this case, the model of Eq. (20) should be generalized to accommodate these couplings:

$$|\Psi_k\rangle \approx \alpha_k|\phi_k\rangle + \sum_{v=1}^{N_k} \beta_{kv}|\chi_v\rangle \tag{22}$$

where the coefficients α_k and β_{kv}, and the delocalization P_{del}, are given by

$$\begin{aligned} \alpha_k &= \left(1 - \sum_{v=1}^{N_k} S_{kv}^2\right)^{-1/2} \\ \beta_{kv} &= -\alpha_k S_{kv} \\ P_{\mathrm{del}} &= \sum_{v=1}^{N_k} |\beta_{kv}|^2 P_{\mathrm{del}}(\chi_v) \end{aligned} \tag{23}$$

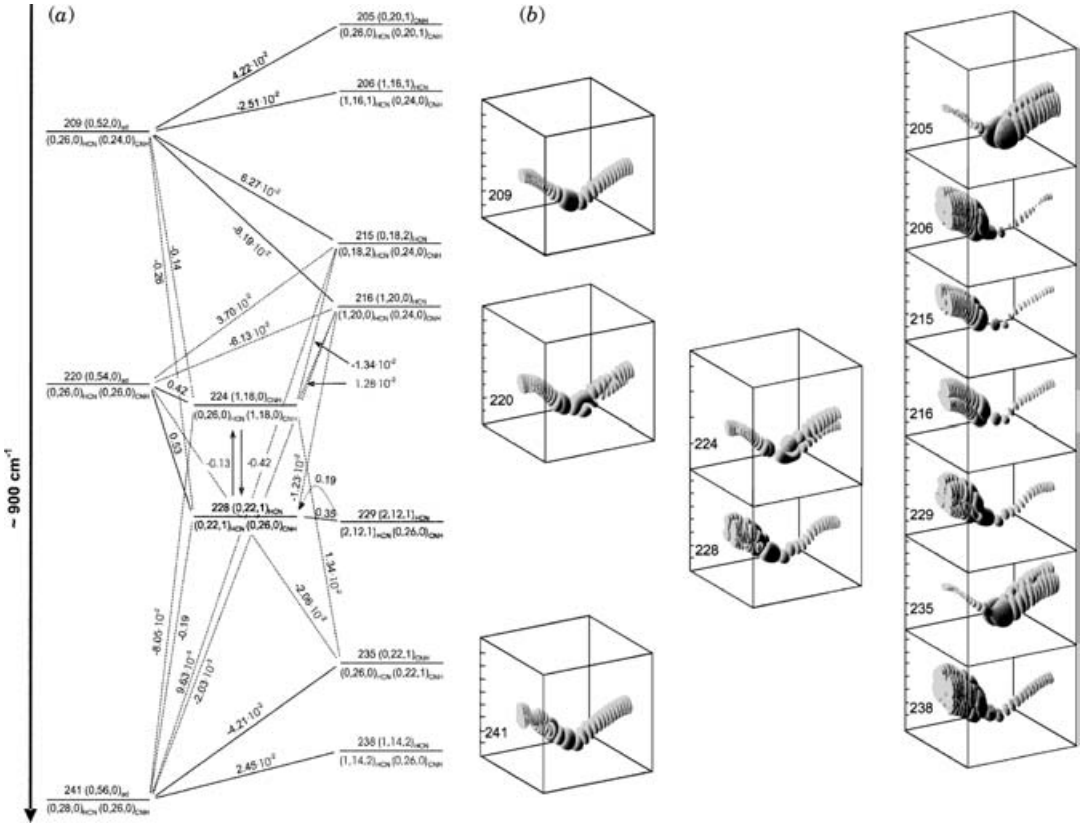

Figure 8. The scheme of interstate couplings leading to nonadiabatic delocalization in HCN ↔ CNH, in an energy window of 900 cm^{-1} centered around 16,200 cm^{-1} above the quantum mechanical ground state. (**a**) The structure of the energy levels, their assignments (upper, adiabatic; lower, according to the nodal structure in the isolated wells), and overlap integrals S_{kv} (numbers on the lines connecting pairs of states). The extent of delocalization diminishes from left to right. (**b**) Wavefunctions of the energy levels shown in (*a*). The wavefunctions are shown in the same representation as in Fig. 6.

This model can be used to uncover the complicated network of interstate couplings leading to nonadiabatic delocalization. An example of such a coupling scheme is presented in Fig. 8a. These states lie approximately 16,000 cm^{-1} above the ground vibrational state. The energy interval of about 900 cm^{-1} comprises 37 states, of which only three are adiabatically delocalized. They belong to the progression $(0, v_2, 0)$ and are collected in the left column of Fig. 8a. The adiabatically delocalized states lie above the respective barrier $V^+_{0,0}$. All other states belong to progressions, which are adiabatically trapped below the respective adiabatic barriers $V^+_{v_1,v_3}$. Nevertheless, all the trapped states are nonadiabatically delocalized. This is clearly seen in Fig. 8b, which shows some of the corresponding wavefunctions. Nonadiabatic delocalization of two states, 224 and 228, is particularly strong, with respective values $P_{\text{del}} = 20.0\%$ (224) and $P_{\text{del}} = 6.9\%$ (228). These states are shown in the middle column of the diagram in Fig. 8a. The states in the right column are more weakly delocalized ($P_{\text{del}} = 1.1\%$). Strong and weak couplings between eigenstates are indicated by the solid and dotted lines, respectively. The numbers above the lines are the values of the overlap integrals S_{kv} for the pair of states in question. This scheme can be considered as a pictorial guide to the choice of the coupling model for a particular state. For example, states 205 and 206 are perturbed only by the adiabatically delocalized state $(0, 52, 0)_{\text{ad}}$ in the left column. For them, Eq. (20) is appropriate. For most other states in the right and middle columns, the multiple perturber model of Eq. (22) appears to be more adequate.

Figure 8 demonstrates how the delocalization, initially carried by three adiabatically delocalized states, spreads over the adjacent eigenfunctions. Note that one can distinguish between direct and indirect interactions of eigenstates. Delocalization of states 205 and 206 is a result of the direct coupling with the adiabatically delocalized state 209. More complicated is the example of state 229 (right column in Fig. 8). In the zeroth-order approximation, this state is assigned as $(2, 12, 1)_{\text{HCN}}$. Its (weak) nodal structure in the CNH well coincides with that of the adiabatically delocalized state 220 (left column), although the direct overlap between these two states is vanishingly small. In fact, the nodal structure of state 229 in the CNH well is due to its coupling to the neighboring state 228 (middle column), which, in turn, is strongly coupled to the adiabatic state 220. The coupling scheme in Fig. 8 contains even more complicated coupling chains, which develop between the localized and delocalized states, thus leading to spreading of the weak delocalization over the entire spectrum. Adiabatically delocalized eigenfunctions play the role of critical nuclei necessary to initiate this process. The avalanche-like expansion of weak delocalization, initiated by the adiabatically delocalized states, is the main reason for the increase in the density of states with $P_{\text{del}} \geq 1\%$ with growing energy. This is illustrated in Fig. 9, where the total density of states is compared with the density of delocalized states.

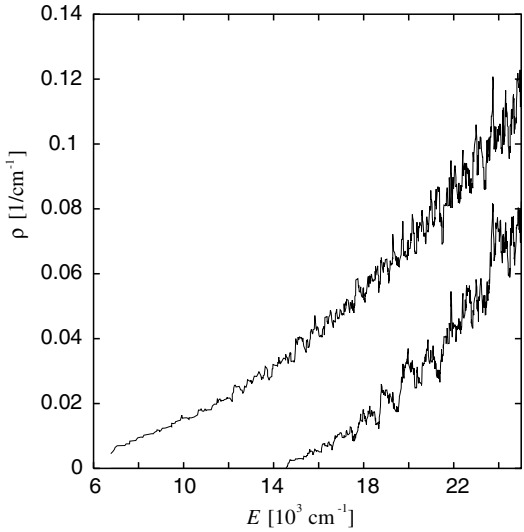

Figure 9. The density of states in the HCN ↔ CNH system as a function of energy above the ground vibrational state. The upper curve shows the full density of states. The lower curve corresponds to the density of delocalized states with $P_{\text{del}} > 1\%$.

III. RESONANTLY COUPLED ISOMERIZING AND DISSOCIATING SYSTEMS

Section II dealt with the system HCN ↔ CNH, for which the various degrees of freedom can be nearly separated. Section III is instead devoted to the description of the dynamics of the isomerizing and dissociating systems HCP ↔ CPH, HOCl → HO + Cl and HOBr → HO + Br, for which there exists a strong coupling (namely, a 1:2 Fermi resonance) between the reactive degree of freedom and a perpendicular one. A feature that is common to isomerization and dissociation reactions is the large anharmonicity along the reaction pathway. Based on the analysis of two integrable models—the Dunham expansion and the Fermi resonance Hamiltonian—Section III.A describes how the folding of the polyads (i.e., the closely spaced groups of states coupled by the Fermi resonance) caused by these large anharmonicities combines with the Fermi nonlinear coupling to produce a saddle-node bifurcation, where quantum states, which stretch along the reaction pathway, are created. These saddle-node bifurcations are, however, just the first step of the subtle pattern of bifurcations, which these systems must undergo in order to reach the reaction threshold. Relying mostly on the classical analysis of the ab initio PESs, Section III.B describes this pattern in

more detail, particularly emphasizing the correspondence between the quantum mechanical and classical descriptions.

A. Polyad Folding and Saddle-Node Bifurcations

It has been shown recently that the vibrational spectra of HCP [33–36], HOCl [36–39], and HOBr [40,41] obtained from quantum mechanical calculations on global ab initio surfaces can be reproduced accurately in the low to intermediate energy regime (75% of the isomerization threshold for HCP, 95% of the dissociation threshold for HOCl and HOBr) with an integrable Fermi resonance Hamiltonian. Based on the analysis of this Hamiltonian, this section proposes an interpretation of the most salient feature of the dynamics of these molecules, namely the first saddle-node bifurcation, which takes place in the intermediate energy regime.

The Fermi resonance Hamiltonian consists of two terms. The first one, H_D, is the Dunham expansion, which characterizes the uncoupled system, while the second term, H_F, is the Fermi resonance coupling, which describes the energy flow between the reactive mode and one perpendicular mode. For the three systems, HCP $\leftrightarrow$ CPH, HOCl $\rightarrow$ HO + Cl and HOBr $\rightarrow$ HO + Br, the reactive degree of freedom is the slow component of the Fermi pair and will therefore be labeled s, while the fast component will be labeled f. Thus, the resonance condition writes $\omega_f \approx 2\omega_s$. More explicitly, for HCP the slow reactive mode is the bend (mode 2) and the fast one is the CP stretch (mode 3), while for HOCl and HOBr the slow mode is the OX stretch (X = Cl,Br) (mode 3) and the fast one is the bend (mode 2). The third, uncoupled mode—that is, the CH stretch (mode 1) for HCP and the OH stretch (mode 1) for HOCl and HOBr—will be labeled u. With these notations, the Dunham expansion writes in the form

$$H_D = \sum_{i=s,f,u} \omega_i I_i + \sum_{i,k} x_{ik} I_i I_k + \sum_{i,k,m} y_{ikm} I_i I_k I_m + \cdots \tag{24}$$

where

$$I_i = \frac{1}{2}(p_i^2 + q_i^2) = a_i^+ a_i + \frac{d_i}{2} = v_i + \frac{d_i}{2} \tag{25}$$

In Eq. (25), (p_i, q_i) is the set of conjugate dimensionless normal coordinates for mode i, a_i^+ and a_i are the corresponding creation and annihilation operators, v_i is the quantum number for this degree of freedom, and d_i is its degeneracy (d_i is equal to 2 for the bend in HCP and equal to 1 for all other degrees of freedom considered here). I_i is the classical action integral for mode i and Eq. (25) just

expresses the Einstein–Brillouin–Keller (EBK) quantization rule [42–45] for this mode. Quantum mechanically, the Fermi resonance term is written as

$$H_F = (a_s a_s a_f^+ + a_s^+ a_s^+ a_f)\left(k_0 + \sum_{i=s,f,u} k_i I_i + \cdots\right) \tag{26}$$

while its classical expression involves the angles $\varphi_i = -\tan^{-1}(p_i/q_i)$ conjugate to the I_i's, that is,

$$H_F = 2\cos(\varphi_f - 2\varphi_s) I_s \sqrt{I_f}\left(k_0 + \sum_{i=s,f,u} k_i I_i + \cdots\right) \tag{27}$$

See Table I of Ref. 34, Table II of Ref. 39 and Table I of Ref. 41 for numerical values of the coefficients ω_i, x_{ik}, y_{ikm}, k_i, ... Note that there are two misprints in Table II of Ref. 39: One should read $y_{233} = +0.2503\,\mathrm{cm}^{-1}$ and $y_{123} = -0.4304\,\mathrm{cm}^{-1}$.

Let us first neglect the Fermi resonance and analyze the dynamics of the uncoupled systems described by the Dunham expansion alone [Eq. (24)]. Because of the resonance condition $\omega_f \approx 2\omega_s$, quantum states are organized in clumps, or "polyads." Each polyad is defined by two quantum numbers, namely the number v_u of quanta in the uncoupled degree of freedom and the so-called polyad number P:

$$P = 2v_f + v_s \tag{28}$$

A polyad with quantum numbers v_u and P is labeled $[v_u, P]$. Polyads are separated by large energy gaps at low energies but overlap more and more widely as energy increases. It turns out that for the three molecules HCP, HOCl, and HOBr, the difference $2\omega_s - \omega_f$ is small (resonance condition) *and* positive. Therefore, at low P values, polyad $[v_u, P]$ organizes as follows. The state with lowest energy has quantum numbers $(v_s, v_f) = (0, P/2)$ (if P is even) or $(v_s, v_f) = (1, (P-1)/2)$ (if P is odd). The state with highest energy has quantum numbers $(v_s, v_f) = (P, 0)$. In between, the energies of the $\mathrm{int}(P/2) + 1$ states of the polyad increase monotonously with the number of quanta v_s in the reactive degree of freedom. Because of the large (negative) anharmonicity along the reaction pathway, this description does not hold for large values of P. Indeed, if P (and therefore v_s) becomes sufficiently large, then the *linear* harmonic energy gap $2\omega_s - \omega_f$ between two successive states of the polyad can become smaller than the *quadratic* (or higher-order) anharmonic corrections. For these higher values of P, the energies of the $\mathrm{int}(P/2) + 1$ states of the polyad are an increasing function of v_s up to a certain value of v_s, and then a *decreasing* function of v_s.

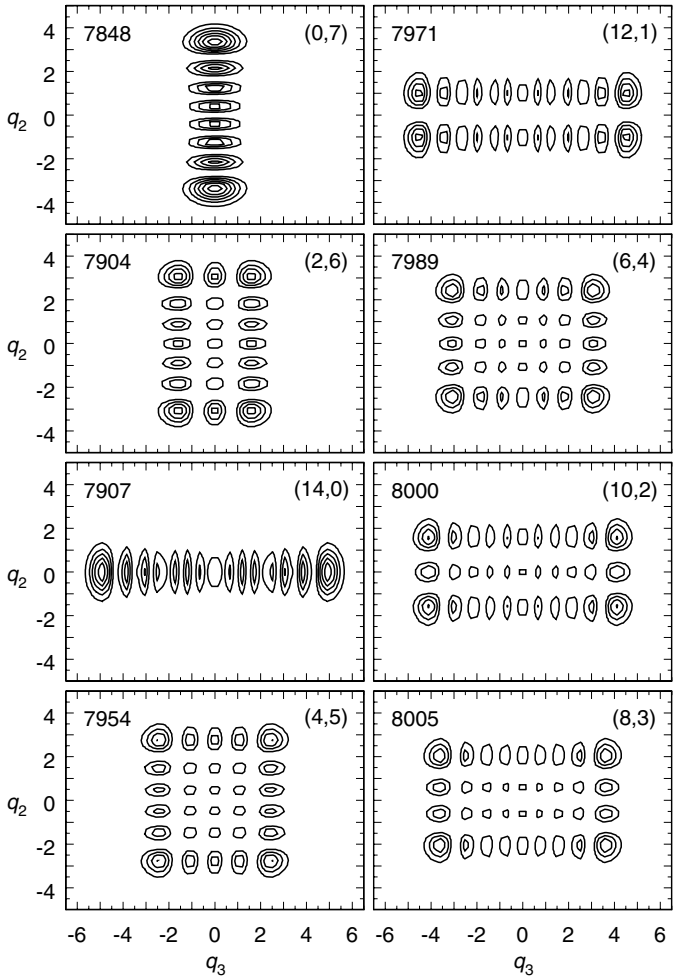

Figure 10. Density probability in the (q_3, q_2) plane for the eight states of "uncoupled" HOBr belonging to polyad $[v_u, P] = [0, 14]$. The Hamiltonian is the Dunham expansion of Eq. (24) with parameters from Table I of Ref. 41. q_3 (OBr stretch) ranges from to -6.5 to 6.5, and q_2 (bend) ranges from -5.0 to 5.0. The energy (in cm^{-1}) above the quantum mechanical ground state, as well as the good quantum numbers $(v_s, v_f) = (v_3, v_2)$, are indicated for each state.

Stated in other words, the polyad folds. The wavefunctions for the eight states belonging to polyad $[v_u, P] = [0, 14]$ of uncoupled HOBr ($H = H_D$) are plotted in Fig. 10 as an example. It is seen that the energy of the states is an increasing function of v_s from $v_s = 0$ to $v_s = 8$, but a decreasing one from $v_s = 8$ to $v_s = 14$. As a result, the polyad appears rather scrambled.

Numerically, this is most easily analyzed by rewriting the Dunham expansion of Eq. (24) in terms of coordinates, which are adapted to the polyad structure of the spectrum. One defines new sets (J_u, ψ_u), (J_P, ψ_P), and (J_0, ψ_0) of conjugate action-angle-like coordinates, according to

$$\begin{aligned}(J_u, \psi_u) &= (I_u, \varphi_u) \\ (J_P, \psi_P) &= (2I_f + I_s, \varphi_s) \\ (J_0, \psi_0) &= (2I_f, \varphi_s - \varphi_f/2)\end{aligned} \tag{29}$$

which are connected to the (I_i, φ_i) $(i = u, f, s)$ ones by a linear canonical transformation. In terms of these new variables, the Hamiltonian of Eqs. (24) and (27) is rewritten in the form

$$\begin{aligned}H_D &= \sum_{i=u,P,0} \Omega_i J_i + \sum_{i,k} X_{ik} J_i J_k + \sum_{i,k,m} Y_{ikm} J_i J_k J_m + \cdots \\ H_F &= \cos(2\psi_0)(I - J_0)\sqrt{J_0}(K + \sum_{i=u,P,0} K_i I_i + \cdots)\end{aligned} \tag{30}$$

with trivial linear relationships between the spectroscopic coefficients of Eqs. (24) and (27) and those of Eq. (30). According to Eq. (25), the quantized values of J_u and J_P associated with the quantum mechanical polyad $[v_u, P]$ are

$$\begin{aligned}J_u &= v_u + \frac{d_u}{2} \\ J_P &= P + d_f + \frac{d_s}{2}\end{aligned} \tag{31}$$

Clearly, polyad $[v_u, P]$ of the uncoupled system $H = H_D$ is folded if equation

$$\frac{\partial H_D}{\partial J_0} = 0 \tag{32}$$

has a real solution $J_0 = J_F$, such that $0 \leq J_0 \leq J_P$ (J_F is a function of J_u and J_P). The result is displayed in Fig. 11 (top) for the states of HOBr with no excitation in the OH stretch ($v_u = 0$). This figure shows the energy of (i) the pure bending trajectory [b], that is, $H_D(J_0 = J_P)$, (ii) the pure stretching trajectory [s], that is, $H_D(J_0 = 0)$, and (iii) the folding point [F], that is, $H_D(J_0 = J_F)$, as a function of P (more precisely, as a function of J_P, but the abscissa scale is converted to artificially continuous values of P according to Eq. (31)). The energies are plotted relative to the energy of [b], because they are all nearly degenerate (because of the resonance condition) and essentially linear functions of P. It is

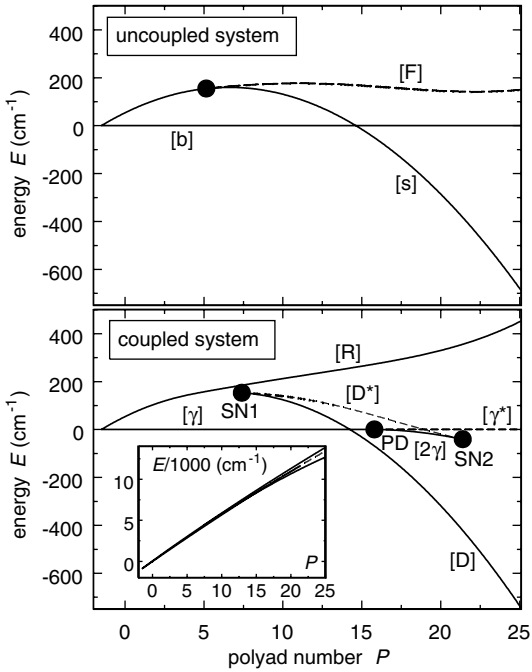

Figure 11. (**Top**) Plot, as a function of the polyad number P, of the energies of the pure bending trajectory [b], the pure stretching trajectory [s], and the folding point [F] for the states of "uncoupled" HOBr with no excitation in the OH stretch ($v_u = v_1 = 0$). The Hamiltonian is the Dunham expansion of Eq. (24) with parameters from Table I of Ref. 41. All energies are plotted relative to the energy of the bending trajectory [b]. (**Bottom**) Plot, as a function of the polyad number P, of the energies of the periodic orbits for the states of HOBr with no excitation in the OH stretch ($v_u = v_1 = 0$). The Hamiltonian is the Fermi resonance model of Eqs. (24) and (27), with parameters from Table I of Ref. 41. The small insert depicts the energies of the PDs relative to the energy of the quantum mechanical ground state. In the main figure, the energies are plotted relative to the energy of the pure bending periodic orbit [γ]. The heavy dots marked SN1, SN2, and PD indicate the two saddle-node and the period-doubling bifurcations, respectively. Stable periodic orbits are indicated by solid lines, while unstable periodic orbits are represented by dashed curves.

seen that polyads are folded above $P \approx 5$ and that the energy of the pure stretching trajectory [s] becomes *smaller* than the energy of the pure bending trajectory [b] at $P \approx 15$. The energies of quantum states always occur between the energies of the two outermost lines, that is, [b] and [s] up to $P = 5$, [b] and [F] from $P = 5$ to $P = 15$, and [s] and [F] above $P = 15$. Therefore, pure stretching states are located at the top of the polyads up to $P = 5$; they then migrate from the top to the bottom of the polyads between $P = 5$ and $P = 15$, and they finally reach the bottom of the polyads above $P = 15$. Conversely, pure bending states

are located at the bottom of the polyads up to $P = 15$ and then migrate inside the polyad. It is also emphasized, as can be checked in Fig. 10, that the states located at the top of the polyads above $P = 5$ are not associated with any particular motion, but are instead just combination states with $P - J_F + 1$ (or the integer closest to this value) nodes along the slow reactive coordinate and $(J_F - 1)/2$ nodes along the fast one. Similar features are observed for HOCl and HCP (in the later case, the CP stretch plays the role of the HOBr bend, and the HCP bend plays that of the OBr stretch).

Let us now consider the dynamics of the coupled system with Hamiltonian $H = H_D + H_F$. J_u and J_P remain good quantum numbers for this Hamiltonian and are quantized according to Eq. (31). It is known that the dynamics of the coupled system is governed by the shape of its stable periodic orbits (POs) in the subspace (p_s, q_s, p_f, q_f) of the normal coordinates involved in the Fermi resonance. The reason for this is that these POs act as the "backbones" (or nodal lines) of the quantum mechanical wavefunctions. Moreover, it is not necessary to consider the POs in the full six-dimensional space as long as the third mode u remains decoupled from s and f. The four-dimensional POs are most easily obtained in terms of the conjugate coordinates of Eq. (29). Indeed, they consist of the line $J_0 = J_P$, plus the fixed points in the (J_0, ψ_0) space. These fixed points satisfy

$$\begin{aligned} \frac{dJ_0}{dt} &= -\frac{\partial H}{\partial \psi_0} = 0 \\ \frac{d\psi_0}{dt} &= \frac{\partial H}{\partial J_0} = \frac{\partial H_D}{\partial J_0} + \frac{\partial H_F}{\partial J_0} = 0 \end{aligned} \tag{33}$$

Note that the first equation has trivial solutions $\psi_0 = 0$ and $\psi_0 = \pi/2$ (sometimes it also has less trivial solutions). Moreover, the derivative of H_F, in the second equation, is always much smaller than the derivative of H_D, except in the neighborhood of $J_0 = 0$, where $\partial H_F/\partial J_0$ goes to infinity, and in the neighbourhood of $J_0 = J_F$ (if the polyad folds), where $\partial H_D/\partial J_0$ goes to zero. Consequently, the coupled system has at least one fixed point with $J_0 \approx 0$ and another one with $J_0 \approx J_F$. Since, as stated above, the $J_0 = J_P$ line also corresponds to a PO in the (p_s, q_s, p_f, q_f) subspace, one can conclude that the coupled system $H = H_D + H_F$ necessarily has periodic orbits, which remain energetically close to the bend [b] and the stretch [s] trajectories, as well as the folding line [F], of the uncoupled system, for all values of P (the coupled system can have additional principal families of POs, see below). One therefore expects the continuation/bifurcation (C/B) diagram [46–48] of the coupled system—that is, the plot of the energies of the POs as a function of the polyad number P, not to be too different from the plot of the energies of [s], [b], and [F] for the uncoupled system. This point can be checked in the case of HOBr by comparing the top and

bottom plots of Fig. 11. At first glance, they are indeed rather similar. There are, however, important discrepancies that will now be discussed.

At low P values ($P \leq 7.4$), the coupled system $H = H_D + H_F$ has two stable POs, called [γ] and [R], which coincide, respectively, with the bend [b] and stretch [s] trajectories of the uncoupled system $H = H_D$. Since both [b] and [γ] satisfy $J_0 = J_P$, their energies coincide through the whole range of P values. In contrast, starting with the P value where the polyad first folds (i.e., $P = 5$), the [R] PO deviates from [s] and follows instead the folding line [F]. In agreement with the conclusions of the preceding paragraph, a stable PO, which remains close to the [s] line, that is which is essentially pure OBr stretch in the case of HOBr, however appears at $P = 7.4$. This PO, which is called [D] in the case of HOBr and HOCl, is born at a saddle-node bifurcation, which is indicated in Fig. 11 (bottom) as a black dot labeled SN1. Saddle-node bifurcations are singularities of the phase space, where a stable and an unstable PO are created simultaneously [45,49–51] (the unstable PO [D*] is indicated with a dashed line in Fig. 11). From the preceding discussion it should be clear that the saddle-node bifurcation SN1 represents the *nonlinear response of the coupled system to the folding of the polyads of the uncoupled system*. Stated in other words, it is the consequence of the coexistence of the Fermi resonance and the strong anharmonicity along the reaction pathway.

Saddle-node bifurcations taking place for the reasons just described have been observed for HOBr [41], HOCl [36,38,39], and HCP [34–36]. For HOBr and HOCl, the stable PO born at the saddle-node bifurcations is called [D] for ''dissociation,'' because this PO stretches along the dissociation pathway and scars OBr- or OCl-stretch quantum mechanical wavefunctions (see Fig. 11e of Ref. 38, Figs. 3b and 3g of Ref. 41, or Section III.B). In the case of HCP, the stable PO born at the bifurcation is better called [I], for ''isomerization,'' because this PO stretches along the isomerization pathway and scars bending quantum mechanical wavefunctions (see Figs. 6b and 6d of Ref. 35 or Figs. 7b and 7d of Ref. 36).

Despite the general resemblance of the energy curves in Fig. 11, the Fermi resonance has a dramatic effect on the wavefunctions, as can be checked by comparing Fig. 10 and Fig. 12, which show the wavefunctions of the eight states of polyad $[v_u, P] = [0, 14]$ for ''uncoupled'' ($H = H_D$) and ''coupled'' ($H = H_D + H_F$) HOBr, respectively. The principal reason for this striking difference is that, in addition to the OH stretch, the uncoupled system has only two degrees of freedom (the bend [b] and the OBr stretch [s]), while the coupled system has three possible types of motion above the saddle-node bifurcation: the bend [γ], an almost pure OBr stretching motion along the [D] PO, and a resonant-type motion along the [R] PO (the pronounced horseshoe shape of this later PO reflects a strong energy transfer between the OBr stretch and the bend). As a consequence, the polyads of the coupled system can no longer be described,

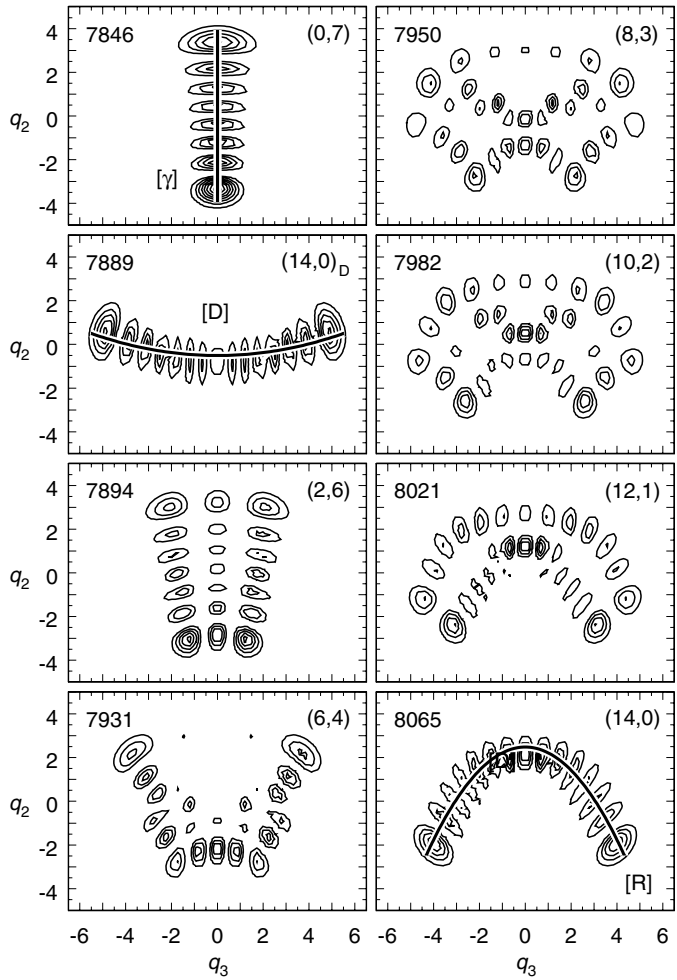

Figure 12. Density probability in the (q_3, q_2) plane for the eight states of "coupled" HOBr belonging to polyad $[v_u, P] = [0, 14]$. The Hamiltonian is the Fermi resonance Hamiltonian of Eqs. (24) and (26) with parameters from Table I of Ref. 41. q_3 (OBr stretch) ranges from to -6.5 to 6.5 and q_2 (bend) from -5.0 to 5.0. The energy (in cm^{-1}) above the quantum mechanical ground state, as well as approximate quantum numbers $(v_s, v_f) = (v_3, v_2)$, are indicated for each state. The three periodic orbits for this polyad, [R], [D], and [γ], are plotted on top of some of the density probabilities.

above $P = 5$, as the folding of regular sequences of states that evolve from a pure bending state (along [b]) to a pure OBr stretching state (along [s]). They are instead better described as sequences of states, which evolve from pure bending states (scared by the [γ] PO) to *resonant-type states* (scared by the [R] PO) and are perturbed, above the saddle-node bifurcation, by the birth and proliferation of OBr-stretching states (scared by the [D] PO).

The most detailed understanding of the evolution of the polyads of the coupled system is obtained by plotting the third action integral of the system as a function of energy E for given values of J_u and J_P. This action integral is expressed as

$$\Im = \Im(E, J_u, J_P) = \frac{1}{2\pi} \int_{\psi_0 \in [0,\pi]} J_0 \mathrm{d}\psi_0 \tag{34}$$

while the corresponding EBK quantization rule reads

$$\Im = n + \tfrac{1}{2} \tag{35}$$

where n is an integer, either positive or negative. Figure 13 provides examples of such plots for polyads $[v_u, P] = [0, 7]$, [0, 14] and [0, 30] of HOBr. The plot for polyad $[v_u, P] = [0, 7]$, which is located below the bifurcation, contains only one branch, which extends from the energy of the [γ] PO to the energy of the [R] PO and is denoted by (a). According to Eq. (35), the semiclassical energies are the values of E at which $\Im$ is half-integer. These values are indicated with filled circles in Fig. 13. It is emphasized that the quantum and semiclassical energies are in very good agreement, with the difference between the two sets of values never exceeding a few cm^{-1}. Branch (a) contains members of the normal progression of states, which evolve from a state aligned along [γ] to a state aligned along [R]. At the SN1 bifurcation, the branch (a) of the action integral splits into two branches (a) and (b). These two branches again support quantum states belonging to the normal progression. However, one state of this progression disappears each time the energy gap between (a) and (b) becomes sufficiently wide to encompass an additional half-integer value of $\Im$. For example, it can be checked in Fig. 12 that the third state of the normal progression (i.e., the state with four nodes along the [R] PO) is missing from the normal progression, because the half-integer value $\Im = -11/2$ lies in the gap between (a) and (b) (see Fig. 13). Still, the number of states in polyad P remains equal to $\mathrm{int}(P/2) + 1$, because each state, which disappears from the normal progression, is replaced by a member of the new progression of ''dissociation'' states, which is supported by branch (c). This third branch also appears at the saddle-node bifurcation SN1 and extends between the energies of the stable [D]

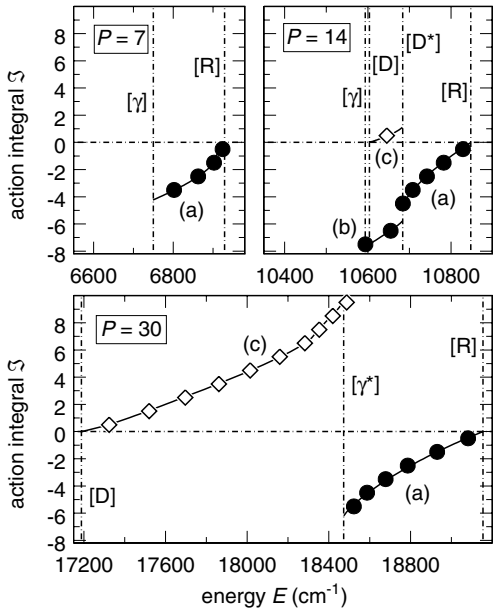

Figure 13. Plot of the action integral ϑ as a function of the absolute energy E for polyads $[v_u, P] = [0, 7]$, $[0, 14]$, and $[0, 30]$ of HOBr. The Hamiltonian is the Fermi resonance Hamiltonian of Eqs. (24) and (27) with parameters from Table I of Ref. 41. The vertical lines indicate the energies of the various periodic orbits. The quantum mechanical states belonging to the normal and the "new" progression are indicated by filled circles and open diamonds, respectively. Note that the horizontal energy scale for polyads $P = 7$ and $P = 14$ is expanded twice compared to $P = 30$.

and unstable [D*] POs born at the bifurcation (see $P = 14$ in Fig. 13). One additional dissociation state appears in the quantum spectrum each time branch (c) widens sufficiently to encompass an additional half-integer value of ϑ. For example, it can be checked in Figs. 12 and 13 that the dissociation state of polyad $[v_u, P] = [0, 14]$ (i.e., the second lowest state) corresponds to $\vartheta = 1/2$ on branch (c). It should be realized that the number of states in polyad P remains equal to $\text{int}(P/2) + 1$, because branches (b) and (c) are parallel in the energy interval where they overlap (the classical frequency is the same for the two branches).

B. Bifurcations at Higher Energies

The saddle-node bifurcations discussed in Section III.A play a crucial role in the dynamics of the molecules investigated, because the stable PO born at the bifurcation follows the reaction pathway over a large energy range. Consequently, the quantum states that are scarred by this PO stretch further and further along the reaction pathway and can be considered as the precursors of the

isomerization and dissociation reactions. Nonetheless, increasing the energy deposited in the vibrational degrees of freedom of these molecules results in additional bifurcations, which are discussed in this section.

Part of these additional bifurcations are reproduced by the Fermi resonance Hamiltonian. For example, the C/B diagram of HOBr in Fig. 11 displays, in addition to SN1, two further bifurcations, PD and SN2, which take place at $P = 15.8$ and $P = 21.4$, respectively. PD is a period-doubling bifurcation, where the bending-type PO [γ], defined by $J_0 = J_P$, becomes unstable, while the double-period daughter PO remains stable. This stable PO with double period, called [2γ], is found in a rather restricted interval of P values, since it disappears at the second saddle-node bifurcation SN2. In contrast with SN1, where the stable [D] and the unstable [D*] POs were *born* simultaneously, SN2 corresponds to a discontinuity of the classical phase space, where the stable [2γ] and the unstable [D*] POs are *destroyed* simultaneously. At SN2, branch (b) disappears from the plot of the action integral $\Im$ as a function of energy E. Therefore, for polyads $[v_u = 0, P]$ where $P \geq 22$, the accessible classical phase space extends between the two remaining stable POs—that is, [D] and [R]—with the unstable PO [$\gamma*$] playing the role of a separatrix between the two kinds of motion (see Fig. 13, $P = 30$). Quantum mechanically, all the members of the new progression are located below [$\gamma*$], on the (c) branch, while all the remaining members of the normal progression are located above [$\gamma*$], on the (a) branch (see Fig. 13, $P = 30$). The question regarding why polyads $[v_u, P]$ with $22 \leq P \leq 35$ look simpler than polyads at lower energies is explained by the following facts: (i) There remain only two stable POs, and therefore two possible backbones for quantum mechanical wavefunctions, and (ii) members of the normal and new progression can no longer be interwoven. This point can be checked in Fig. 5 of Ref. 41, which shows the wavefunctions for the 16 states belonging to polyad $[v_u, P] = [0, 30]$ of HOBr.

To conclude this analysis based on the Fermi resonance Hamiltonian, let us mention that HOCl, behaves very much like HOBr. Indeed, Fig. 10b of Ref. 36 shows that for this molecule the saddle-node bifurcation SN1 takes place at $P = 21.8$, (for $v_u = 0$), the period-doubling bifurcation PD occurs at $P = 24.6$, and the second saddle-node bifurcation SN2 takes place at around $P = 38$, very close to the dissociation threshold. In contrast, the dynamics of HCP is somewhat simpler, in the sense that the first saddle-node bifurcation SN1 is indeed observed at $P = 14.3$, but PD and SN2 do not take place (see Fig. 13 of Ref. 35 or Fig. 10a of Ref. 36).

Most of the bifurcations, which take place in the high-energy regime, are however not reproduced by the Fermi resonance Hamiltonian, essentially because they result from the superposition of the 1:2 Fermi-resonance and higher-order ones. In order to gain information on the dynamics close to the reaction threshold, one therefore has to analyze the dynamics on the PES by

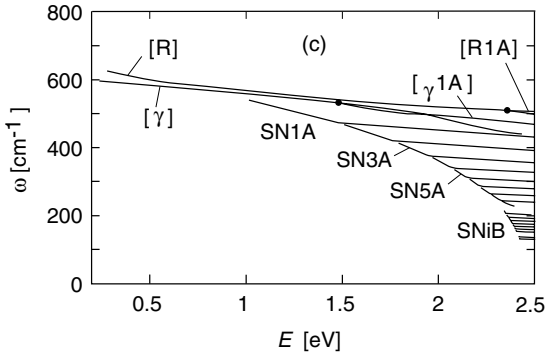

Figure 14. Plot, as a function of the absolute energy E, of the frequencies of the classical periodic orbits belonging to various families. The frequencies of the [γ]-type POs are divided by two, whereas the frequencies of the [R1A] family are multiplied by two. The energy scale is shifted to higher energies by 0.23 eV—that is, the zero-point energy of the OH stretch mode. See the text for more details.

classical mechanics. These studies have been performed for the three molecules already discussed—that is, HOBr [41], HOCl [38], and HCP [35,36]. It turns out that cascades of saddle-node bifurcations seem to be the rule when approaching the reaction threshold. One can distinguish between two different types of cascades, according to the types of motion involved in the bifurcations.

The first type of cascade has been observed for all three of the molecules, HOBr, HOCl, and HCP. Figure 14 shows, for example, the classical C/B diagram obtained for HOBr (see Fig. 5d of Ref. 38 for the classical C/B diagram of HOCl and Fig. 9b of Ref. 35 or Fig. 8b of Ref. 36 for the classical C/B diagram of HCP). Since there is no conserved quantity, except the energy E, classical C/B diagrams necessarily represent the evolution with respect to E of a given property of the POs, like, for example, their frequencies, as in Fig. 14. In this diagram it is seen that the SN1 bifurcation and the smooth [D] curve of the Fermi resonance model in Fig. 11 are replaced by a series of SNiA bifurcations and corresponding [SNiA] curves $(i = 1, 2, 3, \ldots)$, which all exhibit the same pattern, namely, a short segment with a relatively large anharmonicity and a second segment for which the slope is very small. The nearly flat segment of each curve is probably due to a resonance between motion along the successive [SNiA] POs and the OH stretch [41]. Roughly speaking, the [D] line of the Fermi resonance model in Fig. 11 is just the smooth interpolation between successive segments with large anharmonicities. Since the POs that scar dissociating quantum states (i.e., states stretching along the dissociation pathway) all belong to the more anharmonic segments of the [SNiA] curves, the more harmonic segments of the C/B diagram in Fig. 14 are not essential to

understand the features of the quantum mechanical spectrum: The [D] line joining the more anharmonic segments contains all the important information.

The successive [SN*i*A] POs follow closely the dissociation pathway up to [SN7A], while they acquire a pronounced S-type shape and ultimately avoid the dissociation pathway for $i \geq 8$, as is illustrated in Figs. 15b and 15f. This happens in the same energy range where a second cascade of saddle-node bifurcations SN*i*B and related stable POs [SN*i*B] are first observed (see Fig. 14). This is not by chance. What one observes here is indeed just the repetition—with a different ratio of the classical frequencies—of the scheme, which gives rise to the SN*i*A family of saddle-node bifurcations at lower energies. More precisely, in Section III.A it was seen that the 1:2 Fermi resonance between motions along [R] (OBr stretch) and [γ] (bend) is responsible for (i) the pronounced U shape that [R] acquires with increasing energies (see Fig. 15c), and (ii) the occurrence of the saddle-node bifurcations SN1 (or SN*i*A), where a new motion along [D] (or [SN*i*A]) is born, which follows the reaction pathway (see Fig. 15b). Because of the large anharmonicity along the reaction pathway, the frequency of the motion along [SN*i*A] however steadily decreases with increasing energies, so that at a certain point a 1:3 resonance with the motion along the bending type PO [γ] is established. As happened for the 1:2 resonance between [R] and [γ], the 1:3 resonance between [SN*i*A] and [γ] is responsible for (i) the pronounced S-shape that [SN*i*A] aquires above SN7A (see Fig. 15f) and (ii) the occurrence of a second family of saddle-node bifurcations, SN*i*B, where a new motion along the [SN*i*B] POs is born, which follows the reaction pathway (see Fig. 15g). Note that because of resonances with the OH-stretch degree of freedom, each [SN*i*B] curve has the same pattern as the [SN*i*A] ones, namely, a short segment with a relatively large anharmonicity and a second segment for which the slope is very small.

From the classical point of view, the high-energy bifurcation pattern of HOBr thus consists of two nested cascades of saddle-node bifurcations. The principal cascade, R $\rightarrow$ SN*i*A $\rightarrow$ SN*i*B $\rightarrow$ . . ., results from the successive 1:2, 1:3, and so on, resonances between the OBr stretch and the bend. Each member of the principal family, in turn, consists of a cascade of bifurcations, SN1A $\rightarrow$ SN2A $\rightarrow$ SN3A $\rightarrow$ . . . and SN1B $\rightarrow$ SN2B $\rightarrow$ SN3B $\rightarrow$ . . ., because of resonances between the OBr stretch and the OH stretch. From the quantum mechanical point of view, one observes, above the onset of the 1:3 resonance, states that are scared by the three possible ''stretching''-type POs, that is, [R] (U-shaped wavefunctions), [SN*i*A] (S-shaped wavefunctions), and [SN*i*B] (wavefunctions stretching along the dissociation pathway).

Two points are worth noting before concluding. First, the ab initio PES for HOBr [40,41] is the only realistic molecular model, for which such a subtle pattern of bifurcations has been detected so far: For HOCl [38] and HCP [35], the SN*i*B family of saddle-node bifurcations could not be found. Moreover, both

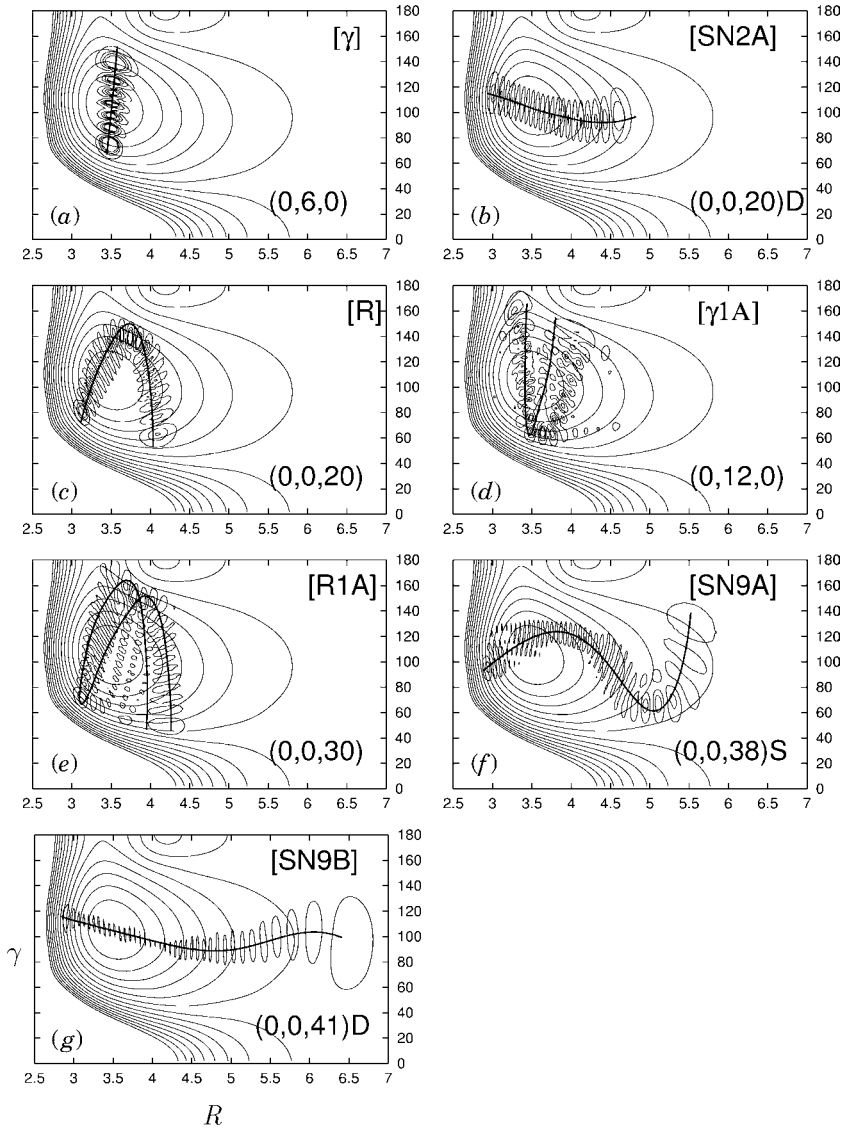

Figure 15. Contour plots of wavefunctions for different types of quantum mechanical states as functions of R and γ. The OH-stretch coordinate r is integrated over. The solid lines represent corresponding classical periodic orbits calculated at comparable energies.

HOCl and HOBr display a couple of additional bifurcations, which were not discussed here because they are not directly related to the dissociation reaction. The interested reader is referred to Refs. 38 and 41 for more details.

IV. SUMMARY

The character of vibrational states of a polyatomic molecule is expected to drastically change with increasing internal energy. This has been demonstrated in this review for several triatomic molecules: HCN, HCP, HOCl, and HOBr. For the first two examples, increasing the energy gradually ''drives'' the molecule toward the isomerization barrier, while for the other two examples it pushes the molecule toward the dissociation channel. In both cases, the types of vibrational motion are very different from the motion at low energies. Exact quantum mechanical, classical, and semiclassical methods have been utilized to discuss this development from low to high energies.

For HCN, a molecule with no resonance between the three fundamental frequencies, we have demonstrated that a sequence of canonical transformations leads to a nearly separable Hamiltonian, the diagonalization of which quantitatively predicts the eigenenergies. Moreover, this approximate Hamiltonian is well suited to describe the localized as well as part of the delocalized states of the system and leads to a consistent assignment of most of the states. Nevertheless, the remaining couplings, which are ignored in the transformed Hamiltonian, lead to interesting delocalized states, which require a full quantum mechanical description. These states, which have different stretching excitations in the HCN and the CNH wells, have been termed ''nonadiabatically delocalized'' states, because they are due to couplings between states belonging to different adiabatic channels.

The other three molecules are different in that they show already at low energies a 1:2 Fermi resonance between the reaction (isomerization or dissociation) coordinate and another coordinate. This resonance, together with the polyad folding due to the strong anharmonicity in the isomerization or dissociation mode, leads to saddle-node bifurcations, at which new types of states come into existence and members of progressions characteristic for the lower-energy regime disappear. The new family of states advances the molecule toward the isomerization barrier or the dissociation channel. The existence of saddle-node bifurcations usually makes the spectrum of eigenenergies and the organization in terms of polyads quite complex. However, we have also shown how a detailed analysis of the structure of the classical phase space in terms of periodic orbits and continuation/bifurcation diagrams can be used to understand the quantum mechanical spectrum. Saddle-node bifurcations seem to be characteristic features of many molecules. However, up to now an experimental example has only been observed for HCP [35].

A detailed understanding of the intramolecular motion of highly excited molecules is important for understanding the dissociation dynamics, because the sequences of bound states just below the dissociation threshold continue as resonances to energies above the threshold [52]. Whether the dynamics around the threshold is chaotic or whether the eigenstates show characteristic features will have consequences for the lifetime of the excited complex and therefore on the dissociation rate. The same is true, of course, also for the inverse process—that is, the stabilization of complexes in collisions with gas atoms.

References

1. M. Joyeux and D. Sugny, *Can. J. Phys.* **80**, 1459 (2002).
2. D. Sugny, M. Joyeux, and E. L. Sibert III, *J. Chem. Phys.* **113**, 7165 (2000).
3. D. Sugny and M. Joyeux, *J. Chem. Phys.* **112**, 31 (2000).
4. K. Efstathiou, M. Joyeux, and D.A. Sadovskii, *Phys. Rev. A*, **69**, 032504 (2004).
5. M. Joyeux, D. A. Sadovskii, and J. Tennyson, *Chem. Phys. Lett.* **382**, 439 (2003).
6. J. Robert and M. Joyeux, *J. Chem. Phys.* **119**, 8761 (2003).
7. T. van Mourik, G. J. Harris, O. L. Polyansky, J. Tennyson, A. G. Csaszar, and P. J. Knowles, *J. Chem. Phys.* **115**, 3706 (2001).
8. G. J. Harris, O. L. Polyansky, and J. Tennyson, *Spectrochim. Acta A* **58**, 673 (2002).
9. E. B. Wilson, J. C. Decius, and P. C. Cross, *Molecular Vibrations*, Dover, New York, 1955, Chapter 4.
10. J. H. Van Vleck, *Phys. Rev.* **33**, 467 (1929).
11. O. M. Jordahl, *Phys. Rev.* **45**, 87 (1934).
12. E. C. Kemble, *The Molecular Principles of Quantum Mechanics*, McGraw-Hill, New York, 1937, Section 48c.
13. E. L. Sibert III, *J. Chem. Phys.* **88**, 4378 (1988).
14. D. Lessen, J. S. Baskin, C. M. Jones, T. He, and E. Carrasquillo-Molina, *J. Chem. Phys. A* **107**, 5697 (2003).
15. I. Shavitt and L. T. Redmon, *J. Chem. Phys.* **73**, 5711 (1980).
16. A. J Dragt and J. M. Finn, *J. Math. Phys.* **17**, 2215 (1976).
17. A. J Dragt and J. M. Finn, *J. Math. Phys.* **20**, 2649 (1979).
18. A. J Dragt and E. Forest, *J. Math. Phys.* **24**, 2734 (1983).
19. G. D. Birkhoff, *Dynamical Systems*, Vol. 9, AMS colloquium, AMS, New York, 1966.
20. F. G. Gustavson, *Astron. J.* **71**, 670 (1966).
21. R. T. Swimm and J. B. Delos, *J. Chem. Phys.* **71**, 1706 (1979).
22. A. M. Smith, S. L. Coy, W. Klemperer, and K. K. Lehmann, *J. Mol. Spectrosc.* **134**, 134 (1989).
23. X. Yang, C. A. Rogaski, and A. M. Wodtke, *J. Opt. Soc. Am. B* **7**, 1835 (1990).
24. D. M. Jonas, X.Yang, and A. M. Wodtke, *J. Chem. Phys.* **97**, 2284 (1992).
25. S. C. Farantos, J. M. Gomez Llorente, O. Hahn, and H. S. Taylor, *J. Chem. Phys.* **93**, 76 (1990).
26. D. Romanini, and K. K. Lehmann, *J. Chem. Phys.* **102**, 633 (1995).
27. A. Maki, W. Quapp, S. Klee, G. C. Mellau, and S. Albert, *J. Mol. Spectrosc.* **180**, 323 (1996).
28. F. J. Northrup, G. A. Bethardy, and R. G. Macdonald, *J. Mol. Spectrosc.* **186**, 349 (1997).

29. J. M. Bowman, B. Gazdy, J. A. Bentley, T. K. Lee, and C. E. Dateo, *J. Chem. Phys.* **99**, 308 (1993).
30. Z. Bacic, R. M. Whitnell, D. Brown, and J. C. Light, *Comput. Phys. Comm.* **51**, 35 (1988).
31. A. J. Dobbyn, M. Stumpf, H.-M. Keller, and R. Schinke, *J. Chem. Phys.* **103**, 9947 (1995).
32. D. J. Nesbitt and R. W. Field, *J. Phys. Chem.* **100**, 12735 (1996).
33. C. Beck, R. Schinke, and J. Koput, *J. Chem. Phys.* **112**, 8446 (2000).
34. M. Joyeux, D. Sugny, V. Tyng, M. E. Kellman, H. Ishikawa, R. W. Field, C. Beck, and R. Schinke, *J. Chem. Phys.* **112**, 4162 (2000).
35. H. Ishikawa, R. W. Field, S. C. Farantos, M. Joyeux, J. Koput, C. Beck, and R. Schinke, *Annu. Rev. Phys. Chem.* **50**, 443 (1999).
36. M. Joyeux, S. C. Farantos, and R. Schinke, *J. Phys. Chem. A* **106**, 5407 (2002).
37. S. Skokov, K. A. Peterson, and J. M. Bowman, *J. Chem. Phys.* **109**, 2662 (1998).
38. J. Weiss, J. Hauschildt, S. Yu. Grebenshchikov, R. Düren, R. Schinke, J. Koput, S. Stamatiadis, and S. C. Farantos, *J. Chem. Phys.* **112**, 77 (2000).
39. R. Jost, M. Joyeux, S. Skokov, and J. M. Bowman, *J. Chem. Phys.* **111**, 6807 (1999).
40. K. A. Peterson, *J. Chem. Phys.* **113**, 4598 (2000).
41. T. Azzam, R. Schinke, S. C. Farantos, M. Joyeux, and K. A. Peterson, *J. Chem. Phys.* **118**, 9643 (2003).
42. A. Einstein, *Verh. Dtsch. Phys. Ges.* **19**, 82 (1917).
43. L. Brillouin, *J. Phys.* **7**, 353 (1926).
44. J. Keller, *Ann. Phys.* **4**, 180 (1958).
45. M. Tabor, *Chaos and Integrability in Nonlinear Dynamics*, John Wiley & Sons, New York, 1989.
46. S. Wiggins, *Global Bifurcations and Chaos*, Springer, Berlin, 1988.
47. S. Wiggins, *Introduction to applied nonlinear dynamical systems and chaos*, Springer, New York, 1990.
48. S. C. Farantos, *Int. Rev. Phys. Chem.* **15**, 345 (1996).
49. P. Berge, Y. Pomeau, and C. Vidal, *Order Within Chaos*, John Wiley & Sons, New York, 1984.
50. M. C. Gutzwiller, *Chaos in Classical and Quantum Mechanics*, Springer, New York, 1990.
51. J. Guckenheimer and P. Holmes, *Nonlinear Oscillations, Dynamical Systems, and Bifurcations of Vector Fields*, Springer, Berlin, 1983.
52. S. Yu. Grebenshchikov, R. Schinke, and W. L. Hase, *State-Specific Dynamics of Unimolecular Dissociation*, in N. J. B. Green, ed., *Comprehensive Chemical Kinetics*, Vol. 39, Part I, Elsevier, Amsterdam, 2003.

CHAPTER 6

CLASSICAL COULOMB THREE-BODY PROBLEM

MITSUSADA M. SANO

Graduate School of Human and Environmental Studies, Kyoto University, Sakyo, Kyoto, 606-8501, Japan

CONTENTS

I. Introduction
II. *N*-Body Problem in Celestial Mechanics
III. Coulomb Three-Body Problem: The 2D Case with Zero Angular Momentum
IV. The Collinear eZe Case: Mass Ratio Effect
  A. Triple Collision Manifold
  B. Triple Collision Orbits
  C. Experimental Manifestation
V. Free-Fall Problem
VI. Summary
Acknowledgments
References

I. INTRODUCTION

The three-body problem appears in various physical and chemical systems—that is, celestial systems (e.g., the sun, the earth, and the moon), atomic systems (e.g., two electrons and one nucleus), and molecular systems (e.g., $D + H_2 \rightarrow DH + H$ reaction). Due to historical reasons, the three-body problem in celestial mechanics is the oldest. In order for our ancestors to make the calender, they observed the motion of the sun and the moon for agricultural and fishery purposes and also for daily life. After Copernicus, they knew that the earth itself moves. But they did not know the law of the motion of stars and planets. By

Geometric Structures of Phase Space in Multidimensional Chaos: A Special Volume of Advances in Chemical Physics, Part A, Volume 130, edited by M. Toda, T Komatsuzaki, T. Konishi, R.S. Berry, and S.A. Rice. Series editor Stuart A. Rice.
ISBN 0-471-70527-6

Newton's work, they had the law of the motion of these three bodies—that is, the equations of motion. The three-body problem of sun–earth–moon became important in the sense that they could actually predict the motion of these three bodies by using the equations of motion formally. For the sun–earth–moon problem, see [1]. Although many mathematicians and astronomers contributed to this problem, it was not solved analytically. Finally Poincaré has shown that for three-body problem, one can not construct general solutions [2]. What Poincaré found in final stage of his study is what we now call "chaos." If we use mathematical terminology of the present days, he found the existence of the homoclinic or heteroclinic entanglement of the stable and unstable manifolds for fix points on the Poincaré section. Entering the twentieth century, the innovation of computers assisted physicists and astronomers to investigate various N-body problems. Following Poincaré, mathematicians also continued to contribute to this problem (see, for instance, Ref. 3). Some important mathematical developments will be reviewed in the next section. However, our understanding even about three-body problem is far from complete. The investigation is still going on.

In the beginning of the twentieth century, a mechanics in small world was constructed, namely quantum mechanics. In the early stage of making quantum mechanics, Bohr found a rule to obtain some part of the energy spectrum of a hydrogen atom (i.e., the two-body problem: one electron and one nucleus) [4]. He showed that the action integral of classical periodic orbit of electron should be integer multiple of the Planck constant h. Now this rule is called the Bohr–Sommerfeld (BS) quantization condition. With this success, many physicists tried to apply the BS-quantization condition to helium atom (i.e., the three-body problem: two electron and nucleus). But they failed. Einstein extended the BS quantization condition to the higher-dimensional case (this new quantization condition is now called the Einstein–Brillouin–Keller (EBK) quantization condition) and warned that in the situation that Poincaré found, namely the three-body problem, the EBK-quantization condition cannot work [5]. By the works of Heisenberg, Schrödinger, and Dirac, a complete form of quantum mechanics was constructed. Due to great success of quantum mechanics, the problem on the spectrum of helium atom pointed out by Einstein was forgotten by almost all physicists. But some physicists still considered this problem—for example, Langmuir [6], van Vleck [7], Heisenberg and Sommerfeld (see the corresponding section in Ref. 8).

About 50 years after Einstein, Gutzwiller applied the path integral method with a semiclassical approximation and succeeded to derive an approximate quantization condition for the system that has fully chaotic classical counterpart. His formula expresses the density of states in terms of unstable periodic orbits. It is now called the Gutzwiller trace formula [9,10]. In the last two decades, several physicists tested the Gutzwiiler trace formula for various

systems. As an application to the atomic three-body problem, semiclassical quantization was carried out for the hydrogen negative ion [11] and the helium atom [12] in the collinear eZe configuration.[1] In these works, it was revealed that their classical dynamics in the collinear eZe configuration is fully chaotic, probably hyperbolic, and that the collinear eZe configuration gives the eigenenergies of $n\mathbf{s}m\mathbf{s}$ $(n, m \geq 1,\ n \leq m)$ with reasonable accuracy. For the former result, we do not know why these systems exhibit full chaoticity. The first aim of this chapter is to elucidate mechanism of strong chaoticity in two-electron atoms and ions in the collinear eZe configuration. The latter result is in strong contrast to the result of the CI calculation in quantum chemistry. This apparently astonishing result implies that the semiclassical quantization using the Gutzwiller trace formula precisely incorporates the correlations among two electrons, although the energy levels obtained in their work are limited to $n\mathbf{s}m\mathbf{s}$ $(n, m \geq 1,\ n \leq m)$. For the correlations of two electrons in quantum mechanics, see Ref. 13. In addition, for helium atom, the intermittency in its classical dynamics is semiclassically quantized to yield the quantum defects for $n\mathbf{s}m\mathbf{s}$ $(n, m \geq 1,\ n \leq m)$ with reasonable accuracy [14]. The regularity in chaos—that is, intermittency, gives the regularity in the quantum defects. For classical dynamics and the quantum aspect of two-electron atoms, mainly helium atom, see Ref. 8 for bound states and Ref. 15 for scattering states.

The first systematic study on classical two-electron atoms and ions was done by Wannier [16]. He calculated the ionization rate for two-electron atom and ions near $E = 0$ but $E > 0$. His result is $\sigma(E) \sim E^{1.12689}$ for $Z = 1(\mathrm{H}^-)$. This threshold law was also calculated in quantum mechanical and semiclassical treatments. The experimental result agrees with the classical result quite well near $E = 0$ but $E > 0$, but it deviates from the classical result when E becomes large (see Figs. 8 and 9 in Ref. 15). The classical dynamics of two-electron atoms and ions was mainly investigated for some restricted configurations—that is, the collinear eZe configuration, the collinear eeZ configuration, and the Wannier ridge configuration [17]. It is known that the collinear eZe configuration is very unstable, that the collinear eeZ configuration is unstable for $Z = 1$, but relatively stable for $Z \geq 2$, and that the Wannier ridge configuration is relatively stable. The Wannier ridge configuration includes the Langmuir orbit (torus). The EBK quantization for the Langmuir orbit for helium gives some energy levels [6]. Recently the Langmuir problem is extended to the N electrons plus nucleus system [18].In addition, the dynamics of the eeZ configuration has proved that it is nonintegrable, by using the Ziglin analysis [19]. These restricted configurations mentioned above have zero

[1] "eZe" stands for the order of electron(e)–nucleus(Z)–electron(e) on a line.

angular momentum. In the two-dimensional (2D) case as a more general situation, a few kinds of tori were found. One is planetary orbits that have zero angular momentum [20]. The others are tori with nonzero angular momentum [21].

The above investigations on classical dynamics of two-electron systems is mainly based on numerical findings. We need some firm analytical tools to explore the fine geometrical structure in the phase space. For this purpose, we focus on some similarities between the gravitational systems and the Coulomb systems—that is, their singular nature. In this direction, the McGehee's blow-up technique [22] was applied to the two-electron system having a nucleus with infinite mass [23].[2] The second aim of this chapter is to apply the McGehee's blow-up technique to our Coulomb systems—that is, the 2D case having nucleus with infinite mass in Section III and the collinear eZe configuration with finite masses in Section IV.

The organization of this chapter is as follows. In Section II, we review the results on N-body problem, developed by several mathematicians in celestial mechanics. One of them, namely the McGehee's blow-up technique, will be used in the later sections. In Section III, our attention is turned to the Coulomb three-body problem. We treat the 2D system with zero total angular momentum, that one of three particles has infinite mass. A set of regularized equations of motion and the triple collision manifold (TCM) are derived by using the hyperspherical coordinates. It is found that only two equilibrium points for the total flow exist. These two equilibrium points are on the TCM. This finding implies that triple collisions occur, asymptotically approaching the collinear eZe configuration. Thus only homothetic solution of collinear eZe type exists. The stability analysis for these two equilibrium points is done. The collinear eZe configuration and the Wannier ridge configuration are mutually orthogonal in the phase space. In these configurations, the stable and unstable manifold of two equilibrium points are numerically calculated. Behavior of the whole dynamics in this system is still unknown. But some aspects were elucidated by a participant of this conference and his colleagues [24]. In Section IV, the system of three particles with finite masses in the collinear eZe configuration is considered. In particular, a series of atoms and ions (i.e., H^-, He, Li^+, Be^{2+}, etc.), in the collinear eZe configuration are extensively investigated. The main result in this section is the following conjecture: **Thanks to a large mass ratio between nucleus and electron of these atom and ions, the classical dynamics of these atoms and ions in the collinear eZe configuration is probably hyperbolic**. For the case of small mass ratio, the dynamics of such systems in

[2]According to Ref. 15, the first application of the McGehee's method to the Coulomb systems was, probably, done by B. Eckhardt in his habilitation thesis.

the collinear eZe configuration is nonhyperbolic—that is, there exist tori. The candidates for such systems are proton–antiproton–proton(p–$\overline{p}$–p), positronium negative ion(e–$\overline{e}$–e, sometimes denoted by Pr−), and H_2^+ in the collinear ZeZ configuration. Experimental manifestation of this finding is suggested. In Section V, in order to find tori in the 2D case with zero angular momentum (all masses are finite), the free-fall problem is considered. The free-fall problem treats the initial conditions with zero velocities. Thanks to the scaling property of the Coulomb systems, the initial condition space is bounded and compact. The results for H^-, He, and Pr− are presented. In Section VI, the results of this chapter and future perspective are summarized.

II. *N*-BODY PROBLEM IN CELESTIAL MECHANICS

In this section, mathematical results in celestial mechanics is reviewed. If the reader need a complete historical review, see Ref. 25.[3] One of these results—that is, the McGehee's blow-up technique—will be used in Sections III and IV.

In celestial mechanics, our attention focuses on the behavior of planets and/or comets around the sun, which is described by the following Hamiltonian:

$$H = \sum_{i=1}^{N} \frac{\mathbf{p}_i^2}{2m_i} - \sum_{i<j} \frac{Gm_i m_j}{|\mathbf{q}_i - \mathbf{q}_j|} \tag{1}$$

If we consider the sun and one planet, namely a two-body case, the equations of motion for this case is solvable. We have the famous Kepler motion.It is well known that there are four types of orbits, namely the circle ($\epsilon = 0$), the elliptic curve ($0 < \epsilon < 1$), the parabolic curve ($\epsilon = 1$), and the hyperbolic curve ($\epsilon > 1$), where ϵ is the eccentricity.

If one more planet or comet is added to this system, the system becomes three-body. For instance, consider the system having the sun, the earth, and the moon. To investigate this system was indispensable for our ancestors, because it was directly related to the calender. The calender is necessary for agriculture and fishery and also for daily life. By such demand, many astronomers and mathematicians investigated the three-body problem. In 1885–1986, it was announced in *Acta Mathematica* that the King Oscar prize may be awarded for a person who has solved general solutions for N-body problem. Many mathematicians struggled with this problem. Many articles were written after this announcement. Finally, Poincaré received this prize in 1889. If shortly summarized, his answer is that the three-body problem is generally not solvable

[3]Reference 25 is written for general readers. But the list of references is substantial and useful for graduate students and researchers who are interested in mathmematical development on this subject.

or generally hard to solve it. He used qualitative and geometrical methods.Then he found the homoclinic or heteroclinic tangle of the stable manifold and unstable manifolds of the fixed points on the Poincaré section. Nowadays we know that what he found was what we now call ''chaos.'' His results were collected in Ref. 2.

After Poincaré, Painlevé considered singularities of solutions of differential equations in N-body problem. He found that if singularities exist, there are two types of singularities in N-body problem. The first type of singularities is collisional singularities. An obvious example is binary collisions. Consider the Kepler motion, namely, the two-body problem. As a limiting case of three types of orbits—namely, the elliptic, the parabolic, and the hyperbolic curves—there exists a collisional orbit. Two planets are on a line. One planet collides with the other planet successively. The elastic bounces continue endlessly.[4] If we consider three-body problem, there exist triple collisions. As we will see later, binary collisions and triple collisions also exist in Coulomb system. The second type of singularities is noncollisional singularities. Painlevé has shown that in the three-body problem there exist only collisional singularities. Thus Painlevé conjectured that noncollisional singularities may exist in the N-body problem ($N \geq 4$).

A first attack to Painlevé's conjecture was done by von Zeipel [26]. von Zeipel considered how the ''size'' of an N-body system evolves in time. He chose the moment of inertia $I = \sum_i m_i |\mathbf{q}_i|^2$ as the size of the N-body system. He has shown that a necessary condition for a solution having noncollisional singularity is that the motion of the system becomes unbounded in finite time.

Next for the three-body problem, McGehee has elucidated the behavior near triple collisions in the collinear configuration [22]. If three bodies get closer, the escaping one attains a higher velocity. This property is very important for Painlevé's conjecture, since high velocity can be gained by encountering near-triple collisions, which is needed to noncollisional singularities. He focused on the ''size'' of the three-body system, namely the moment of inertia I as done by von Zeipel. He blew up the whole system by scaling the size ''$r = \sqrt{I}$'' of the system. After that, he removed singularities of binary collisions. For the equations of motion and the energy relation obtained, setting $r = 0$ (and/or $E = 0$), he obtained the energy surface with $r = 0$, namely a set of points that exhibit just triple collisions in the phase space. This energy surface is called the triple collision manifold (TCM). Thanks to the TCM and the regularized equations of motion that he derived, he has shown how the orbits near triple collisions behave. His method was immediately applied to the isosceles

[4]The elastic bounce cannot occure in actual astronomical phenomena. A nonelastic collision must occure. For instance, remember the comet Shoemaker–Levy collision with Jupiter in 1994.

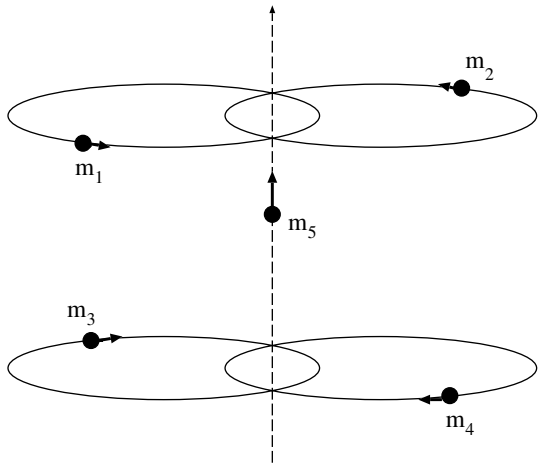

Figure 1. Xia's example of a noncollisional singularity.

configuration for the gravitational three-body problem by Devaney [27], which corresponds to the Wannier ridge configuration for the Coulomb three-body problem.

Finally using the McGehee's blow-up technique to five-body system, Xia proved Painlevé conjecture [28] (for review, see Ref. 25). Precisely he showed an example of noncollisional singularity. For the collinear case, the bodies necessarily exhibit binary collisions. Therefore, five bodies should be in higher-dimensional space. He considered two sets of binary bodies and one body (say m_5) moving between two sets of binary bodies (see Fig. 1). The body m_5 approaches one of binary bodies. Then encountering orbits near triple collision, the body m_5 is going back to other binary bodies gaining their velocities and encountering orbits near another triple collision. In this process, two binary bodies are moving away from each other. In this way, the body m_5 is endlessly going back and forth between two of binary bodies. In this process, the time interval between triple collisions becomes shorter and shorter exponentially (like $T_n \simeq C \exp(-nA)$) even though two of binary bodies are going away. The body m_5 is accelerated very rapidly. Thus if we sum up all time intervals where the sum is like a geometrical series, then we find that the total time is finite. Therefore in finite time, the five-body system in this configuration becomes unbounded without collisions.

The McGehee's blow-up technique is essential to investigate the detailed structure of N-body problem in celestial mechanics. If the particles have a different sign of charge, such a Coulomb system has the same type of

singularities—that is, binary collisions and triple collisions. Thus the McGehee's blow-up method is applicable to the Coulomb systems. It is natural that someone have a question, "Are there noncollisional singularities in Coulomb systems?" The answer is probably "No," because the repulsive interaction between the same charged particles prevents the Coulomb systems from having noncollisional singularities. This may be easily guessed from the result on the triple collision manifold for the Coulomb system (i.e., the difference between the gravitational system and the Coulomb system) in the next section.

In the next two sections, we shall apply the McGehee's method to our Coulomb three-body problem.

III. COULOMB THREE-BODY PROBLEM: THE 2D CASE WITH ZERO ANGULAR MOMENTUM

In this section we derive a set of regularized equations of motion and a triple collision manifold (TCM) for the Coulomb three-body system. Three particles (electron, nucleus, and electron) have masses $m_1 = m_e$, $m_2 = m_n$ and $m_3 = m_e$ and charges $-e$, Ze, and $-e$. We consider the Coulomb three-body system whose Hamiltonian is

$$H = \sum_{i=1}^{3} \frac{\mathbf{p}_i^2}{2m_i} - \frac{Ze^2}{|\mathbf{q}_1 - \mathbf{q}_2|} - \frac{Ze^2}{|\mathbf{q}_2 - \mathbf{q}_3|} + \frac{e^2}{|\mathbf{q}_1 - \mathbf{q}_3|} \tag{2}$$

After certain scaling, we have the Hamiltonian in a dimensionless form

$$H = \frac{\mathbf{p}_1^2}{2} + \frac{\mathbf{p}_2^2}{2\xi} + \frac{\mathbf{p}_3^2}{2} - \frac{1}{|\mathbf{q}_1 - \mathbf{q}_2|} - \frac{1}{|\mathbf{q}_2 - \mathbf{q}_3|} + \frac{1}{Z|\mathbf{q}_1 - \mathbf{q}_3|} \tag{3}$$

where $\xi = m_n/m_e$. There is an important property.

Property 1. Triple collision orbits have zero angular momentum.

Thus if we consider the case that the orbit exhibits triple collision, the system should have zero angular momentum. In addition, if the system has zero angular momentum, the orbit is confined in the 2D plane. So we have to consider the 2D case with zero angular momentum. There are three distinct configurations:

1. *The Collinear eZe Configuration*. In this configuration, three particles are arranged in the order of electron(e)–nucleus(Z)–electron(e) on a line.
2. *The Collinear eeZ Configuration*. In this configuration, three particles are arranged in the order of electron(e)–electron(e)–nucleus(Z) on a line.

3. *The Wannier Ridge Configuration*. In this configuration, the distance r_1 between electron 1 and nucleus is equal to the distance r_2 between electron 2 and nucleus. In this case, three particles forms isosceles.

Our system consists of one nucleus and two electrons.We set the mass of the nucleus to be infinite in this section, namely $\xi = \infty$. In the following section, we shall consider the case that all masses are finite for the collinear eZe configuration. The Hamiltonian in a dimensionless form in the hyperspherical coordinates is given by

$$H = \tfrac{1}{2}\left\{p_r^2 + \frac{4}{r^2}p_\chi^2 + \frac{4}{r^2\sin^2(\chi)}(p_\alpha^2 + L'^2) + \frac{2}{r^2}\left(\frac{1}{\cos^2(\frac{1}{2}\chi)} - \frac{1}{\sin^2(\frac{1}{2}\chi)}\right)p_\alpha L'\right\}$$
$$- \frac{1}{r}\left(\frac{1}{\cos(\frac{1}{2}\chi)} + \frac{1}{\sin(\frac{1}{2}\chi)} - \frac{1}{Z(1-\sin(\chi)\cos(\alpha))^{1/2}}\right) \tag{4}$$

where $r_1 = r\cos(\frac{1}{2}\chi)$ (or $r_2 = r\sin(\frac{1}{2}\chi)$) represents the distances between nucleus and electron 1 (or 2). $r = (r_1^2 + r_2^2)^{\frac{1}{2}}$ is the hyperradius. $\chi = 2\arctan(r_2/r_1)$ is the hyperangle that is valued as $0 \le \chi \le \pi$. α is the angle between two vectors that start from the nucleus to the electron 1 and from the nucleus to the electron 2. Note that $L = 2L'$ stands for the total angular momentum. Since we are interested in the case $L = 0$ by setting $L = 0$ the Hamiltonian is reduced to

$$H = \tfrac{1}{2}\left\{p_r^2 + \frac{4}{r^2}p_\chi^2 + \frac{4p_\alpha^2}{r^2\sin^2(\chi)}\right\}$$
$$- \frac{1}{r}\left\{\frac{1}{\cos(\frac{1}{2}\chi)} + \frac{1}{\sin(\frac{1}{2}\chi)} - \frac{1}{Z(1-\sin(\chi)\cos(\alpha))^{1/2}}\right\}$$
$$= T + \frac{1}{r}V(\chi,\alpha) \tag{5}$$

where

$$V(\chi,\alpha) = -\frac{1}{\cos(\frac{1}{2}\chi)} - \frac{1}{\sin(\frac{1}{2}\chi)} + \frac{1}{Z(1-\sin(\chi)\cos(\alpha))^{1/2}} \tag{6}$$

The scaled potential surface of $V(\chi,\alpha)$ is depicted in Fig. 2. In the hyperspherical coordinates, the variables for the configuration are automatically separated into

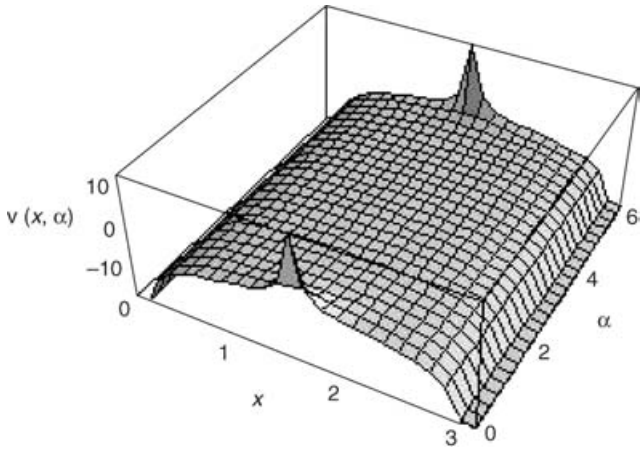

Figure 2. The scaled potential surface of $V(\chi, \alpha)$: $Z = 2$.

the "size" variable (i.e., the hyperradius r) and the "conformation" variables (i.e., the variables χ and α). The equations of motion are now given by

$$\frac{dr}{dt} = p_r \tag{7}$$

$$\frac{d\chi}{dt} = \frac{4p_\chi}{r^2} \tag{8}$$

$$\frac{d\alpha}{dt} = \frac{4p_\alpha}{r^2 \sin^2(\chi)} \tag{9}$$

$$\frac{dp_r}{dt} = \frac{4p_\chi^2}{r^3} + \frac{4p_\alpha^2}{r^3 \sin^2(\chi)} + \frac{1}{r^2} V(\chi, \alpha) \tag{10}$$

$$\frac{dp_\chi}{dt} = \frac{4p_\alpha^2 \cos(\chi)}{r^2 \sin^3(\chi)} - \frac{1}{r} \frac{\partial}{\partial \chi} V(\chi, \alpha) \tag{11}$$

$$\frac{dp_\alpha}{dt} = -\frac{1}{r} \frac{\partial}{\partial \alpha} V(\chi, \alpha) \tag{12}$$

We employ the scaling transformation

$$u = r^{1/2} p_r, \qquad v = r^{-1/2} p_\chi, \qquad w = r^{-1/2} p_\alpha \tag{13}$$

and the time transformation $d\tau = r^{-3/2}dt$ (i.e., the McGehee's blow-up transformation) [22]. Then we obtain the following energy relation:

$$\tfrac{1}{2}\left(u^2 + 4v^2 + \frac{4w^2}{\sin^2(\chi)}\right) + V(\chi,\alpha) - rE = 0 \tag{14}$$

where E represents the value of the Hamiltonian H. The equations of motion become

$$\frac{dr}{d\tau} = ru \tag{15}$$

$$\frac{d\chi}{d\tau} = 4v \tag{16}$$

$$\frac{d\alpha}{d\tau} = \frac{4w}{\sin^2(\chi)} \tag{17}$$

$$\frac{du}{d\tau} = \tfrac{1}{2}u^2 + \left(4v^2 + \frac{4w^2}{\sin^2(\chi)}\right) + V(\chi,\alpha) \tag{18}$$

$$\frac{dv}{d\tau} = -\tfrac{1}{2}uv + \frac{4w^2\cos(\chi)}{\sin^3(\chi)} - \frac{\partial}{\partial\chi}V(\chi,\alpha) \tag{19}$$

$$\frac{dw}{d\tau} = -\tfrac{1}{2}uw - \frac{\partial}{\partial\alpha}V(\chi,\alpha) \tag{20}$$

What is rested is to regularize the binary collisions between electron and nucleus. To do so, we first set

$$x = \sin(\chi)v \tag{21}$$

After that, we employ the time transformation.

$$\frac{d\tau}{dt} = \sin(\chi) \tag{22}$$

Note that t is not one that is defined in the first equations of motion: Eqs. (7)–(12). The energy relation finally becomes

$$\sin^2(\chi)u^2 + 4x^2 + 4w^2 + 2\sin^2(\chi)V(\chi,\alpha) - 2\sin^2(\chi)rE = 0 \tag{23}$$

The equations of motion are given by

$$\frac{dr}{dt} = \sin(\chi) ru \tag{24}$$

$$\frac{d\chi}{dt} = 4x \tag{25}$$

$$\frac{d\alpha}{dt} = \frac{4w}{\sin(\chi)} \tag{26}$$

$$\frac{du}{dt} = -\sin(\chi)\left(\tfrac{1}{2}u^2 + V(\chi,\alpha) - 2rE\right) \tag{27}$$

$$\frac{dx}{dt} = -\sin(\chi)\cos(\chi)(u^2 + 2V(\chi,\alpha) - 2rE) - \tfrac{1}{2}\sin(\chi)ux - \sin^2(\chi)\frac{\partial}{\partial\chi}V(\chi,\alpha) \tag{28}$$

$$\frac{dw}{dt} = -\tfrac{1}{2}\sin(\chi)uw - \sin(\chi)\frac{\partial}{\partial\alpha}V(\chi,\alpha) \tag{29}$$

The TCM is obtained by setting $r = 0$ and/or $E = 0$ in Eq. (23):

$$\sin^2(\chi)u^2 + 4x^2 + 4w^2 + 2\sin^2(\chi)V(\chi,\alpha) = 0 \tag{30}$$

The dimension of the TCM is four. The flow on the TCM is given by

$$\frac{d\chi}{dt} = 4x \tag{31}$$

$$\frac{d\alpha}{dt} = \frac{4w}{\sin(\chi)} \tag{32}$$

$$\frac{du}{dt} = -\sin(\chi)\left(\tfrac{1}{2}u^2 + V(\chi,\alpha)\right) \tag{33}$$

$$\frac{dx}{dt} = -\sin(\chi)\cos(\chi)(u^2 + 2V(\chi,\alpha)) - \tfrac{1}{2}\sin(\chi)ux - \sin^2(\chi)\frac{\partial}{\partial\chi}V(\chi,\alpha) \tag{34}$$

$$\frac{dw}{dt} = -\tfrac{1}{2}\sin(\chi)uw - \sin(\chi)\frac{\partial}{\partial\alpha}V(\chi,\alpha) \tag{35}$$

In the right-hand side of Eq. (32), one may think that there are still singularities $4w/\sin(\chi)$. This term is not singular. The reason is as follows. The total angular

momentum is $L = p_{\theta_1} + p_{\theta_2}$, where p_{θ_1} and p_{θ_2} are the momenta for azimuthal direction of the electron 1 and the electron 2. θ_1 and θ_2 are the azimuthal angles of the electrons 1 and 2, respectively. Suppose that the electron 1 exhibits a binary collision with the nucleus, that is, $\chi = \pi$. At the moment of this binary collision, $p_{\theta_1} = 0$. Now the total angular momentum is $L = 0$. Thus, at this moment, it implies that $p_{\theta_2} = 0$.On the other hand, the momentum p_α is given by $p_{\theta_1} = p_\alpha$, $p_{\theta_2} = -p_\alpha$. Then we have $p_\alpha = 0$, equivalently $w = 0$. Thus the term $4w/\sin(\chi)$ in Eq. (32) is harmless. When the electron 2 exhibits a binary collision, a similar discussion holds.

Property 2. For $H = E < 0$, the orbits run inside of the TCM, that is, $\sin^2(\chi)u^2 + 4x^2 + 4w^2 + 2\sin^2(\chi)V(\chi, \alpha) \leq 0$. For $H = E > 0$, the orbits run outside of the TCM, that is, $\sin^2(\chi)u^2 + 4x^2 + 4w^2 + 2\sin^2(\chi)V(\chi, \alpha) \geq 0$. For $H = E = 0$, the orbits run just on the TCM, that is, $\sin^2(\chi)u^2 + 4x^2 + 4w^2 + 2\sin^2(\chi)V(\chi, \alpha) = 0$.

To analyze the behavior of the flow on the TCM, we check positions of equilibrium points of the total flow [Eqs. (24)–(29)]. This is done by setting the right-hand side of Eqs. (24–29) to be zero. It is easily shown that the total flow has only two equilibrium points.

$$(r, \chi, \alpha, u, x, w) = \left(0, \frac{\pi}{2}, \pi, u^{(+)}, 0, 0\right) \quad \text{and} \quad \left(0, \frac{\pi}{2}, \pi, u^{(-)}, 0, 0\right) \tag{36}$$

where $u^{(\pm)} = \pm\sqrt{-2V(\frac{\pi}{2}, \pi)}$. We call the former equilibrium point A and the latter B. This is in contrast to the case of the gravitational three-body problem. For the planar isosceles gravitational three-body problem, there are six equilibrium points on the TCM (in this case, its dimension is two) [27]. Two equilibrium points correspond to collinear-type triple collisions. The other four equilibrium points correspond to equilateral-type triple collisions. Back to the present Coulomb problem, the above-mentioned two equilibrium points correspond to the collinear-type triple collision. Actually, there is a collinear homothetic solution from the equilibrium point A to the equilibrium point B. Therefore, for our Coulomb problem, it implies that only collinear-type triple collisions, whose orbit asymptotically approach to(or leave from) the triple collision in the collinear eZe configuration, occur. This is physically understood as follows. For our Coulomb system, the interaction between electrons is repulsive. Since the total energy is fixed, the electrons cannot be close each other. Thus the equilateral-type triple collision cannot occur for our Coulomb system.

What to do next is the stability analysis of two equilibrium points A and B. Omitting the details of calculation, the stability exponents for the critical point

A are given by

$$\lambda_1^{(A)} = u^{(+)} \tag{37}$$

$$\lambda_{2,3}^{(A)} = \frac{u^{(+)}}{4}\left(-1 \pm \sqrt{\frac{4Z-9}{4Z-1}}\right) \tag{38}$$

$$\lambda_{4,5}^{(A)} = \frac{u^{(+)}}{4}\left(-1 \pm \sqrt{\frac{100Z-9}{4Z-1}}\right) \tag{39}$$

On the other hand, due to the symmetry relation, the stability exponents for the critical point B have signs opposite to those for the critical points A.

$$\lambda_1^{(B)} = -u^{(+)} \tag{40}$$

$$\lambda_{2,3}^{(B)} = \frac{u^{(+)}}{4}\left(1 \mp \sqrt{\frac{4Z-9}{4Z-1}}\right) \tag{41}$$

$$\lambda_{4,5}^{(B)} = \frac{u^{(+)}}{4}\left(1 \mp \sqrt{\frac{100Z-9}{4Z-1}}\right) \tag{42}$$

If we restrict the system to the collinear eZe configuration (i.e., $\alpha = \pi$), the corresponding TCM is topologically equivalent to a spherical shell with four holes.

$$\sin^2(\chi)u^2 + 4x^2 + 2\sin^2(\chi)V(\chi, \alpha = \pi) = 0 \tag{43}$$

This is identical to one obtained by Bai, Gu, and Yuan [23]. In Fig. 3a, the stable and unstable manifolds of the critical points A and B on the TCM is depicted for the collinear eZe configuration. If we restrict the system to the Wannier ridge configuration (i.e., $\chi = \pi/2$), the corresponding TCM is topologically equivalent to a spherical shell.

$$u^2 + 4w^2 + 2V(\chi = \frac{\pi}{2}, \alpha) = 0 \tag{44}$$

In Fig. 3b, the stable and unstable manifolds of the critical points A and B on the TCM is depicted for the Wannier ridge configuration. The stability exponents $\lambda_{4,5}^{(A,B)}$ correspond to those for the case of the collinear eZe configruation(i.e., $\alpha = \pi$). On the other hand, the stability exponents $\lambda_{2,3}^{(A,B)}$ correspond to those for the case of the Wannier ridge configuration (i.e., $\chi = \pi/2$).

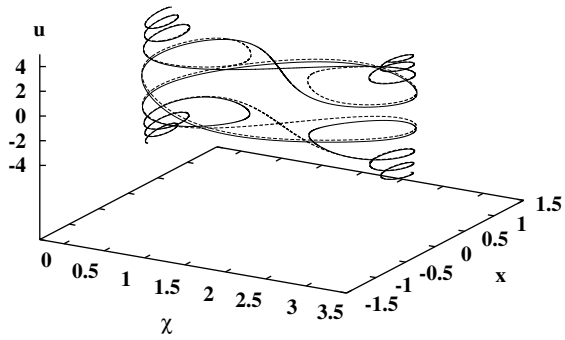

(*a*)

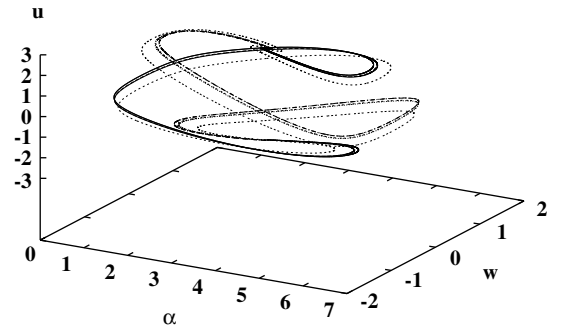

(*b*)

Figure 3. The stable and unstable manifolds of the critical points A and B on the TCM for $Z = 2$. (*a*) The collinear eZe configuration ($\alpha = \pi$). The critical points A and B on the TCM are hyperbolic fixed points. (*b*) The Wannier ridge configuration ($\chi = \pi/2$). The critical points A and B on the TCM are a stable focus and an unstable focus, respectively.

IV. THE COLLINEAR eZe CASE: MASS RATIO EFFECT

In this section, we consider the case that all three particles have finite masses. The contents of this section is a short summary of Ref. 29. We consider three particles 1, 2, and 3 whose masses are $m_1 = m_e$, $m_2 = m_n = \xi m_e$, and $m_3 = m_e$ and whose charges are $-e$, Ze, and $-e$, respectively. Suppose that three particles are arranged on a line in the order 1, 2, and 3 from left to right—that is, the collinear eZe configuration. The mass ratio ξ is given by $\xi = m_n/m_e$.

After some scaling transformation, we have the following Hamiltonian H for this system:

$$H = \frac{p_1^2}{2} + \frac{p_2^2}{2\xi} + \frac{p_3^2}{2} - \frac{1}{|q_1 - q_2|} - \frac{1}{|q_2 - q_3|} + \frac{1}{Z|q_1 - q_3|} \tag{45}$$

The parameters of this system is the charge Z and the mass ratio ξ. For numerical calculations in this section, we shall set $H = -1$ for our convenience.

A. Triple Collision Manifold

As shown for the 2D case with infinite nucleus mass in Section III, in this subsection we shall construct the TCM for the collinear eZe case with finite masses and shall elucidate the behavior near triple collisions. We use the McGehee's original transformation [22].The derivation of the TCM is successive application of tricky transformations to the equations of motion and the energy conservation relation. We do not show all of the derivation. The readers are strongly recommended to consult with Refs. 22 and 29 for details.

With the energy conservation and the zero total momentum, we transform the variables as $(q_1, q_2, q_3, p_1, p_2, p_3) \to (r, x, \phi, \psi)$. r is the squre root of the moment of inertia; that is, $r = \sqrt{q_1^2 + \xi q_2^2 + q_3^2}$. x is valued as $|x| \leq 1$. The transformations consist of the McGehee's blow-up transformation, the regularization of binary collisions, and the others. The energy relation is given as

$$2 - \frac{2\psi^2}{1 - x^2} = \frac{2(1 - x^2)}{W(x)}(\phi^2 - 2rE) \tag{46}$$

E is the value of the Hamilonian. The equations of motion is given by

$$\frac{dr}{d\tau} = \frac{\lambda(1 - x^2)}{W(x)^{1/2}} r\phi \tag{47}$$

$$\frac{d\phi}{d\tau} = \frac{\lambda}{2} W(x)^{1/2} \left[1 - \frac{1 - x^2}{W(x)}(\phi^2 - 4rE)\right] \tag{48}$$

$$\frac{dx}{d\tau} = \psi \tag{49}$$

$$\frac{d\psi}{d\tau} = -x + \frac{2x(1 - x^2)}{W(x)}(\phi^2 - 4rE) + \frac{1}{2}\frac{W'(x)}{W(x)}(1 - x^2 - \psi^2) - \frac{\lambda(1 - x^2)}{2W(x)^{1/2}}\phi\psi \tag{50}$$

where

$$W(x) = 2(1-x^2)\sin(2\lambda)\left[\frac{1}{(b_2-b_1)\sin(\lambda(1+x))} + \frac{1}{(a_3-a_2)\sin(\lambda(1-x))} - \frac{1}{Z\{(b_2-b_1)\sin(\lambda(1+x))+(a_3-a_2)\sin(\lambda(1-x))\}}\right] \tag{51}$$

$$\cos(2\lambda) = \frac{1}{\xi+1} \tag{52}$$

$$\mathbf{a} = \left(-\frac{1}{\sqrt{(1+\xi)(2+\xi)}}, -\frac{1}{\sqrt{(1+\xi)(2+\xi)}}, \frac{1+\xi}{\sqrt{(1+\xi)(2+\xi)}}\right) \tag{53}$$

$$\mathbf{b} = \left(-\frac{1+\xi}{\sqrt{(1+\xi)(2+\xi)}}, \frac{1}{\sqrt{(1+\xi)(2+\xi)}}, \frac{1}{\sqrt{(1+\xi)(2+\xi)}}\right) \tag{54}$$

Here λ is valued as $0 \le \lambda \le \pi/4$. In order to obtain the TCM , we set $r = 0$ and/or $E = 0$. The energy relation becomes

$$\psi^2 + x^2 + (1-x^2)^2 W(x)^{-1}\phi^2 = 1 \tag{55}$$

Equation (55) defines a surface in (x, ϕ, ψ) coordinates, that is, the TCM.The TCM is topologically equivalent to a spherical shell with four holes. A schematic picture for the TCM is depicted in Fig. 4a. The flow on the TCM is determined by the following equations of motion:

$$\frac{d\phi}{d\tau} = \frac{\lambda}{2}W(x)^{1/2}\left[1 - \frac{1-x^2}{W(x)}\phi^2\right] \tag{56}$$

$$\frac{dx}{d\tau} = \psi \tag{57}$$

$$\frac{d\psi}{d\tau} = -x + \frac{2x(1-x^2)}{W(x)}v^2 + \frac{1}{2}\frac{W'(x)}{W(x)}(1-x^2-\psi^2) - \frac{\lambda}{2}\frac{1-x^2}{W(x)^{1/2}}\phi\psi \tag{58}$$

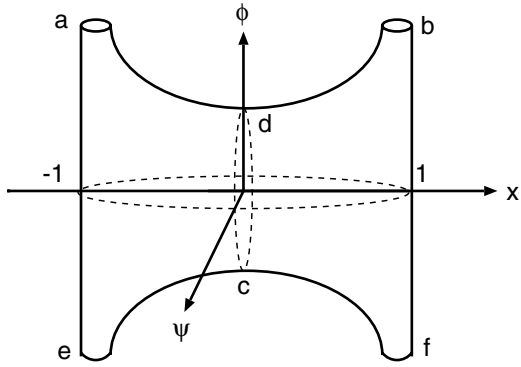

Figure 4. Schematic picture of the triple collision manifold (TCM). There are two critical points c and d. [Reprinted with permission from M. M. Sano, *Journal of Physics A*: *Mathematical and General* **37**, 803 (2004). Copyright © 2004, IOP Publishing Ltd.]

For the TCM, there are two critical points $c = (0, -\phi_c, 0)$ and $d = (0, \phi_c, 0)$, two infinite arms (a and b), and two infinite legs (e and f), where $\phi_c = W(0)^{1/2}$.

Similar to Property 2, we have the following.

Property 3. For $H = E < 0$, the orbits runs inside of the TCM. For $H = E > 0$, the orbits runs outside of the TCM. For $H = E = 0$, the orbits run just on the TCM.

As shown in the previous section for the 2D case with infinite nucleus mass, we also carry out stability analysis for the critical point c and d. The critical points c and d are the equilibrium points of the flow [Eqs. (56)–(58)]. At the same time, they are the equilibrium points of the total flow [Eqs. (47)–(50)]. The stability analysis of the equilibrium points c and d gives that $\dim(\mathcal{W}^s(c)) = 2, \dim(\mathcal{W}^u(c)) = 1$ and $\dim(\mathcal{W}^s(d)) = 1, \dim(\mathcal{W}^u(d)) = 2$, where $\mathcal{W}^s(x)$ and $\mathcal{W}^u(x)$ are the stable and unstable manifolds of x, respectively. We investigate the stable and unstable manifolds on the TCM numerically to show the global topological property of the triple collision orbits. We call them $\mathcal{W}_{TCM}(c)$ and $\mathcal{W}_{TCM}(d)$. For later use, we call the part of the TCM between two critical points c and d *the body of the TCM*: $\{(x, \phi, \psi); |\phi| \leq \phi_c, \psi^2 + x^2 + (1 - x^2)^2 W(x)^{-1}\phi^2 = 1\}$.

We are interested in the actual two-electron atom and ions.Thus we need to investigate the ξ-dependence of the flow on the TCM. Thanks to the similarity between celestial problem and Coulomb problem, for our Coulomb systems, the same argument is easily shown following the discussion of Ref. [22].

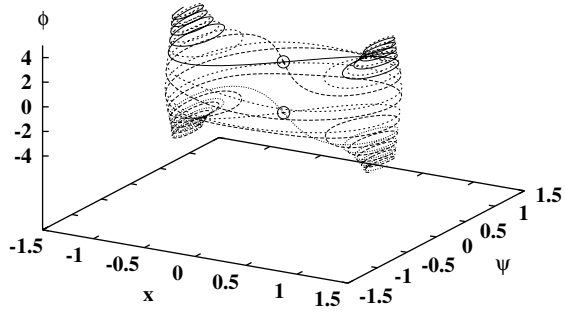

Figure 5. The stable and unstable manifolds of the critical points c and d on the TCM for $(Z, \xi) = (1, 1)$. Two circles indicate the positions of two critical points c and d. [Reprinted with permission from M. M. Sano, *Journal of Physics A*: *Mathematical and General* **37**, 803 (2004). Copyright © 2004, IOP Publishing Ltd.]

Property 4. When $\xi \to 0$, the orbits on the TCM wind around the body of the TCM *infinitely often*.

However, this limit has some trouble as mentioned in Ref. [30]. For numerical consideration, we do not take this limit. Only the behavior for small ξ is needed.

In order to show the ξ-dependence of the flow on the TCM for large ξ, we numerically calculate the stable and unstable manifolds on the TCM. Figure 5 depicts them for $(Z, \xi) = (1, 1)$. We confirmed the following things. When ξ is increased, the winding number $\mathcal{N}$ of the stable and unstable manifolds of c and d on the TCM around the body of the TCM is *monotonically* decreased. From numerical observation, $\mathcal{N}$ is saturated to certain value in the limit $\xi \to \infty$. For even relatively small value of ξ, $\mathcal{N}$ is almost saturated—for instance, $\xi < 100$ for $Z = 1, 2, 3, 4, 5$.

B. Triple Collision Orbits

In this subsection, we consider triple collision orbits on a Poincar'e section. We take the Poincaré surface of section at the plane $x = 0$ in (x, ϕ, ψ) coordinates. We define $\mathscr{D} = \{(x, \phi, \psi) | x = 0,\ \psi^2 + W(0)^{-1}\phi^2 \leq 1\ \}$. We divide $\mathscr{D}$ as $\mathscr{D} = \mathscr{D}_1 \cup \mathscr{D}_2$, where $\mathscr{D}_1 = \{(x, \phi, \psi) | x = 0,\ \psi \geq 0,\ \psi^2 + W(0)^{-1}\phi^2 \leq 1\}$ and $\mathscr{D}_2 = \{(x, \phi, \psi) | x = 0,\ \psi \leq 0,\ \psi^2 + W(0)^{-1}\phi^2 \leq 1\}$. We also define the boundary of $\mathscr{D}$, that is, $\partial\mathscr{D} = \{(x, \phi, \psi) | x = 0,\ \psi^2 + W(0)^{-1}\phi^2 = 1\ \}$.

As done in Refs. [29,31,32], by using the symbolic dynamics, we can specify the location of the triple collision orbits. We skip the detail of this method. The triple collision orbits that experience a triple collision in the future will form curves on the Poincaré section. Then we call them the triple collision curves.

For later use, we denote them by $\mathscr{C}_{TC}$. Figures 6a and 7a depict the triple collision curves $\mathscr{C}_{TC}$ for the case of $(Z, \xi) = (1, 1)$ and the case of the helium, respectively. For the case of $(Z, \xi) = (1, 1)$ (Fig. 6a), there are two tori in $\mathscr{D}_1$ and $\mathscr{D}_2$, namely the region around $(\phi, \psi) = (0, \pm 0.35)$. They are triangular-shaped. The simple stable orbits (the torus) may correspond to the Schubart orbits in the celestial problem [33]. In Fig. 6a, the region of these orbitsis shown as a triangle area. On the other hand, for the case of the helium (Fig. 7a)—that is, large ξ—there is no torus. In Figs. 6a and 7a, we plot $\mathscr{C}_{TC}$. In Figs. 6b and 7b,

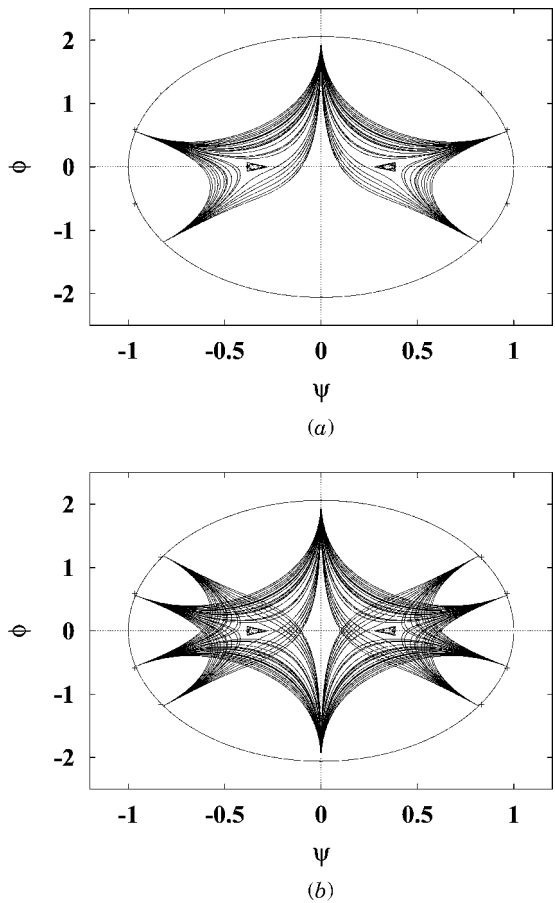

Figure 6. The triple collision curves $\mathscr{C}_{TC}$ and $\mathscr{C}'_{TC}$ on the Poincaré section for $(Z, \xi) = (1, 1)$. (*a*) Only $\mathscr{C}_{TC}$ is depicted. (*b*) Both $\mathscr{C}_{TC}$ and $\mathscr{C}'_{TC}$ are depicted. [Reprinted with permission from M. M. Sano, *Journal of Physics A*: *Mathematical and General* **37**, 803 (2004). Copyright © 2004, IOP Publishing Ltd.]

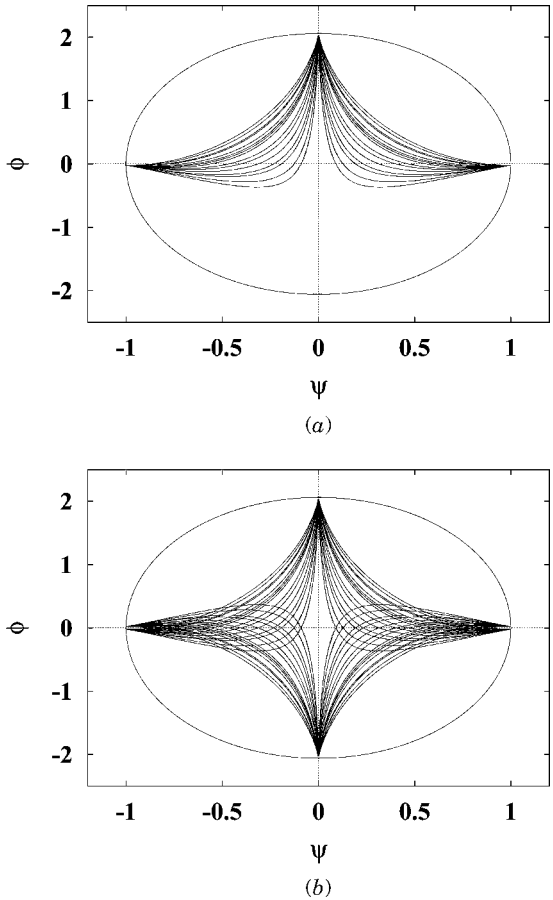

Figure 7. The triple collision curves $\mathscr{C}_{TC}$ and $\mathscr{C}^t_{TC}$ on the Poincaré section for $(Z, \xi) = (1, 7)$. (*a*) Only $\mathscr{C}_{TC}$ is depicted. (*b*) Both $\mathscr{C}_{TC}$ and $\mathscr{C}^t_{TC}$ are depicted. [Reprinted with permission from M. M. Sano, *Journal of Physics A*: *Mathematical and General* **37**, 803 (2004). Copyright © 2004, IOP Publishing Ltd.]

we also plot the triple collision curves whose orbits experienced the triple collision in the past, we denote them by $\mathscr{C}^t_{TC}$. By symmetry, $\mathscr{C}_{TC}$ and $\mathscr{C}^t_{TC}$ are symmetric against the line $\phi = 0$.

In order to examine the hyperbolicity of the system, we investigate the foliated structure of $\mathscr{D}$. In Figs. 6b and 7b, we depict the triple collision curves whose orbit is started and/or ended at a triple collision for the case of $(Z, \xi) = (1, 1)$ and the case of the helium, respectively. It is clearly seen that for Fig. 7b $\mathscr{C}_{TC}$ and $\mathscr{C}^t_{TC}$ transversely cross each other, while for Fig. 6b $\mathscr{C}_{TC}$ and

$\mathscr{C}^t_{TC}$ transversely cross each other except near the torus. Since the dynamics of our system is continuous, we expect that $\mathscr{C}_{TC}$ and $\mathscr{C}^t_{TC}$ do not cross the stable and unstable manifolds except on $\partial\mathscr{D}$. In fact, it is numerically confirmed that when ξ is sufficiently large, the triple collision curves $\mathscr{C}_{TC}(\mathscr{C}^t_{TC})$ are parallel to the stable (unstable) manifolds in the Poincaré section for the Poincaré map, respectively. Therefore, Fig. 7b (sufficiently large ξ) manifests that the dynamics of the helium in the collinear eZe configuration is hyperbolic. With some parameter values when the torus exists (for small value of ξ), $\mathscr{C}_{TC}$ and $\mathscr{C}^t_{TC}$ do not foliate. In this case, the tangency of the $\mathscr{C}_{TC}$ and $\mathscr{C}^t_{TC}$ is observed. This may manifest the tangency of the stable and unstable manifolds.

Furthermore, we investigate the detailed structure of the Poincaré surface of section for the case of $(Z, \xi) = (1, 1)$. In this case, there are tori. These tori have the periodic points with period 6 in their outermost part. Here we counted the number of vertices of two triangle, namely $2 \times 3 = 6$. These periodic points is associated to one orbit in the whole phase space, which is an antisymmetric orbit in the configuration space. These periodic points have stable and unstable manifolds. In Fig. 8a, we depict the stable manifolds of the these periodic points. In Fig. 8b, we also depict the unstable manifolds by using the symmetry. The stable and unstable manifolds of these periodic points go to $\partial\mathscr{D}$. It should be noted that the reached points of them on $\partial\mathscr{D}$ is the accumulation points of $\mathscr{C}_{TC}$ and $\mathscr{C}^t_{TC}$. Comparing Figs. 6a and 6b with Fig. 8, it is confirmed that $\mathscr{C}_{TC}$ in Figs. 6a and 6b is nearly parallel to the stable manifolds and $\mathscr{C}^t_{TC}$ in Fig. 6b is nearly parallel to the unstable manifolds. Therefore, it is understood that the foliated structure of $\mathscr{C}_{TC}$ and $\mathscr{C}^t_{TC}$ manifests the foliation of the stable and unstable manifolds—that is, hyperbolic structure.

The connection between the observation in Fig. 5 and the observation in Figs. 6b and 7b is unknown here. Now we elucidate this connection. Figure 6b for $(Z, \xi) = (1, 1)$ shows one branch of $\mathscr{W}_{TCM}(c)$ and the triple collision orbits on the Poincaré section. A remarkable point is that the triple collision curves $\mathscr{C}_{TC}$ and $\mathscr{C}^t_{TC}$ accumulate at 10 points on $\partial\mathscr{D}$. As shown in Fig. 9a, these points are the points at which $\mathscr{W}_{TCM}(c)$ and $\mathscr{W}_{TCM}(d)$ cross the plane $x = 0$ and which are, of course, just on $\partial\mathscr{D}$. We denote these points by $P_{TCM,r=0}$. It is clear that the number of points of $P_{TCM,r=0}$ is related to the existence of tori in the Poincaré section $\mathscr{D}$. If the tori exist, its outer most torus has periodic points. These periodic points have the stable and unstable manifolds. Branches of these stable and unstable manifolds run toward $\partial\mathscr{D}$, precisely $\mathscr{W}_{TCM}(c)$ and $\mathscr{W}_{TCM}(d)$ on $\partial\mathscr{D}$. This situation was observed in Fig. 8. Therefore, the number of the points of $P_{TCM,r=0}$ is related to the existence of the tori. At the same time, the number of the points of $P_{TCM,r=0}$ just corresponds to the winding number $\mathscr{N}$ of $\mathscr{W}_{TCM}(c)$ or $\mathscr{W}_{TCM}(d)$ around the body of the TCM as mentioned in the previous subsection. In Figs. 7b and 9b, the case of $(Z, \xi) = (1, 7)$ is shown. As the result of the previous subsection, when ξ is large enough, the winding

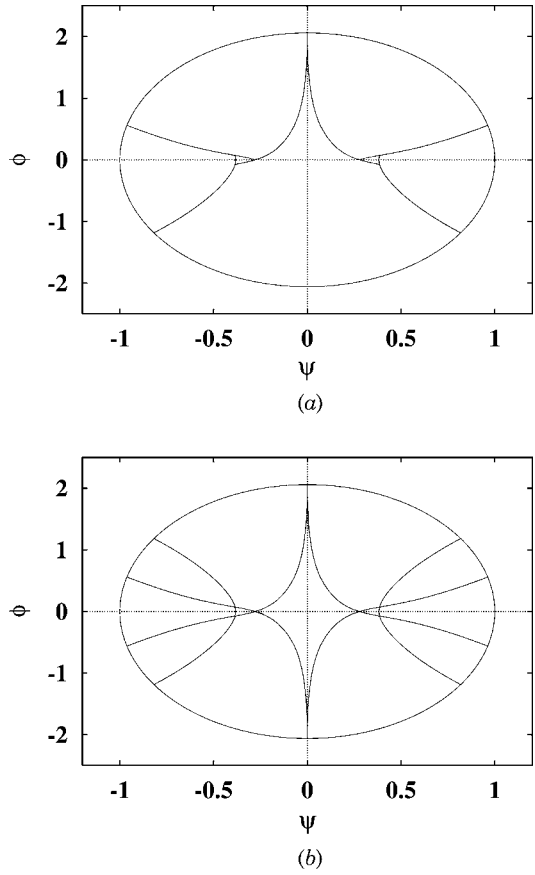

Figure 8. The stable and unstable manifolds of the periodic points of the outermost tori for the case of $(Z, \xi) = (1, 1)$. (*a*) The stable manifolds. (*b*) The unstable manifolds are also added to (*a*).

number of $\mathscr{W}_{TCM}(c)$ and $\mathscr{W}_{TCM}(d)$ saturates to certain value. For $Z = 1$, the critical value $\xi_c(Z = 1)$ is in the interval $(6.0, 7.0)$. This is clearly shown in Fig. 10 for $(Z, \xi) = (1, 6)$ and $(1, 7)$. In other words,when ξ is large enough, the number of the points of $P_{TCM,r=0}$ also saturates to a certain value that is, in fact, 6 (i.e., no torus case). Thus, the existence of tori in the Poincaré section $x = 0$ is monitored by the number of points of $P_{TCM,r=0}$. When ξ is large enough, the tori disappear and the triple collision curves $\mathscr{C}_{TC}$ transversely cross $\mathscr{C}^t_{TC}$. This would be a strong evidence of hyperbolicity of the system with large ξ, since it is numerically confirmed that $\mathscr{C}_{TC}(\mathscr{C}^t_{TC})$ is parallel to the stable (unstable)

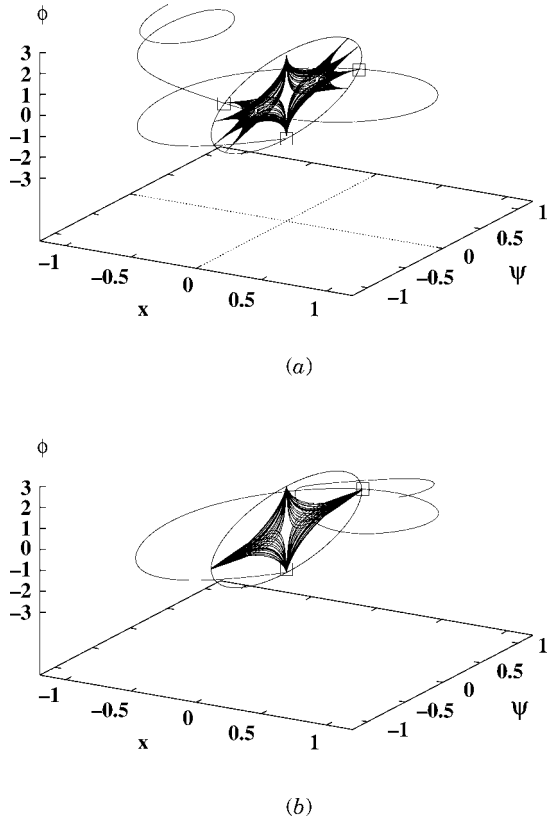

Figure 9. The triple collision curves $\mathscr{C}_{TC}$ and $\mathscr{C}^{t}_{TC}$ on the Poincaré section and one branch of the unstable manifold of the critical point c in (x, ϕ, ψ) coordinates. (*a*) For the case of $(Z, \xi) = (1, 1)$. (*b*) For the case of $(Z, \xi) = (1, 7)$. The points where the unstable manifold of the critical point c crosses the plane $x = 0$, are indicated by squares. [Reprinted with permission from M. M. Sano, *Journal of Physics A*: *Mathematical and General* **37**, 803 (2004). Copyright © 2004, IOP Publishing Ltd.]

manifold for the Poincaré map, respectively. We also confirmed that this scenario holds for the other Z cases (e.g., $Z = 1, 2, ..., 100$). The critical value of $\xi_c(Z)$ at which the winding number $\mathscr{N}$ saturates is calculated. In Fig. 11, we summarize the result. For $Z = 1, 2, 3, 4, 5$, the critical value $\xi_c(Z)$ is order of $O(10)$. This critical value is numerically obtained. The profile of Fig. 11 is almost linear.

From the above numerical observation, we can state two conjectures. (1) **For the system Eq. (45) with** (Z, ξ)**,** $Z \geq 1$**, there exists the critical value** $\xi_c(Z)$

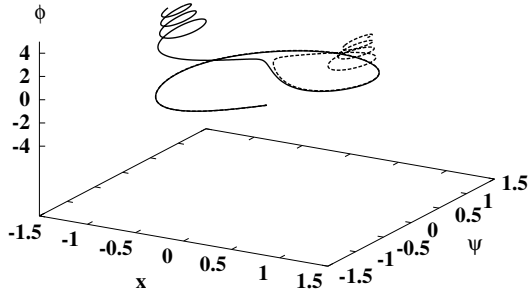

Figure 10. One branch of the unstable manifold of the critical point c for $(Z, \xi) = (1, 6)$ and $(1, 7)$. When $(Z, \xi) = (1, 6)$, the unstable manifold winds around the left arm a. When $(Z, \xi) = (1, 7)$, the unstable manifold winds around the right arm b. When ξ is increased and crosses the critical value $\xi_c(Z = 1)$, the unstable manifold changes the direction and winds around the right arm b.

such that for $\xi > \xi_c(Z)$ the system is hyperbolic. (2) **For the system Eq. (45) with $(Z, \xi_c(Z))$, $Z \geq 1$, the stable (unstable) manifold of the critical points c on the TCM degenerates the unstable (stable) manifold of the critical points d, namely totally degenerate.** Since for actual two-electron atom or ions the mass ratio is large, (i.e., $m_p/m_e \approx 1840$), this means that the classical dynamics of H^-, He, Li^+, Be^{2+}, and so on, in collinear eZe configuration is hyperbolic.

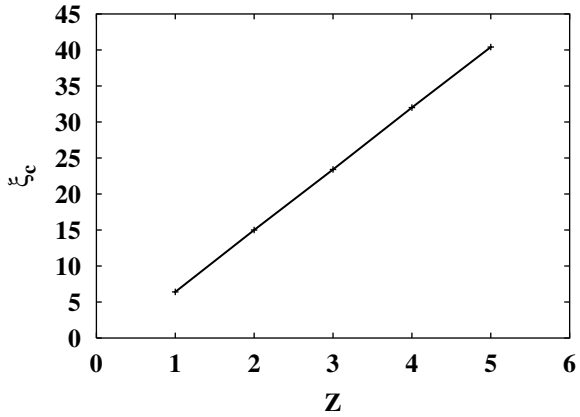

Figure 11. The critical value $\xi_c(Z)$ versus Z.

C. Experimental Manifestation

Systems in the collinear eZe configuration which have tori would be the antiproton–proton–antiproton ($\overline{p}$–p–$\overline{p}$) system, the positronium negative ion (Pr–(e–$\overline{e}$–e)), which corresponds to the case of $Z = 1, \xi = 1$, and H_2^+. If these systems have bound states, we can see the effect of our finding in the Fourier transform of the density of states for the spectrum. For a positronium negative ion, the EBK quantization was done [34]. Stable antisymmetric orbits were obtained and were quantized to explain some part of the energy spectrum. As hyperbolic systems, H^- and He have been already analyzed in Refs. 11 and 17, respectively. Thus, Li^+ is the next candidate. We might see the effect of the intermittency for this system in quantum defect as shown for helium [14].

V. FREE-FALL PROBLEM

Finding tori in the 2D case is very difficult, because the dimension of the phase space is 6. Some elaborate method to find tori is needed. In this section, we consider the free-fall problem. We treat three particles with finite masses.

Since we are interested in the case with zero total angular momentum, we have chosen such initial conditions for three particles. However, the phase space of the entire initial conditions is too big—in fact, infinite. Therefore, for numerical investigation, we have to restrict the initial conditions to some subspace of the entire initial conditions. If three particles have zero velocity at some moment, then the orbit associated to this initial condition has zero angular momentum, since $\mathbf{L} = \sum_{i=1}^{3} \mathbf{q}_i \times \mathbf{p}_i$. Thus we consider the initial conditions with zero velocities of three particles at time zero. These are just the initial conditions of the free-fall. So this problem is sometimes called the free-fall problem. The free-fall problem in gravitational three-body problem was well investigated [35–38].

The Coulomb system has the famous scaling relation. The positions, the momenta, and the energy of three particles are easily scaled. In this study, we set the total energy to be negative. If we consider the initial conditions for the free-fall problem, only the conformation of three particles is important—that is, the shape of the triangle formed by three particles. The scale of the position does not matter. Now we consider three particles. Two particles are the same (for instance, electrons), denoted by α_1 and α_2. One particle is different from two (for instance, nucleus), denoted by β. Since the total angular momentum is zero, the motion of three particles is confined in the 2D space. Set the particle β at the origin $(x, y) = (0, 0)$ in the 2D plane. Set the particle α_1 at $(x, y) = (1, 0)$. Another particle α_2 can be set anywhere in the 2D plane. In order to include all shapes of the triangle of three particles, where can we put another particle α_2? The answer is that the particle α_2 can be set in the region

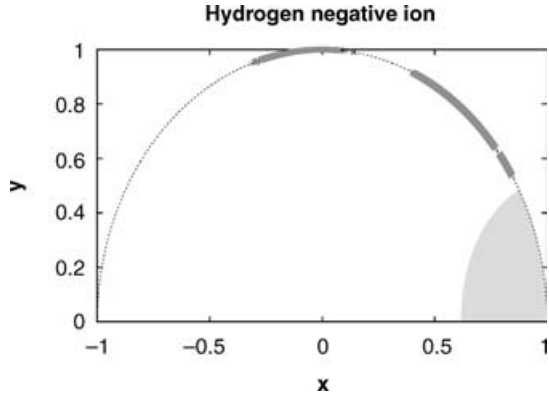

Figure 12. Candidates of tori in the initial condition space for the free-fall problem: hydrogen negative ion, H^-. The painted region near the corner $(x, y) = (1, 0)$ represents the initial conditions with positive total energy.

$D = \{(x, y) : x^2 + y^2 \leq 1 \text{ and } y \geq 0\}$, that is, inside of unit semicircle. Fortunately the region D is compact! To explore this region is numerically possible.

We numerically calculate the plot for three systems, namely H^-, He, and Pr− in the following way. Set three particles as in the above initial conditions. Start a free fall. If after some time interval three particles are still staying near the origin, then we regard the corresponding initial condition as a candidate for torus and plot this initial condition. The results are depicted in Figs. 12, 13, and

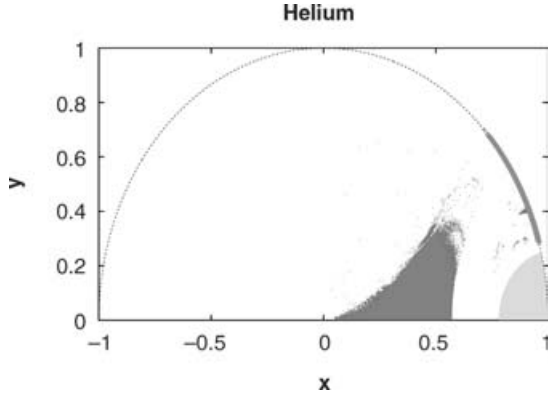

Figure 13. Candidates of tori in the initial condition space for the free-fall problem: helium atom, He. The painted region near the corner $(x, y) = (1, 0)$ represents the initial conditions with positive total energy.

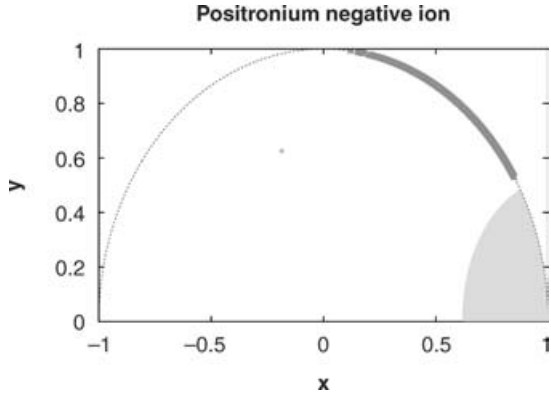

Figure 14. Candidates of tori in the initial condition space for the free-fall problem: positronium negative ion, Pr−. The painted region near the corner $(x, y) = (1, 0)$ represents the initial conditions with positive total energy.

14. The painted region near $(x, y) = (1, 0)$ corresponds to the initial conditions with positive total energy. We disregard this region. Figure 12 is the result for H^-. The thick lines on the semicircle correspond to the initial conditions for a family of tori. For H^-, there is no other possibilities for tori. Figure 13 is the result for He. Compared to the case of H^-, there are relative large region for candidates of tori around $0 \leq x \leq 0.6,\ 0 \leq y \leq 0.6$. The initial conditions in this region corresponds to the planetary orbits (tori), which were first discovered by Richter and Wintgen [20]. The thick line on the semicircle correspond to the initial conditions for a family of tori in Wannier ridge configuration, which probably includes a kind of Langmuir orbit. Near this thick line, there is some small region which includes candidates of tori. Figure 14 is the result for Pr−. The thick line on the semicircle correspond to the initial conditions for a family of tori. In this case, one exceptional candidate is near $(x, y) = (-0.2, 0.65)$. This may not be torus because of finite time evolution in numerical calculation. A reason why there is a difference between the $Z = 1$ case (H^- and Pr−) and the $Z = 2$ case (He), namely the existence of planetary orbits for He, is that the eeZ configuration is stable for the $Z = 2$ case and unstable for the $Z = 1$. It is numerically confirmed that the bending perturbation is generally stable. If the eeZ configuration is stable, adding the bending perturbation, the perturbed orbits are sometimes stable. Thus the planetary orbits exist for He.

VI. SUMMARY

In this chapter, we presented the geometry of the orbits near triple collisions in the Coulomb three-body problem for the collinear eZe configuration and the 2D case with zero angular momentum.

In Section III, for the 2D case with zero angular momentum, the TCM and a set of regularized equations of motion were derived. The dimension of the TCM for this case is four. The most remarkable point is that only two equilibrium points exist for the total flow. Therefore, as homothetic solutions, only collinear-type homothetic solution is allowed. This implies that all triple collisions occur asymptotically approaching to the collinear eZe configuration. This is in sharp contrast to the gravitational case that has more equilibrium points and allows the equilateral-type homethetic solution. In this sense, the Coulomb three-body problem is much simpler than the gravitational three-body problem. The stability analysis for two equilibrium points was carried out. In the collinear eZe configuration and the Wannier ridge configuration, the local property of the flow on the TCM was revealed. However, at present, the whole dynamics for the 2D case with zero angular momentum is not known very well. A partial result was presented in this conference by Choi, Lee, and Tanner [24].

In Section IV, for the collinear eZe case, McGehee's method was directly applied to the system with finite masses. The mass ratio ξ plays an important role in this problem. When the value of ξ is increased, the flow on the TCM is changed, especially how many times $\mathscr{W}^{(u)}_{TCM}(c)$ winds around the body of the TCM, say $\mathscr{N}$. When ξ goes to infinity, $\mathscr{N}$ is saturated to certain value. This property is directly related to the existence of tori inside the TCM (the dynamics with $E \leq 0$). Thanks to a large mass ratio ξ, H^-, He, Li^+, Be^{2+}, and so on, in the collinear eZe configuration are probably hyperbolic. This hyperbolicty and the intermittency would reflect the behavior of the quantum defects of H^-, He, Li^+, Be^{2+}, and so on. Nonhyperbolic systems are also predicted by our finding, that is e–$\bar{e}$–e, p–$\bar{p}$–p, and H_2^+.

In Section V, we presented the result on the free fall problem. It was shown that the value of Z is very important for the existence of tori in the 2D plane.

For future problems, the TCM and a set of regularized equations of motion derived in Section III will be used to investigate the whole dynamics of the 2D case with zero angular momentum. This task would be hard both numerically and theoretically. But fortunately the dynamics is relatively simpler than that of the gravitational case. For theoretical aspect, the scheme of this conference, namely normally hyperbolic invariant manifold (NHIM) [39] may be possibly applied to our Coulomb three-body problem. See the scaled potential surface of $V(\chi, \alpha)$ in Fig. 2. The collinear eZe configuration (i.e., $\alpha = \pi$) and the Wannier ridge configuration (i.e., $\chi = \pi/2$) are mutually orthogonal. The intersection set of the collinear eZe confguration and the Wannier ridge configuration includes the collinear homothetic solution. If we neglect the "size" variable r, the scaled potential $V(\chi, \alpha)$ has the ridge, namely the Wannier ridge. In the direction to the collinear eZe configuration, the dynamics is unstable, probably hyperbolic as mentioned in the conjecture. On the other hand, in the direction to the Wannier ridge configuration, the dynamics is relatively stable. This situation is very similar to the setting up for an NHIM. Anyway the collinear homothetic

solution may play a central role for the dynamics in the 2D case with $L = 0$. If we elucidate the whole dynamics in the 2D case with $L = 0$, we will be able to carry out semiclassical quantization to yield the full spectrum of $^1S^e$ and we will know the correlations in two-electron atoms or ions both in classical-sense and in quantum-sense through semiclassics.

Acknowledgments

The author is grateful to the organizers of this conference, Professor Mikito Toda, Professor Tamiki Komatsuzaki, Professor Tetsuro Konishi, Professor R.Stephen Berry, and Professor Stuart A. Rice. He is also grateful to Professor Kiyotaka Tanikawa for stimulating discussion on three-body problem in celestial mechanics.He thanks Dr. M. Alvarez-Ramírez for sending him Ref. [30]. He also thanks the following institute and the organizations for financial support: Japan Society of the Promotion of Science, Yukawa Institute for Theoretical Physics at Kyoto University, Inoue Foundation for Science, and Grants-in-Aid for scientific research in priority areas by the Japanese Ministry of Education, Culture, Sports, Science and Technology, entitled ''Control of molecules in intense laser fields.''

References

1. M. C. Gutzwiller, *Rev. Mod. Phys*. **70**, 589 (1998).
2. H. Poincaré, *Les méthods nouvelles de la méchanique céleste I, II et III*, Gauthier-villars, Paris, 1899.
3. S. L. Siegel and J. K. Moser, *Lectures on Celestial Mechanics*, Springer-Verlag, Berlin, 1971.
4. N. Bohr, *Philos. Mag.* **26**, 492 (1913).
5. A. Einstein, *Verh. Dtsch. Phys. Ges.* **19**, 82 (1917).
6. I. Langmuir, *Phys. Rev.* **17**, 339 (1921).
7. J. H. van Vleck, *Philos. Mag.* **44**, 842 (1922).
8. G. Tanner, K. Richter, and J.-M. Rost, *Rev. Mod. Phys.* **72**, 497 (2000).
9. M. C. Gutzwiller, *J. Math. Phys.* **12**, 343 (1971).
10. M. C. Gutzwiller, *Chaos in Classical and Quantum Mechanics*, Springer, New York, 1990.
11. P. Gaspard and S. A. Rice, *Phys. Rev. A* **48**, 54 (1993).
12. G. S. Ezra, K. Richter, G. Tanner, and D. Wintgen, *J. Phys. B* **24**, L413 (1991).
13. U. Fano, *Rep. Prog. Phys.* **46**, 97 (1983).
14. G. Tanner and D. Wintgen, *Phys. Rev. Lett.* **75**, 2928 (1995).
15. J.-M. Rost, *Phys. Rep.* **297**, 271 (1998).
16. G. H. Wannier, *Phys. Rev.* **90**, 817 (1953).
17. K. Richter, G. Tanner, and D. Wintgen, *Phys. Rev. A* **48**, 4182 (1993).
18. F. Diacu and E. Peréz-Chavela, *J. Phys. A* **36**, 9053 (2003).
19. M. A. Almeida, A. López-Castillo, and T. J. Stuchi, *J. Phys. A* **36**, 4805 (2003).
20. K. Richter and D. Wintgen, *Phys. Rev. Lett.* **65**, 1965 (1990).
21. T. Yamamoto and K. Kaneko, *Phys. Rev. Lett.* **70**, 1928 (1993).
22. R. McGehee, *Invent. Math.* **27**, 191 (1974).
23. Z.-Q. Bai, Y. Gu, and J.-M. Yuan, *Physica D* **118**, 17 (1998).

24. N. N. Choi, M.-H. Lee, and G. Tanner, *Private communication*. The poster presentation in this conference entitled "Electron-positive helium ion scattering as a three-body Coulomb problem," 2003; N. N. Choi, M.-H. Lee and G. Tanner, *Phys. Rev. Lett.* **93** 054302 (2004).
25. F. Diacu and P. Holmes, *Celestial Encounter: The Origin of Chaos and Stability*, Princeton University Press, Princeton, 1996.
26. H. von Zeipel, *Arkiv Math. Astron. Fysik.* **4**, 1 (1908).
27. D. L. Devaney, *Invent. Math.* **60**, 249 (1980).
28. Z. Xia, *Ann. Math.* **135**, 411 (1992).
29. M. M. Sano, *J. Phys. A* **37**, 803 (2004).
30. M. Alvarez-Ramírez and J. Delagado, *Discrete and Continuous Dynamical Systems.* **9**, 1149 (2003).
31. K. Tanikawa and S. Mikkola, *Celest. Mech. Dyn. Astron.* **76**, 23 (2000).
32. K. Tanikawa and S. Mikkola, *Chaos* **10**, 649 (2000).
33. J. Schubart, *Astron. Nachr.* **283**, 17 (1956).
34. N. Simonovic and J.-M. Rost, *Eur. Phys. J. D* **15**, 155 (2001).
35. H. Umehara, *The Free-Fall Three-Body Problem: Escape and Collision*, Ph.D. Thesis, Department of Astronomical Science, School of Mathematical and Physical Science, The Graduate University for Advanced Studies, Japan, 1997.
36. T. A. Agekian and J. P. Anosova, *Astron. Zh.* **44**, 1261 (1967).
37. K. Tanikawa, H. Umehara, and H. Abe, *Celest. Mech. Dyn. Astron.* **62**, 335 (1995).
38. R. A. Broucke, On the role of the moment of inertia in three-body scattering, in *From Newton to Chaos* (A. Roy and B. Steves, eds.) Plenum Press, New York (1995).
39. S. Wiggins, *Normally Hyperbolic Invariant Manifolds in Dynamical Systems*, Springer-Verlag, Berlin, 1994.

CHAPTER 7

GLOBAL ASPECTS OF CHEMICAL REACTIONS IN MULTIDIMENSIONAL PHASE SPACE

MIKITO TODA

Physics Department, Nara Women's University, Nara, 630-8506, Japan

CONTENTS

I. Introduction
  A. Simplify Dynamics Using NHIMs
  B. Connections Among NHIMs
  C. Bifurcation in the Skeleton
  D. Purpose of the Chapter
II. Singular Perturbation Theory
III. Normally Hyperbolic Invariant Manifolds (NHIMs)
IV. Lie Perturbation
V. Melnikov Integral
VI. Arnold Model
VII. Tangency
VIII. Chaotic Itinerancy
IX. Breakdown of Normal Hyperbolicity
X. Crisis in Multidimensional Chaos
XI. Summary
Appendix A: Melnikov Integral for Example 1
Appendix B: Melnikov Integral for Example 2
Acknowledgments
References

I. INTRODUCTION

In the conventional theory of chemical reactions, the assumption of local equilibrium plays a crucial role. This assumption enables us to limit our attention to local structures of the phase space—that is, transition states—and it replaces

Geometric Structures of Phase Space in Multidimensional Chaos: A Special Volume of Advances in Chemical Physics, Part A, Volume 130, edited by M. Toda, T Komatsuzaki, T. Konishi, R.S. Berry, and S.A. Rice. Series editor Stuart A. Rice.
ISBN 0-471-70527-6

global aspects of the reaction dynamics with equilibrium properties. In this way, we can estimate physical quantities such as reaction rates using only information about the saddle regions of the potential function.

Recently, however, experimental studies of reaction processes have cast doubt on the local equilibrium assumption. When that assumption is not valid, understanding of reaction processes requires the study of global aspects of the phase space in multidimensional chaotic dynamics [1].

In order to proceed, we propose the following three-stage strategy. First, we simplify the description of the dynamics locally in the phase space. This is done in an analogous and extended fashion similar to that used in the conventional Transition State Theory. Second, we study how the local dynamics in different regions of the phase space are related to each other. Thus, identification and understanding of global structures of the phase space is our target for this stage. (This will be the main focus of this review, since the first part is discussed in detail by Refs. 2 and 3.) Third, we examine bifurcation in the global structures of the phase space.

In the following, we explain these three stages in more detail.

A. Simplify Dynamics Using NHIMs

First, in order to simplify the description of the dynamics we separate the whole system, locally in the phase space, into two parts based on a gap in characteristic time scales. This is done using the concept of normally hyperbolic invariant manifolds (NHIMs) [4–8]. Here, the characteristic time scales are estimated as the inverses of the absolute values of the local Lyapunov exponents [5,6]. Then, the Fenichel normal form offers a simplified description of the local dynamics near a NHIM [7].

In constructing NHIMs, those degrees of freedom with smaller absolute values of the local Lyapunov exponents correspond to the directions that are tangent to the NHIM. Those with larger absolute values of the local Lyapunov exponents describe movements that are normal to the NHIM. The gap between smaller and larger absolute values of the local Lyapunov exponents is the key in this construction.

The dynamics of approaching and leaving a NHIM are described by the orbits on the stable and unstable manifolds of the NHIM.

In constructing the stable manifold of the NHIM we follow, backward in time, the normal directions of the NHIM with negative local Lyapunov exponents. For the unstable manifold we follow forward in time the normal directions of the NHIM with positive local Lyapunov exponents.

In reaction dynamics, NHIMs and their stable and unstable manifolds exist in the phase space above saddles of the potential function. In the first stage of our strategy, these saddles are at the focus of our interest.

Let N denote the number of the degrees of freedom of a system. We also use the term "the index of the saddle" to indicate the number of negative eigenvalues of the Hessian matrix of the potential function at the saddle.

Suppose we have a saddle with index 1. Then, a NHIM of $2N-2$ dimension exists above it in the phase space, with two directions that are normal to it. Along these normal directions, with negative and positive Lyapunov exponents, $(2N-1)$-dimensional stable and unstable manifolds exist, respectively. The normal directions of the saddle correspond to the degree of freedom that is the reaction coordinate near the saddle, and they describe how the reaction proceeds locally near the NHIM.

These NHIMs are of the largest dimension in the phase space. In the $(2N-1)$-dimensional equi-energy surface, the dimension of these NHIMs is $2N-3$, and that of their stable and unstable manifolds is $2N-2$. Therefore, their stable and unstable manifolds separate the equi-energy surface locally into two regions. This separation corresponds to separating the equi-energy surface locally into the reactant and product sides.

Thus, based on NHIMs with saddles with index 1, we can construct a theory that is a rigorous reformulation of the conventional Transition State Theory [9,10]. Moreover, the use of the Lie perturbation brings the system locally into the Birkhoff normal form with one inverse harmonic potential [2]. This form is nothing but the Fenichel normal form.

As reactions proceed further, the system will go through multiple saddles of the potential function. Thus, we are led to ask how dynamics near these saddles are connected with each other. This is the problem we face in the second stage.

B. Connections Among NHIMs

Second in our strategy, we ask how the dynamics near NHIMs are connected with each other. Here, intersections between the stable and unstable manifolds of the NHIMs play a major role.

Suppose that the unstable manifold of a NHIM intersects with the stable manifold of another NHIM (or the same NHIM); such intersections are called heteroclinic (or homoclinic). This means that there exists a path that connects these two NHIMs (or a path that leaves from and comes back to the NHIM). Thus, their intersections offer the information on how the NHIMs are connected.

In multidimensional systems, these intersections would exhibit much more variety than they do in the lower-degrees-of-freedom systems that have been traditionally studied in nonlinear physics. One of the new aspects is "tangency", which was found in the predissociation of a van der Waals complex of three bodies [11,12]. The tangency gives birth to transition in chaos [12], which is called a crisis [13]. Then, the extention of the concept of reaction rates to multidimensional chaos, which was first proposed in Ref. 9, breaks down [11,14].

Thus, instead of trying to extend the concept of reaction rates, we follow a different route.

We regard the intersections between stable and unstable manifolds as a skeleton of reaction paths. The skeleton has the structure of a network, since one NHIM can be connected with multiple NHIMs. Then, branching in the skeleton will manifest itself as tangency [1]. This observation suggests the importance of tangency in multidimensional reaction dynamics.

Moreover, the NHIM with a saddle with index 1 can be connected with NHIMs with saddles with indexes larger than 1. To see this possibility, let us count the dimension of the intersections. Suppose we have a saddle with index L. Then, the NHIM of $2N - 2L$ dimension exists with $(2N - L)$-dimensional stable and unstable manifolds. In the equi-energy surface, the dimension of the NHIM is $2N - 2L - 1$, and that of its stable and unstable manifolds is $2N - L - 1$. Thus, the dimension of the intersection, if any, between its stable manifold and the unstable manifold of the NHIM with a saddle with index 1 is $2N - L - 2$. If its value is larger than 0, a path exists which connects these two NHIMs. Therefore, the allowed values of L for systems of 3 degrees of freedom (for example) are 1 and 2, when we also take into account the condition that $2N - 2L - 1$ (i.e., the dimension of the NHIM with a saddle with index L in the equi-energy surface) should not be negative.

In addition to the NHIMs with saddles, other kinds of NHIMs can also become important when intramolecular vibrational energy redistribution (IVR) comes into play. They are NHIMs with whiskered tori that are created by nonlinear resonances within the potential well [5]. In the network of nonlinear resonances, which is called the Arnold web [16,17], these NHIMs will be connected in an interwoven way with each other and also with NHIMs with saddles.

Thus, orbits in the skeleton of reaction paths will wander around from one NHIM to another, following the complicated structure of the network. Such behavior reminds us of the dynamics called ‘‘chaotic itinerancy’’ [18–21].

To investigate this behavior, we have two methods available at present: One is the Melnikov integral, which is used by Arnold in Ref. 15 to see if the stable and unstable manifolds of whiskered tori intersect. The other is Lie perturbation theory, which is used in astrophysics to control orbiters in the universe [22].

The Melnikov integral is more suitable for theoretical purposes to prove theorems using model Hamiltonians. On the other hand, Lie perturbation theory is applicable to realistic systems such as clusters. For an application of Lie perturbation theory to clusters, see Ref. 23.

C. Bifurcation in the Skeleton

Up until now we have fixed the energy and parameters of the system in considering the skeleton of reaction paths. In the third stage of our strategy we vary these quantities to see what will happen in the skeleton.

Here, we mention only two possibilities, though we could have other cases. The first is that the condition of normal hyperbolicity breaks down for some NHIMs. Then, what happens to those NHIMs? Do they bifurcate into other NHIMs, or do they disappear at all? The second possibility is that intersections between the stable and unstable manifolds of NHIMs change into tangency. This could lead to bifurcation in the way NHIMs are connected by their stable and unstable manifolds.

At present, study of this stage is very limited [7]. We expect that future progress will reveal details of how the skeleton varies.

D. Purpose of the Chapter

In this chapter, we present the basic ideas that are necessary to carry out our strategy. In particular, we focus attention on the tangency mentioned in the second stage, since study of tangency will give a clue to understand the features of branching in the skeleton of reaction paths. For this reason, we investigate a simple model Hamiltonian both numerically and analytically using the Melnikov integral.

We will also discuss the relevance, in the context of chemical reactions, of the possibilities pointed out in the third program stage, which enables us to go beyond the condition of normal hyperbolicity, and the need for the gap in the characteristic time scales. Moreover, bifurcation in the skeleton can offer a mechanism by which reaction processes evolve, thereby opening a new arena in the study of chemical reactions.

In the following, we give an overview of the chapter.

The basic ideas that are necessary for the first program stage are explained in Sections II, III, and IV. In Section II, we formulate the problem of how to analyze a system that has a gap in characteristic time scales. Our method is to use perturbation theory with respect to a parameter that is the ratio between a long time scale and a short time scale, which is a version of singular perturbation theory. The reason will be explained in Section II. In Section III, the concept of NHIMs is introduced in the context of singular perturbation theory. We will give an intuitive description of NHIMs and explain how the description is implemented, leaving the precise formulation of the NHIM concept to the literature in mathematics. In Section IV, we will show how Lie perturbation theory can be used to transform the system into the Fenichel normal form locally near a NHIM with a saddle with index 1. Our explanation is brief, since a detailed exposition has already been published [2].

The Melnikov integral, which plays a key role in the second program stage, is presented in Sections V, VI, and VII. In Section V, we derive the Melnikov integral following the presentation in Ref. 24. We limit our explanation to a simplified situation to avoid discussion of the convergence of the integral. In Section VI, we discuss the Arnold model [15] to show, using the Melnikov

integral, a sufficient condition for intersections to occur between the stable and unstable manifolds of whiskered tori with different action values. In the historical context, this argument implies the behavior called the Arnold diffusion, though the term ''diffusion'' could be problematic [25]. The core of this chapter is Section VII. Here, we investigate the Arnold model numerically and analytically, using the Melnikov integral to reveal the tangency. We also discuss the universality of the tangency in multidimensional chaos.

In Section VIII, we give a summary of the viewpoint obtained from the second program stage—in particular, its resemblance to chaotic itinerancy. This section bridges our argument from the second program stage to the third program stage.

The third stage of our strategy is discussed in Sections IX and X. Our discussion is speculative, since quantitative analysis is lacking at present. In Section IX, we point out that, in reaction dynamics, breakdown of normal hyperbolicity would also play an important role. Such cases would include phase transitions in systems with a finite number of degrees of freedom. In Section X, we will discuss the possibility of bifurcation in the skeleton of reaction paths, and we point out that it corresponds to crisis in multi-dimensional chaos. This approach offers an interesting mechanism for chemical evolution.

In the Section XI, we summarize the major points of this chapter. We will also propose future development of our strategy with application to systems with many degrees of freedom—for example, the dynamics of protein folding. We suggest that coarse graining of the phase-space structure may need to be incorporated to tackle such a problem.

II. SINGULAR PERTURBATION THEORY

The existence of a gap in characteristic time scales of a dynamical system is the key to this chapter. The meaning of ''the characteristic time'' scales will be made clear in the following.

In the field of chemical reactions, separating the system into fast and slow degrees of freedom is a standard method. It is based on the gap in characteristic time scales for motion of electrons and nuclei. This is the Born–Oppenheimer approximation, and it is used for constructing potential surfaces for the motion of the nuclei.

In this chapter, focus attention on a different method to analyze those systems that consist of fast and slow variables. It is called singular perturbation theory, and is suitable for understanding chaotic behavior in systems with many degrees of freedom. The reason for the term ''singular'' will be explained later.

In this and the next sections, we will present the basic ideas of singular perturbation theory without going into mathematical rigor.

Let us consider the following coupled ordinary differential equations:

$$\begin{aligned} \varepsilon \frac{d\boldsymbol{x}}{dt} &= \boldsymbol{f}(\boldsymbol{x}, \boldsymbol{y}) \\ \frac{d\boldsymbol{y}}{dt} &= \boldsymbol{g}(\boldsymbol{x}, \boldsymbol{y}) \end{aligned} \tag{1}$$

where ε is a small constant which satisfies $0 < \varepsilon \ll 1$. Here, $\boldsymbol{x}$ and $\boldsymbol{y}$ are vectors on Euclidean spaces.

The constant ε represents the gap in characteristic time scales between the dynamics of $\boldsymbol{x}$ and that of $\boldsymbol{y}$; suppose that the values of $\boldsymbol{f}(\boldsymbol{x}, \boldsymbol{y})$ and $\boldsymbol{g}(\boldsymbol{x}, \boldsymbol{y})$ are of the same order. Then, the magnitude of $d\boldsymbol{x}/dt$ is ε^{-1} times larger that that of $d\boldsymbol{y}/dt$. This means that $\boldsymbol{x}$ varies ε^{-1} times faster than $\boldsymbol{y}$ does. Thus, $\boldsymbol{x}$ is a fast variable and $\boldsymbol{y}$ is a slow one.

We will introduce a new time variable $\tau \equiv t/\varepsilon$ which describes fast changes of the coupled equations Eq. (1). Using the fast time variable τ, the equations Eq. (1) become

$$\begin{aligned} \frac{d\boldsymbol{x}}{d\tau} &= \boldsymbol{f}(\boldsymbol{x}, \boldsymbol{y}) \\ \frac{d\boldsymbol{y}}{d\tau} &= \varepsilon \boldsymbol{g}(\boldsymbol{x}, \boldsymbol{y}) \end{aligned} \tag{2}$$

The coupled equations Eq. (1) and (2) are equivalent for a finite value of ε. However, they will reveal different asymptotic behavior in the limit $\varepsilon \searrow 0$.

Let us consider Eq. (2) first. When we set $\varepsilon = 0$ in Eq. (2), we obtain

$$\begin{aligned} \frac{d\boldsymbol{x}}{d\tau} &= \boldsymbol{f}(\boldsymbol{x}, \boldsymbol{y}) \\ \frac{d\boldsymbol{y}}{d\tau} &= \boldsymbol{0} \end{aligned} \tag{3}$$

There is no time development of $\boldsymbol{y}$ in Eq. (3). Intuitively speaking, the slow variable $\boldsymbol{y}$ looks like a constant in the asymptotic limit $\varepsilon \searrow 0$, when we view $\boldsymbol{y}$ using the fast time variable τ.

In Fig. 1, a schematic picture of the flow under Eq. (3) is shown. There, the thick arrows indicate the directions of the flow. They are parallel to the $\boldsymbol{x}$ axis since there is no time development of $\boldsymbol{y}$. The thin curve shows the locations where $d\boldsymbol{x}/d\tau = \boldsymbol{0}$; that is, both $\boldsymbol{x}$ and $\boldsymbol{y}$ do not vary.

On the other hand, when we set $\varepsilon = 0$ in Eq. (1), we obtain the following equations:

$$\begin{aligned} \boldsymbol{0} &= \boldsymbol{f}(\boldsymbol{x}, \boldsymbol{y}) \\ \frac{d\boldsymbol{y}}{dt} &= \boldsymbol{g}(\boldsymbol{x}, \boldsymbol{y}) \end{aligned} \tag{4}$$

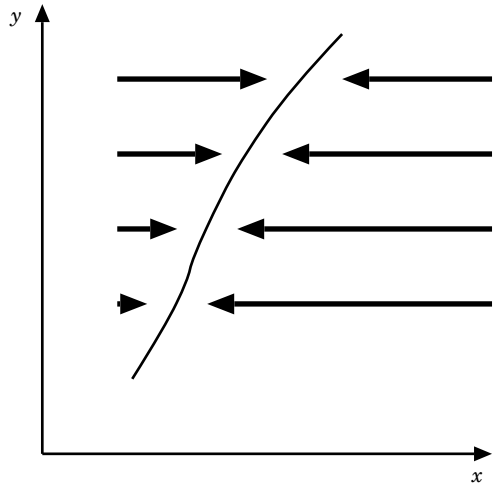

Figure 1. A schematic picture of the flow for Eq. (3).

Note the following significant fact for Eq. (4). While the original coupled equations (1) have a solution for an arbitrary initial condition $(\boldsymbol{x}, \boldsymbol{y})$, Eqs. (4) have one only for an initial condition that satisfies $\mathbf{0} = \boldsymbol{f}(\boldsymbol{x}, \boldsymbol{y})$. In other words, Eqs. (4) have solutions only on the manifold where $d\boldsymbol{x}/dt = \mathbf{0}$ in the original equations (1).

Let $(\boldsymbol{x} = \boldsymbol{x}_0(\boldsymbol{y}), \boldsymbol{y})$ denote one of the graphs of the manifold $\mathbf{0} = \boldsymbol{f}(\boldsymbol{x}, \boldsymbol{y})$. Then, substituting $\boldsymbol{x} = \boldsymbol{x}_0(\boldsymbol{y})$ in the second equation of Eq. (4)—that is, $d\boldsymbol{y}/dt = \boldsymbol{g}(\boldsymbol{x}, \boldsymbol{y})$—we obtain a closed equation for $\boldsymbol{y}$ as follows:

$$\frac{d\boldsymbol{y}}{dt} = \boldsymbol{g}(\boldsymbol{x}_0(\boldsymbol{y}), \boldsymbol{y}) \tag{5}$$

A schematic picture of a solution for Eq. (5) is shown in Fig. 2.

Here, we explain the origin of the term "singular." It is used in contrast with the expression "regular." In general, regular perturbation theory presupposes that the solution obtained by setting $\varepsilon = 0$ resembles the one for a small and positive ε. However, for Eq. (4), there exist no solutions at all for arbitrary initial conditions when we set $\varepsilon = 0$.

The reason why such situations occur is that, when we set $\varepsilon = 0$, the degree of the equations is reduced. The freedom of specifying conditions to determine the unique solution depends on the degree of the differential equations. Thus, reducing the degree of the equations results in decreasing our freedom to select initial conditions, leading to the nonexistence of solutions for arbitrary initial conditions. Then, we call such perturbation methods "singular."

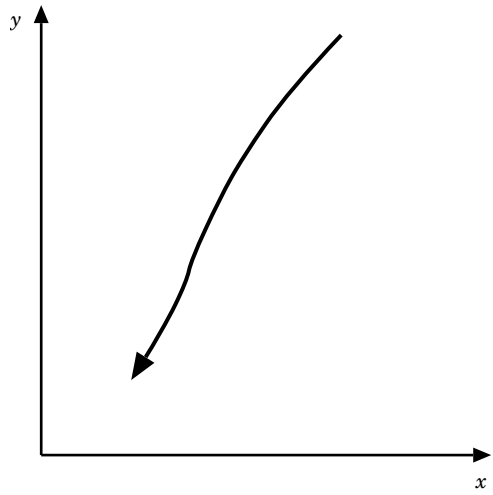

Figure 2. A schematic picture of the flow for Eq. (4).

A typical example is seen in hydrodynamics when we set the viscosity equal to zero. Since the viscosity appears in the term of the highest differential degree in the Navier–Stokes equation, setting the viscosity equal to zero reduces the degree of the equation, leading to nonexistence of solutions for arbitrary boundary conditions.

In our case, by combining both Fig. 1 and Fig. 2, we can display a schematic picture of the flow for $\varepsilon = 0$ in Fig. 3. Here, in order to indicate that there exist two time scales, we use double arrows for fast movement and use a single arrow for slow movement.

Based on Fig. 3, we expect a flow for a small and positive ε as shown in Fig. 4. In Fig. 4, the behavior of the system consists of the two types of movement: the fast one, which runs almost parallel to the $\boldsymbol{x}$ axis, and the slow one on the manifold $(\boldsymbol{x}_0(\boldsymbol{y}), \boldsymbol{y})$.

Thus, the singular perturbation generates a hierarchical structure consisting of fast and slow movements. Clearly, we must now ask under what criterion we can justify, based on the flow in Fig. 3, that the flow for a small and positive ε would be the one in Fig. 4.

III. NORMALLY HYPERBOLIC INVARIANT MANIFOLDS (NHIMs)

Normal hyperbolicity enables us to derive the flow for $\varepsilon > 0$ from the singular case with $\varepsilon = 0$. This criterion was presented by Fenichel in Refs. 4–6 and was

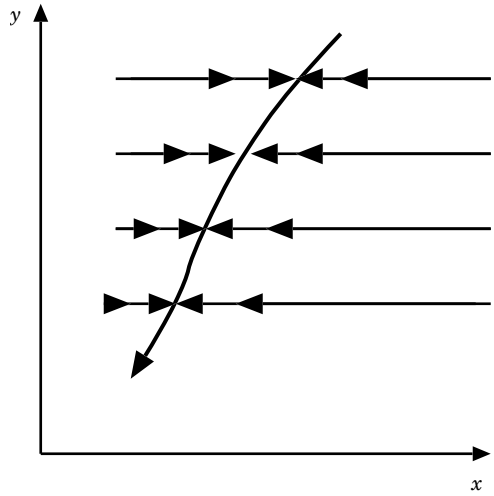

Figure 3. A schematic picture of the flow Eq. (1) for $\varepsilon = 0$, which is obtained by combining the flows described by Eqs. (3) and (4).

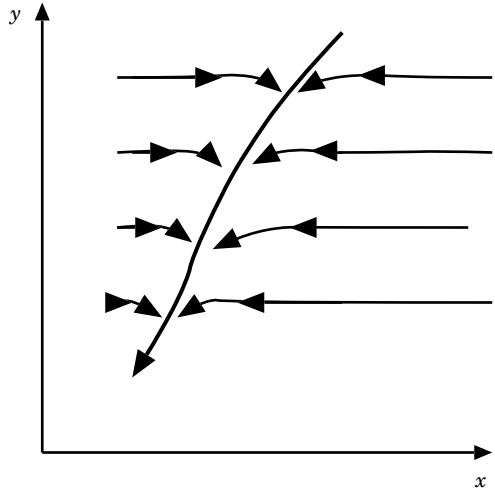

Figure 4. A schematic picture of the flow Eq. (1) for a small and positive ε which is expected from Fig. 3.

described independently by Hirsch et al. in Ref. 8. Readable accounts of their works can be found in Refs. 26 and 27. See also Refs. 28 and 29 for more detailed accounts. Here, we provide an intuitive representation of the ideas presented in these articles and show how they work.

Let M_0 denote the manifold that is defined by the graph $(\boldsymbol{x}_0(\boldsymbol{y}), \boldsymbol{y})$ for $\varepsilon = 0$. Roughly speaking, normal hyperbolicity of the manifold M_0 means that the absolute values of the Lyapunov exponents along the normal directions of M_0 are much larger than those along the tangent directions of M_0. In other words, there exists a gap between them.

The normal directions of the manifold M_0 would have negative and positive Lyapunov exponents. By following, backward in time, the directions with the negative Lyapunov exponents, we construct the stable manifold W_0^s of M_0. By following, forward in time, the directions with the positive Lyapunov exponents, we construct the unstable manifold W_0^u of M_0. In Fig. 3 where a schematic picture of a NHIM M_0 is displayed, we only show the stable manifold of M_0. In general, however, a NHIM M_0 has both stable and unstable manifolds.

As for the term "invariant," it means that orbits starting on a NHIM stay on it at least locally in time for both forward and backward directions. However, due attention must be paid to the following. In general, a NHIM will have boundaries where orbits starting on it flow off the manifold. This is because the flow on it could reach those locations where normal hyperbolicity breaks down. Later in this chapter we will mention an example of this behavior.

For the case of normal hyperbolicity, the theorem proved by Fenichel and independently by Hirsch et al. guarantees the following: For a small and positive ε, there exists a NHIM M_ε with stable and unstable manifolds, W_ε^s and W_ε^u, respectively. The NHIM M_ε varies smoothly with respect to the parameter ε. Moreover, W_ε^s and W_ε^u also vary smoothly with respect to the parameter ε at least locally near the NHIM M_ε.

In the following, we derive an explicit expression for M_ε using the facts that M_ε is invariant and that it depends smoothly on ε. Then, we will see that the singular perturbation with respect to the parameter ε becomes regular [7].

First, we derive the condition that M_ε is invariant under the flow of Eqs. (1). Let $(\boldsymbol{x} = \boldsymbol{x}_\varepsilon(\boldsymbol{y}), \boldsymbol{y})$ denote one of the graphs of the manifold M_ε. Then, its invariance is expressed as follows.

Let us take a derivative of $\boldsymbol{x}_\varepsilon(\boldsymbol{y}(t))$ with respect to t and multiply it by ε, that is,

$$\varepsilon \frac{d\boldsymbol{x}_\varepsilon}{dt} = \varepsilon \frac{d\boldsymbol{x}_\varepsilon}{d\boldsymbol{y}} \cdot \frac{d\boldsymbol{y}}{dt} \tag{6}$$

In order for the graph $\boldsymbol{x}_\varepsilon(\boldsymbol{y}(t))$ to be invariant, the time development of $\boldsymbol{x}$ caused by the time development of $\boldsymbol{y}$ should coincide with that of $\boldsymbol{x}$ under the flow of

Eqs. (1). This means that the equation obtained by substituting the second of Eqs. (1) for $d\boldsymbol{y}/dt$ in the right-hand side of Eq. (6) should be the same as the one obtained by substituting the first of Eqs. (1) for the left-hand side of Eq. (6), that is,

$$\boldsymbol{f}(\boldsymbol{x}_\varepsilon(\boldsymbol{y}),\boldsymbol{y}) = \varepsilon \frac{d\boldsymbol{x}_\varepsilon}{d\boldsymbol{y}} \cdot \boldsymbol{g}(\boldsymbol{x}_\varepsilon(\boldsymbol{y}),\boldsymbol{y}) \tag{7}$$

This is the condition that the manifold defined by $\boldsymbol{x} = \boldsymbol{x}_\varepsilon(\boldsymbol{y})$ is invariant under the flow of Eqs. (1).

Second, because of the smooth dependence of M_ε on ε, the graph $\boldsymbol{x}_\varepsilon(\boldsymbol{y})$ can be expanded with respect to ε as follows:

$$\boldsymbol{x}_\varepsilon(\boldsymbol{y}) = \boldsymbol{x}_0(\boldsymbol{y}) + \varepsilon \boldsymbol{x}_0^{(1)}(\boldsymbol{y}) + O(\varepsilon^2) \tag{8}$$

Note that this expansion can be continued to higher orders, as far as the condition for smoothness guarantees.

Now, let us combine Eqs. (7) and (8). Substitute the expansion Eq. (8) into the condition for the invariance, Eq. (7), and use the Taylor expansion for $\boldsymbol{f}(\boldsymbol{x}, \boldsymbol{y})$ and $\boldsymbol{g}(\boldsymbol{x}, \boldsymbol{y})$ with respect to $\boldsymbol{x}$ around $\boldsymbol{x}_0(\boldsymbol{y})$. We then obtain the following:

$$\begin{aligned} &\boldsymbol{f}(\boldsymbol{x}_0(\boldsymbol{y}),\boldsymbol{y}) + \varepsilon \frac{\partial \boldsymbol{f}}{\partial \boldsymbol{x}}(\boldsymbol{x}_0(\boldsymbol{y}),\boldsymbol{y}) \cdot \boldsymbol{x}_0^{(1)}(\boldsymbol{y}) + O(\varepsilon^2) \\ &= \varepsilon \left(\frac{d\boldsymbol{x}_0}{d\boldsymbol{y}}(\boldsymbol{y}) + O(\varepsilon) \right) \cdot (\boldsymbol{g}(\boldsymbol{x}_0(\boldsymbol{y}),\boldsymbol{y}) + O(\varepsilon)) \end{aligned} \tag{9}$$

Here, note that $\boldsymbol{f}(\boldsymbol{x}_0(\boldsymbol{y}),\boldsymbol{y}) = \boldsymbol{0}$. Then, Eq. (9) can be solved successively with respect to the order of ε. In other words, the perturbation using Eq. (9) is regular.

For example, the equation for the lowest-order correction $\boldsymbol{x}_0^{(1)}(\boldsymbol{y})$ is the following:

$$\frac{\partial \boldsymbol{f}}{\partial \boldsymbol{x}}(\boldsymbol{x}_0(\boldsymbol{y}),\boldsymbol{y}) \cdot \boldsymbol{x}_0^{(1)}(\boldsymbol{y}) = \frac{d\boldsymbol{x}_0}{d\boldsymbol{y}}(\boldsymbol{y}) \cdot \boldsymbol{g}(\boldsymbol{x}_0(\boldsymbol{y}),\boldsymbol{y}) \tag{10}$$

Thus, when the matrix $A \equiv \partial \boldsymbol{f}/\partial \boldsymbol{x}(\boldsymbol{x}_0(\boldsymbol{y}),\boldsymbol{y})$ is invertible, $\boldsymbol{x}_0^{(1)}(\boldsymbol{y})$ is obtained using Eq. (10) as follows:

$$\boldsymbol{x}_0^{(1)}(\boldsymbol{y}) = \left(\frac{\partial \boldsymbol{f}}{\partial \boldsymbol{x}}(\boldsymbol{x}_0(\boldsymbol{y}),\boldsymbol{y}) \right)^{-1} \cdot \frac{d\boldsymbol{x}_0}{d\boldsymbol{y}}(\boldsymbol{y}) \cdot \boldsymbol{g}(\boldsymbol{x}_0(\boldsymbol{y}),\boldsymbol{y}) \tag{11}$$

The higher-order corrections with respect to ε can be obtained similarly.

The condition that the matrix A has an inverse plays a crucial role in the above derivation. Here, we explain that this condition is satisfied when the manifold M_0 is normally hyperbolic. Let us study the time development of a small deviation $\delta\boldsymbol{x}$ from the manifold M_0 under the fast time variable τ. Substitute $\boldsymbol{x}(\tau) = \boldsymbol{x}_0(\boldsymbol{y}) + \delta\boldsymbol{x}(\tau)$ into Eq. (3) and note that the slow variable $\boldsymbol{y}$ is constant. Then, the linear equation for $\delta\boldsymbol{x}$ is

$$\frac{d\delta\boldsymbol{x}}{d\tau} = \frac{\partial \boldsymbol{f}}{\partial \boldsymbol{x}}(\boldsymbol{x}_0(\boldsymbol{y}), \boldsymbol{y}) \cdot \delta\boldsymbol{x}(\tau) \tag{12}$$

Recall that normal hyperbolicity of M_0 means that the movement along directions normal to M_0 is hyperbolic even when we use the fast time variable. In other words, the matrix A has eigenvalues with nonzero real parts. Thus, A has an inverse.

Based on the above, we see that the eigenvectors of the matrix A give us the linear approximation to the stable and unstable manifolds of M_0. The coordinate system which is based on these eigenvectors for M_0 changes smoothly to the coordinate system for the flow near M_ϵ. Using this coordinate system, the flow near M_ϵ is expressed in the Fenichel normal form. Moreover, the Fenichel normal form shows the remarkable property that the flow on the stable and unstable manifolds of M_ε is "foliated" [7,26,27], as we now explain.

First, transform the variables to read $(\boldsymbol{x}', \boldsymbol{y}) = (\boldsymbol{x} - \boldsymbol{x}_0(\boldsymbol{y}), \boldsymbol{y})$, and let $(\boldsymbol{x}, \boldsymbol{y})$ denote $(\boldsymbol{x}', \boldsymbol{y})$ for simplicity. For the normal directions of the manifold M_0, the eigenvectors of the matrix $A \equiv \frac{\partial \boldsymbol{f}}{\partial \boldsymbol{x}}(\boldsymbol{0}, \boldsymbol{y})$ offer the linear approximation to the stable and unstable manifolds of M_0; the coordinates beyond the linear approximation are obtained by following these eigenvectors in the backward and forward directions in time, respectively. Let $\boldsymbol{a}$ and $\boldsymbol{b}$ denote the coordinates thus obtained along the unstable and stable manifolds, respectively. Then, the stable manifold W_0^s is given by $\boldsymbol{a} = \boldsymbol{0}$, and the unstable manifold W_0^u is given by $\boldsymbol{b} = \boldsymbol{0}$ and $\boldsymbol{x} = (\boldsymbol{a}, \boldsymbol{b})$. A schematic picture of these manifolds is shown in Fig. 5.

Using the coordinate system $(\boldsymbol{a}, \boldsymbol{b}, \boldsymbol{y})$ and the fast time variable τ, the flow along the normal directions near the NHIM M_0 is given by

$$\begin{aligned} \frac{d\boldsymbol{a}}{d\tau} &= f_{\boldsymbol{a}}(\boldsymbol{a}, \boldsymbol{b}, \boldsymbol{y}) \cdot \boldsymbol{a} \\ \frac{d\boldsymbol{b}}{d\tau} &= f_{\boldsymbol{b}}(\boldsymbol{a}, \boldsymbol{b}, \boldsymbol{y}) \cdot \boldsymbol{b} \end{aligned} \tag{13}$$

where the vectors $\boldsymbol{a}$ and $\boldsymbol{b}$ are factored out of $\boldsymbol{f}(\boldsymbol{a}, \boldsymbol{b}, \boldsymbol{y})$, leaving the matrices denoted by $f_{\boldsymbol{a}}$ and $f_{\boldsymbol{b}}$, respectively. This result comes from the invariance of the manifolds W_0^s and W_0^u defined, respectively, by $\boldsymbol{a} = \boldsymbol{0}$ and $\boldsymbol{b} = \boldsymbol{0}$.

For a small and positive ε, the stable and unstable manifolds W_ε^s and W_ε^u of the NHIM M_ε also exist because of the theorem by Fenichel and Hirsch et al.

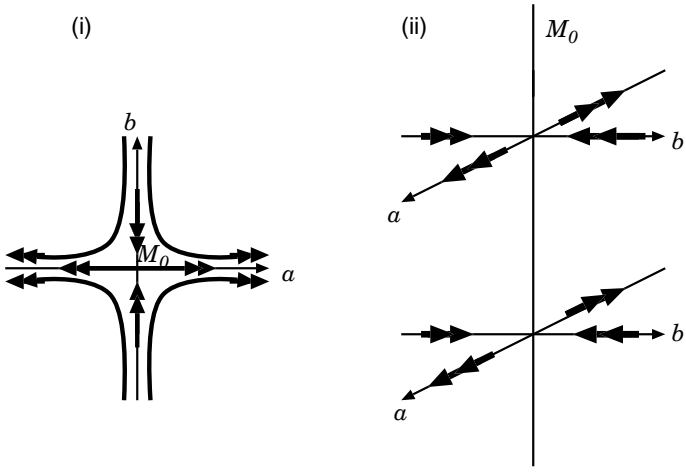

Figure 5. The stable and unstable manifolds of M_0.

Moreover, they smoothly depend on the parameter ε. Then, we can transform Eqs. (2) locally near M_ε into the following form:

$$\begin{aligned}
\frac{d\boldsymbol{a}}{d\tau} &= f_{\boldsymbol{a}}(\boldsymbol{a},\boldsymbol{b},\boldsymbol{y})\cdot\boldsymbol{a} \\
\frac{d\boldsymbol{b}}{d\tau} &= f_{\boldsymbol{b}}(\boldsymbol{a},\boldsymbol{b},\boldsymbol{y})\cdot\boldsymbol{b} \\
\frac{d\boldsymbol{y}}{d\tau} &= \varepsilon(\boldsymbol{g}_0(\boldsymbol{y}) + g_1(\boldsymbol{a},\boldsymbol{b},\boldsymbol{y})\cdot\boldsymbol{ab})
\end{aligned} \tag{14}$$

Eqs. (14) are called the Fenichel normal form. Here, $(\boldsymbol{a},\boldsymbol{b})$ represent the coordinate system along the normal directions of M_ε obtained by a smooth transformation from $(\boldsymbol{a},\boldsymbol{b})$ of M_0. We use the same notation for both of the coordinate systems of M_0 and M_ε. In the third equation of Eqs. (14), $\boldsymbol{ab}$ represents the tensor product between $\boldsymbol{a}$ and $\boldsymbol{b}$. The kth element of $g_1(a,b,y)\cdot\boldsymbol{ab}$ stands for $\sum_{i,j}\{g_1(\boldsymbol{a},\boldsymbol{b},\boldsymbol{y})\}_{k,i,j}a_ib_j$.

A remarkable aspect of the Fenichel normal form is that, in the third equation of Eqs. (14), the coupling term between the tangent directions and the normal directions involves only the tensor product $\boldsymbol{ab}$. This means that for $\boldsymbol{a}=\boldsymbol{0}$ (or $\boldsymbol{b}=\boldsymbol{0}$) the time development along the normal directions does not affect the movement of the base points, which are obtained by projecting points on W^s_ε (or W^u_ε) to M_ε. See Fig. 6 for a schematic picture of orbits on W^s_ε and the movement of their base points on M_ε.

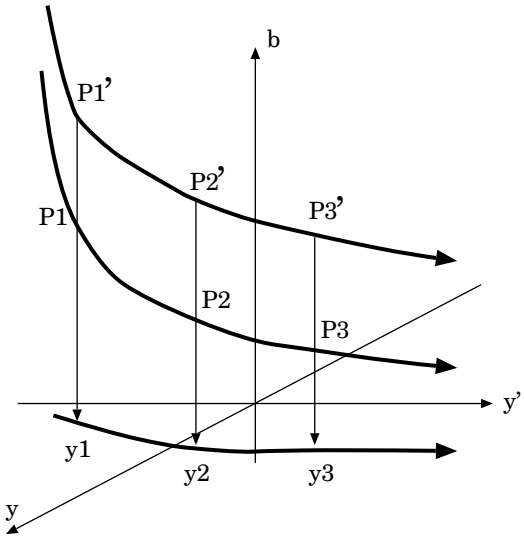

Figure 6. Foliation of the stable manifold by the Fenichel normal form.

In Fig. 6, the dynamics on the three-dimensional stable manifold is shown near the two-dimensional NHIM. Here, b denotes the coordinate along the normal direction, and (y, y') denotes the coordinates on the NHIM.

In Fig. 6, the dynamics on W^s_ε can be decomposed into the movement along the normal directions and the flow on the manifold M_ε. Note that the time development of b does not affect the movement of the base points. Suppose two points P1 and P1′ on W^s_ε with the same base point y1. Then, the orbit from P1 through P2 reaching P3 and the one from P1′ through P2′ reaching P3′ are projected to the same movement of the base points on M_ε from y1 through y2 reaching y3. In other words, the three-dimensional invariant manifold W^s_ε consists of two-dimensional invariant manifolds that correspond to the movements of the base points. Then, in mathematics, we say that the three-dimensional stable manifold is ''foliated'' by two-dimensional leaves. This structure is called ''foliation'' [28,30].

Thus, the Fenichel normal form provides us with foliation of the stable and unstable manifolds of the NHIM M_ε. Moreover, their foliation smoothly depends on the parameter ε from $\varepsilon = 0$ to a small and positive ε locally near the NHIM.

Points that are on neither W^s_ε nor W^u_ε behave as follows near the manifold M_ε. First, they move almost parallel to the flow on the stable manifold W^s_ε. After coming close to M_ε, they move following the slow movement on M_ε. Finally, they leave M_ε almost parallel to the flow on the unstable manifold W^u_ε. We show these features in Fig. 7.

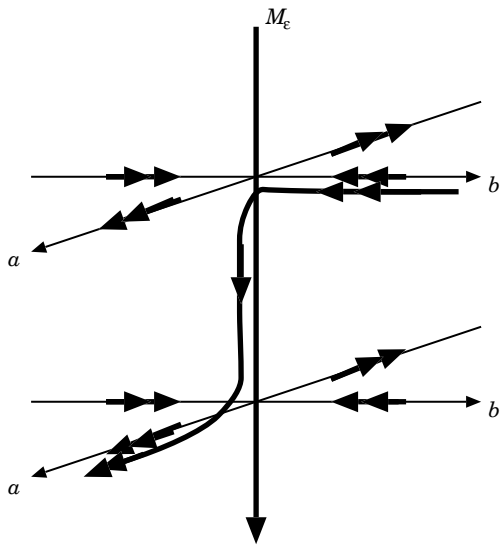

Figure 7. A schematic picture of the flow near M_ε.

IV. LIE PERTURBATION

Until now, we have discussed NHIMs in general dynamical systems. In this section, we limit our argument to Hamiltonian systems and show how singular perturbation theory works. In particular, we discuss NHIMs in the context of reaction dynamics. First, we explain how NHIMs appear in conventional reaction theory. Then, we will show that Lie perturbation theory applied to the Hamiltonian near a saddle with index 1 actually transforms the equation of motion near the saddle to the Fenichel normal form. This normal form can be considered as an extension of the Birkhoff normal form from stable fixed points to saddles with index 1 [2]. Finally, we discuss the transformation near saddles with index larger than 1.

Let $\boldsymbol{q} = (q_1, q_2, \ldots, q_N)$ and $\boldsymbol{p} = (p_1, p_2, \ldots, p_N)$ denote the positions and the momenta for a system of N degrees of freedom, respectively, where q_m and $p_m (m = 1, 2, \ldots, N)$ are canonically conjugate. For a saddle with index 1, let q_1 denote the coordinate along the eigenvector with the negative eigenvalue of the Hessian matrix of the potential.

In the conventional theory, a saddle with index 1 corresponds to a transition state. Near a saddle, the NHIM M_0 exists above it in the phase space. The NHIM M_0 consists of those orbits with $q_1 = 0$ and $p_1 = 0$—that is, the vibrational motions involving (q_n, p_n) for $n = 2, \ldots, N$ above the saddle. Thus, its

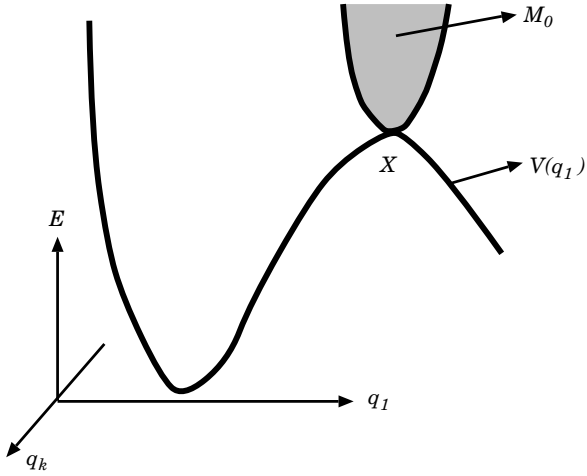

Figure 8. A saddle of the potential and the NHIM above it.

dimension is $2N-2$ in the phase space. See Fig. 8 for a schematic picture showing the saddle $\boldsymbol{X}$ with index 1 and the NHIM M_0 above it. Here, the direction perpendicular to the q_1 axis schematically indicates vibrational degrees of freedom. Similarly for a saddle with index L, a NHIM with dimension $2N-2L$ exists above it in the phase space.

In the following, suppose that $\boldsymbol{q}=\boldsymbol{0}$ is a saddle of the potential. Then, using a Taylor expansion around $\boldsymbol{q}=\boldsymbol{0}$, the Hamiltonian can be written in the form

$$H(\boldsymbol{p},\boldsymbol{q})=\sum_{j=2}^{\infty}H_j(\boldsymbol{p},\boldsymbol{q}) \tag{15}$$

where H_j consists of the terms of jth degree with respect to q_m and $p_m (m=1,2,\ldots,N)$. The lowest-order term, H_2, is given by

$$H_2(\boldsymbol{p},\boldsymbol{q})=\tfrac{1}{2}\omega_1(p_1^2-q_1^2)+\tfrac{1}{2}\sum_{n=2}^{N}\omega_n(p_n^2+q_n^2) \tag{16}$$

Since (q_1,p_1) is the degree of freedom corresponding to the negative eigenvalue of the Hessian matrix of the potential, the sign of its lowest potential term is minus—that is, the inverse harmonic potential. For other degrees of freedom, the lowest-order terms of their potentials describe harmonic oscillators. Therefore, they are vibrational degrees of freedom. In Eq. (16), we normalize the coefficients of the Hamiltonian so that they are written as $\omega_m\,(m=1,2,\ldots,N)$.

Now, we apply Lie perturbation theory to the Hamiltonian (15) to derive the Fenichel normal form. In the Lie transformation, we use the variables $(\boldsymbol{z},\bar{\boldsymbol{z}})$ for convenience. For the vibrational degrees of freedom, $(z_n,\bar{z}_n)$ are the following complex conjugate variables:

$$z_n = p_n + iq_n, \qquad \bar{z}_n = p_n - iq_n \qquad (n = 2,\ldots,N) \tag{17}$$

and, for the reaction coordinate, the following pair of real variables,

$$z_1 = p_1 + q_1, \qquad \bar{z}_1 = p_1 - q_1 \tag{18}$$

Then, the Poisson bracket is expressed in $(\boldsymbol{z},\bar{\boldsymbol{z}})$ as follows:

$$[f,g] = 2\left(\frac{\partial f}{\partial z_1}\frac{\partial g}{\partial \bar{z}_1} - \frac{\partial f}{\partial \bar{z}_1}\frac{\partial g}{\partial z_1}\right) + 2i\sum_{n=2}^{N}\left(\frac{\partial f}{\partial z_n}\frac{\partial g}{\partial \bar{z}_n} - \frac{\partial f}{\partial \bar{z}_n}\frac{\partial g}{\partial z_n}\right) \tag{19}$$

Suppose that $(\boldsymbol{q},\boldsymbol{p})$ is transformed into $(\boldsymbol{q}',\boldsymbol{p}')$, and the transformed Hamiltonian is $K(\boldsymbol{q}',\boldsymbol{p}')$. For $(\boldsymbol{q},\boldsymbol{p})$ we define $(\boldsymbol{z},\bar{\boldsymbol{z}})$, and for $(\boldsymbol{q}',\boldsymbol{p}')$ we use $(\boldsymbol{z}',\bar{\boldsymbol{z}}')$, by Eqs. (17) and (18), respectively. Let e^F denote the Lie transformation, which transforms $(\boldsymbol{z}',\bar{\boldsymbol{z}}')$ to $(\boldsymbol{z},\bar{\boldsymbol{z}})$:

$$\begin{aligned} \boldsymbol{z} &= e^F\boldsymbol{z}' \\ \bar{\boldsymbol{z}} &= e^F\bar{\boldsymbol{z}}' \end{aligned} \tag{20}$$

Then, the transformed Hamiltonian $K(\boldsymbol{z}',\bar{\boldsymbol{z}}')$ is given by

$$\begin{aligned} K(\boldsymbol{z}',\bar{\boldsymbol{z}}') &= H(\boldsymbol{z}(\boldsymbol{z}',\bar{\boldsymbol{z}}'),\bar{\boldsymbol{z}}(\boldsymbol{z}',\bar{\boldsymbol{z}}')) \\ &= H(e^F\boldsymbol{z}', e^F\bar{\boldsymbol{z}}') \\ &= e^F H(\boldsymbol{z}',\bar{\boldsymbol{z}}') \end{aligned} \tag{21}$$

Here, we use the same notation for Hamiltonians in the variables $(\boldsymbol{z},\bar{\boldsymbol{z}})$ as those in $(\boldsymbol{q},\boldsymbol{p})$. There will not be any confusion with this notation, since only the expressions using $(\boldsymbol{z},\bar{\boldsymbol{z}})$ will appear from now on.

In the last line of Eq. (21), only the variables $(\boldsymbol{z}',\bar{\boldsymbol{z}}')$ appear. From now on, we will use $(\boldsymbol{z},\bar{\boldsymbol{z}})$ instead of $(\boldsymbol{z}',\bar{\boldsymbol{z}}')$ for convenience.

We will use the Lie transformation where F in Eq. (20) is given by a polynomial f_k, which consists of kth-order terms as follows:

$$F_k g \equiv [g, f_k] \tag{22}$$

Using F_k for k which is greater than or equal to 3, we define a series of Lie transformations as follows:

$$\begin{aligned} K^{(2)} &= H \\ K^{(k)} &= e^{F_k} K^{(k-1)} \qquad (k \geq 3) \end{aligned} \tag{23}$$

When we use $K^{(k)} = \sum_{j=2}^{\infty} K_j^{(k)}$, where $K_j^{(k)}$ is a polynomial that consists of jth-order terms, we have the following expressions:

$$\begin{aligned} K_j^{(k)} &= K_j^{(k-1)} \qquad (k-1 \geq j \geq 2) \\ K_k^{(k)} &= K_k^{(k-1)} + F_k K_2^{(k-1)} = K_k^{(k-1)} + F_k H_2 \end{aligned} \tag{24}$$

Note that in the variables $(z, \bar{z})$ the second-order terms are of the following form:

$$H_2 = \tfrac{1}{2} \sum_{m=1}^{N} \omega_m \bar{z}_m z_m \tag{25}$$

Therefore, the Lie transformation of the second-order terms is given by

$$F_k H_2 = \tfrac{1}{2} \sum_{m=1}^{N} [\omega_m \bar{z}_m z_m, f_k] = \omega_1 \left(\frac{\partial f_k}{\partial \bar{z}_1} \bar{z}_1 - \frac{\partial f_k}{\partial z_1} z_1 \right) + \sum_{n=2}^{N} i\omega_n \left(\frac{\partial f_k}{\partial \bar{z}_n} \bar{z}_n - \frac{\partial f_k}{\partial z_n} z_n \right) \tag{26}$$

Let us calculate $F_k H_2$ for polynomials f_k that consist of kth-order terms. In general, polynomials $f_k (k \geq 3)$ are given by

$$f_k = \sum_{\substack{\alpha_1, \ldots, \alpha_N \\ \beta_1, \ldots, \beta_N \\ \sum \alpha_m + \sum \beta_m = k}} A_{\boldsymbol{\alpha}, \boldsymbol{\beta}} z_1^{\alpha_1} \cdots z_N^{\alpha_N} \bar{z}_1^{\beta_1} \cdots \bar{z}_N^{\beta_N}. \tag{27}$$

Here, $A_{\boldsymbol{\alpha}, \boldsymbol{\beta}}$ denote constant coefficients, and the sum runs over all the possible $\boldsymbol{\alpha} = (\alpha_1, \alpha_2, \ldots, \alpha_N)$ and $\boldsymbol{\beta} = (\beta_1, \beta_2, \ldots, \beta_N)$, where α_m and β_m $(m = 1, 2, \ldots, N)$ are nonnegative integers and they sum to k. Then, the Lie transformation $F_k H_2$ defined by a polynomial f_k is expressed as follows:

$$F_k H_2 = \sum_{\boldsymbol{\alpha}, \boldsymbol{\beta}} A_{\boldsymbol{\alpha}, \boldsymbol{\beta}} \left\{ \omega_1 (\beta_1 - \alpha_1) + \sum_{n=2}^{N} i\omega_n (\beta_n - \alpha_n) \right\} z_1^{\alpha_1} \cdots z_N^{\alpha_N} \bar{z}_1^{\beta_1} \cdots \bar{z}_N^{\beta_N} \tag{28}$$

The sum $\sum_{\boldsymbol{\alpha}, \boldsymbol{\beta}}$ in Eq. (28) runs the same way as that in Eq. (27).

From Eq. (28), we know that all the terms in $K_k^{(k-1)}$ except for those with $\alpha_1 = \beta_1$ can be eliminated by the Lie transformation—that is, by suitably choosing the coefficients $A_{\boldsymbol{\alpha},\boldsymbol{\beta}}$ in the second equation of Eq. (24). This means that the degree of freedom $(z_1, \bar{z}_1)$, which corresponds to the reaction coordinate, only appears as a product of $z_1\bar{z}_1$ in the transformed Hamiltonian $K(\boldsymbol{z}, \bar{\boldsymbol{z}})$ as follows:

$$K(\boldsymbol{z}, \bar{\boldsymbol{z}}) = z_1\bar{z}_1 v(z_1\bar{z}_1, z_2, \bar{z}_2, \ldots, z_N, \bar{z}_N) + u(z_2, \bar{z}_2, \ldots, z_N, \bar{z}_N) \tag{29}$$

Then, the equations of motion for z_1 and $\bar{z}_1$ consist solely of those terms that are at least of first order in z_1 and $\bar{z}_1$, respectively. For vibrational degrees of freedom, the coupling terms with $(z_1, \bar{z}_1)$, involve only products of $z_1\bar{z}_1$ as follows:

$$\begin{aligned}
\frac{dz_1}{dt} &= z_1 v_1(z_1\bar{z}_1, z_2, \bar{z}_2, \ldots, z_N, \bar{z}_N) \\
\frac{d\bar{z}_1}{dt} &= \bar{z}_1 \bar{v}_1(z_1\bar{z}_1, z_2, \bar{z}_2, \ldots, z_N, \bar{z}_N) \\
\frac{dz_n}{dt} &= u_n(z_2, \bar{z}_2, \ldots, z_N, \bar{z}_N) + z_1\bar{z}_1 v_n(z_1\bar{z}_1, z_2, \bar{z}_2, \ldots, z_N, \bar{z}_N) \\
\frac{d\bar{z}_n}{dt} &= \bar{u}_n(z_2, \bar{z}_2, \ldots, z_N, \bar{z}_N) + z_1\bar{z}_1 \bar{v}_n(z_1\bar{z}_1, z_2, \bar{z}_2, \ldots, z_N, \bar{z}_N) \qquad (n = 2, \ldots, N)
\end{aligned} \tag{30}$$

Here, the functions u_m and v_m for $m = 1, \ldots, N$ are derived from u and v using Hamilton's equations of motion, and $\bar{u}_m$ and $\bar{v}_m$ are the complex conjugates of u_m and v_m, respectively. This set of equations Eq. (30) is the Fenichel normal form.

Note that, for those terms with $\alpha_1 = \beta_1$, the problem of eliminating higher-order terms is the same as that in the Birkhoff normal form for stable fixed points. Then, it is possible to eliminate higher-order terms as long as the set of frequencies ω_n $(n = 2, \ldots, N)$ satisfies the nonresonance condition

$$\sum_{n=2}^{N} \omega_n(\alpha_n - \beta_n) \neq 0 \tag{31}$$

for any sets of nonnegative integers α_n, β_n $(n = 2, \ldots, N)$. In other words, as long as frequencies ω_n $(n = 2, \ldots, N)$ are nonresonant, we can eliminate all of the terms in $K_k^{(k-1)}$ except for those with $\alpha_n = \beta_n$ $(\forall n = 2, \ldots, N)$.

Thus, all the terms that cannot be eliminated by the Lie transformation are products of the form $|z_2|^2, \ldots, |z_N|^2$. By noting the relation

$$|z_n|^2 = p_n^2 + q_n^2 = 2I_n \tag{32}$$

where I_n denotes the action of the harmonic oscillator, we see that these terms are represented by the action variables of the harmonic oscillators. Therefore, if the limit converges, after multiplying the Lie transformations with successively larger k—that is, if the expression

$$e^{F_k} e^{F_{k-1}} \cdots e^{F_3} \tag{33}$$

converges as $k \to \infty$—the transformed Hamiltonian is written solely with the action variables of the vibrational motions and the reaction coordinate.

The above situation is the same as for the celebrated theorem of Kolmogorov–Arnold–Moser (KAM)—that is, the problem of small denominators. The convergence can be proved for sufficiently nonresonant combinations of the vibrational frequencies [31]. In other words, when tori of the vibrational motions on the NHIM M_0 are sufficiently nonresonant, they survive under small perturbations.

Thus, the Lie transformation brings the Hamiltonian locally near a saddle with index 1 into the Fenichel normal form. In addition, we find that, on the NHIM, tori with sufficiently nonresonant frequencies survive.

For saddles with index L with $L > 1$, note the following point when we use the Lie transformation. For these saddles, one may wonder whether "resonance" can occur among the normal directions in the following sense. If a set of nonnegative integers $n_{l'}$ $(l' = 1, \ldots, L)$ exists where all of its elements are not zero, such that $\sum_{l'=1}^{L} \omega_{l'} n_{l'} = 0$ holds, then "resonance" occurs among the normal directions of the NHIM of the saddle. Here, $l' = 1, \ldots, L$ stand for the degrees of freedom corresponding to the negative eigenvalues of the Hessian matrix of the potential at the saddle. However, "resonance" does not matter in transforming to the Fenichel normal form as we explain now.

For saddles with index L with $L > 1$, the Hamiltonian has L degrees of freedom

$$z_l = p_l + q_l, \qquad \bar{z}_l = p_l - q_l \qquad (l = 1, \ldots, L) \tag{34}$$

which correspond to the negative eigenvalues of the Hessian matrix, and $N - L$ degrees of freedom

$$z_n = p_n + iq_n, \qquad \bar{z}_n = p_n - iq_n \qquad (n = L + 1, \ldots, N) \tag{35}$$

which correspond to the positive eigenvalues of the Hessian matrix. Here, $(z_1 = 0, \ldots, z_L = 0)$ gives the linear approximation of the stable manifold and $(\bar{z}_1 = 0, \ldots, \bar{z}_L = 0)$ gives that of the unstable manifold.

For saddles where "resonance" does not take place, we can use the Lie transformation in a similar way to saddles with index 1. Then, only those terms

with $\alpha_{l'} = \beta_{l'}$ $(\forall l' = 1, \ldots, L)$ remain in the transformed Hamiltonian—that is, those terms where $z_{l'}, \bar{z}_{l'}$ appear as products $z_{l'}\bar{z}_{l'}$ $(l' = 1, \ldots, L)$. On the other hand, for saddles where "resonance" occurs, those terms with $\alpha_{l'} \neq \beta_{l'}$ $(\exists l' = 1, \ldots, L)$ also remain in the transformed Hamiltonian. However, these terms always involve coordinates of both the stable and unstable manifolds. In other words, they have both $z_{l'}$ and $\bar{z}_{l''}$ for some l', l'' $(l', l'' = 1, \ldots, L)$, because, in order to satisfy the condition $\sum_{l'=1}^{L} \omega_n(\alpha_n - \beta_n) = 0$, $\alpha_{l'}$ and $\beta_{l''}$ must be nonzero for some l', l'' $(l', l'' = 1, \ldots, L)$. Thus, even when "resonance" takes place, the transformed Hamiltonian takes the Fenichel normal form.

V. MELNIKOV INTEGRAL

Until now we have discussed local aspects of the dynamics near NHIMs with saddles with index 1. In the second stage of our strategy, we are interested in how the dynamics near these NHIMs are connected with each other. The information on this feature of the dynamics is offered by the intersections between the stable and unstable manifolds of NHIMs.

In this section, we will introduce the Melnikov integral, which estimates the gaps between stable and unstable manifolds. Thus, if the Melnikov integral attains the value zero, this signals the existence of intersections between stable and unstable manifolds. If the intersection is transversal, it implies the existence of horseshoe dynamics [32], that is, chaotic behavior. On the other hand, if the intersection is tangent [11], it implies that the system is at a transition between different kinds of dynamics [12]. Such transitions of chaotic behavior are called crisis [13]. The tangency will be further analyzed in Section VII.

The Melnikov integral also offers a method to estimate the reaction rates for systems with two degrees of freedom. This idea comes from the work of Davis and Gray [9]. However, their idea breaks down for systems with more than two degrees of freedom because of tangency [11,14]. This breakdown requires a new conceptual structure to describe the reaction dynamics from the viewpoint of multiple-dimensional chaos. What we propose for this new concept is the skeleton of reaction paths, where the connections among NHIMs are the focus of our study.

In this section we derive the Melnikov integral, following Ref. 24 with some corrections.

We consider a model Hamiltonian that consists of a one-degree-of-freedom reaction coordinate coupled with n degrees of freedom that are vibrational modes. Thus, the total number, N, of the degrees of freedom is $n + 1$. The reaction coordinate is a degree of freedom that has an unstable fixed point. The position of the fixed point corresponds to a saddle with index 1 of the whole system—that is, a transition state in the conventional sense. The n-degrees-of-freedom vibrational modes are, in general, nonlinear. Moreover, when the

coupling between the vibrational modes and the reaction coordinate vanishes, they are integrable.

The reaction processes result from interactions between the reaction coordinate and the vibrational modes. The Melnikov integral estimates the gap caused by these interactions. The integral also gives the reaction rate—that is, the magnitude of the flow over the saddle when there exists no tangency.

Let $\boldsymbol{x} = (q, p)$ denote the one-degree-of-freedom reaction coordinate. For n-degrees-of-freedom vibrational modes, $\boldsymbol{I} \in \mathbf{R}^n$ and $\boldsymbol{\theta} \in \mathbf{T}^n$ denote their action and angle variables, respectively, where $\mathbf{T} = [0, 2\pi]$. These action and angle variables would be obtained by the Lie transformation, as we have discussed in Section IV. In reaction dynamics, the variables $(\boldsymbol{I}, \boldsymbol{\theta})$ describe the degrees of freedom of the intramolecular and possibly the intermolecular vibrational modes that couple with the reaction coordinate. In the conventional reaction rate theory, these vibrational modes are supposed to play the role of a heat bath for the reaction coordinate $\boldsymbol{x}$.

Now, we introduce the model Hamiltonian. Let the Hamiltonian H consist of two parts H_0 and H_1,

$$H(\boldsymbol{x}, \boldsymbol{I}, \boldsymbol{\theta}) = H_0(\boldsymbol{x}, \boldsymbol{I}) + \varepsilon H_1(\boldsymbol{x}, \boldsymbol{I}, \boldsymbol{\theta}) \tag{36}$$

Here, H_0 is an unperturbed part of the total Hamiltonian H and is supposed to describe the reaction coordinate and the vibrational modes when they are decoupled. H_1 consists of interactions between the reaction coordinate and the vibrational modes, and is considered as a perturbation to H_0. The constant ε is supposed to be small, that is, $0 < \varepsilon \ll 1$.

Furthermore, we suppose that H_0 is of the following form,

$$H_0(\boldsymbol{x}, \boldsymbol{I}) = H_0^r(\boldsymbol{x}, \boldsymbol{I}) + H_0^b(\boldsymbol{I}) \tag{37}$$

This means that the unperturbed motion of $\boldsymbol{x}$ may depend on the action variables of the vibrational modes. Thus, we do not need a separable Hamiltonian as the unperturbed part. The second term H_0^b describes vibrational motions, which are integrable and, in general, nonlinear.

As for the dynamics of $\boldsymbol{x}$ under the unperturbed Hamiltonian $H_0^r(\boldsymbol{x}, \boldsymbol{I})$, we assume that the reaction coordinate $\boldsymbol{x}$ has a saddle $\boldsymbol{X}(\boldsymbol{I}) = (Q(\boldsymbol{I}), P(\boldsymbol{I}))$. Its location, in general, depends on the action variables $\boldsymbol{I}$. Suppose that the saddle $\boldsymbol{X}(\boldsymbol{I})$ has a separatrix orbit $\boldsymbol{x}_0(t, \boldsymbol{I})$ connecting it with itself. See Fig. 9 for a schematic picture of the phase space $\boldsymbol{x} = (q, p)$ under the unperturbed Hamiltonian $H_0^r(\boldsymbol{x}, \boldsymbol{I})$. Here, we show the saddle $\boldsymbol{X}$ and the separatrix orbit on the two-dimensional phase space $\boldsymbol{x} = (q, p)$.

Nonseparable Hamiltonians will be necessary to describe reactions where the potential function and the saddle vary as the vibrational motions are excited. See

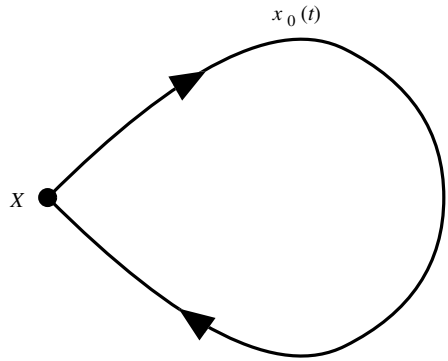

Figure 9. The fixed point and the separatrix of H_0^r.

Fig. 10 for an example where the potential explicitly depends on $\boldsymbol{I}$ as $V(q_1, \boldsymbol{I})$. Reaction processes involving enzymes can correspond to such cases. These reactions take place within a specific range of temperature. This temperature dependence results from the dependence of the saddle on $\boldsymbol{I}$, where the height of the saddle decreases for a specific range of the action values of the vibrational modes. Then, the reaction proceeds at those temperatures where the action variables are excited specifically to these values.

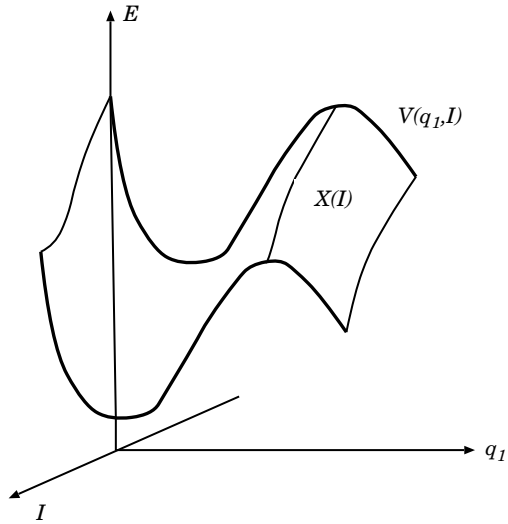

Figure 10. Potential function that depends on I.

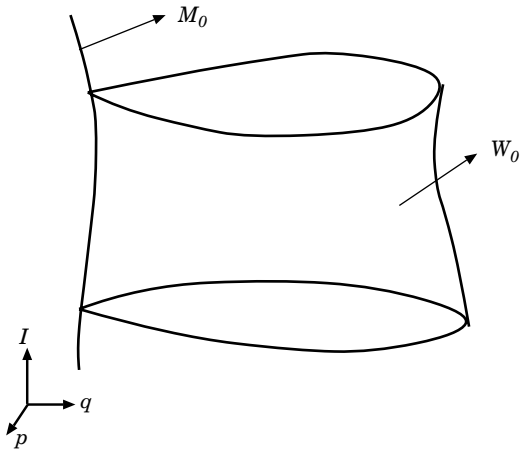

Figure 11. Invariant manifolds under the time development by H_0.

Here, we limit our argument to a system with a homoclinic connection—that is, a separatrix connecting a saddle with itself. The following argument can be straightforwardly extended to a system with a heteroclinic connection—that is, a separatrix connecting different saddles.

In the $(2n+2)$-dimensional phase space $(\boldsymbol{x}, \boldsymbol{I}, \boldsymbol{\theta})$, the saddle $\boldsymbol{X}(\boldsymbol{I})$ corresponds to an n-dimensional torus $T_0(\boldsymbol{I}) = \{(\boldsymbol{X}(\boldsymbol{I}), \boldsymbol{I}, \boldsymbol{\theta}) | \boldsymbol{\theta} \in \mathbf{T}\}$. It is a hyperbolic torus with an $(n+1)$-dimensional separatrix $S_0(\boldsymbol{I}) = \{(\boldsymbol{x}_0(t, \boldsymbol{I}), \boldsymbol{I}, \boldsymbol{\theta}) | \boldsymbol{\theta} \in \mathbf{T}, t \in \mathbf{R}\}$. The set of these tori constitutes an $2n$-dimensional NHIM $M_0 = \{(\boldsymbol{X}(\boldsymbol{I}), \boldsymbol{I}, \boldsymbol{\theta}) | \boldsymbol{I} \in \mathbf{I}_f, \boldsymbol{\theta} \in \mathbf{T}\}$ with $W_0 = \{(\boldsymbol{x}_0(t, \boldsymbol{I}), \boldsymbol{I}, \boldsymbol{\theta}) | \boldsymbol{I} \in \mathbf{I}_f, \boldsymbol{\theta} \in \mathbf{T}, t \in \mathbf{R}\}$ as its $(2n+1)$-dimensional separatrix. Here, $\mathbf{I}_f$ denotes the region in the action space where the saddles $X(\boldsymbol{I})$ exist. See Fig. 11 for a schematic picture of these manifolds in the space $(\boldsymbol{x}, \boldsymbol{I})$. Since the locations of the tori $T_0(\boldsymbol{I})$ and the separatrices $S_0(\boldsymbol{I})$ depend on the action variables, we show in this figure, their dependence using the axis of action as the third direction. Note that the dimension of the action variables can be greater than one.

Since the manifold M_0 is a NHIM, it changes continuously, under a small perturbation, into a new NHIM M_ε. Moreover, the separatrix W_0 changes, continuously and locally near M_ε, into the stable manifold W^s_ε and the unstable one W^u_ε of the NHIM M_ε. Note, however, that, in general, W^s_ε and W^u_ε no longer coincide with each other to form a single manifold globally. Then, the Lie transformation method brings the total Hamiltonian $H(\boldsymbol{x}.\boldsymbol{I}, \boldsymbol{\theta})$ into the Fenichel normal form locally near the manifold M_ε.

The Fenichel normal form offers a complete description of the dynamics at least locally near the NHIM. However, it does not give a full understanding of

the global aspects of the system. For example, estimation of the gap between the stable and unstable manifolds lies outside the scope of the Fenichel normal form. This is the place where the Melnikov integral plays a role.

Now, we derive the Melnikov integral. The derivation of the Melnikov integral is perturbative. We will expand the orbit $(\boldsymbol{x}(t), \boldsymbol{I}(t), \boldsymbol{\theta}(t))$ under the total Hamiltonian H in powers of the small parameter ε.

Under the Hamiltonian H_0, the equation of motion for $\boldsymbol{x}$ is written as

$$\dot{\boldsymbol{x}} = JD_{\boldsymbol{x}}H_0(\boldsymbol{x}, \boldsymbol{I}) \tag{38}$$

where the matrix J is given by

$$J = \begin{pmatrix} 0 & 1 \\ -1 & 0 \end{pmatrix} \tag{39}$$

and $D_{\boldsymbol{x}}$ means the partial derivative with respect to $\boldsymbol{x} = (q, p)$, that is, $D_{\boldsymbol{x}} = (\partial/\partial q, \partial/\partial p)$. In the following, $D_{\boldsymbol{I}}$ and $D_{\boldsymbol{\theta}}$ are defined similarly.

Then, the time development under the total Hamiltonian H is given by

$$\begin{aligned} \dot{\boldsymbol{x}} &= JD_{\boldsymbol{x}}H_0(\boldsymbol{x}, \boldsymbol{I}) + \varepsilon JD_{\boldsymbol{x}}H_1(\boldsymbol{x}, \boldsymbol{I}, \boldsymbol{\theta}) \\ \dot{\boldsymbol{I}} &= -\varepsilon D_{\boldsymbol{\theta}}H_1(\boldsymbol{x}, \boldsymbol{I}, \boldsymbol{\theta}) \\ \dot{\boldsymbol{\theta}} &= D_{\boldsymbol{I}}H_0(\boldsymbol{x}, \boldsymbol{I}) + \varepsilon D_{\boldsymbol{I}}H_1(\boldsymbol{x}, \boldsymbol{I}, \boldsymbol{\theta}) \end{aligned} \tag{40}$$

For simplicity, we assume in the following that, for points on M_0—that is, for $(\boldsymbol{x} = \boldsymbol{X}(\boldsymbol{I}), \boldsymbol{I}, \boldsymbol{\theta}(t))$—the following hold:

$$\begin{aligned} \dot{\boldsymbol{x}} &= \boldsymbol{0} \\ \dot{\boldsymbol{I}} &= \boldsymbol{0} \end{aligned} \tag{41}$$

These assumptions imply that the perturbation does not change the location of the manifold M_0 and the dynamics on it. More specifically, they mean that all of the tori $S_0(\boldsymbol{I})$ on M_0 survive under the perturbation caused by the coupling between $\boldsymbol{x}$ and $(\boldsymbol{I}, \boldsymbol{\theta})$.

These assumptions simplify the derivation of the Melnikov integral. Otherwise, the NHIM M_ε would shift from M_0, and some tori on M_ε would be destroyed due to perturbations, as discussed in Section IV. Then, a discussion which is similar to the KAM theorem says that nonresonant tori remain on the NHIM M_ε [31]. Using the stable and unstable manifolds of these tori, the derivation of the Melnikov integral follows [24].

Under the perturbation, the separatrix orbit $(\boldsymbol{x}_0(t, \boldsymbol{I}_0), \boldsymbol{I}_0, \boldsymbol{\theta}_0(t))$ will split into the following two orbits: $(\boldsymbol{x}_s(t), \boldsymbol{I}_s(t), \boldsymbol{\theta}_s(t))$ on the stable manifold W^s_ε, and

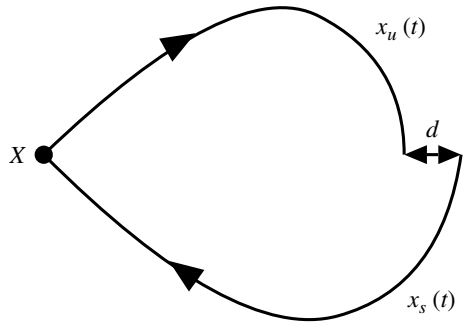

Figure 12. The gap between $\boldsymbol{x}_s$ and $\boldsymbol{x}_u$.

$(\boldsymbol{x}_u(t), \boldsymbol{I}_u(t), \boldsymbol{\theta}_u(t))$ on the unstable manifold W^u_ε. The Melnikov integral estimates the gap in the plane (q, p) between these two orbits up to the first order in ε. See Fig. 12 for a schematic picture of the gap.

Let us first expand, using ε, the deviations of $(\boldsymbol{x}_s, \boldsymbol{I}_s, \boldsymbol{\theta}_s)$ and $(\boldsymbol{x}_u, \boldsymbol{I}_u, \boldsymbol{\theta}_u)$ from $(\boldsymbol{x}_0, \boldsymbol{I}_0, \boldsymbol{\theta}_0)$, respectively,

$$\begin{aligned} \boldsymbol{x} &= \boldsymbol{x}_0 + \varepsilon \boldsymbol{x}_1 \\ \boldsymbol{I} &= \boldsymbol{I}_0 + \varepsilon \boldsymbol{I}_1 \\ \boldsymbol{\theta} &= \boldsymbol{\theta}_0 + \varepsilon \boldsymbol{\theta}_1 \end{aligned} \tag{42}$$

In Eq. (42), $\boldsymbol{x}$ means either $\boldsymbol{x}_u$ or $\boldsymbol{x}_s$. For $\boldsymbol{I}$ and $\boldsymbol{\theta}$, similar notations are used. In the following, we will use these simplified expressions unless we state otherwise.

One may wonder if this expansion is possible for chaotic orbits, since the distance between the original orbit and the one under the perturbation increases exponentially in time for chaotic evolution. We will present an intuitive answer to this question. For example, the distance between $\boldsymbol{x}_0(t)$ and $\boldsymbol{x}_u(t)$ increases exponentially for $t \to \infty$. Then, the perturbative analysis will break down for this time interval. On the other hand, their distance shrinks exponentially for $t \to -\infty$, since they go to the same saddle. Similar reasoning would also hold for the stable orbit $\boldsymbol{x}_s(t)$. Thus, for some time t_0, the perturbative analysis will be applicable to $\boldsymbol{x}_u$ for $t \in [-\infty, t_0]$ and to $\boldsymbol{x}_s$ for $t \in [t_0, \infty]$, respectively.

In the above reasoning, we have utilized the assumptions given in Eq. (41), when we state that $\boldsymbol{x}_0(t)$ and $\boldsymbol{x}_u(t)$ (or $\boldsymbol{x}_0(t)$ and $\boldsymbol{x}_s(t)$) go to the same fixed point. For general perturbations, the shift of M_ε has to be taken into account with that of tori on it. Moreover, only those orbits $\boldsymbol{x}_u(t)$ (or $\boldsymbol{x}_s(t)$) that approach the surviving tori on M_ε can be dealt with. Otherwise, slow movements caused by the perturbation on the NHIM M_ε would tear apart the orbit under the perturbation and the one $\boldsymbol{x}_0(t)$ without it.

Expanding the orbits on the stable and unstable manifolds up to the first order in ε, respectively, we obtain the equations of motion for their first-order corrections,

$$\begin{aligned}\dot{\boldsymbol{x}}_1 &= \langle \boldsymbol{x}_1, D_{\boldsymbol{x}} \rangle J D_{\boldsymbol{x}} H_0(\boldsymbol{x}_0, \boldsymbol{I}_0) + \langle \boldsymbol{I}_1, D_{\boldsymbol{I}} \rangle J D_{\boldsymbol{x}} H_0(\boldsymbol{x}_0, \boldsymbol{I}_0) \\ &\quad + J D_{\boldsymbol{x}} H_1(\boldsymbol{x}_0, \boldsymbol{I}_0, \boldsymbol{\theta}_0) \\ \dot{\boldsymbol{I}}_1 &= -D_{\boldsymbol{\theta}} H_1(\boldsymbol{x}_0, \boldsymbol{I}_0, \boldsymbol{\theta}_0)\end{aligned} \tag{43}$$

where $\langle \boldsymbol{x}_1, D_{\boldsymbol{x}} \rangle$ denotes the operator defined by the inner product between $\boldsymbol{x}_1$ and $D_{\boldsymbol{x}} = (\partial/\partial q, \partial/\partial p)$, and $\langle \boldsymbol{I}_1, D_{\boldsymbol{I}} \rangle$ denotes the operator defined by the inner product between $\boldsymbol{I}_1$ and $D_{\boldsymbol{I}}$, respectively. In the following, $<, >$ will denote the inner product. We do not use the equation for $\boldsymbol{\theta}_1$ in the following, so we omit it.

To estimate the gap between $(\boldsymbol{x}_u, \boldsymbol{I}_u)$ and $(\boldsymbol{x}_s, \boldsymbol{I}_s)$ on the $(2N-1)$-dimensional equi-energy surface in $2N$-dimensional phase space, we need $N-1$ independent quantities [24]. We measure the gap using the energy of the unperturbed Hamiltonian $H_0^r(\boldsymbol{x}, \boldsymbol{I})$, and the actions $I_l\,(l = 1, \ldots, n-1)$. In the following, we derive the expression for the difference $d(t)$ in terms of $H_0^r(\boldsymbol{x}, \boldsymbol{I})$. For other quantities involving $I_l\,(l = 1, \ldots, n-1)$, expressions can be derived using their equations of motion.

Now, we derive the difference $d(t)$ in terms of $H_0^r(\boldsymbol{x}, \boldsymbol{I})$—that is, the values of the unperturbed Hamiltonian for the reaction coordinate,

$$\begin{aligned}d(t) &= H_0^r(\boldsymbol{x}_u(t), \boldsymbol{I}_u(t)) - H_0^r(\boldsymbol{x}_s(t), \boldsymbol{I}_s(t)) \\ &= \varepsilon \{ \langle (\boldsymbol{x}_{1u}(t) - \boldsymbol{x}_{1s}(t)), D_{\boldsymbol{x}} \rangle H_0^r(\boldsymbol{x}_0, \boldsymbol{I}_0) \\ &\qquad + \langle (\boldsymbol{I}_{1u}(t) - \boldsymbol{I}_{1s}(t)), D_{\boldsymbol{I}} \rangle H_0^r(\boldsymbol{x}_0, \boldsymbol{I}_0) \} \\ &\qquad + \text{second and higher-order terms in } \varepsilon\end{aligned} \tag{44}$$

Let $d_1(t)$ denote the first-order term of the gap $d(t)$ in Eq. (44) involving $(\boldsymbol{x}_u(t), \boldsymbol{I}_u(t))$ and $(\boldsymbol{x}_s(t), \boldsymbol{I}_s(t))$, respectively,

$$d_1(t) = \left\langle \boldsymbol{x}_1(t), D_{\boldsymbol{x}} H_0^r(\boldsymbol{x}_0(t), \boldsymbol{I}_0(t)) \right\rangle + \left\langle \boldsymbol{I}_1(t), D_{\boldsymbol{I}} H_0^r(\boldsymbol{x}_0(t), \boldsymbol{I}_0(t)) \right\rangle \tag{45}$$

Differentiating Eq. (45) with respect to t, and substituting Eq. (43) to $\dot{\boldsymbol{x}}_1$ and $\dot{\boldsymbol{I}}_1$, we find the equation of motion for $d_1(t)$ to be

$$\begin{aligned}\dot{d}_1 &= \left\langle \boldsymbol{x}_1, \frac{d}{dt} D_{\boldsymbol{x}} H_0^r(\boldsymbol{x}_0, \boldsymbol{I}_0) \right\rangle + \left\langle \dot{\boldsymbol{x}}_1, D_{\boldsymbol{x}} H_0^r(\boldsymbol{x}_0, \boldsymbol{I}_0) \right\rangle \\ &\quad + \left\langle \boldsymbol{I}_1, \frac{d}{dt} D_{\boldsymbol{I}} H_0^r(\boldsymbol{x}_0, \boldsymbol{I}_0) \right\rangle + \left\langle \dot{\boldsymbol{I}}_1, D_{\boldsymbol{I}} H_0^r(\boldsymbol{x}_0, \boldsymbol{I}_0) \right\rangle \\ &= \left\langle \boldsymbol{x}_1, \left\langle J D_{\boldsymbol{x}} H_0^r, D_{\boldsymbol{x}} \right\rangle D_{\boldsymbol{x}} H_0^r \right\rangle + \left\langle \left\langle \boldsymbol{x}_1, D_{\boldsymbol{x}} \right\rangle J D_{\boldsymbol{x}} H_0^r, D_{\boldsymbol{x}} H_0^r \right\rangle \\ &\quad + \left\langle \left\langle \boldsymbol{I}_1, D_{\boldsymbol{I}} \right\rangle J D_{\boldsymbol{x}} H_0^r, D_{\boldsymbol{x}} H_0^r \right\rangle + \left\langle J D_{\boldsymbol{x}} H_1, D_{\boldsymbol{x}} H_0^r \right\rangle \\ &\quad + \left\langle \boldsymbol{I}_1, \left\langle J D_{\boldsymbol{x}} H_0^r, D_{\boldsymbol{x}} \right\rangle D_{\boldsymbol{I}} H_0^r \right\rangle + \left\langle -D_{\boldsymbol{\theta}} H_1, D_{\boldsymbol{I}} H_0^r \right\rangle\end{aligned} \tag{46}$$

where all of the variables in the second equation are $(\boldsymbol{x}_0(t, \boldsymbol{I}_0), \boldsymbol{I}_0, \boldsymbol{\theta}_0(t))$.

In Eq. (46), we note that the first term + the second term = 0 and the third term + the fifth term = 0, that is,

$$\langle \boldsymbol{x}_1, \langle JD_{\boldsymbol{x}}H_0^r, D_{\boldsymbol{x}}\rangle D_{\boldsymbol{x}}H_0^r\rangle + \langle \langle \boldsymbol{x}_1, D_{\boldsymbol{x}}\rangle JD_{\boldsymbol{x}}H_0^r, D_{\boldsymbol{x}}H_0^r\rangle = 0 \tag{47}$$

and

$$\langle \langle \boldsymbol{I}_1, D_{\boldsymbol{I}}\rangle JD_{\boldsymbol{x}}H_0^r, D_{\boldsymbol{x}}H_0^r\rangle + \langle \boldsymbol{I}_1, \langle JD_{\boldsymbol{x}}H_0^r, D_{\boldsymbol{x}}\rangle D_{\boldsymbol{I}}H_0^r\rangle = 0 \tag{48}$$

for an arbitrary $\boldsymbol{x}_1$ and $\boldsymbol{I}_1$, respectively. They can be derived when we differentiate the Poisson bracket $[H_0^r, H_0^r] = \langle D_{\boldsymbol{x}}H_0^r, JD_{\boldsymbol{x}}H_0^r\rangle = 0$ with respect to $\boldsymbol{x}$ and $\boldsymbol{I}$, respectively, leading to the equations

$$\langle D_{x_i}D_{\boldsymbol{x}}H_0^r, JD_{\boldsymbol{x}}H_0^r\rangle + \langle D_{\boldsymbol{x}}H_0^r, D_{x_i}JD_{\boldsymbol{x}}H_0^r\rangle = 0 \qquad (i = 1, 2) \tag{49}$$

and

$$\langle D_{I_l}D_{\boldsymbol{x}}H_0^r, JD_{\boldsymbol{x}}H_0^r\rangle + \langle D_{\boldsymbol{x}}H_0^r, D_{I_l}JD_{\boldsymbol{x}}H_0^r\rangle = 0 \qquad (l = 1, \ldots, n) \tag{50}$$

where $x_1 = q$ and $x_2 = p$ in Eq. (49).

Thus, we finally obtain a differential equation for $d_1(t)$,

$$\begin{aligned} \dot{d}_1 &= \langle D_{\boldsymbol{x}}H_0^r, JD_{\boldsymbol{x}}H_1\rangle - \langle D_{\boldsymbol{I}}H_0^r, D_{\boldsymbol{\theta}}H_1\rangle \\ &= [H_0^r, H_1](\boldsymbol{x}_0(t, \boldsymbol{I}_0), \boldsymbol{I}_0, \boldsymbol{\theta}_0(t)) \end{aligned} \tag{51}$$

where the Poisson bracket $[H_0^r, H_1]$ is defined in terms of $(\boldsymbol{x}, \boldsymbol{I}, \boldsymbol{\theta})$. The inner product $\langle,\rangle$ in the first term is defined in the space $\boldsymbol{x} = (q, p)$, and the one in the second term is in $(\boldsymbol{I}, \boldsymbol{\theta}) = (I_1, \ldots, I_n, \theta_1, \ldots, \theta_n)$.

One of the remarkable aspects of Eq. (51) is that its right-hand side is given only using the unperturbed orbit $(\boldsymbol{x}_0(t, \boldsymbol{I}_0), \boldsymbol{I}_0, \boldsymbol{\theta}_0(t))$. Thus, in obtaining the quantity $d_1(t)$, we do not need any information on perturbed orbits. This is one of the merits of using the Melnikov integral to estimate the gap between the stable and unstable manifolds.

In the following, d_{1s} denotes the first-order term $d_1(t)$ for the stable manifold and denotes d_{1u} for the unstable manifold. In order to obtain d_{1s} and d_{1u}, we integrate Eq. (51). As already explained, for a time t_0 the perturbation analysis is applicable to x_u for $t \in [t_u, t_0]$ and applicable to x_s for $t \in [t_0, t_s]$ as $t_u \to -\infty$ and $t_s \to \infty$. Therefore, we integrate Eq. (51) from $-\infty$ to t_0 to obtain d_{1u}, and from t_0 to ∞ to obtain d_{1s}, respectively. Strictly speaking, in order to achieve convergence of the integral, the limiting processes $t_u \to -\infty$ and $t_s \to \infty$ have to be such that the orbits approach the same points on the whiskered tori, respectively.

Then, we are led to the equations

$$d_{1u}(t_0) = \int_{-\infty}^{t_0} [H_0^r, H_1](\boldsymbol{x}_0(t, \boldsymbol{I}_0), \boldsymbol{I}_0, \boldsymbol{\theta}_0(t))\, dt \tag{52}$$

and

$$d_{1s}(t_0) = \int_{\infty}^{t_0} [H_0^r, H_1](\boldsymbol{x}_0(t, \boldsymbol{I}_0), \boldsymbol{I}_0, \boldsymbol{\theta}_0(t))\, dt \tag{53}$$

respectively.

Thus, the gap between $(\boldsymbol{x}_u(t), \boldsymbol{I}_u(t))$ and $(\boldsymbol{x}_s(t), \boldsymbol{I}_s(t))$ at $t = t_0$ in terms of the difference of the unperturbed energy H_0^r is given by

$$\begin{aligned} d_1(t_0) &= d_{1u}(t_0) - d_{1s}(t_0) \\ &= \int_{-\infty}^{\infty} [H_0^r, H_1](\boldsymbol{x}_0(t, \boldsymbol{I}_0), \boldsymbol{I}_0, \boldsymbol{\theta}_0(t))\, dt \end{aligned} \tag{54}$$

The integral in Eq. (54) is called the Melnikov integral. Note that the final expression given in Eq. (54) does not explicitly involve any dependence on the time t_0.

It is instructive to examine the intuitive meaning of the Melnikov integral in Eq. (54). The integrand $[H_0^r, H_1]$ of the Melnikov integral gives the time development of the unperturbed Hamiltonian H_0^r under the influence of the total Hamiltonian $H = H_0^r + H_0^b + \varepsilon H_1$ because $[H_0^r, H_0^r + H_0^b] = 0$. By integrating the integrand, we obtain the net change of the value of H_0^r under the perturbation.

In order to estimate the gap on the equi-energy surface, we also need the quantities involving $I_l\,(l = 1, \ldots, n-1)$. Thus, we construct the Melnikov vector for the gap. In Section VI, we will use the Melnikov vector to study intersections between the stable and unstable manifolds of whiskered tori with different action values.

In the following, we consider two examples where the Melnikov integral is explicitly calculable. The first example serves as a standard case for the calculation of the integral. The results will be used in the later sections where we study the Arnold model and tangency. The second one serves as a prototype for molecular systems under time-dependent electric fields.

Example 1. The total Hamiltonian is given by

$$H(q, p, I, \theta) = \frac{p^2}{2} - \cos q + \omega I - \varepsilon \cos\theta(\cos q + 1) \tag{55}$$

The unperturbed Hamiltonian H_0 of the system

$$H_0(q,p,I) = \frac{p^2}{2} - \cos q + \omega I \tag{56}$$

consists of the two parts H_0^r and H_0^b as follows:

$$H_0^r(q,p,I) = \frac{p^2}{2} - \cos q \tag{57}$$

$$H_0^b(I) = \omega I \tag{58}$$

The perturbation H_1 is as follows:

$$H_1(q,p,I,\theta) = -\cos\theta(\cos q + 1) \tag{59}$$

The equation of motion under the total Hamiltonian is then

$$\begin{aligned}
\dot{q} &= \frac{\partial H}{\partial p} = p \\
\dot{p} &= -\frac{\partial H}{\partial q} = -(1 + \varepsilon\cos\theta)\sin q \\
\dot{I} &= -\frac{\partial H}{\partial \theta} = -\varepsilon\sin\theta(\cos q + 1) \\
\dot{\theta} &= \frac{\partial H}{\partial I} = \omega
\end{aligned} \tag{60}$$

In the interval $q \in [-\pi, \pi]$, hyperbolic fixed points of the unperturbed Hamiltonian H_0 are given by

$$p = 0, \qquad q = \pm\pi \tag{61}$$

There exist two kinds of separatrix orbits connecting $(q = -\pi, p = 0)$ and $(q = \pi, p = 0)$:

$$\begin{aligned}
q_\pm(t-\tau) &= \pm 2\sin^{-1}(\tanh(t-\tau)) \\
p_\pm(t-\tau) &= \pm\frac{2}{\cosh(t-\tau)}
\end{aligned} \tag{62}$$

where τ is a constant showing dependence on initial conditions. The orbits with a plus sign lie on the plane (q,p) with $p > 0$, and the ones with a minus sign lie on the plane (q,p) with $p < 0$. A schematic picture of these orbits is shown in Fig. 13.

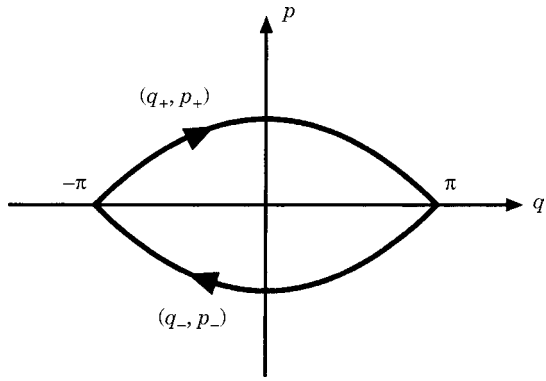

Figure 13. The flow of the pendulum in phase space.

In this system, the unstable fixed points $(q = \pm\pi, p = 0)$ of the unperturbed Hamiltonian survive the perturbation. Moreover, $\dot{I} = 0$ holds for $(q = \pm\pi, p = 0, I, \theta(t))$. Thus, the assumptions given by Eq. (41) hold. Therefore, the derivation of the Melnikov integral is applicable to this Hamiltonian.

Substituting the separatrix orbits $(q_+(t-\tau), p_+(t-\tau), I, \theta(t) = \omega t + \alpha)$ with a constant α into the integrand of the Melnikov integral,

$$\begin{aligned}[H_0^r, H_1] &= \frac{\partial H_0^r}{\partial q}\frac{\partial H_1}{\partial p} - \frac{\partial H_0^r}{\partial p}\frac{\partial H_1}{\partial q} + \frac{\partial H_0^r}{\partial \theta}\frac{\partial H_1}{\partial I} - \frac{\partial H_0^r}{\partial I}\frac{\partial H_1}{\partial \theta} \\ &= -p\cos\theta\sin q \end{aligned} \tag{63}$$

and estimating the integral, we obtain

$$d(\tau, \alpha) = \varepsilon\frac{2\pi\omega^2}{\sinh\frac{\pi}{2}\omega}\sin(\omega\tau + \alpha) \tag{64}$$

See Appendix A for details of the calculation.

Equation (64) shows that the distance $d(\tau, \alpha)$ exhibits an oscillatory dependence as a function of τ. In other words, $d(\tau, \alpha)$ changes between plus and minus values as initial conditions shift on the separatrix. This means that the stable and unstable manifolds have transverse intersections. See Fig. 14 showing how the oscillatory change of the integral implies the occurrence of transverse intersections. The existence of transverse intersections between stable and unstable manifolds leads to horseshoe dynamics—that is, chaos. Thus, the Melnikov integral given by Eq. (64) indicates that this system exhibits chaotic behavior.

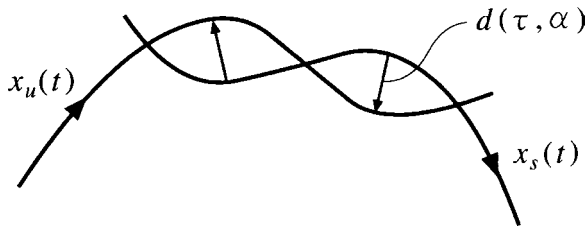

Figure 14. An oscillatory change of the Melnikov integral.

Following the idea of Davis and Gray, the reaction rate is related to the area of those regions that are surrounded by pieces of the stable and unstable manifolds. In Fig. 15, the shaded region indicates one of them. The reaction rate is proportional to the net area of those regions that pass the saddle per unit time.

On the other hand, the net area of these regions is given by the amplitude $d(\omega)$ of the Melnikov integral as we show in the following.

The area of the region shadowed in Fig. 15 is given approximately by

$$\text{the amplitude of } d(\tau, \alpha) \times \omega^{-1} \tag{65}$$

because the area is the product of the gap between the stable and unstable manifolds and the distance between successive intersections. While the gap is measured by energy and is equal to $d(\omega)$—that is, the amplitude of the Melnikov integral—the distance between successive intersections is measured by time and is roughly equal to ω^{-1}. Then, the product of the two quantities has the unit of area in phase space and equals $d(\omega) \times \omega^{-1}$. The number of those regions that pass the saddle per unit time is proportional to ω, since it is equal to the inverse of the period of the external force.

Thus, the net area of those regions which pass the saddle per unit time is proportional to the amplitude $d(\omega)$ of the Melnikov integral. Therefore, the reaction rate is proportional to the amplitude $d(\omega)$ of the Melnikov integral.

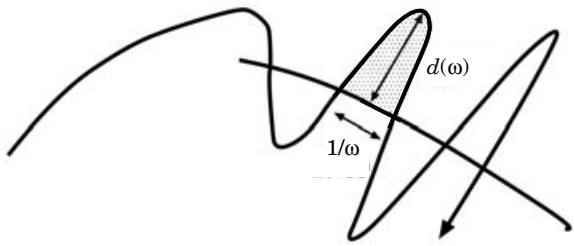

Figure 15. The area surrounded by stable and unstable manifolds.

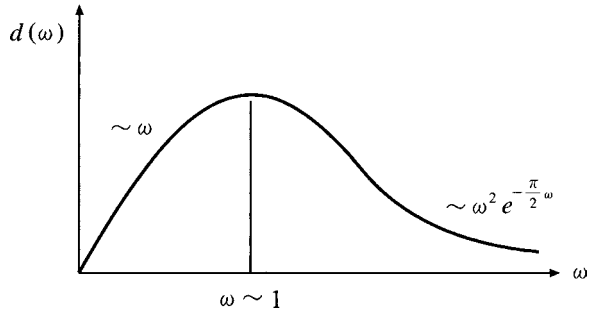

Figure 16. The amplitude of $d(\omega)$ versus ω.

Figure 16 shows how the amplitude $d(\omega)$ of the Melnikov integral depends on the frequency ω of the external force. Remember that the characteristic time scale of the unperturbed Hamiltonian is 1. Then, the fact that $d(\omega)$ attains a maximum at $\omega \sim 1$ implies that chaos is caused by resonance between the unperturbed system and the external force.

Example 2. The total Hamiltonian is given by

$$H = \frac{p^2}{2m} + D(e^{-2aq} - 2e^{-aq}) + \varepsilon q \sin(\omega t + \alpha) \tag{66}$$

This Hamiltonian models a molecule composed of two atoms acted on by an oscillatory electric field. Thus, it is a prototype of diatomic molecules in laser fields.

The unperturbed Hamiltonian H_0 of the system is given by

$$H_0 = \frac{p^2}{2m} + D(e^{-2aq} - 2e^{-aq}) \tag{67}$$

and the perturbation H_1 is

$$H_1 = q \sin(\omega t + \alpha) \tag{68}$$

The separatrix orbit of H_0 is given by

$$\begin{aligned} e^{aq} &= \frac{1 + \omega_0^2 (t - \tau)^2}{2} \\ p &= \frac{m}{a} \frac{2\omega_0^2 (t - \tau)}{1 + \omega_0^2 (t - \tau)^2} \end{aligned} \tag{69}$$

where $\omega_0 = \sqrt{\frac{2a^2}{m}D}$ is a frequency of the Morse oscillator in the harmonic approximation. τ is a constant representing the dependence on initial conditions.

This Hamiltonian has an unstable fixed point at $(p = 0, q = \infty)$. However, it is not hyperbolic, since the rate of approaching the fixed point is not exponential but polynomial as $p(t) \sim t^{-1} \quad (t \to \infty)$ shows in Eq. (69).

In spite of this, the Melnikov integral

$$d = \varepsilon \int_{-\infty}^{\infty} [H_0, H_1]\, dt \tag{70}$$

can be estimated in the same way as in the previous section. Here the Poisson bracket is defined in terms of (x, p),

$$\begin{aligned}[H_0, H_1] &= \frac{\partial H_0}{\partial x}\frac{\partial H_1}{\partial p} - \frac{\partial H_0}{\partial p}\frac{\partial H_1}{\partial x} \\ &= -\frac{p}{m}\sin(\omega t + \alpha)\end{aligned} \tag{71}$$

Estimating the integral, we obtain the following result:

$$d(\tau, \alpha) = -\varepsilon \frac{2\pi}{a} e^{-\frac{\omega}{\omega_0}} \cos(\omega\tau + \alpha) \tag{72}$$

This results is wrong at $\omega = 0$. Therefore, we have to be careful in using it for those cases where the frequency of the external field is small compared to the characteristic inverse time scale of the Morse Hamiltonian. See Appendix B for details.

VI. ARNOLD MODEL

Chaos in systems with N degrees of freedom with $N \geq 3$ has characteristics that are not shared by chaos in systems with two degrees of freedom. In this section, we show that the Melnikov integral reveals one of these characteristics. They are exhibited in the intersections between the stable and unstable manifolds of whiskered tori with different action values.

In systems with two degrees of freedom, two-dimensional tori separate the equi-energy surface into two disjoint parts. Thus, orbits on one part of the equi-energy surface cannot go into the other. Therefore, the existence of two-dimensional tori in systems of two degrees of freedom results in nonergodic behavior of the system.

To the contrary, for systems of N degrees of freedom with $N \geq 3$, N-dimensional tori no longer separate the equi-energy surface. This implies that going around tori would be possible. One of the possible mechanisms for such behavior is movement along nonlinear resonances.

In his celebrated article, Arnold actually constructed a model where these movements take place [15]. In this model, orbits move along a nonlinear resonance under the influence of other resonances. From the results of this study, it is found that the dynamics on the network of nonlinear resonances is characteristic for systems of N degrees of freedom with $N \geq 3$. The network is called the Arnold web [16,17].

The Arnold web is supposed to play an important role in intramolecular vibrational energy redistribution (IVR) [1]. However, in order to reveal its role for IVR, the following two problems must be investigated.

The first is that the diffusive dynamics on the web (the Arnold diffusion) is very slow. Indeed, its time scale is so long that Arnold diffusion would be irrelevant in IVR. The second is that a recent study shows that diffusive behavior across nonlinear resonances is much more prominent than that along resonances [28,33,34]. Then, movement along resonances would be surpassed by movement across resonances.

Bearing these problems in mind, we will study the Arnold model as an example of the Melnikov integral. This section will also serve as an introduction leading to the argument on tangency in the next section.

The Arnold model is a time-dependent Hamiltonian with two degrees of freedom,

$$H = \frac{p^2}{2} - V\cos q + \frac{I^2}{2} - \varepsilon(\cos q + 1)\cos\theta - \varepsilon\cos q\cos\omega t \tag{73}$$

where ε is a small parameter.

The unperturbed Hamiltonian is obtained by setting $\varepsilon = 0$ in the Hamiltonian H,

$$H_0 = \frac{p^2}{2} - V\cos q + \frac{I^2}{2} \tag{74}$$

Thus, the unperturbed Hamiltonian H_0 decouples into two subsystems (q, p) and (I, θ). The perturbation H_1 is given by

$$H_1 = -(\cos q + 1)\cos\theta - \cos q\cos\omega t \tag{75}$$

The degree of freedom (q, p) has a resonant term $V\cos q$. There exist unstable fixed points $(q = \pm\pi, p = 0)$, and the separatrix orbits connecting them. The separatrix orbits of the nonlinear resonance are given by the following:

$$\begin{aligned} p_{\pm}(t-\tau) &= \pm\frac{2\sqrt{V}}{\cosh\sqrt{V}(t-\tau)} \\ q_{\pm}(t-\tau) &= \pm 2\sin^{-1}\Big(\tanh\sqrt{V}(t-\tau)\Big) \end{aligned} \tag{76}$$

The degree of freedom (I, θ) describes movements on tori,

$$I = \Omega, \qquad \theta = \Omega t + \alpha \tag{77}$$

where we assume $\Omega \neq 0$. Removal of this assumption needs a different analysis (see Xia [35]). Furthermore, in the next section, we will show that the case with $\Omega = 0$ reveals another new phenomenon, which we will call "tangency."

The dynamics under the unperturbed Hamiltonian has a two-dimensional NHIM

$$M_0 = \left\{(q, p, I, \theta) \;\middle|\; q = \pm\pi, p = 0, I \in \mathbf{I}_f, \theta \in \mathbf{T}\right\} \tag{78}$$

Note that this model also satisfies the assumptions given by Eq. (41).

In the following, we are interested in the dynamics that result in transport along the variable I. In order to see the behavior along the direction of I, orbits on the stable and unstable manifolds will be studied, that is,

$$\begin{aligned} I_{1u} &= I_{10} + \varepsilon I_u, \quad p_{1u} = p_+ + \varepsilon p_u, \quad q_{1u} = q_+ + \varepsilon q_u \\ I_{2s} &= I_{20} + \varepsilon I_s, \quad p_{2s} = p_+ + \varepsilon p_s, \quad q_{2s} = q_+ + \varepsilon q_s \end{aligned} \tag{79}$$

Then, how these manifolds intersect will be investigated using the Melnikov integral. See Fig. 17 for a schematic picture of the stable and unstable manifolds with a shift in the variable I.

The gap between the stable and unstable manifolds is estimated using the following quantity, $H_{10} = \frac{p^2}{2} - V\cos q$ and $H_{20} = \frac{I^2}{2}$. See Fig. 18, which shows the displacement of the unstable orbit (q_u, p_u, I_u) from the one without the perturbation.

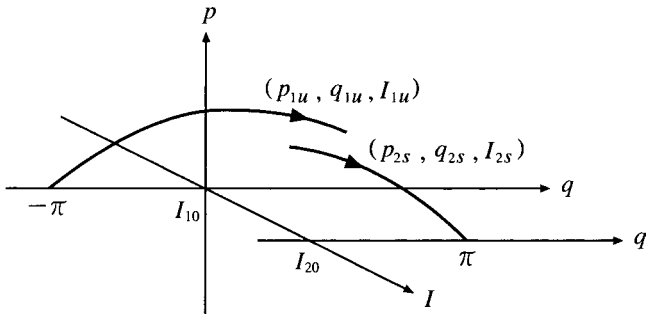

Figure 17. Dynamics under the unperturbed Hamiltonian of the Arnold model.

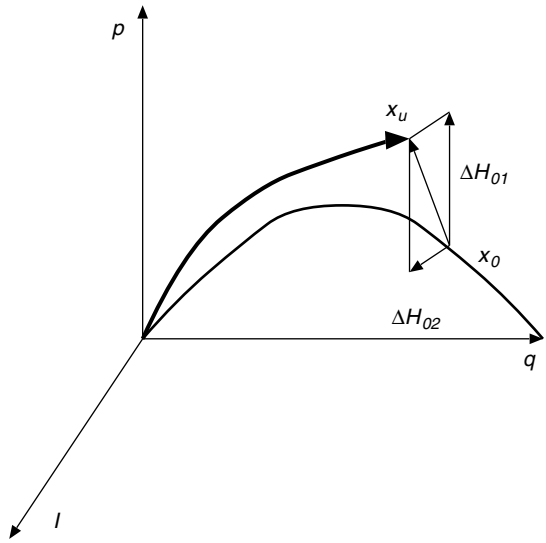

Figure 18. Displacement ΔH_{10} and ΔH_{20} in the space (q,p,I) from $\boldsymbol{X}_0 = (q_0, p_0, I_0)$ to $\boldsymbol{X}_u = (q_u, p_u, I_u)$.

In order to measure the displacement, we need two quantities H_{10} and H_{20}, since the system has a time-dependent two-degrees-of-freedom Hamiltonian, that is,

$$\begin{aligned} d_{10} &= H_{10}(q_{1u}, p_{1u}) - H_{10}(q_{2s}, p_{2s}) \\ &= \varepsilon\{D_q H_{10}(q_+, p_+) \cdot (q_u - q_s) + D_p H_{10}(q_+, p_+) \cdot (p_u - p_s)\} \\ &\quad + \text{second- and higher-order terms in } \varepsilon \end{aligned} \tag{80}$$

$$\begin{aligned} d_{20} &= H_{20}(I_{1u}) - H_{20}(I_{2s}) \\ &= H_{20}(I_{10}) - H_{20}(I_{20}) + \varepsilon D_I H_{20}(I_{10}) \cdot (I_u - I_s) \\ &\quad + \text{second- and higher-order terms in } \varepsilon \end{aligned} \tag{81}$$

For the first-order terms in ε,

$$d_1 = D_q H_{10} \cdot (q_u - q_s) + D_p H_{10} \cdot (p_u - p_s) \tag{82}$$

$$d_2 = D_I H_{20} \cdot (I_u - I_s) \tag{83}$$

an argument that is similar to the one in the previous section leads to the expression

$$d_1 = \int_{-\infty}^{\infty} [H_{10}, H_1]\, dt \tag{84}$$

$$d_2 = \int_{-\infty}^{\infty} [H_{20}, H_1]\, dt \tag{85}$$

Here, the variables in H_{10} and H_{20} are the orbits under the unperturbed Hamiltonian.

The vector (d_1, d_2) is called the Melnikov vector. For systems of more than two degrees of freedom, as well as for time-dependent systems of two degrees of freedom, we need the Melnikov vectors to investigate intersections between the stable and unstable manifolds of NHIMs.

Substituting the orbits under the unperturbed Hamiltonian into the Melnikov vector, we obtain

$$\begin{aligned} d_1 &= -\int_{-\infty}^{\infty} \frac{\partial H_{10}}{\partial p}\frac{\partial H_1}{\partial q}\, dt \\ &= -\int_{-\infty}^{\infty} p \sin q(\cos\theta + \cos\omega t)\, dt \end{aligned} \tag{86}$$

$$\begin{aligned} d_2 &= -\int_{-\infty}^{\infty} \frac{\partial H_{20}}{\partial I}\frac{\partial H_1}{\partial \theta}\, dt \\ &= -\int_{-\infty}^{\infty} I(\cos q + 1)\sin\theta\, dt \end{aligned} \tag{87}$$

Estimating these integrals, the final results are the following:

$$d_1 = \frac{2\pi\omega^2/V}{\sinh\frac{\pi\omega}{2\sqrt{V}}}\sin\omega\tau + \frac{2\pi\Omega^2/V}{\sinh\frac{\pi\Omega}{2\sqrt{V}}}\sin(\Omega\tau + \alpha) \tag{88}$$

$$d_2 = -\frac{2\pi\Omega^2/V}{\sinh\frac{\pi\Omega}{2\sqrt{V}}}\sin(\Omega\tau + \alpha) \tag{89}$$

In order for Arnold diffusion to take place, we need a transverse intersection of the stable and unstable manifolds. In other words, there must be a (τ_0, α_0) that satisfies the following conditions:

$$\begin{aligned} d_{10} &= \varepsilon d_1(\tau_0, \alpha_0) = 0 \\ d_{20} &= H_{20}(I_{10}) - H_{20}(I_{20}) + \varepsilon d_2(\tau_0, \alpha_0) = 0 \end{aligned} \tag{90}$$

and the matrix defined by

$$\begin{pmatrix} \dfrac{\partial d_1}{\partial \tau} & \dfrac{\partial d_2}{\partial \tau} \\ \dfrac{\partial d_1}{\partial \alpha} & \dfrac{\partial d_2}{\partial \alpha} \end{pmatrix} \tag{91}$$

has the inverse at (τ_0, α_0).

These conditions can be understood as follows. Since the system is time-dependent, we consider the phase-space structure at a fixed time t. Then, the stable and unstable manifolds are two-dimensional manifolds, and they are parametrically represented using (τ, α). Their intersections, if any, are points in the four-dimensional phase space (q, p, I, θ). (Note that the equi-energy surface does not exist.) Let (τ_0, α_0) denote an intersection. In order to have transverse intersections between the stable and unstable manifolds, there must be an inverse function $f : (d_1, d_2) \to (\tau, \alpha)$ in the neighborhood of the intersection (τ_0, α_0). See Fig. 19 for the difference between transverse and tangent intersections between two curves on the plane. The condition for the existence of the inverse is that $\left.\frac{\partial(d_1,d_2)}{\partial(\tau,\alpha)}\right|_{\substack{\tau=\tau_0 \\ \alpha=\alpha_0}}$ is regular.

The sufficient condition for the existence of intersections is given by the following:

$$|H_{20}(I_{10}) - H_{20}(I_{20})| \leq \varepsilon \min\left\{ \frac{2\pi\omega^2/V}{\sinh \frac{\pi\omega}{2\sqrt{V}}}, \frac{2\pi\Omega^2/V}{\sinh \frac{\pi\Omega}{2\sqrt{V}}} \right\} \tag{92}$$

When the inequality holds, we see that $\left.\frac{\partial(d_1,d_2)}{\partial(\tau,\alpha)}\right|_{\substack{\tau=\tau_0 \\ \alpha=\alpha_0}}$ is regular.

The above argument is only of first order in ε. However, even with higher-order terms in ε the argument holds since transverse intersections do not disappear under small perturbations. Thus, there exists a chain of tori $I_{10}, I_{20}, \ldots$ such that transverse intersections between stable and unstable manifolds of neighboring tori $I_{i0}, I_{i+1,0} (i = 1, 2, \ldots)$ result in the transport along the direction

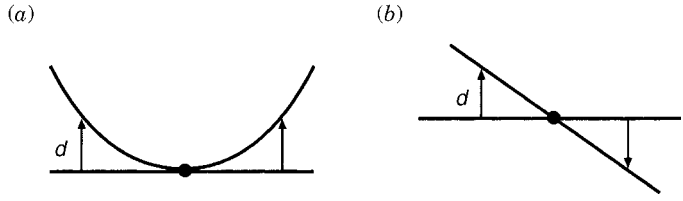

Figure 19. (*a*) Two curves do not intersect transversally, (*b*) Two curves intersect transversally.

of I. Such behavior is called Arnold diffusion. (However, see Ref. 25 showing that Arnold diffusion is not diffusive.)

For generic cases where the assumptions Eq. (41) do not hold, there is a hole in the above discussion. This hole comes from the fact that, under general perturbations, some tori are destroyed creating gaps in the chain of tori $I_{10}, I_{20}, \ldots$. If the widths of these gaps do not satisfy the inequality (92), Arnold diffusion would be impossible. This problem is called the gap problem. The gap problem raises the question as to whether Arnold diffusion is generic or not. Recently, Xia has made progress in studying this problem. See Ref. 36 for his results.

Also note that the inequality Eq. (92) implies that there would be no Arnold diffusion for $\Omega = 0$. To the contrary, Xia proved that there still exists a diffusive movement even for $\Omega = 0$. He called it pseudo-Arnold diffusion [35].

In the next section, we will also study the Arnold model with $\Omega = 0$ from a different point of view. We show that the model exhibits tangency and that the condition for tangency can be derived using the Melnikov integral.

VII. TANGENCY

Branching is one of the important features of the skeleton of paths. It is revealed in the tangency of intersections between the stable and unstable manifolds of NHIMs. This is understood as follows.

In systems of N degrees of freedom with $N \geq 3$, one NHIM would be connected with multiple NHIMs. Figure 20 shows a schematic picture of a

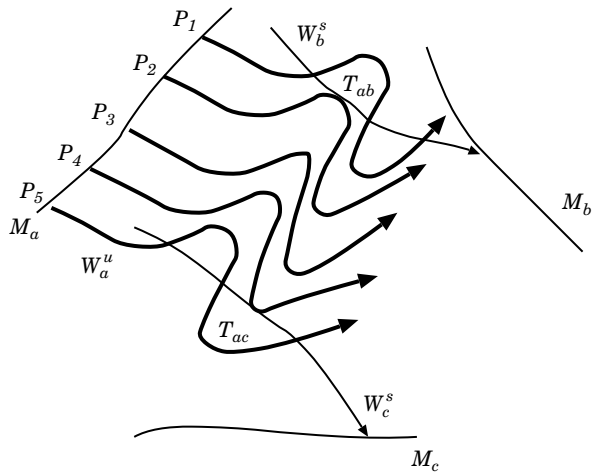

Figure 20. When branching exists, tangency takes place as initial conditions continuously vary on the unstable manifold.

NHIM M_a connected with two other NHIMs, M_b and M_c. There, the unstable manifold W_a^u of the NHIM M_a has intersections with the stable manifolds W_b^s and W_s^c of the NHIMs M_b and M_c, respectively. As initial conditions continuously vary from P1 through P2, P3, and P4 to P5 on W_a^u, its intersections with the stable manifolds change as follows. The transverse intersection with W_b^s for P1 first changes into tangency with W_b^s at T_{ab} for P2, then no intersection for P3, tangency with W_c^s at T_{ac} for P4, and finally transverse intersection with W_c^s for P5. Thus, we expect that whenever branching exists, tangency occurs as initial conditions continuously vary on the unstable manifolds.

This suggests that tangency is a universal phenomenon in the skeleton of reaction paths for multiple dimensional chaos.

In this section, we study a model Hamiltonian where the condition for tangency can be derived using the Melnikov integral. The Hamiltonian is the Arnold model with $\Omega = 0$. We will show that the Arnold model with $\Omega = 0$ exhibits tangency when the strength of the perturbation exceeds a threshold. Thus, this model offers a clue to understand the branching structure of the skeleton.

The Arnold model with $\Omega = 0$ corresponds to scattering processes. In the planar Coulomb three-body problem, the asymptotic limit where one of the three bodies goes to infinity corresponds to the Arnold model with $\Omega = 0$ [35]. For three-body clusters interacting with van der Waals potential, the Arnold model with $\Omega = 0$ also arises when one of the three bodies goes to infinity [37].

We can also regard the Arnold model with $\Omega = 0$ as a system with three resonances. In other words, it models the dynamics around resonance intersections. This is because the condition $\Omega = 0$ is regarded as a resonance condition, where the movement θ becomes slow. Then, the term $\cos\theta$ cannot be averaged out but must be kept in the analyses. Thus, in addition to the term $V\cos q$, the model has another resonance term $\cos\theta$. Therefore, the Arnold model with $\Omega = 0$ can be regarded as a model of a resonance intersection.

Figure 21 shows the reason why branching is expected at resonance intersections. There, three resonances are indicated by the thick lines on the equi-energy surface $E = \text{const}$ in the action space (I_1, I_2, I_3). The point P indicates the location of a resonance intersection. An orbit starting form the point A can go either to the point B or to the point C along resonance lines. Thus, at the resonance intersection, two reaction paths exist: one from the point A to B and the other from A to C. Therefore, branching of reaction paths is expected at resonance intersections.

As is mentioned in the previous sections, the dynamics around resonance intersections is more important than was supposed before [33,34]. As yet, however, branching of reaction paths at resonance intersections has not been studied.

Thus, the Arnold model with $\Omega = 0$ belongs to a universal and important class of dynamical systems.

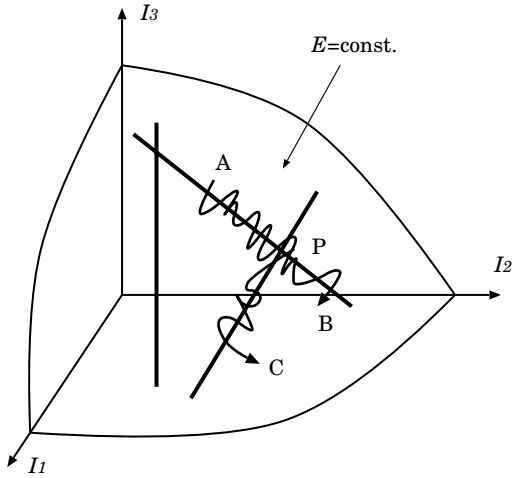

Figure 21. Branching is expected at resonance intersections.

The model is a time-dependent Hamiltonian with two degrees of freedom,

$$H = \frac{p^2}{2} - V\cos q + \frac{I^2}{2} - \mu(\cos q + 1)\cos\theta - \varepsilon\cos q\cos\omega t \qquad (93)$$

This model is the same as the Arnold model except that Eq. (93) has two small parameters ε and μ. In the following analysis we will consider ε and μ separately.

First, we consider those orbits starting from the initial conditions with $(I = 0, \theta = \theta_0)$ and (q, p) on the separatrix Eq. (76) near the unstable fixed point $(q = -\pi, p = 0)$. In other words, we will see how a piece of the unstable manifold with a different initial value of θ intersects with the stable manifold of the NHIM with $(q = \pi, p = 0)$. Here, the dimension of the pieces of the unstable manifold is 1, since we fix the initial conditions of (I, θ), and the dimension of the stable manifold is 3.

In Fig. 22, projections to the plane (q, p) are shown for the development of these pieces of the unstable manifold (solid lines) and the stable manifold (dotted lines). We choose $V = 1.0$, $\omega = 1.0$, $\varepsilon = 0.1$, and $\mu = 0.22$, and the initial values θ_0 for these pictures are the following: (a) $\theta_0 = -0.9\pi$, (b) $\theta_0 = -0.8\pi$, (c) $\theta_0 = -0.78\pi$, (d) $\theta_0 = -0.77\pi$, (e) $\theta_0 = -0.76\pi$, (f) $\theta_0 = -0.74\pi$.

In Figs. 22a–c, intersections are transverse. They become tangent in Fig. 22d, and no intersections exist in Figs. 22e and 22f. The name ''tangency'' is based on these pictures. Note that tangency here means that intersections become tangent as we continuously vary initial conditions on the unstable manifold. It

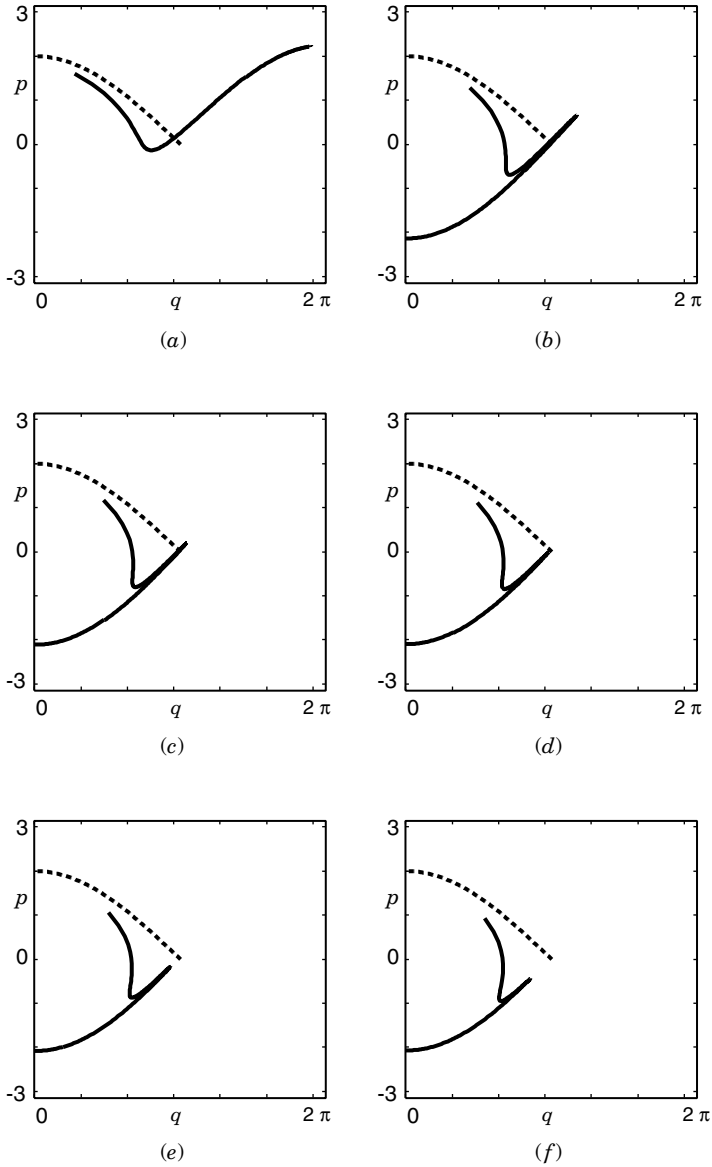

Figure 22. How intersections between stable manifolds (dotted lines) and unstable manifolds (solid lines) change as θ_0 varies. Tangency takes place at (*d*). We choose $V = 1.0$, $\omega = 1.0$, $\varepsilon = 0.1$, and $\mu = 0.22$, and the initial values θ_0 for these pictures are the following: (*a*) $\theta_0 = -0.9\pi$, (*b*) $\theta_0 = -0.8\pi$, (*c*) $\theta_0 = -0.78\pi$, (*d*) $\theta_0 = -0.77\pi$, (*e*) $\theta_0 = -0.76\pi$, (*f*)$\theta_0 = -0.74\pi$.

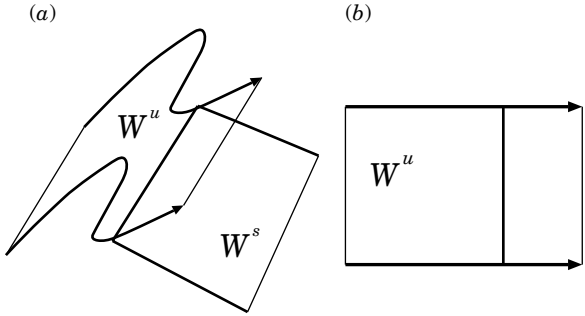

Figure 23. Schematic picture of intersections (*a*) shown in phase space and (*b*) displayed on the unstable manifold.

does not necessarily mean that the whole intersection between the three-dimensional unstable and stable manifolds becomes tangent.

The above intersections take place in the four-dimensional phase space. It is preferable to study them in a space of reduced dimensionality, which we introduce so as to see the intersections in a lower-dimensional space [12]. Figure 23 indicates a schematic picture of our idea, and Fig. 24 shows the results.

In Fig. 23a, an intersection between two-dimensional stable and unstable manifolds is displayed in a three-dimensional phase space. In order to see the intersection in a space of reduced dimensionality, only its location is indicated on the unstable manifold in Fig. 23b. Thus, we can single out the information on how they intersect, although we sacrifice the information on how these manifolds are folded as they intersect. (How they are folded can be also studied in a similar way using the Lagrangian singularity caused by folding. See the details in Ref. 12.)

In Fig. 24, intersections take place between two-dimensional pieces of the unstable manifold and the three-dimensional stable manifold in the four-dimensional phase space. Here, two-dimensional pieces of the unstable manifold are specified by the initial condition $I = 0$. In other words, we continuously vary initial conditions on the unstable manifold by changing the values of θ_0 with $I = 0$.

In Fig. 24, the abscissa is θ_0, and the ordinate indicates the direction of (q, p) along which the unstable manifold becomes stretched. We choose $V = 1.0$, $\omega = 1.5$, and $\varepsilon = 0.1$, and we vary the value of μ as follows: (a) $\mu = 0.19700$, (b) $\mu = 0.19750$, (c) $\mu = 0.19810$, (d) $\mu = 0.19834$, (e) $\mu = 0.19900$, (f) $\mu = 0.19950$.

We can see that in Fig. 24d a qualitative change takes place in the way intersection lines are connected. In Figs. 24a–c, tangency does not occur and

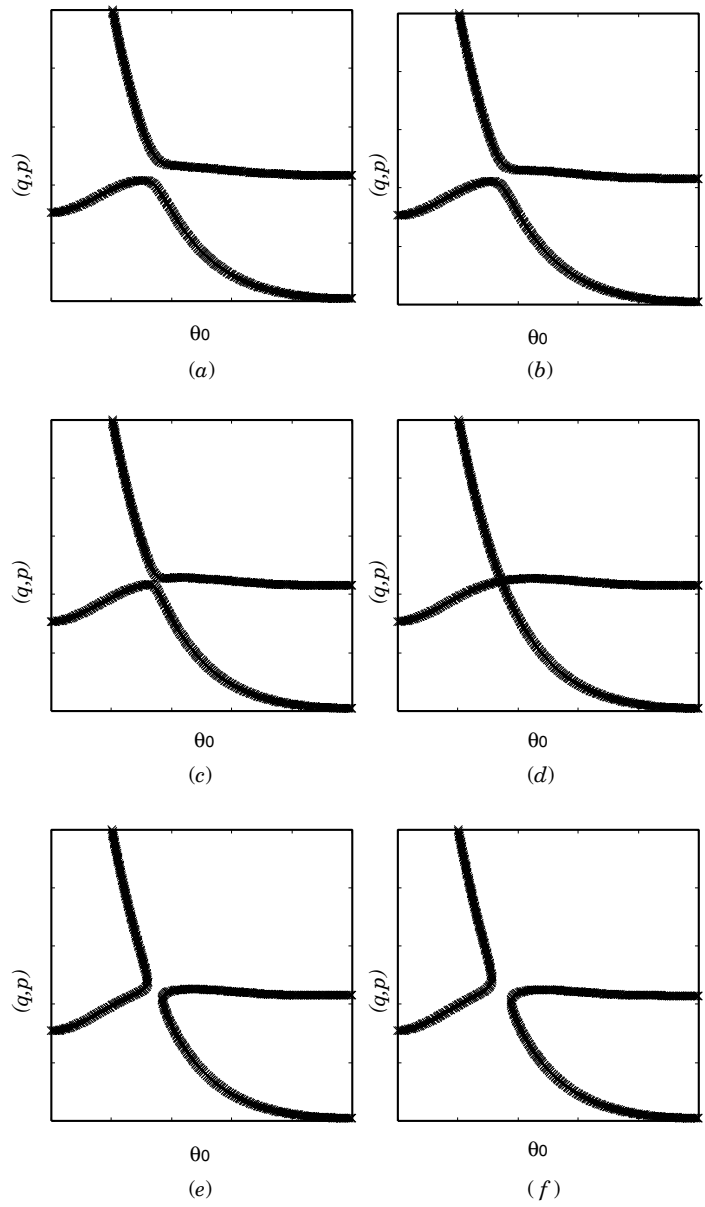

Figure 24. Intersection displayed on the unstable manifold. Qualitative change of intersections takes place at (*d*). We choose $V = 1.0$, $\omega = 1.5$, and $\varepsilon = 0.1$ and vary the value of μ as follows: (*a*) $\mu = 0.19700$, (*b*) $\mu = 0.19750$, (*c*) $\mu = 0.19810$, (*d*) $\mu = 0.19834$, (*e*) $\mu = 0.19900$, (*f*) $\mu = 0.19950$.

intersections are always transverse. On the other hand, in Figs. 24e and 24f, tangency occurs as initial conditions θ_0 change. Thus, a topological transition must be seen in the dynamical behavior of the system, as the value of μ varies.

In the following, we estimate the value of μ when the transition takes place. Our method is based on the following idea concerning the large difference among the characteristic time scales.

The characteristic time scale for (q,p) is of the order of $(\sqrt{V})^{-1}$, and that for the external force is ω^{-1}. On the other hand, the characteristic time scale for (I,θ) is Ω^{-1}. Thus, in the asymptotic limit where Ω goes to zero, the behavior of (I,θ) is supposed to be very slow in comparison to that of (q,p) and the external force. Therefore, we can consider the dynamics as composed of (a) the interaction between (q,p) and the external force and (b) the interaction between (q,p) and (I,θ). Then, the energy balance for (q,p) is estimated to see how (q,p) behaves with the above interactions combined.

To estimate the energy change of (q,p) caused by the external force, we use the Melnikov integral. To estimate the change caused by the coupling to (I,θ), we resort to the sudden approximation. By adding these two changes, we can qualitatively see the dynamics of (q,p). This argument gives a reasoning for the perturbation analysis using two small parameters ε and μ. In Figs. 25 and 26, we show a schematic explanation of our idea.

In Fig. 25a, the energy change caused by the external force is shown as an oscillatory feature of the unstable manifold (the solid line). There, the unstable

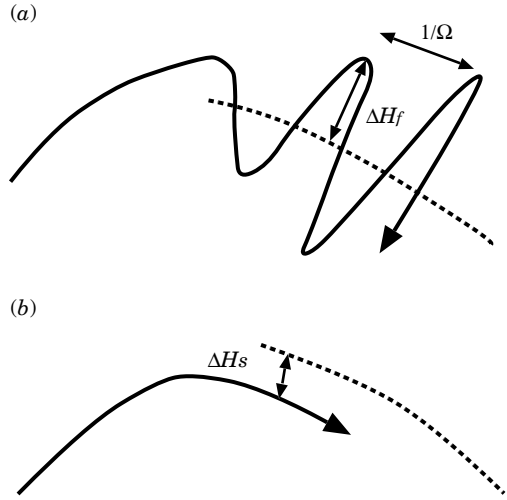

Figure 25. Energy changes (*a*) caused by external force and (*b*) caused by interaction with (I,θ).

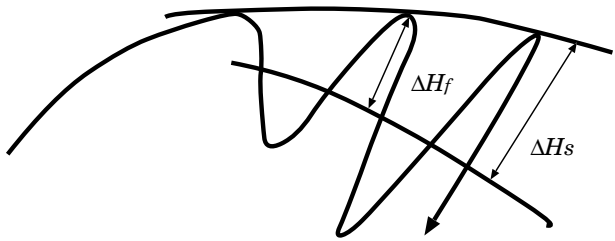

Figure 26. Schematic picture showing how to estimate tangency.

manifold intersects with the stable manifold (the dotted line). This feature is estimated using the Melnikov integral, that is,

$$\Delta H_f = \varepsilon \frac{2\pi\omega^2/V}{\sinh\left(\frac{\pi\omega}{2\sqrt{V}}\right)} \sin(\omega\tau) \tag{94}$$

Note that the frequency of the oscillatory feature of the manifold is given by the frequency of the interaction. Therefore, if the frequency of the interaction goes to zero, the feature of the manifold changes from the oscillation to a shift shown in Fig. 25b as ΔH_s. To estimate this shift, we have to resort to a different method.

Combining these two changes—that is, the oscillation and the shift—we can understand the dynamics of (q, p). If the energy change caused by the external force ΔH_f and the change ΔH_s caused by (I, θ) are equal, that is,

$$\Delta H_f + \Delta H_s = 0 \tag{95}$$

tangency takes place. We use Eq. (95) to estimate μ when tangency takes place. See Fig. 26 for a schematic explanation of how to estimate μ when tangency takes place.

In order to implement the above idea, we need to estimate ΔH_s. We use the sudden approximation as follows. The equation of motion for I is given by the following:

$$\dot{I} = -\mu \sin\theta(\cos q + 1) \tag{96}$$

where $q(t)$ is the separatrix orbit. The behavior of (q, p) is much faster than that of (I, θ). Therefore, we regard the influence of (q, p) on the separatrix to (I, θ) as an impact, that is,

$$\cos q + 1 = \frac{2}{\cosh^2(\sqrt{V}t)} \sim 4\delta(\sqrt{V}t) \tag{97}$$

Then, the variable I changes its value from the initial value $I = 0$ by the following amount:

$$\Delta I = -\frac{4\mu \sin \theta_0}{\sqrt{V}} \tag{98}$$

where we regard the variable θ as fixed in its initial condition θ_0.

The change ΔI of the variable I causes a decrease of the energy possessed in (q, p) by an amount ΔH_s:

$$\Delta H_s = -(\Delta I)^2/2 \tag{99}$$

Substituting Eq. (98) to Eq. (94), we obtain ΔH_s in the form

$$\Delta H_s = -\frac{8\mu^2 \sin^2 \theta_0}{V} \tag{100}$$

In estimating μ by Eq. (95), we use Eq. (94) and Eq. (100). When we omit the dependence on θ_0 in Eq. (100), and the oscillatory dependence in Eq. (94), the condition Eq. (95) for tangency becomes

$$\varepsilon \frac{2\pi\omega^2/V}{\sinh\left(\frac{\pi\omega}{2\sqrt{V}}\right)} = \frac{8\mu^2}{V} \tag{101}$$

In Fig. 27, we compare the results of our numerical calculations (shown as crosses) with those obtained in Eq. (101) shown as the solid line. We choose $V = 1.0$ and $\varepsilon = 0.1$ here. We can see that the two results coincide very well, supporting the validity of our ideas for the analysis.

In this section, we have discussed the condition for tangency using the Melnikov integral and the sudden approximation. The analyses in this section needs to be further developed in the following directions: First, the sudden approximation should be improved to take into account the movement of the slow variable, that is, (I, θ). Second, the assumptions Eq. (41) should be removed so that the analyses can be applied to more generic cases. Third, the condition that μ is small must be removed so that intersections between resonances of full strength can be analyzed. Fourth, realistic reactions should be analyzed so that the content of this section has more direct relevance to reaction processes.

VIII. CHAOTIC ITINERANCY

In this section, we discuss the branching structure of the skeleton of paths and chaotic itinerancy, which are seen as orbits wander around among NHIMs.

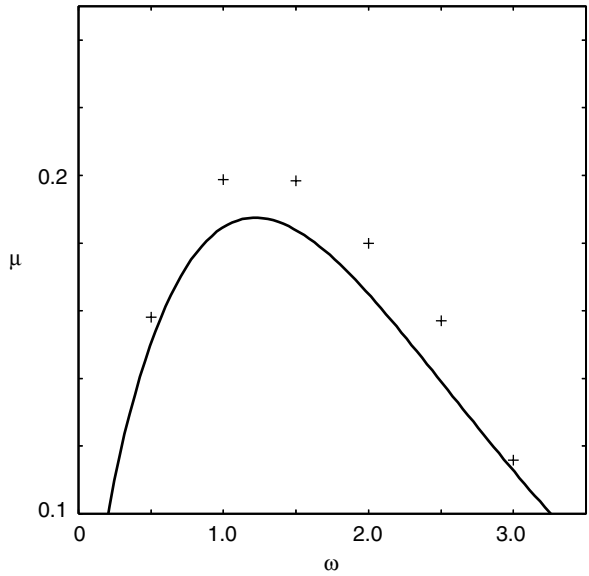

Figure 27. Comparison between numerical calculations and analytical results Eq. (101). We choose $V = 1.0$ and $\varepsilon = 0.1$.

We will also show that the skeleton has a property called ‘‘structural stability.’’ We will then use this property to bridge our discussion from the second stage to the third one.

As reactions proceed, the system goes through multiple saddles and potential wells. Then, the reaction proceeds wandering around NHIMs of saddles with index 1, those with index larger than 1, and also NHIMs of whiskered tori. When leaving NHIMs, an orbit moves along their unstable manifolds, and when approaching NHIMs, it goes along their stable manifolds. The intersection between the stable and unstable manifolds works as a switch that determines which NHIM is connected to which. Since one NHIM would be connected with multiple NHIMs in chaos of multiple degrees of freedom, these connections have the structure of a network. Thus, in these wandering processes, intersections between the stable and unstable manifolds of NHIMs play the role of the skeleton of reaction paths.

Based on this idea, we draw Figs. 28 and 29, which show how orbits in the phase space would flow in the large.

In Fig. 28, we display multiple connections among NHIMs. Depending on initial conditions near the NHIM, one orbit can approach one NHIM, another can approach a different one. If we could choose initial conditions near the

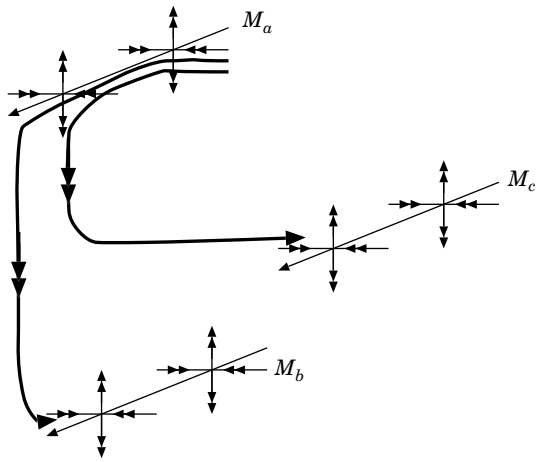

Figure 28. One NHIM is connected with multiple NHIMs.

starting NHIM, this would lead to control of the succeeding reaction processes, showing the importance of knowing the condition of tangency.

In Fig. 29, orbits approach a NHIM flowing almost parallel to its stable manifold. When coming near it, they move following the slow movement on it. After that, they leave it almost parallel to its unstable manifold. Then, through the intersections between its unstable manifold and the stable manifolds of other NHIMs, they approach different NHIMs following their stable manifolds. They would repeat such behavior forever.

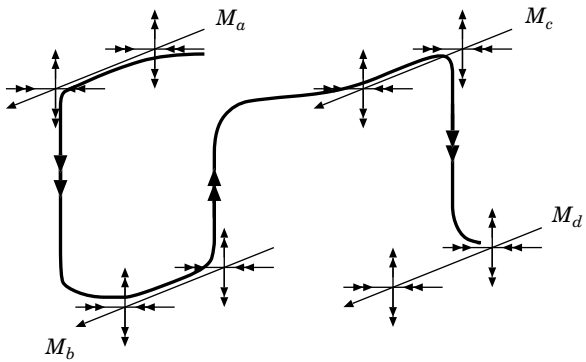

Figure 29. Chaotic itinerancy where an orbit wanders around multiple saddles.

This behavior reminds us of ''chaotic itinerancy'' found in dynamical systems with many degrees of freedom [18,19,21,38]. Chaotic itinerancy is the behavior where orbits repetitively approach and leave invariant structures of the phase space. Such behavior has been found in coupled maps [19], turbulence [18], neural networks [38], and Hamilton systems [21]. The mechanism of chaotic itinerancy is not yet fully understood. The study of NHIMs and how their stable and unstable manifolds intersect could offer some clues in revealing its mechanism [20].

In chemical reactions, orbits on stable and unstable manifolds of NHIMs describe movements of reaction coordinates. In some cases, these reaction coordinates are those degrees of freedom describing the behavior of individual nuclei such as a bond length between a pair of atoms. In other cases such as protein folding, reaction coordinates describe collective behavior where multiple nuclei participate. In either case, the processes of leaving a NHIM and approaching another one involve reformulation of reaction coordinates. In particular, when reaction coordinates are collective variables, reformulation processes themselves are of interest. We think that the study of intersections is crucial to understand how a certain collective movement is replaced by another one.

Thus, while the system wanders around multiple NHIMs, those degrees of freedom that constitute the reaction coordinates change as the reaction proceeds. This is the viewpoint that we would like to establish in the second stage of our strategy, where global aspects of the phase space is the target.

One of the important properties of this viewpoint is that it is ''structurally stable.'' Structural stability means that characteristic features of the systems do not change qualitatively as their parameters vary by sufficiently small amounts. In mathematics, this means that the systems we consider constitute an open set under a suitable topology [39].

In our study, NHIMs and their stable and unstable manifolds, at least locally near the NHIM, smoothly depend on parameters of the system. This is guaranteed by the theorem of Fenichel and Hirsch et al. Moreover, transverse intersections between stable and unstable manifolds are structurally stable. This is because their existence and characteristics do not change as the parameters vary by sufficiently small amounts. Thus, all of the features except possibly for tangency are structurally stable.

Structural stability implies that those features do not change qualitatively even when the system is under the influence of other possibly random effects, as far as their effects are sufficiently small. In this sense, we can single out robust features of the system using the concepts of NHIMs, their stable and unstable manifolds, and the intersections among them.

As we move on to the third stage, we pay attention to other features that are not structurally stable. The first is breakdown of the condition of normal

hyperbolicity, and the second is related to bifurcation in the connections among NHIMs.

IX. BREAKDOWN OF NORMAL HYPERBOLICITY

Until now, our main interest has been in those aspects of the skeleton that are structurally stable. However, in reaction processes of complex systems, other features that are not structurally stable also play a crucial role. For example, in the processes of evolution, life acquires new reaction mechanisms that emerge from old ones. Other examples are phase transitions in systems with finite degrees of freedom, such as clusters. Thus, qualitative jumps in reaction mechanism are also of importance. Here and also in the next sections, we consider how to incorporate those features that are not structurally stable into our strategy. Since the study in this stage is premature, our argument will be intuitive. We will also foresee future development in these two sections.

In this section, we consider the breakdown of the condition of normal hyperbolicity. First, we explain a simple example where breakdown of normal hyperbolicity leads to a bifurcation in reaction processes. In the Belousov–Zhabotinsky (BZ) reaction [40], the bifurcation from the stable fixed point to the limit cycle takes place through the breakdown of normal hyperbolicity. This is the simplest case where mathematical analyses are in progress [41].

Second, we point out the possibility that normal hyperbolicity breaks down for NHIMs with saddles as the energy of the vibrational modes increases at saddles. These cases seem to be much more difficult than that in the BZ reaction. At present, no attempt to analyze these cases has been made. However, considering that we face these cases frequently in reactions, the study of the breakdown of normal hyperbilicity is urgent.

Now, we explain the breakdown in the BZ reaction. The simplest equation that models the reaction is given by

$$\begin{aligned} \varepsilon \frac{dx}{dt} &= f(x, y) \\ \frac{dy}{dt} &= x - y \end{aligned} \tag{102}$$

where both x and y are one-dimensional variables and $0 < \varepsilon \ll 1$. In Eq. (102), x is a fast variable and y is a slow one.

We do not give a concrete form of the function $f(x, y)$ for the BZ reaction, because its expression is complicated [40]. Instead, we use the following function:

$$f(x, y) = y - a(x - x_1)(x - x_2)(x - x_3) - b \tag{103}$$

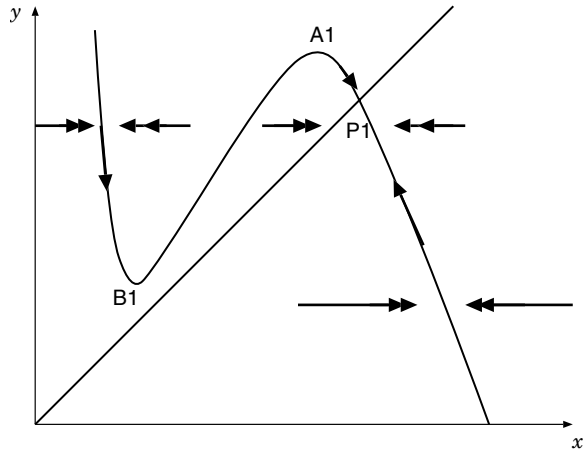

Figure 30. Flow of BZ reaction when stable fixed point exists.

since the essence of the following argument does not change. Here, the constants of $f(x, y)$ satisfy $a < 0, b > 0, 0 < x_1 < x_2 < x_3$.

In Figs. 30 and 31, the flow under Eq. (102) is displayed in the phase space (x, y). Figure 30 shows a case where the reaction terminates at the fixed point, and Fig. 31 shows a case where the limit cycle exists. In these figures, the NHIMs M_0 are graphs $x = x(y)$ that are obtained by solving $f(x, y) = 0$ for x,

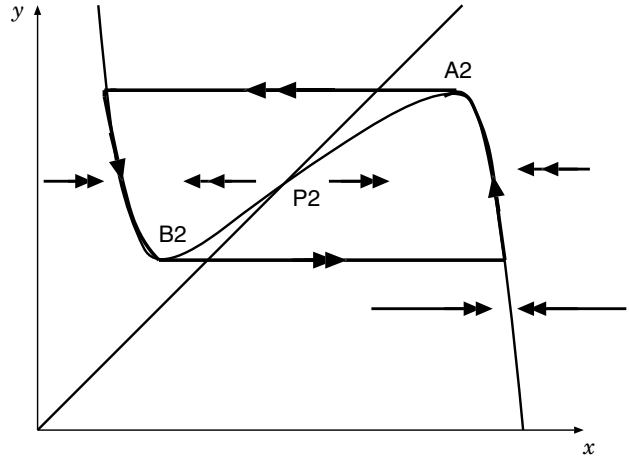

Figure 31. Flow of BZ reaction when limit cycle exists.

and there we have $dx/dt = 0$. There, we also display the locations where $dy/dt = 0$ holds, that is, $x = y$.

Since x varies much faster than y does, in these figures the flow runs almost parallel to the x axis. On the other hand, slower movements take place along $f(x, y) = 0$. The slower movements change their directions at the point where $dy/dt = 0$ holds, that is, $x = y$. The intersections between two curves $f(x, y) = 0$ and $x = y$—that is, the points P1 and P2—are fixed points. While P1 is a stable fixed point, P2 is unstable.

Note in these figures that the manifold defined by $f(x, y) = 0$ does not constitute a single NHIM. This is because the fast movement goes parallel to the tangent direction of the manifold $f(x, y) = 0$ at the points A1 and B1 in Fig. 30, and at the points A2 and B2 in Fig. 31, respectively. In other words, there exist three NHIMs, which are separated from each other by these points where $dy/dx = 0$. Thus, normal hyperbolicity breaks down at these four points. Therefore, the manifold $f(x, y) = 0$ consists of three NHIMs that are separated at A1 and B1 in Fig. 30, and A2 and B2 in Fig. 31, respectively.

This indicates that NHIMs in general have boundaries, and orbits flow off NHIMs at their boundaries.

Moreover, the breakdown of normal hyperbolicity leads to the bifurcation from the fixed point to the limit cycle. Suppose that under a smooth variation of parameters we change the flow from the one in Fig. 30 to the one in Fig. 31. Then, in order for the fixed point P1 in Fig. 30 to shift to P2 in Fig. 31, it should go through the point where normal hyperbolicity breaks down.

Thus, we speculate that, in the processes where qualitatively different flows emerge, the system would experience the situation where normal hyperbolicity breaks down. This speculation is based on the argument that, in order for the flows along the normal directions of NHIMs to bifurcate, one of the Lyapunov exponents of the normal directions must change its sign from plus to minus or from minus to plus. In the middle of these changes, normal hyperbolicity breaks down.

In reaction dynamics, NHIMs with saddles would lose normal hyperbolicity as the energy of the vibrational modes increases at saddles. This is shown schematically in Fig. 32. Here, a saddle X of the potential function is displayed with its NHIM above in the phase space. When the reaction takes place with only a small amount of the energy in the vibrational modes, orbits go over the saddle where the vibrational motions are quasi-periodic. In Fig. 32, this is shown by the dotted arrow with tori on the NHIM. As the energy of the vibrational modes increases, however, orbits go over the saddle where the vibrational motions are chaotic because of the coupling among the vibrational modes. In Fig. 32, this is shown by the solid arrow with chaos (shown by the wavy line) on the NHIM. If the Lyapunov exponents of these chaotic motions become larger than those of the normal directions, the condition of normal hyperbolicity breaks down.

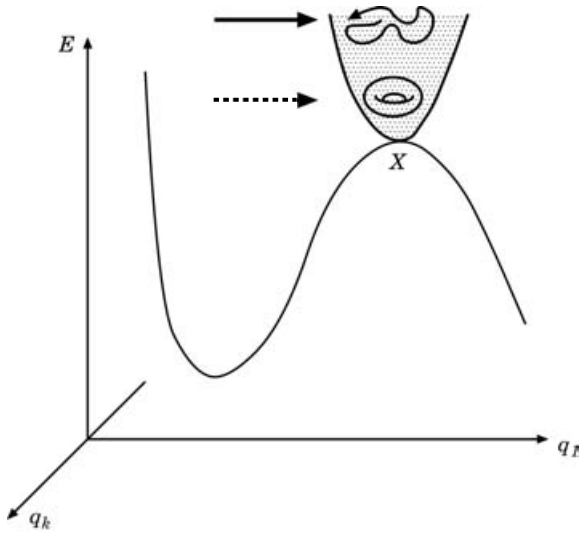

Figure 32. Breakdown of normal hyperbolicity at a saddle.

These situations take place when we raise the energy of clusters. Then, clusters would frequently change their structures, crossing over multiple saddles with considerable vibrational energy [42,43]. This leads to a phase transition of the cluster from the solid to the liquid state. Thus, a phase transition in systems with finite degrees of freedom belongs to the class of cases where the breakdown of normal hyperbolicity plays a crucial role.

Contrary to the previous example where normal hyperbolicity breaks down at points, here it would break down over a region where chaotic orbits move around. In these cases, we do not know at all what could happen to the original NHIM. Considering that we frequently face those cases shown in Fig. 32, we definitely need to investigate them.

X. CRISIS IN MULTIDIMENSIONAL CHAOS

In the previous section, we explained the bifurcation on NHIMs which would result from breakdown of normal hyperbolicity. Here, we speculate on bifurcation in the connections among NHIMs. In Fig. 33, we schematically display how the connections among NHIMs would change. As parameters of the system vary, transverse intersections between the unstable manifold W_a^u of a NHIM M_a and the stable manifold W_b^s of a NHIM M_b [see Fig. 33(i)] disappear. Instead, transverse intersections between the unstable manifold W_a^u of the NHIM M_a and the stable manifold W_c^s of another NHIM M_c [see Fig. 33(ii)] appear.

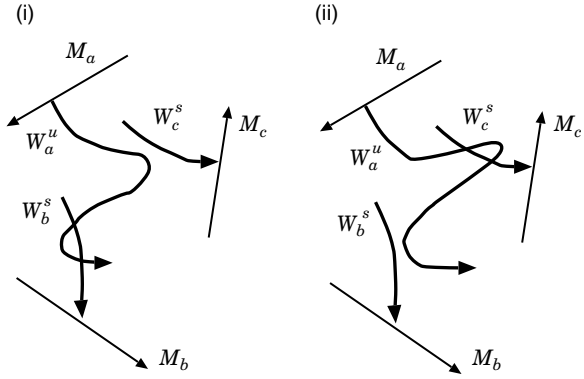

Figure 33. Change of intersections between stable and unstable manifolds.

When intersections disappear or new intersections appear, these intersections are tangent. Thus, we suggest that tangency signals bifurcation in the connections among NHIMs. Moreover, we expect that the tangency of intersections gives birth to a transition of chaos.

This mechanism can be considered as crisis in multidimensional chaos. Qualitative changes resulting from bifurcation of the skeleton would offer a clue to understanding how reaction processes exhibit phase transitions and how they evolve from older reaction processes.

Connections among NHIMs in multidimensional phase space is impossible to visualize directly. Thus, we need methods to detect their connections indirectly based on, for example, time series of orbits. We discuss this problem briefly.

The conventional theory of reaction processes relies on equilibrium statistical physics where the equi-energy surface is uniformly covered by orbits as shown in Fig. 34. To the contrary, the phase space in multidimensional chaos has various invariant structures, and orbits wander around these structures as shown in Fig. 35. In these processes, those degrees of freedom that constitute the movement along stable or unstable manifolds vary from NHIM to NHIM. Their variance reveals how reaction coordinates change during successive processes in reaction dynamics.

To characterize these invariant structures and the changes of reaction coordinates, the concept of finite-time Lyapunov exponents can be useful [44]. The original definition of the Lyapunov exponents needs ergodicity (see, e.g., Ref. 45) to make sure that the time average of the exponents converges. However, for chaotic itinerancy, the exponents would not converge. Moreover, the finite-time Lyapunov exponents can be more useful to detect whether

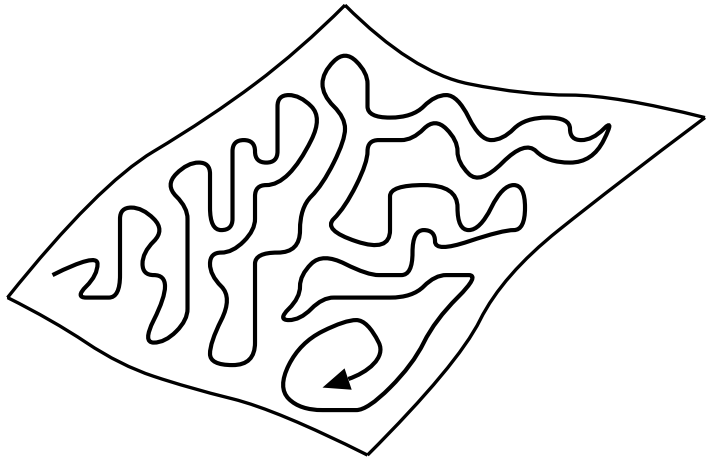

Figure 34. Dynamics on a uniformly ergodic equi-energy surface.

(a) orbits are staying near NHIMs where slow movements are dominant or (b) orbits are leaving or approaching NHIMs. Then, detailed investigation into which degrees of freedom participate in the changes of the finite Lyapunov vectors will be important for understanding chaotic initerancy in reaction dynamics. Furthermore, bifurcation of the finite Lyapunov exponents and their

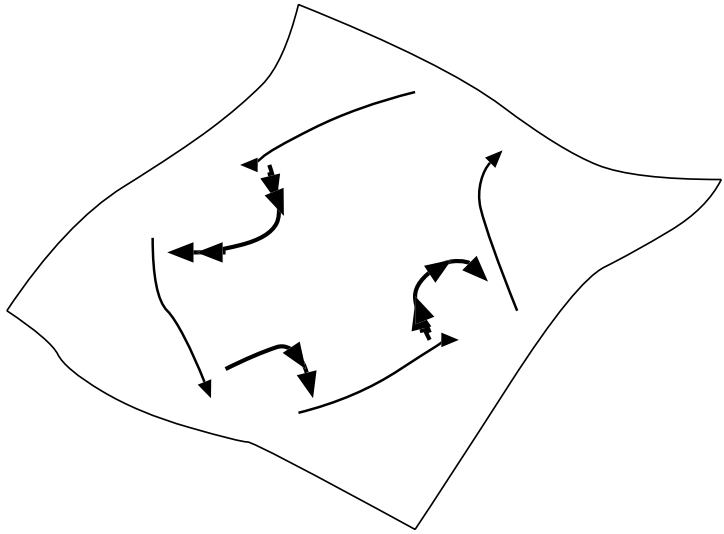

Figure 35. Wandering among invariant structures in the phase space.

vectors will give crucial clues for realizing the mechanism of how new reaction processes emerge from old ones. These ideas will provide us with concrete methods to study connections among NHIMs.

XI. SUMMARY

In this chapter, we have proposed a strategy for studying the dynamical processes associated with reactions from the standpoint of multidimensional chaos. Our strategy consists of the following three stages. First, we analyze local structures of the phase space based on the concepts of NHIMs and their stable and unstable manifolds. Second, we pay attention to global aspects of the dynamics based on the intersections of the stable and unstable manifolds. There, tangency will reveal branching structure of the skeleton of reaction paths. Third, we focus attention on bifurcation in the skeletons based on the breakdown of normal hyperbolicity and crisis.

For further development of our strategy to more complex systems such as protein folding, we need methods to coarse-grain the phase-space structure. For example, a statistical approach to the skeleton of paths could be an interesting idea. Closely related to this is the analyses of the rugged energy landscape, in which many saddles and wells exist. Then, simply following the stable and unstable manifolds of NHIMs would be cumbersome. Here also, we need methods to coarse-grain the phase-space structure. These problems can be tackled within our strategy, the results of which will be published in the future.

APPENDIX A. MELNIKOV INTEGRAL FOR EXAMPLE 1

Since the separatrix orbit is given by $q(t-\tau) = 2\sin^{-1}(\tanh(t-\tau))$, we have, for $-\pi \le q \le \pi$, the following expression:

$$\sin\frac{q}{2} = \tanh(t-\tau)$$

$$\cos\frac{q}{2} = \frac{1}{\cosh(t-\tau)} \tag{A.1}$$

$$\sin q = 2\tanh(t-\tau)\cdot\frac{1}{\cosh(t-\tau)} = 2\frac{\sinh(t-\tau)}{\cosh^2(t-\tau)} \tag{A.2}$$

Then, the integrand of the Melnikov integral is given by the following:

$$\begin{aligned}[H_0^r, \varepsilon H_1] &= -\varepsilon p\cos\theta\sin q \\ &= -\varepsilon\frac{2}{\cosh(t-\tau)}\cos(\omega t+\alpha)\frac{2\sinh(t-\tau)}{\cosh^2(t-\tau)}\end{aligned} \tag{A.3}$$

In integration, only the even functions contribute. Therefore, by setting $t' = t - \tau$, we have the following expression:

$$\begin{aligned} d &= \varepsilon \int_{-\infty}^{\infty} \frac{4 \sinh t' \cdot \sin \omega t'}{\cosh^3 t'} dt' \sin(\omega\tau + \alpha) \\ &= -2\varepsilon \sin(\omega\tau + \alpha) \left\{ \left[\frac{\sin \omega t}{\cosh^2 t} \right]_{-\infty}^{\infty} - \int_{-\infty}^{\infty} \frac{\omega \cos \omega t}{\cosh^2 t} dt \right\} \\ &= 2\varepsilon\omega \sin(\omega\tau + \alpha) \int_{-\infty}^{\infty} \frac{\cos \omega t}{\cosh^2 t} \, dt \end{aligned} \tag{A.4}$$

Thus, we have to estimate the following integral

$$d = 2\varepsilon\omega \sin(\omega\tau + \alpha) \int_{-\infty}^{\infty} \frac{\cos \omega t}{\cosh^2 t} \, dt \tag{A.5}$$

We estimate the integral in the complex t plane. See Fig. A.1 for the path for integration and the poles. Notice that the integrand has poles of second order at $t_n = i\pi(n + \frac{1}{2})$. Finally, we obtain the following:

$$\begin{aligned} \mathrm{Re} \int_{-\infty}^{\infty} \frac{e^{i\omega t}}{\cosh^2 t} \, dt &= 2\pi i \sum_{n=0}^{\infty} \mathrm{Re}\left(-i\omega e^{i\omega t_n}\right) \\ &= 2\pi\omega e^{-\frac{\pi}{2}\omega} \sum_{n=0}^{\infty} e^{-n\pi\omega} \\ &= \frac{\pi\omega}{\sinh \frac{\pi}{2}\omega} \end{aligned} \tag{A.6}$$

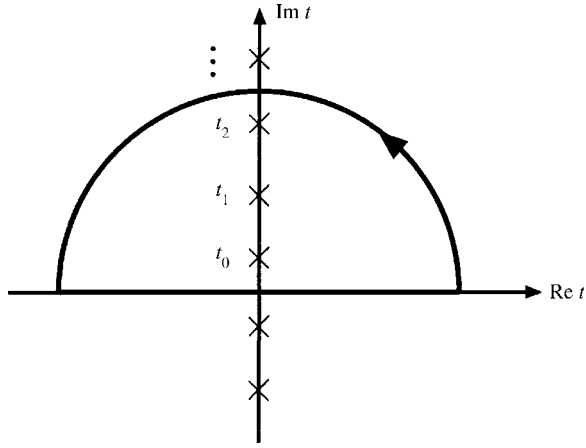

Figure A.1. The path in the complex t plane for the Melnikov integral.

Using these expressions, the gap d is given as follows:

$$\therefore \quad d = \varepsilon \frac{2\pi\omega^2}{\sinh \frac{\pi}{2}\omega} \sin(\omega\tau + \alpha) \tag{A.7}$$

APPENDIX B. MELNIKOV INTEGRAL FOR EXAMPLE 2

The gap is expressed as follows:

$$\begin{aligned} d &= -\frac{\varepsilon}{m}\int_{-\infty}^{\infty} p \sin(\omega t + \alpha)\, dt \\ &= -\varepsilon \frac{2\omega_0^2}{a}\int_{-\infty}^{\infty} \frac{t-\tau}{1+\omega_0^2(t-\tau)^2}\sin(\omega t + \alpha)\, dt \end{aligned} \tag{B.1}$$

Only even functions contribute in the integral.

By setting $t' = t - \tau$, we have

$$d = -\varepsilon \frac{2\omega_0^2}{a}\cos(\omega\tau + \alpha)\int_{-\infty}^{\infty} \frac{t' \sin \omega t}{1+(\omega_0 t')^2}\, dt' \tag{B.2}$$

where the integral is done in the complex t plane. See Fig. B.1 for the complex t plane, the pole and the path for integration. Thus, we obtain the following:

$$\int_{-\infty}^{\infty} \frac{\omega_0^2 t e^{i\omega t}}{1+(\omega_0 t)^2} dt = \pi i e^{-\frac{\omega}{\omega_0}} \tag{B.3}$$

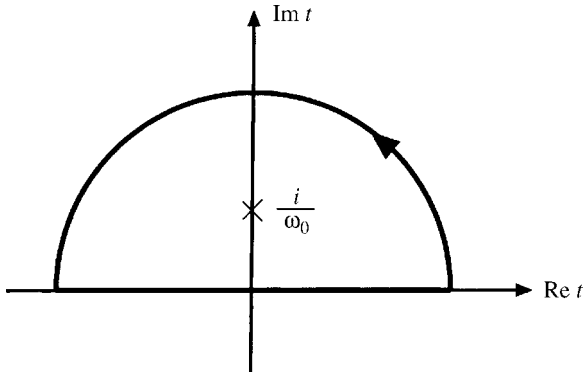

Figure B.1. The complex t plane for the Melnikov integral.

Then, we finally obtain the following result:

$$\therefore \quad d = -\varepsilon \frac{2\pi}{a} e^{-\frac{\omega}{\omega_0}} \cos(\omega\tau + \alpha) \tag{B.4}$$

Note that this integral does not converge for $\omega = 0$. This means that the Melnikov integral loses its meaning in the limiting cases near $\omega = 0$. This results from the fact that the fixed point is not hyperbolic as $p(t) \sim t^{-1} \quad (t \to \infty)$ shows.

Acknowledgments

The author would like to thank Dr. Fuchigami for his help in the initial stage of this work. This work is supported by the Grant-in-Aid for Scientific Research on Priority Areas "Control of Molecules in Intense Laser Fields" from the Japanese Ministry of Education, Science, Sports, and Culture.

References

1. M. Toda, *Adv. Chem. Phys.* **123**, 153 (2002).
2. T. Komatsuzaki and R. S. Berry, *Adv. Chem. Phys.* **123**, 79 (2002).
3. C. Jaffé, S. Kawai, J. Palacián, P. Yanguas, and T. Uzer, A New Look at the Transition State: Wigner's Dynamical Perspective Revisited, *Adv. Chem. Phys.* **130**, 171 (2005).
4. N. Fenichel, *Indiana Univ. Math. J.* **21**, 193 (1971).
5. N. Fenichel, *Indiana Univ. Math. J.* **23**, 1109 (1974).
6. N. Fenichel, *Indiana Univ. Math. J.* **26**, 81 (1977).
7. N. Fenichel, *J. Diff. Eq.* **31**, 53 (1979).
8. M. W. Hirsch, C. C. Pugh, and M. Shub, *Invariant Manifolds*, Lecture Notes in Mathematics, Vol. 583, Springer, New York, 1977.
9. M. J. Davis and S. K. Gray, *J. Chem. Phys.* **84**, 5389 (1986).
10. S. Wiggins, *Chaotic Transport in Dynamical Systems*, Springer, New York, 1992.
11. R. E. Gillilan and G. S. Ezra, *J. Chem. Phys.* **94**, 2648 (1991).
12. M. Toda, *Phys. Rev. Lett.* **74**, 2670 (1995).
13. Y. C. Lai, C. Grebogi, R. Blumel, and I. Kan, *Phys. Rev. Lett.* **84**, 2212 (1993).
14. S. Wiggins, *Physica* **D44**, 471 (1990).
15. V. I. Arnold, *Soviet Math. Dokl.* **5**, 581 (1964).
16. B. V. Chirikov, *Phys. Rep.* **52**, 265 (1979).
17. A. J. Lichtenberg and M. A. Lieberman, *Regular and Chaotic Dynamics*, Springer, New York, 1992.
18. K. Ikeda, K. Otsuka and K. Matsumoto, *Prog. Theor. Phys. Suppl.* **99**, 295 (1989).
19. K. Kaneko, *Physica* **D41**, 137 (1990).
20. M. Komuro, *A Mechanism of Chaotic Itinerancy in Globally Coupled Maps*, International Conference on New Directions in Dynamical Systems (NDDS 2002), A satellite conference of ICM 2002, August 5–15, 2002, Ryukoku University and Kyoto University, Kyoto, Japan.
21. T. Tsuchiya, N. Goda, and T. Konishi, *Astrophys. Space Sci.* **257**, 319 (1997).

22. Koon, W. S., M. Lo, J. E. Marsden, and S. Ross, *Chaos* **10**, 427 (2000).
23. T. Komatsuzaki, K. Hoshino, and Y. Matsunaga, Regularity in Chaotic Transitions on Multi-Basin Landscapes, *Adv. Chem. Phys. Part B* **130**, 257 (2005).
24. S. Wiggins, *Global Bifurcation and Chaos—Analytical Methods*, Springer, New York, 1988.
25. T. Konishi, Slow Dynamics in Multidimensional Phase Space: Arnold Model Revisited, *Adv. Chem. Phys. Part B* **130**, 423 (2005).
26. C. K. R. T. Jones, in *Dynamical Systems*, L. Arnold, ed., Lecture Notes in Mathematics, Vol. 1609, Springer, New York, 1995, p. 44.
27. T. J. Kaper, in *Analyzing Multiscale Phenomena Using Singular Perturbation Methods*, J. Cronin and R. E. O'Malley, Jr., eds., Proceedings of Symposia in Applied Mathematics, Vol. 56, American Mathematical Society, Rhode Island, 1999, p. 85.
28. G. Haller, *Chaos Near Resonance*, Springer, New York, 1999.
29. S. Wiggins, *Normally Hyperbolic Invariant Manifolds in Dynamical Systems*, Springer, New York, 1994.
30. S. Wiggins, *Introduction to Applied Nonlinear Dynamical Systems and Chaos*, Springer, New York, 2003.
31. S. M. Graff, *J. Diff. Eq.* **15**, 1 (1974).
32. J. Moser, *Stable and Random Motions in Dynamical Systems*, Annals of Mathematical Studies, Vol. 77, Princeton University Press, Princeton, 1973.
33. S. Honjo and K. Kaneko, Structure of Resonances and Transport in Multidimensional Hamiltonian Dynamical Systems, *Adv. Chem. Phys. Part B* **130**, 437 (2005).
34. L. Lasker, *Physica* **D67**, 257 (1993).
35. Z. Xia, *J. Diff. Eq.* **110**, 289 (1994).
36. Z. Xia, *Arnold Diffusion and Instabilities in Hamiltonian Dynamics*, preprint, see the web site <http://math.nwu.edu/~xia/preprint/arndiff.ps>.
37. M. Toda, to be published.
38. S. Nara and P. Davis, *Prog. Theor. Phys.* **88**, 845 (1992).
39. M. W. Hirsch and S. Smale, *Differential Equations, Dynamical Systems and Linear Algebra*, Academic Press, New York, 1974.
40. S. K. Scott, *Oscillations, Waves and Chaos in Chemical Kinetics*, Oxford University Press, Oxford, 1994.
41. M. Diener, *Math. Intell.* **6**, 38 (1984).
42. R. S. Berry, Atomic Clusters: Powerful Tools to Probe Complex Dynamics, *Adv. Chem. Phys. Part B* **130**, 3 (2005).
43. K. Takatsuka, Temperature, Geometry, and Variational Structure in Microcanonical Ensemble for Structural Isomerization Dynamics of Clusters: A Multichannel Chemical Reaction Beyond the Transition-State Concept, *Adv. Chem. Phys. Part B* **130**, 25 (2005).
44. T. Okushima, Finite-Time Lyapunov Exponents in Many-Dimensional Dynamical Systems, *Adv. Chem. Phys. Part B* **130**, 501 (2005).
45. E. Ott, *Chaos in Dynamical Systems*, 2nd ed., Cambridge University Press, Cambridge, 2002.

CHAPTER 8

CLASSICAL MECHANISM OF MULTIDIMENSIONAL BARRIER TUNNELING

KIN'YA TAKAHASHI

The Physics Laboratories, Kyushu Institute of Technology, Iizuka, 820-8502, Japan

KENSUKE S. IKEDA

Department of Physical Sciences, Faculty of Science and Engineering, Ritsumeikan University, Kusatsu, 525-8577, Japan

CONTENTS

I. Introduction: Global Aspects of Multidimensional Tunneling
II. Fringed Tunneling and Semiclassical Method
  A. Model System and Fringed Tunneling
  B. Semiclassical Method
III. Static Barrier
  A. A Classical Solution of the Static Barrier
  B. Singularities and Integration Paths of Classical Trajectories
IV. Semiclassical Results
  A. Effects of the Periodic Perturbation
  B. Local Structure of $\mathcal{M}$-Set Near the Critical Point
  C. Global Structure of Branches Contributing to the Fringed Tunneling
V. Theoretical Analyses
  A. Brief Sketch of Our Analyses
  B. Low-Frequency Approximation
  C. Contributions of Multiple Characteristic Trajectories to the Fringed Tunneling
  D. Characteristic Perturbation Strength
VI. Summary
Appendix A: Fringed Tunneling in a 2D Barrier System
Appendix B: Melnikov Method
Acknowledgments
References

Geometric Structures of Phase Space in Multidimensional Chaos: A Special Volume of Advances in Chemical Physics, Part A, Volume 130, edited by M. Toda, T Komatsuzaki, T. Konishi, R.S. Berry, and S.A. Rice. Series editor Stuart A. Rice.
ISBN 0-471-70527-6

Multidimensionality of systems significantly affects tunneling phenomena. In particular, if a system under consideration is classically nonintegrable, then very complicated tunneling phenomena, referred to as called *chaotic tunneling*, are observed. The aim of this short review is to explain the underlying classical mechanism of multidimensional barrier tunneling by using the semiclassical method based on classical dynamics extended to the complex domain—that is, the complex semiclassical method. The tunneling probability of multidimensional barrier systems is still well reproduced by using the complex semiclassical method even in the chaotic tunneling regime, in which a characteristic tunneling phenomenon (i.e., the fringed tunneling) is observed. However, the classical trajectories guided by complexified stable and unstable manifolds dominantly contribute to the tunneling probability, which gives quite a different picture of the tunneling from that given by the ordinary instanton mechanism.

I. INTRODUCTION: GLOBAL ASPECTS OF MULTIDIMENSIONAL TUNNELING

The semiclassical method of multidimensional tunneling [1–3] is a long-standing problem which seems to be far from completion. If one wishes to apply the semiclassical method to the analysis of tunneling, he has to take into account classical trajectories going into the complex domain in order to reach a classically forbidden region where the tunneling wave is observed [4]. The instanton, which is a trajectory evolving in imaginary time [5], is a good example of such complexified trajectories used to explain the tunneling in terms of the semiclassical method. Indeed, it well reproduces the tunneling phenomena in one-dimensional (1D) systems as well as in multidimensional but classically (nearly) integrable systems [6–8]. The great success of the instanton theory seems to provide us with a good reason to expect that the tunneling of general multidimensional systems is easily manageable with the semiclassical method based on it.

However, a multidimensional system is generally classically nonintegrable, and so the existence of classical chaos, which more or less appears in the (complex) phase space, introduces some intrinsic difficulties to applying the semiclassical method to multidimensional tunneling. Even if we restrict ourselves to the real domain, which means that we don't take into account tunneling phenomena, the existence of chaos is a real obstacle to endowing the semiclassical method with the rigorously mathematical basis, while some practical applications of the semiclassical method work well in prediction of quantal quantities which are used to characterize the quantum chaotic nature of a system under consideration [9,10]. The extension of the phase space to the complex domain will introduce further complexities and difficulties, and there is

almost nothing known about the complex-domain chaos of more than one-dimensional systems.

Nevertheless, the manifestation of chaos in multidimensional tunneling phenomena has been attracting much attention [11–13], and there have been some successful attempts in application of the (complex-domain) semiclassical method to multidimensional tunneling in classically nonintegrable systems [14–17]. For example, it is well known as the chaos assisted tunneling that the tunneling between quasi-degenerate doublets located on twin tori of KAM islands for systems with a tori-chaos mixed phase-space structure becomes very sensitive to the presence of the chaotic sea between them. Bohigas et al. [11] applied some semiquantum approach based on the level spectrum analysis for giving a phenomenological explanation of a mechanism of the chaos-assisted tunneling. Recently, there have been some reports of experiments that succeeded in measurement of tunneling phenomena predicted by the theory of chaos-assisted tunneling: microwave spectra in the superconducting cavity, momentum distributions of cold atoms in an amplitude-modulated standing wave of light, and so on [13].

More mathematically rigorous application of the semiclassical method to the tunneling in classically chaotic systems was performed by Shudo and Ikeda taking a kicked rotator as a model system of chaotic tunneling. Actually they have investigated the tunneling probability penetrating from tori to a chaotic sea, and they have demonstrated that the semiclassical method using the complexified classical trajectories can well reproduce every detail of the complicated features of the tunneling wavefunction penetrating into the chaotic region [15]. Furthermore, it has been suggested that there are some deep connections between the tunneling problem and key concepts of complex dynamical systems such as Julia sets, Böttcher coordinates, and so on [18].

However, it is still unclear if their approach and results concerning with the quantum maps could be applicable to the tunneling problem of ordinary multidimensional systems that are evolved in time by the continuous-time Schrödinger equation. This is because the underlying classical dynamics of time-continuous systems is essentially different in the complex domain from that of the map systems. In particular, the complexified classical trajectory of time-continuous systems generally has movable singularities, whose positions on complex time plane move depending on its initial condition, while there is no singularity of the trajectory in maps, since the discretized time has no analytical extension to the complex domain. It should be noted that the existence of movable singularities is well known in the field of the Painlevé analysis, and the analysis of movable singularities not only plays a key role in the judgment of integrability of a given system [19], but also, if it is not integrable, provides further information on the nature of chaotic motion inherent in the system [19,20]. Therefore it is considered that the movable singularities

probably play a key role of understanding chaotic tunneling phenomena with the semiclassical method, but, at the same time, their existence may introduce some difficulties in practical construction of the semiclassical method for time-continuous systems.

To our knowledge, the first pioneering work that treated the multidimensional tunneling for ordinary systems evolved in continuous time is a series of works by Miller et al. They developed a semiclassical formula of the S matrix [2], and they applied their formula to the case of collinear $H + H_2$ reaction. As a result, they found an intrinsic multidimensional tunneling phenomenon reproduced by novel complex tunneling paths that were never predicted by the one-dimensional approach based on the adiabatic approximation [1]. They have, however, treated a rather regular case—that is, ground-state to ground-state tunneling—then the tunneling trajectories they found seem not to be affected by any classical chaos.

The energy barrier tunneling problem in multidimensional autonomous systems has attracted several author's attentions [3,14]. In particular, the tunneling in 2D double well potentials has been investigated along the line of trace formula by Creagh and Whelan [14]. They studied the case in which the energy is sufficiently less than the potential saddle, then classical trajectories are localized in one well or other, but exhibit ergodic behavior in each well. They found that the major statistical behavior, namely mean behavior of the tunneling splitting induced by quasi-doublet states, is well described by the complex orbit penetrating through the energy potential barrier in pure imaginary time evolution, which gives the minimum imaginary action. It seems that the tunneling picture based on a single instanton orbit still works effectively in the energy barrier tunneling of multi-dimensions. However, in order to reproduce more detail statistical behavior in energy splitting sequence—that is, an characteristic oscillatory component observed in the sequence due to the chaos in both potential well—they had to take into account the contributions not only from a major instanton but from many other instanton-like orbits. Such instanton-like orbits are running very close the original instanton path in imaginary time and are connected with orbits homoclinic to the real orbit extended from the original instanton. It means that a single instanton orbit as well as a bunch of instanton-like orbits running under the potential barrier simultaneously contribute to the semiclassical formula.

The other important scenario in multidimensional tunneling is of the dynamical tunneling that is observed in 1.5D and 2D systems [21]. In this case, the classical phase space is separated not by the energy barrier but by the invariant surface (e.g., KAM tori). Such a situation is realized, for example, in periodically perturbed one-dimensional (1.5D) barrier potentials and also in 2D barrier systems when the total energy is taken over the potential saddle. In a series of recent articles [22–25], we have found a new class of tunneling phenomena

seeming to be influenced by classical instability in 1.5D scattering barrier systems. The tunneling component penetrating through the oscillating barrier is still described by the standard instanton theory (or its modified version) in a weak perturbation regime, but it becomes accompanied by a remarkable fringed pattern as the perturbation strength exceeds a certain characteristic value; that is, the so-called fringed tunneling is observed. It should be noted that similar fringed patterns are also observed in the tunneling component in a certain class of 2D barrier systems with a suitable choice of the total energy and the input channel [24,26,27]. Thus the appearance of fringed pattern on the tunneling component is quite generic for multidimensional barrier systems.

The aim of this chapter is to provide a short review of our recent studies based on the complex domain semiclassical method, in which we have elucidated the underlying classical mechanisms of the fringed tunneling [23,24,25]. We will demonstrate that the feature of complex trajectories contributing via the semiclassical method to the fringed tunneling observed in the strong perturbation regime is essentially different from that of the instanton picture which well works in unperturbed or weakly perturbed systems. This point should be extremely stressed.

A set of complex trajectories satisfying the classical initial condition form an invariant manifold in the complex phase space, which is a classical counterpart of the incident plane wave. Some of those trajectories that satisfy the output boundary condition at the observatory point become contributing to the tunneling. Under the influence of the perturbation, the incoming wave manifold is entangled with the complexified stable manifold of the unstable periodic orbit at the top of the barrier, making heteroclinic-like entanglement. Such an entanglement always occurs in the complex domain for any nonzero strength of perturbation, even if it disappears in the real domain for a sufficiently weak perturbation. However, when the strength of perturbation is weak enough, the heteroclinic-like entanglement occurs in a much deeper side of the complex domain, and trajectories with smaller imaginary parts making major contributions to the tunneling obey the instanton scenario being saved from any significant influence of the complex entanglement. As the perturbation becomes stronger, the entanglement gets closer to the real axis, and thereby major contributing trajectories become subject to it. Such trajectories always start in the neighborhood of the heteroclinic-like point and are traveling in the complex phase space being guided by the complexified stable and unstable manifolds, which are the fundamental objects generating complexity of chaos in classically nonintegrable systems. As a result, the feature of trajectories contributing to the fringed tunneling observed in the strong perturbation regime is essentially different from that of the instanton picture that well works in unperturbed or weakly perturbed systems. Such trajectories are regarded as the simplest case of the complex trajectories contributing to chaotic tunneling appearing in general

multidimensional systems. Surprisingly enough, the entanglement among complexified invariant manifolds, which is a key to understanding the classical mechanism of the chaotic tunneling, is accompanied by singular behavior exhibited by singularities of the complexified trajectory, namely a singular dependence of singularities on its initial condition induces a topological switching of the integration path with change of the initial condition and plays a crucial rule in construction of the heteroclinic-like entanglement.

Some theoretical tools developed in Ref. 25—that is, the adiabatic classical solution in the low-frequency limit and the Melnikov method extended into the complex domain—allow us to prove almost every facts needed of theoretically understanding the underlying classical mechanism of the fringed tunneling. In particular, Section V is devoted to the theoretical analyses by using the adiabatic solution together with the Melnikov method. In Section VI we briefly discuss similarity and difference between maps and time-continuous systems in chaotic tunneling regimes [17]. Consequently, it is suggested that there exists a comprehensive story that gives a global aspect on the multidimensional tunneling independent of map and time-continuous systems.

II. FRINGED TUNNELING AND SEMICLASSICAL METHOD

A. Model System and Fringed Tunneling

First of all, we will briefly introduce the fringed tunneling and the complex-domain semiclassical method applied to it.

We take a periodically perturbed Eckart type-potential [28] as a model system of the fringed tunneling. The Hamiltonian of the model system is given as follows:

$$\begin{aligned} H(Q,\hat{P},\omega t) &= \tfrac{1}{2}\hat{P}^2 + V(Q,\omega t) \\ &= \tfrac{1}{2}\hat{P}^2 + V_0(Q) + \epsilon v(Q,\omega t) \end{aligned} \tag{1}$$

where Q is the coordinate and $\hat{P} = -i\hbar\frac{\partial}{\partial Q}$ is the momentum operator. The potentials $V_0(Q)$ and $v(Q,\omega t)$ are defined by

$$V_0(Q) = \mathrm{sech}^2(Q), \qquad v(Q,\omega t) = \sin(\omega t)\mathrm{sech}^2(Q) \tag{2}$$

where V_0 denotes a nonperturbed potential independent of time and v is a periodic function of time that acts as a perturbation. The parameter ϵ indicates the strength of perturbation.

The incident wave is coming from the right-hand side with a constant momentum $P_1(<0)$. If the incident energy $E_1(=\frac{1}{2}P_1^2)$ is taken small enough,

then the quantum probability observed in the transmissive side is due to the tunneling effect.

The stationary solution is given by the Floquet solution [29],

$$\Psi_{P_1}(Q_2, t_2) = \mathrm{e}^{-iE_1 t_2/\hbar} \langle Q_2 | \hat{\Omega}_1^+(\omega t_2) | P_1 \rangle \tag{3}$$

and the periodic part of the Floquet solution $\langle Q_2 | \hat{\Omega}_1^+(\omega t_2) | P_1 \rangle$ is the wave matrix for periodically perturbed systems [22,30]. Its convenience representation is obtained as follows [22]:

$$\begin{aligned} \langle Q_2 | \hat{\Omega}_1^+(\omega t_2) | P_1 \rangle = & \lim_{|Q_1| \to \infty} \sqrt{\frac{|P_1|}{2\pi\hbar}} e^{iP_1 Q_1/\hbar} \\ & \times \int_0^\infty ds \langle Q_2 | \hat{U}(\omega t_2 : \omega t_2 - \omega s) | Q_1 \rangle \exp\left\{ i \frac{E_1 s}{\hbar} \right\} \end{aligned} \tag{4}$$

where $\hat{U}$ denotes the time propagator of the system defined by

$$\hat{U}(\theta + \omega t : \theta) = \mathscr{T} \exp\left\{ -\frac{i}{\hbar} \int_0^t ds \hat{H}(\theta + \omega s) \right\} \tag{5}$$

where $\mathscr{T}$ is a time ordering operator. Then, the wave operator is nothing more than the time-dependent analogue of the energy domain Green function.

Let's see the numerical results (see Fig. 1). The tunneling wave changes depending on the strength of the perturbation ϵ. The result of the week perturbation regime, $\epsilon = 0.05$, is shown in Fig. 1a, in which the quantum probability is drawn as a function of the coordinate Q. The potential is localized near the origin, and its width is very small in this scale. Then the probability for negative Q indicates the tunneling component. There is a regular spatial oscillation in the tunneling component. On the other hand, in the strong perturbation regime ($\epsilon = 0.2$) in Fig. 1b, we find the complicated fringes superposed on the simple spatial oscillation in the tunneling component, namely the fringed tunneling. Appearance of such complicated patterns is a manifestation of the multidimensionality of the system in the tunneling phenomenon. As shown in Appendix A, similar fringed patterns are observed in a certain class of 2D autonomous systems [24,26,27]. Hereafter, we concentrate on the strong perturbation regime—that is, the fringed tunneling.

B. Semiclassical Method

The main tool attacking such complicated tunneling phenomena is the complex-domain semiclassical method, and the appearance of fringed patterns in the

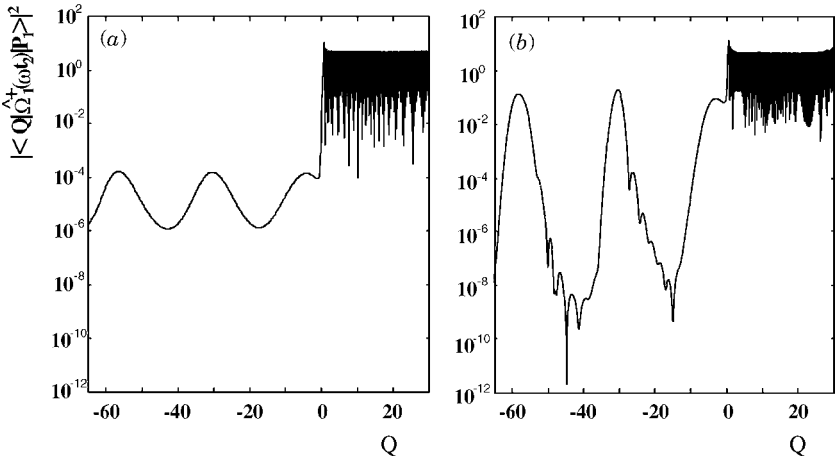

Figure 1. Snapshots of quantum probabilities. (*a*) Weak perturbation regime: $\epsilon = 0.05$. (*b*) Strong perturbation regime: $\epsilon = 0.2$. The other parameters are set as follows: $E_1 = 0.75, \omega = 0.3$, $\hbar = 1000/(3\pi \times 2^{10}) \sim 0.1036$, and $\omega t_2 = 0(\mathrm{mod} 2\pi)$.

tunneling component should be explained in terms of complexified semiclassical method.

By applying the saddle point approximation to its formula, the semiclassical expression of the wave matrix is given as follows [22]:

$$\langle Q_2|\hat{\Omega}_1^+(t_2)|P_1\rangle \sim \sum_{\text{c.t.}} \lim_{Q_1\to\infty} \sqrt{\frac{|P_1|}{2\pi\hbar}} e^{iP_1Q_1/\hbar} \left(\frac{1}{P_1}\frac{\partial^2 S_\Omega}{\partial E_1 \partial Q_2}\right)^{1/2} \times \exp\left[\frac{i}{\hbar} S_\Omega(Q_2, t_2, Q_1, E_1)\right] \tag{6}$$

where the classical action is defined by

$$S_\Omega(Q_2, t_2, Q_1, E_1) \equiv \int_{t_1}^{t_2} [P(t)^2/2 - V(Q, \omega t)]\, dt + E_1(t_2 - t_1(Q_2, t_2, Q_1, E_1)) \tag{7}$$

The classical action is a function of the initial coordinate Q_1, initial energy E_1, end time t_2, and end coordinate Q_2; thus the initial time t_1 is not an independent variable.

The notation $\sum_{\text{c.t.}}$ in Eq. (6) means to sum over all the classical trajectories satisfying the boundary condition which is decided by the independent variables

of the classical action [Eq. (7)]. In particular, in order to calculate the tunneling probability by the semiclassical method, we should take into account the classical trajectories going into the complex domain of the phase space, with the classical equation of motion,

$$\frac{d^2Q}{dt^2} = -\frac{\partial V(Q, \omega t)}{\partial Q} \tag{8}$$

The initial and final sets of dynamical variables deciding the classical action, namely (Q_1, E_1) and (Q_2, t_2) in this case, are the quantum observables specifying the initial and final states. Then we should assign real numbers to them. Since t_1 is canonically conjugate to E_1 and cannot be observed quantum mechanically, we can choose any complex number for it and the lapse times $s = t_2 - t_1$ may take a complex number. To our knowledge, such prescription for complexifying canonically paired observables was first presented by Miller [2].

A convenient way to find the trajectory satisfying the boundary condition is to take t_1 as a complex search parameter. In order to obtain the quantum probability as a function of Q_2, we should change the end coordinate Q_2 in the real line with fixed t_2 real, then the search parameter t_1 will trace a 1D set on the complex plane—that is, 1D curves. According to Shudo and Ikeda [15], we call such a set on the complex initial time plane t_1 the $\mathscr{M}$-set, which is defined by [22]

$$\mathscr{M} = \{t_1 = \xi + i\eta \,|\, (\xi, \eta) \in \mathbf{R}^2, \operatorname{Im} Q(t_2 - t_1, t_1, P_1, Q_1) = 0\} \tag{9}$$

where ξ and η denote the real and imaginary parts of t_1; thus the $t_2 - (\xi - i\eta)$ is the lapse time. The $\mathscr{M}$-set is in general composed of disconnected curves and we call each piece of disconnected components the complex branch. A single branch is not always enough to reconstruct the quantum probability; two or more branches and sometimes an infinite number of branches may simultaneously contribute to it, as will be shown later. The $\mathscr{M}$-set enables us to visualize the structure of the set of initial conditions of contributing trajectories on the search plane.

We also introduce the $\mathscr{L}$-set [22]:

$$\begin{aligned} \mathscr{L} = \{(Q_2, P_2) | Q_2 &= Q(t_2 - t_1, t_1, P_1, Q_1), \\ P_2 &= P(t_2 - t_1, t_1, P_1, Q_1), t_1 \in \mathscr{M}\} \end{aligned} \tag{10}$$

which is the set of the end point (Q_2, P_2) at a given time t_2 of the trajectories satisfying the initial condition given by the $\mathscr{M}$-set.

There are two problems peculiar to the complex domain semiclassical method which introduce some difficulties in handling of the semiclassical wave matrix.

One is the Stokes phenomenon [31–35]. The Stokes phenomenon is a very important subject of semiclassical method, but we won't describe it in detail in this chapter (for details see Ref. [22,35]).

The other is of the singularities of the complex classical trajectories [19], which is peculiar to time-continuous systems and plays an important role to understand tunneling phenomena of barrier potentials [25]. First, we briefly explain the role of singularities of classical trajectory by taking the static Eckart barrier as a simple example.

III. STATIC BARRIER

A. A Classical Solution of the Static Barrier

In the limit of $\epsilon = 0$, the classical equation of motion given by Eq. (8) can be integrated [28], and for the case in which the incident energy E_1 is less than the potential barrier (i.e., $0 < E_1 < 1$) the solution with the incident condition, $Q = Q_1 \gg 1, P = P_1 < 0$ at $t = t_1$, is given by

$$Q(t - t_1, t_1, Q_1, P_1) = \sinh^{-1}(\lambda \cosh(\sqrt{2E_1}(t - t_0))) \tag{11}$$

where the parameter λ is defined by

$$\lambda \equiv \sqrt{1/E_1 - 1} \tag{12}$$

At $t = t_0$ the trajectory hits the turning point given by

$$Q_{turn} = Q(t_0 - t_1) = \log[\lambda + \sqrt{\lambda^2 + 1}] \tag{13}$$

The lapse time $t_0 - t_1$, which is the time for the trajectory to spend until the turning point, is represented by

$$t_0 - t_1 = (Q_1 - \log \lambda)/\sqrt{2E_1} \equiv t_{01} \tag{14}$$

B. Singularities and Integration Paths of Classical Trajectories

The solution has singularities whose position on the complexified lapse time plane (i.e., s-plane) is decided by

$$Sg_n^{\pm} = \left(Q_1 - \log \lambda \pm \sinh^{-1}(1/\lambda)\right)/\sqrt{2E_1} + i(-n + 1/2)\Delta t_I/2 \tag{15}$$

where Δt_I is defined by $\Delta t_I \equiv 2\pi/\sqrt{2E_1}$. Note that the singularities $Sg_n^{\pm}$ are just lapse times at which $Q_{sg} = i\pi(m + 1/2)$, where the potential V_0 diverges. It can easily be checked that the branch point of the type $(s - Sg_n^{\pm})^{1/2}$ appears when the

trajectory hits $Q = Q_{sg}$, because the classical equation of motion is asymptotically given by $d^2Q/dt^2 \propto (Q - Q_{sg})^{-3}$ close to Q_{sg}. Also note that if the initial position Q_1 and momentum P_1 are fixed, the singularities on the s-plane are independent of t_1, because of the time-translational symmetry in autonomous systems.

As shown in Fig. 2a, the singularities are categorized into two groups, namely, Sg_n^- and Sg_n^+. Sg_n^- and Sg_n^+ are located periodically with the interval $\Delta t_I/2$ on the two lines parallel to the $\mathrm{Im}\{s\}$ axis, respectively. The interval of the two lines—that is, the distance between Sg_n^+ and Sg_n^-—is decided by the $\frac{2}{\sqrt{2E_1}}\sinh^{-1}(1/\lambda)$. The point t_{01}, at which the trajectory hits the turning point, is located at the middle of the two lines.

Figure 2a also shows how the physically significant integration paths are going among the singularities in topologically different ways. In a practical calculation, we can take a path homotopic to one of such representative integration paths $\{C_n^{\pm}\}$. In Fig. 2b, we see the complex trajectories $(Q(t), P(t))$

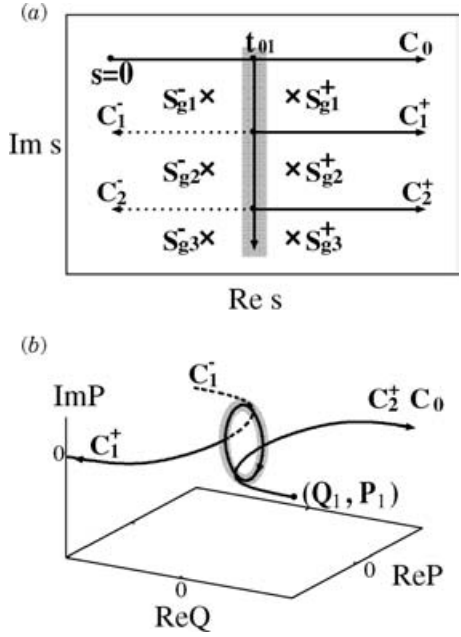

Figure 2. Relation between the integration paths and the complexified trajectories of the unperturbed barrier system. (*a*) Singularities and representative integration paths on the s-plane. (*b*) Complex trajectories obtained along various integration paths depicted in (*a*) for the case of $E_1 < 1$. The instanton trajectory in the classically forbidden region in (*b*), as well as the corresponding integration path in (*a*), is indicated by a hatched halo around it.

which are obtained along various integration paths in Fig. 2a for the case of $E_1 < 1$.

Each path $C_n^{\pm}$ defines a branch of the solution. The trajectory starting at the initial point (Q_1, P_1) hits the classical turning point at $s = t_{01}$; after that, it rotates along a complex elliptic orbit, in the classically forbidden region of the potential barrier. Such a complex bouncing trajectory is often celled an instanton. After rotating along the ellipse $n/2$ times, the trajectory is reflected back to $Q = +\infty$ for even integration paths, C_n^+ $(n = 2m)$, and tunnels toward $Q = -\infty$ for odd integration paths, C_n^+ $(n = 2m - 1)$.

Therefore, the existence of singularities leads to an infinite number of Riemann sheets on the complex lapse time plane, half of which contribute to the reflection and the other half of which yield transmissive components. The destination of the trajectory—that is, which side is it ending up, transmissive side or the reflective side?—changes depending on a choice of integration paths.

It should be noted that all the trajectories with odd integration paths contribute to the tunneling component, but the major contribution to it comes from the trajectory with the path C_1^+, because more round trips along the complex ellipse result in a larger imaginary part of the classical action. Thus, contributions of the other integration paths $C_{2m-1}^+ (m > 1)$ are extremely small and negligible. It should be also noted that the trajectories with the integration paths C_n^- disagree with the causality and make unphysical contributions, but such contributions are removed by the proper treatment of the Stokes phenomenon (for details, see Ref. 22).

IV. SEMICLASSICAL RESULTS

A. Effects of the Periodic Perturbation

We would like to return to the oscillating Eckart barrier. With simple intuitive consideration, we can predict what happens, if a periodically perturbation is applied to the system. In the following argument, we assume that the perturbation is sufficiently slow, namely the low-frequency limit, in which the fringed tunneling is typically observed.

Let's consider the effect of perturbation on classical trajectories in the complex domain. Since the perturbation changes periodically in the real-time domain, namely a sinusoidal function, the effective perturbation strength in the complex-time domain is amplified exponentially; that is, $\epsilon \to \epsilon e^{\omega|\mathrm{Im}t|}$ (see Fig. 3b).

Even when the input energy E_1 is small enough so that the particle cannot go through the barrier by a real trajectory, we can always find a particular initial time t_{1c}, taking suitable choice of its imaginary depth and real initial phase, at which the trajectory hits the top of barrier. Therefore, the trajectory starting at t_{1c} is a trajectory on the complexified stable manifold of the unstable periodic

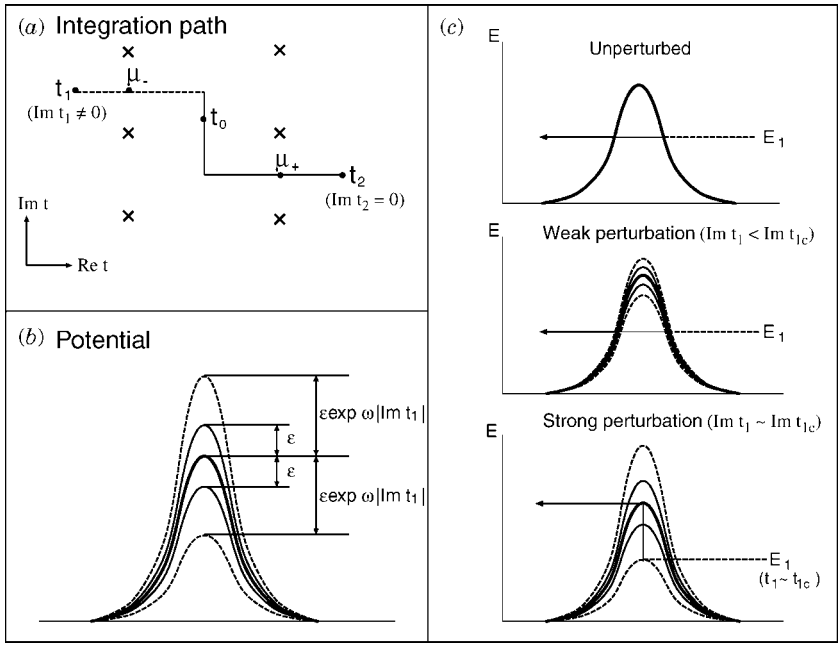

Figure 3. Effects of the periodic perturbation. (*a*) Integration path on the complex time plane. (*b*) Deformation of the potential by the periodical perturbation. In the case where $\mathrm{Im}\, t = \mathrm{Im}\, t_1 \neq 0$—that is, the part of integration path indicated by the same broken line in (*a*)—the oscillation of complexified potential is amplified exponentially as shown by the broken lines. (*c*) Change of the tunneling trajectory with increase of the perturbation strength. In the bottom figure, a trajectory stating at t_1 in the close neighborhood of t_{1c} is drawn.

orbit at the top of the barrier. It means that the initial search plane t_1 intersects with the stable manifold in the complex domain, even if the intersection disappears in the real domain. Let's call t_{1c} "the critical point" [24, 25]. It is found numerically that the critical point t_{1c} is always found in the initial time plane t_1 independent of the strength of the perturbation ϵ.

As the perturbation strength becomes smaller, the "critical point" t_{1c} goes into the deeper imaginary side. Therefore, if the strength of perturbation is taken small enough, a trajectory with the major integration path C_1^+ is not affected by the critical point. Let's call such a situation "weak perturbation regime." In the weak perturbation regime, the tunneling trajectory is well approximated by the instanton (see the middle figure of Fig. 3c).

However, if ϵ is large enough, then the critical point t_{1c} moves toward the real axis and may drastically disturb the original nature of the trajectories defined along the major integration path C_1^+ (see the bottom of Fig. 3c). This is a typical

situation generically observed in the strong perturbation regime, in which the fringed patterns on the tunneling component are observed.

B. Local Structure of $\mathscr{M}$-Set Near the Critical Point

When the observatory time t_2 is fixed, we can decide the $\mathscr{M}$-set defined by Eq. (9). Concerning the $\mathscr{M}$-set, there exists a remarkable fact that the critical point t_{1c} is always accompanied by a characteristic part of the branch passing very close to it, say $\mathscr{M}_c$, which plays an important role in the construction of the fringed wave pattern on the tunneling component with the semiclassical formula. Let's see a numerical example. Figure 4a gives a blown-up picture of $\mathscr{M}$-set near a certain critical point. We can find an $\mathscr{M}_c$ running very close to the critical point t_{1c}.

A remarkable feature of the critical point is that the singularities Sg_n^+ as functions of t_1 logarithmically diverge at the critical point $t_1 = t_{1c}$. Figure 4b shows the movement of singularities on the lapse time plane together with the integration path C_1^+. When the initial time t_1 is at the point 1, the topology of the integration path is essentially the same as the case of $E_1 < 1$ in the static limit,

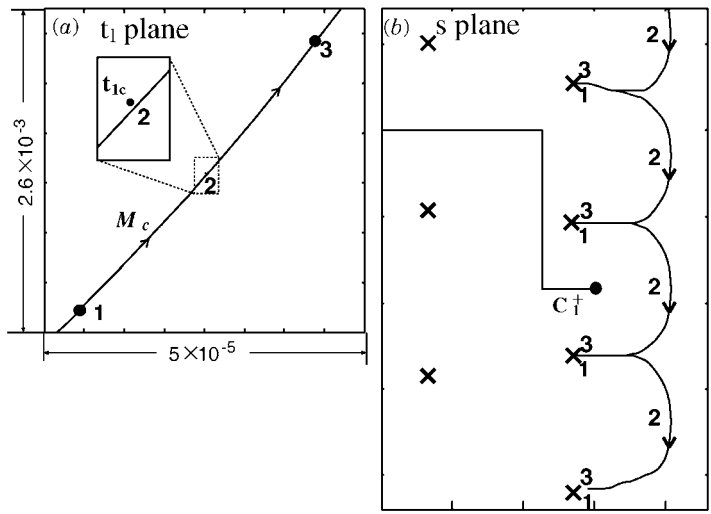

Figure 4. Switching of the path topology induced by the divergence movement of the singularities Sg_n^+ at a critical point under a strong perturbation. The parameters are the same as in Fig. 1. (*a*) Blow-up picture of the vicinity of the critical point t_{1c}, which corresponds to the first critical point in Fig. 5a. The characteristic subset $\mathscr{M}_c$ (branch **1** in Fig. 5*a*) exists passing close to the critical point t_{1c}. (*b*) The singularities Sg_n^+ simultaneously shift down as $1 \to 2 \to 3$ detouring the integration path C_1^+ on the lapse time plane, when t_1 varies as $1 \to 2 \to 3$ along $\mathscr{M}_c$ on the t_1-plane in (*a*).

and the trajectory reaches the transmissive side at $t = t_2$. Moving the initial time t_1 along $\mathscr{M}_c$ from point 1 to point 3, the singularities Sg_n^+ simultaneously shift down avoiding the integration path because of their own divergence behavior. It means that although the integration path C_1^+ is fixed, its topological nature with respect to the singularities changes from transmissive one to reflective one during that process, thereby inducing the drastic change in the destination of the trajectory. Therefore, the end of the trajectory traverses the phase space from the transmissive quadrant ($P_2 < 0, Q_2 < 0$) to the reflective one ($P_2 > 0$, $Q_2 > 0$), as t_1 passes close to t_{1c} along $\mathscr{M}_c$. The corresponding $\mathscr{L}$-set, namely the set of end points of the trajectories with their initial points on $\mathscr{M}_c$, should form a *merged* object composed of the tunneling and reflective branches, which are defined along the topologically different paths C_1^+ and C_2^+ in the unperturbed limit, respectively. It should be remarked that in the rigorous sense the end point of the integration path moves with t_1, namely $s = t_2 - t_1(t_2 \quad \text{fixed})$, but its movement is negligible, because the distance between points 1 and 3 is negligibly small.

C. Global Structure of Branches Contributing to the Fringed Tunneling

In order to understand the relation between the critical point and fringed tunneling in terms of the semiclassical method, we have to see the global picture of the $\mathscr{M}$-set and $\mathscr{L}$-set. Figure 5a shows a typical example of the $\mathscr{M}$-set obtained in the strong perturbation regime, and Fig. 5b is the corresponding $\mathscr{L}$-set. On the t_1-plane in Fig. 5a, three critical points each indicated by an X appear periodically at the period of the perturbation $T(= 2\pi/\omega)$ due to the periodicity of the perturbation. Let's call them the first, second, and third critical points in order from right to left. The structure of an $\mathscr{M}$-set is very complicated, but we can find that branch 1 is passing very close to the first critical point. The first critical point and branch 1, respectively, correspond to t_{1c} and $\mathscr{M}_c$ in Fig. 4a. Branches 2 and 5 are also running very close to the second and third critical points, respectively. Branch 5 is too small in this scale to identify, but it is confirmed in a blown-up picture that it exists very close to the third critical point, which is not, however, shown here.

In the $\mathscr{L}$-set, all these branches, 1, 2, and 5, stretch over the reflective quadrant ($P > 0, Q > 0$) and the transmissive quadrant ($P < 0, Q < 0$), passing close to the origin. Then, as discussed above, they can be interpreted as the *merged* object composed of the tunneling and reflective branches of the unperturbed system. Furthermore, a part of such a characteristic branch follows, to some extent, the real unstable manifold of the unstable periodic orbit at the origin going into both transmissive and reflective sides. The length in which each branch extends along the real unstable manifold becomes longer and longer while increasing the lapse time—that is, with increase of the branch number.

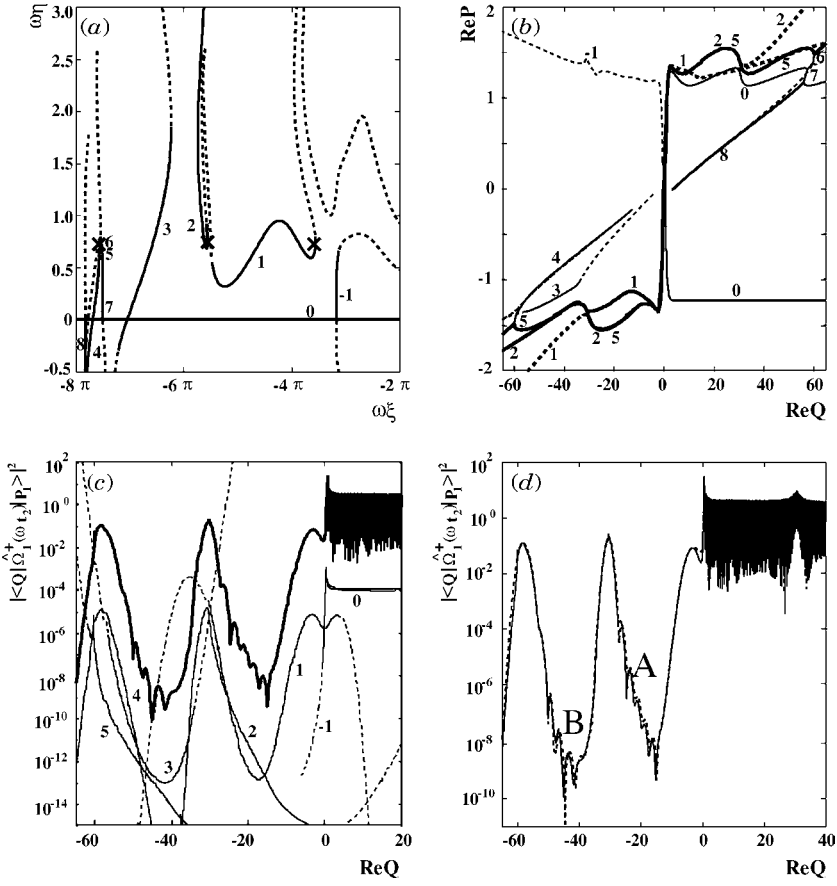

Figure 5. Results of the semiclassical calculation in the strong perturbation regime. The parameters are the same as in Fig. 1. (*a*) $\mathscr{M}$-set. The critical points are indicated by $\times$. (*b*) $\mathscr{L}$-set projected onto the real plane. The characteristic branches 1, 2, and 5 are drawn by thick lines. (*c*) The semiclassical probability amplitude (thick line) and weights of the branches (thin lines). All the probabilistic weights are multiplied by 10^{-4} for convenience of comparison with the total probability. (*d*) The semiclassical probability amplitude (thick line) compared with the fully quantum probability amplitude (broken line).

It should be noted that the parts of branches drawn by broken lines indicate noncontributing parts that make unphysical contributions, and they can be removed by the proper treatment of the Stokes phenomenon. After such a procedure, we can sum up all the contributions from the physically legal parts of the branches in the $\mathscr{M}$-set. We find the probabilistic weights of the branches together with the total probability obtained by the sum formula [Eq. (6)] in Fig. 5c. In Fig. 5d, the tunneling probability obtained by the sum formula is

compared with the result of the purely quantum computation. The semiclassical method reproduces well the tunneling wave including the complicated fringed patterns in the ranges indicated by A and B.

The appearance of fringes on the tunneling component is the result of a simultaneous contribution of multiple tunneling trajectories to the sum formula. Indeed, in the $\mathscr{L}$-set (Fig. 5b), we can find that two or more branches exist in the ranges of the fringed tunneling (e.g., 1, 2 for A and 3, 4, 5 for B), and these groups of branches have nearly equal weights in the regions A and B, respectively(see Fig. 5c). The additional branches 3 and 4 contributing to the fringe are considered as ones bifurcated from the branch 2 in time evolution, and form a chain structure with 2 and 5.

Therefore, the series of branches 1, 2, 5 respectively associated with the first, second, and third critical points seems to play an important role in the construction of interference fringes on the tunneling component. In the $\mathscr{L}$-set, they traverse the phase space and thus contribute simultaneously to the wave matrix forming the remarkable fringe pattern on the tunneling wavefunction.

V. THEORETICAL ANALYSES

A. Brief Sketch of Our Analyses

In order to clarify the underlying classical mechanism of the fringed tunneling, we developed theoretical analyses in the low-frequency regime based on a complex adiabatic solution [25], together with the Melnikov method extended to the complex domain [25].

Some important facts about the critical point and the branch associated with it, which are numerically observed, can be proven with the Melnikov method and the adiabatic solution in the low-frequency regime. They are summarized as follows [25]:

1. The intersection between the complexified stable manifold and the incident beam set $\mathscr{I}$—that is, $\{Q, P, t_1 | Q = Q_1, P = P_1, t_1 \in \mathbf{C}\}$—exists at an arbitrary perturbation strength, and if t_{1c} is the intersection, then $t_{1c} + T$ is also intersection because of the periodic nature of the perturbation.

2a. The intersection t_{1c} becomes the critical point of the singularities Sg_n^+ in the sense that in the limit of $t_1 \to t_{1c}$ the singularity diverges as $Sg_n^+ \sim -\log(t_1 - t_{1c})/\sqrt{2}$.

2b. A branch of the $\mathscr{M}$-set passing close to a critical point, say $\mathscr{M}_c$, always exists.

3. As t_1 is moved along $\mathscr{M}_c$, the end point of the trajectory $(Q(t_2 - t_1, t_1), P(t_2 - t_1, t_1))$ traverses continuously but abruptly from the transmissive side to reflective side (and vice versa) passing close to the origin O.

As shown in Appendix B, item 1 is proven by using the Melnikov method. It means that the heteroclinic-like entanglement between the complexified stable manifold and the initial time plane t_1 occurs.

Items 2a and 2b are justified by using the adiabatic solution [25]. Indeed, the adiabatic solution enables us to prove the anomalous behavior of the singularities Sg_n^+ at the critical point (i.e., item 2a), as well as the local structure of the characteristic branch $\mathscr{M}_c$ near the critical point (i.e., item 2b).

Furthermore, by using the adiabatic solution with the items 2a and 2b proven, we can explain the remarkable feature of the characteristic branches in the $\mathscr{L}$-set, (i.e., item 3), which is observed numerically [25]. Especially the topological switching of the integration path induced by the divergence behavior of the singularities Sg_n^+ at the critical point (i.e., item 2a) is the key to understanding why and how the characteristic branches dominantly contributing to the fringed tunneling are generated in the strong perturbation regime.

Therefore, all the important properties concerning with the critical point and the associated branch, which are numerically observed, can be explained analytically. However, we won't show details of the proofs of items 2a,2b and 3, since they are rather technically complicated and understanding them requires readers to make an additional effort. For one who wants to see the details, refer to Ref. 25.

In the following subsections, we instead concentrate on explaining, by using the adiabatic solution, geometrical features of the complex trajectories contributing to the fringed tunneling, which clarifies what is the chaotic tunneling trajectory.

B. Low-Frequency Approximation

First we briefly introduce the adiabatic solution in the low-frequency limit, which was developed in our previous work [25]. The classical equation of the motion is given by

$$\ddot{Q} = 2a(t)\frac{\sinh Q}{\cosh^3 Q} \tag{16}$$

and the equation of the energy is also obtained as follows:

$$\dot{E} = \frac{\partial H}{\partial t} = \frac{\dot{a}(t)}{\cosh^2 Q} = \dot{a}(t)h(t) \tag{17}$$

where the function $a(t)$ and $h(t)$ are, respectively, defined by

$$a(t) \equiv 1 + \epsilon \sin \omega t, \quad h(t) \equiv \frac{1}{\cosh^2 Q} \tag{18}$$

In order that the formal solution

$$\sinh Q = Y(t) = r(t)\cosh\phi(t) \tag{19}$$

becomes the solution of Eq. (16), $\phi(t)$ and $r(t)$ should satisfy the following equation:

$$\frac{d}{dt}\{r^2\dot{\phi}\}\sinh(\phi) - [2E(t) - \dot{\phi}^2]r^2\cosh(\phi) + r\ddot{r}\cosh(\phi) = 0 \tag{20}$$

If we take $a(t)$ constant, the energy becomes constant and the solution satisfying Eq. (20) gives a solution of the static barrier.

In the low-frequency limit ($\omega \ll 1$ and $d^2r(t)/dt^2 \sim 0$), the relation given by Eq. (20) can be reduced to two equations:

$$\dot{\phi}(t) = \sqrt{2E(t)} \tag{21}$$

$$\frac{d}{dt}\{r(t)^2\dot{\phi}(t)\} = 0, \quad \text{namely} \quad r(t) = \frac{\alpha}{\{2E(t)\}^{1/4}} \tag{22}$$

where α is a certain constant of motion, which plays an important role in analyses in the following.

We put the initial time of the adiabatic solution t_0 in the scattering region, so that $\phi(t_0) = 0$. For the unperturbed system, t_0 indicates the time at which the classical trajectory reaches the turning point. At $t = t_0$, the energy $E_0 = E(t_0)$ satisfies the relation

$$E_0 = a(t_0)/\{1 + \alpha^2/\sqrt{2E_0}\} \tag{23}$$

From the numerical results in Section IV, it is considered that the complex trajectories contributing to the fringed tunneling pass close to the unstable periodic orbit at the origin and so the energy varies near the origin as $E(t) \sim a(t_0) +$ small correction. Then, it is quite natural to assume that α is a smallness parameter.

To clarify the physical meaning of the parameter α and to provide explicit forms of $E(t)$ and $\phi(t)$, it is convenient to introduce the characteristic times called "gates" $\mu_{\mp}$. As shown in Fig. 6, the gates $\mu_{\mp}$ are put at the middle points of two adjacent singularities, $t_{sg} = Sg_n^{\mp} + t_1$ and $t'_{sg} = Sg_{n+1}^{\mp} + t_1$, respectively. Thus, $\mu_{\mp}$ respectively play the entrance and exit gates of the scattering region. We can assume that the integration path always passes through the gates $\mu_{\mp}$ as shown in Fig. 6a. Roughly speaking, the function $h(t)$ takes nonzero value only between the two gates, and the particle travels freely at a constant momentum outside the gates (see Fig. 6b).

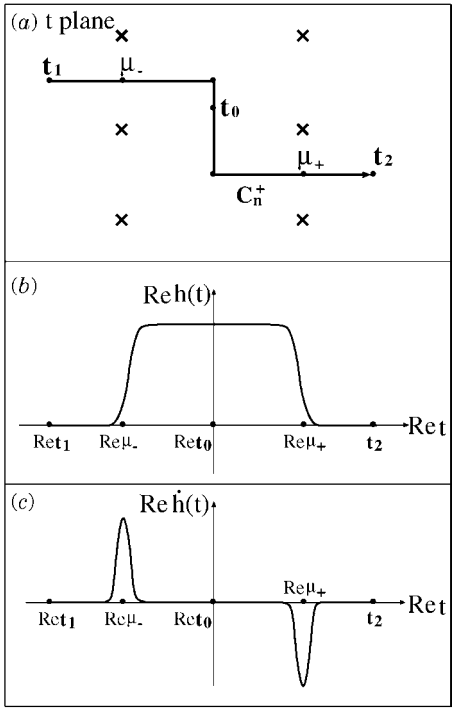

Figure 6. Behavior of the function $h(t)$ near the gate $\mu_{\mp}$. (*a*) Positions of the gates $\mu_{\mp}$ on the complex t plane. An integration path C_n^+ passing through the gates $\mu\mp$ is also drawn. (*b*) $\mathrm{Re}\, h(t)$ along the path C_n^+. Note that if $|\alpha| \ll 1$, then $|\mathrm{Re}\, h(t)| \gg |\mathrm{Im}\, h(t)|$ (*c*) $\mathrm{Re}\, \dot{h}(t)$ along the path C_n^+.

From the feature of $h(t)$, the positions of gates $\mu_{\pm}$ should be defined by

$$d^2h(t)/d\phi^2|_{t=\mu_{\pm}} = 0 \tag{24}$$

and $\phi(\mu_{\pm})$ are respectively related to $r(\mu_{\pm})$ as follows:

$$e^{\pm\phi(\mu_{\pm})} = 2e^{in_{\pm}\pi}[1 + r(\mu_{\pm})^2/4 + O(|\alpha|^4)]/r(\mu_{\pm}) \tag{25}$$

where $n_{\pm}$ are integers decided by the choice of the integration path—that is, the imaginary depths of the gates μ_+ and μ_-.

Integrating the energy gain equation (17) by using the lowest-order approximation, which is essentially the same as the Melnikov method, gives the

expression of the time-dependent energy,

$$E(t) = \begin{cases} a(\mu_-)h(t_0) = E_1 & (\text{if } \mathrm{Re}\, t \ll \mathrm{Re}\, \mu_-) \\ a(t)h(t_0) & (\text{if } \mathrm{Re}\, \mu_- \ll \mathrm{Re}\, t \ll \mathrm{Re}\, \mu_+) \\ a(\mu_+)h(t_0) = E_2 & (\text{if } \mathrm{Re}\, t \gg \mathrm{Re}\, \mu_+) \end{cases} \tag{26}$$

From the initial condition ($Q = Q_1(\gg 1), P = P_1 = -\sqrt{2E_1} < 0$, at $t = t_1$), we can obtain the following relations:

$$E_1 = P_1^2/2 = a(\mu_-)h(t_0) = E(\mu_-) \sim a(\mu_-)[1 - \alpha^2/\sqrt{2}] \tag{27}$$

$$Q_1 = \log 2 + \alpha^2 \left\{4\sqrt{2E_1}\right\}^{-1} - \sqrt{2E_1}(t_1 - \mu_-) \tag{28}$$

Then the initial energy E_1 is decided as a function of the input gate μ_- together with the parameter α, and the initial coordinate Q_1 is defined from μ_-, t_1 and α.

Since the observables E_1 and Q_1 are fixed at real values, Eqs. (27) and (28) are reduced into a relation that represents the parameter α as a function of μ_- or t_1:

$$\alpha^2 = A_1(t_1 - t_{1c}) = A_2(\mu_- - \mu_{-c}) \tag{29}$$

where t_{1c} and μ_{-c} respectively denote t_1 and μ_- at $\alpha = 0$, and

$$A_1 \sim A_2 = \sqrt{2}\{a(\mu_{-c})\}^{-1} \frac{da(\mu_-)}{d\mu_-}\Big|_{\mu_- = \mu_{-c}} \tag{30}$$

As will be shown in the following, the solution at $\alpha = 0$ gives a trajectory on the complexified stable manifold, and t_{1c} is nothing more than the critical point. Then, the significance of the smallness parameter α^2 is clarified in terms of the boundary condition.

For convenience of the following arguments, we introduce a different phase function φ defined by

$$\varphi(t) = \phi(t) + \log 2 - \log\left\{\alpha(2E(t))^{-1/4}\right\} \tag{31}$$

It is important that φ takes, at $t = \mu_-$, an almost zero value,

$$\varphi(\mu_-) = -\alpha^2\left\{4\sqrt{2E_1}\right\}^{-1} + O(\epsilon\omega) \sim 0 \tag{32}$$

which makes the following analyses easier.

Applying the input-boundary condition for the formal solution, we can derive, after some tedious calculations, an explicit expression of φ:

$$\varphi(t) = \begin{cases} \sqrt{2E_1}(t - t_1) - Q_1 + \log 2 + O(\epsilon\omega) \\ \qquad\qquad\qquad\qquad\qquad\qquad (\text{if Re } t \leq \text{Re } \mu_-) \\ \int_{\mu_-}^{t} \sqrt{2a(s)h(t_0)}\, ds + \frac{1}{4}\log\left(\frac{E(t)}{E(\mu_-)}\right) + \varphi(\mu_-) + O(\epsilon\omega) \\ \qquad\qquad\qquad\qquad\qquad\qquad (\text{if Re } \mu_- \leq \text{Re } t \leq \text{Re } \mu_+) \\ \sqrt{2E_2}(t - \mu_+) + \frac{1}{4}\log\left(\frac{E(t)}{E(\mu_+)}\right) + \varphi(\mu_+) + O(\epsilon\omega) \\ \qquad\qquad\qquad\qquad\qquad\qquad (\text{if Re } t \geq \text{Re } \mu_+) \end{cases} \tag{33}$$

By using $\varphi(t)$ and $E(t)$ obtained above with the parameter α, the adiabatic solution is given by

$$\sinh Q(t) = \alpha^2 e^{\varphi(t)}/(4\sqrt{2E(t)}) + e^{-\varphi(t)} \tag{34}$$

$$P(t) = \operatorname{sech} Q(t)[\alpha^2 e^{\varphi(t)}/4 - \sqrt{2E(t)}e^{-\varphi(t)}] \tag{35}$$

where the first term on the right-hand side of both equations indicates an unstable part with order α^2 and the second term is a stable part. Then, $\alpha = 0$ gives a solution for the stable manifold of the unstable periodic orbit at the origin.

As mentioned in the previous subsection, the adiabatic solution (34) together with the Melnikov method enables us to prove items 1, 2a, 2b, and 3. Then the significant properties of tunneling trajectories and of the branches consisting of them, which are numerically observed, can be explained in terms of the adiabatic approximation associated with the Melnikov method.

C. Contributions of Multiple Characteristic Trajectories to the Fringed Tunneling

Let's consider the geometrical feature of the solution obtained. Since $\phi = 0$ and $\varphi \sim -\log\alpha$ at $t = t_0$, then the unstable term balances, in order, with the stable term in both Eqs. (34) and (35). As a result, the stable term overcomes the unstable term in the region Re $t \ll$ Re t_0, although the unstable term dominates over the other in the region Re $t \gg$ Re t_0.

Therefore, we can summarize the feature of the solution as follows.

4a. In the first stage of time evolution, the trajectory with t_1 in a small neighborhood of t_{1c} traces the particular trajectory on the complexified stable manifold, which starts at $(Q = Q_1, P = P_1, t = t_{1c}(\alpha = 0))$:

$$(Q(t), P(t)) = (\sinh^{-1}\{e^{-\varphi(t)}\}, \quad -\mathrm{sech}Q(t)\sqrt{2E(t)}e^{-\varphi(t)}) \tag{36}$$

4b. In the next stage, the trajectory swings across the scattering region guided by the stable and unstable manifolds.

4c. In the final stage, the trajectory is scattered along the complexified unstable manifold.

4d. The tunneling trajectories selected to satisfy the output boundary condition, (i.e., $t_1 \in \mathscr{M}_c$) move close to the real plane sticking to the unstable manifold.

The last item coming from the output boundary condition can actually be proven by putting the output boundary condition to the adiabatic solution [25].

From item 2b, the characteristic $\mathscr{M}$-set (i.e., $\mathscr{M}_c$) passes very close to the critical point and items 3 and 4d signify that the corresponding $\mathscr{L}$-set transverses the phase space from the transmissive quadrant to the reflective quadrant along the real unstable manifold.

Now, we should remember that the critical points appear periodically on the initial time plane t_1 due to the periodicity of the perturbation (see Fig. 7a). In Fig. 7a, the critical points are assigned by a integer n such that $t_{1c}^{(n)} = t_{1c}^{(0)} - nT \quad (n \in \mathbf{N})$, where $t_{1c}^{(0)}$ is a properly chosen critical point. Each critical point $t_{1c}^{(n)}$ is accompanied by a characteristic branch $\mathscr{M}_c^{(n)}$. The lapse time of the trajectory stating at a point on $\mathscr{M}_c^{(n)}$ is estimated by

$$s \sim t_2 - t_{1c}^{(n)} = t_2 - t_{1c}^{(0)} + nT \tag{37}$$

It should be noted that the effective length of the branch in the $\mathscr{L}$-set, in which it is well extended along the unstable manifold, becomes longer and longer as increasing the lapse time, namely with increase of the branch number n. As a result, an infinite number of branches of the $\mathscr{L}$-set each corresponding to a different $\mathscr{M}_c^{(n)}$ with a sufficiently large number n are passing through the region of the fringed tunneling.

The imaginary part of the classical action defined by Eq. (7)—that is, Im S_Ω—is the primary factor controlling the weight of the contributing trajectory, and it is almost the same for any choice of the initial point, $t_1 \in \mathscr{M}_c^{(n)}$, where n is arbitrary. This is because every trajectory traces the same orbit in the phase space, $(Q, P, t(\mathrm{mod}\ T))$, guided by the complexified stable manifold, until it approaches to the real plane; thus Im S_Ω gained in this process is almost

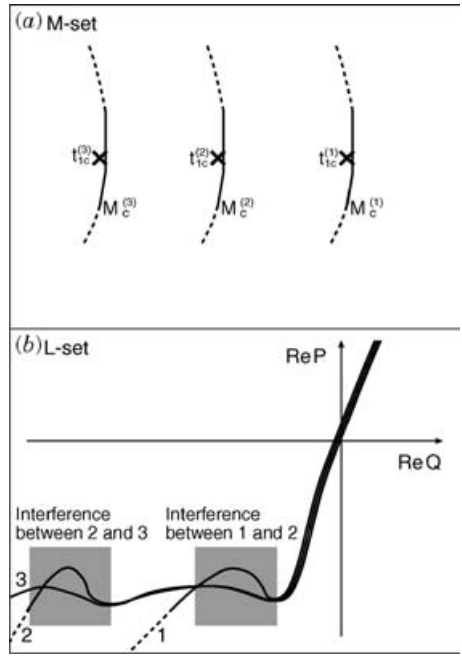

Figure 7. A sketch: How do multiple branches contribute to the interference fringe. (*a*) Periodicity of critical points in t_1 plane, each of which is accompanied by a branches passing close to it. (*b*) The branches in the $\mathscr{L}$-set. The fringed patterns are created by the interference of the branches in the hatched regions.

the same. It indicates a possibility that for given t_2 and Q_2, an infinite number of trajectories may simultaneously contribute to the semiclassical wave matrix (6).

However, the numerical result shows that only a few of branches practically contributes to the tunneling probability in each region of fringed tunneling. It means that there is an additional factor making difference in weights of the contributing branches.

Indeed, the difference in weights comes from the amplitude factor of the semiclassical wave matrix, which is given from Eqs. (6) and (7) by

$$\begin{aligned} |\partial^2 S_\Omega/\partial E_1 \partial Q_2|^{1/2} &= |\partial Q_2(t_2, t_1, P_1, Q_1)/\partial t_1|^{-1/2} \\ &= |4\sqrt{2E(t_2)}\cosh(Q_2) e^{-\varphi(t_2)}/A_1|^{1/2} \end{aligned} \tag{38}$$

The lapse time increases with n as shown in Eq. (37); thus from its expression given by Eq. (33), φ is roughly proportional to the lapse time. Therefore,

for a large n, namely for the trajectory with a long lapse time, the amplitude factor decays exponentially as $|\partial^2 S_\Omega/\partial E_1 \partial Q_2|^{1/2} \propto \mathrm{e}^{-nT/2}$. Consequently, among an infinite number of the possibly contributing tunneling trajectories, only the finite number of $\mathscr{M}_c^{(n)}$ with a relatively small n, namely a short lapse time, actually contribute to the tunneling probability at the observatory coordinate Q_2.

As shown in the numerical calculation, the interference of the characteristic branches 1 and 2 makes the fringed pattern in the region A, while branch 5 together with branches 3 and 4, which are bifurcated from branch 2 in time evolution, contributes in region B. Hence, it is confirmed that the branches associated with the critical points have a significant effect on the construction of the fringed pattern, and we come to a whole understanding of underlying mechanism of the fringed tunneling.

D. Characteristic Perturbation Strength

From the above argument it is clarified that the tunneling mechanism in the strong perturbation regime, which yields the fringes on the tunneling component, is quite different from the (perturbed) instanton mechanism of the tunneling in the weak perturbation regime [22,23]. It is worthwhile to discuss how the transition of the tunneling mechanism occurs as the perturbation strength is increased.

As was stressed in Sections IV.A and V.A, there always exist the critical points t_{1c}, even if the strength of the perturbation is arbitrarily small. Such critical points, however, have a large imaginary component and are located so deeply in the imaginary domain of the complex plane that they do not affect the dominating instanton branches with the integration path C_1^+. As the perturbation increases, the imaginary part of the critical points decreases, thereby finally going across the dominant branches with the path C_1^+. This is the case that the structure of the branches are broken up and reconstructed by the influence of the critical points.

Using the above criterion, it is possible to estimate the characteristic value of the perturbation strength, above which the critical point significantly influences the dominant branches resulting in the fringed tunneling. The imaginary depth of the dominant branches of the $\mathscr{M}$-set is roughly estimated as $|\mathrm{Im}(t_2 - t_1)| \sim \pi/\sqrt{2}$. Therefore, the characteristic value $\epsilon = \epsilon_c$ is the value at which the critical point t_{1c} passing through the border of the Riemann sheets of the dominant and next order branches, whose imaginary depth is estimated as $\sim 3\pi/2\sqrt{2}$:

$$|\mathrm{Im}\, t_{1c}| \sim 3\pi/2\sqrt{2} \tag{39}$$

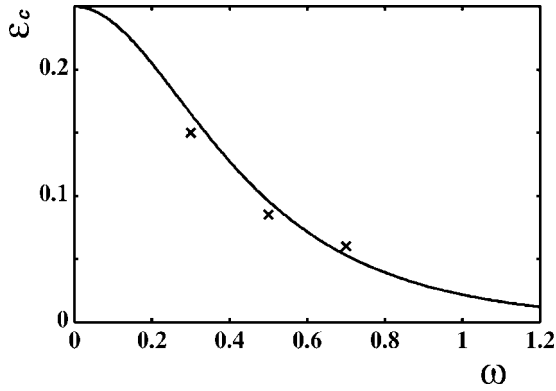

Figure 8. The characteristic strength ϵ versus ω. The full line indicates the theoretical estimate of the characteristic strength ϵ_c as a function of ω, while the values of ϵ_c that are numerically decided at three relatively small ωs are marked by ×.

Substituting the estimation of $\mathrm{Im}\, t_{1c}$ by the Melnikov method [Eq. (B.11)] into Eq. (39), we get the characteristic perturbation strength

$$\epsilon_c \sim (1 - E_1)/\{(1 - \chi(\omega))\cosh(3\omega\pi/2\sqrt{2})\} \tag{40}$$

above which the fringed tunneling may be observed. In other words, if ϵ is given, the fringed tunneling is observed above the characteristic energy

$$E_{1c} = 1 - \epsilon\{(1 - \chi(\omega))\cosh(3\omega\pi/2\sqrt{2})\} \tag{41}$$

Sufficiently below it the one-dimensional instanton picture works well.

Finally we compare in Fig. 8 the above theoretical value of ϵ_c with the numerical ϵ_c, above which the tunneling component exhibits a definite fringed pattern. The numerical ϵ_c is given at three relatively small ωs. The agreement of the theory with the numerical data seems to be satisfactory.

VI. SUMMARY

In the present chapter, we have pursued the underlying classical mechanism of the multidimensional (dynamical) tunneling in classically nonintegrable systems by taking the periodically perturbed Eckart potential as a simple example [36]. In the strong perturbation regime, the remarkable tunneling phenomenon, referred to as *fringed tunneling*, is observed, and we have elucidated its classical

mechanism by using some analytical tools—that is, the adiabatic solution of classical equation of motion in the low-frequency limit as well as the Melnikov method extended into the complex domain.

The remarkable fact that we found through the numerical and theoretical analyses is that the nature of trajectories contributing to the fringed tunneling is essentially different from that of instanton, which still provides a good tunneling picture as long as the system of multidimensions is integrable or extremely nearly integrable. For integrable or very nearly integrable systems, which correspond to the weak perturbation regime in our case, the tunneling trajectory is well approximated by the instanton. However, the trajectories contributing to the fringed tunneling in the strong perturbation regime no longer obey the instanton picture.

Indeed they are trajectories guided by the complexified stable and unstable manifolds: The trajectories that have their initial points in a very short distance to the complexified stable manifold make major contributions to the fringed tunneling; then they are approaching, in time evolution, the unstable periodic orbit at the top of the barrier, and they are finally scattered toward an asymptotic region along the (real) unstable manifold. In other words, the property of such trajectories is subject to the complexified *heteroclinic-like entanglement* between the complexified stable manifold and the incident wave manifold that is formed by the trajectories satisfying the input boundary condition of the semiclassical wave matrix. In this sense, the trajectories contributing to the fringed tunneling are regarded as the simplest case of chaotic tunneling trajectories in general multidimensional systems.

The heteroclinic point appears as a critical point t_{1c} on the initial time plane t_1. For the periodicity of the perturbation, the critical points t_{1c} actually appear periodically at the period of perturbation T. The initial points of trajectories making major contributions to the fringed tunneling form the characteristic branches, say $\mathscr{M}_c$, which repeatedly appear in the $\mathscr{M}$-set, each passing very close to an individually different critical point t_{1c}. Simultaneous contributions of such periodically appearing branches make the remarkable fringed patterns on the tunneling component. The weight of each contributing branch is appropriately calculated with the semiclassical formula.

In time-continuous systems extended to complex domain, the classical trajectory becomes a function of complex time and generally has singularities. The divergence behavior of the singularities is the important nature associated with the tunneling trajectories contributing to the fringed tunneling. In the present chapter, we have briefly explained how important a role the critical behavior of singularities of trajectories on the stable (and unstable) manifold(s) does play in creation of the geometrically merged object—that is, the characteristic branch embodied in the $\mathscr{L}$-set, which is composed of the topologically different branches in the unperturbed limit (i.e., tunneling and

reflective branches). Unfortunately, we did not fully discuss this problem in the present chapter. For one who wishes to understand more detail mechanism, we refer to Ref. 25, which provides a whole understanding of underlying mechanism of the fringed tunneling.

It is very important to point out that similar tunneling phenomena are quite commonly observed not only for periodically perturbed 1D-barrier systems but also for 2D-barrier systems with a harmonic channel. Thus, we can naturally expect that a similar complexified *heteroclinic-like entanglement* between the incident beam set and the complexified stable manifold generally occurs for 1.5D and 2D barrier systems [37,38] and it changes the nature of tunneling trajectories, from instanton to chaotic tunneling trajectory, thereby yielding to the fringed tunneling.

It is worthwhile to mention the characteristic dynamical process commonly observed in chaotic tunneling phenomena of quantum maps [16,18]. That is, the physical interpretation of the tunneling process in map systems seems to provide a common picture similar to that of multidimensional barrier systems at least on the phenomenological level: The major contributing tunneling trajectories obey the stable and unstable manifolds in the complex phase space. However, the mathematical structure of the tunneling mechanism is quite different in the quantum map models, because the quantum map has no continuous time and thus has no counterparts of the time singularities and of the multiple-Riemann sheets associated with them. Such a difference in the mathematical structure is a real obstacle to discussing in terms of semiclassical method the correspondence in the tunneling phenomena between time-continuous and map systems. For example, the presence of a complex-domain chaos (i.e., homoclinic tangle in complex phase space) and its relationship to the predominant tunneling trajectories are remarkable facts clarified just by using the Gaussian map [16,17]. Such a fully chaotic dynamical structure underlying the new tunneling mechanism is the issue that still remains inaccessible by the time-continuous system. It is strongly desired to clarify the similarities and differences between time-continuous systems and maps, as well as to construct a comprehensive story that gives a global aspect on the problems of multidimensional tunneling.

APPENDIX A: FRINGED TUNNELING IN A 2D BARRIER SYSTEM

An example of 2D systems for which fringed tunneling similar to that of the periodically perturbed 1D barrier is observed is given by [24,26]

$$H_{\text{tot}}(Q,P,q,p) = \tfrac{1}{2}P^2 + V_0(Q) + \beta v_2(Q,q) + H_{\text{ch}}(q,p) \qquad \text{(A.1)}$$

where H_{ch} is the channel Hamiltonian,

$$H_{\mathrm{ch}}(q,p) = p^2/2 + \omega^2 q^2/2 \tag{A.2}$$

and the potential terms are given by

$$V_0(Q) = \operatorname{sech}^2 Q, \quad v_2(Q,q) = q \operatorname{sech}^2 Q \tag{A.3}$$

The incident plane wave coming from $Q = +\infty$ with a constant momentum $P = P_1 < 0$ along the reaction path and with a given quantum number n_1 of the channel eigenstate is given by

$$\text{Incident wave} \propto \exp(iP_1 Q/\hbar) w_{n_1}(q) \qquad (Q \to \infty) \tag{A.4}$$

where w_{n_1} is an eigenstate of H_{ch} with the quantum number n_1. For such a incident condition, a scattering eigenstate $\Psi_{P_1,n_1}(Q,q)$ specified by P_1 and n_1 is obtained. Introducing the classical action and angle of the harmonic oscillator (I,θ), the Hamiltonian may be written by

$$H_{\mathrm{tot}}(Q,P,\theta,I) = \tfrac{1}{2}P^2 + V_0(Q) + \beta v_2(Q,\theta,I) + \omega I \tag{A.5}$$

The numerical results of the pure quantum calculation are shown in Fig. A.1, which gives the quantum probability in the phase-represented scattering eigenstate that is defined by

$$\langle Q,\theta|\Psi_{P_1,n_1}\rangle = \int dq \langle q|\ \theta\rangle^* \Psi_{P_1,n_1}(Q,q) \tag{A.6}$$

where $\langle q|\theta\rangle$ denotes the phase eigenstate [24,26,39],

$$\langle q|\theta\rangle = \lim_{M\to\infty} \sum_{n=0}^{M} e^{in\theta} w_n(q)/\sqrt{M+1} \tag{A.7}$$

The effective strength of the interaction between the reaction and channel coordinates increases with the quantum number n_1 of the input channel, because the strength of interaction is proportional to the channel coordinate q. At a small quantum number $n_1 = 4$, namely when the effective strength of the interaction is small, the tunneling wave component drawn by broken line forms a regular spatial oscillation. On the other hand, at an strong coupling case with $n_1 = 71$, it is observed that the complicated fringes are superposed on the simple spatial oscillation in the tunneling component. It is nothing more than the fringed

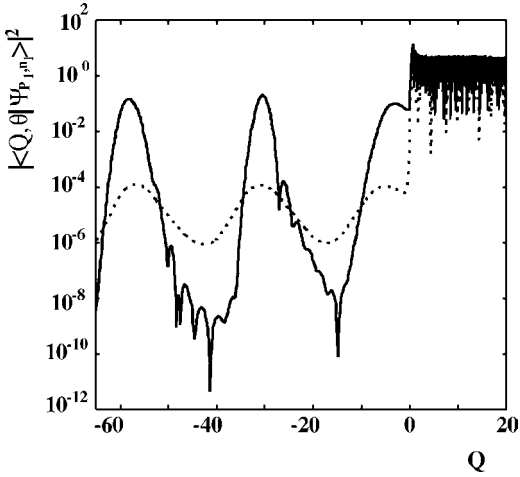

Figure A.1. The tunneling component ($Q < 0$) of the phase-represented scattering eigenfunction $|\langle Q, \theta|\Psi_{P_1,n_1}\rangle|^2$. Broken line: $n_1 = 4$. Solid line: $n_1 = 71$. $\omega = 0.3$, $\beta = 0.0289$, $\hbar = 1000/(3\pi \times 2^{10})$, and $\theta = 0$.

tunneling. Therefore, the tunneling phenomena observed in the 2D system are, in both weak and strong perturbation regimes, very similar to those of the periodically perturbed 1D barrier system (see Fig. A.1). Why are similar tunneling phenomena observed for 1.5D and 2D barrier systems? The answer is as follows.

In the case that n_1 is large, the corresponding classical motion of the channel coordinate q is well approximated by a periodic motion $q \sim \epsilon \sin\theta$ ($\theta \sim \omega t$); thus the Hamiltonian may be approximated as follows:

$$H_{\text{tot}}(Q, P, \theta, I) \sim \tfrac{1}{2}P^2 + V_0(Q) + \epsilon \sin\theta \,\text{sech}^2 Q + \omega I \tag{A.8}$$

where $\epsilon = \sqrt{2n_1\hbar/\omega}\beta$. As well known in Floquet theory [29], this approximated Hamiltonian is equivalent to the periodically perturbed 1D barrier system whose Hamiltonian is the same one given by Eq. (1) [24], namely,

$$H(Q, P, \omega t) = \tfrac{1}{2}P^2 + V_0(Q) + \epsilon v(Q, \omega t) \tag{A.9}$$

where $v(Q, \omega t) = \sin\omega t \,\text{sech}^2 Q$ corresponds to v_2 in the 2D system.

Finally, it should be noted that the fringed tunneling in 2D systems is observed only when the total energy beyond the potential saddle. Then real

classical trajectories satisfying the input condition are not restricted by the energy potential barrier but by the invariant surface formed in phase space, which is specified by the total energy and the quantum number of the initial channel. Therefore it induces the dynamical tunneling.

APPENDIX B: MELNIKOV METHOD

Item 1 in Section V.A is proved by using Melnikov method which is extended into the complex domain [25]. Suppose that the Hamiltonian is written by

$$H(Q,P,\omega t)=\tfrac{1}{2}P^2+V_0(Q)+\epsilon v(Q,\omega t)=H_0(Q,P)+H_1(Q,t) \tag{B.1}$$

where $H_0(=\frac{1}{2}P^2+V_0)$ and $H_1(=\epsilon v)$ denote the unperturbed and perturbed parts, respectively, and also suppose that the unperturbed system has a unstable fixed point; then it usually changes to an unstable periodic orbit when the periodic perturbation is applied.

The energy of a trajectory on the stable manifold of the unstable periodic orbit is given by

$$H(Q_s(t_1),P_s(t_1),t_1)=H(Q_{\mathrm{ups}}(t_1),P_{\mathrm{ups}}(t_1),t_1)+\Delta H_M \tag{B.2}$$

where

$$\Delta H_M=\int_{\infty}^{t_1}\left\{\frac{\partial H_1}{\partial t}(Q_s,t)-\frac{\partial H_1}{\partial t}(Q_{\mathrm{ups}}(t),P_{\mathrm{ups}}(t),t)\right\}dt \tag{B.3}$$

Here, $(Q_{\mathrm{ups}},P_{\mathrm{ups}})$ denotes the unstable periodic orbit, and (Q_s,P_s) also denotes a trajectory on the stable manifold. In the limit of t going to infinity, the energy of the trajectory (Q_s,P_s) converges to that of the unstable periodic orbit $(Q_{\mathrm{ups}},P_{\mathrm{ups}})$.

Under the lowest-order approximation, a trajectory on the unperturbed stable manifold denoted by (Q_{s0},P_{s0}) takes place of (Q_s,P_s). Actually Q_{s0} is given by

$$Q_{s0}(t)=\sinh^{-1}(\mathrm{e}^{-\sqrt{2}(t-\mu)}) \tag{B.4}$$

where μ is a parameter defined by the initial condition, that is,

$$\mu\equiv t_1+(Q_1-\log 2)/\sqrt{2} \tag{B.5}$$

Equation (B.3) in which (Q_s, P_s) are replaced by (Q_{s0}, P_{s0}) is nothing more than the Melnikov function [40].

The evaluation of the Melnikov function for our system in Eq. (1), is carried out immediately. As a result, the energy at the initial time $t = t_1$ is given as follows:

$$H(t_1) \sim 1 + \epsilon(1 - \chi(\omega)) \sin \omega\mu \tag{B.6}$$

where

$$\chi(\omega) \equiv 2\omega \int_0^\infty \frac{\sin \omega s}{1 + e^{2\sqrt{2}s}}\, ds \tag{B.7}$$

Since the initial energy $E_1 (= P_1^2/2)$ takes a real value, the intersection between the stable manifold and the incident beam surface is given by

$$E_1 = P_1^2/2 = \mathrm{Re}\,\{1 + \epsilon(1 - \chi(\omega)) \sin \omega\mu\} \tag{B.8}$$

$$0 = \mathrm{Im}\,\{1 + \epsilon(1 - \chi(\omega)) \sin \omega\mu\} \tag{B.9}$$

Using the definition of the parameter μ given by Eq. (B.5), the intersection t_{1c} is decided by the above relations, (B.8) and (B.9). When E_1 is considerably less than 1, the real intersections (i.e., $\mathrm{Im}\, t_{1c} = \mathrm{Im}\, \mu_c = 0$) exist only for a sufficiently strong perturbation strength such that $\epsilon \geq \epsilon_{th} \equiv |(1 - E_1)/(1 - \chi(\omega))|$, but if the intersection is allowed to be complex, it may exist at an arbitrarily weak perturbation strength. Indeed, the complex intersections

$$\begin{aligned} \mathrm{Re}\, t_{1c} &= \mathrm{Re}\, \mu_c - (Q_1 - \log 2)/\sqrt{2} \\ &= (3/2 + 2n)\pi/\omega - (Q_1 - \log 2)/\sqrt{2} \end{aligned} \tag{B.10}$$

$$\mathrm{Im}\, t_{1c} = \mathrm{Im}\, \mu_c = \omega^{-1} \cosh^{-1}\{\epsilon^{-1}(1 - E_1)/(1 - \chi(\omega))\} \tag{B.11}$$

exist periodically at the interval $T = 2\pi/\omega$, even if the real intersections disappear in the weaker range of perturbation such that $\epsilon < \epsilon_{th}$. We comment that the evaluation of Eq. (B.11) agrees nicely with the numerical estimation of $\mathrm{Im}\, t_{1c}$.

Acknowledgments

The authors are very grateful to A. Shudo, T. Onishi, and A. Yoshimoto for valuable discussions and comments. The present work was supported by Grant-in-Aid for Scientific Research (C) No.13640410, from Japan Society for the Promotion of Science (JSPA) and Grant-in-Aid for Scientific Research on Priority Areas(2) Nos. 14077220 and 15035212 from the Ministry of Education, Culture, Sports, Science and Technology.

References

1. W. H. Miller and T. F. George, *J. Chem. Phys.* **56**, 5668 (1972); T. F. George and W. H. Miller, *J. Chem. Phys.* **57**, 2458 (1972).
2. W. H. Miller, *J. Chem. Phys*, **53**, 1949 (1970); *Adv. Chem. Phys.* **25**, 69 (1974).
3. M. Wilkinson, *Physica* **21D**, 341 (1986); M. Wilkinson and J. H. Hannay, *Physica* **27D**, 201 (1987).
4. J. B. Keller, *Proc. Symp. Appl. Math.* **8**, 27 (1958); B. Seckler and J. B. Keller, *J. Acoust. Soc. Am.* **31**, 192 (1959); A. Z. Patashinskii, V. L. Pokrovskii, and I. M. Khalatnikov, *Sov. Phys. JETP* **17**, 1387 (1963); **18**, 522, 683 (1964); V. P. Maslov, *Sov. Phys. Dokl*. **6**, 666 (1964).
5. L. S. Schulman, *Techinques and Applications of Path Integration*, John Wiley & Sons, New York, 1981.
6. V. A. Benderskii, D. E. Makarov, and C. A. Wight, *Adv. Chem. Phys.* **LXXXVIII**, 1 (1994); R. A. Marcus and M. E. Coltrin, *J. Chem. Phys.* **67**, 2609 (1977); B. C. Garrett, D. G. Truhlar, A. F. Wagner, and T. H. Dunning, Jr., *J. Chem. Phys.* **78**, 4400 (1983); D. G. Truhlar, A. D. Isaacson, R. T. Skodje, and B. C. Garrett, *J. Phys. Chem.* **86**, 2252 (1982); N. Shida, P. F. Barbara, and J. Almlof, *J. Chem. Phys* **91**, 4061 (1989); **94**, 3633 (1991); **95**, 10457 (1991); W. H. Miller, B. A. Ruf, and Y.-T. Chang, *J. Chem. Phys.* **89**, 6298 (1988).
7. J. Knoll and R. Schaeffer, *Ann. Phys. (NY)* **97**, 307 (1976).
8. W. H. Miller, *J. Phys. Chem.* **83**, 960 (1979).
9. M. C. Gutzwiller, *J. Math. Phys.* **8**, 1979 (1967); *J. Math. Phys.* **10**, 1004 (1969); *J. Math. Phys.* **11**, 1791 (1970); *J. Math. Phys.* **12**, 343 (1971); *J. Math. Phys.* **14**, 139 (1973); *J. Math. Phys.* **18**, 806 (1977).
10. M. C. Gutzwiller, *Chaos in Classical and Quantum Mechanics*, Springer-Verlag, New York, 1990.
11. O. Bohigas, S. Tomsovic, and D. Ullmo, *Phys. Rev. Lett.*, **65**, 5 (1990); *Phys. Rep.* **223**, 45 (1993); O. Bohigas, R. Egydo de Carvalho, and V. Marvulle, *Nucl. Phys. A (Netherland)* **560**, 197 (1993); F. Leyvraz and D. Ullmo, *J. Phys. A* **29**, 2529 (1996); O. Brodier, P. Schlagheck, and D. Ullmo, *Phys. Rev. Lett.* **87**, 064101 (2001); O. Brodier, P. Schlagheck, and D. Ullmo, *Ann. Phys. (NY)* **300**, 88 (2002); S. C. Creagh, N. D. Whelan, *Ann. Phys. (NY)* **272**, 196 (1999); S. C. Creagh, N. D. Whelan, *Phys. Rev. Lett.* **84**, 4084 (2000); S. C. Creagh, S. Y. Lee, N. D. Whelan, *Ann. Phys. (NY)* **295**, 194 (2002); W. E. Bies, L. Kaplan, E. J. Heller, *Phys. Rev.E* **64**, 016204 (2001).
12. S. C. Creagh, *Tunnelling in Two Dimensions* in *Tunneling in Complex Systems*, S. Tomsovic, ed., World Sientific, Singapore, 1998, pp. 35–100.
13. D. A. Steck, W. H. Oskay, M. G. Raizen, *Science* **293**, 274 (2001); W. K. Hensinger, H. Haffer, A. Browaeys, N. R. Heckenberg, K. Helmerson, C. McKenzie, G. J. Milburn, W. D. Phillips, S. L. Rolston, H. Rubinsztein-Dunlop, and B. Upcroft, *Nature* **412**, 52 (2001).
14. S. C. Creagh and N. D. Whelan, *Phys. Rev. Lett.* **77**, 4975 (1996); *Phys. Rev. Lett.* **82**, 5237 (1999).
15. A. Shudo and K. S. Ikeda, *Phys. Rev. Lett.* **74**, 682 (1995); A. Shudo and K. S. Ikeda, *Physica* **D115**, 234 (1998).
16. T. Onishi, A. Shudo, K. S. Ikeda, and K. Takahashi, *Phys. Rev. E* **64**, 025201 (2001); *Phys. Rev. E* **68**, 056211 (2003).
17. A. Shudo, T. Onishi, K. S. Ikeda, and K. Takahashi, *Dynamical and Energetic Barrier Tunneling in the Presence of Chaos in Complex Phase Space* in *Fundamental Aspects of Quantum Physics*, L. Accardi and S. Tasaki, eds., World Sientific, Singapore, 2003, pp. 157–176.

18. A. Shudo, Y. Ishii, and K. S. Ikeda, *J. Phys. A* **35**, L225 (2002). See also forthcoming publications.
19. See, for example, A. Ramani, B. Grammaticos, and T. Bountis, *Phys. Rep.* **180**, 159–245 (1989); also see references therein.
20. A. Goriely and M. Tabor, *Physica D* **85**, 93 (1995).
21. M. J. Davis and E. J. Heller, *J. Chem. Phys.* **75**, 246 (1981).
22. K. Takahashi and K. S. Ikeda, *Ann. Phys. (NY)* **283**, 94 (2000).
23. K. Takahashi and K. S. Ikeda, *Found. Phys.* **31**, 177 (2001).
24. K. Takahashi, A. Yoshimoto, and K. S. Ikeda, *Phys. Lett. A* **297**, 370 (2002).
25. K. Takahashi and K. S. Ikeda, *J. Phys. A: Math. Gen.* **36**, 7953 (2003).
26. A. Yoshimoto, *Rep. Math. Phys.* **46**, 303 (2000).
27. K. Takahashi and K. S. Ikeda, Supplement C to *J. Phys. Soc. Jpn.* **72**, 87 (2003).
28. J. D. Doll, T. G. George, and W. H. Miller, *J. Chem. Phys.* **58**, 1343 (1973).
29. G. Floquet, *Ann. Ec. Norm. Suppl.* **12**, 47 (1883); H. Sambe, *Phys. Rev. A* **207**, 315 (1973); J. S. Howland, *Math. Ann.* **207**, 315 (1974).
30. R. G. Newton, *Scattering Theory of Waves and Particles*, 2nd ed., Springer-Verlag, New York, 1982.
31. G. G. Stokes, *Trans. Cambridge Philos. Soc.* **10**, 106 (1864); R. B. Dingle, *Asymptotic Expansions: Their Derivation and Interpretation*, Academic Press, London, 1973; for a very recent development on the study of Stokes phenomenon, see, for example, B. Y. Sternin and V. E. Shatalov, *Borel–Laplace Transform and Asymptotic Theory*, CRC Press, Boca Raton, FL, 1996.
32. M. V. Berry and K. E. Mount, *Rep. Prog. Phys.* **35**, 315 (1972).
33. A. Voros, *Ann. Inst. H. Poincaré*, **39**, 211 (1983).
34. S. Adachi, *Ann. Phys. (NY)* **195**, 45 (1989).
35. A. Shudo and K. S. Ikeda, *Phys. Rev. Lett.* **76**, 4151 (1996).
36. One applies the Painlevé test—that is, the singularity analysis for judging if a considering system is integrable or nonintegrable [19]—to the system studied in the present chapter, then he easily finds that it is nonintegrable in the sense of Painlevé test.
37. M. J. Davis and S. K. Gray, *J. Chem. Phys.* **84**, 5389 (1986).
38. S. Wiggins, L. Weisenfeld, C. Jaffe, and T. Uzer, *Phys. Rev. Lett*. **86**, 5478 (2001).
39. R. Loudon, *The Quantum Theory of Light*, 1st ed., Oxford University Press, Oxford, 1973.
40. S. Wiggins, *Introduction to Applied Nonlinear Dynamical Systems and Chaos*, Springer-Verlag, New York, 1990.

CHAPTER 9

COARSE-GRAINED PICTURE FOR CONTROLLING QUANTUM CHAOS

TOSHIYA TAKAMI[†]

Institute for Molecular Science, Okazaki 444-8585, Japan

HIROSHI FUJISAKI

Department of Chemistry, Boston University, Boston, Massachusetts, 02215, USA

TAKAYUKI MIYADERA

Department of Information Sciences, Tokyo University of Science, Noda City, 278-8510, Japan

CONTENTS

I. Introduction
II. Optimal Control of Quantum Chaos
  A. Controlled Random Matrix System
  B. Controlled Quantum Kicked Rotor
III. Coarse-Grained Picture
  A. Coarse-Grained Rabi State and Frequency
  B. Actual Coarse-Graining Procedure
  C. Smooth Transition Between Random Vectors
IV. Analytic Expression for the Optimal Field
  A. Coarse-Grained Transition Element
  B. Analytic Solution for Perfect Control
V. Summary and Discussion
Acknowledgments
References

[†]Present address: Computing and Communications Center, Kyushu University, Fukuoka, 812-8581, Japan

Geometric Structures of Phase Space in Multidimensional Chaos: A Special Volume of Advances in Chemical Physics, Part A, Volume 130, edited by M. Toda, T Komatsuzaki, T. Konishi, R.S. Berry, and S.A. Rice. Series editor Stuart A. Rice.
ISBN 0-471-70527-6

I. INTRODUCTION

Controlling quantum systems is one of hot topics in physics and chemistry as illustrated in the fields of quantum information processings [1–3] and laser control of atomic and molecular processes [4]. As for the latter, there have been devised various control schemes: A π pulse is a simple example to induce a transition between two eigenstates [5]. As a generalization of the π pulse or adiabatic rapid passage [6], we can utilize the nonadiabatic transitions induced by laser fields [7]. For more than three-level systems, the STIRAP scheme uses a counterintuitive pulse sequence to achieve a perfect population transfer between two eigenstates [8]. When more than two electronic states are involved in the controlled system, we can use a pulse-timing control (Tannor–Rice) scheme to selectively break a chemical bond on a desired potential surface by using a pump and dump pulses with an appropriate time interval [9]. When the controlled system has more than two pathways from an initial state to a target state, quantum mechanical interference between them can be utilized to modify the ratio of products, which is called a coherent control (Shapiro–Brumer) scheme [10].

These control schemes are very effective for a certain class of processes but are not versatile and ineffective for, for example, multilevel–multilevel transitions we shall consider in this chapter. There exist several mathematical studies that investigate controllability of general quantum mechanical systems [11,12]. The theorem of controllability says that quantum mechanical systems with a discrete spectrum under certain conditions have complete controllability in the sense that an initial state can be guided to a chosen target state after some time. Although the theorem guarantees the existence of optimal fields, it does not tell us how to construct such a field for a given problem.

One of the method to practically design an optimal field is optimal control theory (OCT) [12,13] or genetic algorithms [4,14]. In this chapter we focus on the former as a theoretical vehicle. The equations derived from OCT are highly nonlinear (and coupled), so we must solve them using some iterative procedures. There exist some effective algorithms to carry out this procedure numerically; however, the field thus obtained is so complicated that it is difficult to analyze the results: What kinds of dynamical processes are involved in the controlled dynamics? In addition, the cost of the computation becomes larger if we want to apply OCT to realistic problems with many degrees of freedom. Several efforts have been made to reduce computational costs; Zhu and Rabitz [15] have introduced a noniterative algorithm for the optimal field.

On the other hand, we know that some chemical reaction systems, especially when highly excited, exhibit quantum chaotic features [16]; that is, statistical properties of eigenenergies and eigenvectors are very similar to those of random matrix systems [17]. We call such systems *quantum chaos systems*. Researchers have also studied how these quantum chaos systems behave under some external

parameters [18–20]. These statistical properties of quantum chaos systems stem from multilevel–multilevel interactions of eigenstates, which are related to the existence of many avoided crossings [21]. Hence it is necessary to consider the interaction between many eigenstates when we study dynamics in such a system. Furthermore, if our purpose is to control a Gaussian wavepacket in a quantum chaos system, the process also becomes a multilevel–multilevel transition because a Gaussian wavepacket in such a system contains many eigenstates. These are our motivations why we treat multilevel–multilevel transitions and want to control them.

This chapter is organized as follows. In Section II, we show how quantum chaos systems can be controlled under the optimal fields obtained by OCT. The examples are a random matrix system and a quantum kicked rotor. (The former is considered as a strong-chaos-limit case, and the latter is considered as mixed regular-chaotic cases.) In Section III, a ''coarse-grained'' Rabi state is introduced to analyze the controlled dynamics in quantum chaos systems. We numerically obtain a smooth transition between time-dependent states, which justifies the use of such a picture. In Section IV, we derive an analytic expression for the optimal field under the assumption of the CG Rabi state, and we numerically show that the field can really steer an initial state to a target state in random matrix systems. Finally, we summarize the chapter and discuss further aspects of controlling quantum chaos.

II. OPTIMAL CONTROL OF QUANTUM CHAOS

We study optimal control problems of quantum chaos systems. Our goal of control is to obtain an optimal field $\varepsilon(t)$ that guides a quantum chaos system from an initial state $|\varphi_i\rangle$ at $t = 0$ to a given target state $|\varphi_f\rangle$ at some specific time $t = T$. One such method is optimal control theory (OCT), which has been successfully applied to atomic and molecular systems [4].

OCT is usually formulated as a variational problem under constraints as follows: We start from the following functional used by Zhu–Botina–Rabitz [13]:

$$J = J_0 - \alpha \int_0^T [\varepsilon(t)]^2 \, dt - 2\mathrm{Re}\left[\langle \phi(T)|\varphi_f\rangle \int_0^T \langle \chi(t)| \frac{\partial}{\partial t} - \frac{H[\varepsilon(t)]}{i\hbar} |\phi(t)\rangle \, dt \right] \tag{1}$$

The first term on the right-hand side is the squared absolute value of the final overlap,

$$J_0 = |\langle \phi(T)|\varphi_f\rangle|^2 \tag{2}$$

The second term is the penalty term with respect to an amplitude of the external field $\varepsilon(t)$. The factor $\langle\phi(T)|\varphi_f\rangle$ in the last term is introduced to decouple the conditions for the state $|\phi(t)\rangle$ and the inversely evolving state $|\chi(t)\rangle$, both of which evolve under the Hamiltonian $H[\varepsilon(t)]$ [4,13]. The variation of J with respect to $|\phi(t)\rangle$ and $|\chi(t)\rangle$ gives Schrödinger's equations,

$$i\hbar\frac{d}{dt}|\phi(t)\rangle = H[\varepsilon(t)]|\phi(t)\rangle, \qquad i\hbar\frac{d}{dt}|\chi(t)\rangle = H[\varepsilon(t)]|\chi(t)\rangle \tag{3}$$

Here we impose the following boundary conditions:

$$|\phi(0)\rangle = |\varphi_i\rangle, \qquad |\chi(T)\rangle = |\varphi_f\rangle \tag{4}$$

Another variation of J with respect to $\varepsilon(t)$ gives an expression for the external field

$$\varepsilon(t) = \frac{1}{\alpha\hbar}\mathrm{Im}\left[\langle\phi(t)|\chi(t)\rangle\langle\chi(t)|\frac{\partial H[\varepsilon(t)]}{\partial\varepsilon(t)}|\phi(t)\rangle\right] \tag{5}$$

In actual numerical calculations, we usually solve these equations with some iteration procedure [13] because they are nonlinear with respect to $|\phi(t)\rangle$ and $|\chi(t)\rangle$. The optimal field, Eq. (5), is finally given after a local maximum of the functional is reached.

In the following subsections, we numerically demonstrate to control multilevel–multilevel transition problems in quantum chaos systems: One is a random matrix system, and the other is a quantum kicked rotor.

A. Controlled Random Matrix System

The random matrix was first introduced by E. P. Wigner as a model to mimic unknown interactions in nuclei, and it has been studied to describe statistical natures of spectral fluctuations in quantum chaos systems [17]. Here, we introduce a random matrix system driven by a time-dependent external field $\varepsilon(t)$, which is considered as a model of highly excited atoms or molecules under an electromagnetic field. We write the Hamiltonian

$$H[\varepsilon(t)] = H_0 + \varepsilon(t)V \tag{6}$$

where H_0 and V are $N \times N$ random matrices subject to the Gaussian Orthogonal Ensemble (GOE), which represent generic quantum systems with time-reversal symmetry. The matrix elements of H_0 and V are scaled so that both the nearest-neighbor spacing of eigenvalues of H_0 and the variance of the off-diagonal elements of V become unity.

Once we fix the initial state $|\varphi_i\rangle$ and the final state $|\varphi_f\rangle$, the optimal field $\varepsilon(t)$ is obtained by some numerical procedures for appropriate values of the target time T and the penalty factor α. Though there should be many situations corresponding to the choice of $|\varphi_i\rangle$ and $|\varphi_f\rangle$, we only consider the case where they are *Gaussian random vectors*. It is defined by

$$|\varphi\rangle = \sum_j c_j |\phi_j\rangle \tag{7}$$

where c_j are complex numbers determined from the following Gaussian distribution,

$$P(c_j) \propto \exp\left(-|c_j|^2\right) \tag{8}$$

and $|\phi_j\rangle$ is an orthonormal basis.[1] We take this state because it is typical in a random matrix system.

We show two numerical examples for a 64×64 random matrix Hamiltonian: One is the relatively short-time case with $T = 20$ and $\alpha = 1$ shown in Fig. 1, and the other is the case with $T = 200$ and $\alpha = 10$ shown in Fig. 2. In both cases, we obtain the optimal field $\varepsilon(t)$ after 100 iterations using the Zhu–Botina–Rabitz (ZBR) scheme [13] with $\varepsilon(t) = 0$ as an initial guess of the field. The initial and the target state is chosen as Gaussian random vectors as mentioned above. The final overlaps are $J_0 = 0.971$ and 0.982, respectively.

One sees that the ZBR scheme is effective enough for random matrix systems; that is, the optimal fields can be obtained even for this type of complicated problem of multilevel–multilevel transitions. However, it seems that the further analysis is difficult because the power spectra for the optimal fields, Figs. 1b and 2b, are very "complex"; that is, they contain many frequency components.[2]

B. Controlled Quantum Kicked Rotor

The kicked rotor (or the standard map) is one of famous models in chaotic dynamical systems, and it has been studied in various situations [17]. One feature of its chaotic dynamics is the *deterministic diffusion* along the momentum direction. It is also well known that if we quantize this system, this diffusion is

[1] In numerical studies below, we obtain such vectors with normalization after generating random complex elements subject to the distribution.

[2] In the insets of Figs. 1c and 2c, we show the overlaps $|\langle\phi(t)|\varphi_f\rangle|^2$ near $t = T$ in a magnified scale. They exhibit almost the same curves in spite of the different optimal fields. This is because the optimal field is small enough so that the dynamics is not affected in this time scale.

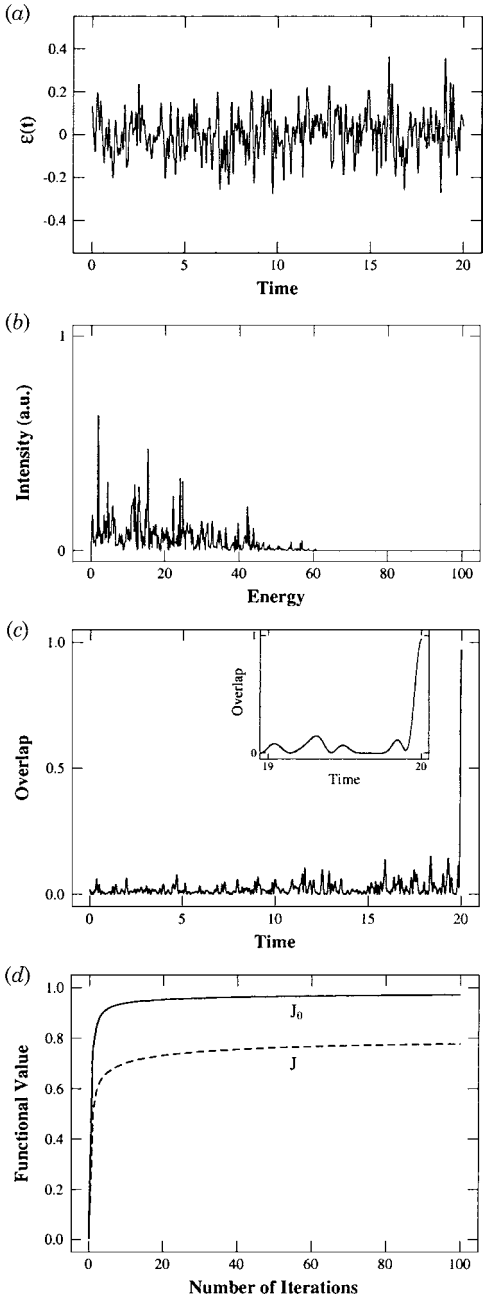

Figure 1. Optimal control between Gaussian random vectors in a 64×64 random matrix system by the Zhu–Botina–Rabitz scheme with $T = 20$ and $\alpha = 1$. (*a*) The optimal field after 100 iterations; (*b*) its power spectrum; (*c*) the optimal evolution of the squared overlap with the target $\left|\langle\phi(t)|\varphi_f\rangle\right|^2$ as well as its magnified values near the target time in the inset; (*d*) the convergence behavior of the overlap J_0 (solid curve) and the functional J (dashed curve) versus the number of iteration steps.

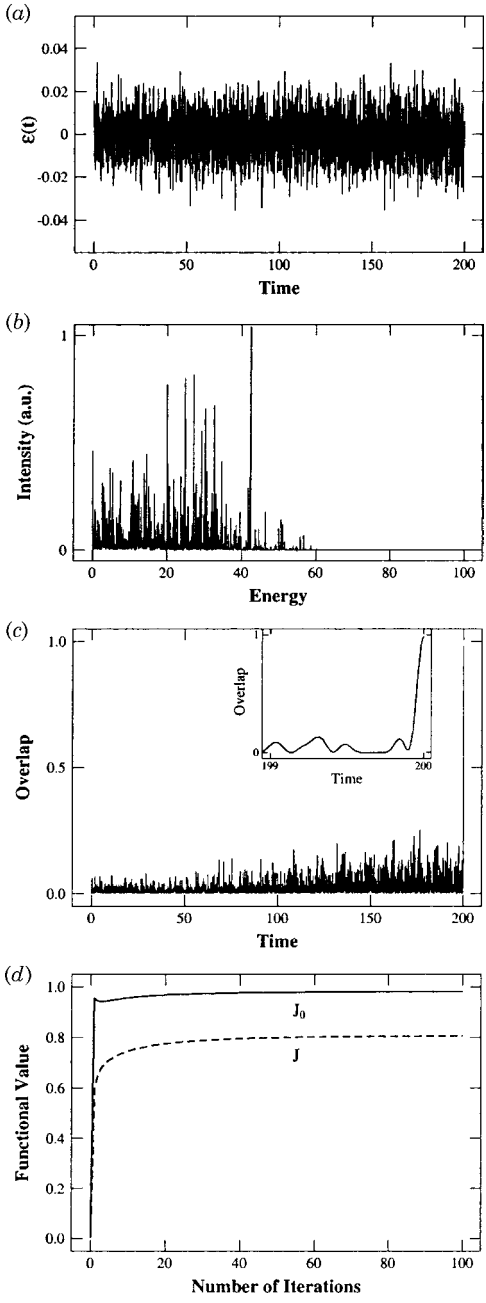

Figure 2. Optimal control between Gaussian random vectors in a 64×64 random matrix system by the Zhu–Botina–Rabitz scheme with $T = 200$ and $\alpha = 10$. (*a*) The optimal field after 100 iterations; (*b*) its power spectrum; (*c*) the optimal evolution of the squared overlap with the target, $\left|\langle\phi(t)|\varphi_f\rangle\right|^2$ as well as its magnified values near the target time in the inset; (*d*) the convergence behavior of the overlap J_0 (solid curve) and the functional J (dashed curve) versus the number of iteration steps.

suppressed by the effects of the wavefunction localization in momentum space [16].

Here we employ the quantum kicked rotor as a simple model of quantum chaos systems. The Hamiltonian of a kicked rotor is written as

$$H_{\mathrm{KR}}(t) = \frac{p^2}{2} + \frac{K}{\tau}\cos\theta \sum_{n=-\infty}^{\infty} \delta(t - n\tau) \tag{9}$$

where θ is an angle (mod 2π), p momentum, K a kick strength, and τ a period between kicks. An external field $\varepsilon(t)$ is applied through the coupling Hamiltonian

$$H_{\mathrm{I}}[\varepsilon(t)] = -\mu(\theta)\varepsilon(t) \tag{10}$$

where the dipole moment is assumed to be

$$\mu(\theta) = -\cos(\theta + \delta\theta_0) \tag{11}$$

The extra phase $\delta\theta_0$ is introduced to break symmetry of the system. We take $\delta\theta_0 = \pi/3$ in the numerical calculations throughout this chapter. The total Hamiltonian is given by

$$H[\varepsilon(t)] = H_{\mathrm{KR}}(t) + H_{\mathrm{I}}[\varepsilon(t)] \tag{12}$$

For easiness of computation, we impose a periodic boundary condition for p as well as θ; the phase space of the corresponding classical system becomes a two-dimensional torus [22,23]. In this case, Planck's constant is given by $\hbar = 2\pi M/\tau N$, where $p = \pm M\pi$ defines the periodic boundaries in the momentum space, and N is the number of discrete points describing θ and p. In the actual calculations, we set $\tau = 1$.

The kicked rotor is often described only at discrete time immediately after/before the periodic kicks. In our control problem, however, we must represent dynamics driven by $\varepsilon(t)$ between those kicks. Then, we can apply the Zhu–Botina–Rabitz scheme as usual. According to Eq. (5), the optimal external field is given by

$$\varepsilon(t) = -\frac{1}{\alpha\hbar}\mathrm{Im}[\langle\phi(t)|\chi(t)\rangle\langle\chi(t)|\mu(\theta)|\phi(t)\rangle] \tag{13}$$

Note that because $\mu(\theta)$ commutes with the unitary operator $e^{-iK\cos\theta/\hbar}$ of a kick, $\varepsilon(t)$ is obtained as a continuous function of time even at the moment of the delta kicks.

In Figs. 3 and 4, we show numerical results for the quantum kicked rotor[3] as in Section II.A. The system parameters are chosen to pick up a regular dynamics (Fig. 3) and a chaotic dynamics (Fig. 4), and the others are $T = 400$ and $\alpha = 1$. The optimal field after 100 iterations for the regular case (Fig. 3a) is much simpler than that for the chaotic case (Fig. 4a). (See also Figs. 3b and 4b.) This is because more states are involved in the latter chaotic process.

Next we investigate the wavepacket dynamics in phase space using the Husimi representation [24]. The initial and final states, $|\varphi_i\rangle$ and $|\varphi_f\rangle$, are chosen as minimum uncertainty (Gaussian) packets centered at (θ_i, p_i) and (θ_f, p_f), respectively. In Fig. 5a, we show the result for the regular case corresponding to Fig. 3. Optimal control is achieved for a wavepacket motion within a torus with $J_0 = 0.989$.[4] Figure 5b shows the controlled dynamics for the chaotic case corresponding to Fig. 4. In this case, the wavepacket once spreads all over the phase space due to the chaotic nature of the system, but it gets together at the target time T with $J_0 = 0.969$. In both regular and chaotic cases, the ZBR–OCT scheme works well for the quantum kicked rotor [25].

III. COARSE-GRAINED PICTURE

If we apply a resonant external field to a two-level system, we can observe a Rabi oscillation. In such a case, the quantum state is well described by

$$|\phi(t)\rangle = e^{E_1 t/i\hbar}|\phi_1\rangle \cos[|\Omega|t] - ie^{-i\theta}e^{E_2 t/i\hbar}|\phi_2\rangle \sin[|\Omega|t] \tag{14}$$

where $|\phi_1\rangle$ and $|\phi_2\rangle$ (E_1 and E_2) are two eigenstates (eigenenergies) of the system, $|\Omega| \equiv |\varepsilon_0 \mu_{12}|/\hbar$ is the Rabi frequency, $\mu_{12} \equiv \langle\phi_1|\hat{\mu}|\phi_2\rangle$ is a matrix element of a dipole operator $\hat{\mu}$, ε_0 is an amplitude of the field, and θ is a certain phase parameter.

In this section, we study the controlled dynamics from an initial state $|\varphi_i\rangle$ at $t = 0$ to a target state $|\varphi_f\rangle$ at $t = T$ in a multistate quantum mechanical system described by Eq. (6). By introducing a "coarse-grained" picture, which means neglecting highly oscillating terms as the case of rotating-wave approximation (RWA) [5] and assuming that $|\varphi_i\rangle$ and $|\varphi_f\rangle$ contain many eigenstates without any correlation between them, we show that the controlled dynamics can be represented as a transition between a pair of time-dependent states [26].

[3]We use the parameters $N = 128$ and $M = 7$. Thus the quantum states are represented by 128 discrete points, and the range of momentum is from -7π to 7π. The value of $\hbar = 2\pi M/N$ is 0.3436.
[4]When the control purpose is to steer a wavepacket in a torus to another place in another torus, OCT fails. This is because the wavepacket is trapped in one torus, and it is very hard to escape from the torus with a weak external field.

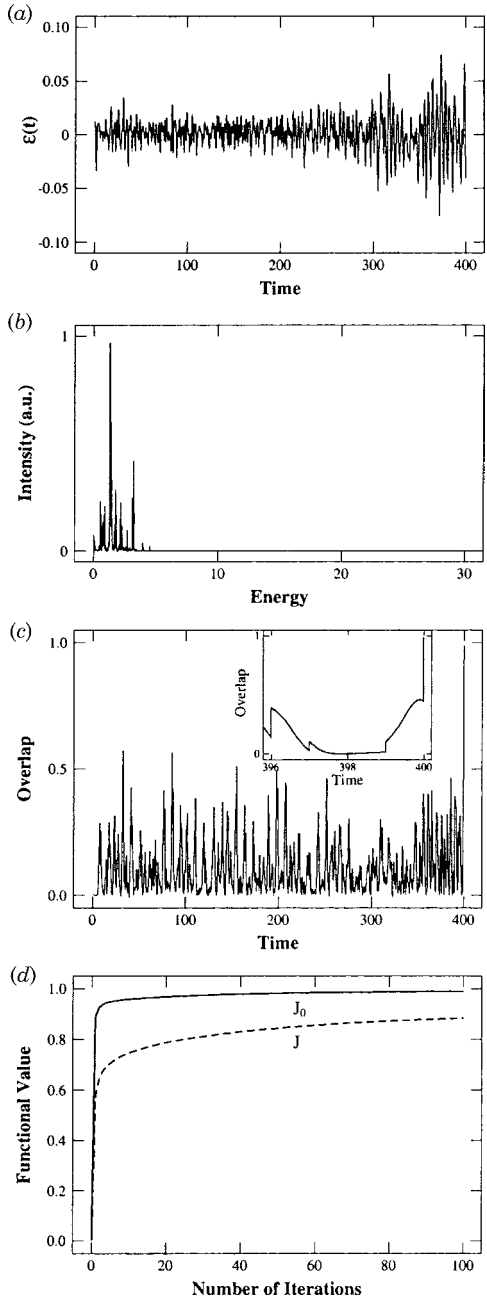

Figure 3. Optimal control in a regular kicked rotor with $K = 1$ and $\hbar = 0.3436$ by the Zhu–Botina–Rabitz scheme with $T = 400$ and $\alpha = 1$. (*a*) the optimal field after 100 iterations; (*b*) its power spectrum; (*c*) the optimal evolution of the squared overlap with the target $\left|\langle\phi(t)|\varphi_f\rangle\right|^2$ as well as its magnified values near the target time in the inset; (*d*) the convergence behavior of the overlap J_0 (solid curve) and the functional J (dashed curve) versus the number of iteration steps.

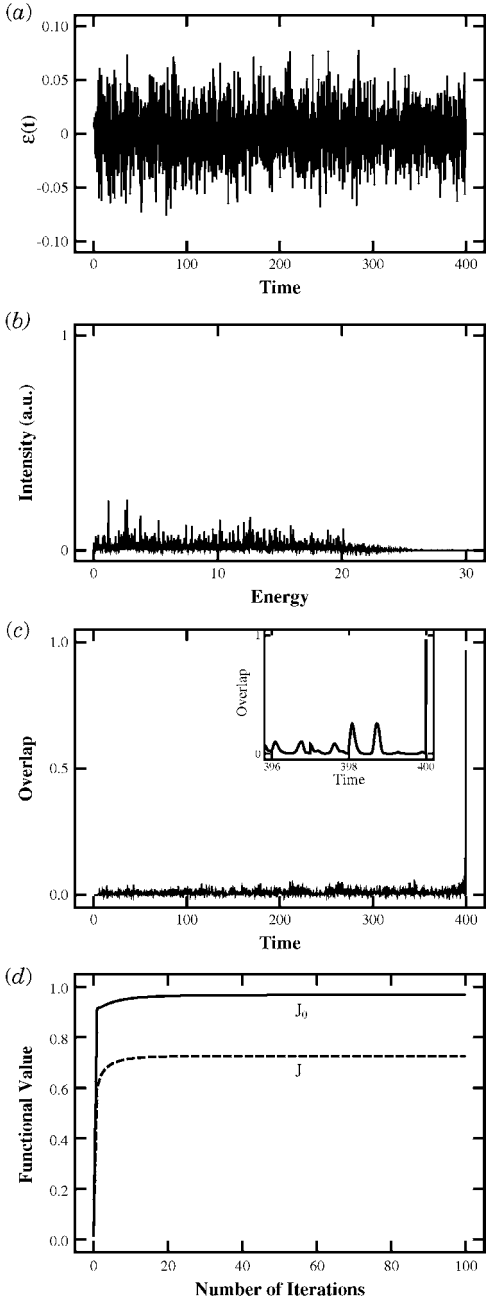

Figure 4. Optimal control in a chaotic kicked rotor with $K = 7$ and $\hbar = 0.3436$ by the Zhu–Botina–Rabitz scheme with $T = 400$ and $\alpha = 1$. (*a*) The optimal field after 100 iterations; (*b*) its power spectrum; (*c*) the optimal evolution of the squared overlap with the target, $\left|\langle\phi(t)|\varphi_f\rangle\right|^2$ as well as its magnified values near the target time in the inset; (*d*) the convergence behavior of the overlap J_0 (solid curve) and the functional J (dashed curve) versus the number of iteration steps.

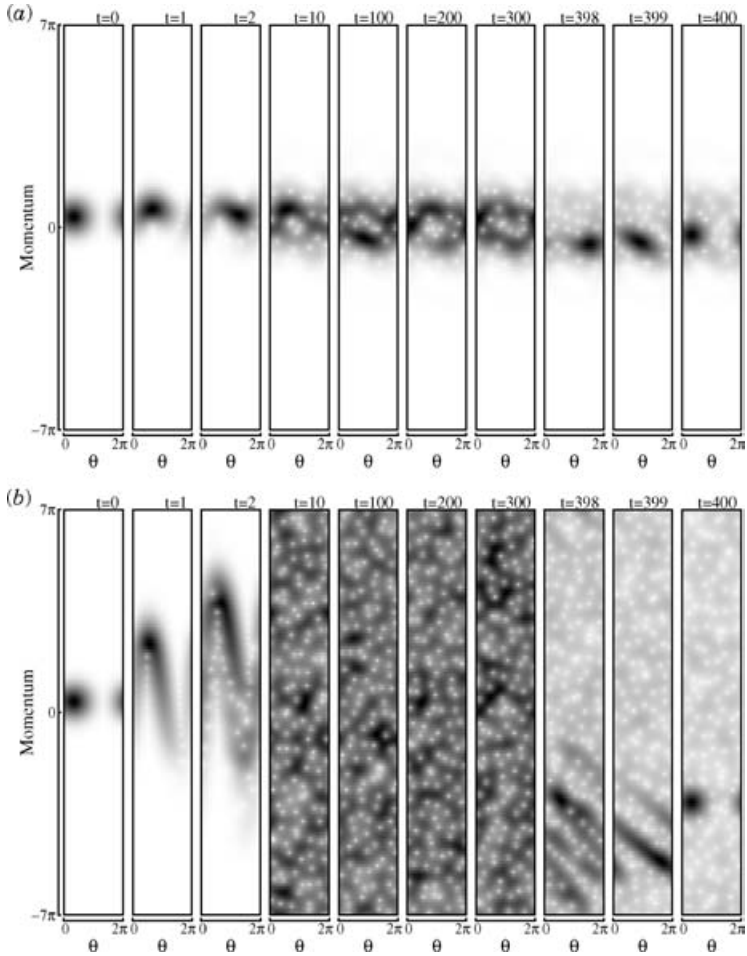

Figure 5. Time evolution of the Husimi distribution for quantum kicked rotors with $\hbar = 0.3436$ under an optimal field after 100 iterations. The Zhu–Botina–Rabitz scheme was used with the penalty factor $\alpha = 1$ and the target time $T = 400$. From left to right, quantum states immediately after the kick at $t = 0$, 1, 2, 10, 100, 200, 300, 398, 399, and 400 are depicted. (*a*) The parameters are $K = 1$ (regular case), $(\theta_i, p_i) = (1.0, 1.0)$ and $(\theta_f, p_f) = (1.0, -1.0)$; (*b*) $K = 7$ (chaotic case), $(\theta_i, p_i) = (1.0, 1.0)$ and $(\theta_f, p_f) = (1.0, -10.0)$.

A. Coarse-Grained Rabi State and Frequency

As shown in Section II.A, the overlap in the controlled dynamics rapidly oscillates because the system contains many states. To analyze this complicated behavior more easily, we introduce the following two time-dependent states,

$$|\phi_0(t)\rangle = \hat{U}_0(t, 0)|\varphi_i\rangle, \qquad |\chi_0(t)\rangle = \hat{U}_0(t, T)|\varphi_f\rangle \tag{15}$$

where

$$\hat{U}_0(t_2, t_1) = e^{-iH_0(t_2-t_1)/\hbar} \tag{16}$$

is a "free" propagator with H_0 from $t = t_1$ to t_2, and T is a target time. These states are an analogue of eigenstates in the usual Rabi state (1.14), and we try to describe the controlled dynamics as a transition from $|\phi_0(t)\rangle$ to $|\chi_0(t)\rangle$.

We introduce another quantum state by a linear combination of the two time-dependent states,

$$|\phi(t)\rangle = |\phi_0(t)\rangle c(t) + |\chi_0(t)\rangle s(t) \tag{17}$$

where $c(t)$ and $s(t)$ are functions satisfying a normalization condition:

$$|c(t)|^2 + |s(t)|^2 = 1 \tag{18}$$

If we require $|\phi(t)\rangle$ to satisfy Schrödinger's equation, we obtain

$$i\hbar\left[|\phi_0(t)\rangle \frac{d}{dt}c(t) + |\chi_0(t)\rangle \frac{d}{dt}s(t)\right] = \varepsilon(t)V[|\phi_0(t)\rangle c(t) + |\chi_0(t)\rangle s(t)] \tag{19}$$

Multiplying $\langle\phi_0(t)|$ and $\langle\chi_0(t)|$ from the left gives the following equations for $c(t)$ and $s(t)$

$$i\hbar\frac{d}{dt}\begin{pmatrix} c(t) \\ s(t) \end{pmatrix} = \begin{pmatrix} \langle\phi_0(t)|\varepsilon(t)V|\phi_0(t)\rangle & \langle\phi_0(t)|\varepsilon(t)V|\chi_0(t)\rangle \\ \langle\chi_0(t)|\varepsilon(t)V|\phi_0(t)\rangle & \langle\chi_0(t)|\varepsilon(t)V|\chi_0(t)\rangle \end{pmatrix}\begin{pmatrix} c(t) \\ s(t) \end{pmatrix} \tag{20}$$

where we have used

$$|\langle\phi_0(t)|\chi_0(t)\rangle| \ll 1 \tag{21}$$

which is satisfied when $|\varphi_i\rangle$ and $|\varphi_f\rangle$ are random vectors with a large number of elements.

Our aim is not to solve Eq. (20) exactly, but to find a coarse-grained (CG) solution by ignoring rapidly oscillating terms when the target time T is large enough. If we use the well-optimized field $\varepsilon(t)$, we expect that the conditions

$$|\langle\phi_0(t)|\varepsilon(t)V|\phi_0(t)\rangle|, |\langle\chi_0(t)|\varepsilon(t)V|\chi_0(t)\rangle| \ll |\langle\phi_0(t)|\varepsilon(t)V|\chi_0(t)\rangle| \tag{22}$$

are satisfied for $T \to \infty$ under the coarse-grained picture. The validity of this condition will be checked in Section III.B.

Under this condition, we obtain the following simple equations:

$$i\hbar \frac{d}{dt}\begin{pmatrix} c(t) \\ s(t) \end{pmatrix} = \begin{pmatrix} 0 & \hbar\Omega \\ \hbar\Omega^* & 0 \end{pmatrix}\begin{pmatrix} c(t) \\ s(t) \end{pmatrix} \tag{23}$$

where

$$\Omega \equiv \left\langle \frac{\langle \phi_0(t)|\varepsilon(t)V|\chi_0(t)\rangle}{\hbar} \right\rangle_{\mathrm{CG}} \tag{24}$$

is a frequency defined by ignoring rapidly oscillating terms. We also expect that Ω has a constant (time-independent) value, which will be justified below. Then, the boundary conditions $c(0) = 1$ and $s(0) = 0$ gives a solution

$$c(t) = \cos[|\Omega|t], \qquad s(t) = -ie^{-i\theta}\sin[|\Omega|t] \tag{25}$$

where $e^{i\theta} = \Omega/|\Omega|$. The final expression of the controlled dynamics is

$$|\phi(t)\rangle = |\phi_0(t)\rangle\cos[|\Omega|t] - ie^{-i\theta}|\chi_0(t)\rangle\sin[|\Omega|t] \tag{26}$$

Note that this state is interpreted to represent a transition between $|\phi_0(t)\rangle$ and $|\chi_0(t)\rangle$ or that between $|\varphi_i\rangle$ and $|\varphi_f\rangle$. Since this is very similar to the usual Rabi state, Eq. (14), we call this state, Eq. (26), ''CG Rabi state'' and call the frequency, Eq. (24), ''CG Rabi frequency.''

B. Actual Coarse-Graining Procedure

In the previous subsection, we have introduced the concept ''coarse-graining'' (CG) to define the CG Rabi frequency Ω, Eq. (24). In the actual calculations, we carry out this procedure by averaging over a certain time interval,

$$\langle A(t)\rangle_{\mathrm{CG}} \equiv \frac{1}{t_2 - t_1}\int_{t_1}^{t_2} A(t')\,dt' \tag{27}$$

Though this result depends on the choice of t_1, t_2 in general, we consider that there exists a natural time scale where the time averaging is meaningful. In optimal control problems, if we choose the target time T large enough, we can substitute the range of the integration into above expression, i.e., $t_1 = 0$ to $t_2 = T$.

To check when the condition, Eq. (22), is fulfilled, and when the CG Rabi frequency Ω defined in Eq. (24) becomes constant, we introduce the

following integrals:

$$F(t) = \int_0^t \langle \phi_0(t') | \varepsilon(t') V | \chi_0(t') \rangle \, dt' \tag{28}$$

$$g_\phi(t) = \int_0^t \langle \phi_0(t') | \varepsilon(t') V | \phi_0(t') \rangle \, dt' \tag{29}$$

$$g_\chi(t) = \int_0^t \langle \chi_0(t') | \varepsilon(t') V | \chi_0(t') \rangle \, dt' \tag{30}$$

Though the integrands are rapidly oscillating, a certain smoothness can be observed in those integrals, especially for $F(t)$. In such a case, we judge that "coarse-graining" (CG) is appropriate. Note that $F(t)$ is a linear function of t when the CG Rabi frequency Ω is constant.

Figure 6 shows $|F(t)|$, $|g_\phi(t)|$, and $|g_\chi(t)|$ obtained from the numerical results in Section II.A. For the case of $T = 20$ in Fig. 6a, the values of $g_\phi(t)$ and $g_\chi(t)$ are small compared to $F(t)$, but $F(t)$ cannot be considered as a linear function of t. Thus, CG is not appropriate in this case. On the other hand, examining the case of $T = 200$ in Fig. 6b, we realize that the condition, Eq. (22), is satisfied, and $F(t)$ is regarded as a linear function of t. Hence we conclude that CG for random matrix systems is appropriate for a rather large target time T, and in such a case the CG Rabi frequency becomes constant.

C. Smooth Transition Between Random Vectors

In Section II.A, we have already obtained the optimal field $\varepsilon(t)$ by the numerical calculation for the random matrix systems, Eq. (6). However, only the overlap between the time-evolving controlled state $|\phi(t)\rangle$ and the target state $|\varphi_f\rangle$ was shown there. In this section, we show the overlaps between the time-dependent states defined by Eq. (15) and $|\phi(t)\rangle$, and we find a smooth transition picture.

In Fig. 7a, we show the overlap $|\langle \phi_0(t) | \phi(t) \rangle|^2$ and $|\langle \chi_0(t) | \phi(t) \rangle|^2$ that are obtained from the dynamics driven by the same external field shown in Fig. 1a. Those curves in the figure are not smooth, and it seems to be difficult to approximate them by the CG Rabi state, Eq. (26), with a constant Ω. In Fig. 7b, on the other hand, we see a smooth transition from $|\phi_0(t)\rangle$ to $|\chi_0(t)\rangle$, which is induced by the optimal field shown in Fig. 2a. In this case, the dynamics can be well represented by the CG Rabi state with a constant Ω.

IV. ANALYTIC EXPRESSION FOR THE OPTIMAL FIELD

In the previous sections, we have studied the controlled dynamics when an optimal field is first given by the ZBR–OCT scheme. In this section, in turn, we

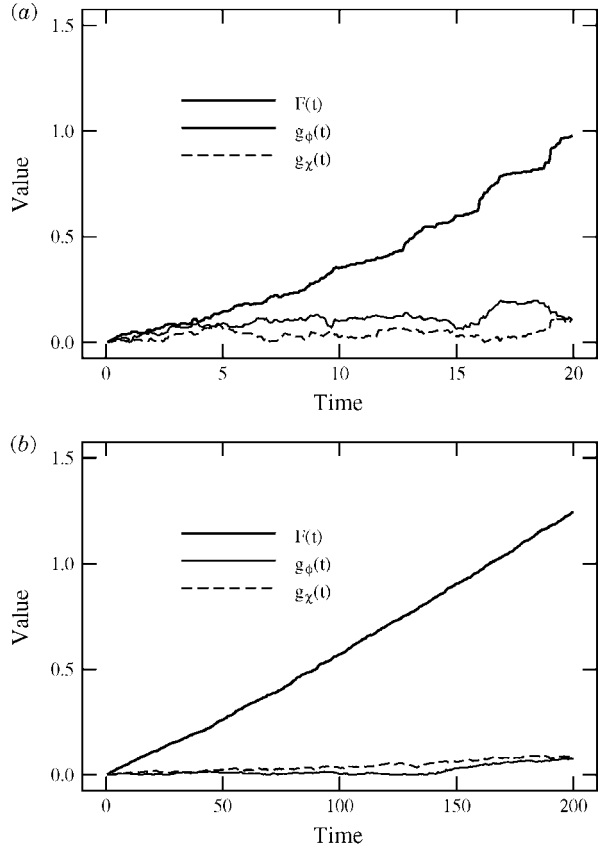

Figure 6. Absolute values of the functions $F(t)$, $g_\phi(t)$, and $g_\chi(t)$ (see the main text) are shown. (*a*) $T = 20$ and $\alpha = 1$; (*b*) $T = 200$ and $\alpha = 10$. The external fields used in these calculations are already shown in Fig. 1a and Fig. 2a, respectively.

first assume that the dynamics is well approximated by the CG Rabi state and then try to derive an analytic optimal field by using OCT [26].

A. Coarse-Grained Transition Element

We start from an assumption that optimally controlled quantum states are represented by the CG Rabi states; that is, the forwardly evolving state $|\phi(t)\rangle$ and the inversely evolving state $|\chi(t)\rangle$ are assumed to be

$$|\phi(t)\rangle = |\phi_0(t)\rangle \cos[|\Omega|t] - ie^{-i\theta}|\chi_0(t)\rangle \sin[|\Omega|t] \tag{31}$$

$$|\chi(t)\rangle = -ie^{i\theta}|\phi_0(t)\rangle \sin[|\Omega|(t-T)] + |\chi_0(t)\rangle \cos[|\Omega|(t-T)] \tag{32}$$

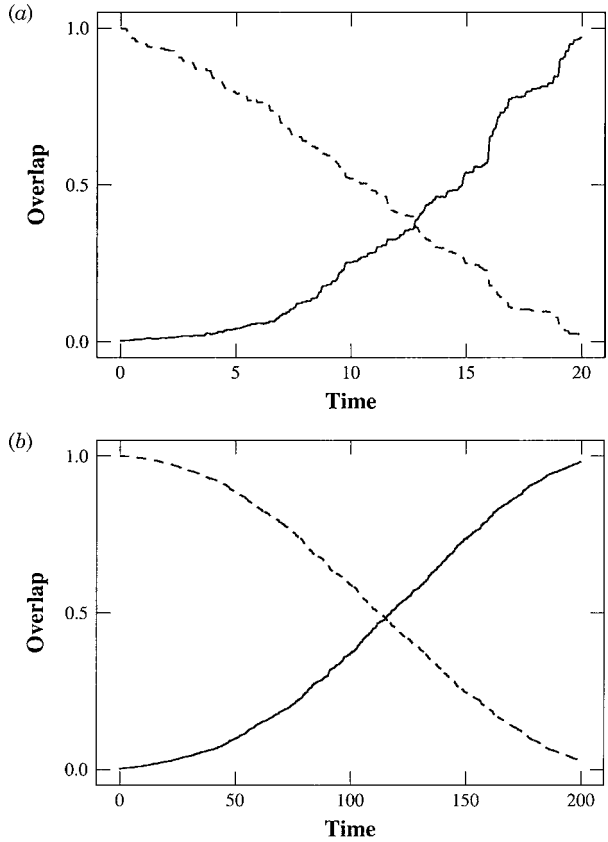

Figure 7. The overlaps $|\langle\phi_0(t)|\phi(t)\rangle|^2$ - - - and $|\langle\chi_0(t)|\phi(t)\rangle|^2$ —— are shown. (*a*) $T = 20$ and $\alpha = 1$; (*b*) $T = 200$ and $\alpha = 10$. The external fields used in these calculations are already shown in Figs. 1a and 2a, respectively.

As we have seen numerically in Section III.C, the optimal field induces a smooth transition between $|\phi_0(t)\rangle$ and $|\chi_0(t)\rangle$. In this section, we employ OCT to study an analytic formulation of the optimal field. Substituting Eqs. (31) and (32) into the expression of the optimal field, Eq. (5), and after some manipulations, we obtain

$$\varepsilon(t) = \frac{\sin 2[|\Omega|T]}{2\alpha\hbar}\,\mathrm{Re}\left[e^{-i\theta}\langle\phi_0(t)|V|\chi_0(t)\rangle\right] \tag{33}$$

where $|\langle\phi_0(t)|\chi_0(t)\rangle| \ll 1$ has been used as before. This is an analytic expression for the optimal field while the value of the CG Rabi frequency Ω and the phase parameter θ have not been determined yet.

The definition of the CG Rabi frequency, Eq. (24), is used to determine $|\Omega|$. Substituting Eq. (33) and using the relation $\Omega = e^{i\theta}|\Omega|$, we obtain

$$|\Omega| = \frac{\bar{V}^2 \sin[2|\Omega|T]}{4\alpha\hbar^2} \tag{34}$$

where

$$\bar{V}^2 \equiv \left\langle |\langle\phi_0(t)|V|\chi_0(t)\rangle|^2 + \left[e^{-i\theta}\langle\phi_0(t)|V|\chi_0(t)\rangle\right]^2 \right\rangle_{\mathrm{CG}} \tag{35}$$

is a CG transition element. This equation gives $|\Omega|$ when the penalty factor α and the target time T are fixed. For a large T, the second term in the right-hand side is considered small compared to the first term. In order to see this, we represent the initial and final state using the eigenstates $|\phi_k\rangle$ of H_0 as

$$|\varphi_i\rangle = \sum_j c_j|\phi_j\rangle, \qquad |\varphi_f\rangle = \sum_k d_k|\phi_k\rangle \tag{36}$$

with the coefficients c_j and d_j. For a large T, we can ignore oscillating terms to obtain

$$|\langle\phi_0(t)|V|\chi_0(t)\rangle|^2 = \sum_{j,k} |c_j|^2|V_{jk}|^2|d_k|^2 + |R(T)|^2 \tag{37}$$

$$[\langle\phi_0(t)|V|\chi_0(t)\rangle]^2 = (R(T))^2 \tag{38}$$

where

$$R(T) \equiv \sum_j c_j^* V_{jj} d_j e^{-E_j T/i\hbar} \tag{39}$$

becomes small for $N \to \infty$ when $|\varphi_i\rangle$ and $|\varphi_f\rangle$ are random vectors (without any special correlation). Thus Eq. (35) is simplified as

$$\bar{V}^2 \approx \sum_{j,k} |c_j|^2|V_{jk}|^2|d_k|^2 \tag{40}$$

If the condition

$$\frac{\bar{V}^2 T}{2\alpha\hbar^2} > 1 \tag{41}$$

is satisfied, at least one $|\Omega|$ ($\Omega \neq 0$) is obtained from Eq. (34). Using this $|\Omega|$, the final overlap J_0 is given by

$$J_0 = \sin^2[|\Omega|T] \tag{42}$$

and the averaged amplitude $\bar{\varepsilon}$ of the external field (1.33) is calculated as

$$\bar{\varepsilon} \equiv \sqrt{\frac{1}{T}\int_0^T |\varepsilon(t)|^2 dt} \approx \frac{\sqrt{2}\hbar|\Omega|}{\bar{V}} \tag{43}$$

In Fig. 8, we compare the predicted values, Eqs. (42) and (43), with the numerical results for the random matrix system. Those results agree well each other especially for a large T; that is, the CG picture is valid and useful especially for a large target time T.[5]

B. Analytic Solution for Perfect Control

In the ZBR scheme, we must choose a small penalty factor α to make the final overlap large enough. In our analytical results, if we take the limit $\alpha \to 0$, we find that

$$|\Omega| = \frac{(2k-1)\pi}{2T} \qquad (k = 1, 2, \ldots) \tag{44}$$

satisfies Eq. (34), and then $J_0 = 1$; that is, perfect control is achieved. Using Eqs. (33) and (34), the optimal field for the perfect control in the small α limit is obtained as

$$\varepsilon(t) = \frac{(2k-1)\pi\hbar}{\bar{V}^2 T}\mathrm{Re}\left[e^{-i\theta}\langle\phi_0(t)|V|\chi_0(t)\rangle\right] \tag{45}$$

where θ can be determined by a normalization condition as

$$e^{2i\theta} = \frac{\langle\phi_0(T)|\varphi_f\rangle}{\langle\varphi_f|\phi_0(T)\rangle} \tag{46}$$

This field is expected to be the optimal field that steers the quantum state $|\varphi_i\rangle$ at $t = 0$ to $|\varphi_f\rangle$ at $t = T$, and it also induces a CG Rabi oscillation beween $|\phi_0(t)\rangle$

[5]Note that there exists a threshold $T_c = 2\alpha\hbar^2/\bar{V}^2$, the smallest target time satisfying the condition, Eq. (41). If we choose a smaller T than T_c, there is no external field that induces the smooth transition described by the CG Rabi state. On the other hand, the numerical method can give finite solutions for such cases because there is no assumption (restriction) about the dynamics except that it obeys the Schrödinger equation.

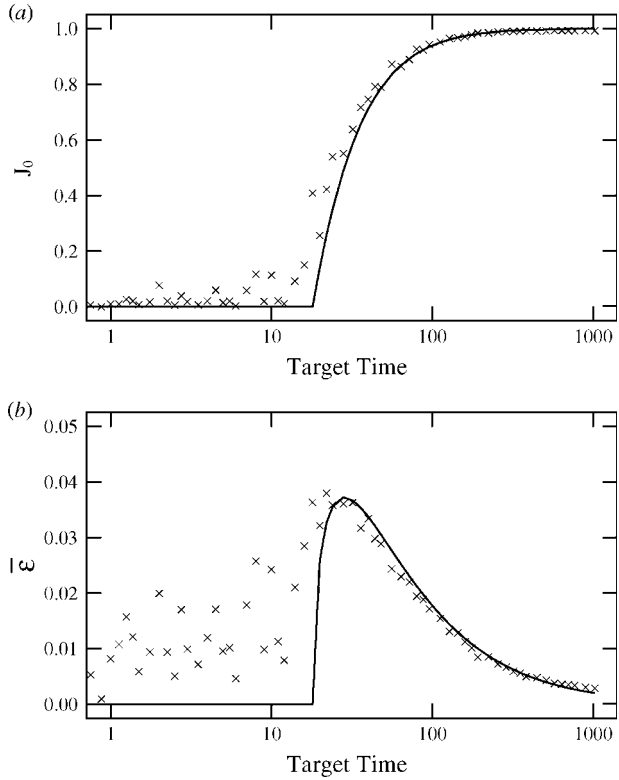

Figure 8. (*a*) The final overlap $J_0 = \left|\langle\phi(T)|\varphi_f\rangle\right|^2$ and (*b*) the averaged field amplitude $\bar{\varepsilon}$ for a 64×64 random matrix system are shown as a function of the target time T. Crosses ($\times$) represent the numerical results by the Zhu–Botina–Rabitz scheme. Solid curves represent our analytic results under the assumption of the CG Rabi state.

and $|\chi_0(t)\rangle$. Note that the penalty factor α does not appear in Eq. (45), so this is different from other non-iterative optimal fields discussed in Ref. 15.

We next examine when and how the analytic optimal field works for a random matrix system (256×256 GOE random matrix). Figure 9 demonstrates the coarse-grained Rabi oscillation induced by the analytic field, Eq. (45), with $k = 3$, where smooth oscillations of $|\langle\phi_0(t)|\phi(t)\rangle|^2$ and $|\langle\chi_0(t)|\phi(t)\rangle|^2$ are observed. The initial and the target states are both Gaussian random vectors with 256 elements. This result shows that the field actually produces the CG Rabi oscillation in the random matrix system.

Finally, in Fig. 10, we show the performance of the analytic field, Eq. (45), for the same type of control problem with various matrix sizes. The abscissa and the ordinate are the target time T and the residual probability $1 - J_0$,

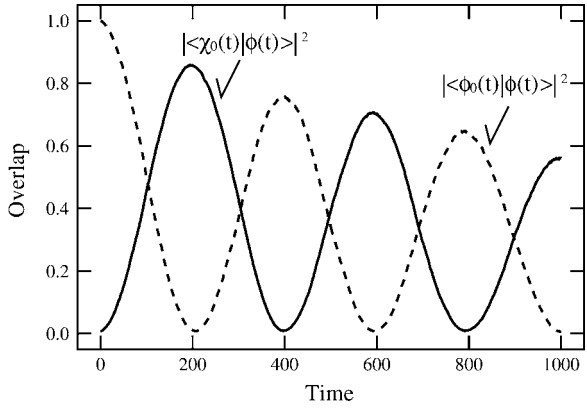

Figure 9. The coarse-grained Rabi oscillation induced by the analytical external field for perfect control is shown for the case $k = 3$ in Eq. (45). The solid curve represents $|\langle\chi_0(t)|\phi(t)\rangle|^2$, and the dashed curve represents $|\langle\phi_0(t)|\phi(t)\rangle|^2$. The initial and the target states are Gaussian random vectors in a 256×256 GOE random matrix system.

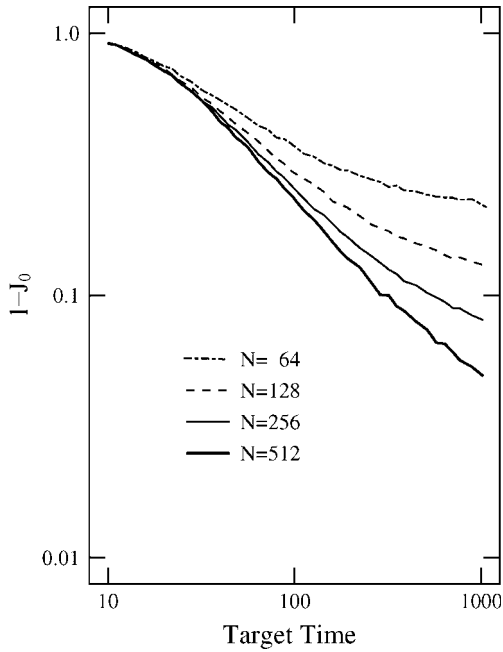

Figure 10. The target-time dependence of the final overlap J_0 by the analytic optimal field with $k = 1$ is shown. The residual probability $1 - J_0$ from perfect control $J_0 = 1$ is depicted for various matrix sizes N of GOE random matrices. The initial and the final states are Gaussian random vectors.

respectively. This result shows that the final overlap J_0 approaches unity; that is, perfect control is achieved as the target time and the matrix size become both large.

V. SUMMARY AND DISCUSSION

We have studied optimal control of random matrix systems and a quantum kicked rotor as examples of quantum chaos systems. Using the ZBR-OCT scheme, we numerically achieved almost perfect control for the above systems where the initial state $|\varphi_i\rangle$ and the target state $|\varphi_f\rangle$ are random vectors (except the case of a quantum kicked rotor with $K = 1$). However, the optimal fields and the overlap $|\langle\phi(t)|\varphi_f\rangle|^2$ thus obtained are too complicated to be analyzed as shown in Figs. 1, 2, 3, and 4. On the other hand, as shown in Fig. 7, the overlaps $|\langle\phi_0(t)|\phi(t)\rangle|^2$ and $|\langle\chi_0(t)|\phi(t)\rangle|^2$ are rather smooth where $|\phi_0(t)\rangle$ ($|\chi_0(t)\rangle$) represents a free forward (backward) evolution of the system, so we can introduce coarse grained concepts: a CG Rabi state and a CG Rabi frequency. The CG Rabi state is an analogue of a usual Rabi state, but it describes a transition between $|\phi_0(t)\rangle$ and $|\chi_0(t)\rangle$ as in Eq. (26). The CG Rabi frequency is defined by ignoring rapidly oscillating terms as in Eq. (24). We applied this picture to OCT and obtained an analytic expression for the optimal field, Eq. (45). We also numerically confirmed that the analytic field actually works in controlling random vectors when the target time and the matrix size are both large enough.

In closing, we discuss future directions of this study: (a) We mainly studied strong-chaos limit cases as random matrix systems, and we applied the coarse grained ideas to them. Thus, the next problem should be addressed on less chaotic cases as banded random matrix systems. A quantum kicked rotor with a small K will be a good example for that purpose [27]. (b) The other interesting problem is the semiclassical limit of the controlled dynamics. Though we have shown that quantum chaos systems can be controlled, we don't know its semiclassical behavior since there are many difficulties in taking the semiclassical limit $\hbar \to 0$. There are, on the other hand, many works studying *chaos control* in classical mechanics, and there are some examples utilizing stochastic features of phase space in "targeting" problems [28,29]. In this respect, it is strongly desirable to study chaos control from semiclassical points of view [30,31]. (c) In connection with quantum information processings, control of quantum entanglement in quantum chaos systems [32] will be another interesting subject to be pursued.

Acknowledgments

The authors thank Prof. S. A. Rice, Prof. H. Rabitz, Prof. M. Toda, Prof. H. Nakamura, Prof. H. Kono, Prof. S. Tasaki, Prof. A. Shudo, Dr. Y. Ohtsuki, and Dr. G. V. Mil'nikov for useful discussions.

References

1. M. A. Nielsen and I. L. Chuang, *Quantum Computation and Quantum Information*, Cambridge University Press, Cambridge, 2000.
2. V. Ramakrishna and H. Rabitz, *Phys. Rev.* A **54**, 1715 (1996).
3. C. M. Tesch and R. de Vivie-Riedle, *Phys. Rev. Lett.* **89**, 157901 (2002); J. P. Palao and R. Kosloff, *Phys. Rev. Lett.* **89**, 188301 (2002).
4. S. A. Rice and M. Zhao, *Optical Control of Molecular Dynamics*, John Wiley & Sons, New York, 2000.
5. L. Allen and J. H. Eberly, *Optical Resonance and Two-level Atoms*, Dover, New York, 1987.
6. J. S. Melinger, S. R. Gandhi, A. Hariharan, D. Goswami, and W. S. Warren, *J. Chem. Phys.* **101**, 6439 (1994).
7. Y. Teranishi and H. Nakamura, *Phys. Rev. Lett.* **81**, 2032 (1998); K. Nagaya, Y. Teranishi, and H. Nakamura, *J. Chem. Phys.* **117**, 9588 (2002); H. Fujisaki, Y. Teranishi, and H. Nakamura, *J. Theor. Comp. Chem.* **1**, 245 (2002).
8. K. Bergmann, H. Theuer, and B. W. Shore, *Rev. Mod. Phys.* **70**, 1003 (1998).
9. D. J. Tannor and S. A. Rice, *J. Chem. Phys.* **83**, 5013 (1985).
10. M. Shapiro and P. Brumer, *J. Chem. Phys.* **84**, 4103 (1986); M. Shapiro and P. Brumer, *Principles of the Quantum Control of Molecular Processes*, John Wiley & Sons, New York, 2003.
11. G. M. Huang, T. J. Tarn, and J. W. Clark, *J. Math. Phys.* **24**, 2608 (1983).
12. A. P. Peirce, M. A. Dahleh, and H. Rabitz, *Phys. Rev.* A **37**, 4950 (1988).
13. W. Zhu, J. Botina, and H. Rabitz, *J. Chem. Phys.* **108**, 1953 (1998).
14. R. S. Judson and H. Rabitz, *Phys. Rev. Lett.* **68**, 1500 (1992).
15. W. Zhu and H. Rabitz, *J. Chem. Phys.* **110**, 7142 (1999).
16. M. C. Gutzwiller, *Chaos in Classical and Quantum Mechanics*, Springer-Verlag, New York, 1990.
17. F. Haake, *Quantum Signatures of Chaos*, 2nd ed., Springer-Verlag, Heidelberg, 2001.
18. P. Gaspard, S. A. Rice, H. J. Mikeska, and K. Nakamura, *Phys. Rev.* A **42**, 4015 (1990).
19. T. Takami, *J. Phys. Soc. Jpn.* **60**, 2489 (1991); T. Takami and H. Hasegawa, *Phys. Rev. Lett.* **68**, 419 (1992).
20. J. Zakrzewski and D. Delande, *Phys. Rev.* E **47**, 1650 (1993).
21. T. Takami, *Phys. Rev. Lett.* **68**, 3371 (1992); T. Takami, *Phys. Rev.* E **52**, 2434 (1995).
22. F. M. Izrailev, *Phys. Rev. Lett.* **56**, 541 (1986).
23. S.-J. Chang and K.-J. Shi, *Phys. Rev.* A **34**, 7 (1986).
24. K. Takahashi, *Prog. Theor. Phys. Suppl.* **98**, 109 (1989).
25. T. Takami, H. Fujisaki, and T. Miyadera, Optimal Control of Quantum Chaotic Dynamics, unpublished.
26. T. Takami and H. Fujisaki, *J. Phys. Soc. Jpn.* (in press).
27. Coherent control of a quantum kicked rotor was studied in J. Gong and P. Brumer, *Phys. Rev. Lett.* **86**, 1741 (2001); *J. Chem. Phys.* **115**, 3590 (2001).
28. E. Ott, *Chaos in Dynamical Systems*, 2nd ed., (Cambridge University Press, Cambridge, 2002; T. Shinbrot, E. Ott, C. Grebogi, and J. A. Yorke, *Phys. Rev. Lett.* **65**, 3215 (1990).

29. C. D. Schwieters and H. Rabitz, *Phys. Rev.* A **44**, 5224 (1991); J. Botina, H. Rabitz, and N. Rahman, *Phys. Rev.* A **51**, 923 (1995).

30. V. S. Batista and P. Brumer, *Phys. Rev. Lett.* **89**, 143201 (2002).

31. H. Fujisaki, Y. Teranishi, A. Kondorskiy, and H. Nakamura, Semiclassical approaches to controlling chemical reaction dynamics, e-print quant-ph/0302025.

32. A. Tanaka, H. Fujisaki, and T. Miyadera, *Phys. Rev.* E **66**, 045201(R) (2002); H. Fujisaki, T. Miyadera, and A. Tanaka, *Phys. Rev.* E **67**, 066201 (2003).

AUTHOR INDEX

Numbers in parentheses are reference numbers and indicate that the author's work is referred to although his name is not mentioned in the text. Numbers in *italic* show the pages on which the complete references are listed. Letter in **boldface** indicates the volume.

Abarbanel, H. D.-I.: **B:**285(77), **B:**288(77), **B:**289(80), **B:**294(77), **B:***312*; **B:**502(5), **B:**506(5), **B:***518*
Abe, H., **A:**330(37), **A:***35*
Abel, M., **B:**522(13), **B:**531-533(13), **B:***541*
Abou-Chacra, R., **B:**212(80), **B:***253*
Abraham, E. R., **B:**522(11), **B:***541*
Abrahams, E., **B:**499(40), **B:***500*
Adachi, S., **A:**410(34), **A:***434*
Adams, J. E.: **B:**74-75(47), **B:***85*; **B:**89(10), **B:**108(20), **B:***127*
Adrover, A., **B:**502(16), **B:***518*
Agekian, T. A., **A:**330(36), **A:***335*
Aizawa, Y.: **B:**270(63), **B:**273(63,67-68,71), **B:**274(71), **B:***312*; **B:**359(20), **B:***371*; **B:**381(25-26), **B:**385(26,38), **B:***419*; **B:**465(1-2), **B:**466(5-6,8,10-11), **B:**469(6), **B:**470(6,8), **B:**471-472(10-11), **B:**474(6,8,13-15), **B:**475(17-20), **B:***475*; **B:**477(6-7), **B:***499*; **B:**502(10), **B:***518*
Ajayan, P. M., **B:**156(2-3), **B:***176*
Akimoto, T., **B:**474(14), **B:***475*
Akiyama, R., **B:**200(43), **B:***203*
Albert, R., **B:**453(23), **B:***463*
Albert, S., **A:**289(27), **A:***302*
Alberts, B.: **B:**180(12), **B:***201*; **B:**558(27), **B:***598*
Aldredge, R. C., **B:**537(42-43), **B:***542*
Alexander, S., **B:**208(35-36), **B:**230(35), **B:**232-233(35), **B:**241(35-36), **B:**246(36), **B:**250(35-36), **B:***252*
Alhassid, Y., **B:**7(5), **B:***23*
Allan, D. W., **B:**270(61), **B:***312*
Allen, J. P., **B:**228(133), **B:***255*
Allen, L., **A:**436(5), **A:**443(5), **A:***457*
Allen, P. B.: **B:**190(32), **B:**195(32), **B:**198(32), **B:***202*; **B:**208(40), **B:**223(109), **B:**238(146), **B:**240(146), **B:**243(146), **B:**250(40), **B:***252,* **B:***254–255*
Alligood, K. T., **B:**307(99), **B:***313*
Almeida, M. A., **A:**307(19), **A:***334*
Almlof, J., **A:**402(6), **A:***433*
Almöf, J. E., **B:**131-132(34), **B:***153*
Alvarez, M. M., **B:**502(16), **B:***518*
Alvarez-Ramírez. M., **A:**323(30), **A:***335*
Amar, F. G.: **B:**35(26), **B:**46(26), **B:**68(26), **B:***84*; **B:**130(6), **B:**139(6), **B:***152*; **B:**156(5), **B:***176*
Amitrano, C.: **A:**146(26-27), **A:***169*; **A:**178(58,61), **A:***214*; **B:**13(11), **B:**17(11,13), **B:***23*; **B:**90(25), **B:**106(25), **B:***127*; **B:**130(13), **B:**139(13), **B:**143(13), **B:***153*
Anderson, J., **B:**406(77), **B:***421*
Anderson, P. W.: **B:**212(80), **B:***253*; **B:**499(40), **B:***500*
Andreoni, W., **B:**180(18), **B:**201(18), **B:***202*
Anfinrud, P. A., **B:**200(36), **B:***202*
Angelescu, D. E., **B:**221(102), **B:***254*
Anosova, J. P., **A:**330(36), **A:***335*
Anteneodo, C., **B:**480-481(30), **B:***500*

Geometric Structures of Phase Space in Multidimensional Chaos: A Special Volume of Advances in Chemical Physics, Part A, Volume 130, edited by M. Toda, T Komatsuzaki, T. Konishi, R.S. Berry, and S.A. Rice. Series editor Stuart A. Rice.
ISBN 0-471-70527-6

Antoni, M., **B:**479(12,16), **B:**480(12), **B:**481(12,35), **B:**494(16), **B:***500*
Antoniou, D., **B:**206(14), **B:***251*
Antoniou, I., **B:**475(19), **B:***475*
Apkarian, V. A., **B:**186(28), **B:***202*
Aquilanti, V., **B:**89(13-15), **B:**96-97(13), **B:**111(13), **B:**114-115(14), **B:***127*
Ariizumi, T., **B:**553(22), **B:***598*
Arimondo, E., **B:**479(13), **B:***500*
Arnold, V. I.: **A:**173-174(13), **A:**184-186(13), **A:***213*; **A:**221(20-21), **A:***263*; **A:**340-341(14), **A:**358(14), **A:**372(14), **A:***398*; **B:**424(1), **B:**425(6), **B:**427(1), **B:**429(1), **B:**435(1), **B:***436*; **B:**438(4), **B:***462*; **B:**465(4), **B:***475*
Asashima, M., **B:**553(22), **B:***598*
Ashurst, W. T., **B:**534(38), **B:***542*
Atela, P., **B:**481(34), **B:***500*
Aubry, S., **B:**379(16), **B:**383(31-32), **B:***419*
Audoly, B., **B:**522(15), **B:**531(15), **B:***541*
Aurell, E., **B:**301(92-93), **B:***313*
Austin, R. H., **B:**207(26-27), **B:**209(26-27), **B:***252*
Avellaneda, M., **B:**525(22-23), **B:***541*
Awazu, A., **B:**556(25), **B:***598*
Azzam, T., **A:**287-288(41), **A:**291(41), **A:**293-294(41), **A:**296-299(41), **A:**310(41), **A:***303*

Baba, A., **B:**477(1), **B:***499*
Babikov, D., **A:**257(85), **A:***265*
Bachuber, K., **B:**406(79), **B:***421*
Bacic, Z.: **A:**198(106), **A:***215*; **A:**280(30), **A:***303*
Bader, J. S., **B:**180(4), **B:**183-185(4), **B:***201*
Badii, R., **B:**502(11), **B:**513(11), **B:***518*
Baer, T., **A:**5(6), **A:***140*, **B:**215(85), **B:**220(91), **B:***253–254*
Bagley, R. J.: **B:**427(10), **B:***436*; **B:**438(10), **B:***463*; **B:**550(11), **B:***597*
Bai, Y., **B:**180(14), **B:***201*
Bai, Z.-I., **A:**308(23), **A:**318(23), **A:***334*
Baldan, O., **B:**378(12), **B:**398(12), **B:**401(12), **B:***418*
Baldin, O., **B:**499(46), **B:***500*
Balk, M. W., **B:**220(97), **B:***254*
Ball, K. D.: **A:**178(66), **A:***214,* **B:***26(1),* **B:***83*
Bandrauk, A. D., **A:**198(136), **A:***216*
Barbáasi, A. L., **B:**453(23), **B:***463*
Barbara, P. F., **A:**402(6), **A:***433*, **B:**131-132(34), **B:***153*
Barbieri, M., **B:**329(12), **B:***351*
Barkai, E., **B:**228(123), **B:***254*
Barré, J., **B:**489(39), **B:***500*
Barrick, D., **B:**200(35), **B:***202*
Barthel, J., **B:**406(79), **B:***421*
Batista, V. S., **A:**456(30), **A:***459*
Beck, C., **A:**287(33-34), **A:**284(34), **A:**287(35), **A:**293(34-35), **A:**298-299(35), **A:**301(35), **A:***303*, **B:**364(13), **B:***371*
Beck, T. L.: **A:**178(53), **A:***214*, **B:**5(4), **B:***23*; **B:**45(31), **B:**53(31,34), **B:**54(34), **B:**56(31), **B:***84*; **B:**90(22), **B:***127*; **B:**130(5,8-10,21), **B:**135(5), **B:**139(5,8-10,21), **B:**143(10), **B:***152–153*; **B:**156(5), **B:***176*; **B:**209(54), **B:***253*
Becker, O. M., **B:**261(22), **B:**262(28), **B:**267(28), **B:***311*
Begleiter, H., **B:**338(19), **B:**341(19), **B:***351*
Bembenek, S. D., **B:**391(52), **B:***420*
Ben-Avraham, D., **B:**208(33), **B:**230(33), **B:***252*
Benderskii, V. A., **A:**402(6), **A:***433*
Ben-Eli, D., **B:**573(34), **B:**579(34), **B:***598*
Benettin, G.: **B:**31(22), **B:**46(22), **B:***84*; **B:**378(12-13), **B:**381(24), **B:**396(66), **B:**397(70), **B:**398(12-13,73), **B:**399(13), **B:**401(12-13,73), **B:***418–420*; **B:**429(25), **B:***436*; **B:**499(45-46), **B:***500*; **B:**502(19), **B:**506(19), **B:***518*
Benito, R. M., **A:**167(72), **A:***170*
Benjamin, I., **B:**7(5), **B:***23*
Ben-Shaul, A., **B:**72(41), **B:***84*
Bensimon, D.: **A:**5(10), **A:**18(10), **A:**30(10), **A:***140*; **A:**177(41), **A:***214*
Bentley, J. A.: **A:**198(114,120), **A:***216*; **A:**280(29), **A:***303*
Beratan, D. N., **B:**201(45), **B:***203*
Berblinger, M., **B:**43(28), **B:***84*
Berendsen, H. J. C., **B:**267(60), **B:**273(70), **B:**309(60), **B:***312*
Beresytcki, H., **B:**522(15), **B:**531(15), **B:***541*
Berge, P., **A:**293(49), **A:***303*
Bergmann, K., **A:**436(8), **A:***457*
Berne, B. J.: **A:**144(12), **A:***168*; **A:**228(40), **A:***264*; **B:**180(1,4), **B:**183-185(4), **B:***201*; **B:**205(2), **B:***251*
Bernstein, R. B., **B:**27-29(2), **B:**71-73(2), **B:**75(2), **B:**79-80(2), **B:***83*

Berry, M. V.: **A:**106(71), **A:**107(73), **A:***142*; **A:**410(32), **A:***434*; **B:**4(1), **B:***23*; **B:**56(36), **B:***84*
Berry, R. S.: **A:**7(26), **A:**137(26), **A:***140*; **A:**146(25-31), **A:***169*; **A:**173(5), **A:**178(5,53-54,57-58,61-63,65-66,69-74), **A:**179(69-73), **A:**186(63,69), **A:***213–215*; **A:**218-219(4), **A:**229(4), **A:**234(4,50), **A:**245(50), **A:***263–264*; **A:**338-339(2), **A:**341(2), **A:**352(2), **A:**392(42), **A:***398–399*; **B:**4(3), **B:**5(4), **B:**10(8-9), **B:**13(9,11), **B:**16(9), **B:**17(11-12), **B:**21(16-18), **B:**22(20-21), **B:***23–24*; **B:**26(1), **B:**35(26), **B:**45(31), **B:**46(26), **B:**52(31), **B:**53-54(34), **B:**56(31), **B:**66(39-40), **B:**68(26), **B:***83–84*; **B:**90(22,25-27), **B:**106(25), **B:***127*; **B:**130(5-16,26), **B:**135(5), **B:**139(5-16,26), **B:**143(10,12-13), **B:***152–153*; **B:**156(5-6), **B:**170(6), **B:***176*; **B:**209(53-55), **B:***253*; **B:**260(13-20), **B:**261(21), **B:**262(29), **B:**263(13-20), **B:**265(13-20), **B:**266(29,56), **B:**284(56), **B:**300(13-20), **B:***310–311*; **B:**388(46), **B:***420*; **B:**438(2), **B:***462*
Bessi, U., **B:**427(17), **B:***436*
Bestiale, S., **B:**130(28), **B:**139(28), **B:***153*
Beswic, J. A., **A:**63(43), **A:***141*
Bethardy, G. A., **A:**278(28), **A:***302*, **B:**210(77), **B:***253*
Bhalla, K., **B:**180(13), **B:***201*
Bhatia, P., **A:**228(42), **A:***264*
Bies, W. E., **A:**403(11), **A:***433*
Biferale, L., **B:**521(5), **B:**525(5), **B:***541*
Bigwood, R., **A:**137(99), **A:***141*, **B:**206-207(20), **B:**209(20,50), **B:**212(20), **B:**214(20), **B:**217(20), **B:***252*
Bihary, Z., **B:**186(28), **B:***202*
Birkhoff, G. D., **A:**278(19), **A:***302*
Bizzarri, A. R.: **B:**228(119), **B:***254*; **B:**265(52), **B:***311*
Blencowe, M. P., **B:**221(103), **B:***254*
Blumel, R., **A:**339(13), **A:**358(13), **A:***398*
Blumen, A., **B:**264(51), **B:***311*
Blumenfeld, R., **B:**228(116), **B:***254*
Boczko, E. M., **B:**266-257(59), **B:***311*
Boerlijst, M., **B:**549(8), **B:**573(8), **B:***597*
Boffetta, G.: **B:**301(92-94), **B:***313*; **B:**537(45), **B:***542*
Bogomolny, E. B., **A:**107(74), **A:***142*
Boguski, M. S., **B:**348(21), **B:***351*
Bohigas, O., **A:**403(11), **A:***433*, **B:**210(72), **B:***253*
Bohr, N., **A:**306(4), **A:***334*
Bolhuis, P. G., **A:**232(43), **A:***264*
Boltzmann, H., **B:**378(10), **B:**401(10), **B:***418*
Boltzmann, L., **B:**499(42), **B:***500*
Bonnet, L., **A:**249(75), **A:***265*
Boozer, A. H., **B:**502(16), **B:***518*
Borg, I., **B:**318-319(5), **B:***351*
Borkovec, M.: **A:**144(12), **A:***168*; **A:**228(37), **A:***264*; **B:**180(1), **B:***201*; **B:**205(2), **B:***251*
Bossy-Wetzel, E., **B:**180(13), **B:***201*
Botina, J., **A:**436(13), **A:**437-439(13), **A:**456(29), **A:***457–458*
Botstein, D., **B:**348(21), **B:***351*
Bouchaud, J.-P.: **B:**228(120), **B:***254*; **B:**520-521(2), **B:**526(28), **B:***541–542*
Bouchet, F., **B:**489(39), **B:***500*
Boudon, V., **A:**248(66), **A:***265*
Bountis, T., **A:**403(19), **A:**410(19), **A:***434*
Bourlioux, A., **B:**535(40), **B:***542*
Bovin, J. O., **B:**156(2), **B:***176*
Bowman, J. M.: **A:**198(113-119), **A:***216*; **A:**280(29), **A:**287(37,39), **A:**288(39), **A:**293(39), **A:***303*
Boxer, S. G., **B:**200(37), **B:***203*
Braier, P. A., **B:**90(27), **B:***127*
Braunstein, D., **B:**228(115), **B:***254*
Bray, D.: **B:**180(12), **B:***201*; **B:**558(27), **B:***598*
Brayer, G. D., **B:**180(17), **B:***202*
Breen, J. J., **A:**61(41-42), **A:***141*
Briant, C. L., **B:**130(1), **B:**139(1), **B:***152*
Brillouin, L., **A:**288(43), **A:***303*, **B:**545(4), **B:***597*
Brodier, O., **A:**403(11), **A:***433*
Brody, T. A., **B:**210(63), **B:**214(63), **B:***253*
Brooks, B. R.: **B:**190(33), **B:***202*; **B:**228-229(126), **B:***255*
Brooks, C. L. III: **B:**190(33), **B:***202*; **B:**228(128), **B:***255*; **B:**266-257(59), **B:***311*
Broucke, R. A., **A:**330(38), **A:***335*
Browaeys, A., **A:**403(13), **A:***433*
Brown, D., **A:**280(30), **A:***303*
Brown, P. O., **B:**348(21), **B:***351*
Brown, R.: **B:**289(80), **B:***312*; **B:**364(16), **B:***371*
Brown, R. C., **A:**128(91), **A:***142*
Bruccoleri, R. E., **B:**190(33), **B:***202*

Brumer, P.: **A:**8(31), **A:**20(35), **A:**27(35), **A:**114(83), **A:**128(97), **A:**134(97), **A:**140(103), **A:***141–142*; **A:**436(10), **A:**456(27,30), **A:***457–458*; **B:**43(27), **B:***84*
Brunet, J. P., **B:**89(10), **B:***127*
Bryngelson, J. D., **B:**263-264(38), **B:***311*
Bu, L.: **B:**180(9,16), **B:**197(9), **B:***201–202*; **B:**228(137), **B:***255*
Buch, V., **B:**186(28), **B:***202*
Buchheim, M. A., **B:**332(15), **B:***351*
Buldum, A., **B:**221(107), **B:***254*
Bunimovich, L., **B:**387(41-42), **B:***419*
Bunker, P. R., **A:**198(86), **A:***215*
Burghardt, I., **A:**218(3), **A:**228(3), **A:**232(45), **A:**237(55), **A:**244(55), **A:***263–265*
Burleigh, D., **B:**210(78), **B:***253*
Burton, J. J., **B:**130(1), **B:**139(1), **B:***152*
Bushnell, G. W., **B:**180(17), **B:***202*
Buss, L. W., **B:**553(24), **B:***598*

Cahill, D. G., **B:**221(99), **B:***254*
Cai, J., **B:**180(13), **B:***201*
Cairns-Smith, A. G., **B:**550(12), **B:***597*
Calenbuhr, V., **B:**591(39), **B:***598*
Campbell, D. M., **B:**207(31), **B:**219(31), **B:**249(31), **B:***252*
Campolieti, G., **A:**114(83), **A:***142*
Cannistraro, S.: **B:**228(119,134), **B:***254–255*; **B:**265(52), **B:***311*
Cao, L., **B:**290(81-82), **B:**291(81-82), **B:**300(82), **B:***312*
Cao, W., **B:**180(14), **B:***201*
Carcía, A. E., **B:**180(15), **B:***202*
Cardenas, A. E., **B:**180(15), **B:***202*
Careri, G., **B:**221(155), **B:**248(155), **B:***255*
Carlini, P.: **B:**228(119), **B:***254*; **B:**265(52), **B:***311*
Carrington, T., **A:**124(89), **A:***142*
Carry, J. R., **A:**146(46), **A:***169*
Carter, D., **A:**20(34), **A:***141*
Carter, S.: **A:**96(65), **A:***142*; **A:**198(110), **A:**199-200(142), **A:**202(142), **A:***215–216*
Casati, G., **A:**7(28), **A:**128(28), **A:***141*
Casdagli, M., **B:**285(75), **B:**286(79), **B:**300(75), **B:**307-309(75), **B:***312*
Castiglione, P., **B:**526-527(26), **B:***541*
Cavalli, S., **B:**89(13-15), **B:**96-97(13), **B:**111(13), **B:**114-115(14), **B:***127*
Cederbaum, L. S., **B:**210(64-65,71), **B:***253*
Celani, A., **B:**522(13), **B:**531-533(13), **B:***541*
Celleti, A., **B:**442(21), **B:***463*
Cencini, M., **B:**534(37), **B:**537(37,45), **B:**539(37), **B:***542*
Cerbelli, S., **B:**502(16), **B:***518*
Cerjan, C. J.: **B:**132(35), **B:***153*; **B:**171(14), **B:***177*
Chakravarty, C.: **B:**31(20), **B:**39(20), **B:**45(20), **B:***84*; **B:**209(57), **B:***253*
Champion, P. M., **B:**180(14), **B:**200(35), **B:***201–202*
Chan, H. S., **B:**90(32), **B:***128*
Chan, W.-T., **A:**198(129), **A:***216*
Chandler, D., **B:**205(7), **B:**207(7), **B:**209(7), **B:**217(7,17), **B:**218(7), **B:***251,* **B:***253*
Chandra, A. K., **A:**198(131-132), **A:***216*
Chang, S.-J., **A:**442(23), **A:***457*
Chang, Y.-T., **A:**402(6), **A:***433*
Chapman, R. L., **B:**332(15), **B:***351*
Chapuisat, X., **A:**198(133-134), **A:***216*, **B:**89(8-10), **B:***127*
Chatfield, D. C., **A:**174(23), **A:**178(23), **A:***213*
Chawanya, T., **B:**301(90), **B:***313*
Chelkowski, S., **A:**198(136), **A:***216*
Chenciner, A., **A:**219(15), **A:***263*
Chernov, N. I., **B:**387(43), **B:***419*
Chesnavich, W. J., **A:**249(73), **A:***265*
Chiang, J., **A:**96(100), **A:***142*
Chierchia, L.: **B:**396(66), **B:***420*; **B:**427(17), **B:***436*
Child, M. S.: **A:**176(37), **A:***213*; **A:**223(35), **A:**228(39), **A:**230(39), **A:**232(39), **A:***264*
Chin, J. K., **B:**180(10), **B:**199(10), **B:***201*
Chirikov, B. V.: **A:**7(28), **A:**128(28), **A:***141*; **A:**340(16), **A:**372(16), **A:***398*; **B:**383(27-28), **B:**397(69), **B:***419–420*; **B:**424(2), **B:**427(2), **B:**430(2), **B:***436*; **B:**438(5), **B:**441(17-18), **B:**457(5), **B:***462–463*; **B:**477(5), **B:***499*
Chiti, F., **B:**264(46), **B:***311*
Cho, M.: **B:**229(139), **B:***255*; **B:**391(54), **B:***420*
Choi, D., **B:**396(64), **B:***420*
Choi, M. Y., **B:**479(14), **B:***500*
Choi, N. N., **A:**308(24), **A:***335*
Chow, T. S., **B:**208(34), **B:**233(142), **B:***252,* **B:***255*
Christiansen, F., **B:**502(20), **B:***518*
Christoffel, K. M., **A:**198(119), **A:***216*
Chuang, I. L., **A:**436(1), **A:***457*
Cicogna, A., **B:**427(15), **B:***436*

Cincotta, P. M.: **B:**424(3), **B:**427(3), **B:***436*; **B:**438(7), **B:***462*
Ciraci, S., **B:**221(107), **B:***254*
Clark, J. W., **A:**436(11), **A:***457*
Cline, J. I., **A:**63(44-46), **A:**65(48), **A:***141*
Cohen, E., **B:**354(1-2), **B:***370*
Cohen, E. D. D., **B:**364(13), **B:***371*
Coltrin, M. E., **A:**402(6), **A:***433*
Connor, J. N. L., **A:**249(74), **A:***265*
Conroy, J. A., **B:**324(9), **B:***351*
Constantin, P., **B:**522(14,16), **B:**531-533(14), **B:***541*
Costley, J., **B:**106(34), **B:***128*
Coy, S. L., **A:**278(22), **A:***302*, **B:**210(66), **B:***253*
Creagh, S. C.: **A:**218(7), **A:***263*; **A:**403(11-12,14), **A:**404(14), **A:***433*; **B:**414(83), **B:***421*
Cresson, J., **B:**427(18), **B:***436*
Crisanti, A.: **B:**301(92-94), **B:***313*; **B:**521(4-5), **B:**525(5), **B:**537(4), **B:***541*
Crooks, G. E., **B:**354(4), **B:***370*
Cross, M. C., **B:**221(102), **B:***254*
Cross, P. C.: **A:**271(9), **A:***302*, **B:**89(16), **B:**93(16), **B:**95(16), **B:**106(16), **B:***127*; **B:**187(30), **B:***202*
Csaszar, A. G., **A:**269(7), **A:**274-275(7), **A:**277(7), **A:***302*
Curioni, A., **B:**180(18), **B:**201(18), **B:***202*
Cushman, R., **A:**248(63), **A:***265*
Cvitanovic, P., **B:**380(18), **B:***419*

Dahleh, M. A., **A:**436(12), **A:***457*
D'Alessandro, M., **B:**395(61), **B:***420*
Dana, I., **A:**177(41), **A:***214*
D'Aquino, A., **B:**395(61), **B:***420*
Dateo, C. E.: **A:**198(114,116), **A:***216*; **A:**280(29), **A:***303*
Daubechies, I., **B:**316(2), **B:***351*
Dauxois, T., **B:**479(13), **B:**485(37), **B:**489(39), **B:***500*
Davidson, G. S., **B:**348(20), **B:***351*
Davis, D. J., **A:**31(36), **A:***141*
Davis, H. L.: **B:**90(22), **B:***127*; **B:**130(7), **B:**139(7), **B:***152*
Davis, M. J.: **A:**5(11), **A:**6(12), **A:**20(33), **A:**31(36), **A:**35(11), **A:**39(12), **A:**59-60(11-12), **A:**65(11), **A:***140–141*; **A:**145(17), **A:**166(17), **A:**167(71), **A:***169–170*; **A:**177(42-44), **A:**198(91,94-95), **A:***214–215*; **A:**228(29), **A:***264*; **A:**339(9), **A:***398*; **A:**404(21), **A:**428(37), **A:***434*; **B:**205(9), **B:**209(9,58,62), **B:**210(77), **B:***251,* **B:***253*; **B:**260(10), **B:***310*; **B:**442(19), **B:***463*
Davis, P., **A:**388(38), **A:***399*
Dawson, S., **B:**502(14), **B:***518*
De Almeida, A. M., **A:**7(25), **A:**75(25), **A:***140*
De Carvalho, A., **B:**380(20), **B:***419*
Decatur, S. M., **B:**200(37), **B:***203*
Decius, J. C.: **A:**271(9), **A:***302*, **B:**89(16), **B:**93(16), **B:**95(16), **B:**106(16), **B:***127*; **B:**187(30), **B:***202*
Delagado, J., **A:**323(30), **A:***335*
DeLeon, N.: **A:**7(23-25), **A:**75(23-25), **A:**83-84(56), **A:**87(23,57), **A:**88(59), **A:**90(59), **A:**94(23,63), **A:***140–141*; **A:**146(35-37), **A:**153(35-37), **A:**159(36), **A:***169*; **A:**178(56), **A:**198(127), **A:***214–216*; **A:**228(40), **A:**232(48), **A:**250(48), **A:***264*; **B:**48(33), **B:**82(33), **B:***84*
DeLorenzi, G., **A:**173(9), **A:***213*
Delos, J. B., **A:**278(21), **A:***302*
DeLuca, J., **B:**395(62), **B:***420*
Delwiche, C. F., **B:**332(15), **B:***351*
De Marsily, G., **B:**525(24), **B:***541*
De Micheli, E., **A:**249(77), **A:***265*
Demidov, A. A., **B:**180(14), **B:**200(35), **B:***201–202*
Demikhovskii, V. Ya., **A:**131(95-96), **A:***142*, **B:**209(59), **B:***253*
Demtröder, W., **B:**210(64), **B:***253*
Deprit, A., **A:**178-179(75), **A:**194(75), **A:***215*
De Sousa Dias, M. E. R., **A:**248(71), **A:***265*
Devaney, D. L., **A:**311(27), **A:**317(27), **A:***335*
De Vivie-Riedl, R., **A:**436(3), **A:***457*
DeVore, R. A., **B:**316(2), **B:***351*
Dewey, T. G., **B:**228(130), **B:**237(130), **B:***255*
Diacu, F., **A:**307(18), **A:**309(25), **A:**330(25), **A:***334–335*
Dian, B. C., **B:**249(157), **B:***255*
Dickerson, R. E., **B:**180(11), **B:***201*
Diener, M., **A:**389(41), **A:***399*
Dill, K. A., **B:**90(32), **B:***128*
DiNola, A., **B:**267(60), **B:**309(60), **B:***312*
Dion, C. M., **A:**198(136), **A:***216*
Dlott, D. D., **B:**200(37), **B:***203*
Dobbyn, A. J., **A:**280(31), **A:***303*
Dobson, C. M., **B:**264(46), **B:***311*

Doll, J. D.: **A:**406(28), **A:**410(28), **A:***434*, **B:**130(21-22), **B:**139(21-22), **B:***153*; **B:**209(56), **B:***253*
Donoho, D. L., **B:**316(2), **B:***351*
Dorsey, N. E., **B:**225-227(113), **B:**247(113), **B:***254*
Doster, W., **B:**228(115), **B:***254*
Doye, J. P. K.: **B:**90(27), **B:***127*; **B:**130(25), **B:**139(25), **B:***153*; **B:**266-267(57), **B:**284(57), **B:***311*
Dragt, A. J.: **A:**167(74-75), **A:***170*; **A:**277(16-18), **A:***302*
Drews, A. R., **B:**228(134), **B:***255*
Drobits, J. C., **A:**66(52), **A:***141*
Duke, K., **B:**348(20), **B:***351*
Dumont, R. S., **B:**43(27), **B:***84*
Dunning, T. H., **A:**402(6), **A:***433*
Duppen, K., **B:**200(42), **B:***203*
Düren, R., **A:**287(38), **A:**298-299(38), **A:**301(38), **A:***303*
Dyre, J. C., **B:**392(56), **B:***420*
Dyson, F., **B:**549(9), **B:***597*

Easton, R. W., **B:**427(13), **B:***436*
Eberly, J. H., **A:**436(5), **A:**443(5), **A:***457*
Eckart, C., **B:**89(19), **B:**93(19), **B:**106(19), **B:***127*
Eckhardt, B., **A:**173(8), **A:***213*
Eckmann, J.-P., **B:**502(1), **B:***517*
Edler, J., **B:**200(44), **B:***203*
Efstathiou, K., **A:**269(4), **A:***302*
Egorov, S. A., **B:**180(6), **B:**183-185(6), **B:***201*
Eguchi, J., **B:**207(30), **B:**219(30), **B:**249(30), **B:***252*
Egydo de Carvalho, R., **A:**403(11), **A:***433*
Eigen, M., **B:**547-548(7), **B:**573(31), **B:***597–598*
Einstein, Albert: **A:**288(42), **A:***303*; **A:**306(5), **A:***334*
Eisen, M. B., **B:**348(21), **B:***351*
Eisenberg, D., **B:**378(6), **B:**405(6), **B:***418*
Eizinger, A., **B:**348(20), **B:***351*
Elber, R.: **B:**180(15), **B:**186(28), **B:***202*; **B:**223(110), **B:**228(110,117,131-132), **B:**235(131-132), **B:**238(144), **B:**257(131), **B:***254–255*
Ellegaard, C., **B:**210(75), **B:***253*
Ellinger, Y., **A:**198(130), **A:***216*
Elliott, S. R., **B:**208(42), **B:**250(42), **B:***252*
Elmaci, N., **B:**262(29), **B:**266(29,56), **B:**284(56), **B:***311*
Elran, Y., **A:**262(86), **A:***265*
Embid, P. F., **B:**534(36), **B:***542*
Engholm, J. R., **B:**207(25), **B:**209(25), **B:**239(25), **B:***252*
Englander, S. W., **B:**180(14), **B:***201*
Entin-Wohlman, O., **B:**208(36-37), **B:**241(36-37), **B:**246(36-37), **B:**250(36-37), **B:***252*
Era, M., **B:**180(19), **B:***202*
Erskin, J., **B:**354(12), **B:***371*
Esaki, S., **B:**265(53), **B:**299(53), **B:***311*
Estebaranz, J. M., **A:**167(72), **A:***170*
Etters, R. D., **B:**130(2-4), **B:**139(2-4), **B:***152*
Eubank, S., **B:**286(79), **B:***312*
Evans, D., **B:**354(1), **B:***370*
Evans, M. G.: **A:**144(4), **A:***168*; **A:**176(28), **A:***213*; **B:**258(3), **B:***310*
Evard, D. D., **A:**63(44-46), **A:**65(48), **A:***141*
Eyring, H.: **A:**144(3), **A:***168*; **A:**172(3), **A:**176(3,27), **A:***213*; **B:**258(2), **B:***310*
Ezra, G. S., **A:***264*; **A:**6(18), **A:**20(33), **A:**48(18), **A:***140–141*; **A:**145(20), **A:**146(48), **A:**166(20), **A:**167(71), **A:***169–170*; **A:**178(55), **A:***214*; **A:**307(12), **A:***334*; **A:**339(11), **A:**358(11), **A:***398*; **B:**205(10), **B:**209(10,58), **B:***251,* **B:***258*; **B:**438(1), **B:**442(19), **B:***462–463*

Fabian, J.: **B:**190(32), **B:**195(32), **B:**198(32), **B:***202*; **B:**208(40), **B:**238(145-146), **B:**240(145-146), **B:**243(145-146), **B:**250(40), **B:***252,* **B:***255*
Fair, J. R., **A:**178(64), **A:***214*, **B:**48(33), **B:**82(33), **B:***84*
Falcioni, M., **B:**521(4), **B:**537(4,45), **B:***541–542*
Falkovich, G., **B:**520(3), **B:**523(3), **B:***541*
Fano, U., **A:**307(13), **A:***334*
Farantos, S.: **A:**198(99-104), **A:***215*; **A:**228(42), **A:***264*; **A:**278(25), **A:**287(35-36,38), **A:**292(45), **A:**293(35-36,38), **A:**298(35-36,38), **A:**299(35,38), **A:**301(35,38), **A:***302–303*
Farmer, J. D.: **B:**286(79), **B:***312*; **B:**550(11), **B:***597*

Farrelly, D.: **A:**173(6,10,18), **A:**177(6,18), **A:**180-181(6,18), **A:**198(85), **A:***213,* **A:***215*; **A:**219(13), **A:**234(13,51), **A:**248(65), **A:***263–265*
Faure, A., **A:**245(58-59), **A:**248(58), **A:**256(58,84), **A:**257-258(59), **A:***265*
Fayer, M. D.: **B:**180(5), **B:**183-184(5), **B:**189-190(5), **B:**200(35,37,43), **B:***201–203*; **B:**207(28), **B:**209(28), **B:**239(28), **B:***252*
Federov, D. G., **B:**201(47), **B:***203*
Fein, A. E.: **B:**190(31), **B:***202*; **B:**238(143), **B:***255*
Feldman, J. L., **B:**208(40), **B:**250(40), **B:***252*
Felker, P. M., **B:**209(43), **B:**220(43,94-95), **B:***252,* **B:***254*
Feller, W., **B:**450(22), **B:***463*
Fenichel, N., **A:**338(4-7), **A:**340(5), **A:**341(7), **A:**349(7), **A:***398*
Fermi, E., **B:**376(1), **B:**393(1), **B:***418*
Ferrer, S., **A:**238(57), **A:***265*
Fersht, A., **B:**263(35), **B:***311*
Field, R. W., **A:**282(32), **A:**287(34-35), **A:**288(34), **A:**293(34-35), **A:**298-299(35), **A:**301(35), **A:***303*, **B:**210(66), **B:***253*
Finn, J. M.: **A:**167(74-75), **A:***170*; **A:**277(16-17), **A:***302*
Firpo, M.-C., **B:**481(32), **B:***500*
Fisher, M. E., **B:**526(27), **B:***542*
Fisher, R. A., **B:**521-522(10), **B:***541*
Flach, S., **B:**395(60), **B:***420*
Fleming, G. R.: **B:**220(97), **B:**229(139), **B:***254–255*; **B:**391(54), **B:***420*
Fleming, P. R., **A:**198(105), **A:***215*
Fleurat-Lesard, P., **A:**257(85), **A:***265*
Floquet, G., **A:**407(29), **A:**430(29), **A:***434*
Flores, J., **B:**210(63), **B:**214(63), **B:***253*
Floudas, C. A., **A:**198(138), **A:***216*
Flynn, C. P., **A:**173(9), **A:***213*, **B:**228(133), **B:***255*
Fontana, W., **B:**553(24), **B:***598*
Fontich, E., **B:**427(16), **B:***436*
Ford, J., **B:**376(2), **B:**393(2), **B:***418*
Forest, E., **A:**277(18), **A:***302*
Forst, W., **A:**176(30), **A:***213*
Founargiotakis, M, **A:**198(99,103), **A:***215*
Francisco, J. E.: **B:**27-28(7), **B:**71-72(7), **B:**75(7), **B:**79-80(7), **B:***84*; **B:**90(29), **B:***127*; **B:**180(1), **B:***201*
Franks, F., **B:**405(7), **B:***418*
Frantz, D. D., **B:**130(22), **B:**139(22), **B:***153*
Fraser, A. M., **B:**292-293(83), **B:***312*
Frauenfelder, H., **B:**228(114-115), **B:***254*
Fredj, E., **B:**186(28), **B:***202*
Freed, K. F., **B:**210(69), **B:***253*
Freeman, D. L., **B:**130(21-22), **B:**139(21-22), **B:***153*
Freidlin, M., **B:**530-531(35), **B:***542*
French, J. B., **B:**210(63), **B:**214(63), **B:***253*
Fried, L. E., **A:**146(48), **A:***169*
Friedman, R. S., **A:**174(23), **A:**178(23), **A:***213*
Frisch, U., **B:**523(18), **B:***541*
Froeschlé, C.: **B:**427(12,14), **B:***436*; **B:**438(9), **B:**442(21), **B:***463*
Frost, W., **A:**5(5), **A:***140*
Froyland, G., **B:**290-291(82), **B:**300(82), **B:***312*
Fuchigami, S., **B:**200(40), **B:***203*
Fuchikami, N., **B:**396(64), **B:***420*
Fujimoto, H., **B:**74(46), **B:***85*
Fujimura, Y., **A:**198(136-137), **A:***216*
Fujisaki, H., **A:**436(7), **A:**443(25), **A:**456(31-32), **A:***457–458*
Fukui, K.: **B:**74(46), **B:***85*; **B:**130(30), **B:***153*
Fukuzawa, K., **B:**201(47), **B:***203*
Fulton, N. G., **A:**220(19), **A:***263*
Funatsu, T., **B:**265(55), **B:**299(55), **B:***311*
Furusawa, C., **B:**551(16), **B:**553(16), **B:**556(16,26), **B:**557(26), **B:**573(16), **B:**593(26,41), **B:**594(41), **B:**595(26,41), **B:**597(16), **B:***598*

Gadre, S. R., **A:**198(121), **A:***216*
Galbraith, H. W., **B:**89(17), **B:**106(17), **B:***127*
Galgani, L.: **B:**31(22), **B:**46(22), **B:***84*; **B:**378(12-13), **B:**396(66), **B:**397(70,72), **B:**398(12-13), **B:**399(13), **B:**401(12-13), **B:**402(72), **B:***418–420*; **B:**499(45), **B:***500*; **B:**502(19), **B:**506(19), **B:***518*
Gallavotti, G.: **B:**354(2), **B:***370*; **B:**396(66), **B:**397(70), **B:***420*; **B:**429(25), **B:***436*
Gandhi, S. R., **A:**436(6), **A:***457*
Garbary, D. J., **B:**332(15), **B:***351*
García, A. E.: **B:**228(116), **B:***254*; **B:**264(40), **B:**267-268(42), **B:**300(40), **B:***311*
Garrett, B. C.: **A:**144(10,14), **A:**163(10), **A:***168–169*; **A:**174(23), **A:**178(23), **A:***213*; **A:**218(2), **A:***263*; **A:**402(6), **A:***433*; **B:**258(6), **B:**300(6), **B:***310*

Gaspard, P.: **A:**22(35), **A:**27(35), **A:***141*; **A:**218(3), **A:**228(3), **A:**232(45-46), **A:**237(55), **A:**244(55), **A:***263–265*; **A:**307(11), **A:**330(11), **A:***334*; **A:**436-437(18), **A:***457*; **B:**83(51), **B:***85*; **B:**386-387(40), **B:***419*
Gatti, F., **A:**198(133-134), **A:***216*
Gawedzki, K., **B:**520(3), **B:**523(3), **B:***541*
Gazdy, B.: **A:**198(113-114,116,118), **A:***216*; **A:**280(29), **A:***303*
Geisel, T.: **A:**128(92), **A:***142*, **B:**383-384(37), **B:***419*; **B:**479(21,28), **B:***500*
Geist, K., **B:**502-503(17), **B:***518*
Gelbart, W. M., **B:**210(69), **B:***253*
George, T. G., **A:**406(28), **A:**410(28), **A:***434*
Georges, A.: **B:**228(120), **B:***254*; **B:**520-521(2), **B:**526(28), **B:***541–542*
Gerber, R. B.: **B:**186(28), **B:***202*; **B:**228(117), **B:**238(144), **B:***254–255*
Geva, E., **B:**186(26), **B:***202*
Gibson, J., **B:**286(79), **B:***312*
Gillilan, R. E., **A:***264*; **A:**6(18), **A:**48(18), **A:***140*; **A:**145(20), **A:**166(20), **A:***169*; **A:**178(55), **A:***214*; **A:**339(11), **A:**358(11), **A:***398*; **B:**205(10), **B:**209(10), **B:***251*; **B:**438(1), **B:***462*
Giona, M., **B:**502(16), **B:***518*
Giorgilli, A.: **B:**378(12-13), **B:**396(66), **B:**397(70-72), **B:**398(12-13), **B:**399(13), **B:**401(12-13,71), **B:**402(72), **B:***418–420*; **B:**499(45), **B:***500*
Girifalco, L. A., **B:**159(12), **B:**160(13), **B:**167(13), **B:***176–177*
Giugliarelli, G., **B:**228(134), **B:***255*
Glansdorff, P., **B:**354(9), **B:***370*
Glotzer, S. C., **B:**392(56), **B:***420*
Go, J., **B:**210(77), **B:***253*
Go, N.: **B:**223-224(112), **B:**228-229(112), **B:***254*; **B:**261(24-25), **B:**264(37), **B:**301(24-25), **B:***311*
Goda, N., **A:**340(21), **A:**388(21), **A:***398*
Gogonea, V., **B:**201(46), **B:***203*
Gojobori, T., **B:**328(11), **B:***351*
Goldhirsch, I., **B:**502-503(9), **B:***518*
Goldstein, H., **A:**219(16), **A:***263*, **B:**115(36), **B:***128*
Gollub, J. P., **B:**527(31), **B:***542*
Golub, G. H., **B:**502-504(18), **B:**506(18), **B:**510(18), **B:**517(18), **B:***518*
Gomez Llorente, J. M.: **A:**198(100-102,104), **A:***215*; **A:**278(25), **A:***302*
Gong, J. B.: **A:**128(97), **A:**134(97), **A:**140(103), **A:***142*; **A:**147(55), **A:**153(55), **A:***170*; **A:**218(1), **A:**228(1), **A:***263*; **A:**456(27), **A:***457*
Gonzalez, L., **A:**198(137), **A:***216*
Goriely, A., **A:**403(20), **A:***434*
Goswami, D., **A:**436(6), **A:***457*
Goto, S., **B:**427(23), **B:***436*
Gotze, W., **B:**391(51), **B:***420*
Gouda, N., **B:**479(17), **B:***500*
Gower, J. C., **B:**262(26-27), **B:***311*
Graff, S. M., **A:**357(31), **A:**362(31), **A:***399*
Grammaticos, B., **A:**403(19), **A:**410(19), **A:***434*
Grandy, W. T., **B:**38(14), **B:**72(14), **B:***84*
Grassberger, P., **B:**7(6-7), **B:***23*
Gray, H. B., **B:**201(45), **B:***203*
Gray, S. K.: **A:**5(11), **A:**6(12), **A:**35(11), **A:**39(12), **A:**59-60(11-12), **A:**65(11,47,49,51,55), **A:**66(49), **A:**124(90), **A:***140–142*; **A:**145(17-18), **A:**166(17), **A:***169*; **A:**177(43), **A:**178(52), **A:**198(90-93,95), **A:***214–215*; **A:**228(29), **A:***264*; **A:**339(9), **A:***398*; **A:**428(37), **A:***434*; **B:**205(9), **B:**209(9), **B:***251*; **B:**260(10-11), **B:***310*
Grebenshchikov, S. Yu., **A:**287(38), **A:**293(52), **A:**298-299(38), **A:**301(38), **A:***303*
Grebogi, C.: **A:**339(13), **A:**358(13), **A:***398*; **A:**456(28), **A:***457*; **B:**364(16), **B:***371*; **B:**502(14), **B:***518*
Green, D. R., **B:**180(13), **B:***201*
Gregurick, S. K., **B:**186(28), **B:***202*
Grice, M. E., **A:**249(73), **A:***265*
Groenen, P., **B:**318-319(5), **B:***351*
Gruebele, M., **A:**137(99-100), **A:***142*, **B:**206(20), **B:**207(20,22), **B:**209(20,22,50-51), **B:**210(22), **B:**212(20), **B:**214(20), **B:**216(22), **B:**217(20,89-90), **B:***252,* **B:***254*
Guckenheimer, I., **A:**293(51), **A:***303*
Guhr, T., **B:**210(73-74), **B:***253*
Guichardet, A., **B:**88(4), **B:***127*
Guijarro, J. I., **B:**264(46), **B:***311*
Guilini, D., **A:**140(101), **A:***142*
Guiraldenq, P., **B:**160(13), **B:**167(13), **B:***177*
Guo, Z., **B:**266-257(59), **B:***311*
Gustavson, F. G., **A:**278(20), **A:***302*
Gutmann, M., **A:**61(41-42), **A:***141*

Gutzwiller, M. C.: **A:**7(27), **A:***141*; **A:**176(34), **A:***213*; **A:**293(50), **A:***303*; **A:**306(1,9-10), **A:**320(9), **A:***334*; **A:**402(9-10), **A:***433*; **A:**436(16), **A:**442(16), **A:***457*; **B:**83(52), **B:***85*
Guzzo, M.: **B:**381(24), **B:***419*; **B:**427(14), **B:***436*

Haak, J. R., **B:**267(60), **B:**309(60), **B:***312*
Haake, F.: **A:**7(29), **A:***141*; **A:**436(17), **A:**438-439(17), **A:***457*
Habib, S., **A:**140(102), **A:***142*, **B:**502(21), **B:**517(21), **B:***518*
Haffer, H., **A:**403(13), **A:***433*
Hahn, O.: **A:**198(100-102, **A:**104), **A:***215*; **A:**278(25), **A:***302*
Haible, B., **B:**431(29), **B:***436*
Halberstadt, N., **A:**65(48), **A:***141*
Halicioglu, T., **B:**55(35), **B:***84*
Hall, T., **B:**380(20), **B:***419*
Haller, G., **A:**347(28), **A:**351(28), **A:**372(28), **A:***399*, **B:**427(21-22), **B:***436*
Halonen, L. O.: **A:**96(65), **A:***142*; **A:**199-200(142), **A:**202(142), **A:***216*
Hamada, D., **B:**264(46), **B:***311*
Hamm, P.: **B:**200(44), **B:***203*; **B:**207(24), **B:**209(24), **B:***252*
Han, S., **B:**180(14), **B:***201*
Handy, N. C.: **A:**198(110), **A:***215*, **B:**74-75(47), **B:***85*; **B:**89(10), **B:**108(20), **B:***127*
Hänggi, P., **A:**228(37), **A:***264*, **B:**221(106), **B:***254*
Harayama, T.: **B:**273(67), **B:***312*; **B:**465(1), **B:***475*; **B:**502(10), **B:***518*
Harding, L., **A:**198(135), **A:***216*
Hariharan, A., **A:**436(6), **A:***457*
Harris, G. J., **A:**269(7-8), **A:**274(7-8), **A:**275(7), **A:**277(7-8), **A:***302*
Harthcock, M. A., **A:**91(61-62), **A:***141*
Haruyama, T., **B:**477(7), **B:***499*
Harvey, S. C., **B:**228(129), **B:***255*
Hase, W. L.: **A:**5(6), **A:***140*; **A:**168(78), **A:***170*; **A:**198(82), **A:***215*; **A:**293(52), **A:***303*; **B:**27-28(7), **B:**71-72(7), **B:**75(7), **B:**79-80(7), **B:***84*; **B:**90(29), **B:***127*; **B:**180(1), **B:***201*; **B:**215(85), **B:***253*; **B:**259(7), **B:***310*
Hasegawa, H.: **B:**200(40), **B:***203*; **B:**326-327(10), **B:***351*; **B:**354(10-11), **B:**356(10), **B:**358(11), **B:**359(10,19), **B:**368(21), **B:***370–371*
Hasha, D. L., **B:**207(30), **B:**219(30), **B:**249(30), **B:***252*
Hashimoto, N., **B:**34(25), **B:**46(32), **B:**56(32), **B:**58(32), **B:***84*
Hashimoto, T., **B:**582(37), **B:***598*
Hasselblatt, B., **B:**378(15), **B:***418*
Hata, H., **B:**502(13), **B:***518*
Hatano, T., **B:**354(8), **B:***370*
Hatori, T., **B:**530(33), **B:***542*
Hauschildt, J., **A:**287(38), **A:**298-299(38), **A:**301(38), **A:***303*
Havlin, S., **B:**208(33), **B:**230(33), **B:***252*
Hayasaka, K., **B:**328(11), **B:***351*
Hayes, W. B., **B:**502(15), **B:***518*
Head-Gordon, T., **B:**411(82), **B:***421*
Heckenberg, N. R., **A:**403(13), **A:***433*
Heidrich, D., **A:**198(109), **A:***215*
Helgaker, T., **B:**131-132(33), **B:***153*
Heller, E. J.: **A:**107(72), **A:**129(93), **A:***142*; **A:**403(11), **A:**404(21), **A:***433–434*; **B:**209(62), **B:**210(68), **B:***253*
Helmerson, K., **A:**403(13), **A:***433*
Henderson, J. R., **A:**220(19), **A:***263*
Henrard, J., **A:**248(67), **A:***265*
Henrichsen, H., **B:**481(35), **B:***500*
Henriksen, E. A., **B:**221(101), **B:***254*
Hensinger, W. K., **A:**403(13), **A:***433*
Herbst, E., **A:**256(82-83), **A:***265*
Hernandez, R.: **A:**146(51-52), **A:**148(60), **A:***169–170*; **A:**178(49,51), **A:***214*; **B:**21(19), **B:***23*; **B:**210(67), **B:***253*
Hershkovitz, E., **A:**228(38), **A:***264*
Hess, B., **B:**561(28), **B:***598*
Hetzenauer, H., **B:**406(79), **B:***421*
Higo, J., **A:**165(66-67), **A:***170*, **B:**302(96), **B:***313*
Hilger, Adam, **B:**376(3), **B:**382-383(3), **B:***418*
Hill, J. R.: **B:**200(37), **B:***203*; **B:**207(28), **B:**209(28), **B:**239(28), **B:***252*
Hinde, R. J.: **A:**146(28), **A:***169*; **A:**178(57,63), **A:**186(63), **A:***214*; **A:**234(50), **A:**245(50), **A:***264*; **B:**10(8-9), **B:**13(9), **B:**16(9), **B:***23*; **B:**66(39-40), **B:***84*; **B:**89(21), **B:**90(25), **B:**106(25), **B:**108(21), **B:***127*; **B:**130(14-15), **B:**139(14-15), **B:***153*; **B:**209(57), **B:***253*

Hirano, T., **A:**198(140), **A:***216*
Hirata, F., **B:**261(24-25), **B:**301(24-25), **B:***311*
Hirata, Y., **B:**477(1), **B:***499*
Hirooka, H., **B:**381(25), **B:***419*
Hirsch, M., **A:**198(109), **A:***215*
Hirsch, M. W., **A:**338(8), **A:**347(8), **A:***398*, **A:**338(39), **A:***399*
Hirschfelder, J. O., **A:**176(29), **A:***213*
Hoare, M. R.: **B:**29(16), **B:**31(16), **B:***84*; **B:**136(39), **B:***153*
Hochstrasser, R. M., **B:**207(24), **B:**209(24), **B:**220(94), **B:**248(152), **B:***252,* **B:***254–255*
Hofbauer, J., **B:**582(35), **B:***598*
Hoff, W., **B:**207(26), **B:**209(26), **B:***252*
Hoffman, D. K., **B:**131(32), **B:**132(32), **B:***153*
Hogeweg, P., **B:**549(8), **B:**573(8), **B:***597*
Hoki, K., **A:**198(137), **A:***216*
Holbrook, K. A., **A:**176(31), **A:***213*
Holme, P., **B:**479(14), **B:***500*
Holme, T. A., **A:**198(96), **A:***215*
Holmes, P.: **A:**293(50-51), **A:***303*; **A:**309(25), **A:**330(25), **A:***335*
Holmes, P. J., **B:**427(8), **B:***436*
Honeycutt, J. D., **B:**266-267(58), **B:***311*
Hong, H., **B:**479(14), **B:***500*
Hong, M. K., **B:**228(115), **B:***254*
Honjo, S., **A:**372(33), **A:**378(33), **A:***399*, **B:**427(19), **B:***436*
Hoover, W. G., **B:**130(28), **B:**139(28), **B:***153*
Horai, S., **B:**328(11), **B:***351*
Horiguchi, H., **B:**72-73(42), **B:***84*
Horita, T., **B:**502(13), **B:***518*
Horiuti, J., **A:**176(38), **A:***213*
Hoshino, K.: **A:**147(59), **A:***170*; **A:**340(23), **A:***399*; **B:**285(74), **B:**301(95), **B:***312–313*
Hotta, K., **B:**83(56), **B:***85*
Huang, C. M., **A:**198(120), **A:***216*
Huang, G. M., **A:**436(11), **A:***457*
Hudson, J. S. Jr., **B:**348(21), **B:***351*
Hudspeth, E., **B:**220(92), **B:***254*
Hufnagel, L., **A:**136(98), **A:***142*
Hummer, G.: **B:**180(15), **B:***202*; **B:**228(116), **B:***254*; **B:**264(40), **B:**300(40), **B:***311*
Hutchinson, J. S., **A:**178(64), **A:**198(96,105), **A:***214–215*, **B:**48(33), **B:**82(33), **B:***84*
Hynes, J. T.: **A:**144(11), **A:**163(11), **A:**164(63), **A:***168,* **A:***170*, **B:**180(7), **B:**187(29), **B:**200(29), **B:***201–202*; **B:**216(86), **B:***254*

Iben, I. E. T., **B:**228(115), **B:***254*
Ibrado, A. M., **B:**180(13), **B:***201*
Ichihashi, T., **B:**156(2), **B:***176*
Ichikawa, Y. H., **B:**530(33), **B:***542*
Ichiki, K., **B:**378(14), **B:**409(14), **B:**411-412(14), **B:***418*
Iijima, S., **B:**156(2), **B:***176*
Ikeda, K. S.: **A:**340(18), **A:**388(18), **A:***398*; **A:**403(15-18), **A:**404(22-25), **A:**405(23-25,27), **A:**406(17,25), **A:**407(22,24,27), **A:**408(22), **A:**409(15,22), **A:**410(22,25,35), **A:**412(22), **A:**413(24-25), **A:**417-418(25), **A:**423(25), **A:**425(22-23), **A:**428(16-18, **A:**24), **A:**429(24), **A:**431(25), **A:***433–434*; **B:**156(8-9), **B:**159-160(11), **B:**167(8,11), **B:**168(11), **B:***176*
Ikegami, T., **B:**582(36-37), **B:***598*
Imaizumi, R., **B:**474(15), **B:***475*
Imig, O., **A:**198(109), **A:***215*
Inadomi, Y., **B:**201(47), **B:***203*
Inoue, A., **B:**83(53-54), **B:***85*
Ionascu, D., **B:**200(35), **B:***202*
Ionov, S., **B:**180(1), **B:***201*
Isaacson, A. D., **A:**402(6), **A:***433*
Ishii, K., **B:**229(138), **B:**242(138), **B:***255*
Ishii, Y.: **A:**403(18), **A:**428(18), **A:***434*, **B:**265(55), **B:**299(55), **B:***311*; **B:**380(19), **B:***419*
Ishikawa, H., **A:**287(34-35), **A:**288(34), **A:**293(34-35), **A:**298-299(35), **A:**301(35), **A:***303*
Ishioka, S., **B:**396(64), **B:***420*
Ito, K., **B:**466(10), **B:**471-472(10), **B:***475*
Ito, Y., **B:**594(43), **B:***598*
Iung, C., **B:**210(79), **B:***253*
Iwai, T., **B:**88(5-6), **B:***127*
Iwane, A. H., **B:**265(53), **B:**299(53), **B:***311*
Iyer, V. R., **B:**348(21), **B:***351*
Izrailev, F. M.: **A:**131(95-96), **A:***142*; **A:**442(22), **A:***457*; **B:**209(59), **B:***253*; **B:**397(69), **B:***420*

Jackson, T. A., **B:**200(36), **B:***202*
Jacucci, G., **A:**173(9), **A:***213*

Jaffé, C.: **A:**7(22), **A:**21(22), **A:***140*; **A:**144(15), **A:**147(15,54,58), **A:**148(15,54), **A:**163(15), **A:***169–170*; **A:**173(6-7,10,18-19,21), **A:**177(6,18-19,45-47), **A:**180-181(6,18), **A:**182(78), **A:**212(19,21), **A:***213–215*; **A:**219(8-9,13), **A:**221(8), **A:**233(9), **A:**234(8,13,51), **A:**235(9), **A:**237(9), **A:**250(8), **A:***263–264*; **A:**338-339(3), **A:**341(3), **A:**352(3), **A:***398*; **A:**428(38), **A:***434*
Jaffe, R. J., **B:**72-73(43), **B:***85*
Jagannathan, A., **B:**208(37), **B:**241(37), **B:**246(37), **B:**250(37), **B:***252*
Jalnapurkar, S. M., **A:**248(72), **A:***265*
Janda, K. C., **A:**63(44-46), **A:**65(48), **A:***141*
Jang, S.: **A:**6(19), **A:**87(58), **A:**88(60), **A:**97-98(19), **A:**104(67), **A:**108(75), **A:**124(88), **A:***140–142*; **A:**168(76), **A:***170*; **A:**198(122), **A:***216*
Jansen, T. I. C., **B:**200(42), **B:***203*
Jarzynski, C., **B:**354(3), **B:**355(17), **B:**356(3), **B:***370–371*
Jaynes, E. T., **B:**28(12), **B:**72(12), **B:***84*
Jean, J. M., **B:**209(44), **B:***252*
Jeans, J. H.: **B:**378(11), **B:**401(11), **B:***418*; **B:**499(43), **B:***500*
Jellinek, J.: **B:**45(31), **B:**53(31,34), **B:**54(34), **B:**56(31), **B:***84*; **B:**90(22), **B:***127*; **B:**130(5,7-8), **B:**135(5), **B:**139(5,7-8), **B:***152*; **B:**156(5), **B:***176*
Jena, P., **A:**178(66), **A:***214*
Jensen, H. J. A., **B:**131-132(33), **B:***153*
Jeon, G. S., **B:**479(14), **B:***500*
Jeong, H.: **B:**453(23), **B:***463*; **B:**546-547(5), **B:***597*
Jiang, M., **B:**348(20), **B:***351*
Jimenez, R., **B:**180(10), **B:**199(10), **B:***201*
Johan, T., **A:**245(59), **A:**257-258(59), **A:***265*
Johnson, B. R., **A:**245(61), **A:***265*
Johnson, J. B., **B:**228(115), **B:***254*
Johnson, K. E., **A:**61-62(39-40), **A:***141*
Johnson, R. W., **B:**73(44), **B:***85*
Jonas, D. M., **A:**278(24), **A:***302*
Jonas, J., **B:**207(30), **B:**219(30), **B:**249(30), **B:***252*
Jones, C. K. R. T., **A:**347(26), **A:**349(26), **A:***399*
Jones, D. P., **B:**180(13), **B:***201*
Joos, E., **A:**140(101), **A:***142*
Jordahl, O. M., **A:**272(11), **A:**277(11), **A:***302*
Jordan, K. D., **B:**171(14), **B:***177*
Jørgensen, P., **B:**131-132(33), **B:***153*
Jortner, J., **A:**63(43), **A:***141*
Jost, R., **A:**287-288(39), **A:**293(39), **A:***303*
Joyeux, M.: **A:**198(141), **A:***216*; **A:**219(10), **A:**223(34), **A:***263–264*; **A:**269(1-6), **A:**274(1), **A:**278(3), **A:**287(34-36,39), **A:**288(34,39), **A:**293(34-36,39), **A:**298(35-36), **A:**299(35), **A:**301(35), **A:***302–303*
Judd, K., **B:**290-291(82), **B:**300(82), **B:***312*
Judson, R. S., **A:**436(14), **A:***457*
Jun, B., **B:**264(45), **B:***311*
Jung, C., **A:**249(76,78), **A:***265*
Jungwirth, P., **B:**186(28), **B:***202*
Justum, Y., **A:**198(133-134), **A:***216*

Kadanoff, L. P.: **A:**5(10), **A:**18(10), **A:**30(10), **A:***140*; **A:**177(41), **A:***214*
Kaelberer, J., **B:**130(2-4), **B:**139(2-4), **B:***152*
Kamimura, T., **B:**530(33), **B:***542*
Kamino, T., **B:**156-157(7), **B:***176*
Kan, I., **A:**339(13), **A:**358(13), **A:***398*
Kaneko, K.: **A:**308(21), **A:***334*; **A:**340(19), **A:**372(33), **A:**388(19), **A:**378(33), **A:***398–399*; **B:**301(89-90), **B:***312–313*; **B:**427(10), **B:***436*; **B:**438(10), **B:**441(14), **B:***463*; **B:**479(24), **B:***500*; **B:**502(12), **B:**513-514(12), **B:***518*; **B:**544(1-2), **B:**551(1-2,13-17,21), **B:**553(15-17), **B:**556(15-16,25-26), **B:**557(15,26), **B:**558(2), **B:**561(29), **B:**562-563(2), **B:**573(16-17,32-33), **B:**575(2,32), **B:**582(36), **B:**583(38), **B:**592(33), **B:**593(26,41), **B:**594(41,43), **B:**595(26,41), **B:**596(44,46), **B:**597(15-16), **B:***597–598*
Kantz, H.: **B:**285(78), **B:**294(78), **B:***312*; **B:**395(63), **B:***420*
Kantz, T. S., **B:**332(15), **B:***351*
Kaper, T. J., **A:**347(27), **A:**349(27), **A:***399*
Kaplan, I., **A:**403(11), **A:***433*
Karney, C. F. F.: **B:**383(29), **B:***419*; **B:**477(4), **B:***499*
Karp, G., **B:**180(12), **B:***201*
Karplus, M.: **B:**180(15), **B:**190(33), **B:***202*; **B:**228(126,128,132), **B:**229(126), **B:**235(132), **B:***255*; **B:**262(28), **B:**263-264(36), **B:**267(28), **B:***311*
Kashiwagi, A., **B:**551(21), **B:**593-595(41), **B:***598*

Kashiwagi, H., **B:**180(19), **B:***202*
Kassel, L. S.: **A:**5(2), **A:***140*; **A:**144(2), **A:***168*
Kataoka, M., **B:**264(46), **B:***311*
Kato, H., **B:**74(46), **B:***85*
Kato, S., **B:**72-73(43), **B:**74(46), **B:***85*
Katok, A., **B:**378(15), **B:**379(34), **B:**383(34), **B:***418–419*
Kauffman, S. A., **B:**550(10), **B:***597*
Kauffmans, S., **B:**550(11), **B:***597*
Kawai, S.: **A:**147(58), **A:***170*; **A:**338-339(3), **A:**341(3), **A:**352(3), **A:***398*
Kawamura, H., **B:**396(64), **B:***420*
Kay, K. G.: **A:**111(77), **A:**114(82), **A:***142*; **A:**262(86), **A:***265*; **B:**209(47), **B:***252*
Keck, J. C.: **A:**144(8), **A:**163(8), **A:***168*; **A:**173(15), **A:**176(15), **A:***213*; **B:**258(5), **B:**300(5), **B:***310*
Keilin, D., **B:**180(11), **B:***201*
Keller, H. M., **A:**280(31), **A:***303*
Keller, J., **A:**288(44), **A:***303*
Keller, J. B., **A:**402(4), **A:***433*
Kellman, M. E., **A:**287-288(34), **A:**293(34), **A:***303*
Kelner, J., **B:**223(109), **B:***254*
Kemble, E. C., **A:**272(12), **A:**277(12), **A:***302*
Kendrick, B. K., **A:**257(85), **A:***265*
Kenkre, V. M., **B:**180(5), **B:**183-184(5), **B:**189-190(5), **B:***201*
Kennel, M. B., **B:**289(80), **B:***312*
Kenny, J. E., **A:**61-62(40), **A:***141*
Keplinski, P., **B:**221(108), **B:***254*
Kerstein, A. R., **B:**522(17), **B:**531(17), **B:**534(17), **B:***541*
Keshavamurthy, S., **A:**178(50), **A:***214*
Keske, J. C., **B:**205(8), **B:**209(8), **B:***251*
Ketzmerick, R., **A:**136(98), **A:***142*
Khalatnikov, I. M., **A:**402(4), **A:***433*
Kholodenko, Y., **B:**248(152), **B:***255*
Khouider, B., **B:**535(40), **B:***542*
Kidera, A.: **B:**181(21), **B:**195(21), **B:***202*; **B:**238(150-151), **B:***255*
Kiefer, C., **A:**140(101), **A:***142*
Kiefer, J. H., **A:**198(135), **A:***216*
Kiefhaber, T., **B:**254(43), **B:***311*
Kifer, Y., **B:**475(16), **B:***475*
Kikuchi, Y.: **B:**273(67), **B:***312*; **B:**477(7), **B:***499*; **B:**502(10), **B:***518*
Kim, B. J., **B:**479(14), **B:***500*
Kim, C. N., **B:**180(13), **B:***201*
Kim, H., **B:**186(27), **B:***202*
Kim, S. B.: **A:**146(32), **A:***169*; **A:**174(24), **A:**178(24), **A:***213*
Kim, S. K., **B:**348(20), **B:***351*
Kimball, G. E., **A:**172(3), **A:**176(3), **A:***213*
Kindt, J. T., **B:**406(80), **B:***421*
Kinsey, J. L., **B:**27-28(4), **B:**71-73(4), **B:**75(4), **B:**79-80(4), **B:***83*
Kiraly, M., **B:**348(20), **B:***351*
Kirczenow, G., **B:**221(104), **B:***254*
Kiselev, A., **B:**522(14,16), **B:**531-533(14), **B:***541*
Kishino, H., **B:**326-327(10), **B:***351*
Kitagawa, T., **B:**200(35), **B:***202*
Kitamura, K., **B:**265(53), **B:**299(53), **B:***311*
Kitao, A., **B:**261(24-25), **B:**301(24-25), **B:***311*
Kitao, O., **B:**390(48), **B:***420*
Kitaura, K., **B:**201(47), **B:***203*
Klafter, J.: **B:**228(122-123), **B:***254*; **B:**264(48,50-51), **B:***311*; **B:**479(22), **B:***500*; **B:**524(21), **B:***541*
Klee, S., **A:**278(27), **A:***302*
Klemperer, W.: **A:**198(87-90), **A:***215*; **A:**278(22), **A:***302*
Klippenstein, S. J.: **A:**144(14), **A:***169*; **A:**218(2), **A:***263*
Kluck, R. M., **B:**180(13), **B:***201*
Knoll, J., **A:**402(7), **A:***433*
Knowles, P. J., **A:**269(7), **A:**274-275(7), **A:**277(7), **A:***302*
Ko, E., **B:**551(19), **B:***598*
Kobayashi, T., **B:**156(9), **B:**159-160(11), **B:**167-168(11), **B:***176*
Kocher, T. D., **B:**324(9), **B:***351*
Koeppl, G. W., **A:**176(39), **A:***214*
Koga, N., **B:**285(74), **B:***312*
Kogumo, N., **B:**475(19), **B:***475*
Koizumi, H., **B:**156(1), **B:***176*
Kolmogorov, A. N.: **B:**425(5), **B:***436*; **B:**521-522(9), **B:***541*
Komatsu, M., **B:**156-157(7), **B:***176*
Komatsuzaki, T.: **A:**7(26), **A:**137(26), **A:***140*; **A:**146(38-45,49-50), **A:**147(41,45,59), **A:**148(38-39,41-45), **A:**151(44-45), **A:**152-153(45), **A:**161(44), **A:**162(38-45,49), **A:**166(42-43), **A:**167(42-44), **A:***169–170*; **A:**173(5), **A:**178(5,67-74), **A:**179(69-73), **A:**186(69), **A:***213–215*; **A:**218-219(4), **A:**229(4), **A:**234(4,50), **A:**235(52), **A:**245(50,62), **A:**247(62), **A:***263–265*; **A:**338-339(2),

A:340(23), **A:**341(2), **A:**352(2), **A:***398–399*; **B:**21(14-18), **B:**22(20-21), **B:***23–24*; **B:**90(26), **B:***127*; **B:**209(53), **B:***253*; **B:**260(13-20), **B:**261(21), **B:**263(13-20), **B:**264(41), **B:**265(13-20), **B:**266-267(41), **B:**274(73), **B:**285(74), **B:**294(41), **B:**300(13-20), **B:**301(73,95), **B:***310–313*; **B:**438(2), **B:***462*
Komeji, Y., **B:**201(47), **B:***203*
Ko-Mitamura, E. P., **B:**551(18), **B:**567(18), **B:**570(18), **B:***598*
Komornicki, A., **B:**72-73(43), **B:***85*
Komuro, M., **A:**340(20), **A:**388(20), **A:***398*
Kondepudi, D., **B:**354(9), **B:***370*
Kondorskiy, A., **A:**456(31), **A:***459*
Konishi, T.: **A:**340(21), **A:**342(25), **A:**377(25), **A:**388(21), **A:***398–399*, **B:**385(39), **B:***419*; **B:**441(14), **B:***463*; **B:**479(17,24,29), **B:***500*; **B:**502(12), **B:**513-514(12), **B:***518*
Kook, H. T., **B:**438(11), **B:**441(11), **B:***463*
Koon, W. S.: **A:**168(77), **A:***170*; **A:**248(68), **A:***265*; **A:**340(22), **A:***399*
Koplik, J., **B:**526(28), **B:***542*
Köppel, H., **B:**210(64-65,71), **B:***253*
Koput, J., **A:**287(33,35,38), **A:**293(35,38), **A:**298-299(35,38), **A:**301(35,38), **A:***303*
Kosloff, R., **A:**436(3), **A:***457*
Kostov, K. S., **B:**264(41), **B:**266-267(41), **B:**294(41), **B:***311*
Kovács, Z., **A:**224(26), **A:**228(41), **A:**249(41), **A:**250(26), **A:***264*
Koyama, H., **B:**479(29), **B:***500*
Kozin, I. N., **A:**248(64,69-70), **A:***265*
Kozlov, V. V., **A:**173-174(13), **A:**184-186(13), **A:***213*
Kramer, F. R., **B:**547(6), **B:***597*
Kramer, P. R., **B:**521(6), **B:***541*
Kramers, H. A., **A:**144(6), **A:**163(6), **A:***168*
Krumhansl, J. A., **B:**228(116), **B:***254*
Kruskal, J. B., **B:**317(3), **B:**319(3), **B:***351*
Kubachewski, O., **B:**157(10), **B:***176*
Kubo, R., **B:**46(32), **B:**56(32), **B:**58(32), **B:***84*
Kugimiya, T., **A:**165(66), **A:***170*
Kuharski, R. A., **B:**205(7), **B:**207(7), **B:**209(7), **B:**217(7,17), **B:**218(7), **B:***251,* **B:***254*
Kulkami, S. A., **A:**198(121), **A:***216*
Kumar, A. T. N., **B:**200(35), **B:***202*
Kumeda, Y., **A:**198(140), **A:***216*
Kundkar, L. R., **B:**220(96), **B:***254*
Kunz, R. E., **B:**26(1), **B:***83*
Kupperman, A., **A:**245(60), **A:***265*, **B:**89(11), **B:**115(11), **B:***127*
Kupsch, J., **A:**140(101), **A:***142*
Kurkal, V., **A:**198(126), **A:***216*
Kurosaki, S., **B:**465(2), **B:***475*
Kurtz, S. R., **B:**228(133), **B:***255*
Kuzmin, M., **B:**209(48), **B:***252*
Kwok, A., **B:**207(28), **B:**209(28), **B:**239(28), **B:***252*

Labastie, P., **B:**90(23), **B:***127*
Lai, Y. C., **A:**339(13), **A:**358(13), **A:***398*
Laird, B. B., **B:**391(52), **B:***420*
Lambert, W. R., **B:**209(43), **B:**220(43,94), **B:***252,* **B:***254*
Lan, B. L., **A:**198(115,117), **A:***216*
La Nave, E., **B:**391(55), **B:***420*
Lancet, D., **B:**573(34), **B:**579(34), **B:***598*
Landau, L., **B:**499(44), **B:***500*
Landolfi, M., **B:**394(57), **B:***420*
Langmuir, I., **A:**306(6), **A:***334*
Langton, C., **B:**553(23), **B:***598*
Lanne, J., **A:**91(61-62), **A:**100(66), **A:***141–142*
Lara, M., **A:**238(57), **A:***265*
Larregaray, P., **A:**249(75), **A:***265*
Lashkari, D., **B:**348(21), **B:***351*
Laskar, J.: **B:**427(20), **B:***436*; **B:**438(13), **B:**442(13,20-21), **B:**453(13), **B:***463*
Lasker, L., **A:**372(34), **A:**378(34), **A:***399*
Latora, V., **B:**479(15,18,20,23), **B:**480(15,18), **B:**481(15,18,31), **B:**485(37), **B:**487(15), **B:***500*
Lauterborn, W., **B:**502-503(17), **B:***518*
Lauvergnat, D., **A:**198(134), **A:***216*
LaViolette, R. A., **B:**250(159), **B:**405(75), **B:***255*, **B:***420*
Leboeuf, P., **A:**219(12), **A:***263*, **B:**530(34), **B:***542*
Lebowitz, J. L., **B:**354(5), **B:***370*
Le Daeron, P. Y., **B:**383(32), **B:***419*
Lee, F., **A:**248(65), **A:***265*
Lee, H. W., **A:**105(68), **A:***142*
Lee, J. C. F., **B:**348(21), **B:***351*
Lee, M.-H., **A:**308(24), **A:***335*
Lee, S. Y., **A:**403(11), **A:***433*
Lee, T. J., **A:**198(114,116), **A:***216*
Lee, T. K., **A:**280(29), **A:***303*
Lega, E., **B:**427(12,14), **B:***436*
Lehman, E. L., **B:**322(8), **B:***351*

Lehmann, K. K.: **A:**198(87-90), **A:***215*; **A:**278(22,26), **A:***302*; **B:**209(45), **B:***252*
Leitner, D. M.: **A:**131(94), **A:***142*; **A:**178(53), **A:***214*; **B:**4(3), **B:**5(4), **B:***23*; **B:**130(10,22,26), **B:**139(10,22,26), **B:**143(10), **B:***152–153*; **B:**180(2,15), **B:**181(22), **B:**190(22), **B:**193(22), **B:**195(21-22), **B:**197(22), **B:***201–202*; **B:**205(3-4,6), **B:**206(4,16-19,21), **B:**207(3-4,6,19,21), **B:**209(16-21,54-57,60-61), **B:**210(16,21,65,70-71,76), **B:**212(20), **B:**213(16,18-19), **B:**214(16-17,20), **B:**217(20), **B:**220(3-4,6), **B:**221(105,107), **B:**223(111), **B:**229(111), **B:**233(141), **B:**238(147-149), **B:**240(111,147-149), **B:**241(111), **B:**242(147), **B:**243(111,147-149), **B:**246(147-148), **B:**247(111), **B:**248(156), **B:**249(3-4,6), **B:**250(111), **B:***251–255*; **B:**424(4), **B:**427(4), **B:***436*
Le Quéré, F., **A:**124(90), **A:***142*
Lessen, D., **A:**276(14), **A:**278(14), **A:***302*
Lester, M. I., **A:**66(52-54), **A:***141*
Letokhov, V., **B:**180(1), **B:***201*
Levin, S. A., **B:**538(47), **B:***542*
Levine, B., **B:**205(6), **B:**207(6), **B:**220(6), **B:**249(6), **B:***251*
Levine, D. J., **B:**214(82), **B:***253*
Levine, R. D.: **A:**116(87), **A:***142*, **B:**7(5), **B:***23*; **B:**27(2-5), **B:**28(2-5,13), **B:**29(2), **B:**71(2-5), **B:**72(2-5,13), **B:**73(2-5), **B:**75(2-5), **B:**79(2-5), **B:**80(2-4), **B:***83–84*
Levitt, M., **B:**228-229(127), **B:***255*
Levy, D. H., **A:**61-62(39-40), **A:***141*
Levy, R. M., **B:**261(23), **B:***311*
Lewis, J.: **B:**180(12), **B:***201*; **B:**558(27), **B:***598*
Lewis, L. A., **B:**332(15), **B:***351*
Leyvraz, F., **A:**403(11), **A:***433*
Li, C.-B., **B:**354(10), **B:**356(10), **B:**359(10), **B:***370*
Li, F.-Y., **B:**26(1), **B:***83*
Lian, T. Q., **B:**248(152), **B:***255*
Liao, Jie-Lou, **A:**218(5), **A:***263*
Lichtenberg, A. J.: **A:**5(7), **A:**8(7), **A:***140*; **A:**146(47), **A:***169*; **A:**176(33), **A:***213*; **A:**340(17), **A:**372(17), **A:***398*; **B:**31(21), **B:**45(21), **B:**68(21), **B:***84*; **B:**376(4), **B:**392(4), **B:**395(62), **B:***418,* **B:***420*; **B:**438(8,12), **B:**441(12), **B:**457(8), **B:**463(12), **B:***462–463*; **B:**478(10), **B:***499*; **B:**502(5), **B:***518*; **B:**529(32), **B:***542*
Lidar, D. A., **B:**228(117), **B:***254*
Lieberman, M. A.: **A:**5(7), **A:**8(7), **A:***140*; **A:**146(47), **A:***169*; **A:**176(33), **A:***213*; **A:**340(17), **A:**372(17), **A:***398*; **B:**31(21), **B:**45(21), **B:**68(21), **B:***84*; **B:**376(4), **B:**392(4), **B:***418*; **B:**438(12), **B:**441(12), **B:**463(12), **B:***463*; **B:**478(10), **B:***499*; **B:**502(5), **B:***518*; **B:**529(32), **B:***542*
Light, J. C.: **A:**124(89), **A:***142*; **A:**280(30), **A:***303*; **B:**4(2), **B:***23*
Lim, M.: **B:**200(36), **B:***202*; **B:**207(24), **B:**209(24), **B:***252*
Ling, S.: **A:**83-84(56), **A:***141*; **A:**146(37), **A:**153(37), **A:***169*; **A:**198(127-128), **A:***216*
Lipp, C., **A:**250(78), **A:***265*
Litke, A., **B:**338(19), **B:**341(19), **B:***351*
Littlejohn, R. G., **A:**220(17), **A:**248(17), **A:**250(17), **A:***263*, **B:**88(7), **B:**89(7,12-14), **B:**91(7), **B:**93-95(7), **B:**96(12-13), **B:**97(13), **B:**108(7), **B:**111(13), **B:***127*
Litvak-Hinenzon, A., **A:**180(77), **A:**182(77), **A:***215*
Liu, X., **B:**180(13), **B:***201*
Livi, R., **B:**395(58,63), **B:***420*
Lo, M. W.: **A:**168(77), **A:***170*; **A:**173(10), **A:***213*; **A:**219(13), **A:**234(13), **A:**248(68), **A:***263,* **A:***265*; **A:**340(22), **A:***399*
Lochak, P.: **B:**397(70), **B:***420*; **B:**429(26-28), **B:***436*
Locke, B., **B:**248(152), **B:***255*
Lockwood, S. F., **B:**324(9), **B:***351*
Logan, D. E.: **B:**180(2), **B:***201*; **B:**206(15), **B:**210(15), **B:**212-213(15), **B:***251*
Longarte, A., **B:**249(157), **B:***255*
López-Castillo, A., **A:**307(19), **A:***334*
Loring, R. F., **B:**200(43), **B:***203*
Losada, J. C., **A:**167(72), **A:***170*
Louck, J. D., **B:**89(17), **B:**106(17), **B:***127*
Loudon, R., **A:**429(39), **A:***434*
Louie, G. V., **B:**180(17), **B:***202*
Lovejoy, E. R.: **A:**146(32-33), **A:***169*; **A:**174(24-25), **A:**178(24-25), **A:***213*
Luck, S., **B:**228(115), **B:***254*
Lund, J., **B:**348(20), **B:***351*
Luthey-Schulten, Z. A., **B:**90(31), **B:***128*

Macdonald, R. G., **A:**278(28), **A:***302*
MacElroy, R. D.: **B:**250(159), **B:***255*; **B:**405(75), **B:***420*

MacKay, R. S.: **A:**5(8-9), **A:**30(8-9), **A:***140*; **A:**177(41), **A:**193(81), **A:***214–215*, **B:**376(3), **B:**382(3), **B:**383(3,35), **B:***418–419*
MacKerrel, A. D.: **B:**190(33), **B:***202*; **B:**261(22), **B:***311*
Madsen, D., **B:**217(89), **B:***254*
Maiti, B., **A:**228(42), **A:***264*
Maitra, N. T., **A:**129(93), **A:***142*
Majda, A. J., **B:**521(6), **B:**525(22), **B:**534(36), **B:**535(40), **B:***541–542*
Makarov, D. E., **A:**402(6), **A:***433*
Maki, A., **A:**278(27), **A:***302*
Malyshev, A. I., **A:**131(95-96), **A:***142*, **B:**209(59), **B:***253*
Mancinelli, R., **B:**527(29), **B:***542*
Manneville, P., **B:**359(18), **B:***371*
Manz, J., **A:**198(137), **A:***216*, **B:**106(35), **B:***128*
Maradudin, A. A.: **B:**190(31), **B:***202*; **B:**238(143), **B:***255*
Marcelin, A., **A:**176(26), **A:***213*
Marcus, R. A.: **A:**5(3-4), **A:***140*; **A:**144(7,16), **A:**146(16), **A:***168–169*; **A:**178(60), **A:***214*; **A:**402(6), **A:***433*; **B:**209(49), **B:**220(96), **B:***252,* **B:***254*
Marinari, E. G., **B:**273(69), **B:***312*
Marks, L. D., **B:**156(2-3), **B:***176*
Marsden, J. E.: **A:**168(77), **A:***170*; **A:**173(10), **A:***213*; **A:**219(13), **A:**221(22), **A:**234(13), **A:**248(22,68,72), **A:***263–265*; **A:**340(22), **A:***399*; **B:**427(8), **B:***436*
Marston, C. C., **A:***215*; **A:**7(23,25), **A:**75(23,25), **A:**87(23), **A:**94(23,63), **A:***140–141*; **A:**232(48), **A:**250(48), **A:***264*
Martens, C. C.: **A:**20(33), **A:***141*; **A:**167(71), **A:***170*; **B:**209(58), **B:***253*; **B:**442(19), **B:***463*
Martin, C. H., **B:**206(12), **B:***251*
Mart'in, P., **B:**427(16), **B:***436*
Martínez, T. J., **B:**205(6), **B:**207(6), **B:**220(6), **B:**249(6), **B:***251*
Martinoli, A., **B:**397(72), **B:**402(97), **B:***420*
Marvulle, V., **A:**403(11), **A:***433*
Maslov, V. P., **A:**402(4), **A:***433*
Mather, J. N., **B:**383(33), **B:***419*
Matheron, G., **B:**525(24), **B:***541*
Matsuda, H., **B:**229(138), **B:**242(138), **B:***255*
Matsumoto, K., **A:**340(18), **A:**388(18), **A:***398*
Matsumoto, M., **B:**390(49-50), **B:***420*
Matsunaga, Y.: **A:**147(59), **A:***170*; **A:**340(23), **A:***399*; **B:**264(41), **B:**266-267(41), **B:**274(73), **B:**285(74), **B:**294(41), **B:**301(73,95), **B:***311–313*
Matsuura, T., **B:**551(18), **B:**567(18), **B:**570(18), **B:***598*
Mayne, L. C., **B:**180(14), **B:***201*
Mayoral, E., **B:**364(15), **B:***371*
Mazzino, A., **B:**523(18), **B:**526-527(26), **B:***541*
McCammon, J. A.: **B:**180(15), **B:***202*; **B:**228(118,129), **B:***254–255*; **B:**261(23), **B:***311*
McCoy, A. B., **A:**198(111-112), **A:***215–216*
McDonald, J. D., **B:**214(81), **B:***253*
McGehee, R., **A:**308(22), **A:**310(22), **A:**315(22), **A:**320(22), **A:**322(22), **A:***334*
McKaye, K. R., **B:**324(9), **B:***351*
McKenzie, C., **A:**403(13), **A:***433*
McLachlan, R. I., **B:**481(34), **B:***500*
McLafferty, F. J., **A:**173(16), **A:**176(16), **A:***213*
McWhorter, D. A., **B:**220(92-93), **B:***254*
Mees, A., **B:**290-291(82), **B:**300(82), **B:***312*
Mehta, M. A., **A:***215*; **A:**7(25), **A:**75(24-25), **A:**88(59), **A:**90(59), **A:***140–141*; **A:**146(35), **A:**153(35), **A:***169*; **A:**232(48), **A:**250(48), **A:***264*; **B:**48(33), **B:**82(33), **B:***84*; **B:**210(63), **B:**214(63), **B:***253*
Meiss, J. D.: **A:**5(8-9), **A:**30(8-9), **A:***140*; **A:**177(41), **A:***214*; **B:**376(3), **B:**382(3), **B:**383(3,35-36), **B:***418–419*; **B:**427(13), **B:***436*; **B:**438(11), **B:**441(11), **B:***463*; **B:**477(8), **B:**478(9), **B:**479(26), **B:***499–500*
Melinger, J. S., **A:**436(6), **A:***457*
Mellau, G. C., **A:**289(27), **A:***302*
Mello, P. A., **B:**210(63), **B:**214(63), **B:***253*
Mel'nikov, V. K., **B:**465(3), **B:***475*
Merchant, K. A., **B:**200(43), **B:***203*
Merz, K. M., **B:**201(46), **B:***203*
Metzler, R., **B:**228(122-123), **B:***254*
Meyer, K. R., **A:**221(24), **A:**234(24), **A:**237(24), **A:**241(24), **A:**250(24), **A:***264*
Meyer, N., **A:**250(78), **A:***265*
Mezey, P. G., **B:**133(36-37), **B:***153*
Mikami, T., **B:**186-187(24), **B:**189(24), **B:**193(24), **B:***202*
Mikhailov, A., **B:**561(28), **B:**591(39), **B:***598*
Mikkola, S., **A:**323(31-32), **A:***335*
Milburn, G. J., **A:**403(13), **A:***433*
Miller, M. A.: **B:**56(37), **B:***84*; **B:**90(27), **B:***127*; **B:**130(19), **B:**139(19), **B:***153*; **B:**266-267(57), **B:**284(57), **B:**301(95), **B:***311,* **B:***313*

Miller, R. J. D., **B:**206(13), **B:**209(13), **B:***251*
Miller, W. H.: **A:**54(37), **A:**57(38), **A:**111(78), **A:**112(80), **A:**114(81), **A:**115(80,84-86), **A:***141–142*; **A:**144(9,13), **A:**146(51), **A:**148(9,60), **A:***168–170*; **A:**172-173(2), **A:**178(48-50), **A:**193(80), **A:**198(83,90), **A:***213–215*; **A:**218(6), **A:**232(6), **A:***263–264*; **A:**402(1-2,6,8), **A:**404(1-2), **A:**406(28), **A:**409(2), **A:**410(28), **A:***433–434*; **B:**74-75(47), **B:***85*; **B:**89(10), **B:**90(30), **B:**108(20), **B:***127*; **B:**132(35), **B:***153*; **B:**171(14), **B:***177*; **B:**186(25), **B:***202*; **B:**210(67), **B:***253*
Mills, D. R., **B:**547(6), **B:***597*
Mills, I. M., **A:**198(110), **A:***215*
Mil'Nikov, G. V., **A:**227(36), **A:***264*
Milnor, J., **B:**380(17), **B:***419*
Minami, Y., **A:**198(140), **A:***216*
Minnhagen, P., **B:**479(14), **B:***500*
Mishler, B. D., **B:**332(15), **B:***351*
Mitchell, K. A., **B:**89(13-14), **B:**96-97(13), **B:**111(13), **B:**114-115(14), **B:***127*
Mitome, M., **B:**156(2), **B:***176*
Miyadera, T., **A:**443(25), **A:**456(32), **A:***457–458*
Miyasaka, T., **B:**475(17), **B:***475*
Miyashita, O.: **B:**181(21), **B:**195(21), **B:***202*; **B:**238(150-151), **B:***255*
Mizutani, Y., **B:**200(35), **B:***202*
Mladenovic, M., **A:**198(106), **A:***215*
Moffatt, H. K., **B:**520-521(1), **B:**537(1), **B:***541*
Montemurro, M. A., **B:**480-481(30), **B:**482(36), **B:***500*
Montgomery, J. A., **B:**205(7), **B:**207(7), **B:**209(7), **B:**217-218(7), **B:***251*
Montgomery, R., **A:**219(15), **A:***263*, **B:**88(1-2), **B:***126*
Montroll, E. W.: **B:**228(121), **B:***254*; **B:**524(20), **B:***541*
Moore, C. B.: **A:**146(32-33), **A:***169*; **A:**174(24-25), **A:**178(24-25), **A:***213*; **B:**210(67), **B:***253*
Moore, G. R., **B:**180(11), **B:***201*
Moore, T., **B:**348(21), **B:***351*
Mordasini, T., **B:**180(18), **B:**201(18), **B:***202*
Mori, H.: **B:**156-157(7), **B:***176*; **B:**502(13), **B:***518*
Morita, T., **B:**502(13), **B:***518*
Moritsugu, K.: **B:**181(21), **B:**195(21), **B:***202*; **B:**238(150-151), **B:***255*
Morokuma, K., **B:**72-73(43), **B:***85*
Morriss, G., **B:**354(1), **B:***370*
Mortenson, P. N., **B:**266-267(57), **B:**284(57), **B:***311*
Moser, J. M., **B:**425(7), **B:***436*
Moser, J. K.: **A:**306(3), **A:***334*; **A:**358(32), **A:***399*
Mouchet, A., **A:**219(12), **A:***263*
Mount, K. E., **A:**410(32), **A:***434*, **B:**56(36), **B:***84*
Moyal, J. E., **A:**106(70), **A:**111(70), **A:***142*
Mudipalli, P. S., **A:**198(135), **A:***216*
Mukamel, D., **B:**499(41), **B:***500*
Müller, S. C., **B:**522(12), **B:***541*
Muller-Groeling, A., **B:**210(74), **B:***253*
Muratore-Ginanneschi, P., **B:**526-527(26), **B:***541*
Murdock, J., **A:**237(54), **A:***264*
Murray, N. V., **A:**177(41), **A:***214*
Murrell, J. N.: **A:**96(65), **A:***142*; **A:**199-200(142), **A:**202(142), **A:***216*
Mutschke, G., **B:**395(60), **B:***420*
Muzzio, F. J., **B:**502(16), **B:***518*

Nagaoka, M.: **A:**146(49-50), **A:**162(49), **A:***169*; **A:**178(67-68), **A:***214*; **A:**235(52), **A:***264*; **B:**21(14-15), **B:***23*; **B:**90(26), **B:***127*
Nagaya, K., **A:**436(7), **A:***457*
Nakamura, H.: **A:**165(66), **A:***170*; **A:**227(36), **A:***264*; **A:**436(7), **A:**456(31), **A:***457–458*
Nakamura, K., **B:**83(51), **B:***85*
Nakanishi, K., **B:**390(48), **B:***420*
Nakano, T., **B:**201(47), **B:***203*
Nakato, M., **B:**475(18), **B:***475*
Nakayama, T., **B:**208(32), **B:***252*
Nara, S., **A:**388(38), **A:***399*
Nauts, A., **A:**198(134), **A:***216*, **B:**89(8,10), **B:***127*
Navarro, J. F., **A:**248(67), **A:***265*
Nayak, S. K.: **A:**178(66), **A:***214*, **B:**31(20), **B:**39(20), **B:**45(20), **B:***84*; **B:**130(27), **B:**139(27), **B:***153*
Neishtadt, A. I., **A:**173-174(13), **A:**184-186(13), **A:***213*, **B:**429(26), **B:***436*
Nekhoroshev, N. N.: **B:**381(23), **B:***419*; **B:**429(24), **B:***436*; **B:**466(9), **B:**469(9), **B:***475*
Nemoto, T., **B:**201(47), **B:***203*
Nesbet, R. K., **B:**27-28(6), **B:**71-72(8), **B:**75(8), **B:**79(8), **B:***84*

Nesbitt, D. J., **A:**282(32), **A:***303*
Neumann, M., **B:**406(76), **B:***421*
Newmeyer, D. D., **B:**180(13), **B:***201*
Newton, R. G., **A:**407(30), **A:***434*
Nguyen, P. H., **B:**200(39), **B:***203*
Nielse, J. K., **B:**391(53), **B:***420*
Nielsen, M. A., **A:**436(1), **A:***457*
Nierwetberg, J., **B:**479(21), **B:***500*
Nilsson, L., **B:**190(33), **B:***202*
Nishikawa, T., **B:**223-224(112), **B:**228-229(112), **B:***254*
Nitzan, A., **B:**221(106), **B:***254*
Noid, D. W., **A:**65(51), **A:***141*
Noid, W. G., **B:**200(43), **B:***203*
Noli, C., **A:**249(74), **A:***265*
Nord, R. S., **B:**131(32), **B:**132(32), **B:***153*
Nordholm, K. S. J., **B:**209(46), **B:***252*
Nordholm, S., **B:**205(5), **B:**207(5), **B:**215(5), **B:***251*
Northrup, F. J., **A:**278(28), **A:***302*
Northrup, S. H.: **B:**180(15), **B:***202*; **B:**216(86), **B:***254*
Nozaki, K., **B:**427(23), **B:***436*
Nyman, G., **B:**186(27), **B:***202*
Nymeyer, H., **B:**267-268(42), **B:***311*

Oberman, A., **B:**522(14), **B:**531-533(14), **B:**537(44), **B:***541–542*
Ohmine, I.: **B:**229(139), **B:**250(158), **B:***255*; **B:**262(30-31), **B:**265(30-31), **B:**273(30), **B:**300(30-31), **B:***311*; **B:**378(8-9), **B:**388(8-9), **B:**389(47), **B:**390(8-9,47-50), **B:**391(54), **B:**397(47), **B:**401(47), **B:**406(78,81), **B:**408(8-9), **B:**409(9), **B:***418,* **B:***420–421*; **B:**477(1), **B:***499*
Ohtaki, Y., **B:**354(10), **B:**356(10), **B:**359(10,19), **B:**368(21), **B:***370–371*
Ohtsuki, Y., **A:**198(137), **A:***216*
Okabe, T., **B:**274(72), **B:***312*
Okazaki, S., **B:**186-187(24), **B:**189(24), **B:**193(24), **B:***202*
Okubo, A., **B:**538(47), **B:***542*
Okumura, K., **B:**200(41), **B:***203*
Okushima, T., **A:**393(44), **B:**508(24), **A:***399*, **B:***518*
Olafson, B. D., **B:**190(33), **B:***202*
Olson, W. K., **B:**261(23), **B:***311*
Oltvai, Z. N., **B:**453(23), **B:***463*
Onishi, T., **A:**403(16-17), **A:**406(17), **A:**428(16-17), **A:***433*
Onuchic, J. N.: **B:**90(31), **B:***128*; **B:**201(45), **B:***203*; **B:**205(1), **B:**206(1), **B:***251*; **B:**267-268(42), **B:***311*
Oono, Y.: **B:**317(4), **B:***351*; **B:**354(6), **B:***370*
Ooyama, N., **B:**381(25), **B:***419*
Orbach, R. L., **B:**208(32,35-39), **B:**230(35), **B:**232-233(35), **B:**241(35-39), **B:**246(36-37), **B:**250(35-37), **B:***252*
Ormos, P., **B:**228(115), **B:***254*
Orszag, S. A., **B:**502-503(9), **B:***518*
Oseledec, V. I., **B:**502(8), **B:**505(8), **B:***518*
Oskay, W. H., **A:**403(13), **A:***433*
Ota, M.: **B:**273(67), **B:***312*; **B:**477(7), **B:***499*; **B:**502(10), **B:***518*
Otsuka, K., **A:**340(18), **A:**388(18), **A:***398*
Ott, E.: **A:**393(45), **A:***399*; **A:**456(28), **A:***457*; **B:**364(16), **B:***371*; **B:**383(36), **B:***419*; **B:**478(9), **B:**479(26), **B:***499–500*; **B:**502(6), **B:***518*
Otto, M. F., **A:**136(98), **A:***142*
Oxtoby, D. W., **B:**180(3), **B:**183-184(3), **B:***201*
Ozorio De Almeida, A. M., **A:***215*; **A:**146(34), **A:**153(34), **A:**159(34), **A:**161(34), **A:***169*; **A:**224(25), **A:**232(48), **A:**250(48), **A:***264*

Pack, R. T., **A:**257(85), **A:***265*
Pal, P.: **B:**29(16), **B:**31(16), **B:***84*; **B:**136(39), **B:***153*
Palacián, J.: **A:**147(54,58), **A:**148(54), **A:***170*; **A:**173(21), **A:**178-179(76), **A:**194(76), **A:**197(76), **A:**212(21), **A:***213,* **A:***215*; **A:**219(9,11), **A:**233(9), **A:**235(9), **A:**237(9), **A:**238(57), **A:***263,* **A:***265*; **A:**338-339(3), **A:**341(3), **A:**352(3), **A:***398*
Paladin, G.: **B:**310(91-93), **B:***313*; **B:**521(4), **B:**537(4), **B:***541*
Palao, J. P., **A:**436(3), **A:***457*
Palmer, R. G., **B:**499(40), **B:***500*
Pandey, A., **B:**210(63), **B:**214(63), **B:***253*
Paniconi, M., **B:**354(6), **B:***370*
Paparella, F., **B:**300(88), **B:**301(94), **B:***312–313*
Parisi, G., **B:**273(69), **B:***312*
Park, J., **B:**248(156), **B:***255*
Park, K., **B:**181(20), **B:**185-186(20), **B:***202*
Parlitz, U., **B:**502-503(17), **B:***518*
Partovi, M. H., **B:**502(22), **B:**517(22), **B:***518*
Pasta, J., **B:**376(1), **B:**393(1), **B:***418*
Patashinskii, A. Z., **A:**402(4), **A:***433*
Pate, B. H., **B:**205(8), **B:**209(8,45), **B:**220(92-93), **B:***251–252,* **B:***254*

Pattanayak, A. K., **B:**538(46), **B:***542*
Patterson, C. W., **A:**198(97), **A:***215*
Pavlichenkov, I. M., **A:**248(69), **A:***265*
Pear, M. P., **B:**180(15), **B:***202*
Pearman, R., **B:**217(89-90), **B:***254*
Pearson, E. M., **B:**55(35), **B:***84*
Pechukas, P.: **A:**173(16-17), **A:**176(16,35-36), **A:**177(35-36), **A:**186(17), **A:**193-194(35), **A:***213–214*; **A:**228(39), **A:**230(39), **A:**232(39), **A:***264*; **B:**106(34), **B:***128*
Peirce, A. P., **A:**436(12), **A:***457*
Pelcovits, R. A., **B:**499(41), **B:***500*
Peng, T.-I., **B:**180(13), **B:***201*
Percival, I. C.: **A:**5(8-9), **A:**30(8-9), **A:***140*; **A:**177(41), **A:***214*; **B:**383(30,35), **B:***419*
Pérez-Chavela, E., **A:**307(18), **A:***334*
Perry, D. S., **B:**210(77), **B:***253*
Persch, G., **B:**210(64), **B:***253*
Peters, N., **B:**521-522(8), **B:**534(8), **B:**539(8), **B:***541*
Peterson, K. A.: **A:**287(37,40), **A:**299(40), **A:***303*, **B:**200(37), **B:***203*; **B:**207(25), **B:**209(25), **B:**239(25), **B:***252*
Peterson, R. L., **B:**547(6), **B:***597*
Petrovskii, I. G., **B:**521-522(9), **B:***541*
Pettigrew, G. W., **B:**180(11), **B:***201*
Pettini, M., **B:**394(57), **B:**395(58-59), **B:***420*
Pettit, B. M., **B:**228(128), **B:***255*
Phillips, J. C., **B:**489(38), **B:***500*
Phillips, W. D., **A:**403(13), **A:***433*
Phillpot, S. R., **B:**221(108), **B:***254*
Piskunov, N. S., **B:**521-522(9), **B:***541*
Platt, N., **B:**300(87-88), **B:***312*
Plotkin, S. S., **A:**164(65), **A:***170*, **B:**264(44), **B:**302(97), **B:***311,* **B:***313*
Pohorill, A.: **B:**250(159), **B:***255*; **B:**405(75), **B:***420*
Poincaré, H.: **A:**176(32), **A:***213*; **A:**306(2), **A:**310(2), **A:***334*
Pokrovskii, V. L., **A:**402(4), **A:***433*
Polanyi, M.: **A:**144(4), **A:***168*; **A:**176(27-28), **A:***213*; **B:**258(3), **B:***310*
Polik, W. F., **B:**210(67), **B:***253*
Pollak, E., **A:**164(64), **A:***170*, **A:**173(17), **A:**176(37), **A:**177(40), **A:**186(17), **A:***213–214*; **A:**218(5), **A:**228(39), **A:**230(39), **A:**232(39), **A:***263–264*; **B:**73(45), **B:***85*; **B:**106(35), **B:***128*; **B:**502(11), **B:**513(11), **B:***518*
Polyanski, O. L.: **A:**220(19), **A:***263*; **A:**269(7-8), **A:**274(7-8), **A:**275(7), **A:**277(7), **A:***302*
Pomeau, Y.: **A:**293(49), **A:***303*, **B:**359(18), **B:***371*; **B:**522(15), **B:**531(15), **B:***541*
Porjesz, B., **B:**338(19), **B:**341(19), **B:***351*
Porter, C. E., **B:**210(63), **B:**214(63), **B:***253*
Posch, H. A., **B:**130(28), **B:**139(28), **B:***153*
Pöschel, J., **B:**397(70), **B:***420*
Postma, J. P. M., **B:**267(60), **B:**309(60), **B:***312*
Potts, A. R., **B:**220(91), **B:***254*
Poulsen, J. A., **B:**186(27), **B:***202*
Pratt, L. R.: **B:**250(159), **B:***255*; **B:**405(75), **B:***420*
Prigogine, I., **B:**354(9), **B:***370*
Pritchard, H. O., **A:**198(129), **A:***216*
Procaccia, I., **B:**7(6-7), **B:***23*
Provat, A., **B:**526(28), **B:***542*
Provenzale, A., **B:**300(88), **B:**301(94), **B:***312–313*
Proykova, A., **B:**26(1), **B:***83*
Pryer, K. M., **B:**329(14), **B:***351*
Pugh, C. C., **A:**338(8), **A:**347(8), **A:***398*

Qi, P. X., **B:**180(14), **B:***201*
Qian, J., **B:**209(44), **B:***252*
Quapp, W.: **A:**198(108-109), **A:***215*; **A:**278(27), **A:***302*
Quenneville, J., **B:**205(6), **B:**207(6), **B:**220(6), **B:**249(6), **B:***251*

Rabii, F., **B:**205(7), **B:**207(7), **B:**209(7), **B:**217-218(7), **B:***251*
Rabitz, H., **A:**436(2,12-15), **A:**437-439(13), **A:**454(15), **A:**456(29), **A:***457–458*
Radons, G., **A:**128(92), **A:***142*, **B:**383-384(37), **B:***419*
Raff, M.: **B:**180(12), **B:***201*; **B:**558(27), **B:***598*
Ragazzo, C. G., **B:**427(11), **B:***436*
Rahman, A.: **B:**135(38), **B:***153*; **B:**388(44), **B:***419*
Rahman, N., **A:**456(29), **A:***458*
Raizen, M. G., **A:**403(13), **A:***433*
Rajaram, S., **B:**322(7), **B:***351*
Ramakrishna, V., **A:**436(2), **A:***457*
Ramani, A., **A:**403(19), **A:**410(19), **A:***434*
Ramaswany, R.: **B:**31(20), **B:**39(20), **B:**45(20), **B:***84*; **B:**130(27), **B:**139(27), **B:***153*
Ramaswarmy, R., **B:**389-390(47), **B:**397(47), **B:**401(47), **B:***420*

Rammal, R., **B:**230-231(140), **B:**233(140), **B:***255*
Ramsperger, H. C.: **A:**5(1), **A:***140*; **A:**144(1), **A:***168*
Rao, V. S., **A:**198(131), **A:***216*
Rapisarda, A., **B:**479(15,18,20,23), **B:**480(15,18), **B:**481(15,18,31), **B:**485(37), **B:**487(15), **B:***500*
Ratiu, T., **A:**221(22), **A:**248(22), **A:***264*
Ratner, M. A.: **B:**182(23), **B:**186(28), **B:***202*; **B:**238(144), **B:***255*
Rayez, J. C., **A:**249(75), **A:***265*
Rechester, A. B., **B:**441(15-16), **B:***463*
Rector, K. D., **B:**207(28), **B:**209(28), **B:**239(28), **B:***252*
Redmon, L. T., **A:**277(15), **A:***302*
Redner, S., **B:**526(28), **B:***542*
Regan, J. J., **B:**201(45), **B:***203*
Rego, L. G. C., **B:**221(104), **B:***254*
Reichl, L. E., **B:**83(51), **B:***85*
Reid, B. P., **A:**65(48), **A:***141*
Reinhardt, P., **B:**140(40), **B:***153*
Reinhardt, W. P.: **A:**166(68-69), **A:***170*; **A:**198(85), **A:***215*; **B:**187(29), **B:**200(29), **B:***202*
Reinsch, M., **A:**220(17), **A:**248(17), **A:**250(17), **A:***263*, **B:**88(7), **B:**89(7,12,14), **B:**91(7), **B:**93-95(7), **B:**108(7), **B:**114(14), **B:**115(12,14), **B:***127*
Rella, C. W.: **B:**200(37), **B:***203*; **B:**207(25,28), **B:**209(25,28), **B:**239(25,28), **B:***252*
Remacle, F., **A:**116(87), **A:***142*
Rencher, A. C., **B:**316(1), **B:**319(1), **B:**330(1), **B:***351*
Renzaglia, K. S., **B:**332(15), **B:***351*
Rey, R., **B:**180(7), **B:***201*
Rice, O. K.: **A:**5(1,3), **A:***140*; **A:**144(1), **A:***168*; **B:**221(98), **B:***254*
Rice, S. A.: **A:**6(12-16,19), **A:**8(30), **A:**20(32), **A:**22(35), **A:**27(35), **A:**39(12), **A:**41(13-14), **A:**59-60(12), **A:**65(51), **A:**66(16,55), **A:**70(15), **A:**85(15), **A:**87(58), **A:**95(64), **A:**99(60), **A:**97-98(19), **A:**104(67), **A:**108(75), **A:**124(88), **A:***140–142*; **A:**145(18-19), **A:**147(55), **A:**153(55), **A:**167(76), **A:***169–170*; **A:**178(52,59), **A:**198(91-93,122-126), **A:***214–216*; **A:**218(1), **A:**222(28), **A:**228(1,28), **A:**232(46), **A:***263–264*; **A:**307(11), **A:**330(11), **A:***334*; **A:**436(4,9), **A:**437-438(4), **A:***457*; **B:**205(9), **B:**209(9,46), **B:**210(68-69), **B:***251–253*; **B:**260(11-12), **B:***310*
Richter, K.: **A:**219(14), **A:**244(14), **A:***263*; **A:**306(8), **A:**307(12,17), **A:***334*; **A:**308(20), **A:***334*
Rick, S. W., **B:**130(22), **B:**139(22), **B:***153*
Risser, S. M., **B:**201(45), **B:***203*
Rist, C., **A:**256(84), **A:***265*
Roberts, G., **B:**427(13), **B:***436*
Roberts, K.: **B:**180(12), **B:***201*; **B:**558(27), **B:***598*
Roberts, R. M., **A:**248(64,70-71), **A:***265*
Robinson, P. J., **A:**176(31), **A:***213*, **B:**215(85), **B:***253*
Robledo, A., **B:**364(15), **B:***371*
Rogaski, C. A., **A:**278(23), **A:***302*
Roitberg, A.: **B:**186(28), **B:***202*; **B:**238(144), **B:***255*
Rolston, S. L., **A:**403(13), **A:***433*
Romanini, D., **A:**278(26), **A:***302*
Römelt, J., **B:**106(35), **B:***128*
Romesberg, F., **B:**180(10), **B:**199(10), **B:***201*
Rom-Kedar, V., **A:**180(77), **A:**182(77), **A:***215*
Ronney, P. D., **B:**534(39), **B:***542*
Rosca, F., **B:**180(14), **B:**200(35), **B:***201–202*
Rose, J. P., **B:**266(56), **B:**284(56), **B:***311*
Rosenbluth, M. N., **B:**441(16), **B:***463*
Ross, B. D., **B:**207(29), **B:**219(29), **B:**249(29), **B:***252*
Ross, D. T., **B:**348(21), **B:***351*
Ross, J., **B:**522(12), **B:***541*
Ross, S. D.: **A:**168(77), **A:***170*; **A:**173(10), **A:**198(86), **A:***213,* **A:***215*; **A:**219(13), **A:**234(13), **A:**248(68), **A:***263,* **A:***265*; **A:**340(22), **A:***399*
Rossky, P. J., **B:**186(27), **B:***202*
Rost, J.-M., **A:**306(8), **A:**307(15), **A:**330(34), **A:***334–335*
Rost, S., **A:**219(14), **A:**244(14), **A:***263*
Roukes, M. L., **B:**221(100-102), **B:***254*
Rousseau, D. L., **B:**180(14), **B:***201*
Roux, B.: **B:**190(33), **B:***202*; **B:**261(22), **B:***311*
Rubinsztein-Dunlop, H., **A:**403(13), **A:***433*
Rubner, J., **A:**128(92), **A:***142*
Ruchayskiy, O., **B:**522(16), **B:***541*
Ruedenberg, K., **B:**131(32), **B:**132(32), **B:***153*
Ruelle, D.: **B:**273(69), **B:***312*; **B:**502(1), **B:***517*
Ruf, B. A., **A:**402(6), **A:***433*

Ruffo, S.: **B:**395(58,62-63), **B:***420*; **B:**479(11-13,18,23), **B:**480(11-12,18), **B:**481(11-12,18,31,35), **B:**485(37), **B:**489(39), **B:***500*
Rupley, J. A., **B:**221(155), **B:**248(154-155), **B:***255*
Rüssmann, H., **B:**396(65), **B:***420*
Ruth, H. H., **B:**502(20), **B:***518*
Ryne, R. D., **B:**502(21), **B:**517(21), **B:***518*
Ryzhik, L., **B:**522(14,16), **B:**531-533(14), **B:***541*

Sadeghi, R., **A:**232(44), **A:***264*
Sadovskii, D. A.: **A:**248(66), **A:***265*; **A:**269(4-5), **A:***302*
Sagnella, D. E.: **B:**180(8), **B:**200(36), **B:***201–202*; **B:**228(135-136), **B:**248(135-136), **B:***255*
Saito, N.: **B:**381(25), **B:***419*; **B:**466(7), **B:**470-471(7), **B:**474(7), **B:***475*
Saito, S.: **B:**229(139), **B:***255*; **B:**262(31,34), **B:**265(31), **B:**300(31), **B:***311*; **B:**378(14), **B:**390(49), **B:**391(54), **B:**406(78,81), **B:**409(14), **B:**411-412(14), **B:***418,* **B:***420–421*; **B:**477(1), **B:***499*
Sakurai, J. J., **B:**182(23), **B:***202*
Sander, C., **B:**228-229(127), **B:***255*
San Juan, J. F., **A:**238(57), **A:***265*
Sannami, A., **B:**380(22), **B:***419*
Sano, M., **B:**502(2), **B:***517*
Sano, M. M., **A:**322-325(29), **A:**328(29), **A:***335*
Santoprete, M., **B:**427(15), **B:***436*
Sasa, S., **B:**354(8), **B:***370*
Sasai, M., **A:**165(66), **A:***170*, **B:**389-390(47), **B:**397(47), **B:**401(47), **B:***420*
Sastry, S., **B:**392(56), **B:***420*
Sathyamurthy, N., **A:**228(42), **A:***264*
Sato, F., **B:**180(19), **B:***202*
Sato, K.: **B:**466(10), **B:**471-472(10), **B:***475*; **B:**594(43), **B:***598*
Sauer, T. D.: **B:**285(75), **B:**300(75), **B:**307(75,99), **B:**308-309(75), **B:***312–313*; **B:**502(3-4,14), **B:***517–518*
Sawada, S., **B:**156(4,8-9), **B:**159-160(11), **B:**165(4), **B:**167(8,11), **B:***176*
Sawada, Y., **B:**502(2), **B:***517*
Scala, A., **B:**391(55), **B:***420*
Schaefer, H. F. III, **A:**198(90), **A:***215*
Schatz, C., **B:**182(23), **B:***202*
Schelling, P. K., **B:**221(108), **B:***254*
Scher, H., **B:**228(121), **B:***254*
Scherer, G. J., **A:**198(87-90), **A:***215*
Schinke, R.: **A:**257(85), **A:***265*; **A:**280(31), **A:**287(33-36,38,41), **A:**288(34,41), **A:**291(41), **A:**293(34-36,38,41,52), **A:**294(41), **A:**296-297(41), **A:**298(35-36,38,41), **A:**299(35,38,41), **A:**301(35,38,41), **A:***303*
Schlagheck, P., **A:**403(11), **A:***433*
Schlesinger, M. F., **B:**524(20-21), **B:***541*
Schlier, C., **B:**43(28), **B:***84*
Schmelcher, P., **B:**209(61), **B:***253*
Schmidt, P. P., **A:**198(139), **A:***216*
Schofield, S. A.: **B:**180(2), **B:***201*; **B:**207(23), **B:**209-210(23), **B:**214(23,83-84), **B:**216(84), **B:***252–253*
Scholz, H. J., **A:**249(76), **A:***265*
Schranz, H. W., **B:**200(38), **B:***203*
Schreiber, T., **B:**285(78), **B:**294(78), **B:***312*
Schroder, T. B., **B:**392(56), **B:***420*
Schubart, J., **A:**324(33), **A:***335*
Schuler, G., **B:**348(21), **B:***351*
Schulman, L. S., **A:**402(5), **A:***433*
Schulte, A., **B:**228(115), **B:***254*
Schulten, K., **B:**206(12), **B:**248(153), **B:***251,* **B:***255*
Schultz, S. L., **B:**209(44), **B:***252*
Schuster, P., **B:**547-548(7), **B:***597*
Schuttenmaer, C. A., **B:**406(80), **B:***421*
Schwab, K., **B:**221(101), **B:***254*
Schwartz, S. D., **A:**111(78), **A:***142*, **B:**206(14), **B:***251*
Schweiters, C. D., **A:**456(29), **A:***458*
Schwenke, D. W., **A:**174(23), **A:**178(23), **A:***213*
Schwettman, H. A., **B:**207(25,28), **B:**209(25,28), **B:**239(25,28), **B:***252*
Sciortino, F., **B:**391(55), **B:***420*
Scoles, G., **B:**209(45), **B:***252*
Scott, S. K., **A:**389(40), **A:***399*
Seckler, B., **A:**402(4), **A:***433*
Segal, D., **B:**221(106), **B:***254*
Segré, D., **B:**573(34), **B:**579(34), **B:***598*
Seideman, T., **A:**144(12), **A:***168*
Sekimoto, K., **B:**354-355(7), **B:***370*
Sekine, S., **B:**402(74), **B:***420*

Seko, C.: **B:**27(8,10), **B:**28(11), **B:**30(19), **B:**33(19), **B:**36(19), **B:**39(19), **B:**43(29-30), **B:**45(19), **B:**47(29), **B:**49(10), **B:**51(10), **B:**52(30), **B:**56(19), **B:**58(30), **B:**60(19,30), **B:**61-63(11), **B:**66(19), **B:**68(19), **B:**67(11), **B:***84*; **B:**90(24), **B:***127*; **B:**130(17-18,20,29), **B:**139(17-18,20,29), **B:**140(17), **B:**143(17), **B:***153*; **B:**270-271(62), **B:***312*
Seligman, T. H., **A:**250(78), **A:***265*
Sepúlveda, M. A., **B:**502(11), **B:**513(11), **B:***518*
Serva, M., **B:**310(91), **B:***313*
Shafin, W., **A:**61-62(40), **A:***141*
Shah, S. P., **A:**198(124-125), **A:***216*
Shalon, D., **B:**348(21), **B:***351*
Shannon, C., **B:**545(3), **B:***597*
Shanz, H., **A:**136(98), **A:***142*
Shapere, A., **B:**88(3), **B:***127*
Shapiro, M.: **A:**8(31), **A:***141*; **A:**436(10), **A:***457*
Shatalov, V. E., **A:**410(31), **A:***434*
Shavitt, I., **A:**277(15), **A:***302*
Sheeran, M., **B:**180(14), **B:***201*
Shen, D., **A:**198(129), **A:***216*
Shen, J., **B:**180(15), **B:***202*
Shen, T. Y., **B:**228(118), **B:***254*
Sheng, P., **B:**208(41), **B:**250(41), **B:***252*
Shepard, R. N., **B:**317(3), **B:**319(3), **B:***351*
Shepelyanski, D. L.: **B:**383(27), **B:***419*; **B:**477(5), **B:***499*
Shewmon, P. G., **B:**160(13), **B:**167(13), **B:***177*
Shi, K.-J., **A:**442(23), **A:***457*
Shi, Q., **B:**186(26), **B:***202*
Shibata, T., **B:**301(89-90), **B:***312–313*
Shibuya, N., **B:**551(18), **B:**567(18), **B:**570(18), **B:***598*
Shida, N.: **A:**402(6), **A:***433*, **B:**30(17), **B:***84*; **B:**131-132(34), **B:***153*; **B:**259(8), **B:***310*
Shiga, M., **B:**186-187(24), **B:**189(24), **B:**193(24), **B:***202*
Shima, Y., **B:**551(18), **B:**567(18), **B:**570(18), **B:***598*
Shimizu, Y., **B:**156(8-9), **B:**159-160(11), **B:**167(8,11), **B:**168(11), **B:***176*
Shimono, M., **B:***311*
Shinbrot, T., **A:**456(28), **A:***457*
Shirai, H., **A:**165(66), **A:***170*
Shirts, R. B.: **A:**166(68-69), **A:***170*; **A:**198(97-98), **A:***215*
Shivanshinsky, G. I., **B:**534(38), **B:***542*
Shizume, K., **A:**140(102), **A:***142*
Shleesinger, M. F., **B:**264(48-49), **B:***311*
Shore, B. W., **A:**436(8), **A:***457*
Shore, J. E., **B:**73(44), **B:***85*
Shrake, A., **B:**217(88), **B:***254*
Shtilerman, M., **B:**180(14), **B:***201*
Shub, M., **A:**338(8), **A:**347(8), **A:***398*
Shudo, A.: **A:**403(15-18), **A:**406(17), **A:**409(15), **A:**410(35), **A:**428(16-18), **A:***433–434*, **B:**262(34), **B:***311*; **B:**378(14), **B:**409(14), **B:**411-412(14), **B:***418*
Sibert, E. L. III: **A:**198(111-112,141), **A:***215–216*; **A:**269(2), **A:**274(13), **A:***302*, **B:**187(29), **B:**200(29), **B:***202*; **B:**210(78), **B:***253*
Siegel, S. L, **A:**306(3), **A:***334*
Sigmund, K., **B:**582(35), **B:***598*
Simó, C., **B:**376(5), **B:***418*
Simó, Carles, **A:**173(20), **A:**175(20), **A:***213*
Simonovic, N., **A:**330(34), **A:***335*
Sinai, Ya. G., **B:**387(41), **B:***419*
Singer, S. J.: **B:**205(7), **B:**207(7), **B:**209(7), **B:**217-218(7), **B:***251*; **B:**217(87), **B:***254*
Sivakumer, N., **A:**63(46), **A:**65(48), **A:***141*
Sjodin, T., **B:**180(14), **B:**200(35), **B:***201–202*
Skene, J. M., **A:**66(52-54), **A:***141*
Skinner, J. L., **B:**180(6), **B:**181(20), **B:**183-184(6), **B:**185(6,20), **B:**186(20), **B:***201–202*
Skodje, R. T.: **A:**232(44), **A:***264*; **A:**402(6), **A:***433*
Skog, J. E., **B:**329(14), **B:***351*
Skokov, S., **A:**287(37,39), **A:**288(39), **A:**293(39), **A:***303*
Sligar, S. G.: **B:**200(35), **B:***202*; **B:**228(114), **B:***254*
Smale, S., **A:**388(39), **A:***399*
Smith, A. M., **A:**278(22), **A:***302*
Smith, A. R., **B:**329(14), **B:***351*
Smith, D. J., **B:**156(2), **B:***176*
Smith, J. Maynard, **B:**573(30), **B:***598*
Smith, R. S., **A:**198(97-98), **A:***215*
Snijder, J. G., **B:**200(42), **B:***203*
Sokolov, I. M., **B:**264(51), **B:***311*
Solina, S. A. B., **B:**210(66), **B:***253*
Solomon, T. H.: **B:**479(25), **B:***500*; **B:**527(31), **B:***542*
Someda, K., **B:**200(40), **B:***203*

Song, K.: **A:**168(78), **A:***170*; **A:**249(73), **A:***265*; **B:**259(7), **B:***310*
Sornette, D., **B:**591(40), **B:***598*
Sosnick, T. R., **B:**180(14), **B:***201*
Souganidis, P. E., **B:**534(36), **B:***542*
Sparpaglione, M., **B:**395(58), **B:***420*
Spiegel, E. A., **B:**300(87-88), **B:***312*
Spiegelman, S., **B:**547(6), **B:***597*
Spohn, H., **B:**354(5), **B:***370*
Srinivasan, A. R., **B:**261(23), **B:***311*
Stamatescu, I. O., **A:**140(101), **A:***142*
Stamatiadis, S.: **A:**228(42), **A:***264*; **A:**287(38), **A:**293(38), **A:**298-299(38), **A:**301(38), **A:***303*
Stanley, H. E., **B:**391(53,55), **B:***420*
Stapleton, H. J., **B:**228(133-134), **B:***255*
Starr, F. W., **B:**391(53,55), **B:***420*
States, D. J., **B:**190(33), **B:***202*
Staudt, L. M., **B:**348(21), **B:***351*
Stauffer, J. R., **B:**324(9), **B:***351*
Steck, D. A., **A:**403(13), **A:***433*
Stein, D. L., **B:**499(40), **B:***500*
Steinbach, P. J., **B:**228(115), **B:***254*
Steinfeld, J. I.: **B:**27-28(7), **B:**71-72(7), **B:**75(7), **B:**79-80(7), **B:***84*; **B:**90(29), **B:***127*; **B:**180(1), **B:***201*
Stern, P. S., **B:**228-229(127), **B:***255*
Sternin, B. Y., **A:**410(31), **A:***434*
Stevens, D.: **B:**479(27), **B:***500*; **B:**527(30), **B:***542*
Stewart, G. M., **B:**214(81), **B:***253*
Stillinger, D., **B:**130(23), **B:**139(23), **B:***153*
Stillinger, F. H.: **B:**30(18), **B:**35(18), **B:***84*; **B:**90(28), **B:***127*; **B:**130(23), **B:**131(31), **B:**139(23), **B:***153*; **B:**262(32-33), **B:***311*; **B:**388(44-45), **B:**411(82), **B:***419,* **B:***421*
Stinson, D. G., **B:**228(133), **B:***255*
Stock, G., **B:**200(39), **B:***203*
Stokes, G. G., **A:**410(31), **A:***434*
Strang, G., **B:**93(33), **B:***128*
Stratt, R. M.: **B:**229(139), **B:***255*; **B:**391(54), **B:***420*
Straub, E., **B:**180(1), **B:**200(36), **B:***201–202*
Straub, J. E.: **A:**144(12), **A:***168*, **B:**180(8-9,16), **B:**197(9), **B:***201–202*; **B:**205(2), **B:**228(135-137), **B:**248(135-136), **B:***251,* **B:***255*
Strelcyn, J. M.: **B:**31(22), **B:**46(22), **B:***84*; **B:**396(66), **B:***420*; **B:**502(19), **B:**506(19), **B:***518*
Stuart, J. M., **B:**348(20), **B:***351*
Stuchebruckhov, A. A., **B:**209(48-49), **B:***252*
Stuchebrukhov, A., **B:**180(1), **B:***201*
Stuchi, T. J., **A:**307(19), **A:***334*
Stumpf, M., **A:**280(31), **A:***303*
Suárez, D., **B:**201(46), **B:***203*
Suen, J., **B:**354(12), **B:***371*
Sugano, S., **B:**156(1,4), **B:***176*
Sugny, D.: **A:**198(141), **A:***216*; **A:**219(10), **A:***263*; **A:**269(1-3), **A:**274(1), **A:**278(3), **A:**287-288(34), **A:**293(34), **A:***302–303*
Sulem, P.-L., **B:**502-503(9), **B:***518*
Sun, L., **A:**168(78), **A:***170*, **B:**259(7), **B:***310*
Sun, X., **A:**115(84-86), **A:***142*
Sutcliffe, B. T., **B:**89(18), **B:**106(18), **B:***127*
Suzuki, T., **B:**593-595(41), **B:***598*
Swaminathan, S., **B:**190(33), **B:***202*
Swimm, R. T., **A:**278(21), **A:***302*
Swinney, H. L.: **B:**292-293(83), **B:***312*; **B:**479(25), **B:***500*
Syage, J. A., **B:**220(94), **B:***254*
Szalay, V., **A:**198(107), **A:***215*
Szathmary, E., **B:**573(30), **B:***598*

Tabor, M.: **A:**288(45), **A:**293(45), **A:***303*; **A:**403(20), **A:***434*; **B:**83(51), **B:***85*
Tachibana, A., **B:**88(5), **B:***127*
Taddei, N., **B:**264(46), **B:***311*
Taguchi, Y.-H., **B:**317(4), **B:***351*
Tai, K., **B:**228(118), **B:***254*
Takada, S., **B:**264(39), **B:**285(74), **B:**299(39), **B:***311–312*
Takagi, H., **B:**583(38), **B:***598*
Takahashi, K.: **A:**403(16-17), **A:**404(22-25), **A:**405(23-25,27), **A:**406(17,25), **A:**407(22, **A:**24,27), **A:**408-409(22), **A:**410(22,25), **A:**412(22), **A:**413(24-25), **A:**417-418(25), **A:**423(25), **A:**425(22-23), **A:**428(16-17,24), **A:**429(24), **A:**431(25), **A:***433–434*; **A:**443(24), **A:***457*
Takahashi, S., **B:**83(56), **B:***85*
Takami, T., **A:**437(21), **A:**443(25-26), **A:**449(26), **A:***457*
Takano, K., **A:**198(140), **A:***216*
Takano, M., **B:**272(64-65), **B:**274(65), **B:***312*
Takatsuka, K.: **A:**220(18), **A:**244-245(18), **A:***263*; **A:**392(43), **A:***399*; **B:**27(8,10), **B:**28(11,15), **B:**30(19), **B:**32(23-24), **B:**33(19), **B:**34(25), **B:**36(19), **B:**39(19), **B:**43(29), **B:**44(30), **B:**45(19), **B:**47(29),

B:49(10), **B:**51(10), **B:**52(30), **B:**56(19), **B:**58(30), **B:**60(19,30), **B:**61-63(11), **B:**64(38), **B:**66(19), **B:**68(19), **B:**67(11), **B:**83(48-50,53-56), **B:***84–85*; **B:**90(24), **B:***127*; **B:**130(17-18,20,29), **B:**139(17-18,20,29), **B:**140(17), **B:**143(17), **B:***153*; **B:**259(9), **B:***310*; **B:**270-271(62), **B:***312*
Takayanagi, K., **B:**156(2), **B:***176*
Takeda, K., **B:**156-157(7), **B:***176*
Takens, F., **B:**285(76), **B:**302(76), **B:***312*
Taketsugu, T., **A:**198(140), **A:***216*
Talbi, D., **A:**198(130), **A:***216*
Talkner, P., **A:**228(37), **A:***264*
Tamarit, F., **B:**480-481(30), **B:***500*
Tanaka, A., **A:**456(32), **A:***459*
Tanaka, H.: **B:**265(53), **B:**299(53), **B:***311*; **B:**378(8-9), **B:**388(8-9), **B:**390(8-9), **B:**408(8-9), **B:**409(9), **B:***418*; **B:**502(10), **B:***518*
Tanaka, K.: **B:**270(63), **B:**273(63,67), **B:***312*; **B:**477(7), **B:***499*
Tang, H.: **A:**6(19), **A:**97-98(19), **A:**104(67), **A:***140,* **A:***142*; **A:**198(122), **A:***216*
Tang, K. T., **A:**252(82), **A:***265*
Tang, X. Z., **B:**502(16), **B:***518*
Tanikawa, K., **A:**323(31-32), **A:**330(37), **A:***335*
Tanimura, Y., **B:**200(41), **B:***203*
Tanishiro, Y., **B:**156(2), **B:***176*
Tanner, G.: **A:**219(14), **A:**244(14), **A:***263*; **A:**306(8), **A:**307(12,14,17), **A:**308(24), **A:**330(14), **A:**333(24), **A:***334–335*
Tannor, D. J., **A:**436(9), **A:***457*
Taraskin, S. N., **B:**208(42), **B:**250(42), **B:***252*
Tarn, T. J., **A:**436(11), **A:***457*
Taylor, G. I., **B:**523(19) 526(25), **B:***541*
Taylor, H. S.: **A:**198(100-102,104), **A:***215*; **A:**278(25), **A:***302*
Teller, E., **B:**499(44), **B:***500*
Tempkin, J. A., **B:**502(3), **B:***517*
Tenenbaum, A., **B:**395(61), **B:***420*
Tennyson, J.: **A:**198(99), **A:***215*; **A:**220(19), **A:**248(64,70), **A:***263,* **A:***265*; **A:**269(5,7-8), **A:**274(7-8), **A:**275(7), **A:**277(7), **A:***302*
Teramoto, H., **B:**83(50), **B:***85*
Teranishi, Y., **A:**436(7), **A:**456(31), **A:***457–458*
Tersigni, S. H., **A:**20(32), **A:***141*
Tesch, C. M., **A:**436(3), **A:***457*
Tesch, M., **B:**248(153), **B:***255*
Thayer, B. D., **B:**228(134), **B:***255*
Theuer, H., **A:**436(8), **A:***457*
Thiffeault, J.-L., **B:**502(16), **B:**503(23), **B:***518*
Thirumalai, D.: **B:**228(117,135), **B:**248(135), **B:***254–255*; **B:**266-267(58), **B:***311*
Thommen, F., **A:**63(44-45), **A:***141*
Thompson, D. E., **B:**200(43), **B:***203*
Thouless, D. J., **B:**212(80), **B:***253*
Thurston, W., **B:**380(17), **B:***419*
Tiller, W. A., **B:**55(35), **B:***84*
Tinghe, T. S., **B:**221(100), **B:***254*
Tiyapan, A., **A:**177(46-47), **A:***214*
Toda, M.: **A:**6(17), **A:**21(17), **A:**138(17), **A:***140*; **A:**145(22-24), **A:**147(56), **A:***169–170*; **A:**234(49), **A:**245(62), **A:**247(62), **A:***264–265*; **A:**338(1), **A:**339(12), **A:**340(1), **A:**358(12), **A:**372(1), **A:**378(37), **A:**381(12), **A:***398–399*; **B:**46(32), **B:**56(32), **B:**58(32), **B:***84*; **B:**205(11), **B:**209(11), **B:***251*; **B:**274(73), **B:**301(73), **B:***312*; **B:**438(3), **B:***462*
Toennies, J. P., **A:**252(82), **A:***265*
Togashi, Y., **B:**561(29), **B:***598*
Tokmakoff, A., **B:**180(5), **B:**183-184(5), **B:**189-190(5), **B:***201*
Toller, M., **A:**173(9), **A:***213*
Tombor, B., **B:**453(23), **B:***463*
Tomita, K., **B:**502(13), **B:***518*
Tomsovic, S., **A:**403(11), **A:***433*, **B:**210(72), **B:***253*
Topper, R. Q.: **A:**75(24), **A:**88(59), **A:**90(59), **A:***140–141*; **A:**146(35), **A:**153(35), **A:***169*; **B:**48(33), **B:**82(33), **B:***84*
Torcini, A.: **B:**479(16), **B:**485(37), **B:**494(16), **B:***500*; **B:**534(37), **B:**537(37), **B:**539(37), **B:***542*
Toulouse, G., **B:**230-231(140), **B:**233(140), **B:***255*
Trautmann, D., **A:**250(78), **A:***265*
Trent, J. M., **B:**348(21), **B:***351*
Tresser, C., **B:**300(87-88), **B:***312*
Tribus, M., **B:**28(13), **B:**72(13), **B:***84*
Tromp, J. W., **A:**111(78), **A:***142*
Trosset, M. W., **B:***351*
True, N. S., **B:**207(29), **B:**219(29), **B:**249(29), **B:***252*
Truhlar, D. G.: **A:**144(10,14), **A:**163(10,61), **A:***168–170*; **A:**174(23), **A:**178(23), **A:***213*; **A:**218(2), **A:***263*; **A:**402(6), **A:***433*; **B:**258(6), **B:**300(6,86), **B:***310,* **B:***312*

Tsai, C. J., **B:**171(14), **B:***177*
Tsallis, C.: **B:**299-300(85), **B:***312*; **B:**364(14), **B:***371*; **B:**479(15,20), **B:**480-481(15), **B:**487(15), **B:***500*
Tsuchiya, T., **A:**340(21), **A:**388(21), **A:***398*, **B:**479(17), **B:***500*
Tsuda, I., **B:**596(45-46), **B:***598*
Tufillaro, N. B., **B:**299-300(84), **B:***312*
Tyng, V., **A:**287-288(34), **A:**293(34), **A:***303*

Uchimaru, T., **A:**198(132), **A:***216*
Ueno, Y., **B:**201(47), **B:***203*
Ulam, S., **B:**376(1), **B:**393(1), **B:***418*
Ullmo, D., **A:**403(11), **A:***433*, **B:**210(72), **B:***253*
Ullo, J. J., **B:**406(77), **B:***421*
Umeda, H., **A:**198(136-137), **A:***216*
Umehara, H., **A:**330(37), **A:***335*
Upcroft, B., **A:**403(13), **A:***433*
Urabe, I., **B:**551(18-21), **B:**567(18), **B:**570(18), **B:***598*
Uzer, T.: **A:**7(22), **A:**21(22), **A:***140*; **A:**144(15), **A:**147(15,54,58), **A:**148(15,54), **A:**163(15), **A:***169–170*; **A:**173(6-7,10,18-19,21), **A:**177(6,18), **A:**180-181(6,18), **A:**182(78), **A:**212(19,21), **A:***213,* **A:***215*; **A:**219(8-9,13), **A:**221(8), **A:**233(9), **A:**234(8,13,51), **A:**235(9), **A:**237(9), **A:**248(64), **A:**250(8), **A:***263–265*; **A:**338-339(3), **A:**341(3), **A:**352(3), **A:***398*; **A:**428(38), **A:***434*; **B:**180(1), **B:***201*; **B:**209(52), **B:***252*

Valdinoci, E., **B:**427(17), **B:***436*
Valiron, P.: **A:**245(58), **A:**248(58), **A:**256(58), **A:***265*; **A:**256(84), **A:***265*
Van der Meer, A. G. F., **B:**207(27), **B:**209(27), **B:***252*
Van der Meer, L., **B:**207(26), **B:**209(26), **B:***252*
Van der Vaart, A., **B:**201(46), **B:***203*
van der Zwan, G., **A:**164(63), **A:***170*
Van Dishoek, E. F., **A:**256(81), **A:***265*
Van erp, T. S., **A:**232(43), **A:***264*
Van Gunsteren, W. F., **B:**267(60), **B:**273(70), **B:**309(60), **B:***312*
van Hecke, Ch., **A:**248(66), **A:***265*
Van Loan, C. F., **B:**502-504(18), **B:**506(18), **B:**510(18), **B:**517(18), **B:***518*
Van Mourik, T., **A:**269(7), **A:**274-275(7), **A:**277(7), **A:***302*
Van Vleck, J. H.: **A:**272(10), **A:**277(10), **A:***302*; **A:**306(7), **A:***334*
Vanzini, S., **B:**397(72), **B:**402(97), **B:***420*
Vecheslavov, V. V., **B:**441(17-18), **B:***463*
Vekhter, B., **B:**266(56), **B:**284(56), **B:***311*
Vela-Arevalo, L. V., **A:**167(73), **A:***170*
Vergassola, M., **B:**520(3), **B:**521(5), **B:**522(18), **B:**523(3), **B:**525(5,23), **B:***541*
Vergni, D., **B:**522(13), **B:**527(29), **B:**531-533(13), **B:**534(37), **B:**537(37), **B:**539(37), **B:***541–542*
Vetterli, M., **B:**316(2), **B:***351*
Viano, G. A., **A:**249(77), **A:***265*
Viartola, A., **A:**238(57), **A:***265*
Vidal, C., **A:**293(49), **A:***303*, **B:**522(12), **B:***541*
Vijay, A., **A:**198(131), **A:***216*
Villa, J., **A:**163(61), **A:***170*, **B:**300(86), **B:***312*
Vittot, M., **B:**396(67), **B:***420*
Vivaldi, F., **B:**438(6), **B:***462*
Vladimirova, N., **B:**522(16), **B:***541*
Von Hardenberg, J. G., **B:**300(88), **B:***312*
Von Zeipel, H., **A:**310(26), **A:***335*
Voros, A., **A:**410(33), **A:***434*
Vulpiani, A.: **B:**310(91-94), **B:***313*; **B:**395(58), **B:***420*; **B:**521(4-5), **B:**522(13), **B:**525(5), **B:**526(26), **B:**527(26,29), **B:**531-533(13), **B:**534(37), **B:**537(4,37), **B:**539(37,45), **B:***541–542*

Wadi, H., **A:**222(33), **A:**232(47), **A:***264*
Wagner, A. F.: **A:**198(135), **A:***216*; **A:**402(6), **A:***433*
Wagner, C., **B:**254(43), **B:***311*
Wagner, G. C., **B:**228(134), **B:***255*
Waite, B. A., **A:**198(83-84), **A:***215*
Wales, D. J.: **A:**146(25), **A:***169*; **A:**178(54,57), **A:***214*; **A:**234(50), **A:**245(50), **A:***264*; **B:**10(8), **B:**12(10), **B:***23*; **B:**26(1), **B:**56(37), **B:**66(39), **B:***83–84*; **B:**90(25,27), **B:**106(25), **B:***127*; **B:**130(11-12,14,19,24-25), **B:**139(11-12,14,19,24-25), **B:**143(12), **B:***152–153*; **B:**209(57), **B:**250(158), **B:***253,* **B:***255*; **B:**258(1), **B:**266(57), **B:**267(1,57), **B:**284(57), **B:**301(95), **B:***310–311,* **B:***313*
Walker, D. M., **B:**299-300(84), **B:***312*
Walker, R. B., **A:**257(85), **A:***265*
Wallenberg, R., **B:**156(2), **B:***176*

Walsh, T. R., **B:**266-267(57), **B:**284(57), **B:***311*
Walter, J., **A:**172(3), **A:**176(3), **A:***213*
Wang, H., **A:**115(85-86), **A:***142*
Wang, Q., **B:**380(21), **B:**394(21), **B:***419*
Wang, W.: **B:**180(14), **B:***201*; **B:**338(19), **B:**341(19), **B:***351*
Wang, X., **B:**180(13), **B:***201*
Wannier, G. H., **A:**307(16), **A:***334*
Warren, W. S., **A:**436(6), **A:***457*
Watanabe, M.: **B:**140(40), **B:***153*; **B:**261(22), **B:***311*
Waterland, R. L., **A:**66(53), **A:***141*
Watson, J. D., **B:**558(27), **B:***598*
Wayne, E., **B:**397(68), **B:***420*
Wazawa, T., **B:**265(55), **B:**299(55), **B:***311*
Weaver, D. L., **B:**264(45), **B:***311*
Weaver, W., **B:**545(3), **B:***597*
Weber, T. A.: **B:**30(18), **B:**35(18), **B:***84*; **B:**90(28), **B:***127*; **B:**131(31), **B:***153*; **B:**262(32-33), **B:***311*; **B:**388(45), **B:***419*
Weeks, E. R., **B:**479(25), **B:***500*
Weiss, J., **A:**287(38), **A:**298-299(38), **A:**301(38), **A:***303*
Weiss, S., **B:**265(54), **B:**299(54), **B:***311*
Weissman, M. C., **B:**273(66), **B:***312*
Weitzner, H.: **B:**479(27), **B:***500*; **B:**527(30), **B:***542*
Weizer, V. G., **B:**159(12), **B:***176*
West, B., **B:**524(21), **B:***541*
Westerberg, K. M., **A:**198(138), **A:***216*
Weyl, H., **A:**105(69), **A:***142*
Wharton, D., **B:**200(35), **B:***202*
Wharton, L., **A:**61-62(39), **A:***141*
Whelan, N. D., **A:**403(11,14), **A:**404(14), **A:***433*
Whetten, R. L., **B:**90(23), **B:***127*
White, R. B., **B:**441(15-16), **B:***463*
Whiteley, T. W. J., **A:**249(74), **A:***265*
Whitnell, R. M., **A:**280(30), **A:***303*, **B:**209(55-56), **B:***253*
Whitney, H., **B:**302(98), **B:**304-305(98), **B:***313*
Wiberg, K. B., **B:**217(88), **B:***254*
Wiedenmüller, H. A., **B:**210(73-74), **B:***253*
Wiesenfeld, L.: **A:**7(22), **A:**21(22), **A:***140*; **A:**144(15), **A:**147(15,57), **A:**148(15), **A:**163(15), **A:**167(70), **A:***169–170*; **A:**173(19), **A:**212(19), **A:***213*; **A:**219(8), **A:**221(8,26), **A:**222(33), **A:**228(38,41), **A:**232(41,47), **A:**234(8), **A:**236(53), **A:**237(53), **A:**238(56), **A:**245(58-59,62), **A:**247(62), **A:**248(56,58), **A:**249(41), **A:**250(8,26), **A:**256(58), **A:**257-258(59), **A:***263–265*; **A:**428(38), **A:***434*
Wiggins, S.: **A:**7(20-22), **A:**20(20-21), **A:**22(21), **A:***140*; **A:**144(15), **A:**145(21), **A:**147(15,53-54), **A:**148(15,54), **A:**163(15,21,53), **A:**167(73), **A:***169–170*; **A:**173(14,19,21), **A:**174(22), **A:**179(14,22), **A:**183(22), **A:**187(22), **A:**203(22), **A:**212(19,21), **A:***213*; **A:**219(8-9), **A:**221(8,23,27), **A:**233(9), **A:**234(8), **A:**235(9), **A:**237(9,23), **A:**238(56), **A:**248(23,56), **A:**250(8), **A:***263–265*; **A:**292(46-47), **A:***303*; **A:**333(39), **A:***335*; **A:**339(10,14), **A:**341(24), **A:**243(29), **A:**351(30), **A:**358(14,24), **A:**362(24), **A:**364(24), **A:***398–399*; **A:**428(38), **A:**432(40), **A:***434*
Wight, C. A., **A:**402(6), **A:***433*
Wigner, E., **B:**258(4), **B:***310*
Wigner, E. P.: **A:**144(5), **A:***168*; **A:**172(4), **A:**173(4,11-12), **A:**176(4,11-12,29), **A:***213*
Wilczek, F., **B:**88(3), **B:***127*
Wilkens, M., **B:**479(13), **B:***500*
Wilkinson, M., **A:**402(3), **A:**404(3), **A:***433*
Willberg, D. M., **A:**61(41-42), **A:***141*
Wilson, E. B.: **A:**271(9), **A:***302*, **B:**89(16), **B:**93(16), **B:**95(16), **B:**106(16), **B:***127*; **B:**187(30), **B:***202*
Wilson, M. A.: **B:**250(159), **B:***255*; **B:**405(75), **B:***420*
Windey, P., **B:**273(69), **B:***312*
Winkler, J. E., **B:**201(45), **B:***203*
Winnewisser, G., **A:**256(83), **A:***265*
Wintgen, D., **A:**307(12,14,17), **A:**308(20), **A:**330(14), **A:***334*
Withnell, R. M., **B:**4(2-3), **B:***23*
Wodtke, A. M., **A:**278(23-24), **A:***302*
Wolf, R. J., **A:**198(82), **A:***215*
Wolynes, P. G.: **A:**131(94), **A:***142*; **A:**164(65), **A:***170*; **B:**90(31), **B:***128*; **B:**180(2,15), **B:***201–202*; **B:**205(1,3,6), **B:**206(1,15,20-21), **B:**207(3,6,19-20,23), **B:**209(16-21,23,60), **B:**210(16,21,23), **B:**212(15,20), **B:**213(15-19), **B:**214(16-17,20,23,83-84), **B:**216(84), **B:**217(20), **B:**220(3,6), **B:**221(105), **B:**228(114), **B:**249(3,6), **B:***251–254*; **B:**263-264(38), **B:**302(97), **B:***311,* **B:***313*; **B:**378(8), **B:**388(8), **B:**390(8), **B:**408(8), **B:***418*; **B:**424(4), **B:**427(4), **B:***436*

Won, Y., **B:**190(33), **B:***202*
Wong, C. F., **B:**180(15), **B:***202*
Wong, S. M., **B:**210(63), **B:**214(63), **B:***253*
Wood, B. P., **B:**438(12), **B:**441(12), **B:**463(12), **B:***463*
Wooten, F., **B:**208(40), **B:**250(40), **B:***252*
Worlock, J. M., **B:**221(100-101), **B:***254*
Wörner, H. J., **A:**128(97), **A:**134(97), **A:***142*
Wozny, C. E., **A:**65(47,49), **A:**66(49), **A:***141*
Wright, K. R., **A:**178(64), **A:***214*, **B:**48(33), **B:**82(33), **B:***84*
Wyatt, R. E.: **A:**128(91), **A:***142*; **A:**198(120), **A:***216*; **B:**180(2), **B:***201*; **B:**210(79), **B:**214(84), **B:**216(84), **B:***253*
Wylie, B. N., **B:**348(20), **B:***351*

Xia, Z.: **A:**311(28), **A:***335*; **A:**373(35-36), **A:**377-378(35), **A:***399*; **B:**427(9), **B:***436*
Xie, A., **B:**207(26-27), **B:**209(26-27), **B:**228(115), **B:***252,* **B:***254*
Xie, X. S., **B:**228(125), **B:***255*
Xin, J., **B:**521-522(7), **B:**530(7), **B:***541*
Xu, D., **B:**206(12), **B:***251*

Yagihara, S., **A:**165(67), **A:***170*, **B:**302(96), **B:***313*
Yakhot, V., **B:**537(41), **B:***542*
Yakubo, K., **B:**208(32), **B:***252*
Yamada, H., **B:**274(72), **B:***312*
Yamaguchi, M., **B:**551(18), **B:**567(18), **B:**570(18), **B:***598*
Yamaguchi, Y., **A:**198(90), **A:***215*
Yamaguchi, Y. Y.: **B:**385(39), **B:***419*; **B:**477(2-3), **B:**479(2,19), **B:**480(2), **B:**485(39), **B:***499–500*
Yamamoto, K.: **B:**273(67), **B:***312*; **B:**477(7), **B:***499*; **B:**502(10), **B:***518*
Yamamoto, T.: **A:**111(79), **A:***142*; **A:**308(21), **A:***334*
Yanagida, T., **B:**265(53,55), **B:**299(53,55), **B:***311*
Yanao, T.: **A:**220(18), **A:**244-245(18), **A:***263*, **B:**28(11), **B:**61-63(11), **B:**64(38), **B:**67(11), **B:**83(48-49), **B:***84–85*; **B:**90(24), **B:***127*
Yang, H., **B:**228(124-125), **B:***255*
Yang, J., **B:**180(13), **B:***201*
Yang, P.-H., **B:**248(154), **B:***255*
Yang, X., **A:**278(23-24), **A:***302*
Yanguas, P.: **A:**147(54,58), **A:**148(54), **A:***170*; **A:**173(21), **A:**178-179(76), **A:**194(76), **A:**197(76), **A:**212(21), **A:***213,* **A:***215*; **A:**219(9,11), **A:**233(9), **A:**235(9), **A:**237(9), **A:**238(57), **A:***263–264*; **A:**338-339(3), **A:**341(3), **A:**352(3), **A:***398*
Yasuda, H., **B:**156-157(7), **B:***176*
Ye, X., **B:**180(14), **B:**200(35), **B:***201–202*
Yeh, S.-R., **B:**180(14), **B:***201*
Yip, S., **B:**406(77), **B:***421*
Yokomizo, T., **A:**165(67), **A:***170*, **B:**302(96), **B:***313*
Yokoyama, K., **B:**317(4), **B:**334(18), **B:***351*
Yomo, T., **B:**544(2), **B:**551(2,13-15,17-21), **B:**553(15,17), **B:**556-557(15), **B:**558(2), **B:**562-563(2), **B:**567(18), **B:**570(18), **B:**573(17), **B:**575(2), **B:**593(41), **B:**594(41,43), **B:**595(41), **B:**597(15), **B:***597–598*
Yonetani, T., **B:**200(37), **B:***202*
Yorke, J. A.: **A:**456(28), **A:***457*, **B:**285(75), **B:**300(75), **B:**307(75,99), **B:**308-309(75), **B:***312–313*; **B:**502(3-4,14), **B:***517–518*
Yoshida, H., **B:**481(33), **B:***500*
Yoshida, T., **B:**265(55), **B:**299(55), **B:***311*
Yoshihiro, T., **B:**180(19), **B:***202*
Yoshimoto, A., **A:**404(24), **A:**405(24,26), **A:**407(24,26), **A:**413(24), **A:**428-429(24,26), **A:***434*
Young, L.-S., **B:**380(21), **B:**394(21), **B:***419*
Young, R. D., **B:**228(115), **B:***254*
Yu, X.: **B:**180(15), **B:**181(22), **B:**190(22), **B:**193(22), **B:**195(21-22), **B:**197(22), **B:***202*; **B:**223(111), **B:**229(111), **B:**233(141), **B:**240-241(111), **B:**243(111), **B:**247(111), **B:**248(156), **B:**250(111), **B:***254–255*
Yuri, M., **B:**470(12), **B:**475(12), **B:***475*

Zacharl, A., **B:**383-384(37), **B:***419*
Zacherl, A., **B:**479(21), **B:***500*
Zanette, D. H., **B:**482(36), **B:***500*
Zaslavsky, G. M.: **B:**264(48), **B:***311*; **B:**479(27), **B:***500*; **B:**527(30), **B:***542*
Zechman, F. W., **B:**332(15), **B:***351*
Zeh, H. D., **A:**140(101), **A:***142*
Zewail, A. H., **A:**61(41-42), **A:***141*, **B:**209(43), **B:**220(43,94-96), **B:***252,* **B:***254*

Zhang, D. H., **A:**65(50), **A:**94(64), **A:**96(100), **A:***141–142*
Zhang, J. Z. H., **A:**65(50), **A:***141*
Zhang, X. L., **B:**338(19), **B:**341(19), **B:***351*
Zhang, Z. Q., **B:**208(41), **B:**250(41), **B:***252*
Zhao, M., **B:**260(12), **B:***310*
Zhao, M. S.: **A:**6(13-16,19), **A:**8(30), **A:**41(13-14), **A:**66(16), **A:**70(15), **A:**85(15), **A:**88(60), **A:**97-98(19), **A:**104(67), **A:**108(75), **A:**124(88), **A:***140–142*; **A:**145(19), **A:**147(55), **A:**153(55), **A:**168(76), **A:***169–170*; **A:**178(59), **A:**198(122-123), **A:***214,* **A:***216*; **A:**218(1), **A:**222(28), **A:**228(1,28), **A:***263–264*; **A:**436-438(4), **A:***457*
Zheng, C., **B:**180(15), **B:***202*
Zhilinskii, B. I., **A:**248(66), **A:***265*
Zhou, M., **B:**208(41), **B:**250(41), **B:***252*
Zhu, W., **A:**436(13,15), **A:**437-439(13), **A:**454(15), **A:***457*
Zimmerman, T., **B:**210(64), **B:***253*
Zipf, G. K., **B:**593(42), **B:***598*
Zumhofen, G., **B:**479(22), **B:***500*
Zumofen, G., **B:**264(50), **B:***311*
Zurek, W. H., **A:**140(102), **A:***142*
Zwanzig, R., **A:**164(62), **A:***170*
Zwier, T. S., **B:**249(157), **B:***255*

SUBJECT INDEX

Letter in **boldface** indicates the volume.

Ab initio calculations:
  intramolecular dynamics, floppy molecules, canonical perturbation theory, **A:**272–278
  resonantly coupled isomerizing/dissociating systems, high energy bifurcations, **A:**299–301
Activation mechanism, rapid alloying, microcluster dynamics:
  nano-sized clusters, **B:**159
  radial and surface diffusion, **B:**168–170
  saddle point energy distribution, **B:**174–175
Adams-Moulton predictor-corrector method, onset dynamics, argon clusters, **B:**135–136
Adiabatic delocalization, isomerizing systems, intramolecular dynamics, *vs.* nonadiabatic, **A:**278–286
Adiabatic invariants:
  fluctuation-dissipation theorem, excess heat production:
    anomalous variance, **B:**361–368
    Hamiltonian chaotic systems, **B:**363–367
  slow relaxation, internal degrees of freedom, Hamiltonian systems, **B:**401–403
Adiabatic solution, multidimensional barrier tunneling:
  low-frequency approximation, **A:**418–422
  Melnikov method, **A:**417–418
Advection-reaction-diffusion equation (ARD), chaotic transitions, inert and reactive substances, **B:**521–522
  FKPP reaction, **B:**530–531
Allan variance, multibasin protein landscapes, chaotic transition, regularity:
  nonstationarity in energy fluctuations, **B:**270–285
  temperature dependence in dimensionality of folding dynamics, **B:**293–299
Alternative Rice, Ramsperger, Kassel and Marcus (ARRKM) rate theory:
  unimolecular reaction:
    Gray-Rice-Davis predissociation theory, **A:**39–41
    helium-iodine predissociation, **A:**60–61
    quantization, **A:**108–111
      rigorous quantum rate *vs.*, **A:**111–114
  unimolecular reaction rate, isomerization theory, **A:**70–75
Amplitude measurements:
  fringed tunneling models, multiple trajectories, **A:**424–425
  phase-space transition states, Melnikov integral, **A:**367–371
Angle-action variables, unimolecular reaction rate theory:
  KAM theorem, **A:**13–14
  phase-space structure, **A:**11–12
  quantum transport, cantori systems, **A:**129–131

Geometric Structures of Phase Space in Multidimensional Chaos: A Special Volume of Advances in Chemical Physics, Part A, Volume 130, edited by M. Toda, T Komatsuzaki, T. Konishi, R.S. Berry, and S.A. Rice. Series editor Stuart A. Rice.
ISBN 0-471-70527-6

Angle space diffusion, globally-coupled Hamiltonian systems, relaxation and diffusion, Hamilton mean field model, **B:**488–498
  equilibrium diffusion, **B:**489–490
  nonstationary state, **B:**494–496
  quasi-stationary state, **B:**491–493
Angular momentum, phase-space transition state geometry, **A:**247–261
  astrophysics applications, **A:**256–261
    inelastic scattering, **A:**257–261
  rotating frame dynamics, **A:**248–256
    relative equilibrium, **A:**249–251
    van der Waals complex, **A:**251–256
  three degrees of freedom, Hénon-Heiles potential, **A:**238–244
  triatomic dynamics, zero angular momentum, **A:**244–247
Anharmonicity:
  heat transfer, quantum energy flow, protein vibrational states, **B:**238–241
  resonantly coupled isomerizing/dissociating systems, **A:**286–287
Anomalous diffusion:
  chaotic transitions, inert substances, **B:**523–527
    strong anomalous diffusion, **B:**527–530
    weak *vs.* strong diffusion, **B:**526–527
  globally-coupled Hamiltonian systems, relaxation and diffusion, Hamilton mean field (HMF) model, **B:**479–480
  heat transfer, quantum energy flow, **B:**227–238
  multidimensional Hamiltonian systems, resonance and transport, **B:**440–442
  slow relaxation, internal degrees of freedom, Hamiltonian systems, mixed-phase space, **B:**379–387
  unimolecular reaction rate, faster-than-classical dynamics, **A:**134–137
Anomalous time series, multichannel chemical isomerization, multi-basin potential, structural transitions, **B:**31–34
Anomalous variance, nonergodic adiabatic invariant, fluctuation-dissipation theorem, excess heat production, **B:**361–368
  Hamiltonian chaotic systems, **B:**363–367
  microcanonical distribution, **B:**361–363
Anti-harmonic oscillator equation, phase-space transition state geometry, one degree of freedom model, linearized Hamiltonian, **A:**225–227
Antiproton-proton-antiproton system, collinear eZe configuration, **A:**330
A priori distribution:
  multichannel chemical isomerization:
    linear surprisal theory, **B:**80
    microcanonical temperature, **B:**58–62
  multichannel isomerization, **B:**28
"Apt" coordinates, Wigner's transition state dynamics, rank-one saddle phase-space structure, **A:**184–186
Argon clusters:
  multibasin landscapes, chaotic transition, regularity, **B:**265–266
  onset dynamics, phase transition:
    analytic techniques, **B:**131–136
    configuration entropy, **B:**140
    configuration space, **B:**140–142
    gradient extremal, **B:**131–133
    Lindemann's criterion, **B:**138–139
      additional potentials, **B:**148–151
    Lyapunov and KS entropy, **B:**142–143
    partitioned cell dynamics, **B:**145–146
    potential energy surface, cell petition, **B:**133–134
    potential function, MD simulation, and temperature, **B:**135–136
    reaction paths, **B:**136–138
    stationary points, **B:**143–145
    structural characteristics, **B:**136
    watershed, **B:**146–148
  power spectra and phase-space dimensions, **B:**5–11
  slow relaxation, internal degrees of freedom, Hamiltonian systems, **B:**389–392
Argon-iodine molecules, unimolecular reaction rate theory, predissociation, **A:**61–63
Arnold diffusion
  atomic clusters, **B:**23
  multidimensional Hamiltonian Systems, resonance and transport, **B:**438, **B:**462
  multidimensional phase space:
    slow dynamics, **B:**427–430
      multi-precision numerical method, **B:**430–435

unimolecular reaction rate theory:
phase-space structure, bottlenecks, many-dimensional systems, **A:**20
quantum transport, classically chaotic systems, **A:**131–134
web model, phase-space transition states:
Melnikov integral derivation, **A:**341–342, **A:**371–377
normally hyperbolic invariant manifold connections, **A:**340
tangency and, **A:**378–385
Arnold model: *see* Arnold diffusion
Arrhenius relation:
isomerization:
atomic clusters, **B:**27–28
multichannel dynamics, **B:**27–28
multichannel isomerization:
isomer lifetimes, **B:**53–70
basic principles, **B:**60–62
canonical temperature, **B:**70
definition, **B:**57–60
density of states evaluation, **B:**55–56
exponential relation, average lifetimes, **B:**62–70
liquid-like ergodicity and nonergodicity, **B:**67–69
M_7 single exponential form case study, **B:**65–67
multiexponential form, **B:**62–63
single exponential form, **B:**64–65
lifetime averaging law, **B:**53–55
local temperatures, **B:**60
microcanonical temperature, numerical calculation, **B:**60–62
rapid alloying, microcluster dynamics, radial and surface diffusion, **B:**167–170
Artificial life (AL) research, recursive cell production and evolution, catalytic reaction network, **B:**553–557
Astrophysics applications, phase-space transition state geometry, angular momentum, **A:**256–261
Asymptotic conditions:
intramolecular dynamics, floppy molecules, canonical perturbation theory, **A:**275–278
phase-space transition states:
angular momentum, astrophysics applications, **A:**261
tangency, **A:**378–385
Atomic clusters:
basic properties, **B:**3–4
Kolmogorov entropy, **B:**5–11
level spacing distributions, **B:**4–5
Lyapunov exponents, **B:**5–11
molecular internal space, isomerization dynamics, **B:**90–91
nonlinear canonical transformation, **B:**21–22
phase-space dimensions, **B:**5–11
power spectra, **B:**5–11
regularity, chaos and ergodicity characteristics, **B:**11–20
Autocatalytic network, recursive cell production and evolution, **B:**573–595
core hypercycle minority, **B:**582–583
evolution models, **B:**585–588
intermingled hypercycle network stabilization, **B:**581–582
molecular models, **B:**574–575
phase states, **B:**575–581
random network localization, **B:**583
statistical law, **B:**588–595
deviation from universal statistics, **B:**593–595
universal statistics, **B:**593
switching mechanism, **B:**584–585
Autocorrelation, fluctuation-dissipation theorem, excess heat production, **B:**357–359
Averaged kinetic temperature controlling method (AKTCM), rapid alloying, microcluster dynamics:
nano-sized clusters, **B:**159
size effect, **B:**161–164
Average mutual information, multibasin landscapes, chaotic transition, regularity, state-space structures, **B:**292–294

Backward reactive trajectories, Wigner's transition state dynamics, rank-one saddle phase-space structure:
normally hyperbolic invariant manifolds, **A:**188–190
transition state principles, **A:**190–191
Ballistic pathway, chaotic transition, regularity, two-basin landscapes, Kramers-Grote-Hynes theory, **A:**164–165

Basin transition:
molecular internal space, democratic centrifugal force, **B:**106
multichannel chemical isomerization, microcanonical temperature, **B:**57–62
Bath interaction:
chaotic transition, regularity, two-basin landscapes, Kramers-Grote-Hynes theory, **A:**164–165
vibrational energy relaxation, force-force-correlation function approximations, **B:**187–190
Wigner's transition state dynamics, theoretical background, **A:**174–175
Belousov-Zhabotinsky (BZ) reaction, phase-space transition states, hyperbolicity breakdown, **A:**389–392
Bending energy fluctuation, multibasin landscapes, chaotic transition, regularity, nonstationarity in, **B:**278–282
Berendsen algorithm, multibasin landscapes, chaotic transition, regularity, constant-temperature molecular dynamics, **B:**309–310
Bernoulli system, multibasin landscapes, chaotic transition, regularity, nonstationarity in energy fluctuations, **B:**274–280
Bifurcation mechanisms:
multichannel isomerization, inter-basin mixing, reaction tubes, **B:**47–50
phase-space transition states:
hyperbolicity breakdown, **A:**391–392
multidimensional chaos crisis, **A:**392–395
resonantly coupled isomerizing/dissociating systems:
high energy bifurcations, **A:**296–301
saddle-node bifurcations, **A:**287–296
Binary clusters, rapid alloying, microcluster dynamics:
floppy surface atoms and PES reaction paths, **B:**170–171
heat of solution, **B:**164–165
molecular dynamics simulation, **B:**160–161
nano-sized clusters, **B:**157–160
procedural characteristics, **B:**157–158
simulation model, **B:**158–160
radial and surface diffusion, **B:**167–170
reaction path numerical simulation, **B:**171–173
saddle point energy distribution, **B:**173–175
size effect, **B:**161–164
solid phase, **B:**165–166
Binary collisions, Coulomb three-body problem, zero angular momentum, **A:**315–319
Birkhoff-Gustavson procedure, intramolecular dynamics, floppy molecules, canonical perturbation theory, **A:**278
Birkhoff normal form, phase-space transition states, normally hyperbolic invariant manifolds, **A:**339–340
BLN protein models, multibasin landscapes, chaotic transition, regularity:
basic properties, **B:**267–270
nonstationarity in energy fluctuations, **B:**270–285
temperature dependence in dimensionality of folding dynamics, **B:**296–299
Body-fixed frame, molecular internal space, kinematics, **B:**88–90
Bohr-Sommerfeld (BS) quantization condition, three-body problem, **A:**306–309
Boltzmann constant, multichannel isomerization:
canonical temperature, **B:**70
density of state evaluation, microcanonical temperature, **B:**55–56
Boltzmann equilibrium distribution:
fluctuation-dissipation theorem, excess heat production:
second law from, **B:**369–370
superstatistical equilibrium distributions, **B:**360–361
thermodynamics, **B:**355–356
multichannel isomerization, linear surprisal theory, **B:**71–74
Boltzmann-Jeans conjecture, slow relaxation, internal degrees of freedom, Hamiltonian systems, **B:**401–403
hypothesis validity, **B:**405–412
Bond energy fluctuation, multibasin landscapes, chaotic transition, regularity, nonstationarity in, **B:**277–278
Born-Oppenheimer approximation, phase-space transition states, singular perturbation theory *vs.,* **A:**342–345
Bottlenecks:
chaotic transition, regularity, two-basin landscapes, normally hyperbolic invariant manifolds (NHIM), **A:**166–168

multibasin landscapes, chaotic transition, regularity, **B:**259–260
protein structures, **B:**265–266
slow relaxation, internal degrees of freedom, Hamiltonian systems, **B:**407–412
unimolecular reaction rate theory:
Davis-Gray predissociation analysis, **A:**30–39
dissociation dynamics, Hamiltonian equations, **A:**123
helium-iodine predissociation, **A:**60–61
phase-space structure:
few-dimensional systems, **A:**18–19
many-dimensional systems, **A:**19–20
quantum scars, **A:**108
quantum transport, cantori systems, **A:**129–131
Zhao-Rice approximation, **A:**41–54
intramolecular dividing surface, **A:**46–48
isomerization theory, **A:**71–75
separatrix crossing rate, **A:**50–54
zeroth-order rate constant, **A:**48–54
Bound-bound coupling potentials, dissociation dynamics, unimolecular reactions, Hamiltonian equations, **A:**116–123
Bound-continuum coupling potentials, dissociation dynamics, unimolecular reactions, Hamiltonian equations, **A:**116–123
Box-counting dimensions, multibasin landscapes, chaotic transition, regularity, embedding theorems, **B:**307–309
Brain wave analysis, nonmetric multidimensional scaling algorithm, **B:**338–341
Branching structure of paths:
fringed tunneling models, **A:**415–417
multiple trajectories, **A:**423–425
multidimensional barrier tunneling:
Melnikov method, **A:**417–418
M-set critical point, **A:**414–415
phase-space transition states:
chaotic itinerancy, **A:**385–389
tangency, **A:**377–385
Brownian motion:
chaotic transitions, inert and reactive substances, **B:**522
multidimensional Hamiltonian systems, resonance and transport structures, **B:**450
Canonical correlation analysis (CCA), nonmetric multidimensional scaling algorithm and:
fern genotype/phenotype, **B:**330–332
green autotrophs, **B:**332–333
Canonical ensemble, globally-coupled Hamiltonian systems, relaxation and diffusion, Hamilton mean field (HMF) model, **B:**480–481
Canonical perturbation theory (CPT), floppy molecules, intramolecular dynamics, **A:**269–278
Canonical temperature, multichannel isomerization, **B:**70
Canonical transformation:
atomic clusters, nonlinear transformation, **B:**21–22
chaotic transition, regularity, two-basin landscapes, saddle regions, dynamical regularity, **A:**148–151
unimolecular reaction rate theory:
phase-space structure, molecular dynamics, **A:**9–10
reaction path analysis, **A:**57–59
Cantori systems:
slow relaxation, internal degrees of freedom, mixed-phase space, **B:**383–387
unimolecular reaction rate, quantum transport, classically chaotic systems, **A:**128–129
Whisker mapping, **A:**129–131
Cao's algorithm, multibasin landscapes, chaotic transition, regularity:
state-space structures, **B:**291–292
temperature dependence in dimensionality of folding dynamics, **B:**296–299
Capped octahedron (COCT) structures, multichannel isomerization:
inter-basin mixing, **B:**46–57
time scales, **B:**50–51
liquid-like phase, **B:**42–44
microcanonical temperature, single exponential form, **B:**66–67
multi-basin potential, **B:**28–30
anomalous time series, **B:**32–34
nonstatistical behavior, low-energy phase, **B:**44–45
Carbon monoxide myoglobin (MbCO):
heat transfer, quantum energy flow, protein vibrational states, anharmonic decay, **B:**238–241

Carbon monoxide myoglobin (MbCO) (*Continued*)
heat transport, quantum energy flow, **B:**250–251
vibrational energy relaxation, cytochrome *c,* CD stretching mode, **B:**200
Carbon-oxygen "wagging," unimolecular reaction rate, isomerization, cyclobutanone, **A:**100–104
Cartesian coordinates:
phase-space transition state geometry, three degrees of freedom, Hénon-Heiles potential, **A:**238–244
vibrational energy relaxation, cytochrome *c,* CD stretching mode, coupling constants, **B:**193–195
Wigner's transition state dynamics, hydrogen cyanide isomerization, **A:**207–210
Cascading saddlebacks, resonantly coupled isomerizing/dissociating systems, high energy bifurcations, **A:**298–301
Catalytic reaction network, recursive cell production and evolution:
autocatalytic network, **B:**573–595
core hypercycle minority, **B:**582–583
evolution models, **B:**585–588
intermingled hypercycle network stabilization, **B:**581–582
molecular models, **B:**574–575
phase states, **B:**575–581
random network localization, **B:**583
statistical law, **B:**588–595
deviation from universal statistics, **B:**593–595
universal statistics, **B:**593
switching mechanism, **B:**584–585
constructive biology, **B:**550–557
chemical reaction networks modeling, **B:**553–557
diverse chemicals, **B:**546–547
Dyson's loose reproduction system, **B:**549–550
Eigen's hypercycle, **B:**547–549
heredity origins, **B:**544–546
minority control hypothesis, **B:**557–573
evolvability, **B:**566–567
experimental protocol, **B:**567–571
growth speed, **B:**565
intermingled hypercycle network production, **B:**595–596
itinerant dynamics, **B:**596
kinetic theory, heredity and, **B:**571–572
model parameters, **B:**557–561
molecule chemical composition, **B:**565–566
molecule preservation, **B:**565
stochastic results, **B:**561–564
universal statistics and fluctuation control, **B:**596–597
Cayley tree topology, unimolecular reaction kinetics, quantum energy flow, local random matrix theory, **B:**212–214
CD stretching mode, vibrational energy relaxation:
basic principles, **B:**180–181
cytochrome *c,* **B:**190–200
carbon monoxide myoglobin (MbCO), **B:**200
classical calculation, **B:**197
coupling constants calculation, **B:**192–195
full width at half maximum spectra, **B:**199–200
lifetime parameter assignment, **B:**195–196
quantum calculation, **B:**197–199
system and bath characteristics, **B:**190–192
force-force-correlation function approximations, **B:**187–190
Celestial mechanics, *n*-body problem in, **A:**309–312
Cell-cell interaction, recursive cell production and evolution, catalytic reaction networks, **B:**597
Cell partition, onset dynamics, argon clusters, potential energy surfaces, **B:**133–134
Cellular flow fronts, chaotic transitions, inert and reactive substances, **B:**531–532
Center manifold:
phase-space transition state geometry, *n* degrees of freedom structures, **A:**237
Wigner's transition state dynamics, stationary points, **A:**179
Centrifugal forces, phase-space transition state geometry, angular momentum, astrophysics applications, **A:**256–261
Chain rule, Wigner's transition state dynamics, Lie transformation, normal-form coordinates, **A:**198

Chaotic itinerancy, phase-space transition states, **A:**385–389
Melnikov integral, **A:**363–371
normally hyperbolic invariant manifold connections, **A:**340
Chaotic transitions. *See also* Quantum chaos
atomic clusters, local characteristics, **B:**11–20
inert substances:
standard and anomalous diffusion, **B:**523–527
strong anomalous diffusion, **B:**527–530
multibasin landscapes, regularity in:
Berendsen algorithm, constant-temperature molecular dynamics, **B:**309–310
embedded techniques:
basic principles, **B:**302–309
phase-space reconstruction, **B:**285–288
energy nonstationarity, protein landscapes, **B:**270–285
bending energy fluctuation, **B:**278–282
bond energy flucation, **B:**277–278
torsional angle energy fluctuation, **B:**282–285
folding dynamic dimensionality, temperature dependency, **B:**294–299
global/local collective coordinates, **B:**261–262
liquid water, **B:**262–263
minimalistic 46-bead protein models, **B:**266–270
phase space transport geometry, **B:**260–261
proteins, **B:**263–266
state-space structure, **B:**285–299
average mutual information, **B:**292–294
false nearest neighbors, **B:**288–292
phase-space reconstruction, embedding of, **B:**285–288
multidimensional barrier tunneling:
global dynamics, **A:**402–406
quantum mapping, **A:**428
multidimensional phase space slow dynamics, global motion, **B:**425–427
phase-space transition states:
angular momentum, astrophysics applications, **A:**261
Arnold model, **A:**371–377
Melnikov integral, **A:**368–371
multidimensional chaos crisis, **A:**392–395
normally hyperbolic invariant manifold connections, **A:**339–340
reacting substances:
front propagation, **B:**537–540
fronts in cellular flows, **B:**531–532
geometric optics limit, **B:**534–537
slow and fast reaction regimes, **B:**532–534
regularity, in two-basin landscapes:
Kramers-Grote-Hynes theory, **A:**163–165
phase space geometrics, **A:**151–163
reactive island theory, **A:**153–163
saddle crossing stochasticity, **A:**165–166
saddle regions, dynamical regularity, **A:**147–151
three-body problem, **A:**306–309
unimolecular reaction rate, **A:**128–137
Arnold diffusion suppression, **A:**131–134
Cantori model, **A:**129–131
faster-than-classical anomalous diffusion, **A:**134–137
CHARMM potential, vibrational energy relaxation:
cytochrome *c,* CD stretching mode, **B:**190–192
coupling constants, **B:**193–195
Chemical molecules, catalytic reaction network, recursive cell production and evolution, **B:**546–547
autocatalytic phases, **B:**575–581
modeling strategy, **B:**553–557
Chirikov-Taylor map, finite-time Lyapunov exponents, multidimensional Hamiltonian dynamical systems, **B:**508
Christoffel symbols, molecular internal space, Eckart subspace dynamics, **B:**109
Clade techniques, nonmetric multidimensional scaling algorithm and, molecular taxonomy, **B:**326–329
Classical autocorrelation function, vibrational energy relaxation:
cytochrome *c,* CD stretching mode, **B:**197
quantum correction factor and, **B:**185–186
Clusters
heat transfer, quantum energy flow, **B:**221–248
unimolecular reaction kinetics:
energy diffusion, **B:**222–223
proteins, **B:**241–248

Clusters (*Continued*)
protein vibrational energy:
anharmonic decay, **B:**237–241
anomalous subdiffusion, **B:**227–237
water clusters, **B:**223–227
nonmetric multidimensional scaling algorithm, **B:**318–320
protein family, **B:**342–343
survival time distribution, Hamiltonian system multiergodicity, **B:**471–474
Coarse-grained representation:
optimal control theory, Zhu-Botina-Rabitz formula, **A:**450–453
quantum chaos systems:
Rabi state and frequency, **A:**446–448
random vector transition, **A:**449
rotating-wave approximation, **A:**440–449
transition element, **A:**450–453
Coexisting phase, rapid alloying, binary clusters, **B:**156–157
Coherent control, quantum chaos, **A:**436
Cohomology equation, intramolecular dynamics, floppy molecules, canonical perturbation theory, **A:**272–278
Collective coordinates:
molecular internal space, four-body systems isomerization, **B:**118–121
multibasin landscapes, chaotic transition, regularity, local-global postulation, **B:**260–266
Collinear electron-electron-nucleus (eeZ) configuration, Coulomb three-body problem, zero angular momentum, **A:**312–319
Collinear electron-nucleus-electron (eZe) configuration:
Coulomb three-body problem:
mass ratio effect, **A:**319–330
antiproton-proton-antiproton system, **A:**330
triple collision manifold, **A:**320–323
triple collision orbits, **A:**323–329
zero angular momentum, **A:**312–319
Collinear transition state, molecular internal space, democratic centrifugal force, **B:**104–106
Compact clusters, rapid alloying, microcluster dynamics, reaction path enumeration, **B:**172–173
Configuration entropy, onset dynamics, argon clusters, **B:**140
Conjugate action-angle-like coordinates, resonantly coupled isomerizing/dissociating systems, polyad folding and saddle-node bifurcation, **A:**290–296
Constrained dynamics, molecular internal space, gauge field reaction rates, **B:**109–110
Constructive biology, recursive cell production and evolution, catalytic reaction network, **B:**550–557
chemical reaction networks modeling, **B:**553–557
Controlled random matrix, optimal control theory, quantum chaos systems, **A:**438–439
Control property, recursive cell production and evolution, catalytic reaction network, heredity kinetics, **B:**571–573
Control schemes, quantum chaos, **A:**436–437
Core hypercycle network, recursive cell production and evolution:
catalytic reaction networks, **B:**581–583
statistical laws, **B:**591–595
evolution models, **B:**586–588
minority molecules, **B:**582–583
Coriolis coupling, unimolecular reaction rate theory, reaction path analysis, **A:**57–59
Correction factor, atomic clusters, nonlinear canonical transformation, **B:**21–22
Correlation dimension, atomic clusters, power spectra and phase-space, **B:**7–11
Correlation function:
globally coupled Hamiltonian systems, relaxation and diffusion:
equilibrium diffusion, **B:**489–490
quasi-stationary state, **B:**491–493
multichannel isomerization, inter-basin mixing, **B:**52–53
Coulomb three-body problem:
Arnold web model, **A:**378
celestial mechanics, **A:**309–312
collinear eZe case, mass ratio effect, **A:**319–330
antiproton-proton-antiproton system, **A:**330
triple collision manifold, **A:**319–323
triple collision orbits, **A:**323–329
free-fall case, **A:**330–332
two-dimensional case, zero angular momentum, **A:**312–319

Coupling coefficients, vibrational energy relaxation, cytochrome *c,* CD stretching mode, **B:**192–195
Coupling states:
  intramolecular dynamics, adiabatic *vs.* nonadiabatic delocalization, **A:**284–286
  resonantly coupled isomerizing/dissociating systems, polyad folding and saddle-node bifurcation, **A:**287–296
C++ programming, multidimensional phase space, slow dynamics, multi-precision numerical method, **B:**431–435
Critical point:
  fringed tunneling models:
    global structure of branches, **A:**415–417
    multiple trajectories, **A:**423–425
    perturbation strength, **A:**425–426
  multidimensional barrier tunneling:
    Melnikov method, **A:**417–418
    M-set local structure, **A:**414–415
    periodic perturbation effects, **A:**413–414
Curvilinear reaction coordinates, multichannel isomerization, linear surprisal theory, **B:**74–76
Cyclobutanone, unimolecular reaction, isomerization, **A:**100–104
Cyclohexane ring inversion, unimolecular reaction kinetics, **B:**216–221
Cylindrical manifolds:
  chaotic transition, regularity, two-basin landscapes, reactive island theory, **A:**154–163
  multibasin landscapes, chaotic transition, regularity, phase-space transition states, **B:**259–260
  phase-space transition state geometry, two degrees of freedom, **A:**232–234
  unimolecular reaction rate, reactive island theory (RIT), **A:**76–80
  Wigner's transition state dynamics, rank-one saddle phase-space structure, normally hyperbolic invariant manifolds, **A:**188–190
Cytochrome *c,* CD stretching mode, vibrational energy relaxation, **B:**190–200
  carbon monoxide myoglobin (MbCO), **B:**200
  classical calculation, **B:**197
  coupling constants calculation, **B:**192–195
  full width at half maximum spectra, **B:**199–200
  lifetime parameter assignment, **B:**195–196
  quantum calculation, **B:**197–199
  system and bath characteristics, **B:**190–192

Damköhler number, chaotic transitions, inert and reactive substances, **B:**522
Data mining, nonmetric multidimensional scaling:
  algorithm characteristics, **B:**320–321
  basic principles, **B:**317–320
  brain wave analysis, **B:**338–341
  embedded point estimation, **B:**322–323
  gene expression, temporal patterns, **B:**348–349
  microarray data, **B:**343–349
  molecular/morphology comparisons, **B:**329–333
    ferns, **B:**329–332
    green autotrophs, **B:**332–333
  molecular taxonomy, **B:**324–329
  pointwise criterion, **B:**321–322
  protein family, **B:**342–343
  soil bacteria biodiversity, **B:**334–338
Davis-Gray rate theory:
  chaotic transition, regularity, two-basin landscapes, **A:**145–147
  phase-space transition states, Melnikov integral, **A:**358
  unimolecular reaction:
    Gray-Rice isomerization theory, **A:**69–70
    predissociation theory, **A:**30–39
Deactivation rate, unimolecular reaction kinetics, LRMT dynamical corrections to RRKM theory, **B:**215–216
Debye frequency:
  rapid alloying, microcluster dynamics, size effect, **B:**162–164
  slow relaxation, internal degrees of freedom, Hamiltonian systems, **B:**408–412
Deflected diffusion, multidimensional Hamiltonian dynamical systems, resonance and transport structures, **B:**460–462
Delocalization, isomerizing systems, intramolecular dynamics, adiabatic *vs.* nonadiabatic, **A:**278–286

Delta function, vibrational energy relaxation, cytochrome *c,* CD stretching mode, **B:**195–196
Democratic centrifugal force (DCF), molecular internal space:
atomic cluster isomerization dynamics, **B:**90–91
classical equations and metric force, **B:**98–99
four-body systems, PAHC equations of motion, **B:**117–118
gauge field suppression, **B:**111–113
kinematics, **B:**89–90
mass-balance asymmetry and trapping trajectories, **B:**103–106
motion trapping, transition state, **B:**121–123
Density functional theory (DFT), vibrational energy relaxation, basic principles, **B:**180–181
Density of states (DOS):
dissociation dynamics, unimolecular reactions, Hamiltonian equations, **A:**123
heat transfer, quantum energy flow, clusters and macromolecules, **B:**221–248
multibasin landscapes, chaotic transition, regularity, minimalistic 46-bead protein models, **B:**268–270
multichannel isomerization, microcanonical temperature, **B:**55–56
multiexponential lifetime averaging, **B:**63
phase-space transition state geometry, angular momentum, astrophysics applications, **A:**256–261
vibrational energy relaxation, cytochrome *c,* CD stretching mode, **B:**190–192
Density probability, resonantly coupled isomerizing/dissociating systems, polyad folding and saddle-node bifurcation, **A:**293–296
Deterministic diffusion, optimal control theory, controlled quantum kicked rotor, **A:**439–443
Deterministic diffusion, slow relaxation, internal degrees of freedom, mixed-phase space, **B:**387
Devil's staircase trajectory, atomic clusters, regularity, chaos, and ergodicity, **B:**16–20
Diffusion coefficient:
globally-coupled Hamiltonian systems, relaxation and diffusion, angle space diffusion:
equilibrium diffusion, **B:**489–490
Hamilton mean field model, **B:**488–498
nonstationary state, **B:**494–496
quasi-stationary state, **B:**491–493
heat transfer, quantum energy flow, proteins, **B:**242–248
multidimensional Hamiltonian dynamical systems, resonance and transport structures, **B:**440–442
deflected diffusion, **B:**460–462
rapid alloying, microcluster dynamics:
nano-sized clusters, **B:**157–158
radial and surface atoms, **B:**167–170
Diffusive stochastic processes, chaotic transition, regularity, two-basin landscapes, saddle regions, dynamical regularity, **A:**149–151
Dimensionality:
atomic clusters, phase-space transition states, **B:**7–11
multibasin landscapes, chaotic transition, regularity, temperature dependency in folding dynamics, **B:**293–299
phase-space transition states:
Hamiltonian dynamics, **A:**221–223
tangency and, **A:**381–385
slow relaxation, internal degrees of freedom, mixed-phase space, **B:**386–387
Diophantine condition, slow relaxation, mixed-phase space, **B:**380–387
Dirac coordinate eigenstate, unimolecular reaction rate, semiclassical approximation, rigorous quantum rate, **A:**115–116
Discrete variable representation (DVR), unimolecular reaction rate, wave packet dynamics, **A:**124–128
Dispersion relation, heat transfer, quantum energy flow, anomalous subdiffusion, **B:**231–238
Dissociation dynamics, unimolecular reactions, Hamiltonian equations, **A:**116–123
DNA molecules, catalytic reaction network, recursive cell production and evolution, minority control hypothesis, **B:**557–573

Double-well systems:
chaotic transition, regularity, two-basin landscapes, reactive island theory, **A:**153–163
multidimensional barrier tunneling, **A:**404–406
slow relaxation, internal degrees of freedom, Hamiltonian systems, **B:**414–418
unimolecular reaction rate:
Gray-Rice isomerization theory *vs.* reactive island theory, **A:**82–84
isomerization in, **A:**84–88
Dunham expansion model, resonantly coupled isomerizing/dissociating systems:
anharmonicity, **A:**286–287
polyad folding and saddle-node bifurcation, **A:**287–296
Dynamical heterogeneity, slow relaxation, internal degrees of freedom, Hamiltonian systems, molecular systems, **B:**392
Dynamical localization, unimolecular reaction rate, quantum transport, classically chaotic systems, **A:**128–129
Dynamical propensity rule, chaotic transition, regularity, two-basin landscapes, saddle regions, dynamical regularity, **A:**151
Dyson's loose reproduction system, recursive cell production and evolution, catalytic reaction networks, **B:**549–550
kinetic heredity, **B:**571–573

Eckart frame, molecular internal space:
gauge-dependent expression, rotation-vibration energy, **B:**93
gauge field isomerization suppression, **B:**106–113
applications, **B:**110–113
Eckart subspace dynamics, **B:**107–109
four-body systems, **B:**123–125
quantitive role, **B:**106–107
reaction rate effects, **B:**109–110
gauge field suppression, subspace parameterization, **B:**110–113
kinematics, **B:**89–90
Eckart type potential:
fringed tunneling, semiclassical method, **A:**406–407
multidimensional barrier tunneling, periodic perturbation effects, **A:**412–414
Edge-bridging saddle, atomic clusters, regularity, chaos, and ergodicity, **B:**16–20
Edge running (ER), rapid alloying, microcluster dynamics:
saddle point energy distribution, **B:**175
Ehrenfest adiabatic state, isomerizing systems, intramolecular dynamics, **A:**278–286
Eigen's hypercycle, recursive cell production and evolution, catalytic reaction networks, **B:**547–549
Eigenstates, intramolecular dynamics, adiabatic *vs.* nonadiabatic delocalization, **A:**278–286
Eigenvalues:
atomic clusters, basic principles, **B:**4
molecular internal space, three-atom clusters, isomerization dynamics, **B:**96–97
phase-space transition state geometry:
one degree of freedom model, linearized Hamiltonian, **A:**224–227
three degrees of freedom, Hénon-Heiles potential, **A:**240–244
Wigner's transition state dynamics:
hydrogen cyanide stationary point geometry, **A:**203–205
saddle region energy landscapes, stability analysis, **A:**181–182
Eigenvector components, unimolecular reaction kinetics, quantum energy flow, **B:**213–214
Eigenvector-following algorithm, onset dynamics, argon clusters, gradient external path, **B:**132–133
Einstein-Brillouin-Keller (EBK) quantization rule:
resonantly coupled isomerizing/dissociating systems, polyad folding and saddle-node bifurcation, **A:**288–296
three-body problem, **A:**306–309
collinear eZe configuration, **A:**330
Einstein-Shannon entropy, fluctuation-dissipation theorem, excess heat production, Boltzmann equilibrium distribution, **B:**355–356
Elastic bounce phenomenon, *n*-body problem in celestial mechanics, **A:**310–312

Embedding theorems:
multibasin landscapes, chaotic transition, regularity, **B:**305–309
false nearest-neighbor, **B:**289–292
future research issues, **B:**300–302
state-space structures, **B:**285–288
temperature dependence in dimensionality of folding dynamics, **B:**296–299
theoretical principles, **B:**302–309
nonmetric multidimensional scaling algorithm, **B:**320–321
brain wave analysis, **B:**338–341
fern genotype/phenotype, **B:**330–332
illustrative case, **B:**323–324
microarray data, **B:**345–349
molecular taxonomy case, **B:**324–329
point estimation, **B:**322–323
protein structures, **B:**342–344
soil bacteria biodiversity, **B:**334–338
Energy barrier tunneling, global dynamics, **A:**404–406
Energy diffusion, heat transfer, quantum energy flow:
anomalous subdiffusion, **B:**232–238
clusters and macromolecules, **B:**222–223
Energy gain equation, multidimensional barrier tunneling, low-frequency approximation, **A:**420–422
Energy gap measurement, phase-space transition states, Melnikov integral, **A:**364–371
Energy level spacings, atomic clusters, distribution in, **B:**4–5
Energy nonstationarity, multibasin landscapes, chaotic transition, regularity, protein structures, **B:**270–285
bending energy fluctuation, **B:**278–282
bond energy flucation, **B:**277–278
torsional angle energy fluctuation, **B:**282–285
Energy surfaces, Wigner's transition state dynamics:
Lie transformation, normal-form coordinates, **A:**197–198
saddle regions, phase-space analysis, **A:**182–183
Entropy deficiency:
fluctuation-dissipation theorem, excess heat production, **B:**354–355
multichannel isomerization, linear surprisal theory, **B:**73–74
Equi-energy surface gaps, phase-space transition states:
Arnold model, **A:**371–377
Melnikov integral, **A:**364–371
multidimensional chaos crisis, **A:**393–395
Equilibrium diffusion, globally-coupled Hamiltonian systems, relaxation and diffusion, **B:**489–490
Ergodicity:
atomic clusters:
local characteristics, **B:**11–20
power spectra and phase-space dimensions, **B:**7–11
Hamiltonian system multiergodicity and nonstationarity:
complex behaviors, **B:**474–475
stagnant motion deviation, **B:**466–469
survival time distribution, clustering motions, **B:**471–474
universality conjecture, **B:**469–471
multichannel isomerization:
global mixing, **B:**47
lifetime averaging uniformity, **B:**35–36
liquid-like dynamics, **B:**67–70
slow relaxation, internal degrees of freedom, Hamiltonian systems, **B:**375–378
nearly integrable systems, **B:**393–398
Error rate, recursive cell production and evolution, autocatalytic network, **B:**574–595
Euclidean distance:
Hamiltonian system multiergodicity, stagnant motion deviation, **B:**466–469
heat transfer, quantum energy flow, anomalous subdiffusion, **B:**230–238
molecular internal space, Eckart subspace dynamics, **B:**107–109
multibasin landscapes, chaotic transition, regularity, state-space structural embedding, **B:**289–292
Euler angles, molecular internal space, gauge-dependent expression, rotation-vibration energy, **B:**91–93
Euler-Lagrangian equations, molecular internal space, gauge-invariant energy, **B:**94
Evolution models, recursive cell production and evolution:
autocatalytic reaction networks, **B:**585–588
catalytic reaction network, itinerant dynamics, **B:**596

Evolvability, recursive cell production and evolution, catalytic reaction networks, **B:**566–567
Excess heat production, fluctuation-dissipation theorem:
  Boltzmann equilibrium distribution, **B:**355–359
    hysteresis loop area, **B:**358–359
    thermodynamics, **B:**355–356
  Jarzynski's nonequilibrium work relation, **B:**368–369
  nonergodic adiabatic invariant, anomalous variance, **B:**361–368
    Hamiltonian chaotic systems, **B:**363–367
    microcanonical distribution, **B:**361–363
  second law, **B:**369–370
  superstatistical equilibrium distributions, **B:**359–361
Exponential decay, multichannel chemical isomerization, lifetime averaging uniformity, **B:**39–42
Exponential relation, microcanonical temperature and average lifetimes:
  linear surprisal theory, **B:**74–80
  multichannel isomerization, **B:**62–70
    liquid-like ergodicity and nonergodicity, **B:**67–69
    M_7 single exponential form case study, **B:**65–67
    multiexponential form, **B:**62–63
    single exponential form, **B:**64–65

"Falling cat" phenomenon, molecular internal space:
  Eckart subspace dynamics, **B:**108–109
  kinematics, **B:**88–90
False nearest-neighbor (FNN), multibasin landscapes, chaotic transition, regularity, state-space structural reconstruction, **B:**288–292
Faster-than-classical quantum anomalous diffusion, unimolecular reaction rate, **A:**134–137
Fast reaction regimes, chaotic transitions, inert and reactive substances, **B:**532–534
Fast switching states, recursive cell production and evolution, catalytic reaction networks, autocatalytic phases, **B:**578–581
Fast transition pathways, multidimensional Hamiltonian, resonance and transport structures, **B:**454–457
Feenberg renormalized perturbation, unimolecular reaction kinetics, quantum energy flow, **B:**212–214
Fenichel normal form, phase-space transition states:
  chaotic itinerancy, **A:**388–389
  Lie perturbation theory, **A:**354–358
  Melnikov integral, **A:**361–371
  normally hyperbolic invariant manifolds, **A:**338–340, **A:**345–352
Fermi-Pasta-Ulam (FPU) computer experiments:
  Hamiltonian system, multiergodicity, **B:**471
  slow relaxation, internal degrees of freedom, Hamiltonian systems:
    hypothesis validity, **B:**406–412
    mixed-phase space, **B:**381–387
    molecular systems, **B:**387–392
    nearly integrable systems, **B:**392–398
Fermi resonance, resonantly coupled isomerizing/dissociating systems:
  anharmonicity, **A:**286–287
  high energy bifurcations, **A:**297–301
  polyad folding and saddle-node bifurcation, **A:**287–296
Fermi's golden rule:
  heat transfer, quantum energy flow, protein vibrational states, anharmonic decay, **B:**238–241
  unimolecular reaction kinetics, quantum energy flow, **B:**214
  vibrational energy relaxation, **B:**180
    general formula, **B:**183–184
    perturbation expansion, **B:**182
Fern genotype/phenotype, nonmetric multidimensional scaling algorithm and, **B:**329–332
Few-dimensional systems, unimolecular reaction rate theory, phase-space structure, bottlenecks, **A:**18–19
Fick equation, chaotic transitions, inert and reactive substances, **B:**522
  FKPP reaction, **B:**531
Final-state interaction, multichannel isomerization, linear surprisal theory, **B:**78

Finger formation pattern, unimolecular reaction rate, wave packet dynamics, **A:**126–128
Finite-horizon configuration, slow relaxation, internal degrees of freedom, mixed-phase space, **B:**387
Finite-time Lyapunov exponents:
multidimensional Hamiltonian dynamical systems:
instability properties, **B:**512–517
correction, **B:**516
order of motion, **B:**512–514
qualitative different instabilities, **B:**514–516
QR method corrections, **B:**506–512
correction procedure, **B:**508–511
finite-time error, **B:**507–508
standard method, **B:**506–507
vectors, **B:**503–505
phase-space transition states, multidimensional chaos crisis, **A:**393–395
First-order kinetics, chaotic transition, regularity, two-basin landscapes, reactive island theory, **A:**158–163
Fisher-Kolmogorov-Petrovsky-Piskunov (FKPP) reaction, chaotic transitions, inert and reactive substances, **B:**521–522
ARD equation, **B:**530–531
Five-body systems, celestial mechanics, **A:**311–312
Floater hopping (FH), rapid alloys:
binary clusters, **B:**174–175
microcluster dynamics, **B:**176
Floaters, rapid alloying, binary clusters:
floppy surface atom reaction paths, **B:**170–171
reaction path enumeration, **B:**172–173
saddle point energy distribution, **B:**173–174
Floppy molecules, canonical perturbation theory, **A:**269–278
Floppy surface atoms, rapid alloying, microcluster dynamics, **B:**170–171
Floquet solution, fringed tunneling, semiclassical method, **A:**407
Fluctuation-dissipation theorem:
excess heat production:
Boltzmann equilibrium distribution, **B:**355–359
hysteresis loop area, **B:**358–359
thermodynamics, **B:**355–356
Jarzynski's nonequilibrium work relation, **B:**368–369
nonergodic adiabatic invariant, anomalous variance, **B:**361–368
Hamiltonian chaotic systems, **B:**363–367
microcanonical distribution, **B:**361–363
second law, **B:**369–370
superstatistical equilibrium distributions, **B:**359–361
recursive cell production and evolution, catalytic reaction networks, **B:**593–595
Flux dynamics, Wigner's transition state dynamics, rank-one saddle phase-space structure, transition state pathway, **A:**193–194
Fokker-Planck equation:
chaotic transitions, inert and reactive substances, **B:**520–522
recursive cell production and evolution, catalytic reaction network, **B:**591–595
Folding dynamics, multibasin landscapes, chaotic transition, regularity, temperature dependence in dimensionality of, **B:**293–299
Foliation, phase-space transition states, normally hyperbolic invariant manifolds, **A:**349–352
Force-force-correlation function approximations, vibrational energy relaxation, **B:**186–190
first term contribution, **B:**187–190
Taylor expansion, **B:**186–187
Forward reactive trajectories, Wigner's transition state dynamics, rank-one saddle phase-space structure:
normally hyperbolic invariant manifolds, **A:**188–190
transition state principles, **A:**191
Four-body systems, molecular internal space, **B:**113–125
collective coordinates, isomerization mechanism, **B:**118–121
gauge field isomerization suppression, Eckart frame, **B:**123–125
principal-axis hyperspherical coordinates, equations of motion, **B:**114–118

transition state trapped motion, DCF effects, **B:**121–123
Four-dimensional degrees of freedom:
phase-space transition state geometry, **A:**243–244
phase-space transition states:
Arnold web model, **A:**375–377
tangency and, **A:**381–385
Four-dimensional free rotor, unimolecular fragmentation mapping, Morse-like kicking field, **A:**27–30
Fourier transform:
chaotic transitions, inert and reactive substances, standard and anomalous diffusion, **B:**525–527
intramolecular dynamics, floppy molecules, canonical perturbation theory, **A:**271–278
multidimensional Hamiltonian systems, resonance and transport, **B:**439
vibrational energy relaxation:
basic principles, **B:**180
cytochrome *c,* CD stretching mode, **B:**197
symmetrized autocorrelation function, **B:**184–185
Fractal distribution:
heat transfer, quantum energy flow, anomalous subdiffusion, **B:**230–238
multichannel isomerization, inter-basin mixing, turning points, **B:**51–53
"Fraction" modes, heat transfer, quantum energy flow, proteins, **B:**241–248
Free-fall problem, Coulomb three-body structures, **A:**330–332
"Freezing" energy, multichannel chemical isomerization, multi-basin potential, **B:**30–31
Frequency-dependent energy diffusion, heat transfer, quantum energy flow, proteins, **B:**243–248
Frequency filter, heat transfer, quantum energy flow, **B:**225–227
Frequency space, multidimensional Hamiltonian, resonance and structure, **B:**442–445
Fringed tunneling models:
global branch structures, **A:**415–417
multiple characteristic trajectories, **A:**422–425
perturbation strength, **A:**425–426
semiclassical technique, **A:**406–407
branch global structures, **A:**415–417
complex-domain method, **A:**407–410
two-dimensional barriers, **A:**428–431
example, **A:**428–431
Froeschlé mapping, multidimensional Hamiltonian, resonance and transport, **B:**438–439
diffusion coefficient, **B:**440–442
frequency and phase space, **B:**443–445
resonance overlap, **B:**457–460
Front propagation, chaotic transitions, inert and reactive substances:
thin front dynamics, **B:**537–540
Fukui's criterion, onset dynamics, argon clusters, **B:**130–131
Full width at half maximum (FWHM), vibrational energy relaxation, cytochrome *c,* CD stretching mode, **B:**199–200
Fully developed chaotic regimes, chaotic transition, regularity, two-basin landscapes, **A:**146–147
saddle crossing stochasticity, **A:**166
"Funnel-like" phenomenon, multibasin landscapes, chaotic transition, regularity, minimalistic 46-bead protein models, **B:**267–270

Γ periodic orbit, phase-space transition state geometry, two degrees of freedom, **A:**230–234
Gap problem, phase-space transition states:
Arnold web model, **A:**377
Melnikov integral, **A:**397–398
Gaspard-Rice mapping:
quantum suppression of Arnold diffusion, **A:**134
unimolecular fragmentation, Morse-like kicking field:
four-dimensional rotor, **A:**27–30
two-dimensional free particles, **A:**24–27
Gauge field isomerization suppression, molecular internal space, **B:**106–113
applications, **B:**110–113
Eckart subspace dynamics, **B:**107–109
four-body systems, Eckart frame, **B:**123–125
quantitive role, **B:**106–107
reaction rate effects, **B:**109–110

Gauge-invariant expression, molecular internal space:
classical equations and metric force, **B:**97–99
metrics and kinetic energy, **B:**93–94
Gauge-theoretical formalism, molecular internal space:
kinematics, **B:**88–90
n-body systems:
gauge-invariant kinetic energy expression, **B:**93–94
rotation-vibration kinetic energy, **B:**91–93
Gaussian distribution, recursive cell production and evolution, catalytic reaction networks, **B:**591–595
Gaussian Orthogonal Ensemble (GOE):
atomic clusters, energy level distribution, **B:**4–5
optimal control theory, perfect control solution, **A:**454–456
quantum chaos systems, random matrix system, **A:**438–439
Gaussian random vectors, quantum chaos systems, optimal control theory, **A:**439–441
Gaussian stochastic force, multibasin landscapes, chaotic transition, regularity, Berendsen algorithm, constant-temperature MD, **B:**309–310
Gaussian wavepacket, quantum chaos systems, **A:**437
Gene expression:
catalytic reaction network, recursive cell production and evolution, **B:**545–546
intermingled hypercycle network production, **B:**595–596
itinerant dynamics, **B:**596
minority control hypothesis, **B:**557–573
evolvability, **B:**566–567
experimental protocol, **B:**567–571
growth speed, **B:**565
kinetic theory, heredity and, **B:**571–573
model parameters, **B:**557–561
molecule chemical composition, **B:**565–566
molecule preservation, **B:**565
stochastic results, **B:**561–564
nonmetric multidimensional scaling algorithm and:
microarray data, **B:**345–348
temporal patterns, **B:**348–349
Genotype/phenotype analysis, nonmetric multidimensional scaling algorithm and, **B:**329–333
ferns, **B:**329–332
green autotrophs, **B:**332–333
Geometrical optics limit, chaotic transitions, inert and reactive substances:
G-equation, **B:**534–537
Geometrics of phase-space:
angular momentum, **A:**247–261
astrophysics applications, **A:**256–261
inelastic scattering, **A:**257–261
rotating frame dynamics, **A:**248–256
relative equilibrium, **A:**249–251
van der Waals complex, **A:**251–256
atomic clusters:
regularity, chaos, and ergodicity, **B:**14–20
chaotic transition, regularity, two-basin landscapes, **A:**151–163
fringed tunneling, multiple trajectories, **A:**422–425
Hamiltonian dynamics, **A:**219–223
dimensions, **A:**221–223
general equations, **A:**219–221
multichannel isomerization, **B:**27–28
inter-basin mixing, **B:**45–53
Markov-type isomers, **B:**45–47
reaction tube bifurcation, **B:**47–50
time scale, **B:**50–51
turning point fractal dimension, **B:**51–53
n degrees of freedom, **A:**234–247
Hénon-Heiles potential, **A:**237–244
normally hyperbolic invariant manifolds, dimensions and, **A:**234–237
geometric characteristics, **A:**236–237
linear regime, **A:**235–236
tri-body dynamics, zero angular momentum, **A:**244–247
one degree of freedom, **A:**223–228
linear case, linearization, **A:**223–227
nonlinearities, **A:**227
two degrees of freedom, **A:**228–234
linear theory, **A:**229–230
periodic orbit dividing serfaces, **A:**230–234
Wigner's transition state dynamics, **A:**174–175
stationary points, **A:**179

Geometric structure:
G-equation, chaotic transitions, inert and reactive substance, geometrical optics limit, **B:**534–537
Gibbs free energy:
binary clusters, microcluster dynamics, rapid alloying, **B:**156–157
globally-coupled Hamiltonian systems, relaxation and diffusion, Hamilton mean field (HMF) model, **B:**481
Global dynamics:
fringed tunneling branches, **A:**415–417
Hamiltonian systems relaxation and diffusion:
angle space diffusion, **B:**488–498
equilibrium diffusion, **B:**489–490
nonstationary state, **B:**494–496
quasi-stationary state, **B:**491–493
model and initial condition, **B:**480–481
probability distribution function of momenta, **B:**484–487
relaxation process, **B:**481–484
slow dynamics, **B:**484
multidimensional barrier tunneling, **A:**402–406
phase-space transition states:
Arnold diffusion model, **A:**371–377
chaotic itinerancy, **A:**385–389
Lie perturbation, **A:**352–358
many degrees of freedom, **B:**425–427
Melnikov integral, **A:**358–371
examples, **A:**395–398
multidimensional chaos, **A:**392–395
normally hyperbolic invariant manifolds, **A:**338–340, **A:**345–352
breakdown, **A:**389–392
singular perturbation theory, **A:**342–345
skeleton bifurcation, **A:**340–341
tangency principles, **A:**341–342, **A:**377–385
Global mixing, multichannel isomerization, **B:**46–47
Gō-like BLN protein models, multibasin landscapes, chaotic transition, regularity:
basic properties, **B:**267–270
nonstationarity in energy fluctuations, **B:**270–285
temperature dependence in dimensionality of folding dynamics, **B:**295–299
G-protein genes, nonmetric multidimensional scaling algorithm and, microarray data, **B:**345–348
Gradient external path (GEP), onset dynamics, argon clusters, **B:**131–133
Gram-Schmidt orthogonalization, unimolecular reaction rate theory, reaction path analysis, **A:**56–59
Gray-Rice-Davis rate theory, unimolecular reaction:
predissociation, ARRKM theory, **A:**39–41
Gray-Rice isomerization theory, unimolecular reaction rate, **A:**66–70
cyclobutanone, **A:**102–104
reactive island theory (RIT) *vs.,* **A:**80–84
Zhao-Rice approximation, **A:**73–75
Green autotrophs, nonmetric multidimensional scaling algorithm and, **B:**332–333
Green fluorescent protein (GFP), heat transfer, quantum energy flow:
anomalous subdiffusion, **B:**228–238
proteins, **B:**242–248
Green function, fringed tunneling, semiclassical method, **A:**407
Growth speed control, recursive cell production and evolution, catalytic reaction networks, **B:**565
Gumbel distribution, Hamiltonian system, multiergodicity, **B:**474–475
Gutzwiller trace formula, three-body problem, **A:**306–309
Gyration radii, molecular internal space:
democratic centrifugal force, **B:**104–106
four-body systems, PAHC equations of motion, **B:**115–118
three-atom clusters, isomerization dynamics, **B:**96–97
topographical mapping, **B:**99–103
Gyration space, molecular internal space:
classical equations and metric force, **B:**97–99
topographical mapping, **B:**101–103

Hamiltonian systems:
atomic clusters, basic principles, **B:**4
chaotic systems, fluctuation-dissipation theorem, excess heat production, adiabatic invariant, **B:**363–367
Coulomb three-body problem, zero angular momentum, **A:**312–319

Hamiltonian systems (*Continued*)
fringed tunneling, semiclassical method, **A:**406–407
globally coupled Hamiltonian systems, relaxation and diffusion:
angle space diffusion, **B:**488–498
equilibrium diffusion, **B:**489–490
nonstationary state, **B:**494–496
quasi-stationary state, **B:**491–493
model and initial condition, **B:**480–481
probability distribution function of momenta, **B:**484–487
relaxation process, **B:**481–484
slow dynamics, **B:**484
intramolecular dynamics:
floppy molecules, canonical perturbation theory, **A:**269–278
resonantly coupled isomerizing/dissociating systems:
high energy bifurcations, **A:**297–301
polyad folding and saddle-node bifurcation, **A:**288–296
multichannel chemical isomerization, multi-basin potential, **B:**28–30
multidimensional dynamical transport and resonance:
basic principles, **B:**450–452
deflected diffusion, **B:**460–462
diffusion coefficient, **B:**440–442
fast transition pathway, **B:**454–457
frequency and phase space, **B:**442–445
model components, **B:**438–439
morphological change, **B:**445–447
overlap, **B:**457–460
residence time distribution, **B:**447–450
rotation number, **B:**439–440
transition diagram, **B:**452–454
multiergodicity and nonstationarity:
complex behaviors, **B:**474–475
stagnant motion deviation, **B:**466–469
survival time distribution, clustering motions, **B:**471–474
universality conjecture, **B:**469–471
phase-space transition states, **A:**219–223
angular momentum:
astrophysics inelastic scattering, **A:**257–261
rotating frame dynamics, **A:**249–256
Arnold web model, **A:**372–377
dimensions, **A:**221–223
general equations, **A:**219–221
global reaction dynamics, **A:**341–342
Lie perturbation theory, **A:**353–358
Melnikov integral, **A:**358–371
tangency, **A:**378–385
three degrees of freedom, Hénon-Heiles potential, **A:**237–244
triatomic dynamics, zero angular momentum, **A:**244–247
two degrees of freedom, periodic orbit dividing surfaces, **A:**230–234
quantum chaos systems:
kicked rotor system, **A:**442–443
random matrix system, **A:**438–439
slow relaxation, internal degrees of freedom:
FPU models, **B:**398–403
mixed-phase space systems, anomalous transport, **B:**379–387
molecular systems, **B:**387–392
nearly integrable picture, applicability, **B:**392–398
validity of hypothesis, **B:**403–412
unimolecular reaction rate:
dissociation techniques, **A:**116–123
isomerization:
cyclobutanone molecule, **A:**100–104
HCN to CHN, **A:**96–100
normally hyperbolic invariant manifolds (NHIM), **A:**7–8
phase-space structure:
canonical transformation, **A:**9–10
normally hyperbolic invariant manifolds (NHIM), **A:**20–22
quantum energy flow, local random matrix theory, **B:**212–214
quantum suppression of Arnold diffusion, **A:**131–134
Zhao-Rice approximation, **A:**41–54
Wigner's transition state dynamics:
Lie transformation normalization, **A:**194–198
rank-one saddle phase-space structure, **A:**183–184
Hamilton-Jacobi equation:
unimolecular reaction rate theory, phase-space structure, **A:**9–10
action/angle variables, **A:**11–12
Wigner's transition state dynamics, hydrogen cyanide isomerization model, **A:**200–202

Hamilton mean field (HMF) model, globally-coupled Hamiltonian systems, relaxation and diffusion:
initial condition, **B:**480–481
probability distribution function of momenta, **B:**484–487
relaxation process, **B:**481–484
Harmonic approximation, unimolecular reaction rate, isomerization theory, cyclobutanone, **A:**103–104
Harmonic oscillator:
heat transfer, quantum energy flow, anomalous subdiffusion, **B:**229–238
intramolecular dynamics, floppy molecules, canonical perturbation theory, **A:**273–278
onset dynamics, argon clusters, configuration entropy, **B:**140
phase-space transition states:
Lie perturbation theory, **A:**353–358
one degree of freedom model, **A:**225–227
slow relaxation, internal degrees of freedom, Hamiltonian systems, **B:**399–403
vibrational energy relaxation:
force-force-correlation function approximations, **B:**187–190
quantum correction factor and, **B:**186
Harthcock-Lane potential energy surface, unimolecular reaction rate, 3-phospholene isomerization, **A:**91–96
Hausdorff dimension, atomic clusters, power spectra and phase-space dimensions, **B:**5–11
Heat of solution, rapid alloying, microcluster dynamics, numerical results, **B:**164–165
Heat reservoir, rapid alloying, microcluster dynamics, nano-sized clusters, **B:**158–160
Heat transfer:
clusters and macromolecules, quantum energy flow, unimolecular reaction kinetics, **B:**221–248
energy diffusion, **B:**222–223
proteins, **B:**241–248
protein vibrational energy:
anharmonic decay, **B:**237–241
anomalous subdiffusion, **B:**227–237
water clusters, **B:**223–227
quantum energy flow, **B:**206
Heaviside step function, multichannel isomerization, inter-basin mixing, **B:**52–53
Heisenberg representation, unimolecular reaction rate, quantized ARRKM theory *vs.* rigorous quantum rate, **A:**112–114
Helium-chloride ($HeCl_2$), unimolecular reaction rate, predissociation theory, **A:**63–66
Helium-iodine-chloride, unimolecular reaction rate, predissociation theory, **A:**66
Helium-iodine (HeI_2), unimolecular reaction:
Gray-Rice-Davis ARRKM theory, **A:**39–41
predissociation:
Davis-Gray analysis, **A:**35–39
intramolecular bottleneck, **A:**60–61
Morse potentials, **A:**59–60
rate constants, **A:**60
Hénon-Heiles potential:
globally coupled Hamiltonian systems, **B:**478–480
multichannel isomerization, **B:**83
phase-space transition state geometry:
angular momentum, **A:**248
three degrees of freedom, **A:**237–244
Heredity, recursive cell production and evolution, catalytic reaction network, **B:**544–546
kinetic theory, **B:**571–573
Hessian matrices:
multichannel isomerization, microcanonical temperature, single exponential form, **B:**66–67
onset dynamics, argon clusters:
cell partition, potential energy surfaces, **B:**133–134
gradient external path, **B:**132–133
phase-space transition state geometry, one degree of freedom model, linearized Hamiltonian, **A:**224–227
phase-space transition states, Lie perturbation theory, **A:**353–358
vibrational energy relaxation, cytochrome *c,* CD stretching mode, **B:**190–192
coupling coefficients, **B:**192–195
Heteroclinicity, multidimensional barrier tunneling:
global dynamics, **A:**405–406

Heterogeneous scenario, slow relaxation, internal degrees of freedom, Hamiltonian systems:
FPU models, **B:**398–403
molecular systems, **B:**392
Hilbert space, unimolecular reaction rate theory:
faster-than-classical anomalous diffusion, **A:**134–137
quantum transport, cantori systems, **A:**129–131
Homeochaos, catalytic reaction networks, **B:**582
Homoclinic tangency:
chaotic transition, regularity, two-basin landscapes:
reactive island theory, **A:**155–163
transition state theory, **A:**145–147
phase-space transition states, Melnikov integral, **A:**361–371
unimolecular fragmentation mapping, Morse-like kicking field, two-dimensional free particle, **A:**24–27
unimolecular reaction rate:
normally hyperbolic invariant manifolds (NHIM), **A:**21–22
reactive island theory (RIT), **A:**78–80
Homogeneous scenario, slow relaxation, internal degrees of freedom, Hamiltonian systems, molecular systems, **B:**392
Homology equation, Wigner's transition state dynamics, Lie transformation normalization, **A:**195–197
Hopping mechanism, heat transport, quantum energy flow, **B:**250–251
Horseshoe dynamics. *See* Chaos theory
Husimi representation, optimal control theory, kicked rotor system, **A:**443
Huygens dynamics, chaotic transitions, inert and reactive substances, front propagation, **B:**538–540
Hydrodynamics, singular perturbation theory, **A:**345
Hydrogen-bond network, slow relaxation, internal degrees of freedom, Hamiltonian systems, molecular systems, **B:**388–392
Hydrogen cyanide (HCN):
intramolecular dynamics:
adiabatic *vs.* nonadiabatic delocalization, **A:**278–286
floppy molecules, canonical perturbation theory, **A:**269–278
canonical transformations, **A:**301–302
isomerization to CHN, unimolecular reaction rate theory:
potential energy surfaces, **A:**96–100
Wigner's transition state dynamics, isomerization, **A:**198–212
Hamiltonian equation, **A:**200–202
model system, **A:**199–200
nonreactive degrees of freedom quantization, **A:**211–212
normal form transformation, **A:**205–207
stationary flow points, **A:**202–205
visualization techniques, **A:**207–210
Hydrogen isocyanide (HNC):
hydrogen cyanide isomerization to, **A:**198–212
intramolecular dynamics:
adiabatic *vs.* nonadiabatic delocalization, **A:**278–286
floppy molecules, canonical perturbation theory, **A:**269–278
Hyperbolicity:
Coulomb three-body problem, collinear eZe configuration, triple collision orbits, **A:**325–329
phase-space transition states:
breakdown of, **A:**341, **A:**389–392
chaotic itinerancy, **A:**388–389
Melnikov integral, **A:**366–371
n degrees of freedom structures, **A:**237
normally hyperbolic invariant manifolds, **A:**345–352
slow relaxation, internal degrees of freedom, Hamiltonian systems, anomalous transport, mixed-phase space, **B:**379–387
Hypercycle structures, recursive cell production and evolution, catalytic reaction networks, **B:**548–549
autocatalytic phases, **B:**578–581
evolution models, **B:**585–588
intermingled hypercycle network, **B:**581–583
kinetics of heredity, **B:**571–573
Hypothesis validity, slow relaxation, internal degrees of freedom, Hamiltonian systems, **B:**403–412
Hysteresis loop, fluctuation-dissipation theorem, excess heat production, **B:**358–359

1/*f*-noise spectral density, multibasin landscapes, chaotic transition, regularity, nonstationarity in energy fluctuations, **B:**272–280
Incident waves, fringed tunneling models, two-dimensional barrier systems, **A:**429–431
Induction time distribution, Hamiltonian system, multiergodicity, **B:**471
Inelastic scattering, phase-space transition state geometry, angular momentum, **A:**257–261
Inequality conditions, phase-space transition states, Arnold web model, **A:**375–377
Inert substances, chaotic transitions:
  standard and anomalous diffusion, **B:**523–527
  strong anomalous diffusion, **B:**527–530
Infinite-horizon configuration, slow relaxation, internal degrees of freedom, mixed-phase space, **B:**387
Inherent structure (IS) surfaces, slow relaxation, internal degrees of freedom, Hamiltonian systems, molecular systems, **B:**388–392
Inhomogeneity, slow relaxation, internal degrees of freedom, Hamiltonian systems, molecular systems, **B:**390–392
Initial value representation (IVR), unimolecular reaction rate, semiclassical approximation, rigorous quantum rate, **A:**114–116
Input-boundary condition, multidimensional barrier tunneling, low-frequency approximation, **A:**422
Instability properties, multidimensional Hamiltonian dynamical systems, finite-time Lyapunov exponents, **B:**512–517
  correction, **B:**516
  order of motion, **B:**512–514
  qualitative different instabilities, **B:**514–516
Instantaneous normal mode (INM) analysis, slow relaxation, internal degrees of freedom, Hamiltonian systems:
  hypothesis validity, **B:**404–412
  molecular systems, **B:**391–392
Instanton trajectory, multidimensional tunneling, **A:**402–406
Integrable systems, global motion, many degrees of freedom, **B:**425–427
Integration paths, classical trajectories, multidimensional barrier tunneling:
  periodic perturbation effects, **A:**412–414
  static barriers, **A:**410–412
Interatomic distances, Wigner's transition state dynamics, hydrogen cyanide isomerization model, **A:**199–200
  Hamiltonian equations, **A:**200–202
Inter-basin mixing, multichannel isomerization, **B:**45–53
  reaction tube bifurcation, **B:**47–50
  time scale, **B:**50–51
  turning point fractal dimension, **B:**51–53
Interlayer mixing (IM), rapid alloying, microcluster dynamics:
  future research issues, **B:**176
  saddle point energy distribution, **B:**175
Intermediate, semi-chaotic regime, chaotic transition, regularity, two-basin landscapes, saddle regions, dynamical regularity, **A:**149–151
Intermingled hypercycle network (IHN), recursive cell production and evolution, catalytic reaction networks, **B:**581–583
  evolution models, **B:**585–588
Intramolecular energy transfer:
  chaotic transition, regularity, two-basin landscapes, dynamical bottlenecks, **A:**166–168
  dissociation dynamics:
    resonantly coupled systems, **A:**286–301
      high-energy bifurcations, **A:**296–301
      polyad folding and saddle-node bifurcations, **A:**287–296
    unimolecular reactions, Hamiltonian equations, **A:**117–123
  isomerization pathways:
    nearly separable systems, **A:**269–286
      adiabatic *vs.* nonadiabatic delocalization, **A:**278–286
      canonical perturbation theory, floppy molecules, **A:**269–278
    resonantly coupled systems, **A:**286–301
      high-energy bifurcations, **A:**296–301
      polyad folding and saddle-node bifurcations, **A:**287–296

Intramolecular energy transfer (*Continued*)
unimolecular reaction rate theory:
Davis-Gray predissociation analysis, **A:**34–39
phase-space quantum scars, **A:**108
3-phospholene isomerization, **A:**94–96
quantum transport, cantori systems, **A:**129–131
Zhao-Rice approximation:
bottleneck dividing surface, **A:**46–48
isomerization theory, **A:**72–75
zeroth-order rate constant, bottleneck crossing, **A:**48–50
Intramolecular vibrational energy relaxation (IVR):
heat transport, **B:**249–251
phase-space transition states:
Arnold web model, **A:**372–377
normally hyperbolic invariant manifold connections, **A:**340
unimolecular reaction kinetics:
cyclohexane ring inversion, **B:**217–221
LRMT dynamical corrections to RRKM theory, **B:**216
quantum energy flow, **B:**208–221
vibrational energy relaxation, **B:**200–201
Invariant measure, unimolecular reaction rate theory, phase-space structure, **A:**10–11
Invariant structures:
chaotic transition, regularity, two-basin landscapes, saddle crossing stochasticity, **A:**165–166
multidimensional barrier tunneling, global dynamics, **A:**404–406
phase-space transition states, multidimensional chaos crisis, **A:**393–395
Inverse harmonic potential, phase-space transition states, Lie perturbation theory, **A:**353–358
In vitro experiments, recursive cell production and evolution, catalytic reaction networks, **B:**567–571
Isomerization:
atomic clusters:
molecular internal space, **B:**90–91
passage-times, **B:**27
chaotic transition, regularity, two-basin landscapes, phase space geometrics, **A:**152–163
intramolecular dynamics:
nearly separable systems, **A:**269–286
adiabatic *vs.* nonadiabatic delocalization, **A:**278–286
canonical perturbation theory, floppy molecules, **A:**269–278
resonantly coupled systems, **A:**286–301
high-energy bifurcations, **A:**296–301
polyad folding and saddle-node bifurcations, **A:**287–296
multichannel chemical clusters:
inter-basin mixing, **B:**45–53
reaction tube bifurcation, **B:**47–50
time scale, **B:**50–51
turning point fractal dimension, **B:**51–53
linear surprisal theory, **B:**70–81
chemical reaction dynamics temperature, **B:**70–71
maximum entropy principle, **B:**72–74
variational structure, **B:**74–80
nonequilibrium stationary flow, **B:**74–76
population ratio, **B:**76–78
prior distribution, **B:**78–80
liquid-like state behavior, **B:**34–45
lifetime averaging uniformity, basin transition, **B:**35–45
accumulated residence time/ergodicity, **B:**35–36
exponential decay expansion uniformity, **B:**39–42
non-RRKM behaviors, **B:**42–45
nonstatistical low-energy behavior, **B:**44–45
passage time and uniformity, **B:**36–39
short-time behavior, **B:**42–44
unimolecular dissociation via transition state, **B:**34–35
Markov-type appearance, **B:**45–47
memory-losing dynamic geometry, **B:**45–53
microcanonical temperature, **B:**53–70
Arrhenius-like relation, **B:**60–62
canonical temperature, **B:**70
definition, **B:**57–60
density of states evaluation, **B:**55–56
exponential relation, average lifetimes, **B:**62–70

liquid-like ergodicity and nonergodicity, **B:**67–69
M_7 single exponential form case study, **B:**65–67
multiexponential form, **B:**62–63
single exponential form, **B:**64–65
lifetime averaging law, **B:**53–55
local temperatures, **B:**60
multi-basin potential, **B:**28–34
anomalous time series, **B:**31–34
M_7-like system, **B:**28–30
solid-liquid transition, **B:**30–31
phase-space transition state geometry, nonzero angular momentum, **A:**247–248
unimolecular reaction kinetics, **A:**66–104
cyclobutanone, **A:**100–104
double-well system, **A:**84–88
Gray-Rice theory, **A:**66–70
reactive island theory *vs.,* **A:**80–84
HCN → CNH, **A:**96–100
3-phospholene, **A:**91–96
reactive island theory, **A:**75–80
Gray-Rice theory *vs.,* **A:**80–84
triple-well system, **A:**88–91
Zhao-Rice approximation, **A:**70–75
Wigner's transition state dynamics, hydrogen cyanide, **A:**198–212
Hamiltonian equation, **A:**200–202
model system, **A:**199–200
nonreactive degrees of freedom quantization, **A:**211–212
normal form transformation, **A:**205–207
stationary flow points, **A:**202–205
visualization techniques, **A:**207–210
Itinerant dynamics, recursive cell production and evolution, catalytic reaction networks, **B:**596

Jacobi vectors:
finite-time Lyapunov exponents, multidimensional Hamiltonian dynamical systems, **B:**503–505
intramolecular dynamics, floppy molecules, canonical perturbation theory, **A:**269–278
molecular internal space:
Eckart subspace dynamics, **B:**107–109
four-body systems, PAHC equations of motion, **B:**114–118
gauge-dependent expression, rotation-vibration energy, **B:**92–93
three-atom clusters, isomerization dynamics, **B:**96–97
Wigner's transition state dynamics, hydrogen cyanide isomerization model, **A:**199–200
Jarzynski's nonequilibrium work relations, fluctuation-dissipation theorem, excess heat production, **B:**368–369

K entropy, multichannel isomerization, microcanonical temperature, single exponential form, **B:**66–67
Keplerian forces, phase-space transition state geometry, triatomic dynamics, zero angular momentum, **A:**244–247
Kicked rotor systems, optimal control theory, quantum chaos systems, **A:**439–446
Kicking potential:
unimolecular fragmentation mapping, Morse-like kicking field:
four-dimensional free rotor, **A:**27–30
two-dimensional free particle, **A:**22–27
unimolecular reaction rate, faster-than-classical anomalous diffusion, **A:**134–137
Kinematics, molecular internal space, **B:**88–90
Kinetic energy:
heat transfer, quantum energy flow:
anomalous subdiffusion, **B:**232–238
clusters and macromolecules, **B:**222–223
molecular internal space, gauge-invariant expression, **B:**93–94
recursive cell production and evolution, catalytic reaction network, **B:**571–573
Kolmogorov-Arnold-Moser (KAM) theorem:
multidimensional Hamiltonian systems, resonance and transport:
diffusion coefficient, **B:**440–442
fast transition pathways, **B:**454–457
multidimensional phase space slow dynamics:
Arnold model, **B:**429–430
global motion, **B:**425–427
phase-space transition states:
Lie perturbation theory, **A:**357–358
Melnikov integral, **A:**362–371

Kolmogorov-Arnold-Moser (KAM) theorem (*Continued*)
slow relaxation, internal degrees of freedom, Hamiltonian systems, **B:**376–378
mixed-phase space, **B:**380–381
nearly integrable systems, **B:**394–398
unimolecular reaction rate theory:
isomerization, cyclobutanone, **A:**102–104
phase-space structure, **A:**12–14
bottlenecks:
few-dimensional systems, **A:**18–19
many-dimensional systems, **A:**19–20
Poincaré surface of section, **A:**14–16
stability analysis, **A:**17–18
Kolmogorov entropy:
atomic clusters:
basic principles, **B:**3–4
power spectra and phase-space dimensions, **B:**5–11
regularity, chaos, and ergodicity, **B:**11–20
chaotic transition, regularity, two-basin landscapes, **A:**146–147
Wigner's transition state dynamics, **A:**178–179
Kolmogorov-Sinai (KS) entropy:
fluctuation-dissipation theorem, excess heat production:
long-period limit, **B:**358–359
multibasin landscapes, chaotic transition, regularity, nonstationarity in energy fluctuations, **B:**274–280
onset dynamics, argon clusters:
results from, **B:**142–143
slow relaxation, internal degrees of freedom
Komatsuzaki-Berry technique, unimolecular reaction, **A:**138–140
Kramers-Grote-Hynes theory, chaotic transition, regularity, two-basin landscapes, **A:**163–165
Kronecker delta, molecular internal space, gauge-dependent expression, rotation-vibration energy, **B:**92–93

Ladder operators, intramolecular dynamics, floppy molecules, canonical perturbation theory, **A:**271–278
Lagrangian equations:
chaotic transitions, inert and reactive substances, **B:**521–522
front propagation, **B:**537–540
standard and anomalous diffusion, **B:**523–527
strong anomalous diffusion, **B:**527–530
molecular internal space:
classical equations and metric force, **B:**98–99
democratic centrifugal force, **B:**104–106
four-body systems, PAHC equations of motion, **B:**115–118
gauge field suppression, **B:**111–113
gauge-invariant energy, **B:**94
onset dynamics, argon clusters, gradient external path, **B:**132–133
Lagrangian singularity, phase-space transition states, tangency and, **A:**381–385
Lagrangian time integral, unimolecular reaction rate, semiclassical approximation, rigorous quantum rate, **A:**115–116
Landau-Teller-Zwanzig (LTZ) formula, vibrational energy relaxation, quantum correction factor and, **B:**186
Langevin capture theory, phase-space transition state geometry, angular momentum, astrophysics applications, **A:**256–261
Langevin dynamics simulations, multibasin landscapes, chaotic transition, regularity, nonstationarity in energy fluctuations, **B:**273–280
Langevin equation:
chaotic transition, regularity, two-basin landscapes, Kramers-Grote-Hynes theory, **A:**163–165
multibasin landscapes, chaotic transition, regularity, Berendsen algorithm, constant-temperature MD, **B:**309–310
recursive cell production and evolution, catalytic reaction network, statistical law, **B:**591–595
Langmuir orbit:
Coulomb three-body problem, free-fall problem, **A:**332
three-body problem, **A:**307–309
Laplace transform, multichannel isomerization, **B:**34–45
Lattice vibrations, Hamiltonian system multiergodicity, **B:**741
LBL bead sequence, multibasin landscapes, chaotic transition, regularity, nonstationarity in, **B:**280–282

Lebesgue measure, unimolecular fragmentation mapping, Morse-like kicking field, two-dimensional free particle, **A:**23–27
Lennard-Jones potential:
atomic reactions:
power spectra and phase-space, **B:**10–11
regularity, chaos, and ergodicity, **B:**13–20
transformation mechanisms, **B:**21–22
cluster dynamics, chaotic transition, regularity, two-basin landscapes, **A:**146–147
molecular internal space, atomic cluster isomerization dynamics, **B:**91
multibasin landscapes, chaotic transition, regularity, nonstationarity in energy fluctuations, **B:**274–280
multichannel chemical isomerization:
liquid-like state, **B:**35
microcanonical temperature, **B:**58–62
multi-basin potential, **B:**28–30
solid-liquid tansition, **B:**30–31
onset dynamics, argon clusters, **B:**135–136
phase-space transition state geometry, angular momentum, astrophysics applications, **A:**256–261
rapid alloying, binary clusters, **B:**156–157
slow relaxation, internal degrees of freedom, Hamiltonian systems, molecular systems, **B:**392
Level shift mechanism, dissociation dynamics, unimolecular reactions, Hamiltonian equations, **A:**117–123
Lévy flight model:
atomic clusters, **B:**23
chaotic transitions, inert and reactive substances, **B:**524–527
Lévy walk model, chaotic transitions, inert and reactive substances, **B:**524–527
Liapunov exponents. *See* Lyapunov exponents
Lie canonical perturbation theory, atomic clusters, nonlinear transformation, **B:**21–22
Lie-Deprit transforms, Wigner's transition state dynamics, theoretical background, **A:**179
Lie perturbation theory, phase-space transition states, **A:**352–358
normally hyperbolic invariant manifold connections, **A:**339–340
Lie transformation algorithm:
canonical perturbation theory:
chaotic transition, regularity, two-basin landscapes, **A:**146–147
unimolecular reaction rate theory, phase-space structure, **A:**10
chaotic transition, regularity, two-basin landscapes:
normally hyperbolic invariant manifolds, **A:**167–168
reactive island theory, **A:**162–163
intramolecular dynamics, floppy molecules, canonical perturbation theory, **A:**277–278
Wigner's transition state dynamics, **A:**178–179
basic principles, **A:**194–197
hydrogen cyanide isomerization, **A:**205–207
visualization techniques, **A:**207–210
normal-form coordinates, dynamics, **A:**197–198
normalization, **A:**194–198
Lie triangle, Wigner's transition state dynamics, Lie transformation normalization, **A:**195–197
Lifetime averaging uniformity, multichannel isomerization:
liquid-like states, **B:**34–45
accumulated residence time and ergodicity, **B:**35–36
exponential decay expression, **B:**39–42
non-RRKM behaviors, **B:**42–45
nonstatistical low energy behavior, **B:**44–45
short-time behavior, **B:**42–44
passage time and uniformity, **B:**36–39
microcanonical temperature/Arrhenius relation, **B:**53–55
exponential relation, **B:**62–70
Lifetime parameter, vibrational energy relaxation, cytochrome *c,* CD stretching mode, **B:**195–196
Limit cycles, phase-space transition states, hyperbolicity breakdown, **A:**390–392
Lindemann's criterion (index):
multichannel isomerization:
lifetime averaging, liquid-like dynamics, **B:**69–70
multi-basin potential, solid-liquid tansition, **B:**30–31
onset dynamics, argon clusters:

Lindemann's criterion (index) (*Continued*)
argon$_5$ clusters, **B:**148–151
configuration entropy, **B:**140–142
phase transition results, **B:**138–139
rapid alloying, microcluster dynamics, solid phase transition, **B:**165–166
unimolecular reaction kinetics, LRMT dynamical corrections to RRKM theory, **B:**215–216
Linear harmonic energy, resonantly coupled isomerizing/dissociating systems, polyad folding and saddle-node bifurcation, **A:**288–296
Linearization, phase-space transition state geometry:
n degrees of freedom structures, normally hyperbolic invariant manifolds, **A:**235–236
one degree of freedom model, **A:**223–227
three degrees of freedom, Hénon-Heiles potential, **A:**240–244
Linear surprisal theory, multichannel isomerization, **B:**70–81
chemical reaction dynamics, temperature, **B:**70–71
maximum entropy principle, **B:**72–74
recent developments in, **B:**80
variational structure, **B:**74–80
nonequilibrium stationary flow, **B:**74–76
population ratio, **B:**76–78
prior distribution, **B:**78–80
Liouville density function, unimolecular reaction rate theory, Wigner function and, **A:**106
Liouville equation, fluctuation-dissipation theorem, excess heat production:
Boltzmann equilibrium distribution, **B:**355–356
microcanonical distribution, **B:**362–363
Lippman-Schwinger equation, multichannel isomerization, linear surprisal theory, **B:**74–76
Liquid-phase dynamics:
multichannel chemical isomerization, **B:**34–45
lifetime averaging uniformity, basin transition, **B:**35–45
accumulated residence time/ergodicity, **B:**35–36
exponential decay expansion uniformity, **B:**39–42
non-RRKM behaviors, **B:**42–45
nonstatistical low-energy behavior, **B:**44–45
passage time and uniformity, **B:**36–39
short-time behavior, **B:**42–44
onset dynamics, argon clusters, **B:**139
Liquid water models:
multibasin landscapes, chaotic transition, regularity, **B:**262–263
slow relaxation, internal degrees of freedom, Hamiltonian systems:
molecular systems, **B:**388–392
nearly integrable systems, **B:**393–398
Lissajous figure, chaotic transition, regularity, two-basin landscapes, reactive island theory, **A:**162–163
Local equilibrium assumption, chaotic transition, regularity, two-basin landscapes, **A:**144–147
Local Random Matrix Theory (LRMT):
unimolecular reaction kinetics:
cyclohexane ring inversion, **B:**217–221
dynamical corrections to RRKM theory, **B:**215–216
quantum energy flow, **B:**209–214
Locking phenomenon, molecular internal space:
four-body systems, collective coordinates, **B:**118–121
topographical mapping, **B:**100–103
Log-normal distribution, recursive cell production and evolution, catalytic reaction networks, **B:**591–595
Long-period limit, fluctuation-dissipation theorem, excess heat production, 358-359
Long-time correlation decay, slow relaxation, internal degrees of freedom, Hamiltonian systems, molecular systems, **B:**388–392
Lorentz gas model, slow relaxation, internal degrees of freedom:
mixed-phase space, **B:**386–387
Lorentzian function:
slow relaxation, internal degrees of freedom, Hamiltonian systems, **B:**402–403
hypothesis validity, **B:**406–412

vibrational energy relaxation, cytochrome *c*, CD stretching mode, **B:**197
Lorenz equation, multibasin landscapes, chaotic transition, regularity:
average mutual information, **B:**293–294
state-space structural embedding, **B:**286–288
Low-energy states, multichannel isomerization, nonstatistical behavior, liquid-like phase, **B:**44–45
Low-frequency approximation, multidimensional barrier tunneling:
adiabatic solution, **A:**418–422
Melnikov method, **A:**431–432
theoretical analysis, **A:**417–418
LR method, finite-time Lyapunov exponents, multidimensional Hamiltonian dynamical systems, **B:**510–512
L-set, fringed tunneling models, global structure of branches, **A:**415–417
Lyapunov exponents. *See also* Maximum Lyapunov exponent (MLE)
atomic clusters:
basic principles, **B:**3–4
power spectra and phase-space dimensions, **B:**5–11
regularity, chaos, and ergodicity, **B:**11–20
chaotic transitions:
inert and reactive substances, front propagation, **B:**537–540
two-basin landscapes, **A:**146–147
finite-time exponents, multidimensional Hamiltonian dynamical systems:
instability properties, **B:**512–517
correction, **B:**516
order of motion, **B:**512–514
qualitative different instabilities, **B:**514–516
QR method corrections, **B:**506–512
correction procedure, **B:**508–511
finite-time error, **B:**507–508
standard method, **B:**506–507
vectors, **B:**503–505
Hamiltonian systems, multiergodicity, **B:**466–469
universality conjecture, **B:**470–471
multibasin landscapes, chaotic transition, regularity:
nonstationarity in energy fluctuations, **B:**274–280
multichannel isomerization:
global mixing, **B:**46–47
inter-basin mixing, reaction tube bifurcation, **B:**49–50
multidimensional Hamiltonian, resonance and transport, frequency and phase space, **B:**443–445
onset dynamics, argon clusters:
results from, **B:**142–143
phase-space transition states:
hyperbolicity breakdown, **A:**391–392
multidimensional chaos crisis, **A:**393–395
normally hyperbolic invariant manifolds, **A:**338–340, **A:**347–352
slow relaxation, internal degrees of freedom, Hamiltonian systems:
anomalous transport, mixed-phase space, **B:**379–387
nearly integrable systems, **B:**394–398
unimolecular reaction rate theory:
phase-space quantum scars, **A:**107–108
phase-space structure, stability analysis, **A:**18
Wigner's transition state dynamics, **A:**178–179

Macromolecules, heat transfer, quantum energy flow, **B:**221–248
unimolecular reaction kinetics:
energy diffusion, **B:**222–223
proteins, **B:**241–248
protein vibrational energy:
anharmonic decay, **B:**237–241
anomalous subdiffusion, **B:**227–237
water clusters, **B:**223–227
Magnetization, globally-coupled Hamiltonian systems, relaxation and diffusion:
Hamilton mean field model, **B:**481–484
probability distribution function, **B:**484–487
Many-dimensional systems, unimolecular reaction rate theory:
phase-space structure, bottlenecks, **A:**19–20
Mapping models, unimolecular fragmentation, **A:**22–30
Morse-like kicking field:
four-dimensional free rotor, **A:**27–30
two-dimensional free particles, **A:**22–27

Mapping time, chaotic transition, regularity, two-basin landscapes, reactive island theory, **A:**159–163
Maradudin-Fein formula, CD stretching mode, **B:**190
Markov-type stochastic process:
  fluctuation-dissipation theorem, excess heat production, **B:**354–355
    Boltzmann equilibrium distribution, **B:**355–356
  multichannel isomerization:
    inter-basin mixing, **B:**45–47
    lifetime averaging unformity, **B:**40–42
  multidimensional phase space, slow dynamics, Arnold diffusion, **B:**434–435
  slow relaxation, internal degrees of freedom, mixed-phase space, **B:**383–387
Mass ratio effect, Coulomb three-body problem, collinear electron-nucleus-electron (eZe) configuration, **A:**319–330
  antiproton-proton-antiproton system, **A:**330
  triple collision manifold, **A:**320–323
  triple collision orbits, **A:**323–329
Mathematical reduction, phase-space transition state geometry, angular momentum, rotating frame dynamics, **A:**248–256
Maximum entropy principle (MEP), multichannel isomerization, linear surprisal theory, **B:**72–74
Maximum Lyapunov exponent, multichannel chamical isomerization, multi-basin potential, **B:**30–31
McGehee's blow-up technique:
  collinear eZe configuration, mass ratio effect, triple collision manifold, **A:**320–323
  n-body problem in celestial mechanics, **A:**309–312
  three-body problem, theoretical background, **A:**308–309
Mean square displacement (MSD), globally-coupled Hamiltonian systems, relaxation and diffusion:
  angle space diffusion, **B:**488–498
  multibasin landscapes, chaotic transition, regularity, protein structures, **B:**264–266
  quasi-stationary state, **B:**491–493
Melnikov-Arnold integral, multidimensional phase space slow dynamics:
  global motion, **B:**427
  slow relaxation, **B:**429–430
Melnikov function:
  fringed tunneling models, perturbation strength, **A:**426
  multidimensional barrier tunneling:
    low-frequency approximation, **A:**420–422
    theoretical analysis, **A:**417–418
    unstable periodic orbits, **A:**431–432
  phase-space transition states:
    Arnold web model, **A:**371–377
    examples using, **A:**395–398
    global reaction dynamics, **A:**341–342
    normally hyperbolic invariant manifold connections, **A:**340, **A:**358–371
    tangency and, **A:**378–385
"Melting" energy, multichannel chemical isomerization, multi-basin potential, **B:**30–31
Memory-losing dynamics:
  multibasin landscapes, chaotic transition, regularity, **B:**259–260
    temperature dependence in dimensionality of folding dynamics, **B:**295–299
  multichannel isomerization:
    inter-basin mixing, **B:**45–53
      reaction tube bifurcation, **B:**47–50
      time scale, **B:**50–51
      turning point fractal dimension, **B:**51–53
Meso time scale, rapid alloying:
  binary clusters, **B:**156–157
  microcluster dynamics, **B:**176
Metric force, molecular internal space:
  internal motion equations, **B:**97–99
  three-atom cluster isomerization, collective coordinates, **B:**94–106
    democratic centrifugal force, mass-balance asymmetry and trapping trajectories, **B:**103–106
    internal motion equations, **B:**97–99
    principal-axis hyperspherical coordinates, **B:**94–97
    topographical mapping, PAHC, **B:**99–103
Metric tensor, molecular internal space, gauge-invariant energy, **B:**93–94
Microarray data, nonmetric multidimensional scaling algorithm and, **B:**343–349
  gene expression patterns, **B:**348–349
  information content, **B:**345–348

Microcanonical distribution, fluctuation-dissipation theorem, anomalous variance, nonergodic adiabatic invariant, **B:**361–363
Microcanonical ensembles, multichannel isomerization:
inter-basin mixing, **B:**45–53
reaction tube bifurcation, **B:**47–50
time scale, **B:**50–51
turning point fractal dimension, **B:**51–53
linear surprisal theory, **B:**70–81
chemical reaction dynamics temperature, **B:**70–71
maximum entropy principle, **B:**72–74
recent developments in, **B:**80
variational structure, **B:**74–80
nonequilibrium stationary flow, **B:**74–76
population ratio, **B:**76–78
prior distribution, **B:**78–80
liquid-like state behavior, **B:**34–45
lifetime averaging uniformity, basin transition, **B:**35–45
accumulated residence time/ergodicity, **B:**35–36
exponential decay expansion uniformity, **B:**39–42
non-RRKM behaviors, **B:**42–45
nonstatistical low-energy behavior, **B:**44–45
passage time and uniformity, **B:**36–39
short-time behavior, **B:**42–44
unimolecular dissociation via transition state, **B:**34–35
Markov-type appearance, **B:**45–47
memory-losing dynamic geometry, **B:**45–53
microcanonical temperature, **B:**53–70
Arrhenius-like relation, **B:**60–62
canonical temperature, **B:**70
definition, **B:**57–60
density of states evaluation, **B:**55–56
exponential relation, average lifetimes, **B:**62–70
liquid-like ergodicity and nonergodicity, **B:**67–69
M_7 single exponential form case study, **B:**65–67
multiexponential form, **B:**62–63
single exponential form, **B:**64–65
lifetime averaging law, **B:**53–55
local temperatures, **B:**60
multi-basin potential, **B:**28–34
anomalous time series, **B:**31–34
M_7-like system, **B:**28–30
solid-liquid transition, **B:**30–31
Microcanonical rate constant, unimolecular reaction, quantized ARRKM theory *vs.* rigorous quantum rate, **A:**112–114
Microcanonical temperature:
multichannel chemical isomerization, **B:**53–70
Arrhenius-like relation, **B:**60–62
canonical temperature, **B:**70
definition, **B:**57–60
density of states evaluation, **B:**55–56
exponential relation, average lifetimes, **B:**62–70
liquid-like ergodicity and nonergodicity, **B:**67–69
M_7 single exponential form case study, **B:**65–67
multiexponential form, **B:**62–63
single exponential form, **B:**64–65
lifetime averaging law, **B:**53–55
local temperatures, **B:**60
multichannel isomerization, future research issues, **B:**82–83
Microscopic mechanisms, rapid alloying, microcluster dynamics, **B:**170–175
floppy surface atoms and PES reaction paths, **B:**170–171
reaction path enumeration, **B:**171–173
saddle point energy distribution, **B:**173–175
Miller-Handy-Adams reaction, unimolecular reaction rate theory, reaction path analysis, **A:**54–59
Minimalistic 46-bead protein models, multibasin landscapes, chaotic transition, regularity, **B:**266–270
Minimum energy path (MEP), intramolecular dynamics, floppy molecules, canonical perturbation theory, **A:**269–278
Minority control hypothesis, recursive cell production and evolution, catalytic reaction network, **B:**557–573
core hypercycles, **B:**582–583
evolvability, **B:**566–567
experimental protocol, **B:**567–571
growth speed, **B:**565

Minority control hypothesis, recursive cell production and evolution, catalytic reaction network (*Continued*)
intermingled hypercycle network production, **B:**595–596
itinerant dynamics, **B:**596
kinetic theory, heredity and, **B:**571–572
model parameters, **B:**557–561
molecule chemical composition, **B:**565–566
molecule preservation, **B:**565
stochastic results, **B:**561–564
Mixed phase space, Hamiltonian systems, anomalous transport, **B:**379–387
Model truncated in reciprocal space (MTRS), multidimensional Hamiltonian dynamical systems, finite-time Lyapunov exponent instability, **B:**512–517
MOIL program, heat transfer, quantum energy flow, anomalous subdiffusion, **B:**228–238
Molecular diffusivity, chaotic transitions, inert and reactive substances, standard and anomalous diffusion, **B:**524–527
Molecular dynamics (MD):
multibasin landscapes, chaotic transition, regularity:
Berendsen algorithm, **B:**309–310
liquid water, **B:**262–263
local/global collective coordinates, **B:**260–266
minimalistic 46-bead protein models, **B:**267–270
nonstationarity in energy fluctuations, **B:**273–280
onset dynamics, argon clusters, **B:**135–136
configuration entropy, **B:**140
phase-space structure, unimolecular reaction rate theory, **A:**9–22
action/angle variables, **A:**11–12
canonical transformation, **A:**9–10
few-dimensional system bottlenecks, **A:**18–19
invariant measure, **A:**10–11
KAM theorem, **A:**12–14
many-dimensional system bottlenecks, **A:**19–20
normally hyperbolic invariant manifold, **A:**20–22
Poincaré surface of section, **A:**14–16
stability analysis, **A:**17–18
rapid alloying, binary clusters:
numerical results, **B:**160–161
research background, **B:**156–157
rapid alloying, microcluster dynamics:
radial and surface diffusion, **B:**169–170
saddle point energy distribution, **B:**175
slow relaxation, internal degrees of freedom, Hamiltonian systems, **B:**377–378
anomalous transport, mixed-phase space, **B:**379–387
molecular systems, **B:**387–392
nearly integrable system, **B:**392–398
Molecular internal space:
atomic cluster isomerization, **B:**90–91
four-body systems, **B:**113–125
collective coordinates, isomerization mechanism, **B:**118–121
gauge field isomerization suppression, Eckart frame, **B:**123–125
principal-axis hyperspherical coordinates, equations of motion, **B:**114–118
transition state trapped motion, DCF effects, **B:**121–123
future research issues, **B:**125–126
gauge field isomerization suppression, **B:**106–113
applications, **B:**110–113
Eckart subspace dynamics, **B:**107–109
quantitive role, **B:**106–107
reaction rate effects, **B:**109–110
gauge-theoretical formalism, *n*-body systems:
gauge-invariant kinetic energy expression, **B:**93–94
rotation-vibration kinetic energy, **B:**91–93
kinematics, **B:**88–90
metric force collective coordinates, three-atom cluster isomerization, **B:**94–106
democratic centrifugal force, mass-balance asymmetry and trapping trajectories, **B:**103–106
internal motion equations, **B:**97–99
principal-axis hyperspherical coordinates, **B:**94–97
topographical mapping, PAHC, **B:**99–103
Molecular systems:
recursive cell production and evolution, catalytic reaction networks:
chemical composition control, **B:**565–566

growth speed control, **B:**565
minority molecule preservation, **B:**565
statistical laws, **B:**593–595
slow relaxation, internal degrees of freedom, **B:**387–392
Molecular taxonomy, nonmetric multidimensional scaling algorithm and, **B:**324–329
Molecule optimal dynamic coordinates (MODC), multibasin landscapes, chaotic transition, regularity, protein structures, **B:**264–266
Monkey saddle points, onset dynamics, argon clusters, **B:**152
Monodromy matrix, unimolecular reaction rate theory, phase-space structure, stability analysis, **A:**17–18
Morphological changes, multidimensional Hamiltonian resonance and transport structures, **B:**445–447
Morse-like kicking field, unimolecular fragmentation mapping:
four-dimensional free rotor, **A:**27–30
two-dimensional free particle, **A:**22–27
Morse potential:
molecular internal space:
atomic cluster isomerization dynamics, **B:**90–91
four-body systems, **B:**113–125
multichannel chemical isomerization, microcanonical temperature, **B:**58–62
multichannel isomerization, inter-basin mixing, **B:**45–43, **B:**52–53
phase-space transition states:
angular momentum, astrophysics applications, **A:**256–261
Melnikov integral, **A:**371
triatomic dynamics, zero angular momentum, **A:**245–247
rapid alloying, microcluster dynamics: **B:**175–176
nano-sized clusters, **B:**159–160
unimolecular reaction rate theory, Zhao-Rice approximation, **A:**42–54
Motion trapping, molecular internal space, democratic centrifugal force, **B:**121–123
MRRKM. *See* Zhao-Rice approximation
M-set:
fringed tunneling models:
global structure of branches, **A:**415–417
multiple trajectories, **A:**423–425
perturbation strength, **A:**425–426
semiclassical techniques, **A:**409–410
multidimensional barrier tunneling:
critical point local structure, **A:**414–415
Melnikov method, theoretical background, **A:**417–418
Multibasin potential:
chaotic transition, regularity on:
Berendsen algorithm, constant-temperature molecular dynamics, **B:**309–310
embedded techniques:
basic principles, **B:**302–309
phase-space reconstruction, **B:**285–288
energy nonstationarity, protein landscapes, **B:**270–285
bending energy fluctuation, **B:**278–282
bond energy flucation, **B:**277–278
torsional angle energy fluctuation, **B:**282–285
folding dynamic dimensionality, temperature dependency, **B:**294–299
global/local collective coordinates, **B:**261–262
liquid water, **B:**262–263
minimalistic 46-bead protein models, **B:**266–270
phase space transport geometry, **B:**260–261
proteins, **B:**263–266
state-space structure, **B:**285–299
average mutual information, **B:**292–294
false nearest neighbors, **B:**288–292
phase-space reconstruction, embedding of, **B:**285–288
multichannel chemical isomerization, **B:**28–34
anomalous time series, **B:**31–34
lifetime averaging uniformity, **B:**35–45
M_7-like system, **B:**28–30
solid-liquid transition, **B:**30–31
slow relaxation, internal degrees of freedom, Hamiltonian systems, **B:**413–418
Multicellular organisms, recursive cell production and evolution, catalytic reaction network, **B:**552–557
Multichannel chemical isomerization:
inter-basin mixing, **B:**45–53
reaction tube bifurcation, **B:**47–50
time scale, **B:**50–51

Multichannel chemical isomerization (*Continued*)
turning point fractal dimension, **B:**51–53
linear surprisal theory, **B:**70–81
chemical reaction dynamics temperature, **B:**70–71
maximum entropy principle, **B:**72–74
recent developments in, **B:**80
variational structure, **B:**74–80
nonequilibrium stationary flow, **B:**74–76
population ratio, **B:**76–78
prior distribution, **B:**78–80
liquid-like state behavior, **B:**34–45
lifetime averaging uniformity, basin transition, **B:**35–45
accumulated residence time/ergodicity, **B:**35–36
exponential decay expansion uniformity, **B:**39–42
non-RRKM behaviors, **B:**42–45
nonstatistical low-energy behavior, **B:**44–45
passage time and uniformity, **B:**36–39
short-time behavior, **B:**42–44
unimolecular dissociation via transition state, **B:**34–35
Markov-type appearance, **B:**45–47
memory-losing dynamic geometry, **B:**45–53
microcanonical temperature, **B:**53–70
Arrhenius-like relation, **B:**60–62
canonical temperature, **B:**70
definition, **B:**57–60
density of states evaluation, **B:**55–56
exponential relation, average lifetimes, **B:**62–70
liquid-like ergodicity and nonergodicity, **B:**67–69
M_7 single exponential form case study, **B:**65–67
multiexponential form, **B:**62–63
single exponential form, **B:**64–65
lifetime averaging law, **B:**53–55
local temperatures, **B:**60
multi-basin potential, **B:**28–34
anomalous time series, **B:**31–34
M_7-like system, **B:**28–30
solid-liquid transition, **B:**30–31
Multidimensional systems:
barrier tunneling:
fringed tunneling models, **A:**406–407
global branch structures, **A:**415–417
multiple characteristic trajectories, **A:**422–425
two-dimensional barriers, **A:**428–431
global dynamics, **A:**402–406
Melnikov integral, **A:**431–432
perturbation strength, **A:**425–426
semiclassical method, **A:**407–410
M-set structure at critical point, **A:**414–415
periodic perturbation effects, **A:**412–414
static barrier, **A:**410–412
classical solution, **A:**410
trajectory singularities and integration paths, **A:**410–412
theoretical analyses:
low-frequency approximation, **A:**418–422
overview, **A:**417–418
Hamiltonian dynamical systems:
finite-time Lyapunov exponents:
instability properties, **B:**512–517
correction, **B:**516
order of motion, **B:**512–514
qualitatively different instabilities, **B:**514–516
QR method corrections, **B:**506–512
correction procedure, **B:**508–511
finite-time error, **B:**507–508
standard method, **B:**506–507
vectors, **B:**503–505
resonance structure:
deflected diffusion, **B:**460–462
diffusion coefficient, **B:**440–442
frequency and phase space, **B:**442–445
model components, **B:**438–439
morphological change, **B:**445–447
overlap, **B:**457–460
residence time distribution, **B:**447–450
rotation number, **B:**439–440
transport structure:
basic principles, **B:**450–452
deflected diffusion, **B:**460–462
diffusion coefficient, **B:**440–442
fast transition pathway, **B:**454–457
model components, **B:**438–439
rotation number, **B:**439–440
transition diagram, **B:**452–454
phase space systems (*See also* Nonmetric multidimensional scaling (nMDS))

chaos crisis in, **A:**392–395
multibasin landscapes, chaotic transition, regularity:
nonstationarity in energy fluctuations, **B:**285
state-space structural embedding, **B:**285–288
normally hyperbolic invariant manifold connections, **A:**339–340
onset dynamics, argon clusters, cell partition, potential energy surfaces, **B:**134
slow relaxation dynamics:
Arnold model, **B:**427–430
future research issues, **B:**435–436
numerical method and results, **B:**430–435
global motion, many degrees of freedom, **B:**425–427
research background, **B:**423–424
Wigner's transition state dynamics, **A:**173–175
Multiergodicity. *See* Ergodicity
Multiexponential lifetime averaging, multichannel isomerization, microcanonical temperature and, **B:**62–63
Multiple parallel reaction paths, recursive cell production and evolution, catalytic reaction networks, **B:**594–595
Multi-precision method, multidimensional phase space slow dynamics, Arnold model, **B:**430–435
Multivariate analysis (MVA), nonmetric multidimensional scaling:
brain wave analysis, **B:**341
data mining applications, **B:**316–320
microarray data, **B:**347–349
soil bacteria biodiversity, **B:**336–338
Murrell, Carter, and Halonen (MCH) potential, Wigner's transition state dynamics, hydrogen cyanide isomerization model, **A:**199–211

Nano-sized clusters, rapid alloying, microcluster dynamics, **B:**157–160
procedural characteristics, **B:**157–158
simulation model, **B:**158–160
Navier-Stokes equation, singular perturbation theory, **A:**345
N-body problem in celestial mechanics, basic principles, **A:**309–312
Nearest-neighbor level spacings:
atomic clusters, energy level distribution, **B:**4–5
rapid alloying, microcluster dynamics, numerical results, **B:**164–165
Nearly integrable system:
global motion, many degrees of freedom, **B:**425–427
slow relaxation, internal degrees of freedom, Hamiltonian systems, **B:**392–398
slow relaxation, mixed-phase space, **B:**380–387
Nearly separable isomerizing systems, intramolecular dynamics, **A:**269–286
adiabatic *vs.* nonadiabatic delocalization, **A:**278–286
canonical perturbation theory, floppy molecules, **A:**269–278
Negative feedback process, recursive cell production and evolution, catalytic reaction networks, **B:**594–595
Negative heat of solution, rapid alloying, microcluster dynamics:
nano-sized clusters, **B:**158–160
numerical results, **B:**164–165
"Negative" temperature, multichannel isomerization, linear surprisal theory, 79-80
Nekhoroshev theorem:
Hamiltonian system multiergodicity and nonstationarity, **B:**466
universality conjecture, **B:**469–471
slow relaxation, internal degrees of freedom, Hamiltonian systems, **B:**376–378, **B:**400–403
mixed-phase space, **B:**381–387
nearly integrable systems, **B:**394–398
Neon-chloride ($NeCl_2$), unimolecular reaction rate, predissociation theory, **A:**63–66
Neon-iodine-chloride, unimolecular reaction rate, predissociation theory, **A:**66
Neon-iodine molecules, unimolecular reaction rate theory, predissociation, **A:**61–63
Newton-Raphson algorithm, onset dynamics, argon clusters, gradient external path, **B:**132–133

Nonadiabatic delocalization, isomerizing systems, intramolecular dynamics, *vs.* adiabatic, **A:**278–286
Noncompact clusters, rapid alloying, microcluster dynamics, reaction path enumeration, **B:**173
Nonequilibrium stationary flow, multichannel isomerization, linear surprisal theory, **B:**74–76
Nonergodicity:
  adiabatic invariant, anomalous variance, fluctuation-dissipation theorem, excess heat production, **B:**361–368
    Hamiltonian chaotic systems, **B:**363–367
    microcanonical distribution, **B:**361–363
  multichannel isomerization, lifetime averaging, liquid-like dynamics, **B:**67–70
Nonhyperbolic systems, slow relaxation, internal degrees of freedom, Hamiltonian systems, **B:**379–387
Nonlinear dynamics:
  atomic clusters, **B:**21–22
  phase-space transition states:
    Arnold model, **A:**371–377
    one degree of freedom model, **A:**227
    three degrees of freedom, Hénon-Heiles potential, **A:**241–244
  Wigner's transition state dynamics, rank-one saddle phase-space structure, normally hyperbolic invariant manifolds, **A:**187–190
Nonmetric multidimensional scaling (nMDS), data mining using:
  algorithm characteristics, **B:**320–321
  basic principles, **B:**317–320
  brain wave analysis, **B:**338–341
  embedded point estimation, **B:**322–323
  gene expression, temporal patterns, **B:**348–349
  microarray data, **B:**343–349
  molecular/morphology comparisons, **B:**329–333
    ferns, **B:**329–332
    green autotrophs, **B:**332–333
  molecular taxonomy, **B:**324–329
  pointwise criterion, **B:**321–322
  protein family, **B:**342–343
  soil bacteria biodiversity, **B:**334–338
  theoretical background, **B:**316–317
Nonreactive trajectories:
  phase-space transition state geometry, one degree of freedom model, **A:**225–227
  Wigner's transition state dynamics:
    hydrogen cyanide isomerization model, quantization, **A:**211–212
    rank-one saddle phase-space structure, normally hyperbolic invariant manifolds, **A:**188–190
Nonstationarity:
  globally-coupled Hamiltonian systems, relaxation and diffusion, angle diffusion, **B:**494–496
  Hamiltonian systems:
    complex behaviors, **B:**474–475
    research background, **B:**465–466
    stagnant motion deviation, **B:**466–469
    survival time distribution, clustering motions, **B:**471–474
    universality conjecture, **B:**469–471
  multibasin landscapes, chaotic transition, regularity, protein structures, **B:**270–285
    bending energy fluctuation, **B:**278–282
    bond energy fluctuation, **B:**277–278
    torsional angle energy fluctuation, **B:**282–285
  slow relaxation, internal degrees of freedom, mixed-phase space, **B:**385–387
Nonstatistical low-energy behavior, multichannel isomerization, liquid-like phase, **B:**44–45
Nonzero angular momentum, phase-space transition state geometry, basic principles, **A:**247–261
No-recrossing rule, transition state theory, Wigner's dynamical perspective, **A:**173–175
No-return assumption, chaotic transition, regularity, two-basin landscapes, **A:**144–147
Normal-Form theory, Wigner's transition state dynamics:
  hydrogen cyanide isomerization, Lie transformation, **A:**205–207
  Lie transformation normalization, **A:**197–198
  rank-one saddle phase-space structure:
    "apt" coordinates, **A:**184–186
    Hamiltonian equations, **A:**184
    normally hyperbolic invariant stable/unstable manifolds, **A:**186–190

transition state structure location, **A:**191–193
Normally hyperbolic invariant manifolds (NHIM):
chaotic transition, regularity, two-basin landscapes:
reactive island theory, **A:**163
skeleton structure, **A:**166–168
transition state theory, **A:**147
Coulomb three-body problem:
collinear eZe configuration, triple collision orbits, **A:**325–329
future research issues, **A:**333–334
multibasin landscapes, chaotic transition, regularity, **B:**259–260
phase-space transition states:
angular momentum, rotating van der Waals complex, **A:**252–256
Arnold web model, **A:**373–377
breakdown of hyperbolicity, **A:**341
chaotic itinerancy, **A:**385–389
global chemical reactions, **A:**338–340, **A:**345–352
breakdown, **A:**389–392
Hamiltonian dynamics, **A:**222–223
hyperbolicity breakdown, **A:**389–392
Lie perturbation theory, **A:**352–358
Melnikov integral, **A:**340, **A:**358–371
multidimensional chaos crisis, **A:**392–395
n degrees of freedom structures, **A:**234–237
three degrees of freedom, Hénon-Heiles potential, **A:**241–244
triatomic dynamics, zero angular momentum, **A:**244–247
tangency, **A:**377–385
unimolecular reaction rate theory:
phase-space structure, **A:**20–22
reactive island theory (RIT), **A:**76–80
Wigner's transition state dynamics:
hydrogen cyanide isomerization model, **A:**200
Lie transformation, **A:**205–207
visualization techniques, **A:**207–210
Lie transformation, stable/unstable manifolds, **A:**197–198
rank-one saddle phase-space structure, **A:**183–194
"apt" coordinates, Normal Form theory, **A:**184–186
n-degree-of-freedom Hamiltonian, **A:**183–184
stable/unstable manifolds, **A:**186–190
transition state defined, **A:**190–191
transition state flux, **A:**193–194
transition state search technique, **A:**191–193
theoretical background, **A:**174–175, **A:**179
Nucleotide sequencing, nonmetric multidimensional scaling algorithm and, molecular taxonomy, **B:**324–329
Number distribution of chemicals, recursive cell production and evolution:
autocatalytic network, **B:**575–581
catalytic reaction network, **B:**547

Octahedral structure, atomic clusters, regularity, chaos, and ergodicity, **B:**14–20
1.5-dimensional scattering barrier:
fringed tunneling models, **A:**430–431
multidimensional barrier tunneling, global dynamics, **A:**404–406
One degree of freedom model, phase-space transition states, **A:**223–228
linear case/linearization, **A:**223–227
Melnikov integral, **A:**358–371
nonlinearities, **A:**227
One-dimensional attractor, multibasin landscapes, chaotic transition, regularity, embedding theorems, **B:**302–309
Onset dynamics, argon cluster phase transition:
analytic techniques, **B:**131–136
configuration entropy, **B:**140
configuration space, **B:**140–142
gradient extremal, **B:**131–133
Lindemann's criterion, **B:**138–139
additional potentials, **B:**148–151
Lyapunov and KS entropy, **B:**142–143
partitioned cell dynamics, **B:**145–146
potential energy surface, cell partition, **B:**133–134
potential function, MD simulation, and temperature, **B:**135–136
reaction paths, **B:**136–138
research background, **B:**129–131
stationary points, **B:**143–145
structural characteristics, **B:**136
watershed, **B:**146–148

Optimal control theory (OCT), quantum chaos systems, **A:**437–443
analytic expression, **A:**449–456
controlled kicked rotor, **A:**439–440
controlled random matrix, **A:**438–439
perfect control solution, **A:**453–456
Order of motion, multidimensional Hamiltonian dynamical systems, finite-time Lyapunov exponent instability, **B:**512–517
Ordinary differential equation (ODE):
phase-space transition state geometry:
Hamiltonian dynamics, **A:**220–221
one degree of fredom model, nonlinear regime, **A:**227
phase-space transition states, singular perturbation theory, **A:**343–345
Oscillatory shifts, phase-space transition states:
Melnikov integral, **A:**366–371
tangency and, **A:**383–385
Overlap mechanisms, multidimensional Hamiltonian resonance, **B:**457–460

Painlevé analysis:
multidimensional barrier tunneling, global dynamics, **A:**403–406
n-body problem in celestial mechanics, **A:**310–312
Pairwise resonances, unimolecular reaction rate theory, Zhao-Rice approximation, bottleneck dividing surface, **A:**48
Parallel sliding, multibasin landscapes, chaotic transition, regularity, nonstationarity in energy fluctuations, **B:**284–285
Parasitic molecules, recursive cell production and evolution, catalytic reaction network, **B:**583–585
Partitioned cell dynamics, onset dynamics, argon clusters, **B:**145–146
Passage time, multichannel chemical isomerization, lifetime averaging uniformity, **B:**36–39
Path integral techniques:
multidimensional barrier tunneling, *M*-set critical point, **A:**414–415
three-body problem, **A:**306–309
Péclet number, chaotic transitions, inert and reactive substances, research background, **B:**522
Pentagonal bipyrimidal (PBP) structures, multichannel isomerization:
inter-basin mixing, **B:**46–57
microcanonical temperature, single exponential form, **B:**65–67
multi-basin potential, **B:**28–30
anomalous time series, **B:**31–34
nonstatistical behavior, low energy phase, **B:**45
Periodic orbit dividing surfaces (PODS):
phase-space transition state geometry, two degrees of freedom, **A:**230–234
resonantly coupled isomerizing/dissociating systems:
high energy bifurcations, **A:**297–301
polyad folding and saddle-node bifurcation, **A:**292–296
Wigner's transition state dynamics:
rank-one saddle phase-space structure, normally hyperbolic invariant manifolds, **A:**186–190
theoretical background, **A:**176–179
Periodic orbit instability, multidimensional barrier tunneling, Melnikov method, **A:**431–432
Periodic perturbation, multidimensional barrier tunneling, semiclassical results, **A:**412–414
Perpendicular coordinates:
intramolecular dynamics, **A:**268–269
resonantly coupled isomerizing/dissociating systems, polyad folding and saddle-node bifurcation, **A:**287–296
Perturbation expansion, vibrational energy relaxation, **B:**181–182
Perturbation theory. *See also* Singular perturbation theory
dissociation dynamics, unimolecular reactions, Hamiltonian equations, **A:**118–123
fringed tunneling:
semiclassical method, **A:**406–407
strength characteristics, **A:**425–426
phase-space transition states:
geometry research, **A:**266
Melnikov integral, **A:**362–371
normally hyperbolic invariant manifolds, **A:**348–352
theoretical background, **A:**218–219

time scales, **A:**341–342
slow relaxation, internal degrees of freedom, Hamiltonian systems, **B:**400–403
future research issues, **B:**413–418
mixed-phase space, anomalous transport, **B:**380–387
Wigner's transition state dynamics, rank-one saddle phase-space structure, normally hyperbolic invariant manifolds, **A:**187–190
Phase categories, recursive cell production and evolution, catalytic reaction networks, **B:**575–581
Phase-space transition states. *See also* Multidimensional phase space systems
atomic clusters, **B:**5–11
nonlinear canonical transformation, **B:**21–22
regularity, chaos, and ergodicity, **B:**11–20
geometry of:
angular momentum, **A:**247–261
astrophysics applications, **A:**256–261
inelastic scattering, **A:**257–261
rotating frame dynamics, **A:**248–256
relative equilibrium, **A:**249–251
van der Waals complex, **A:**251–256
Hamiltonian dynamics, **A:**219–223
dimensions, **A:**221–223
general equations, **A:**219–221
n degrees of freedom, **A:**234–247
Hénon-Heiles potential, **A:**237–244
normally hyperbolic invariant manifolds, dimensions and, **A:**234–237
geometric characteristics, **A:**236–237
linear regime, **A:**235–236
tri-body dynamics, zero angular momentum, **A:**244–247
one degree of freedom, **A:**223–228
linear case, linearization, **A:**223–227
nonlinearities, **A:**227
theoretical background, **A:**218–219
two degrees of freedom, **A:**228–234
linear theory, **A:**229–230
periodic orbit dividing surfaces, **A:**230–234
global chemical reactions:
Arnold model, **A:**371–377
chaotic itinerancy, **A:**385–389
Lie perturbation, **A:**352–358
Melnikov integral, **A:**358–371
examples, **A:**395–398
multidimensional chaos, **A:**392–395
normally hyperbolic invariant manifolds, **A:**338–340, **A:**345–352
breakdown, **A:**389–392
singular perturbation theory, **A:**342–345
skeleton bifurcation, **A:**340–341
tangency principles, **A:**341–342, **A:**377–385
molecular dynamics:
chaotic transition, regularity, two-basin landscapes:
geometrics, **A:**151–163
reactive island theory, **A:**162–163
saddle regions, dynamical regularity, **A:**148–151
unimolecular reaction rate theory, **A:**9–22
action/angle variables, **A:**11–12
ARRKM quantization, **A:**108–111
canonical transformation, **A:**9–10
faster-than-classical quantum anomalous diffusion, **A:**134–137
few-dimensional system bottlenecks, **A:**18–19
invariant measure, **A:**10–11
KAM theorem, **A:**12–14
many-dimensional system bottlenecks, **A:**19–20
normally hyperbolic invariant manifold, **A:**20–22
Poincaré surface of section, **A:**14–16
quantized ARRKM theory *vs.* rigorous quantum rate, **A:**111–114
quantum scars, **A:**106–108
stability analysis, **A:**17–18
wave packet dynamics, **A:**124–128
Wigner function and Weyl's rule, **A:**104–106
multibasin landscapes, chaotic transition, regularity:
geometrical structure, **B:**259–260
state-space structure, **B:**285–299
average mutual information, **B:**292–294
false nearest neighbors, **B:**288–292
phase-space reconstruction, embedding of, **B:**285–288
multichannel chemical isomerization, multi-basin potential, **B:**32–34

Phase-space transition states. (*Continued*)
multidimensional Hamiltonian resonance and structure, **B:**442–445
onset dynamics, argon clusters:
analytic techniques, **B:**131–136
configuration entropy, **B:**140
configuration space, **B:**140–142
gradient extremal, **B:**131–133
Lindemann's criterion, **B:**138–139
additional potentials, **B:**148–151
Lyapunov and KS entropy, **B:**142–143
partitioned cell dynamics, **B:**145–146
potential energy surface, cell partition, **B:**133–134
potential function, MD simulation, and temperature, **B:**135–136
reaction paths, **B:**136–138
stationary points, **B:**143–145
structural characteristics, **B:**136
watershed, **B:**146–148
slow relaxation, internal degrees of freedom, Hamiltonian systems, mixed-phase space, **B:**382–387
Wigner's transition state dynamics, **A:**173–175
hydrogen cyanide isomerization model, **A:**199–200
rank-one saddle structure, **A:**183–194
"apt" coordinates, Normal Form theory, **A:**184–186
n-degree-of-freedom Hamiltonian, **A:**183–184
normally hyperbolic invariant manifolds (NHIMs), stable/unstable manifolds, **A:**186–190
transition state defined, **A:**190–191
transition state flux, **A:**193–194
transition state search technique, **A:**191–193
saddle region energy landscapes, coordinate space *vs.,* **A:**180–181
Phase-space volume, multichannel chemical isomerization, microcanonical temperature, **B:**57–62
3-Phospholene, unimolecular reaction rate, isomerization, **A:**91–96
Photofragment excitation, Wigner's transition state dynamics, **A:**178
Planar dynamics, phase-space transition state geometry, angular momentum, rotating van der Waals complex, **A:**251–256
Planck's constant, unimolecular reaction rate theory:
faster-than-classical anomalous diffusion, **A:**134–137
quantum suppression of Arnold diffusion, **A:**132–134
Pocket formation, chaotic transitions, inert and reactive substances, front propagation, **B:**538–540
Poincaré-Birkhoff theorem:
globally coupled Hamiltonian systems, **B:**478–480
slow relaxation, internal degrees of freedom, Hamiltonian systems, mixed-phase space, **B:**382–387
Poincaré mapping, multidimensional Hamiltonian, resonance and transport, **B:**439
Poincaré surface of section (PSS):
chaotic transition, regularity, two-basin landscapes:
reactive island theory, **A:**154–163
transition state theory, **A:**145–147
n-body problem in celestial mechanics, **A:**309–312
phase-space transition state geometry, Hamiltonian dynamics, **A:**222–223
slow relaxation, internal degrees of freedom, Hamiltonian systems, mixed-phase space, **B:**381–387
three-body problem:
collinear eZe configuration, triple collision orbits, **A:**323–329
research background, **A:**305–309
unimolecular reaction rate theory:
Davis-Gray predissociation analysis, **A:**31–39
double-well isomerization, **A:**85–88
faster-than-classical anomalous diffusion, **A:**1353–137
Gray-Rice isomerization theory, **A:**69–70
isomerization:
cyclobutanone, **A:**102–104
HCN to CHN, **A:**97–100
3-phospholene, **A:**94–96
phase-space structure, **A:**14–16

Zhao-Rice approximation, separatrix crossing rate, **A:**53–54
Pointwise criterion, nonmetric multidimensional scaling algorithm, **B:**321–322
Poisson brackets:
intramolecular dynamics, floppy molecules, canonical perturbation theory, **A:**277–278
phase-space transition states:
Lie perturbation theory, **A:**354–358
Melnikov integral, **A:**365–371
Wigner's transition state dynamics, Lie transformation, normal-form coordinates, **A:**198
Poisson distribution, atomic clusters, energy level distribution, **B:**4–5
Polyad folding, resonantly coupled isomerizing/dissociating systems, **A:**287–296
Polymerase chain reaction (PCR), recursive cell production and evolution, catalytic reaction networks, **B:**567–571
Population ratio, multichannel isomerization, linear surprisal theory, **B:**76–78
Porter-Thomas distribution, unimolecular reaction kinetics, quantum energy flow, **B:**214
Positronium negative ions, collinear eZe configuration, **A:**330
Potential energy surfaces (PES):
Coulomb three-body problem, zero angular momentum, **A:**313–319
intramolecular dynamics, **A:**268–269
adiabatic *vs.* nonadiabatic delocalization, **A:**280–286
nearly separable isomerizing systems, floppy molecules, canonical perturbation theory, **A:**269–278
resonantly coupled isomerizing/dissociating systems, high energy bifurcations, **A:**298–301
molecular internal space:
atomic cluster isomerization dynamics, **B:**90–91
democratic centrifugal force, **B:**104–106
topographical mapping, **B:**101–103
multibasin landscapes, chaotic transition, regularity:
basic principles, **B:**259–260
liquid water, **B:**262–263
local/global collective coordinates, **B:**260–266
minimalistic 46-bead protein models, **B:**267–270
nonstationarity in energy fluctuations, **B:**272–280
multichannel chemical isomerization, microcanonical temperature, **B:**57–62
onset dynamics, argon clusters:
$argon_5$ clusters, **B:**148–151
cell partition, **B:**133–134
configuration entropy, **B:**140–142
stationary points, **B:**143–145
structural analysis, **B:**136
phase-space transition state geometry, three degrees of freedom, Hénon-Heiles potential, **A:**241–244
rapid alloying, microcluster dynamics, floppy surface atom reaction paths, **B:**170–171
slow relaxation, internal degrees of freedom, **B:**416–418
unimolecular reaction rate, isomerization:
cyclobutanone, **A:**101–104
3-phospholene, **A:**91–96
Wigner's transition state dynamics:
hydrogen cyanide isomerization, stationary point geometry, **A:**202–205
saddle region energy landscapes, **A:**180–183
theoretical background, **A:**178–179
Potential function, onset dynamics, argon clusters, **B:**135–136
Power-law distribution, recursive cell production and evolution, catalytic reaction networks, **B:**592–595
Power spectra:
atomic clusters, **B:**5–11
slow relaxation, internal degrees of freedom:
hypothesis validity, **B:**408–412
mixed-phase space, **B:**383–387
Power spectral density function (PSD), Hamiltonian system multiergodicity, stagnant motion deviation, **B:**468–469
complex behaviors, **B:**474–475
Predissociation theory, unimolecular reaction rate, **A:**30–66
Davis-Gray analysis, **A:**30–39
Gray-Rice-Davis ARRKM theory, **A:**39–41
$HeCl_2$ and $NeCl_2$, **A:**63–66

Predissociation theory, unimolecular reaction rate (*Continued*)
HeICl and NeICl, **A:**66
reaction path analysis, **A:**54–59
separatrix rate crossing constant, **A:**50–54
van der Waals molecules, **A:**59–63
HeI_2, **A:**59–61
NeI_2 and ArI_2, **A:**61–63
wave packet dynamics, **A:**126–128
Zhao-Rice approximation (MRRKM), **A:**41–54
intramolecular bottleneck:
approximate dividing surface, **A:**46–48
zeroth-order rate constant calculation for crossing, **A:**48–50
separatrix approximate dividing surface, **A:**45–46
Preservation property, recursive cell production and evolution, catalytic reaction network, heredity kinetics, **B:**571–573
Primitive melting, atomic clusters, power spectra and phase-space dimensions, **B:**7–11
Principal-axis hyperspherical coordinates (PAHC), molecular internal space:
classical equations and metric force, **B:**97–99
four-body systems, **B:**113–125
collective coordinates, **B:**118–121
equations of motion, **B:**114–118
gauge field suppression, **B:**110–113
isomerization topography mapping, **B:**99–103
kinematics, **B:**89–90
three-atom clusters, isomerization dynamics, **B:**94–97
Principal component analysis (PCA):
data mining and, **B:**316–317
multibasin landscapes, chaotic transition, regularity:
future research issues, **B:**300–302
local/global collective coordinates, **B:**260–266
temperature dependence in dimensionality of folding dynamics, **B:**293–299
nonmetric multidimensional scaling algorithm and:
brain wave analysis, **B:**338–341
fern genotype/phenotype, **B:**330–332
green autotrophs, **B:**332–333
microarray data, **B:**345–349
protein family, **B:**342–343
soil bacteria biodiversity, **B:**334–338
Prior distributions, multichannel isomerization, linear surprisal theory, **B:**78–80
Probability distribution function of momenta, globally-coupled Hamiltonian systems, relaxation and diffusion, Hamilton mean field model, **B:**484–487
Prompt states, survival probability, **A:**119–120
Protein folding, chaotic transition, regularity, two-basin landscapes, Kramers-Grote-Hynes theory, **A:**164–165
Protein structures:
heat transfer, quantum energy flow, **B:**241–248
anharmonic decay, vibrational states, **B:**238–241
anomalous subdiffusion of vibrational energy, **B:**227–238
multibasin landscapes, chaotic transition, regularity, **B:**263–266
energy nonstationarity, **B:**270–285
bending energy fluctuation, **B:**278–282
bond energy fluctuation, **B:**277–278
torsional angle energy fluctuation, **B:**282–285
minimalistic 46-bead protein models, **B:**266–270
nonmetric multidimensional scaling, **B:**342–343
Pruning front, slow relaxation, internal degrees of freedom, Hamiltonian systems, **B:**380–387
Pseudo-Arnold diffusion, phase-space transition states, Arnold web model, **A:**377
Pseudometrics, molecular internal space:
Eckart subspace dynamics, **B:**108–109
four-body systems, PAHC equations of motion, **B:**116–118
gauge field effects, **B:**106–107
Pseudo-potential energy curves, intramolecular dynamics:
adiabatic *vs.* nonadiabatic delocalization, **A:**279–286
floppy molecules, canonical perturbation theory, **A:**276–278
Pulse-timing control, quantum chaos, **A:**436

QR methods, finite-time Lyapunov exponents, multidimensional Hamiltonian dynamical systems:

corrections, **B:**506–512
correction procedure, **B:**508–511
finite-time error, **B:**507–508
standard method, **B:**506–507
Quadratic corrections, resonantly coupled isomerizing/dissociating systems, polyad folding and saddle-node bifurcation, **A:**288–296
Qualitative analysis, multidimensional Hamiltonian dynamical systems, finite-time Lyapunov exponent instability, **B:**514–516
Quantitative analysis, molecular internal space, gauge field effects, **B:**106–107
Quantum calculation, vibrational energy relaxation, cytochrome *c,* CD stretching mode, **B:**197–198
Quantum chaos systems:
coarse-grained representation:
procedures, **A:**448–449
Rabi state and frequency, **A:**446–448
random vector transition, **A:**449
rotating-wave approximation, **A:**440–449
transition element, **A:**450–453
optimal control theory, **A:**437–443
analytic expression, **A:**449–456
controlled kicked rotor, **A:**439–440
controlled random matrix, **A:**438–439
perfect control solution, **A:**453–456
Quantum correction factor (QCF), vibrational energy relaxation:
basic principles, **B:**180–181
comparison with other methods, **B:**185–186
cytochrome *c,* CD stretching mode, **B:**199–200
Quantum energy flow:
theoretical background, **B:**206–208
unimolecular reaction kinetics:
cyclohexane ring inversion, **B:**216–221
heat transfer in clusters and macromolecules, **B:**221–248
energy diffusion, **B:**222–223
proteins, **B:**241–248
protein vibrational energy:
anharmonic decay, **B:**237–241
anomalous subdiffusion, **B:**227–237
water clusters, **B:**223–227
localization and rate influence, **B:**208–221
dynamical corrections to RRKM from LRMT, **B:**215–216
local random matrix theory, **B:**209–214
Rice-Ramsperger-Kassel-Marcus theory, **B:**214–215
theoretical background, **B:**206
Quantum flux-flux autocorrelation function, unimolecular reaction, quantized ARRKM theory *vs.* rigorous quantum rate, **A:**111–114
Quantum mapping, multidimensional barrier tunneling, **A:**428
Quantum mechanics:
intramolecular dynamics, adiabatic *vs.* nonadiabatic delocalization, **A:**279–286
phase-space transition states, theoretical background, **A:**218–219
resonantly coupled isomerizing/dissociating systems, polyad folding and saddle-node bifurcation, **A:**288–296
three-body problem, **A:**305–309
unimolecular reaction rate, **A:**104–128
ARRKM theory, **A:**108–111
Hamiltonian approach, **A:**116–123
phase space quantum scars, **A:**106–108
predissociation theory, helium chloride/neon-chloride molecules, **A:**65–66
quantum transport, classically chaotic systems, **A:**128–137
Arnold diffusion suppression, **A:**131–134
Cantori model, **A:**129–131
faster-than-classical anomalous diffusion, **A:**134–137
rigorous quantum rate:
vs. quantized ARRKM, **A:**111–114
semiclassical approximation, **A:**114–116
wave packet dynamics, **A:**123–128
Wigner function and Weyl's rule, **A:**104–106
"Quantum scars," unimolecular reaction rate, phase-space structures, **A:**106–108
Quasi-classical rate theory, unimolecular reaction rate, semiclassical approximation, rigorous quantum rate, **A:**115–116
Quasi-elasticity, phase-space transition state geometry, angular momentum, astrophysics applications, **A:**260–261

Quasi-equilibrium, globally-coupled Hamiltonian systems, relaxation and diffusion, Hamilton mean field (HMF) model, **B:**479–480
Quasi-periodic modes, fluctuation-dissipation theorem, excess heat production, adiabatic invariant, **B:**366–367
Quasi-regular regimes, chaotic transition, regularity, two-basin landscapes, **A:**146–147
  normally hyperbolic invariant manifolds, **A:**167–168
  saddle crossing stochasticity, **A:**165–166
  saddle regions, dynamical regularity, **A:**149–151
Quasi-stationarity:
  fluctuation-dissipation theorem, excess heat production, **B:**356
    microcanonical distribution, **B:**362–363
    superstatistical equilibrium distributions, **B:**360–361
  globally coupled Hamiltonian systems, relaxation and diffusion, Hamilton mean field model, **B:**484
    angle diffusion, **B:**491–493
Quenching technique, multichannel chemical isomerization:
  multi-basin potential, **B:**30
  passage time and uniformity, **B:**36–39

Rabi state and frequency:
  coarse-grained representation:
    optimal control theory, **A:**450–453
    perfect control solution, **A:**453–456
    quantum chaos systems, **A:**446–448
    random vector transition, **A:**449
  optimal control theory, future research, **A:**456
Radial diffusion, rapid alloying, microcluster dynamics, **B:**167–170
Raman scattering, slow relaxation, internal degrees of freedom, Hamiltonian systems, hypothesis validity, **B:**407–412
Random matrix system, optimal control theory, quantum chaos systems, **A:**438–439
Random network localization, recursive cell production and evolution, catalytic reaction network, **B:**583
Random noise, Hamiltonian system multiergodicity, stagnant motion deviation, **B:**474–475
Random phase approximation, multidimensional Hamiltonian resonance and structure, **B:**441–442
Random sampling techniques, multichannel isomerization, lifetime averaging, liquid-like dynamics, **B:**68–70
Random vectors, optimal control theory, quantum chaos systems, smooth transition, **A:**449
Rank-one saddle phase-space structure, Wigner's transition state dynamics, **A:**183–194
  "apt" coordinates, Normal Form theory, **A:**184–186
  n-degree-of-freedom Hamiltonian, **A:**183–184
  normally hyperbolic invariant manifolds (NHIMs), stable/unstable manifolds, **A:**186–190
  transition states:
    defined, **A:**190–191
    flux, **A:**193–194
    search technique, **A:**191–193
Rapid alloying (RA), binary clusters, microcluster dynamics:
  floppy surface atoms and PES reaction paths, **B:**170–171
  future research issues, **B:**175–176
  heat of solution, **B:**164–165
  molecular dynamics simulation, **B:**160–161
  nano-sized clusters, **B:**157–160
    procedural characteristics, **B:**157–158
    simulation model, **B:**158–160
  radial and surface diffusion, **B:**167–170
  reaction path numerical simulation, **B:**171–173
  saddle point energy distribution, **B:**173–175
  size effect, **B:**161–164
  solid phase, **B:**165–166
Rate equations, recursive cell production and evolution, catalytic reaction networks, minority control hypothesis, **B:**562–573
Rayleigh-Bénard convection, chaotic transitions, inert and reactive substances, strong anomalous diffusion, **B:**527–530
Reacting substances, chaotic transitions:
  front propagation, **B:**537–540
  fronts in cellular flows, **B:**531–532
  geometric optics limit, **B:**534–537
  slow and fast reaction regimes, **B:**532–534

Reaction coordinates:
atomic clusters:
regularity, chaos, and ergodicity, **B:**20
separability and regularity of, **B:**22
fringed tunneling models, two-dimensional barrier systems, **A:**429–431
intramolecular dynamics, **A:**268–269
multibasin landscapes, chaotic transition, regularity, **B:**260
multichannel isomerization, linear surprisal theory, nonequilibrium stationary flow, **B:**74–76
onset dynamics, argon clusters, **B:**136–138
configuration entropy, **B:**140–142
phase-space transition states:
Melnikov integral, **A:**358–371
multidimensional chaos crisis, **A:**392–395
normally hyperbolic invariant manifold connections, **A:**339–340
one degree of freedom model, **A:**225–227
rapid alloying, microcluster dynamics:
floppy surface atoms, **B:**170–171
numerical enumeration of, **B:**171–173
resonantly coupled isomerizing/dissociating systems, polyad folding and saddle-node bifurcation, **A:**287–296
unimolecular reaction rate theory, predissociation, **A:**54–59
Reaction network structure, recursive cell production and evolution, diverse chemical molecules, **B:**546–547
"Reaction path Hamiltonian," molecular internal space, kinematics, **B:**89–90
Reaction tubes, multichannel isomerization, inter-basin mixing and bifurcation of, **B:**47–50
Reactive island theory (RIT):
chaotic transition, regularity, two-basin landscapes, phase space geometrics, **A:**153–163
unimolecular reaction rate:
Gray-Rice isomerization theory *vs.*, **A:**80–84
isomerization, **A:**75–80
double-well systems, **A:**85–88
3-phospholene, **A:**95–96
triple-well systems, **A:**90–91
research background, **A:**7–8
Reactive trajectories, Wigner's transition state dynamics, rank-one saddle phase-space structure, normally hyperbolic invariant manifolds, **A:**188–190
Recrossing trajectories:
chaotic transition, regularity, two-basin landscapes:
Kramers-Grote-Hynes theory, **A:**163–165
phase space geometrics, **A:**151–163
reactive island theory, **A:**158–163
saddle regions, dynamical regularity, **A:**149–151
phase-space transition states, theoretical background, **A:**218–219
Recurrence phenomenon, slow relaxation, internal degrees of freedom, Hamiltonian systems, nearly integrable systems, **B:**395–398
Recursive cell production and evolution, catalytic reaction network:
autocatalytic network, **B:**573–595
core hypercycle minority, **B:**582–583
evolution models, **B:**585–588
intermingled hypercycle network stabilization, **B:**581–582
molecular models, **B:**574–575
phase states, **B:**575–581
random network localization, **B:**583
statistical law, **B:**588–595
deviation from universal statistics, **B:**593–595
universal statistics, **B:**593
switching mechanism, **B:**584–585
constructive biology, **B:**550–557
chemical reaction networks modeling, **B:**553–557
diverse chemicals, **B:**546–547
Dyson's loose reproduction system, **B:**549–550
Eigen's hypercycle, **B:**547–549
heredity origins, **B:**544–546
minority control hypothesis, **B:**557–573
evolvability, **B:**566–567
experimental protocol, **B:**567–571
growth speed, **B:**565
intermingled hypercycle network production, **B:**595–596
itinerant dynamics, **B:**596
kinetic theory, heredity and, **B:**571–572
model parameters, **B:**557–561

Recursive cell production and evolution, catalytic reaction network (*Continued*)
molecule chemical composition, **B:**565–566
molecule preservation, **B:**565
stochastic results, **B:**561–564
universal statistics and fluctuation control, **B:**596–597
Regularity characteristics, atomic clusters, **B:**11–20
Relative equilibria (RE), phase-space transition state geometry, angular momentum:
astrophysics inelastic scattering, **A:**257–261
rotating frame dynamics, **A:**249–251
rotating van der Waals complex, **A:**251–256
Relative stability, phase-space transition state geometry, angular momentum, rotating frame dynamics, **A:**248–256
Renormalized diffusion, chaotic transitions, inert and reactive substances, **B:**532
Replication mechanisms, recursive cell production and evolution:
autocatalytic network, **B:**574–595
catalytic reaction networks, **B:**547–549
minority control hypothesis, **B:**560–573
in vitro experiments, **B:**569–571
Repulsion of energy levels:
atomic clusters, spacing distribution, **B:**4–5
heat transfer, quantum energy flow, protein vibrational states, anharmonic decay, **B:**240–241
Residence time distribution:
multichannel chemical isomerization, lifetime averaging uniformity, **B:**35–36
multidimensional Hamiltonian resonance and transport structures, **B:**447–450
Resonance condition:
multidimensional Hamiltonian dynamical systems:
deflected diffusion, **B:**460–462
diffusion coefficient, **B:**440–442
frequency and phase space, **B:**442–445
model components, **B:**438–439
morphological change, **B:**445–447
overlap, **B:**457–460
residence time distribution, **B:**447–450
rotation number, **B:**439–440
phase-space transition states, tangency and, **A:**378–385
resonantly coupled isomerizing/dissociating systems, polyad folding and saddle-node bifurcation, **A:**295–296
Resonantly coupled isomerizing/dissociating systems, intramolecular dynamics, **A:**286–301
high-energy bifurcations, **A:**296–301
polyad folding and saddle-node bifurcations, **A:**287–296
Rice-Ramsperger-Kassel-Marcus (RRKM) rate theory. *See also* Alternative Rice, Ramsperger, Kassel and Marcus rate theory; Zhao-Rice approximation (MRRKM)
atomic clusters, research background, **B:**27–28
multichannel isomerization:
liquid-like state, **B:**34–45
unimolecular reaction:
ARRKM quantization, **A:**108–111
isomerization:
cyclobutanone, **A:**103–104
double-well systems, **A:**87–88
HCN to CHN, **A:**98–100
3-phospholene, **A:**95–96
predissociation, Davis-Gray analysis, **A:**35–39
unimolecular reaction kinetics:
cyclohexane ring inversion, **B:**218–221
LRMT dynamical corrections, **B:**215–216
quantum energy flow, **B:**214–215
theoretical background, **B:**206
unimolecular reaction rate, predissociation theory, helium-iodine, **A:**60–61
Rice-Ramsperger-Kassel (RRK) rate theory, unimolecular reaction, research background, **A:**5–8
Riemann geometrization, Hamiltonian system multiergodicity:
complex behaviors, **B:**475
survival time distribution, **B:**473–474
Riemann sheets:
fringed tunneling models, perturbation strength, **A:**425–426
multidimensional barrier tunneling, static barriers, **A:**412
Rigorous quantum rate, unimolecular reaction:
quantized ARRKM theory and, **A:**111–114
semiclassical approximation, **A:**114–116

Ring inversion rates, unimolecular reaction kinetics, **B:**218–221
Ring puckering coordinate, unimolecular reaction rate, isomerization:
  cyclobutanone, **A:**100–104
  3-phospholene, **A:**91–96
Robustness parameters, chaotic transition, regularity, two-basin landscapes, normally hyperbolic invariant manifolds (NHIM), **A:**166–168
Rotating frame dynamics, phase-space transition state geometry:
  angular momentum, **A:**248–256
    relative equilibrium, **A:**249–251
  van der Waals complex, **A:**251–256
Rotating-wave approximation (RWA), coarse-grained representation, quantum chaos systems, **A:**443, **A:**446
Rotation numbers, multidimensional Hamiltonian, resonance and transport, **B:**439–440
  frequency and phase space, **B:**442–445
Rotation-vibration energy, molecular internal space, gauge-dependent expression, **B:**91–93
Rotor systems:
  faster-than-classical anomalous diffusion, **A:**134–137
  unimolecular fragmentation mapping, Morse-like kicking field, **A:**27–30
Rugged multibasin dynamics, chaotic transition, regularity, two-basin landscapes, **A:**167–168
Rydberg atoms, Wigner's transition state dynamics, saddle region energy landscapes, **A:**180–183

Saddle crossings, chaotic transition, regularity, two-basin landscapes, stochasticity parameters, **A:**165–166
Saddle indexes, phase-space transition states:
  Lie perturbation theory, **A:**352–358
  normally hyperbolic invariant manifolds, **A:**338–340
Saddle-node bifurcations:
  intramolecular dynamics, future research, **A:**301–302
  resonantly coupled isomerizing/dissociating systems, **A:**287–296
    high energy bifurcations, **A:**296–301
Saddle point approximation, fringed tunneling models, semiclassical techniques, **A:**408–410
Saddle regions:
  atomic clusters:
    power spectra and phase-space, **B:**8–11
    regularity, chaos, and ergodicity, **B:**15–20
  chaotic transition, dynamical regularity, two-basin landscapes, **A:**147–151
  molecular internal space, four-body systems, **B:**113–125
  multibasin landscapes, chaotic transition, regularity, **B:**258–260
    phase-space transition states, **B:**259–260
    protein structures, **B:**264–266
  multichannel chemical isomerization, multi-basin potential, **B:**28–30
  onset dynamics, argon clusters, **B:**136
  phase-space transition states, chaotic itinerancy, **A:**386–389
  rapid alloying, microcluster dynamics, energy distribution, **B:**173–174
  Wigner's transition state dynamics:
    energy landscapes, **A:**180–183
    phase space:
      vs. coordinate space, **A:**180–181
      energy landscapes, **A:**182–183
    rank-one saddle phase-space structure, **A:**183–194
      "apt" coordinates, Normal Form theory, **A:**184–186
      n-degree-of-freedom Hamiltonian, **A:**183–184
      normally hyperbolic invariant manifolds (NHIMs), stable/unstable manifolds, **A:**186–190
      transition states:
        defined, **A:**190–191
        flux, **A:**193–194
        search technique, **A:**191–193
    stability, **A:**181–182
    theoretical background, **A:**178–179
Scaling laws:
  globally-coupled Hamiltonian systems, relaxation and diffusion:
  future research issues, **B:**499
    Hamilton mean field model, **B:**484
  Hamiltonian system multiergodicity, universality conjecture, **B:**470–471

Scaling laws (*Continued*)
multibasin landscapes, chaotic transition, regularity, embedding theorems, **B:**307–309
recursive cell production and evolution, catalytic reaction networks, **B:**592–595
Scaling transformation, Coulomb three-body problem:
free-fall problem, **A:**330–332
zero angular momentum, **A:**314–319
Schrödinger equation:
intramolecular dynamics, adiabatic *vs.* nonadiabatic delocalization, **A:**282–286
multidimensional barrier tunneling, global dynamics, **A:**403–406
optimal control theory, quantum chaos systems, **A:**438
Rabi state and frequency, **A:**447–448
unimolecular reaction rate, wave packet dynamics, **A:**123–128
Schubart orbits, Coulomb three-body problem, collinear eZe configuration, **A:**324–329
"Scissors" barriers, Wigner's transition state dynamics:
rank-one saddle phase-space structure, normally hyperbolic invariant manifolds, **A:**188–190
Self-similar island chain:
globally coupled Hamiltonian systems, **B:**478–480
slow relaxation, internal degrees of freedom:
future research issues, **B:**413–418
mixed-phase space, **B:**382–387
Semi-chaotic regime, chaotic transition, regularity, two-basin landscapes, **A:**146–147
saddle crossing stochasticity, **A:**165–166
"Semiclassical eigenfunction hypothesis," unimolecular reaction rate theory, Wigner function, **A:**106–108
Semiclassical techniques:
multidimensional barrier tunneling, **A:**407–410
fringed tunneling models, **A:**406–407
complex-domain method, **A:**407–410
global branch structures, **A:**415–417
multiple characteristic trajectories, **A:**422–425
two-dimensional barriers, **A:**428–431
global dynamics, **A:**402–406
Melnikov integral, **A:**431–432
M-set structure at critical point, **A:**414–415
periodic perturbation effects, **A:**412–414
perturbation strength, **A:**425–426
static barrier, **A:**410–412
classical solution, **A:**410
trajectory singularities and integration paths, **A:**410–412
theoretical analyses:
low-frequency approximation, **A:**418–422
overview, **A:**417–418
three-body problem, **A:**306–309
unimolecular reaction rate, **A:**104–128
ARRKM theory, **A:**108–111
Hamiltonian approach, **A:**116–123
phase space quantum scars, **A:**106–108
predissociation theory, helium chloride/neon-chloride molecules, **A:**65–66
rigorous quantum rate, **A:**114–116
semiclassical approximation, **A:**114–116
vs. quantized ARRKM, **A:**111–114
wave packet dynamics, **A:**123–128
Wigner function and Weyl's rule, **A:**104–106
Semiclassical techniques, multichannel isomerization, future research, **B:**83
Semi-global dynamics, chaotic transition, regularity, two-basin landscapes, reactive island theory, **A:**156–163
Separatrix construction:
multidimensional Hamiltonian resonance and transport, resonance overlap, **B:**458–460
phase-space transition states:
Hamiltonian dynamics, **A:**222–223
Melnikov integral, **A:**359–371
examples using, **A:**395–398
one degree of freedom model, **A:**226–227
tangency and, **A:**384–385
unimolecular reaction rate theory:
Gray-Rice-Davis ARRKM theory, **A:**39–41
Gray-Rice isomerization theory, **A:**67–70
isomerization, cyclobutanone, **A:**102–104
normally hyperbolic invariant manifolds (NHIM), **A:**7–8

quantum suppression of Arnold diffusion, **A:**132–134
Zhao-Rice approximation:
crossing rate constant, **A:**50–54
dividing surface approximation, **A:**45–46
isomerization theory, **A:**70–75
Shannon entropy, multichannel isomerization:
lifetime averaging, liquid-like dynamics, **B:**68–70
linear surprisal theory, **B:**72–74
Shepard plots, nonmetric multidimensional scaling algorithm and, molecular taxonomy, **B:**326–329
Short-period limit, fluctuation-dissipation theorem, excess heat production, **B:**359
Short-time behavior, multichannel isomerization:
liquid-like phase, **B:**42–44
microcanonical temperature/Arrhenius relation, **B:**53–55
Single exponential lifetime averaging, multichannel isomerization, microcanonical temperature, **B:**64–65
Singularities, multidimensional barrier tunneling:
M-set critical point, **A:**414–415
static barriers, **A:**410–412
Singular perturbation theory, phase-space transition states, **A:**342–345
Singular value decomposition (SVD) theorem:
finite-time Lyapunov exponents, multidimensional Hamiltonian dynamical systems:
vectors, **B:**504–505
molecular internal space:
four-body systems, PAHC equations of motion, **B:**114–118
three-atom clusters, isomerization dynamics, **B:**95–97
Size effect:
globally-coupled Hamiltonian systems, relaxation and diffusion, Hamilton mean field (HMF) model, **B:**481
rapid alloying, microcluster dynamics:
nano-sized clusters, **B:**158
numerical results, **B:**161–164
Skeleton reaction profile:
chaotic transition, regularity, two-basin landscapes, **A:**166–168
multibasin landscapes, chaotic transition, regularity, phase-space transition states, **B:**260
phase-space transition states:
bifurcation, **A:**340–341
chaotic itinerancy, **A:**385–389
normally hyperbolic invariant manifold connections, **A:**341
tangency of intersections, **A:**377–385
SKEW structures, multichannel isomerization:
inter-basin mixing, **B:**46––47
time scales, **B:**50–51
liquid-like phase, **B:**43–44
microcanonical temperature, single exponential form, **B:**66–67
nonstatistical behavior, low energy phase, **B:**44–45
Slow relaxation dynamics:
chaotic transitions, inert and reactive substances, **B:**532–534
Hamiltonian systems:
internal degrees of freedom:
FPU models, **B:**398–403
future research issues, **B:**412–418
mixed-phase space systems, anomalous transport, **B:**379–387
molecular systems, **B:**387–392
nearly integrable picture, applicability, **B:**392–398
theoretical background, **B:**375–378
validity of hypothesis, **B:**403–412
multiergodicity and nonstationarity, **B:**466–469
multidimensional phase space systems:
Arnold model, **B:**427–430
numerical method and results, **B:**430–435
global motion, many degrees of freedom, **B:**425–427
Smale horseshoe, unimolecular fragmentation mapping, Morse-like kicking field, two-dimensional free particle, **A:**24–27
Smallness parameter, multidimensional barrier tunneling, low-frequency approximation, **A:**419–422
Smoothing conditions, phase-space transition states, normally hyperbolic invariant manifolds, **A:**348–352

Soil bacteria biodiversity, nonmetric multidimensional scaling algorithm and, **B:**334–338
Solid-liquid transition, multichannel chemical isomerization, multi-basin potential, **B:**30–31
Solid-phase transition, rapid alloying, microcluster dynamics:
  nano-sized clusters, **B:**158
  numerical results, **B:**165–166
Space-fixed frame, molecular internal space, gauge-dependent expression, rotation-vibration energy, **B:**92–93
SPC potential, slow relaxation, internal degrees of freedom, Hamiltonian systems, hypothesis validity, **B:**403–412
Stability analysis:
  Coulomb three-body problem, zero angular momentum, **A:**317–319
  phase-space transition state geometry, triatomic dynamics, zero angular momentum, **A:**245–247
  unimolecular reaction rate theory, phase-space structure, **A:**17–18
  Wigner's transition state dynamics, saddle region energy landscapes, **A:**181–182
Stable/unstable manifolds. *See also* Normally hyperbolic invariant manifolds (NHIM)
  Coulomb three-body problem, zero angular momentum, **A:**317–319
  multidimensional phase space, slow dynamics, Arnold model, **B:**427–430
  phase-space transition states:
    angular momentum, rotating van der Waals complex, **A:**254–256
    Arnold web model, **A:**373–377
    chaotic itinerancy, **A:**386–389
    Melnikov integral, **A:**361–372
    multidimensional chaos crisis, **A:**392–395
    normally hyperbolic invariant manifolds, **A:**347–352
      connections, **A:**339–340
    one degree of freedom model, **A:**227
    tangency and branching, **A:**377–385
  rank-one saddle phase-space structure, **A:**186–190
  Wigner's transition state dynamics, Lie transformation, **A:**197–198
Stagnant motion deviation. *See also* Nonstationarity
  Hamiltonian system multiergodicity and nonstationarity, **B:**466–469
  complexities, **B:**474–475
  universality conjecture, **B:**469–471
Standard diffusion, chaotic transitions, inert substances, **B:**523–527
State-space structure, multibasin landscapes, chaotic transition, regularity, **B:**285–299
  average mutual information, **B:**292–294
  false nearest neighbors, **B:**288–292
  phase-space reconstruction, embedding of, **B:**285–288
Static barrier, multidimensional barrier tunneling, **A:**410–412
  classical solution, **A:**410
  low-frequency approximation, **A:**419–422
  trajectory singularities and integration paths, **A:**410–412
Stationary points:
  onset dynamics, argon clusters, **B:**143–145
  Wigner's transition state dynamics:
    hydrogen cyanide isomerization, **A:**202–205
    saddle region energy landscapes, **A:**180–183
    theoretical background, **A:**179
Statistical law, recursive cell production and evolution, catalytic reaction network, autocatalytic network, **B:**588–595
  deviation from universal statistics, **B:**593–595
  universal statistics, **B:**593
STIRAP scheme, quantum chaos, **A:**436
Stochasticity, chaotic transition, regularity, two-basin landscapes, saddle crossings, **A:**165–166
Stochastic parameter:
  fluctuation-dissipation theorem, excess heat production, adiabatic invariant, **B:**365–367
  recursive cell production and evolution, catalytic reaction networks, minority control hypothesis, **B:**561–573
Stokes phenomenon, fringed tunneling models:
  complex semiclassical techniques, **A:**410
  global structure of branches, **A:**416–417
Stretched exponential function, globally-coupled Hamiltonian systems, relaxation and diffusion, equilibrium diffusion, **B:**489–490

Strong stochasticity threshold (SST), slow relaxation, internal degrees of freedom, Hamiltonian systems, nearly integrable systems, **B:**394–398
Structural analysis, onset dynamics, argon clusters, **B:**136
Structural stability, phase-space transition states, skelton structures, chaotic itinerancy, **A:**386–389
Superstatistical equilibrium distributions, fluctuation-dissipation theorem, excess heat production, **B:**359–361
Surface diffusion, rapid alloying, microcluster dynamics, **B:**167–170
Survival probability, dissociation dynamics, unimolecular reactions, Hamiltonian equations, **A:**118–123
Survival time distribution, Hamiltonian system multiergodicity, clustering motions, **B:**471–474
Switching mechanism, recursive cell production and evolution, catalytic reaction network, **B:**583–585
  evolution models, **B:**587–588
  itinerant dynamics, **B:**596
Symmetrized autocorrelation function, vibrational energy relaxation, **B:**184–185
Symmetry breaking, catalytic reaction network, recursive cell production and evolution, minority control hypothesis, **B:**573

Takens' theorem, multibasin landscapes, chaotic transition, regularity:
  delay coordinates, **B:**306–309
  state-space structural embedding, **B:**288
  temperature dependence in dimensionality of folding dynamics, **B:**297–299
Tangency, phase-space transition states:
  hyperbolicity breakdown, **A:**391–392
  Melnikov integral, **A:**340, **A:**358–371
  normally hyperbolic invariant manifolds:
    branching, **A:**377–385
    connections, **A:**339–340
Tannor-Rice scheme, quantum chaos, **A:**436
Taylor series expansion:
  intramolecular dynamics, floppy molecules, canonical perturbation theory, **A:**270–278
  phase-space transition states:
    Lie perturbation theory, **A:**353–358
    normally hyperbolic invariant manifolds, **A:**348–352
  vibrational energy relaxation:
    cytochrome *c,* CD stretching mode, coupling constants, **B:**192–195
    force-force-correlation function approximations, **B:**186–187
  Wigner's transition state dynamics:
    hydrogen cyanide isomerization, **A:**205–207
    rank-one saddle phase-space structure, "apt" coordinates, **A:**184–186
Temperature dependence:
  multibasin landscapes, chaotic transition, regularity, folding dynamics dimensionality, **B:**293–299
  multichannel isomerization:
    linear surprisal theory, **B:**70–71
    microcanonical states, **B:**53–70
      Arrhenius-like relation, **B:**60–62
      canonical temperature, **B:**70
      definition, **B:**57–60
      density of states evaluation, **B:**55–56
      exponential relation, average lifetimes, **B:**62–70
        liquid-like ergodicity and nonergodicity, **B:**67–69
        M_7 single exponential form case study, **B:**65–67
        multiexponential form, **B:**62–63
        single exponential form, **B:**64–65
      lifetime averaging law, **B:**53–55
      local temperatures, **B:**60
  onset dynamics, argon clusters, **B:**135–136
  phase-space transition states:
    angular momentum, astrophysics applications, **A:**256–261
    Melnikov integral, **A:**360–371
  rapid alloying, microcluster dynamics:
    nano-sized clusters, **B:**158
    radial and surface diffusion, **B:**168–170
Thermal bath, chaotic transition, regularity, two-basin landscapes, Kramers-Grote-Hynes theory, **A:**164–165
Thermal diffusivity, heat transfer, quantum energy flow, clusters and macromolecules, **B:**221–248

Thermally averaged constant, unimolecular reaction, quantized ARRKM theory *vs.* rigorous quantum rate, **A:**111–114
Thermodynamic laws, fluctuation-dissipation theorem, excess heat production, **B:**355–356
  second law from, **B:**369–370
Thomas-Fermi statistics, onset dynamics, argon clusters, configuration entropy, **B:**140
Three-atom clusters:
  celestial mechanics, **A:**309–312
  collinear eZe case, mass ratio effect, **A:**319–330
    antiproton-proton-antiproton system, **A:**330
    triple collision manifold, **A:**319–323
    triple collision orbits, **A:**323–329
  free-fall case, **A:**330–332
  molecular internal space, metric force collective coordinates, **B:**94–106
    democratic centrifugal force, mass-balance asymmetry and trapping trajectories, **B:**103–106
    internal motion equations, **B:**97–99
    principal-axis hyperspherical coordinates, **B:**94–97
    topographical mapping, PAHC, **B:**99–103
  phase-space transition states, Arnold web model and tangency in, **A:**378–385
  theoretical background, **A:**305–309
  two-dimensional case, zero angular momentum, **A:**312–319
Three degrees of freedom structures, phase-space transition state geometry, Hénon-Heiles potential, **A:**237–244
Three-dimensional wavefunctions, intramolecular dynamics, adiabatic *vs.* nonadiabatic delocalization, **A:**279–286
"Three threes," Wigner's formulation of, **A:**172–175
Time autocorrelation function:
  dissociation dynamics, unimolecular reactions, Hamiltonian equations, **A:**118–123
  unimolecular reaction rate, wave packet dynamics, **A:**124–128
Time-continuous systems, multidimensional barrier tunneling:
  global dynamics, **A:**403–406
Time delay coordinate system:
  multibasin landscapes, chaotic transition, regularity:
    average mutual information, **B:**293–294
    state-space structural embedding, **B:**286–288
    Whitney embedding theorem, **B:**305–309
  slow relaxation, internal degrees of freedom, Hamiltonian systems, nearly integrable systems, **B:**395–398
Time-dependent equations:
  coarse-grained representation, quantum chaos systems, **A:**443, **A:**446
    Rabi state and frequency, **A:**446–448
  multidimensional barrier tunneling, low-frequency approximation, **A:**421–422
  phase-space transition states:
    Arnold web model, **A:**372–377
    tangency and, **A:**379–385
Time-evolving wave packet, unimolecular reaction rate, **A:**123–128
Time scales:
  multibasin landscapes, chaotic transition, regularity, nonstationarity in energy fluctuations, **B:**278–282
  multichannel isomerization, inter-basin mixing, **B:**50–51
  phase-space transition states:
    global reaction dynamics, **A:**341–342
    singular perturbation theory, **A:**342–345
    tangency and, **A:**383–385
Time-series analysis, multichannel chemical isomerization, multi-basin potential, **B:**32–34
TIP3 potential, heat transfer, quantum energy flow, **B:**223–227
Top-down technique, Wigner's transition state dynamics, research background, **A:**173–175
Topographical mapping, molecular internal space, principal-axis hyperspherical coordinates (PAHC), **B:**99–103
Tori structures:
  chaotic transition, regularity, two-basin landscapes, reactive island theory, **A:**155–163
  Coulomb three-body problem:
    theoretical background, **A:**307–309
    triple collision orbits, **A:**324–329
  free-fall three-body problem, **A:**330–332

globally coupled Hamiltonian systems, **B:**478–480
multidimensional Hamiltonian systems, resonance and transport:
diffusion coefficient, **B:**440–442
fast transition pathways, **B:**454–457
multidimensional phase space slow dynamics:
Arnold model, **B:**429–430
global motion, **B:**425–427
phase-space transition states:
Arnold model, **A:**371–377
chaotic itinerancy, **A:**386–389
Melnikov integral, **A:**362–371
n degrees of freedom structures, **A:**236–237
slow relaxation, internal degrees of freedom, Hamiltonian systems:
mixed-phase space, **B:**381–387
nearly integrable systems, **B:**396–398
unimolecular reaction rate theory:
isomerization, cyclobutanone, **A:**102–104
KAM theorem, **A:**13–14
Torsional angle energy fluctuation, multibasin landscapes, chaotic transition, regularity, nonstationarity in, **B:**282–285
Total momentum, globally-coupled Hamiltonian systems, relaxation and diffusion, Hamilton mean field (HMF) model, **B:**481
Transition chain crossings, multidimensional phase space, slow dynamics, Arnold model, **B:**428–430
Transition diagram, multidimensional Hamiltonian resonance and transport structures, **B:**452–454
Transition state theory (TST):
chaotic transition, regularity, two-basin landscapes, **A:**144–147
Kramers-Grote-Hynes theory and, **A:**163–165
historical background, **A:**176–179
molecular internal space, democratic centrifugal force, **B:**104–106
motion trapping, **B:**121–123
multibasin landscapes, chaotic transition, regularity, **B:**258–260
multichannel isomerization, liquid-like state, **B:**34–35
phase-space transition state geometry:
angular momentum, **A:**247–261
astrophysics applications, **A:**256–261
inelastic scattering, **A:**257–261
rotating frame dynamics, **A:**248–256
relative equilibrium, **A:**249–251
van der Waals complex, **A:**251–256
Hamiltonian dynamics, **A:**219–223
dimensions, **A:**221–223
general equations, **A:**219–221
n degrees of freedom, **A:**234–247
Hénon-Heiles potential, **A:**237–244
normally hyperbolic invariant manifolds, dimensions and, **A:**234–237
geometric characteristics, **A:**236–237
linear regime, **A:**235–236
tri-body dynamics, zero angular momentum, **A:**244–247
one degree of freedom, **A:**223–228
linear case, linearization, **A:**223–227
nonlinearities, **A:**227
theoretical background, **A:**218–219
two degrees of freedom, **A:**228–234
linear theory, **A:**229–230
periodic orbit dividing serfaces, **A:**230–234
unimolecular reaction, double-well system isomerization, **A:**87–88
Wigner's formulation:
hydrogen cyanide isomerization, **A:**198–212
Hamiltonian equation, **A:**200–202
model system, **A:**199–200
nonreactive degrees of freedom quantization, **A:**211–212
normal form transformation, **A:**205–207
stationary flow points, **A:**202–205
visualization techniques, **A:**207–210
Lie transformation normalization, **A:**194–198
basic principles, **A:**194–197
normal-form coordinates, dynamics, **A:**197–198
rank-one saddle phase-space structure, **A:**183–194
"apt" coordinates, Normal Form theory, **A:**184–186
n-degree-of-freedom Hamiltonian, **A:**183–184
normally hyperbolic invariant manifolds (NHIMs), stable/unstable manifolds, **A:**186–190

Transition state theory (TST) (*Continued*)
transition state:
defined, **A:**190–191
flux, **A:**193–194
search technique, **A:**191–193
research background, **A:**172–175
saddles in energy landscapes, **A:**180–183
phase space energy landscapes, **A:**182–183
phase space *vs.* coordinate space, **A:**180–181
stability, **A:**181–182
Transmission coefficient:
atomic clusters, nonlinear canonical transformation, **B:**21–22
chaotic transition, regularity, two-basin landscapes:
phase space geometrics, **A:**152–163
transition state theory, **A:**145–147
Transporting regular island structures, faster-than-classical anomalous diffusion, **A:**135–137
Transport structure, multidimensional Hamiltonian dynamical systems:
basic principles, **B:**450–452
deflected diffusion, **B:**460–462
diffusion coefficient, **B:**440–442
fast transition pathway, **B:**454–457
model components, **B:**438–439
rotation number, **B:**439–440
transition diagram, **B:**452–454
Trans-stilbene photoisomerization, unimolecular reaction kinetics, **B:**220–221
Trapped motion:
Hamiltonian system multiergodicity, survival time distribution, **B:**472–474
molecular internal space, democratic centrifugal force, **B:**104–106
multichannel isomerization, **B:**83
Triatomic structures, phase-space transition state geometry:
n degrees of freedom, **A:**244–247
nonzero angular momentum, **A:**247–248
Tricapped tetrahedron (IST) structures, multichannel isomerization:
inter-basin mixing, **B:**46–47
inter-basin mixing, time scales, **B:**50–51
nonstatistical behavior, low energy phase, **B:**44–45
Trigonal pyramidal structures, atomic clusters, regularity, chaos, and ergodicity, **B:**14–20
Triple collision manifold (TCM):
collinear eZe configuration:
mass ratio effect, **A:**320–323
theoretical background, **A:**308–309
Coulomb three-body problem:
future research issues, **A:**333–334
zero angular momentum, **A:**312–319
n-body problem in celestial mechanics, **A:**310–312
Triple collision orbits, Coulomb three-body problem:
collinear eZe configuration, mass ratio effect, **A:**323–329
zero angular momentum, **A:**317–319
Triple-well systems, unimolecular reaction, isomerization, **A:**88–91
True dynamics, molecular internal space, gauge field reaction rates, **B:**109–110
Truncation-diagonalization analysis, intramolecular dynamics, adiabatic *vs.* nonadiabatic delocalization, **A:**280–286
Tsallis distribution, fluctuation-dissipation theorem, excess heat production, **B:**354–355
superstatistical equilibrium distributions, **B:**361
Tsallis nonadditive statistical mechanics, multibasin landscapes, chaotic transition, regularity, **B:**300–302
Two-basin landscapes, chaotic transition, regularity:
Kramers-Grote-Hynes theory, **A:**163–165
phase space geometrics, **A:**151–163
reactive island theory, **A:**153–163
saddle crossing stochasticity, **A:**165–166
saddle regions, dynamical regularity, **A:**147–151
Two degrees of freedom models, phase-space transition state geometry, **A:**228–234
linear theory, **A:**229–230
periodic orbit dividing surfaces, **A:**230–234
Two-dimensional barrier systems:
fringed tunneling models, **A:**428–431
multidimensional barrier tunneling, global dynamics, **A:**404–406
Two-dimensional egg-crate potential, globally-coupled Hamiltonian systems, relaxation

and diffusion, nonstationary state, **B:**494–496
Two-dimensional free particle:
Coulomb three-body problem, free-fall problem, **A:**330–332
unimolecular fragmentation mapping, Morse-like kicking field, **A:**22–27
Two-electron structures, theoretical background, **A:**306–309

Unimolecular reaction kinetics:
fragmentation mapping models, **A:**22–30
Morse-like kicking field:
four-dimensional free rotor, **A:**27–30
two-dimensional free particles, **A:**22–27
future research issues, **A:**137–140
isomerization theory, **A:**66–104
cyclobutanone, **A:**100–104
double-well system, **A:**84–88
Gray-Rice theory, **A:**66–70
reactive island theory *vs.,* **A:**80–84
HCN → CNH, **A:**96–100
3-phospholene, **A:**91–96
reactive island theory, **A:**75–80
Gray-Rice theory *vs.,* **A:**80–84
triple-well system, **A:**88–91
Zhao-Rice approximation, **A:**70–75
multichannel isomerization, liquid-like state, **B:**34–35
phase-space structure, molecular dynamics, **A:**9–22
action/angle variables, **A:**11–12
canonical transformation, **A:**9–10
few-dimensional system bottlenecks, **A:**18–19
invariant measure, **A:**10–11
KAM theorem, **A:**12–14
many-dimensional system bottlenecks, **A:**19–20
normally hyperbolic invariant manifold, **A:**20–22
Poincaré surface of section, **A:**14–16
stability analysis, **A:**17–18
predissociation theory, **A:**30–66
Davis-Gray analysis, **A:**30–39
Gray-Rice-Davis ARRKM theory, **A:**39–41
$HeCl_2$ and $NeCl_2$, **A:**63–66
HeICl and NeICl, **A:**66
reaction path analysis, **A:**54–59
separatrix rate crossing constant, **A:**50–54
van der Waals molecules, **A:**59–63
HeI_2, **A:**59–61
NeI_2 and ArI_2, **A:**61–63
Zhao-Rice approximation (MRRKM), **A:**41–54
intramolecular bottleneck:
approximate dividing surface, **A:**46–48
zeroth-order rate constant calculation for crossing, **A:**48–50
separatrix approximate dividing surface, **A:**45–46
quantum energy flow:
cyclohexane ring inversion, **B:**216–221
heat transfer in clusters and macromolecules, **B:**221–248
energy diffusion, **B:**222–223
proteins, **B:**241–248
protein vibrational energy:
anharmonic decay, **B:**237–241
anomalous subdiffusion, **B:**227–237
water clusters, **B:**223–227
localization and rate influence, **B:**208–221
dynamical corrections to RRKM from LRMT, **B:**215–216
local random matrix theory, **B:**209–214
Rice-Ramsperger-Kassel-Marcus theory, **B:**214–215
theoretical background, **B:**206
quantum/semiclassical approaches, **A:**104–128
ARRKM theory, **A:**108–111
Hamiltonian approach, **A:**116–123
phase space quantum scars, **A:**106–108
rigorous quantum rate semiclassical approximation, **A:**114–116
rigorous quantum rate *vs.* quantized ARRKM, **A:**111–114
wave packet dynamics, **A:**123–128
Wigner function and Weyl's rule, **A:**104–106
quantum transport, classically chaotic systems, **A:**128–137
Arnold diffusion suppression, **A:**131–134
Cantori model, **A:**129–131
faster-than-classical anomalous diffusion, **A:**134–137
research background, **A:**4–8

Unitary transformations, intramolecular dynamics, floppy molecules, canonical perturbation theory, **A:**272–278
Universality conjecture, Hamiltonian system multiergodicity, **B:**469–471
Universal statistics, recursive cell production and evolution, catalytic reaction networks, **B:**593
  fluctuation control, **B:**596–597
Unstable periodic orbits:
  chaotic transition, regularity, two-basin landscapes, reactive island theory, **A:**161–163
  unimolecular reaction rate, reactive island theory (RIT), **A:**76–80

Validated computation, multidimensional phase space, slow dynamics, multi-precision numerical method, **B:**430–435
Van der Waals molecules:
  molecular internal space, democratic centrifugal force, **B:**106
  multibasin landscapes, chaotic transition, regularity:
    minimalistic 46-bead protein models, **B:**266–270
    nonstationarity in energy fluctuations, **B:**285
  phase-space transition state geometry, angular momentum, rotating frame dynamics, **A:**251–256
    equilibria, **A:**251–252
    transport, **A:**252–256
  phase-space transition states, tangency in, **A:**378–385
  unimolecular reaction rate theory:
    Davis-Gray predissociation analysis, **A:**34–39
    Gray-Rice-Davis ARRKM theory, **A:**39–41
    predissociation, **A:**59–63
      helium-iodine, **A:**59–61
      neon-iodine/argon iodine, **A:**61–63
    Zhao-Rice approximation, **A:**41–54
      separatrix dividing surface, **A:**45–46
      zeroth-order rate constant, intramolecular bottleneck crossing, **A:**48–50
Van Vleck perturbation:
  chaotic transition, regularity, two-basin landscapes, **A:**146–147
    saddle regions, dynamical regularity, **A:**148–151
  intramolecular dynamics, floppy molecules, canonical perturbation theory, **A:**274–278
"Velocity vector," ARRKM rate quantization, **A:**109–111
Vibrational energy relaxation (VER):
  cytochrome *c* CD stretching, **B:**190–200
    carbon monoxide myoglobin (MbCO), **B:**200
    classical calculation, **B:**197
    coupling constants calculation, **B:**192–195
    full width at half maximum spectra, **B:**199–200
    future research applications, **B:**200–201
    lifetime parameter assignment, **B:**195–196
    quantum calculation, **B:**197–199
    system and bath characteristics, **B:**190–192
  force-force-correlation function approximations, **B:**186–190
    first term contribution, **B:**187–190
    Taylor expansion, **B:**186–187
  general formula, **B:**182–184
  heat transfer, quantum energy flow, anomalous subdiffusion, **B:**228–238
  heat transport, theoretical background, **B:**206–207
  perturbation expansion, **B:**181–182
  quantum correction factor, **B:**185–186
  research background, **B:**180–181
  symmetrized autocorrelation function, **B:**184–185
Vibrational frequency:
  phase-space transition states:
    hyperbolicity breakdown, **A:**391–392
    Lie perturbation theory, **A:**353–358
    Melnikov integral, **A:**359–371
  unimolecular reaction rate theory, Davis-Gray predissociation analysis, **A:**34–39
Vibrational self-consistent field (VSCF) formula, vibrational energy relaxation, quantum correction factor and, **B:**186
Vibrational wave packets, quantum energy flow, theoretical background, **B:**208

Vielbein formalism, molecular internal space, four-body systems, PAHC equations of motion, **B:**117–118
Viscosity measurements, singular perturbation theory, **A:**345
Visualization techniques, Wigner's transition state dynamics, hydrogen cyanide isomerization, **A:**207–210
Vlasov-Poisson equation, globally-coupled Hamiltonian systems, relaxation and diffusion:
  Hamilton mean field (HMF) model, **B:**481
  quasi-stationary state, **B:**491–493
Von Neumann equation, vibrational energy relaxation, perturbation expansion, **B:**181–182

Wannier ridge configuration:
  Coulomb three-body problem:
    free-fall problem, **A:**332
    zero angular momentum, **A:**313–319
  three-body problem, theoretical background, **A:**307–309
Water clusters:
  heat transfer, quantum energy flow, **B:**223–227
  slow relaxation, internal degrees of freedom, Hamiltonian systems, nearly integrable systems, **B:**393–398
Watershed region, onset dynamics, argon clusters, **B:**146–148
Wavefunctions:
  heat transfer, quantum energy flow, **B:**224–227
  intramolecular dynamics, adiabatic *vs.* nonadiabatic delocalization, **A:**282–286
  resonantly coupled isomerizing/dissociating systems, polyad folding and saddle-node bifurcation, **A:**289–296
Wave packet dynamics:
  optimal control theory, kicked rotor system, **A:**443
  unimolecular reaction rate, **A:**123–128
Weibull distribution, Hamiltonian system multiergodicity, **B:**472–474
  complex behavior, **B:**474–475
Weyl's rule, unimolecular reaction rate, **A:**104–106
  semiclassical approximation, rigorous quantum rate, **A:**115–116
Whisker mapping:
  phase-space transition states:
    chaotic itinerancy, **A:**386–389
    tori structures, Melnikov integral, **A:**365–371
  unimolecular reaction rate, quantum transport, classically chaotic systems, **A:**129–131
Whitney's embedding theorem, multibasin landscapes, chaotic transition, regularity, **B:**302–309
Width parameter, vibrational energy relaxation, force-force-correlation function approximations, **B:**190
Wiener-Khinchin theorem, multibasin protein landscapes, chaotic transition, regularity, nonstationarity in energy fluctuations, **B:**270–285
Wigner distribution, atomic clusters, energy level distribution, **B:**4–5
Wigner function, unimolecular reaction rate, **A:**104–106
  phase-space quantum scars, **A:**106–108
  wave packet dynamics, **A:**124–128
Wigner's dynamical perspective, transition state theory:
  hydrogen cyanide isomerization, **A:**198–212
    Hamiltonian equation, **A:**200–202
    model system, **A:**199–200
    nonreactive degrees of freedom quantization, **A:**211–212
    normal form transformation, **A:**205–207
    stationary flow points, **A:**202–205
    visualization techniques, **A:**207–210
  Lie transformation normalization, **A:**194–198
    basic principles, **A:**194–197
    normal-form coordinates, dynamics, **A:**197–198
  rank-one saddle phase-space structure, **A:**183–194
    ''apt'' coordinates, Normal Form theory, **A:**184–186
    n-degree-of-freedom Hamiltonian, **A:**183–184
    normally hyperbolic invariant manifolds (NHIMs), stable/unstable manifolds, **A:**186–190
    transition state defined, **A:**190–191
    transition state flux, **A:**193–194
    transition state search technique, **A:**191–193

Wigner's dynamical perspective, transition state theory (*Continued*)
saddles in energy landscapes, **A:**180–183
phase space energy landscapes, **A:**182–183
phase space *vs.* coordinate space, **A:**180–181
stability, **A:**181–182
Wilson G matrix, vibrational energy relaxation, force-force-correlation function approximations, **B:**187–190
Window function, vibrational energy relaxation, cytochrome *c,* CD stretching mode, **B:**197

Zero angular momentum:
Coulomb three-body problem, **A:**312–319
free-fall problem, **A:**330–332
triatomic dynamics, **A:**244–247
Zero-order vibrational state space, unimolecular reaction kinetics, quantum energy flow, **B:**210–214
Zeroth-order rate constant:
dissociation dynamics, unimolecular reactions, Hamiltonian equations, **A:**116–123
unimolecular reaction rate theory:
isomerization, cyclobutanone, **A:**102–104
Zhao-Rice approximation, intramolecular bottlenecks, **A:**48–50
Zhao-Rice approximation (MRRKM), unimolecular reaction rate:
isomerization theory, **A:**70–75
cyclobutanone, **A:**102–104
double-well potentials, **A:**85–88
HCN to CHN, **A:**97–100
3-phospholene, **A:**91–96
triple-well systems, **A:**88–91
predissociation theory, **A:**41–54
helium chloride/neon-chloride molecules, **A:**63–66
helium-iodine, **A:**60–61
intramolecular bottleneck:
approximate dividing surface, **A:**46–48
zeroth-order rate constant calculation for crossing, **A:**48–50
neon-iodine/argon-iodine molecules, **A:**61–63
separatrix approximate dividing surface, **A:**45–46
wave packet dynamics, **A:**125–128
Zhu-Botina-Rabitz formula, optimal control theory:
coarse-grained transition element, **A:**450–453
kicked rotor system, **A:**442–446
perfect control solution, **A:**453–456
quantum chaos systems, **A:**437–438
random matrix, **A:**439–441
Ziglin analysis, three-body problem, theoretical background, **A:**307–309